Altered mitochondrial dynamics in the NTS affect brown fat morphology and activity

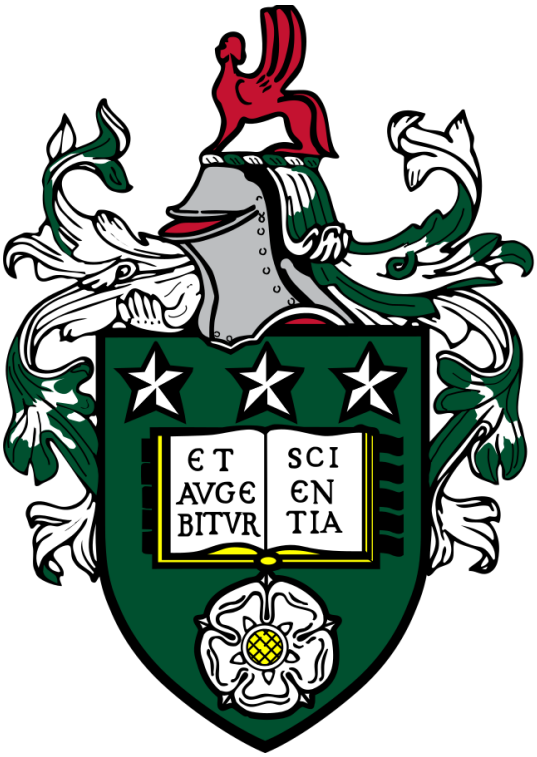

Arianna Fozzato

Submitted in accordance with the requirements for the degree of

Doctor of Philosophy

The University of Leeds

School of Biomedical Sciences

November 2022

The candidate confirms that the work submitted is her own, except where work which has formed part of jointly authored publications has been included. The contribution of the candidate and the other authors to this work has been explicitly indicated below. The candidate confirms that appropriate credit has been given within the thesis where reference has been made to the work of other.

Chapters 3,4 and 5 are based on work from jointly authored publications. This work has been submitted and is currently under review for publication (Fozzato et al., 2022).

Dr. J. Griffiths is responsible for the generation of adenoviruses used in chapters 3,4,5; Dr. L. New is responsible for confocal IHC images of the NTS and provided technical assistance during the PET/CT scans presented in Chapter 3 and 5 and performed the insulin ELISA presented in Chapter 6. The remaining content of Chapters 3,4,5 is directly attributable to myself.

Ethical statement: All experiments were carried out in line with the UK Animals (Scientific Procedures) Act 1986, as well as ethical guidelines set by the University of Leeds Ethical Review Committee. Every effort was made to meet the 3Rs criteria to minimise the number of animals and suffering. All animal work presented in this study was carried out under the following licences:

PPL number: PBF5581CE | Granted: 01 Feb 19 | Amended: 22 Oct 19 | Expires: 30 May 22

PPL number: PP7168482 | Granted: 30 Nov 21 | Expires: 30 Nov 26

PIL number: I80736893 | Granted: 07 Nov 19 | 5 year review: 07 Nov 24

Acknowledgements

The experience of a PhD, from taking your first steps as a scientist into the lab, to writing up your thesis is one of a lifetime and it would have been so much harder without great mentors; I would like to thank my supervisors Dr Beatrice Filippi and Dr Susan Deuchars for teaching me to think outside of the box and for always having a kind word for me. As bad as I am at taking compliments your support got me through many of my bad science days. Thank you for helping me become the confident scientist I am today. I wish you all the very best for the years to come. I would also like to thank my colleagues for making science and life in the lab much more bearable. Thank you, Bianca, Lauryn, Jess, Jo and Niannian. It was a pleasure working with you and thank you for keeping up with my frequent five minutes of panic! Keep showing the world that science needs more great women like you. I wish you all the best for your future career and I am looking forward to coming to visit you up North! For how strange this may sound I would also like to thank the animals that allowed this piece to exist and be presentable today. I am forever grateful to you for making the advance of modern science possible.

I would also like to thank my family and friends, near and far. When I left for the UK, almost five years ago I did not know how long I would have stayed, but not for a single moment I felt like you were not supportive of me and my dreams. I am lucky to have your unconditional love and I miss you every day. Thank you to my parents for teaching me the importance of having dreams and the value of hard work; I hope I made you proud and, dad I wish you were here to see this today. You are always in my heart and not a day goes by without me thinking of you. Thank you to my friends, in particular Fabio, for being on my side since day one; having a friend like you is a true blessing and I am so proud of the person you have grown to be. I would like to thank you, Lorenzo. Words would never be enough to express what it means to me that you are in my life. Thank you for being on my side and supporting me, I can't wait to share with you all the adventures to come. Lastly, I would like to thank my doggos, Ruben and Laika, your waggy tails and loving personalities fill my heart with love and warmth. I am so lucky to have you.

To the me of the future: Always remember that you are worthy and do not ever underestimate yourself. To the me of the past: I hope I made you proud, but I am sort of mad at you for making me write this 390 pages-long book. *Never again.*

Abstract

The nucleus of the solitary tract (NTS) in the dorsal vagal complex (DVC) of the brain controls body weight, food intake, abdominal fat depositions and hepatic glucose and lipid production. High-fat diet (HFD) is known to induce mitochondrial fragmentation in the NTS, which triggers insulin resistance, hyperphagia and body weight gain and alterations in hepatic glucose production (HGP). Brown adipose tissue (BAT) is a thermogenic organ which can uptake circulating glucose and fatty acids to drive non-shivering thermogenesis and increase energy expenditure. The BAT uptakes and metabolises glucose to perform thermogenesis, and this process is directly activated by noradrenergic signalling from sympathetic preganglionic neurons in the central nervous system, which is modulated by the NTS. The dysregulation of signalling molecules in the NTS is linked with altered BAT activity, obesity, and Type two Diabetes Mellitus (T2DM). High-fat diet (HFD) increases mitochondrial fission in the NTS, triggering weight gain, hyperphagia and insulin resistance. In this work we hypothesised that changes in mitochondrial dynamics in the NTS are associated with alterations in BAT glucose metabolism and hepatic lipid metabolism, and particularly, that inhibiting mitochondrial fission in the NTS protects rats from HFD by augmenting BAT glucose uptake and preventing lipid accumulation in the liver.

Here we show that short-term HFD-feeding decreases BAT glucose uptake and alters catecholaminergic innervation to BAT, by decreasing the availability of noradrenaline precursor tyrosine hydroxylase (TH) within BAT. Additionally, we report white lipid droplet infiltration in the BAT tissue. The inhibition of mitochondrial fission in astrocytes of the NTS of HFD-fed rats is sufficient to increase BAT glucose uptake and prevent the effects of HFD on BAT innervation and morphology. We also report that 2-weeks of HFD are sufficient to increase hepatic triglycerides (TG) and induce signs of steatosis in the liver, and this was prevented by the inhibition of mitochondrial fission in astrocytes of the NTS. The inhibition of mitochondrial fission in the astrocytes of the NTS of HFD-fed rats was also associated with a decrease in circulating blood glucose and insulin levels. In regular chow-fed (RC) rats, the activation of mitochondrial fragmentation in astrocytes of the NTS is sufficient to reduce BAT glucose uptake and TH immunoreactivity without affecting BAT morphology and to induce insulin resistance in the NTS and systemic hyperinsulinemia. Moreover, an increase in hepatic

TG content is observed, but no effects on the hepatic cytoarchitecture were observed. In summary, mitochondrial dynamics in the astrocytes of the NTS appear to be important regulators of BAT thermogenesis and hepatic lipid content, and they could constitute a novel therapeutic target to protect from the development of obesity and diabetes.

Table of Contents

List of Figures

List of Tables

Abbreviations

^{18}FDG Fluorodeoxyglucose

α-MSH a-melanocyte-stimulating hormone

AC adenylate cyclase

ADP Adenosine diphosphate

AgRP Agouti-related peptide

AKT Protein kinase B

AMPK Adenosine monophosphate activated protein kinase

ANOVA Analysis of variance

ApoB-100 Alipoprotein B-100 (ApoB-100)

ARC Arcuate nucleus

AP Area postrema

APS Ammonium persulphate

ATP Adenotriphosphate

BAT Brown adipose tissue

BBB Blood brain barrier

BCA Bicinchoninic acid assay

BDNF Brain derived neurotropic factor

BMI Body mass index

BSA Bovine serum albumin

cAMP cycline adenosine monophosphate

CB1R cannabinoid receptor type 1

CL Cardiolipin

CC Central canal

CD137 tumor necrosis factor super family 9

ChAT Choline Acetyltransferase

CEBP CCAAT enhancer binding protein

ChREBP Carbohydrate response element binding protein

CNS Central nervous system

CKK Cholecystokinin

CoQ Coenzyme Q

CPT2 carnitine palmitotltransferase 2

CT computed tomography

CVS Cardiovascular system

DAB 3,3'-Diaminobenzidine

DAPI 4',6-diamidino-2-phenylindole

ddH2O Double distilled water

DGAT 1 diacylglycerol acyltransferase 1

DGAT 2 diacylglycerol acyltransferase 2

DMEM Dulbecco's modified eagle medium

Drp1 Dynamin related protein 1

DMSO Dimethyl sulfoxide

DTT Dithiothreitol

DMX Dorsal motor nucleus of the vagus

DREADD Designer receptor exclusively activated by designer drugs

Drp1:K38-A Dominant negative Dynamin related protein 1

Drp1:S637-A Constitutively active Dynamin related protein 1

DVC Dorsal vagal complex

ER Endoplasmic reticulum

ECL Enhance chemiluminescence

EDTA Ethylenediaminetetraacetic acid

EHMT1 euchromatic histone-lysine N-methyltransferase 1

ERK Extracellular signal-related kinases

FA fatty acids

FAS fatty acid synthase complex

Fis1 Fission 1

FOXO Forkhead box class O

FFA Free fatty acids

FGF21 fibroblast growth factor 21

GABA γ aminobutyric acid

GED GTPase effector domain

GI gastrointestinal

GFAP Glial fibrillary acidic protein

GLP-1 Glucagon-like peptide 1

GLUT 1 Glucose transporter type 1

GLUT 4 Glucose transporter type 4

GFP Green fluorescent protein

G-domain GTPase domain

Glut Glutamate

GSK3b Glucose synthase kinase 3 beta

HFD High fat diet

HGP Hepatic glucose production

HNFα hepatocyte nuclear factor 4a

HRP Horseradish Peroxidase

HSE Health Survey for England

IHC Immunohistochemistry

IF Immunofluorescence

IL Interleukin

IL-6 Interleukin 6

IL-8 Interleukin 8

IRS-1 Insulin receptor substrate 1

IMD index of multiple deprivation

IML Intermediolateral nucleus

IO inferior olive

ICV Intracerebroventricular

IP Intraperitoneal

IMM Inner mitochondrial membrane

iNOS Inducible nitric oxide synthase

INSR Insulin receptor

IRS Insulin receptor substrate

IV Intravenous

JNK c-Jun N-terminal kinases

K_{ATP} ATP sensitive potassium channel

Lepr Leptin receptor

LPL lipoprotein lipase

LPO lateral preoptic area

LH Lateral hypothalamus

LPS Lipopolysaccharide

MAPK mitogen activated protein kinase

MANF mesencephalic astrocyte-derived neurotrophic factor

MBH Mediobasal hypothalamus

MC3R Melanocortin receptor 3

MC4R Melanocortin receptor 4

MDIVI-1 Mitochondrial division inhibitor 1

MiD Mitochondrial dynamic proteins

Mff Mitochondrial fission factor

Mfn Mitofusin

MnPO median preoptic area

MPO medial preoptic area

MOI Multiplicity of infection

mRNA Messenger ribonucleic acid

mtDNA mitochondrial DNA

Myf5 myogenic factor 5

mTORC1 mammalian target of rapamycin complex 1

MTTP microsomal triglyceride transfer protein

NAFLD Non-alcoholic fatty liver disease

NHS National Health Service

NMDA N-methyl-D-aspartate

NeuN Neuronal Nuclei (Hexaribonucleotide binding protein 3)

NPY Neuropeptide Y

NADH Nicotinamide adenine dinucleotide hydrogen

NAD(P)H Nicotinamide adenine dinucleotide phosphate

NO Nitric oxide

NF-kB Nuclear factor kappa-light-chain enhancer of activated B cells

NPY Neuropeptide Y

NP-40 Octyl phenoxypolethoxylethanol 40

NTS Nucleus tractus solitarius

Ob/ob Obese mice

OMM outer mitochondrial membrane

OPA1 Optic atrophy 1

OCT Cryo microtomy embedding medium

OLEFT Spontaneous insulin resistance/obese rat model

OMM Outer mitochondrial membrane

PERK Double stranded RNA-activated protein kinase-like ER kinase

PVN Paraventricular nucleus

PBS Phosphate buffered saline

PBST Phosphate buffered saline with triton\Tween20

PET Positron Emission Tomography

PI3K Phosphoinositide 3 kinase

PNS Peripheral nervous system

Phox2b Paired-like homeobox 2b

PKA Protein kinase A

POMC Proopiomelanocortin

POP preoptic nucleus

PPARGC1A Peroxisome proliferator-activated receptor gamma coactivator 1 α

PPARGC Peroxisome proliferator- activated receptor γ

PPARα Peroxisome proliferator-activated receptor alpha

PRDM16 PR domain zinc finger 16

RrPa Rostral Raphe Pallidus Nucleus

RC Regular Chow

RMR resting metabolic rate

RM raphe magnus

ROS Reactive oxygen species

RPM Rotations per minute

RT Room Temperature

SDS Sodium dodecyl sulphate

SD Sprague Dawley

SREBP-1c Sterol receptor element-binding-protein-1c

T2DM Type II diabetes mellitus

T3 triidothyronine

T4 thyroxine

TBS Tris buffered solution

TBST Tris buffered saline with Triton X\Tween20

TEMED Tetramethylethylenediamine

TG Triglyceride

TH Tyrosine Hydroxylase

TLR Toll like receptors

TMEM26 transmembrane protein 26

TNFα Tumour necrosis factor α

UCP1 Uncoupling protein 1

UPR Unfolded protein response

VLDL very-low density lipoproteins

VMH Ventromedial nucleus

V Volts

WAT White adipose tissue

Chapter 1: General introduction

1.1 Obesity and overweight: a growing epidemic

1.1.1 Facts and figures

Obesity has long been identified as a critical public health risk and it is now reaching epidemic proportions; since 1975 its prevalence worldwide has nearly tripled, with 1.9 billion adults being overweight and of these, 650 million are obese or morbidly obese (WHO Global Health Observatory, 2016). The fundamental cause of obesity is the imbalance of one or more components of energy balance, namely energy intake, energy expenditure and energy storage, and, in particular, in a surplus of energy intake and storage and/or a decrease in energy expenditure, which results in a positive caloric balance (Figure 1.1). According to the National Institute for Health and Care Excellence (NICE) obesity is characterised by a body mass index ([1]BMI) > 29.9 kg/m^2 and a central (abdominal) increase in fat distribution (waist circumference >94 cm for males and >80 cm for females) (NICE, 2022). Importantly, NICE has conveyed that a concomitant increase in BMI and waist circumference are major risk factors for a range of noncommunicable diseases, including cardiovascular disorders, diabetes, and cancer (Figure 1.1). Further, obesity-associated conditions were among the top 10 global causes of death, accounting for 16.8 million of the 56.9 million deaths worldwide in 2016 (WHO Global Health Observatory, 2016).

[1] BMI is an estimation of total body fat and it is defined as the body mass divided by the square of the body height, and it is expressed in kg/m^2.It is used to categorise an individual as underweight, normal weight, overweight, moderately obese, severely obese or very severely obese.

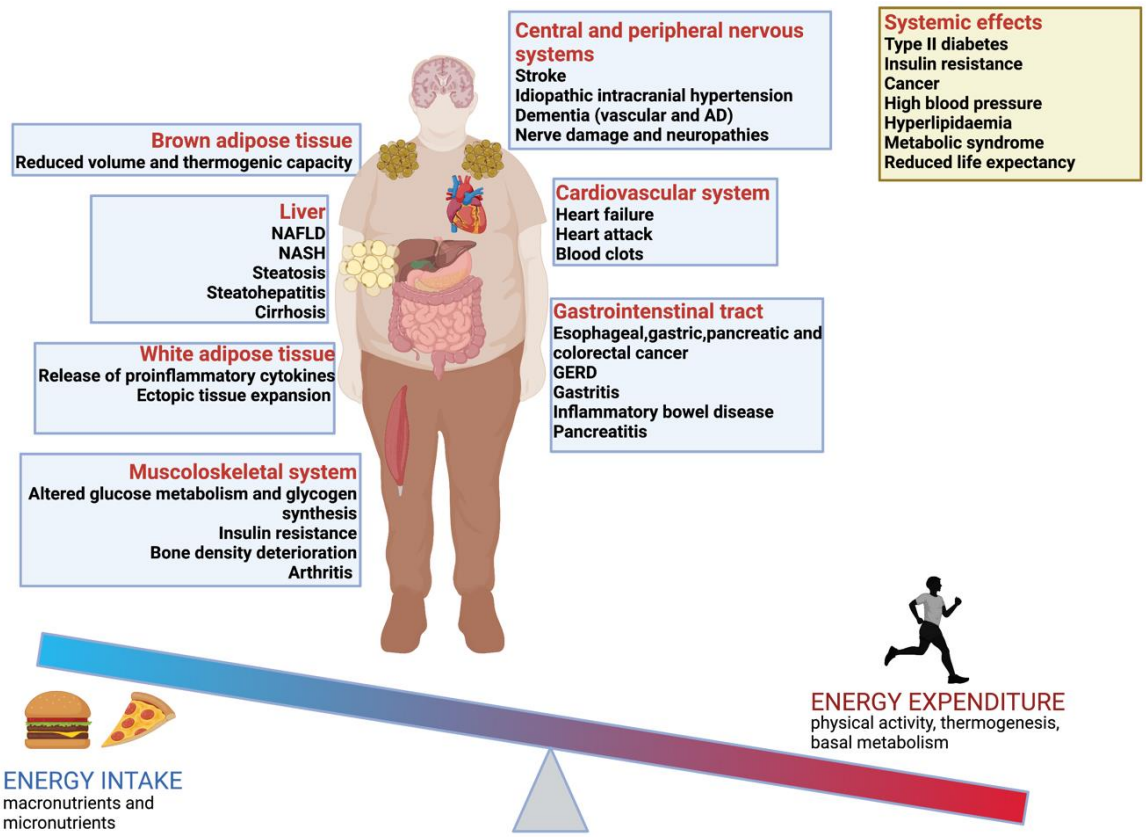

Figure 1. 1: Obesity is a multi-system disease. *AD= Alzheimer's Disease, NAFLD= Nonalcoholic fatty liver disease; NASH= Nonalcoholic steatohepatitis; GERD= Gastroesophageal reflux disease. The fundamental causes of obesity are found in a positive imbalance between energy intake and energy expenditure. Image generated with Biorender.com*

If we focus our attention on England alone, the 2019 Health Survey for England (HSE) found that 28.9 million adults were overweight or obese (63% of adult population), of these 28% were obese, and 3% were morbidly obese (HSE, 2019). Moreover, HSE estimates that in 2019, 28% of children aged 2-15 were overweight or obese in England, including 15% who were obese. Adults and children living in the most deprived areas, as defined by the Index of Multiple Deprivation (IMD), have higher BMI and are more likely to be overweight and obese than those living in the least deprived areas (WHO Global Health Observatory, 2016).

Remarkably, overweight and obesity are linked to more fatalities than underweight, and this occurs in every country worldwide apart from circumscribed regions of Asia and Sub-Saharan Africa (WHO Global Health Observatory, 2016). Without efficient interventions, these trends are expected to increase dramatically with numbers forecast to reach 2.16 billion overweight and 1.12 billion obese people by 2030, (Kelly et al., 2008) causing millions to die from associated complications. The WHO has expressed the need to reverse these growing trends to prevent diet-associated comorbidities and correlated premature deaths. Moreover, obesity comes with significant costs to the wider economy: In the UK in the year 2014/15, the estimated public expenses for obesity prevention programs reached £638 million/year, the costs for the National Health Service (NHS) accounted for 9.8% of the yearly budget (£13.9 billion/year) whilst the costs to the wider economy reached £27 billion/year (Public Health England, 2017). By 2050, the UK-wide NHS costs attributed to the prevention and treatment of overweight and obesity are expected to reach £9.7 billion/year, with a wider cost to the economy projected to reach £49.9 billion/year (Public Health England, 2017). Clearly, obesity and its associated complications represent a severe health crisis, which is, and will be, translating into critical challenges for healthcare and economic systems worldwide.

1.2 Peripheral control of energy balance

The pathogenesis of obesity finds its fundamental causes in chronic dysregulation of energy balance, namely that energy intake is increased, and/or energy expenditure is reduced. However, the essential causes of these processes remain largely unclear, and the aetiology of obesity is a combination of genetic, behavioural, environmental, social, physiological and

cultural factors (Hruby et al., 2016) .Nevertheless, the impact of obesity and overnutrition in human and animal physiology has been largely studied, and they correlate with multisystemic damage, encompassing several organs and systems, including the central (CNS) and peripheral nervous systems (PNS), the cardiovascular system (CVS), the musculoskeletal system, the gastrointestinal (GI) tract, the reproductive system, the adipose tissues and the liver (Kastanias et al., 2017). Here we will review the role of major metabolic effectors, such as the skeletal muscle and the gastrointestinal tract; moreover, to fulfil the scope of this work, we will be discussing in a greater level of detail the physiology of the liver, white adipose tissue, and the CNS in the control of systemic energy expenditure, and the impact of obesity, overnutrition and high fat diet (HFD) on these organs.

1.2.1 Skeletal muscle

The skeletal muscle is critical for the regulation of glucose metabolism and glycogen synthesis, to allow muscle contraction and the maintenance of systemic blood glucose homeostasis; in fact, skeletal muscle increases the rate of glucose uptake across the cell membrane via insulin-dependent Glucose Transporter 4 (GLUT4) translocation to ultimately control glucose utilisation rate (Dimitriadis et al., 2011; Petersen and Shulman, 2018) (Figure 1.2). Moreover, glycolysis occurs in the muscle and the rate of this process is mediated by the action of insulin-dependent enzymes hexokinase and 6-phosphofructokinase. Further, insulin in this tissue can control the rate of glycogen synthesis and breakdown (Dimitriadis et al., 2011). Studies conducted in rats have shown that when insulin concentration is increased from 1 mU/L to 100 mU/L the rate of glycogen synthesis is increased, independently of glucose 6-phosphate (Rossetti and Giaccari, 1990; Dimitriadis et al., 1997). Importantly, obesity leads to the development of insulin resistance in skeletal muscle which involves defects in glucose transport and handling within the muscle (Dohm et al., 1988; Friedman et al., 1994). For example, it has been shown that myotubes from obese patients, with or without Type II Diabetes Mellitus (T2DM) have a decreased rate of glucose uptake and oxidation (Mengeste et al., 2021). Moreover, obese individuals exhibit a depressed insulin signal transduction, which results in decreased glycogen synthesis and glucose transport to myocytes (Houmard et al., 2011; Houmard et al., 2012). Notably, in myotubes from morbidly obese patients, insulin-stimulated insulin receptor substrate 1 (IRS1) active phosphorylation

(tyrosine residue), as well as protein kinase B (Akt) phosphorylation, are blunted. Conversely, IRS1 serine inhibitory phosphorylation was increased (Bell et al., 2010). The muscle can also clear triglycerides (TG) from the circulation in an insulin-dependent manner (Dimitriadis et al., 2011). Importantly, obesity is associated with dysregulation of lipid metabolism in the skeletal muscle, as well as with reduced mitochondrial oxidative capacity and changes in mitochondrial morphology (Boushel et al., 2007; Holloway et al., 2009; Jocken et al., 2010; Gundersen et al., 2019). Altogether this evidence supports the idea that insulin sensitivity in the muscle is critical for the control of several key metabolic functions, and these mechanisms are disrupted by obesity.

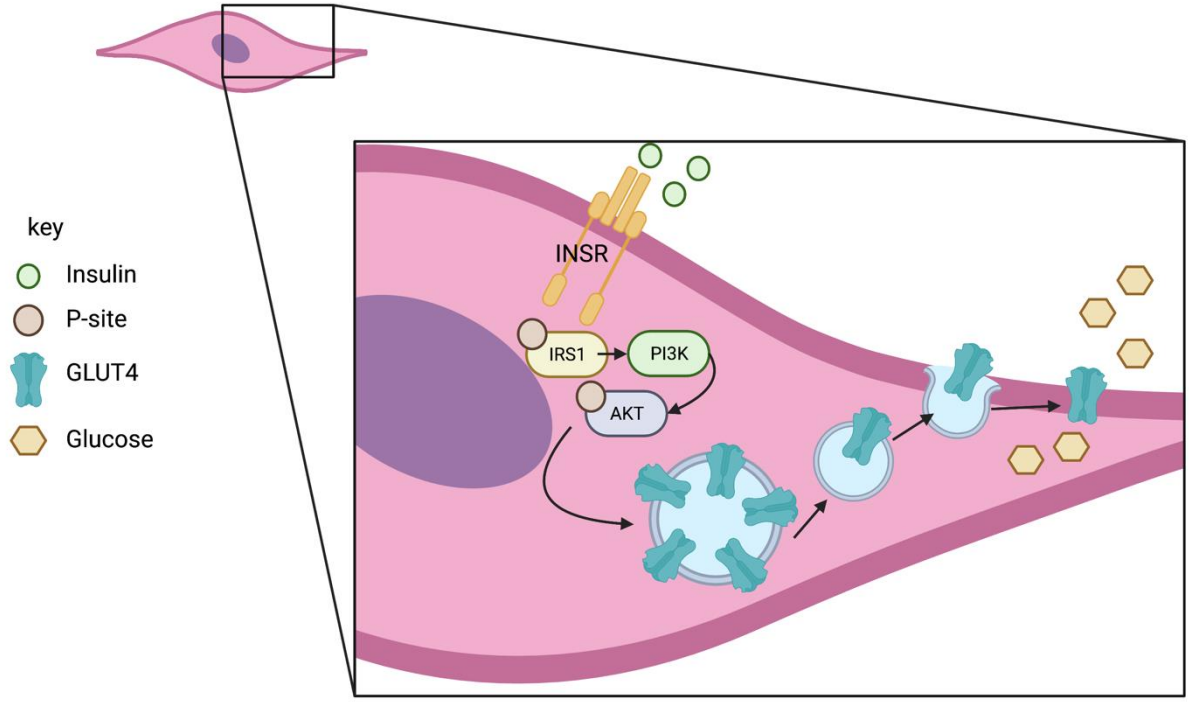

***Figure 1.2**: **Simplified canonical insulin phosphoinositide 3-kinase- protein kinase B (PI3K/AKT) pathway governing glucose uptake in myocytes.** The activation of PI3K/AKT pathway is initiated by the binding of Insulin receptor substrate 1 (IRS1) proteins to PI3K regulatory subunits. This in turn leads to the activation of AKT, which catalyses the translocation of Glucose transporter 4 (GLUT4) from the vesicles in the cytoplasm onto the cell membrane surface, ultimately increasing insulin-dependent glucose transport in myocytes. This process is key in the muscle-mediated maintenance of systemic blood glucose homeostasis. Image generated with Biorender.com.*

1.2.2 Gastrointestinal (GI) tract

The gastrointestinal (GI) tract is also critical to control systemic metabolism, as it acts as an interface between nutrients derived from the ingestion of food and the body requirements of maintaining energetic homeostasis. Signals derived from the gut relay information on incoming nutrients to the brain to control eating behaviours and energy expenditure, to ultimately support whole-body energetic homeostasis. These signals comprise a variety of peptides and hormones secreted by the GI tract, including the orexigenic hormone ghrelin and the anorexigenic hormones Cholecystokinin (CCK), Glucagon-like peptide (GLP1) and leptin (Figure 1.3). In addition, intestinal epithelium-derived signals, lipid-derived molecules and nutrient metabolites derived from the gut microbiota can also signal to the brain (Grenham et al., 2011; Dockray, 2013). Ghrelin, for example, increases appetite and food intake and controls glucose homeostasis, whilst leptin is responsible for short-term regulation of food intake. CCK inhibits stomach emptying and suppresses food intake, whilst GLP1 stimulates insulin release, inhibits glucagon release, suppresses appetite, and favours energy expenditure (Ronveaux et al., 2015; Steinert et al., 2017) (Figure 1.3). Motilin stimulates gastric and small intestine motility, which results in undigested food being moved to the large intestine; importantly, motilin influences hunger and nausea by acting via the vagus nerve and the area postrema in the brainstem (Javid et al., 2013). Further, motilin promotes the release of ghrelin (Zietlow et al., 2010) to increase hunger sensation. PYY3-36 is a gut hormone involved in the generation of satiety, and it is released postprandially in a caloric intake-dependent manner. PYY3-36 can reduce satiety by binding on NPY neurons auto-inhibitory Y2 receptor in the arcuate nucleus (ARC) of the hypothalamus, which is characterized by a permeable blood-brain barrier (BBB) (Blevins et al., 2008). Further, PYY3-36 signalling is conveyed to the nucleus of the solitary tract (NTS) of the brainstem via vagal afferent pathway (Blevins et al., 2008) (Figure 1.3).

Importantly, the stomach and the small intestine (where key processes of digestion and nutrient absorption occur) are highly innervated, which allow these organs to receive signals from the brain. Moreover, the stomach generates a feedback signal to the melanocortin system in the brain, in order to control feeding behaviour and food ingestion, which ultimately

results in delayed gastric content emptying in rats (Richardson et al., 2013; Hussain and Khan, 2017).

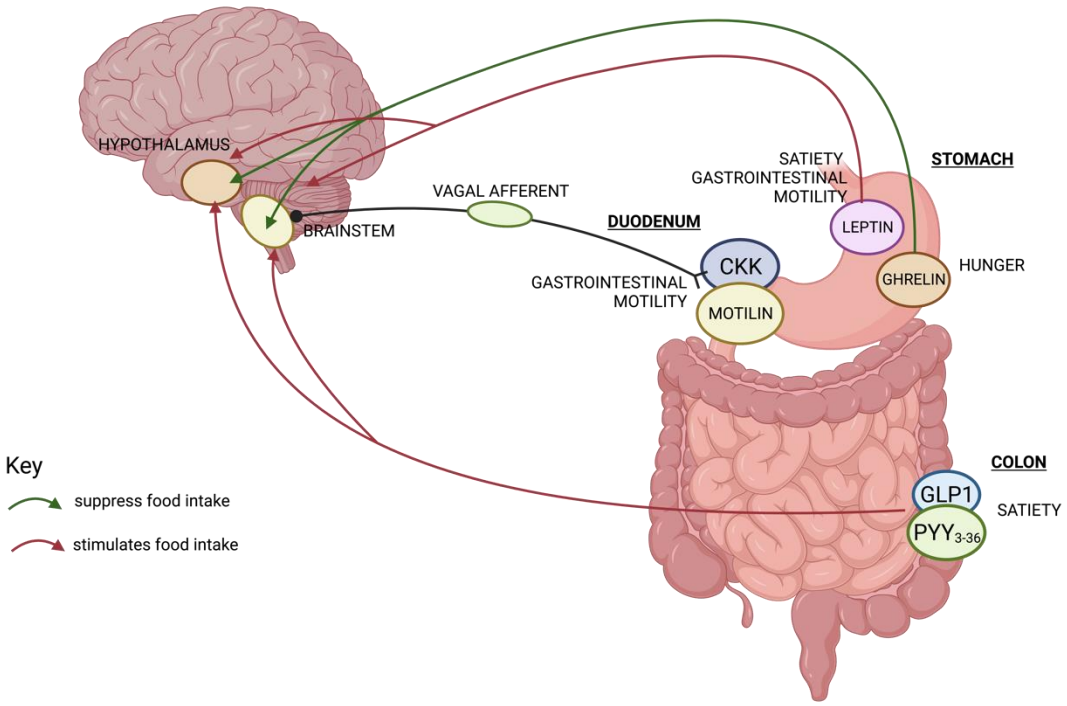

***Figure 1.3**: **GI hormones and their targets in the central nervous system.** Leptin secreted in the gastric mucosa and Glucagon like peptide 1 (GLP1) and Peptide YY$^{3-36}$ synthesised in the intestine target the brainstem and the hypothalamus to suppress appetite. Conversely Ghrelin synthesised in the gastric oxyntic mucosa targets these brain regions to stimulate appetite. Cholecystokinin (CKK) and motilin activate vagal afferents to the NTS to control meal size. Image generated with Biorender.com.*

Interestingly, obese patients exhibit several alterations in plasma ghrelin profile; for example in these subjects, ghrelin levels do not increase during fasting (Gottero et al., 2004), and the physiological nocturnal rise in ghrelin levels is also absent (Perreault et al., 2004). Moreover, in obese patients, ghrelin levels are not suppressed after a meal (Yildiz et al., 2004). Interestingly, in a recent randomised crossover study, the leptin/ghrelin ratio was significantly higher in men who were overweight or obese in both fasting state and postprandially compared to lean men (Adamska-Patruno et al., 2018), which suggests that overweight/obese

subjects may have a diminished feeling of satiety thus contributing to higher caloric intake compared to lean subjects.

Evidence suggests that with obesity the normal pattern of suppression and stimulation of ingestive behaviours is strongly altered in response to changes of GI-derived hormone ghrelin. In rodents, chronic intracerebroventricular infusion of ghrelin increases food intake and independently regulates adipocyte metabolism, leading to a decrease in the utilisation of lipids to generate energy, via a mechanism mediated by the sympathetic nervous system (Theander-Carrillo et al., 2006). Moreover, chronic subcutaneous injections of ghrelin in gastreoctomised mice reversed the gastrectomy-induced reduction of body weight and body fat, suggesting that endogenous ghrelin contributes to maintaining body fat and body weight (De La Cour et al., 2005). Importantly, ghrelin null mice are protected from diet-induced obesity (DIO), however ghrelin deletion influences the preference of metabolic fuels utilised by these animals, which show increased levels of fat oxidation during HFD (Wortley et al., 2004).

DIO is also characterised by reduced sensitivity to intestine-derived CCK, and studies have explored changes in gut microbiota and chronic inflammation occurring during HFD as potential mechanisms of loss of CCK signalling in obesity. For example, studies employing germ-free mice have shown reduced levels of CCK and decreased ability of these animals to sense nutrients in the gut. This incorrect regulatory feedback signalling to the brain leads to increased food intake (Swartz et al., 2012; Duca et al., 2012). Moreover, disturbances in the CCK system can lead to abnormal increases in body weight in rodents, and HFD is associated with increased food intake and body weight which associate with blunted ability of exogenous CCK to reduce food intake in female and male rats (Voits et al., 1996; Savastano and Covasa, 2005). Remarkably this data indicates that HFD and HFD-induced obesity associate with profound changes in the ability of the gut to sense nutrients and relay information about the individual's nutritional status to the brain, showing the importance of the GI tract in the genesis and exacerbation of obesity in both rodents and humans.

1.2.3 Liver

The liver is a key organ in the maintenance of whole-body metabolic homeostasis, performing a vast array of biochemical functions that include regulation of glucose production, protein synthesis and cholesterol production. The liver is densely vascularised, and this characteristic is key to the transport and export of metabolites, hormones, and nutrients to perform its metabolic functions. Importantly the liver accounts for approximately 30% of insulin-dependent disposal of glucose, and for the majority of glucose production within the body (Moore et al., 2012; Han et al., 2016a). The maintenance of glucose homeostasis relies upon insulin-dependent hepatic glucose entry, which prevents TG hydrolysis and limits the gluconeogenesis (Hatting et al., 2018). Upon feeding, insulin induces hepatic glucose uptake via glucose transporters (GLUT1-2-5-8), which facilitates glycogen storage and decreases hepatic glucose production (HGP) by inhibiting gluconeogenesis and glycolysis (Rui, 2014; Hatting et al., 2018). Glucose regulation is a pivotal process carried out by the liver; in fact, Biddinger et al. (2008) showed that liver insulin receptor KO mice (LIRKO) develop dyslipidaemia and were significantly glucose intolerant as they were unable to inhibit HGP. Further, insulin resistance in both pre and post-prandial states results in higher circulating glucose due to inadequate suppression of HGP and stimulation of glucose uptake in the liver (Ferris and Kahn, 2016; Titchenell et al., 2017). T2DM and obesity are characterised by insulin resistance, suggesting that these conditions disrupt insulin regulatory action on hepatic glucose homeostasis.

Excessive accumulation of TG in the liver is associated with alterations in the metabolism of glucose, fatty acids (FA) and lipoproteins, as well as inflammation within this organ (Alves-Bezerra and Cohen, 2017). Obesity and overnutrition are associated with a wide spectrum of abnormalities in the liver, which fall under the umbrella term of “non-alcoholic fatty liver disease” (NAFLD) (Pouwels et al., 2022). NAFLD prevalence in the population is rapidly increasing in both obese and non-obese or lean individuals (Ye et al., 2020). Steatosis is prevalent in 15% of non-obese subjects, 65% of individuals with stage I and II obesity (BMI 30-39.9 kg/m^2) and 85% of extremely obese patients (BMI> 40 kg/m^2). Evidence from the literature also shows that impaired glucose regulation or type 2 diabetes (Ballestri et al., 2016; Younossi, 2019), hypertension, and hyperlipidaemia (Chalasani et al., 2018) are major

metabolic risk factors for this condition. NAFLD is characterised by several pathological hallmarks including intrahepatic TG accumulation (known as “steatosis”), which can be accompanied by an increase in inflammatory markers and fibrosis. Steatosis is the hallmark feature of NAFLD and classically, it has been defined biochemically as intrahepatic TG content of >5% of the liver total volume or weight (Hoyumpa et al., 1975), and histologically as >5% visible intracellular TG infiltration in hepatocytes (Kleiner et al., 2005).

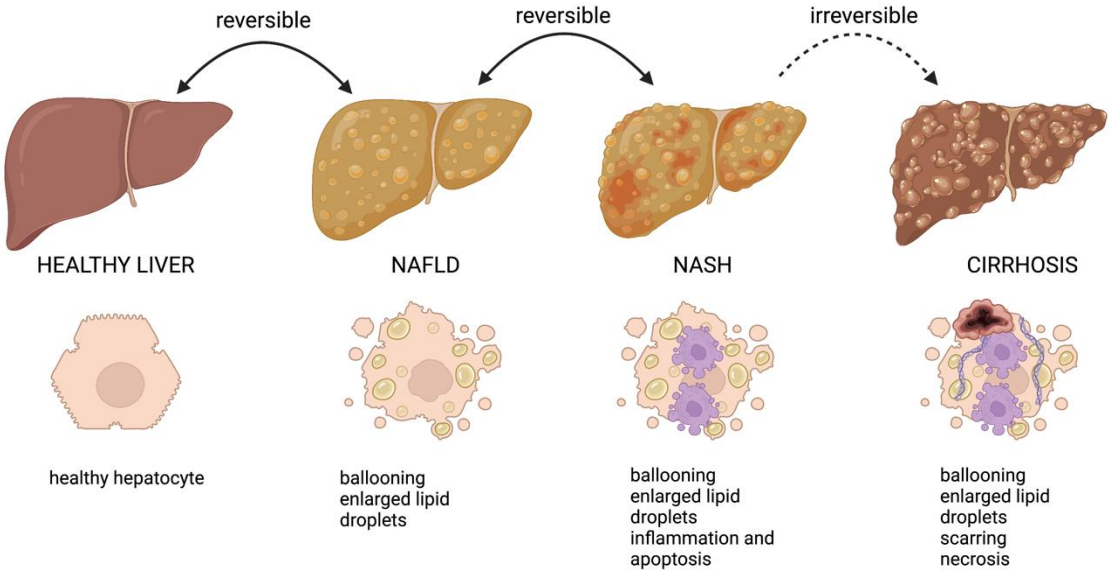

Figure 1. 4 Stages of liver damage*. The first step of liver damage, Non-alcoholic fatty liver disease (NAFLD) is characterised by steatosis and ballooning (hepatocytes swelling); this can progress to non-alcoholic hepatic steatosis (NASH), which is described by inflammation and hepatocellular death. If the disease further progresses, liver fibrosis (scarring)- which consists of excessive accumulation of extracellular matrix proteins, including collagen and proteoglycans- can occur, and this is defined as cirrhosis of the liver. Whilst NAFLD and NASH are reversible, cirrhosis is not.*

(Kleiner et al., 2005). NAFLD can eventually progress to more serious liver disease, with studies showing that ~40% of patients with steatosis progress to non-alcoholic steatohepatitis (NASH)- characterized by fat build-up, inflammation and damage, and of these 7-30% progress to cirrhosis, which is defined as scarring of the liver, which is potentially life-threatening (Singh et al., 2015; Golabi et al., 2016) (Figure 1.4).

1.2.4 In health and disease: physiology and pathophysiology of the liver

The liver has a complex lipid metabolism that is critical to regulate the amount of TG present in this organ, and the processes involved are: (1) fatty acid uptake, (2) *de novo* fatty acid synthesis (3) fatty acid oxidation and (4) fatty acid export of very-low density lipoproteins (VLDL). Fatty acid uptake by the liver is mainly derived from FA released by the adipose tissue, which enter the systemic circulation and are transported to the liver by the hepatic artery and the portal vein, hence this process depends on the availability of FA and liver capacity to transport FA. The rate at which FA are released in the circulation is in direct relationship with the amount of fat mass present in the body tissues, and that applies to both males and females (Mittendorfer et al., 2009), meaning that the higher the adipose tissue mass, the higher is the fatty acid uptake by the liver. Moreover, genes involved in lipid metabolism and FA transport are upregulated in the liver of obese subjects without steatosis (Greco et al., 2008), similar to lipoprotein lipase (*LPL*) mRNA-transcripts that are increased in obese subjects with NAFLD compared to matching controls without NAFLD (Pardina et al., 2009). *De novo* fatty acid synthesis by the liver occurs via a biochemical reaction in which Acetyl CoA is converted by Acetyl CoA Carboxylase to Malonyl CoA and ultimately undergoes a series of metabolic reactions to form a molecule of palmitate. *De novo* lipolysis is controlled by the expression of several genes including fatty acid synthase complex (*FAS*), diacylglycerol acyltransferase (*DGAT*) 1 and 2, and transcription factors including Sterol receptor element-binding-protein-1c (*SREBP-1c*) and Carbohydrate response element binding protein (*ChREBP*). Interestingly, *FAS* KO in the liver reduces diet-induced steatosis in mice (Item et al., 2017), whilst pharmacological inhibition of *DGAT1* using antisense nucleotides protects against HFD-induced fatty liver in a mouse model (Villanueva et al., 2009). Human studies have revealed that obesity is associated with increased *SREBP-1c* mRNA and a concomitant reduction in

Peroxisome proliferator-activated receptor alpha (PPARα) transcripts; interestingly, an increased SRPEBP-1c/PPARα ratio in humans associates with insulin resistance (Pettinelli et al., 2009). Importantly, in lean subjects the contribution of *de novo* lipolysis to total intra-hepatic TG production is small (<5% total incorporated fatty acids) but in subjects with NAFLD it can account for 15-23% of total hepatic TG (Solinas et al., 2015). Interestingly, an increase in *de novo* lipid synthesis may precede and exacerbate NAFLD, via regulation of intra-hepatic TG content through an insulin-dependent mechanism (Smith et al., 2020a) and increases in glucose and insulin concentration in the plasma stimulate hepatic *de novo* lipid synthesis, suggesting that insulin resistance drives this mechanism in NAFLD. Moreover, it has been speculated that insulin resistance in the skeletal muscle may divert carbohydrates from glycogen storage within muscles to increase *de novo* fatty acids synthesis in the liver (Petersen et al., 2007). FA β oxidation is the key pathway for the degradation of fatty acids and plays an essential role in the maintenance of energy homeostasis and it mainly occurs in mitochondria. In the cytosol of hepatocytes, FA are linked to CoA to form fatty Acyl-CoA; FA (carbon chains>14) cannot be directly transported in the mitochondria, so utilise a carnitine shuttle for translocation to the mitochondria. Membrane-bound carnitine palmitoyl transferase 1 exchanges CoA with a carnitine molecule to produce fatty-acylcarnitine, which can then be transported in mitochondria, where carnitine palmitoyl transferase exchanges the carnitine molecule into a CoA molecule to prepare fatty Acyl CoA for β oxidation. During this process, FA are shortened by two carbon units per cycle through a complex biochemical reaction, which is transcriptionally regulated by Peroxisome proliferator-activated receptor alpha (PPARα). Importantly, primary defects in the mitochondrial β oxidation in acyl-CoA dehydrogenase (LCAD) deficient mice lead to steatosis and hepatic insulin resistance (Zhang et al., 2007). Moreover, 28-weeks administration of the PPARα agonist Fenofibrate in OLEFT rats (a rat model of spontaneous insulin resistance and obesity) ameliorated hepatic steatosis and increased mRNA transcripts of FA- β oxidation enzymes in this tissue (Seo et al., 2008). Indeed, historical human studies have shown that fatty acids entering the β oxidation pathway are increased 2-fold when compared to those entering the esterification pathway in lean subjects upon fasting, whilst this effect is not present in obese subjects which show similar proportions of FA entering each pathway (Havel et al., 1970). Interestingly, Lee et al. (2017) paradoxically showed that loss of hepatic FA oxidation in mice carrying a liver-specific

deficiency of mitochondrial long chain fatty acid β-oxidation (Cpt2 KO) renders them resistant to HFD-induced weight gain and adiposity, however these animals exhibited serum dyslipidaemia and hepatic oxidative stress. Beyond mitochondria, the release of Acetyl-CoA via β oxidation in hepatocytes peroxisomes is associated with the inhibition of autophagy and promotion of steatosis in an Acyl-CoA oxidase 1 KO mouse model via mechanistic target of rapamycin complex 1 (mTORC1) activation (He et al., 2020).

The formation of VLDL is another critical process carried out by the liver which converts water insoluble TG into a water-soluble form, which can be exported out of the liver towards other tissues. Hepatic VLDL production constitutes the assembly of alipoprotein B-100 (ApoB-100) with a TG; residual TG that are not oxidized via β oxidation can be esterified for VLDL production - suggesting that VLDL production is important to regulate the levels of intrahepatic TG. For example, the blockage of VLDL production is associated with steatosis in a microsomal TG transfer protein (mttp) KO mouse model (Minehira et al., 2008). HFD induces fat accumulation in the liver via impairment of hepatocyte nuclear factor 4a (*HNF4α*), a nuclear receptor protein that exerts the transcriptional regulation function of genes involved in VLDL secretion on its downstream target ApoB-100, in wild-type mice, in a mechanism mediated by oxidative stress (Yu et al., 2017).

Obesity and overnutrition also affect the liver via other mechanisms: for example, insulin resistance is associated with NAFLD and correlates with steatosis (Korenblat et al., 2008). Furthermore, intrahepatic inflammation is associated with both diet and genetically-induced obesity and is linked with increased signalling of nuclear factor kappa-light chain-enhancer of activated B cells (*NFKB*) and interleukin 6 (IL-6) in the liver of rodents (Carlsen et al., 2009; Luedde and Schwabe, 2011; Kern et al., 2019). Lastly, endoplasmic reticulum (ER) stress is associated with the pathogenesis of NAFLD via interference with hepatic lipid metabolism, in particular via activation of lipogenesis via unfolded protein response (UPR) signalling pathway (Zheng et al., 2010) and inhibition of VLDL secretion and formation (Ota et al., 2008).

1.2.5 White adipose tissue

The white adipose tissue (WAT) is a critical organ in the control of energy homeostasis. Traditionally, WAT has been considered to act only as an energy reservoir; however, it is now well established that WAT senses energy status to secrete endocrine hormones, paracrine factors and adipocyte-derived exosomal micro RNA to regulate diverse processes and mechanisms such as feeding behaviour, energy expenditure, glucose homeostasis and inflammation (Kershaw and Flier, 2004; Vázquez-Vela et al., 2008; Xie et al., 2022).

1.2.6 White adipose tissue physiology and effects of overnutrition

During overnutrition, WAT undergoes cellular hypertrophy, whilst caloric restriction induces lipolysis in this tissue, to support the metabolism of other organs (Birsoy et al., 2013; McLaughlin et al., 2014). In high energy state, WAT releases leptin to reduce food intake by interacting with Agouti-related protein (AgRP) neurons and pro-opiomelanocortin (POMC) neurons in the arcuate nucleus (ARC) of the hypothalamus to inhibit and promote satiety, respectively (Baskin et al., 1999; Cowley et al.,2001), and to increase energy expenditure (Myers et al., 2008). However, in a state of chronic overnutrition, the central effects of leptin become impaired, namely, despite elevated circulating leptin levels in obesity, the hypothalamus develops leptin resistance and becomes unable to respond to the anorexigenic effect of leptin (Münzberg et al., 2004; Enriori et al., 2007).

WAT expansion is a physiological process, achieved by recruitment and differentiation of adipocytes precursor cells. However, adipocyte hypertrophy has been linked with abnormal adipocyte function and can cause insulin resistance (Klöting et al., 2010). WAT hypertrophy is associated with obesity, which is characterised by chronic low-grade inflammation and progressive infiltration of immune cells and upregulation of inflammatory markers (Han et al., 2020).

WAT physiologically hosts leukocytes, with macrophages being the predominant population. WAT macrophages are divided into M1- which are classically activated macrophages and M2, the alternatively activated macrophages (Castoldi et al., 2016). During obesity WAT M1

macrophages increase and are independently associated with WAT inflammation and insulin resistance (Castoldi et al., 2016). Further, chronic overnutrition can increase white adipocyte secreted pro-inflammatory cytokines, such as tumour necrosis factor α (TNFa) (Hotamisligil et al., 1993) and IL-6 and IL-8 (Kobashi et al., 2009; Sindhu et al., 2015; Han et al., 2020), resulting in insulin resistance and inflammation. For example, elevated levels of TNFa in WAT promote insulin resistance via c-Jun amino-terminal kinase (JNK) signalling-via serine phosphorylation of insulin receptor substrate 1 (Hirosumi et al., 2002), whilst IL-6 release by white adipocytes promoters macrophages accumulation in WAT without affecting glucose or insulin tolerance (Han et al., 2020).

These data suggest that HFD-driven WAT expansion impairs adipocyte function via pro-inflammatory mechanisms and insulin impairment to disrupt the regulation of energy metabolism. The blockage of TNFa, via IV delivery of TNF receptor 1 blocking peptide, protected rats from DIO and insulin resistance by blocking local TNFa expression in pancreatic islets, muscle and adipose tissues (Liang et al., 2008). JNK-1 ablation is associated with protection from obesity, insulin resistance and adipose tissue inflammation in HFD-fed mice (Becattini et al., 2016). The evidence presented supports the idea that HFD and obesity profoundly affect WAT and its ability to control systemic metabolism via dysregulation of centrally driven feeding behaviour and pathogenic WAT remodelling. In particular, WAT expansion under chronic overnutrition states is linked with the release of proinflammatory signalling which contributes to insulin resistance.

1.3 Central control of energy balance

The appropriate uptake and release of nutrients is a central mechanism for survival; organs and tissue constantly require the availability of metabolic fuels-such as glucose, fatty acids, and amino acids- to perform the vital cellular function, and for this reason it is necessary that nutrients storage and release are tightly coupled. Whilst several hormones released from peripheral organs, such as insulin and glucagon are critical in the regulation of nutrient management, substantial evidence indicates that the central nervous system (CNS) is the master orchestrator of critical aspects of metabolism (Morton et al., 2006). The brain

monitors changes in nutrient availability and energy state by sensing hormonal and nutrient cues from the circulation and coordinates adaptive responses to nutrient availability and energy expenditure via activation of specialized neuronal networks across several different brain nuclei.

Several brain regions are key to the regulation of metabolism, and these include the (1) hypothalamus, which is divided into the mediobasal hypothalamus (MBH)-containing the ventromedial nuclei (VMH),the arcuate nuclei (ARC), the paraventricular nucleus (PVN) and the lateral hypothalamus (LH) (Lechan and Toni, 2016); and (2) the caudal brainstem, which contains the dorsovagal complex (DVC), composed of the nucleus of the solitary tract (NTS), the area postrema (AP) and the dorsal motor nucleus of the vagus (DMX) (Ngeles Fernández-Gil et al., 2010). These regions are characterised by direct exposure to hormones -including leptin, insulin and ghrelin, due to their proximity to the 3rd and 4th cerebral ventricles, respectively and either a lack of BBB -such as in the AP -or specific transport mechanisms that allow the movement of hormones across BBB to reach the brain (Lechan and Toni, 2016; Ngeles Fernández-Gil et al., 2010) (Figure 1.5).

1.3.1 The hypothalamus

The ARC

The hypothalamus is the most studied region in the control of metabolism, and it exerts a critical role in the control of food intake and energy expenditure (Timper and Brüning, 2017). Importantly, the ARC is considered the key hypothalamic area that senses metabolic cues from the periphery via the systemic circulation; this is due to its proximity to both the median eminence- a circumventricular organ- and the 3rd cerebral ventricle (Broadwell and Brightman, 1976). Notably, two neuronal populations that are critical in the control of feeding behaviour and energy expenditure have been characterised in ARC: the orexigenic neuropeptide Y (NPY) and agouti-related peptide (AgRP)-expressing neurons and the anorexigenic neuropeptide pro-opiomelanocortin (POMC)- expressing neurons. These neurons are the first-order neurons within ARC to relay signalling from hormonal metabolic cues from the circulation (Morton et al., 2006). AgRP neurons physiologically promote food

intake in states of fasting via an N-methyl-D-aspartic acid (NMDA)-mediated mechanism (Hahn et al., 1998; Liu et al., 2012), and acute intracerebral ventricular injections of AgRP in non-fasting animals increase food intake and body weight and reduce energy expenditure in rats (Rossi et al., 1998; Goto et al., 2003). Similarly, optogenetic activation of AgRP causes hyperphagia (Aponte et al., 2011). Moreover, acute activation of AgrP neurons causes insulin resistance by impairing insulin-dependent glucose uptake in the brown adipose tissue of mice (Steculorum et al., 2016), suggesting that this neuronal population exerts control of metabolic functions beyond the regulation of food intake. Similarly, hypothalamic NPY drives food intake and NPY peripheral receptor Y4 KO significantly decreased food intake, body weight and WAT deposition in male mice (Sainsbury et al., 2002).

Oppositely, POMC neurons suppress food intake and favour weight loss (Fan et al., 1997), and intracerebroventricular administration of POMC-derived melanocortins, such as alpha-melanocyte-stimulating hormone (α-MSH) rapidly promotes CCK-mediated suppression of feeding in mice with intact melanocortin 3 and 4 receptors (MC3R/ MC4R) signalling (Fan et al., 1997); similarly, prolonged optogenetic stimulation of POMC neurons in the ARC inhibits food intake (Aponte et al., 2011). Hypothalamic POMC neurons are also critical for the control of energy homeostasis; in fact, it has been recently discovered that hypothalamic POMC neurons express mesencephalic astrocyte-derived neurotrophic factor (MANF), and MANF ablation in these cells induced endoplasmic reticulum (ER) stress and leptin resistance in the hypothalamus, whilst decreasing energy expenditure via blunted brown adipose tissue thermogenesis (Tang et al., 2022). Conversely, MANF overexpression in hypothalamic POMC neurons reversed these effects and protected mice from dietary-induced obesity (Tang et al., 2022). Importantly, a study conducted in obese Zucker rats showed the suppression of *POMC* gene expression in the ARC and *α-MSH* gene expression in the PVN, suggestive of reduced activity of the melanocortin pathway in these brain regions, which led to overnutrition and obesity (Kim et al., 2000). The importance of the melanocortin system in the control of feeding has been demonstrated by the presence of melanocortin 4 receptor (MC4R) mutations in early severe-onset obesity in humans (Yeo et al., 2020; Chami et al., 2020). POMC neurons are also important in the regulation of systemic glucose levels; in fact, selective insulin receptor KO in hypothalamic POMC neurons increased HPG leading to insulin resistance (Hill, 2010; Ruud et al., 2017)

AgRP neurons promote feeding via direct competition with POMC-derived α-MSH for binding with MC3R and MC4R (Krashes et al., 2013). Acute activation of AgRP neurons promotes feeding (Krashes et al., 2013) and studies have shown that the ablation of AgRP neurons in adult mice decreases food intake and body weight (Luquet et al., 2005). Conversely, central administration of AgRP, NPY or GABA agonist promote food intake in mice, and AgRP neurons stimulation using Designer Receptors Exclusively Activated by Designer Drugs (DREADD) revealed that GABA or NPY are required for rapid stimulation of feeding, and MC4R-mediated AgRP action is sufficient to induce feeding over a prolonged period (Krashes et al., 2013). Interestingly, a recent study has revealed that prolonged and continuous HFD resulted in desensitization of AgRP neurons specific to the dietary fats (Beutler et al., 2020); whilst weight loss restored AgRP responsiveness, it failed to rescue AgRP neurons sensitivity to GI hormones and nutrients in mice (Beutler et al., 2020), suggesting that chronic overnutrition leads to dysregulation in hypothalamic AgRP neurons which is not reversed by weight loss. This could provide an insight on the difficulties encountered by obese subjects when trying to maintain or reduce body weight over a long-term.

THE VMH

The ARC is not the only hypothalamic region important to the regulation of whole-body homeostasis; the VMH also plays an important role in glucose sensing and counter-regulatory response to recover from states of hypoglycaemia (Chan et al., 2007; Barnes et al., 2011) and in generating satiety. Remarkably, the VMH is the hypothalamic production site for the anorexigenic neuropeptide, brain-derived neurotrophic factor (BDNF) (Xu et al., 2003) and destruction of VMH induces profound obesity and hyperglycaemia resulting from uncontrolled eating (Shimizu et al., 1987).

Moreover, within the MBH reside two glucose-sensing neuronal populations, namely glucose excited neurons (GE) and glucose inhibited neurons (GI) that increase and decrease their firing rate, respectively, in response to rising glucose levels. GI neurons express NPY, whilst GE neurons express POMC (Levin et al., 2004) inhibited feeding whilst decreasing NPY and AgrP expression; if we consider this data, a failure in suppressing GI neurons or activating GE

neurons firing may explain the impaired glucose-mediated suppression of feeding observed in obesity.

Importantly, in the hypothalamus, insulin activates the phosphoinositide 3-kinase- protein kinase B (PI3K/AKT) pathway of insulin to reduce the sensitivity of GE neurons to drops in glucose sensing, via opening GE ATP sensitive potassium (K_{ATP}) channels (Cotero et al., 2009). Moreover, the data collected by Cotero et al. (2009) indicate that insulin resistance during obesity or T2DM enhances the response of GE neurons in the VMH to decreased levels of glucose, leading to erroneous signalling of energy deficiency in the presence of adequate energy availability. Interestingly, hypothalamic GE neurons from obese Zucker rats display abnormal membrane potential changes in response to fluctuations in extracellular glucose, and they lacked K_{ATP} necessary for glucose sensing (Rowe et al., 1996). Furthermore, long-term HFD impaired hypothalamic glucose sensing and lowered the expression of GLUT2 in this brain region (De Andrade et al., 2015). Notably, Zucker rats present selective insulin resistance in their hypothalamus, with the PI3K, but not the mitogen-activated protein kinase (MAPK) pathway of insulin, being severely impaired in these animals (Carvalheira et al., 2003). Altogether this evidence seems to suggest that insulin sensing is important to regulate food intake via the action of GE neurons via PI3K-dependent glucose sensing, and in presence of chronic overnutrition and hypothalamic insulin resistance, this mechanism is blunted.

Further, mice with insulin receptor deletion restricted to steroidogenic factor 1 (SF-1) neurons are protected from DIO and increased POMC activity during HFD (Klöckener et al., 2011); additionally, the expression of a dominant negative form of AMP-activated protein kinase (AMPK) or inactivation of $\alpha 1$ and $\alpha 2$ subunits of AMPK in SF-1 neurons in the VMH, suppress GI neuronal activity, without affecting the normal response to hypoglycaemia (Quenneville et al., 2020). The VMH is also an important effector site for leptin; for example, increased leptin signalling in SF-1 neurons in the VMH improves glucose homeostasis without affecting body weight (R. Zhang et al., 2008), whilst leptin action in the DMH of mice increases energy expenditure via non-shivering thermogenesis and impacts body weight independently of food intake (Enriori et al., 2011; Rezai-Zadeh et al., 2014).

1.3.2 The brainstem

The brainstem is another key brain region involved in the control of energy homeostasis and processes cues related to energy status at different levels, namely: (1) it senses circulating metabolites and hormones released by peripheral organs, (2) it receives vagal afferents from the gastrointestinal tract, (3) it receives neuronal inputs from other brain regions, such as the hypothalamus, that integrate and process energy related signals, (4) it projects locally and to other brain regions to provide information that will be integrated to control energy balance (Schneeberger et al., 2014) (Figure 1.5) and (5) vagal efferent from the DMX innervate peripheral organs to control motor function and endocrine release in these organs (Figure 1.5). Within the brainstem, the DVC is a key centre for the integration of energy-related information as it relies peripheral signalling via the vagal afferents and projects to the hypothalamus and other key brain regions (Figure 1.5). For example, signals related to satiety from the gastrointestinal tract are relayed to the NTS via the afferent branch of the vagus nerve and the transection of vagal afferents to this brain region decreases meal size and duration (Schwartz, 2000) (Figure 1.5). Similarly to the ARC, the NTS can sense metabolic cues from the periphery due to its proximity with the AP, which is a circumventricular organ, and the 4th ventricle of the brain; moreover, the NTS senses and integrates corticolimbic inputs conveying information on homeostatic, cognitive and motivational aspects of feeding (Grill and Hayes, 2009; Grill and Hayes, 2012). The NTS is also enriched with neurons capable of sensing nutrient, gut hormones and adipokines (Blouet and Schwartz, 2012). The combination of vagal, humoral, and neural inputs renders the NTS a critical negative feedback control centre of short-term satiety, and this function is executed via recruitment of medullary motor outputs (Grill and Hayes, 2009). The NTS also relays information via efferent fibers to the lateral parabrachial nucleus to initiate aversive and avoidance responses to feeding (Palmiter, 2018; Kim et al., 2020) and has extensive reciprocal neuronal projections with the PVN, suggestive of a close connection between the hypothalamus and brainstem (Geerling et al., 2010). Importantly, similarly to the hypothalamus, the DVC is also responsive to insulin however, the ERK1/2 insulin pathway is activated instead of the canonical PI3K/AKT activation observed in the hypothalamus (Carvalheira et al., 2003; Filippi et al., 2012). Filippi et al. (2012) showed that the infusion of the K_{ATP} channel blocker glibenclamide and insulin in the DVC abolished the ability of the DVC to lower HGP and increase glucose infusion rate via the

ERK1/2 insulin pathway. Further, whilst an infusion of insulin in the DVC decreased food intake in rats, molecular inhibition of DVC ERK1/2 in these animals increased food intake and led to obesity after two weeks of HFD (Filippi et al., 2014). This evidence is suggestive of a critical role of insulin sensing in the DVC in the regulation of energy balance.

Neurons within the NTS, similarly to the hypothalamus, produce appetite regulating hormones, including GLP-1, POMC and NPY. NTS POMC ($POMC_{NTS}$) neurons are activated by an exogenous leptin (Ellacott et al., 2006); further studies revealed that endogenous and exogenous leptin increased c-FOS immunoreactivity in a small subset of POMC neurons in the NTS, and their cell activity was shown to be post-synaptic (Georgescu et al., 2020). Interestingly, these cells do not co-localise with established NTS metabolic regulators, namely GLP-1, CCK, BDNF, nesfatin, nitric oxide synthase 1 (nNOS) and seipin, but 100% of $POMC_{NTS}$ neurons express transcription factor paired-like homeobox 2b (Phox2b), a known regulator of afferent visceral pathways (Georgescu et al., 2020). Hayes et al. (2010) reported that specific leptin receptor KO (Lepr KO) in the NTS of rats increased food intake, body weight and adiposity, while Scott et al. (2011), showed that mice in which the Lepr was selectively ablated in the hindbrain under the *Phox2b* promoter exhibited hyperphagia and increased food intake after fasting, as well as a more rapid weight gain compared to matching controls. All together this evidence suggests physiological relevance of leptin in the brainstem in the control of energy homeostasis.

Interestingly, delivery of recombinant adeno-associated virus (rAAV) vector encoding POMC in the NTS of adult rats induced a sustained reduction of food intake, body weight and visceral adiposity, and improved insulin sensitivity in these animals (Li et al., 2007). Moreover, the authors observed an increase in the thermogenic protein, uncoupling protein 1 in the brown adipose tissue, decreased hepatic and serum TG content, and a 21-fold increase in α-MSH in the NTS, but not in the hypothalamus (Li et al., 2007) compared to vehicle-infused controls. This suggests that the mechanisms controlling peripheral energy homeostasis following NTS POMC infusion were not propagated and were therefore restricted to neuronal populations within the NTS. Interestingly, Zhan et al. (2013) revealed different behaviours of POMC neurons in the ARC and in the NTS; in particular, the authors showed that POMC neurons

regulate food intake and energy homeostasis via the integration of long-term adiposity signals from the hypothalamus and short term satiety signals from the brainstem (Zhan et al., 2013).

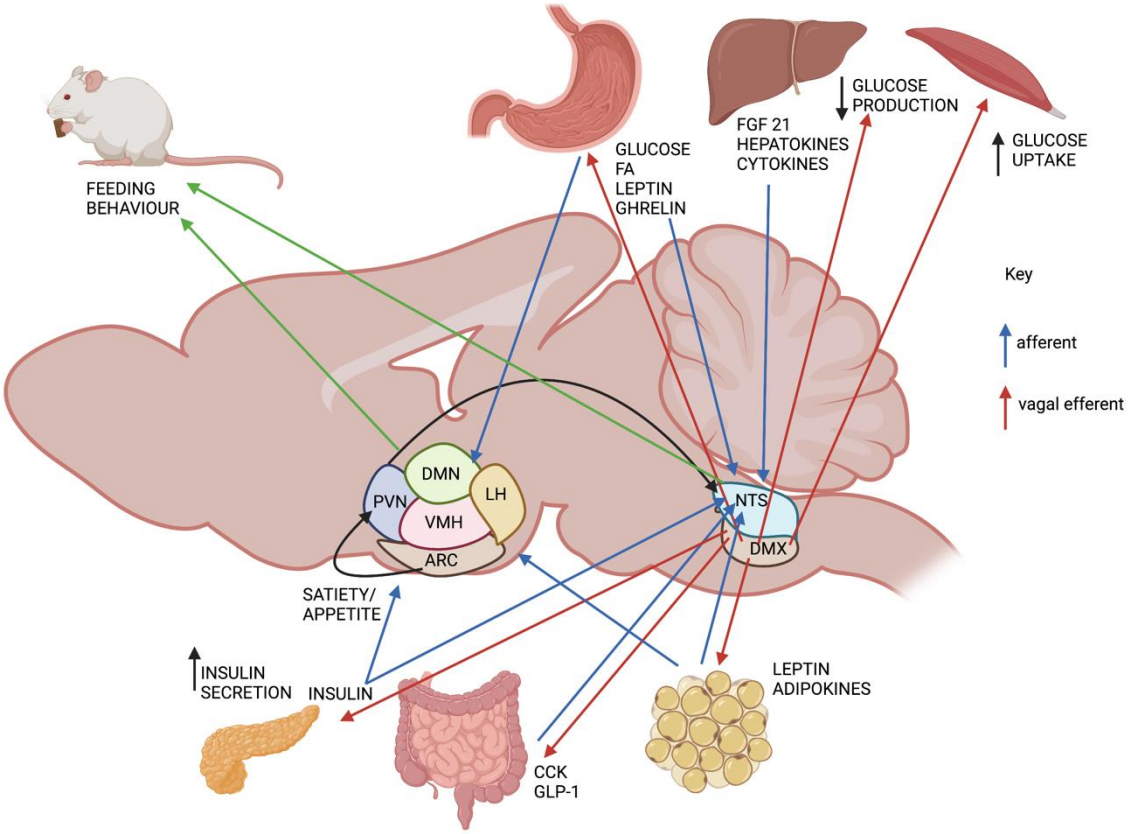

Figure 1.5: Afferent end efferent signalling between the brain and peripheral organs. *The hypothalamus and brainstem are subjected to direct exposure to circulating hormones due to their proximity to the cerebral ventricles and either lack of blood brain barrier (BBB) in the area postrema (AP) or the existence of transport mechanisms allowing hormones to cross the BBB. The brainstem contains vagal efferents arising from the dorsal motor nucleus of the vagus (DMX) that project to peripheral organs, including the gastro intestinal (GI) tract, liver, muscle, and white adipose tissue (WAT) to regulate their physiological functions (red arrows). The nucleus tractus solitarius (NTS) is the destination for vagal afferents arising from the peripheral organs (blue arrows). The complex interaction between the hypothalamus and brainstem and the peripheral organs regulates feeding behaviour and energy homeostasis. BBB: Blood brain barrier; NTS: Nucleus Tractus Solitarius; DMX:Dorsal Motor Nucleus of the Vagus. Image created with Biorender.com*

1.4 Brown adipose tissue – a critical controller of energy balance and thermogenesis

1.4.1 History and discovery

The brown adipose tissue (BAT) was first isolated from the intrascapular area of marmots by Conrad Gesner in 1551, who described it as "neither fat, nor flesh- but something in between". Initially, BAT was believed to be characteristic of hibernating animals, and from mid-1600s it was regarded as a gland, initially associated with the thymus, before being considered an active endocrine gland involved in the formation of blood (1817-1863), and a type of fat tissue involved in the storage of nutrients (1863-1902) (Afzelius,1970). From the beginning of the last century the idea of BAT being an endocrine gland re-emerged, but it was not until 1961 that its role in non-shivering thermogenesis (NST) was identified (Smith and Horwitz, 1969). Initially it was speculated that BAT activation was elicited by a restricted number of stimuli, namely hibernation, cold exposure and cold-induced stress (Smith and Horwitz, 1969). Experiments performed on rabbits and rats in the 1960's established that BAT depots do not only produce heat but also raise the body temperature by providing heat to other organs via the circulatory system (Himms-Hagen, 1989). However, it was not until the late 1970s that evidence from rodent studies showed that BAT, and not skeletal muscle, is the major anatomical site of NST, which led to the idea that BAT plays a major role in adults, newborns and hibernators alike when exposed to cold environments (Foster and Frydman, 1979). Moreover, it was shown that noradrenaline (NA)-induced heat production in BAT leads to a large increase in blood flow to this tissue in rats using a microsphere-based measurement, in which microspheres were injected into the left ventricle of the heart and their accumulation in BAT was assessed via venous sampling (Foster and Frydman, 1979). Whilst this evidence paved the way to BAT research, it was not until the mid 1980's that the molecular mechanisms behind BAT thermogenesis started to be understood. In 1984 Nicholls and Locke proposed a model in which NST occurs via uncoupling of oxidative phosphorylation in the inner mitochondrial membrane (IMM) through a phenomenon defined as "proton leak". Protons are released out of the mitochondrial matrix into the intermembrane space by three complexes of the mitochondrial electron transport chain (ETC), namely Complexes I, III and IV, establishing a proton motive force across the IMM. Moreover, protons re-enter through

Complex V leading to the release of adenosine triphosphate (ATP). However, protons can re-enter the matrix space via alternative means, which allow the bypass of the obligatory ADP-phosphorylation and ATP synthesis steps-to produce heat instead. These alternative routes for protons include direct movement across the membrane, diffusion, and inducible transport via specialised proteins. This latter point was investigated from the late 1970's, leading to the discovery of a 32 kDa transmembrane protein in BAT mitochondria associated with thermogenesis (Ricquier and Kader, 1976; Ricquier et al., 1979), which was later purified from rat tissue and characterised as functional Uncoupling protein 1 (UCP1) in human BAT mitochondria (Ricquier et al., 1982.; Bouillaud et al., 1983a; Garruti et al., 1992; Champigny et al., 1996). However, it was not until the mid 1980's that the proton-translocating activity of UCP1 was understood (Bouillaud et al., 1983b) and it was established that UCP1 is directly activated by adrenergic signalling mediated by β-adrenergic receptors on the surface on brown adipocytes (Di Ricquier et al., 1986). In the years to follow, however, BAT was considered to have little relevance in energy expenditure in humans, as it was deemed to be present and active only in human neonates; for this reason, research in the field was rapidly abandoned, despite anatomical and molecular evidence of BAT and UCP1 in adult humans (Heaton, 1972; Bouillaud et al., 1988).

Importantly, in the first decade of the 2000's a series of incidental findings in nuclear medicine played a critical role in BAT "renaissance". In 2002, Hany and colleagues observed a symmetrical uptake of fluorodeoxyglucose (^{18}FDG) in the cervical and supraclavicular region of adult patients, male and female, via positron electron tomography (PET); importantly, computational tomography (CT) superimposition revealed ^{18}FDG localisation within the fatty tissue of the neck, shoulders and thoracic spine. Interestingly, ^{18}FDG uptake appeared more prominent in underweight patients (Hany et al., 2002). Only two years later, Garcia and colleagues presented a case study, which suggested that ^{18}FDG uptake in BAT is dependent upon ambient temperature, showing that exposing patients to a thermoneutral environment was sufficient to abolish ^{18}FDG uptake in the anatomical regions corresponding to the BAT (Garcia et al., 2004). These results were confirmed in 2009 from a study coming from a larger cohort investigating young and elderly subjects (Saito et al., 2009a); the authors also revealed that ^{18}FDG uptake in BAT follows a seasonal pattern, namely it increases in the winter and decreases in the summer, and it is inversely associated with BMI and total and visceral fat as

estimated from CT images (Saito et al., 2009a). Importantly, this is the first evidence suggesting that BAT is not only present, but also metabolically relevant in adult humans. Further, in the same year it was discovered that BAT in adult humans is UCP1-immunopositive and presents a multilocular lipid droplet morphology, consistent with BAT histology, and the amount of BAT was inversely correlated with age, beta-blockers use and in older patients, with increased body-mass index (Cypess et al., 2009). However, until 2012, the contribution of BAT to human metabolism was not fully elucidated. Remarkably, Ouellet et al. (2012) showed, using PET scans and employing three separate tracers, ^{11}C acetate, ^{18}FDG and ^{18}F-fluoro-thiaheptadecanoic acid (18FHTA), a fatty acid tracer, that BAT contributes to NST in response to cold. The authors found that upon cold stimulation, all subjects recruited in the study showed cold-induced activation of oxidative metabolism restricted to BAT, and this was associated with increased total energy expenditure (Ouellet et al., 2012). Moreover, radio density analysis showed that BAT reduced its TG content upon cold stimulation, suggesting that TG were being converted in FA to fuel β oxidation, Ouellet et al. (2012). These data suggest that the BAT can be targeted to increase its metabolic activity to increase whole-body energy expenditure, which could potentially prevent or reverse HFD-induced obesity.

1.4.2 Structure, origin, and distribution

White adipocytes are sizeable, rounded cells characterised by single large lipid droplets and the cellular nucleus pushed towards the cellular wall. Conversely, brown adipocytes are smaller, and characterised by the presence of numerous and small lipid droplets and a centrally located nucleus that gives them a multilocular aspect. Moreover, BAT brown appearance is due to the presence of a high mitochondrial content which contains respiratory chain cytochrome enzymes and iron acting as a cofactor, and its highly vascularised nature. Together with high vascularisation, BAT is enriched with nerve supplies from the sympathetic branch of the nervous system. In addition to white and brown adipocytes, brite (beige) adipocytes can be found; brite adipocytes share the multilocular morphology and properties of brown adipocytes (e.g. UCP1 expression) but they are predominately located within WAT. They differ from WAT and BAT adipocytes in their developmental origin, size and expression of certain genes (Xue et al., 2007; Waldén et al., 2012; Wu et al., 2012a). Importantly, brite adipocytes are considered to be an inducible form of BAT, which can be induced by cold

exposure or β3 adrenergic stimulation to dissipate energy (Rosenwald et al., 2013; Hoffmann et al., 2016), in a process called “browning”. Conversely, brite adipocytes can be transformed into white adipocytes in response to exposure to a warm environment (Young et al., 1984; Lončar, 1991) (Figure 1.6).

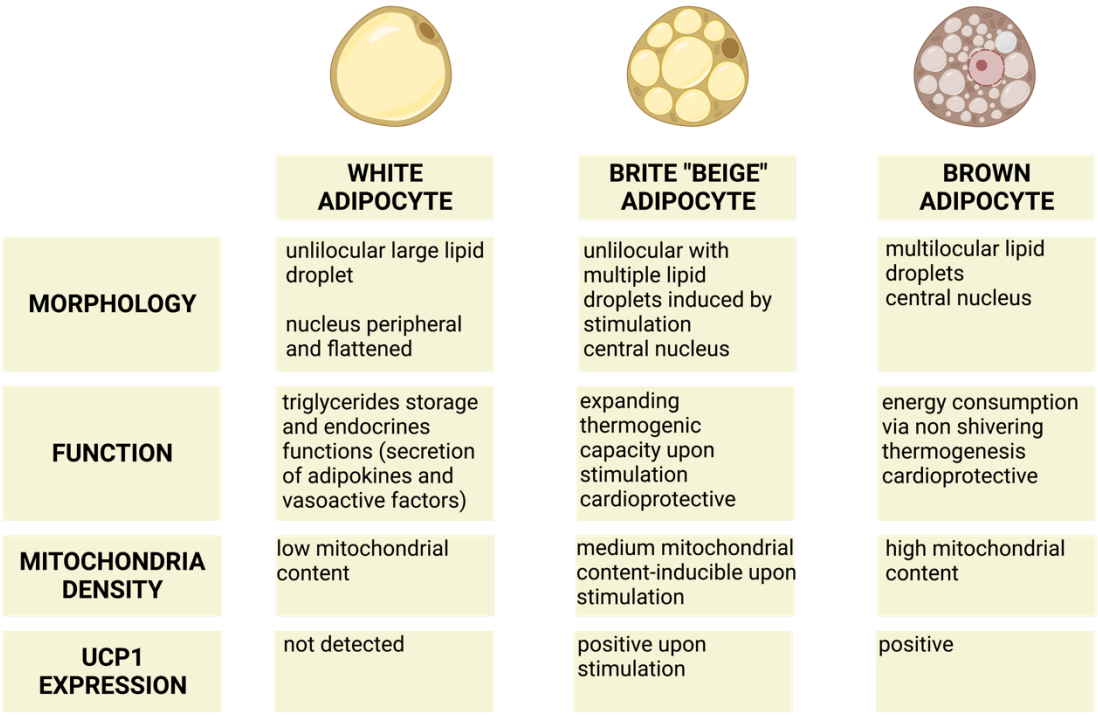

	WHITE ADIPOCYTE	BRITE "BEIGE" ADIPOCYTE	BROWN ADIPOCYTE
MORPHOLOGY	unlilocular large lipid droplet nucleus peripheral and flattened	unlilocular with multiple lipid droplets induced by stimulation central nucleus	multilocular lipid droplets central nucleus
FUNCTION	triglycerides storage and endocrines functions (secretion of adipokines and vasoactive factors)	expanding thermogenic capacity upon stimulation cardioprotective	energy consumption via non shivering thermogenesis cardioprotective
MITOCHONDRIA DENSITY	low mitochondrial content	medium mitochondrial content-inducible upon stimulation	high mitochondrial content
UCP1 EXPRESSION	not detected	positive upon stimulation	positive

Figure 1. 6: Characteristics of white, brite and brown adipocytes. *Image created with Biorender.com*

Both white and brown adipocytes originate from mesenchymal stem cells, which can differentiate into several types of cells, namely adipocytes, myoblasts, chondrocytes, and osteoblasts (Gesta et al., 2007). The genesis of adipocytes consists of a two-step process, the first step is commitment, in which mesenchymal cells are recruited to a specific adipocyte lineage-this step represents the preadipocyte stage- and this is followed by a differentiation step into mature adipocytes.

The commitment to adipogenesis is critical for both white and brown adipocytes as it allows the accumulation of intracellular lipids within the mesenchymal cells, and this process is controlled and regulated by the interaction of several transcription factors, including CCAAT

Enhancer Binding Protein (CEBP) α, β, δ , the peroxisome proliferator activated receptor γ (PPAR γ) and steroid response element binding protein 1c (SREBP1c) (Hansen and Kristiansen, 2006). PPAR γ is the key factor for preadipocyte differentiation and adipogenesis in both WAT and BAT (Figure 1.7). Importantly, brown and white preadipocytes are already fully committed for differentiation in rodents and do not require specific inducers (Cawthorn et al., 2012), suggesting that white and brown adipocytes belong to two different lineages. However, in vitro studies on human-derived preadipocytes and supraclavicular brown adipocytes showed that only fully differentiated cells express UCP1 but this was hardly detectable in precursor cells and fibroblast-like cells derived from patients with detectable BAT activity during ^{18}FDG PET (Lee et al., 2011). This is important evidence to consider when reflecting on the translational value of studies investigating BAT in rodents.

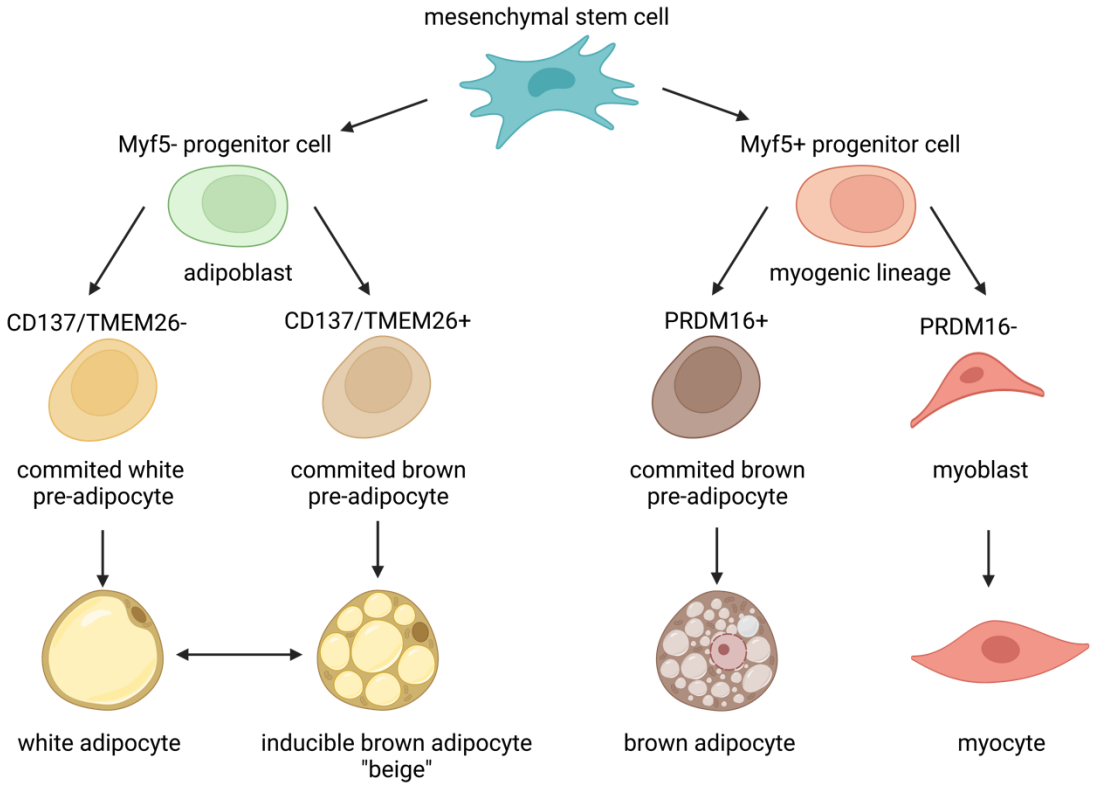

Figure 1. 7: Adipocyte lineage is determined early in the differentiation process. *BAT precursor cells share a common origin with muscle, and both express Myf5, and PRDM16 determines the fate of these precursor cells, with BAT precursor being PRDM16+ and myoblasts being PRDM16-. Conversely, precursor Myf5- cells differentiate into white or brite adipocytes. Their differentiation is determined by CD137 and TMEM26 expression, white adipocytes are CD137/TMEM26- and brite adipocytes are CD137/TMEM26+. Image created with Biorender.com.*

Importantly, BAT precursor cells express the myogenic factor 5 (Myf5), which allows them to differentiate into brown adipocytes or myoblasts. Here, the transcriptional regulator PR Domain Zinc Finger Protein 16 (PRDM16) regulates the fate of these precursor cells, determining their differentiation and allowing the regulation of the thermogenic program in brown adipocytes (Seale et al., 2008) (Figure 1.7). Whilst PRDM16 is required to maintain brown adipocyte lineage and function in mice (Harms et al., 2014), PRDM16-driven differentiation of brown adipocytes lineage is under control of the enzymatic switch euchromatic histone-lysine N-methyltransferase 1 (EHMT1). This enzyme induces PRDM16 stabilisation allowing positive regulation of BAT thermogenic program (Ohno et al., 2013). The role of this enzyme was further confirmed by mice models of EHMT1 adipose-specific deletion, which exhibited a marked reduction of BAT-mediated thermogenesis, insulin resistance and obesity (Ohno et al., 2013). Moreover, mice with PRDM16 deficiency in their BAT exhibited abnormal BAT morphology and reduced thermogenic gene expression markers, as well as increased expression in muscle-specific genes (Seale et al., 2008).

Alternatively, precursor Myf5 negative cells can be induced from mesenchymal stem cells to form white and brite (beige) adipocytes. Importantly, Wu et al. (2012) described for the first time the gene expression signature of brite adipocytes in mice, demonstrating that markers tumor necrosis factor receptor superfamily member 9 (CD137) and transmembrane protein 26 (TMEM26) can be used to select brite preadipocytes from other white preadipocytes (Figure 1.7). The authors provided evidence that human BAT shares the molecular characteristics of brite adipocytes rather than brown adipocytes, showing that human BAT indeed is composed of brite adipocytes, which exhibit higher levels of CD137 and TMEM26 mRNA transcripts when compared to WAT (Wu et al., 2012). This is an important finding as it provides useful information and considerations of the translational value and therapeutic potential of BAT targeting in humans for the treatment of metabolic disorders. As previously discussed, CEBP, SREBP1c and PPAR γ are ultimate differentiators of the three classes of adipocytes, whilst Peroxisome proliferator-activated receptor gamma coactivator 1-alpha (PGC1-α) enrichment is restricted to brite and brown adipocytes, and allows the regulation of mitochondrial biogenesis (Jäer et al., 2007) and response to external stimuli, such as cold temperature (Gill and La Merrill, 2017).

In particular, in brown adipocyte differentiation PGC-1α is a critical co-transcription factor that regulates the synthesis of UCP1 (Sears et al., 1996), and its expression is restricted to BAT whilst it is undetectable in WAT under basal condition; however in WAT and brite adipocytes it can be induced by cold exposure or β adrenergic stimulation (Gill and La Merrill, 2017). Importantly, mice lacking PGC-1α in WAT showed reduced expression of genes associated with thermogenesis and mitochondrial function, and when fed HFD these mice developed insulin resistance and reduced suppression of hepatic glucose output, whilst UCP1 mRNA transcripts in BAT were blunted despite cold exposure (Kleiner et al., 2012).

The largest BAT depots in rodents are located in the intrascapular region (Smith and Hock, 1963), with other depots being located in the cervical, axillary, paravertebral and perirenal regions (Smith and Horwitz, 1969; Nicholls and Locke, 1984). In humans, the biggest BAT depot is located in the supraclavicular region, and smaller pads can be found in the cervical, paravertebral, axillary regions, and around visceral organs (pericardial, perirenal/adrenal, oesophageal, mediastinal) and around core blood vessels, including carotids, aorta, pulmonary and intestinal (mesenteric) vasculature (Sacks and Symonds, 2013). Interestingly, similarly to rodents, human newborns present with large intrascapular BAT depots that disappear rapidly during growth, but supraclavicular, axillary and perirenal depots are seen throughout the life span, up to old age (Ito et al., 1975; Cunningham et al., 1985; Lean et al., 1986a).

1.4.3 Mechanisms of action of BAT

Biochemistry of BAT

Energy expenditure is divided into three distinct components, namely basal energy expenditure, physical activity, and adaptive thermogenesis. As previously discussed, brown adipocytes share their precursor cells with myocytes; in this regard, the existence of a common progenitor could partially explain why BAT presents a large number of mitochondria and is highly metabolically active and capable of adaptive thermogenesis just like muscle cells. Similarly, to other tissues, BAT metabolises nutrients in the form of pyruvate within the cytoplasm, which is fuelled into the ETC of mitochondria. Here, a proton concentration

gradient is generated across the IMM, which is utilised by complex V of the ETC to generate adenosine triphosphate (ATP) from adenosine diphosphate (ADP) and inorganic phosphate (Figure 1.8) and UCP1 can uncouple this reaction and dissipate the ETC proton electrochemical gradient to release energy in form of heat, instead of ATP (Nicholls and Locke, 1984)- this process is defined as non-shivering thermogenesis.

BAT activation

BAT becomes activated in response to cold, diet or β3- adrenergic stimulation, and activation of UCP1 is initiated by a signalling cascade - this starts from the binding of noradrenaline (NA) released by the nerve terminals of the sympathetic branch of the nervous system (SNS) onto the g-coupled adrenergic β3 adrenergic receptor (β3AR) on the surface of brown adipocytes (McCorry, 2007). This first step catalyses the activation of the enzyme adenylate cyclase (AC), which triggers the conversion of ATP to cyclic adenosine monophosphate (cAMP); this, in turn, activates cAMP dependent protein kinase A (PKA). PKA then activates p38 mitogen-activated protein kinase (p38 MAPK) to regulate the expression of several genes including PGC1α, which is required for the modulation of transcription factors including PPAR γ, cAMP response element-binding protein (CREB) and PRDM16, all of which control the regulation of UCP1 transcription (Figure 1.8).

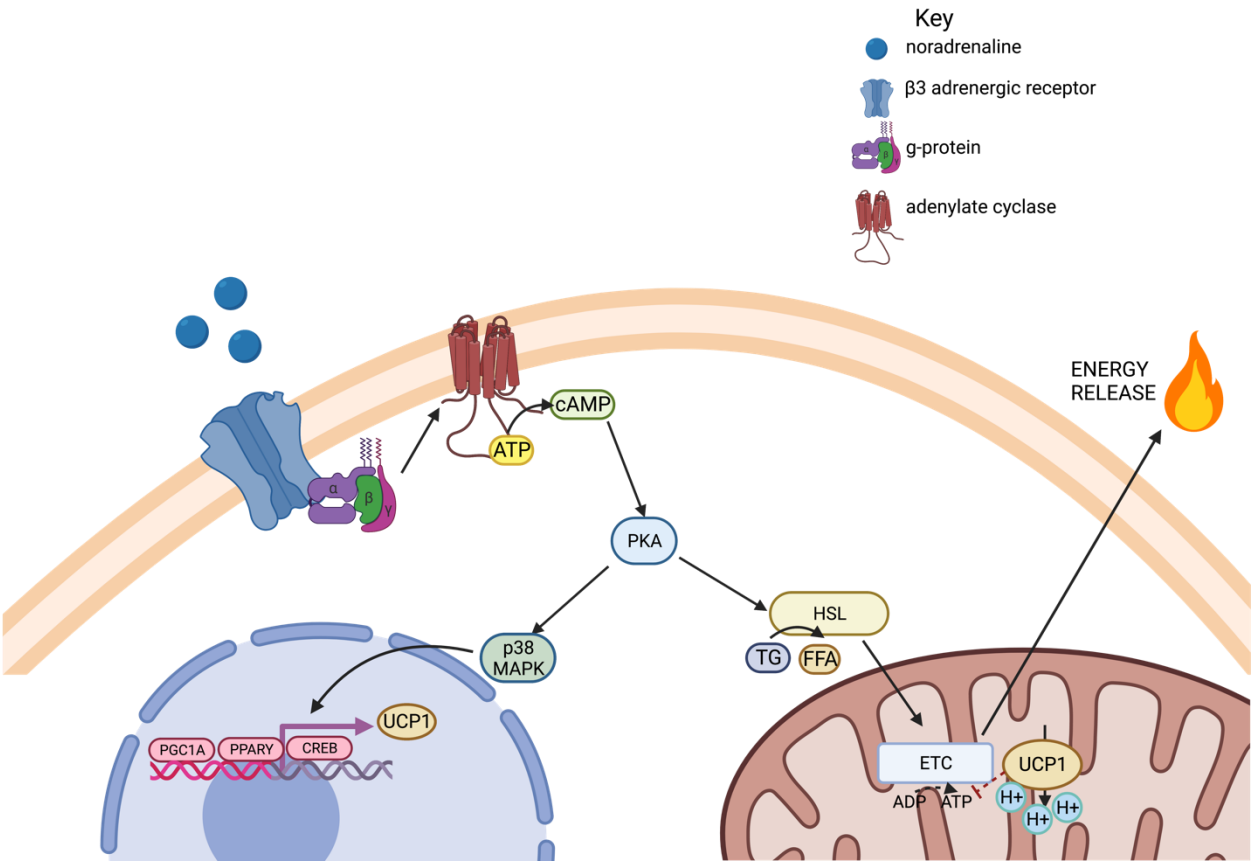

Figure 1.8 UCP1-dependent thermogenesis. *Cold, diet or β3 adrenergic stimulation elicit NA release from the postganglionic BAT sympathetic neurons which bind to β3AR on the surface of brown adipocytes, a g-coupled receptor that catalyses the activation of AC. AC activation allows ATP conversion to cAMP, which activates cAMP-dependent PKA. Two separate signalling cascades are generated: (1) mediated by p38 MAPK activation to regulate PGC1α-dependent modulation of transcription factors and thus UCP1 transcription; (2) lipolysis is stimulated via HSL phosphorylation, resulting in FA release for UCP1 activation and BAT thermogenesis. Image created with Biorender.com*

Moreover, PKA stimulates lipolysis by triggering hormone-sensitive lipase (HSL) phosphorylation, which hydrolyses a range of acyl esters, including TG, which results in FA release. FAs are required for UCP1 activation, which ultimately drives thermogenesis (Figure 1.8). GLUT 1-4 can also participate in FA release via glucose hydrolysis and insertion in the lipogenic cycle. FA can also be introduced directly from the circulation (Weir et al., 2018; McNeill et al., 2020). Examples of the importance of NA as an activator of BAT come from studies of patients with the rare adrenal tumour pheochromocytoma; Lean et al., (1986) found that these patients had significantly higher levels of BAT and BAT ^{18}FDG uptake compared to healthy controls.

Other BAT regulatory factors

Cold exposure and NA-mediated SNS activity are not the only stimulators of BAT; for example, thyroid hormones regulate BAT activity via endocrine and paracrine signalling. Thyroxine (T4) is converted into bioactive Triiodothyronine (T3) by Iodothyronine deiodinase 2 (DiO2), which is highly expressed in BAT. T3 increases UCP1 expression in BAT, leading to increased BAT energy expenditure in mice, which provides protection against obesity and insulin resistance (Watanabe et al., 2006). ICV T3 administration increases BAT thermogenesis in rats via suppression of hypothalamic AMPK and subsequent increase in sympathetic activity and noradrenergic discharge onto BAT (López et al., 2010).

BAT function is characterised by sexual dimorphism, and it has been speculated that sex steroids may play an important role in BAT activation and thermogenesis. Importantly, BAT expresses both androgens and oestrogen receptors (Rodriguez-Cuenca et al., 2007) and *in vitro* studies have shown that oestradiol stimulates UCP1 expression, lipolysis and mitochondrial genesis, whilst these processes are suppressed by testosterone (Pedersen et al., 2001; Rodríguez et al., 2002; Rodríguez-Cuenca et al., 2007). Moreover, studies conducted on rodents have revealed that females have larger and more active BAT pads than males (Rodríguez et al., 2001; Law et al., 2014), and express higher levels of UCP1 in their BAT (Rodríguez et al., 2001; Rodríguez-Cuenca et al., 2002).This pattern was also observed in human studies; in fact, retrospective ^{18}FDG PET/CT scan has revealed that sex was a

determinant of BAT activity, and women often have a more detectable BAT than men (Ouellet et al., 2011; Brendle et al., 2018); however, it is important to consider that differently to rodents, human BAT is more diffuse throughout the body, which may render these depots harder to detect with traditional PET/CT scans.

Diet is also an important regulatory factor for BAT activation; Glick et al. (1981) showed that a single low protein/high carbohydrate meal is sufficient to increase BAT respiration two hours after feeding in rats; moreover, the authors showed that UCP1 activation could be elicited by meal consumption (Glick et al., 1981). More recently, von Essen et al. (2017) revealed that meal consumption induced an increase in glucose utilisation and fatty acid synthesis in rats, but this was significantly blunted by BAT denervation. Similarly in humans, evidence of BAT-mediated diet-induced thermogenesis has been suggested. Studies of single nucleotide polymorphism in thermogenic genes, namely Trp64Arg mutation in the β3AR and A3826G mutation in the *UCP1* gene, are associated with higher WAT depots, lower metabolic rate and blunted weight loss response to caloric deficit (Oppert et al., 1994; Valve et al., 1998; Kogure et al., 1998; Yoneshiro et al., 2012). This evidence suggests that BAT is important in the thermogenic response to food intake. BAT is also activated by humoral factors secreted after the consumption of a meal, such as bile acid and gut hormones (Broeders et al., 2015). Several compounds including tea caffeine, capsaicin, curcumin, retinol acid and resveratrols have been suggested to act as BAT activators via multiple mechanisms of action (Okla et al., 2015; Yoneshiro et al., 2019).

Lastly, fibroblast growth factor 21 (FGF21) has been recently identified to modulate BAT and WAT in rodents; FGF21 subcutaneous infusion in mice increases thermogenic recruitment of WAT by promoting its browning, via a PGC1α- mediated mechanism (Fisher et al., 2012); this action appears to be mediated by the SNS in male mice and an intact adrenergic system was required for FGF21 action as demonstrated by mice lacking β-adrenoceptors (Douris et al., 2015). Moreover, FGF21 is directly secreted by BAT in rodents, suggesting an endocrine role of BAT (Hondares et al., 2011; Fisher et al., 2012).

1.4.4 Relevance as a therapeutic target in obesity and metabolic disorders

Therapeutic targets for obesity are of growing interest, given the global impact and prevalence of this condition and related comorbidities (WHO, 2016). From a thermodynamic perspective, obesity results in an imbalance in energy homeostasis, namely energy intake is greater than energy expenditure. Lifestyle interventions to reduce energy intake (diet) and increase energy expenditure (exercise) are the first line of intervention to ameliorate obesity. However, these have proven to be insufficient to prevent and manage of obesity, due to scarce long-term adherence to these interventions. Effective strategies to prevent or counteract obesity are therefore needed.

BAT plays an important role in energy metabolism and obesity in rodents; for example, transcript levels of genes related to the transport and catabolism of glucose and fatty acids in BAT are increased upon cold-induced BAT stimulation at 4°C for 48 hours (Hiroshima et al., 2018). Moreover, intermittent cold exposure in HFD-fed mice increased metabolic rate 2-fold during the temperature challenge and recruited BAT, triggering its activation. However, these animals compensated for the upregulation in energy expenditure by increasing their food intake, thus there was no reduction in body weight and adiposity, however cold-exposed animals showed an improvement in glucose homeostasis compared to non-challenged controls (Ravussin et al., 2014).

Importantly, acute cold exposure (2-4 hours, 16-19°C) in humans induced BAT activation, which resulted in 13-27% increase in resting energy potential (van Marken Lichtenbelt et al., 2009; Yoneshiro et al., 2011; Chondronikola et al., 2014), whilst chronic but mild (2 hours, 17°C, daily) cold exposure for 9 weeks led to increased thermogenesis and reduced body fat in adults subjects (Yoneshiro et al., 2013), suggesting the importance of BAT in regulating whole body energy expenditure and adiposity.

Increasing BAT activity to enhance energy expenditure and restore energy balance in obese patients appears to be a logical approach, especially if one considers that there is a potential for improvement of metabolic homeostasis via lipid clearance from the circulation and

increased glucose utilisation to fuel thermogenesis (Nedergaard and Cannon, 2010; Bartelt and Heeren, 2013; Moonen et al., 2019).

A small but sustained imbalance in favour of energy expenditure would be sufficient to ameliorate obesity and it is estimated that at basal level, BAT can account for 1 to 5% of resting metabolic rate (RMR), but it has been suggested that upon stimulation this value can reach up to 16% of RMR (Lans et al., 2013; Moonen et al., 2019). Moreover, estimates have shown that cold-induced BAT activation could increase daily energy expenditure by 200-400 kcal (Kajimura and Saito, 2014), and despite its small mass, under cold exposure it accounts for nearly half of total TG and over 75% of glucose derived from meal disposal and metabolism (Bartelt et al., 2011a).

This suggests that BAT can rapidly sequester and combust TG and glucose postprandially, which suggests that the therapeutic benefit of BAT is not restricted to weight loss, but may also be critical in managing hyperglycaemia and hyperlipidaemia in obese and/or diabetic patients (Nedergaard et al., 2011).

Whilst cold exposure clearly elicits a stimulatory response in BAT, multiple long periods of exposure to cold could be impractical and create discomfort in patients, potentially leading to low adherence to the procedure over the long-term. Importantly, another largely explored method to induce BAT thermogenesis consists in the stimulation of the β3AR via β3-adrenergic agonists (Arch, 2002), and this is well established in rodents (Bachman et al., 2002).

In 2015 Cypess et al. demonstrated the relevance of β3- adrenergic agonists in BAT stimulation in humans; importantly, the authors revealed that Mirabegron, a β3- adrenergic agonist used for the treatment of over reactive bladder, could stimulate BAT compared to placebo, leading to higher BAT metabolic activity, as measured with ^{18}FDG /CT scans and increased resting metabolic rate. This suggests that BAT activation could be a useful approach to increase thermogenesis *in vivo* to treat metabolic disorders such as obesity. More recent studies have also demonstrated that Mirabegron positively affects circulating adipokines, glucose metabolism (O'Mara et al., 2020) and regulates lipid droplet size (Hao et al., 2019)

and, unlike other β3- adrenergic agonists, presents a very high safety profile, with minimal effect on cardiovascular function at a dosage of up to 100 mg/day (Loh et al., 2019).

Whilst these approaches constitute exogenous adrenergic stimulation of BAT, very little is known about the modulation of BAT activation via endogenous increase of adrenergic discharge to BAT. Both the hypothalamus and the brainstem are key brain regions involved in the modulation of sympathetic stimulation to BAT. Here we aim to investigate the contribution of the CNS, and in particular of the NTS of the DVC in modulating BAT activity, to investigate whether this brain region may represent a novel therapeutic target for the treatment of obesity.

1.5 Central control of the brown adipose tissue

The role of BAT in energy balance regulation requires the involvement of brain circuits to control thermogenesis via the sympathetic nervous system. (Cannon and Nedergaard, 2004a; Bartness et al., 2010). The thermoregulatory network in the CNS comprises the pathways through which changes in cutaneous and visceral cold and warm sensation and brain temperature trigger fluctuations in thermoregulatory effector tissues, such as BAT, to protect against temperature changes in the brain and other key organs (Morrison et al., 2012). Importantly, most circuits that control BAT thermogenesis are also involved in energy balance regulation (Richard and Picard, 2011; Chechi et al., 2013), and key centres for the autonomic control of BAT are found in the hypothalamus and brainstem (Richard, 2015). Here we report the importance of hypothalamic energy regulatory pathways to BAT activation and the emerging role of the DVC of the brainstem in the modulation of BAT activity.

1.5.1 Hypothalamus

Several hypothalamic nuclei have been involved with the control of BAT-thermogenesis namely, the ARC, POA, DMH, PVH, LH and VHM, which form the hypothalamic energy homeostasis regulatory pathway. The POA is a major coordinator of thermoregulation as it

receives inputs from thermoreceptors of the skin, and it comprises the median preoptic area (MnPO), the medial preoptic area (MPO), the lateral preoptic area (LPO) and the preoptic nucleus (POP). Cooling of the skin or of POA triggers BAT activation in rodents via the SNS. Cold sensation is transmitted via glutamatergic signalling and processed by third-order neurons in the external lateral parabrachial nucleus (LPBel), whilst warm sensation is processed by the dorsal lateral parabrachial nucleus (LPBd), and thermosensory information is then relayed on the POA. Within the POA, cold signalling is mainly occurring in the MnPO, in which GABAergic neurons suppress the activity of other GABAergic neurons within the MPO (Labbé et al., 2015; Hrvatin et al., 2020; Takahashi et al., 2020). Conversely, warm stimuli activate glutamatergic neurons in the MnPO which, in turn, induce activation of GABAergic neurons in the MPO (Labbé et al., 2015). The POA also sends projections to the DMH, which is an important effector in the regulation of BAT metabolism (Labbé et al., 2015; Hrvatin et al., 2020; Takahashi et al., 2020); in fact, glutamatergic neurons within the DMH receive GABAergic negative tonic inhibition from the MPO (Chen et al., 1998) and chemical stimulation of DMH neurons with parenchymal injections of glutamate, or disinhibition of this cell population with $GABA_A$ receptor antagonist, led to an increase of BAT thermogenesis and core body temperature (Zaretskaia et al., 2002; WH et al., 2004; DiMicco and Zaretsky, 2007; Morrison and Nakamura, 2011). The involvement of the DMH in BAT activation has been shown in studies interrogating the role of DMH lesions in this mechanism, which revealed that DMH lesions completely abolish BAT thermogenesis mediated by both external cooling and POA stimulation (Hogan et al., 1982; Preston et al., 1989; Monge-Roffarello et al., 2014). Interestingly, a subset of warm-activated cholinergic neurons within the DMH have been associated with decreased BAT activity and core body temperature (Jeong et al., 2015), which is suggestive of the involvement of multiple neuronal populations in the control of BAT. Importantly, the DMH does not directly project to BAT sympathetic preganglionic neurons, instead it monosynaptically projects to the raphe pallidus nucleus (RPa) in the rostral ventral medulla, which is the main site of BAT premotor neurons (Nakamura et al., 2005; Yoshida et al., 2009) and this is referred to as POA-DMH-RPa thermoregulatory pathway of BAT (Figure 1.9).

Thermoregulatory pathways are not the sole route of hypothalamic control of BAT thermogenesis; in fact, circuits involved in energy homeostasis regulation across the ARC,

PVH, LH and VMH also play an important role (Chechi et al., 2013b; Stefanidis et al., 2014; Richard, 2015). For example, descending projections from the PVH, encompassing the NTS, DMX , AP and nucleus ambiguous, to the sympathetic intermediolateral cell column (IML) of the thoracic spinal cord have been discovered using anterograde tracing in rats, suggestive of PVH direct integration with medullary and spinal autonomic regulatory nuclei (Zheng et al., 1995). The importance of the VMH in the regulation of BAT thermogenesis is also well established as this nucleus integrates peripheral signals-including thyroid hormones (Alvarez-Crespo et al., 2016), leptin (Tanida et al., 2013), and GLP1 (Beiroa et al., 2014), to coordinate thermogenesis via regulation of BAT sympathetic tone. This occurs via projections from the VMH to the rostral raphe pallidus nucleus (rRPa) and inferior olive (IO) in the brainstem (Morrison, 1999; Uno and Shibata, 2001). Remarkably, prostaglandin E2 injection in the anterior POA elicits an increase in BAT thermogenesis in a dose-dependent manner, and its effect could be blocked by GABA receptor agonist muscimol injections in the ipsilateral VMH in rats; conversely, infusion of excitatory neurotransmitters and neuropeptides such as glutamate, NA, serotonin and tryptophan in the VMH activate BAT (Sakaguchi and Bray, 1989; Amir, 1990; Hugie et al., 1992).

Several neuronal populations, including the melanocortin and endocannabinoid systems, have been shown to play an important role in hypothalamic regulation of BAT thermogenesis. The melanocortin system comprises POMC and AgRP neurons as well as neurons expressing MC3R and MC4R. Evidence has shown that POMC neuronal activity is related to increased thermogenesis of BAT via direct projections from the ARC to the thoracic IML (Tsou et al., 1986; Elias et al., 1998) which in turn project to the postganglionic sympathetic neurons innervating BAT (Bamshad et al., 1999; Oldfield et al., 2002). Interestingly, recent evidence has shown that POMC neuronal regulation of BAT thermogenesis is mediated by MANF (Tang et al., 2022). In fact, mice with MANF KO in POMC neurons were prone to DIO, ER stress and leptin resistance in the hypothalamus and decreased sympathetic discharge and BAT thermogenesis; while MANF overexpression in these neurons increased BAT thermogenesis and protected the mice from DIO (Tang et al., 2022). Conversely, intracerebroventricular infusion of AgRP suppresses BAT thermogenesis and temperature, suggesting a bidirectional involvement of POMC and AgRP neurons in regulating BAT. MC4R neurons are synaptically, and potentially polysynaptically, connected to BAT (Song et al., 2008) and central

administration of a melanocortin receptor agonist in the PVH activates BAT thermogenesis (Song et al., 2008; Monge-Roffarello et al., 2014). Further, intracerebroventricular administration of MC3/4R antagonist in APOE3-Leiden mice-a well-established model of diet induced hyperlipidaemia and atherosclerosis-and in wild-type mice, resulted in increased food intake and body fat and reduced BAT activity, measured as uptake of VLDL-TG, fat oxidation and alterations of BAT cytoarchitecture (Kooijman et al., 2014).

The endocannabinoid system is also an important component of hypothalamic BAT regulation, and it comprises neurons expressing the cannabinoid receptor type 1 (CB1R). CB1R are present in several hypothalamic nuclei, and at greater density in the PVN (Hillard et al., 2016), one of the major hypothalamic regions containing sympathetic premotor neurons (Allen, 2002). importantly, IP administration of CB1R antagonist has shown to increase BAT thermogenesis (Verty et al., 2009). Moreover, evidence has suggested that endogenous endocannabinoids could exert a pre-synaptic effect on the IML or brainstem to inhibit PVH MC4R-mediated BAT activation (Monge-Roffarello et al., 2014); whilst inactivation of CB1R endocannabinoid ligand 2 arachidonoyglycerol in the hindbrain of mice increases BAT activity and UCP1 expression, moreover these animals are resistant to DIO (Jung et al., 2012). Overall, this evidence suggests that the hypothalamic endocannabinoid system suppressed BAT activation via direct and indirect mechanisms.

Signalling derived from other hormones and nutrient, such as leptin, insulin and GLP1 can influence the hypothalamic sympathetic output to BAT. For example, hypothalamic administration of insulin influences BAT activity in a dose-dependent manner, with higher doses stimulating BAT thermogenesis and low doses suppressing it (Rahmouni et al., 2004). Analogously, central leptin administration induces BAT sympathetic output (Collins et al., 1996; Sivitz et al., 1997) and increased NA turnover (Collins et al., 1996; Minokoshi et al., 1999; Caron et al., 2018), UCP1 (Scarpace and Matheny, 1998; Rouru et al., 1999; Commins et al., 2000; Ukropec et al., 2006) and PGC1α mRNA (Kakuma et al., 2000), and increased glucose uptake in this tissue (Minokoshi et al., 1999; Haque et al., 1999; D'souza et al., 2017). Moreover, intracerebroventricular administration of pre-proglucagon-derived peptides increases BAT thermogenesis by boosting SNS activity to this organ (Lockie et al., 2012), suggesting that central pharmacological GLP1R activation contributes to energy balance.

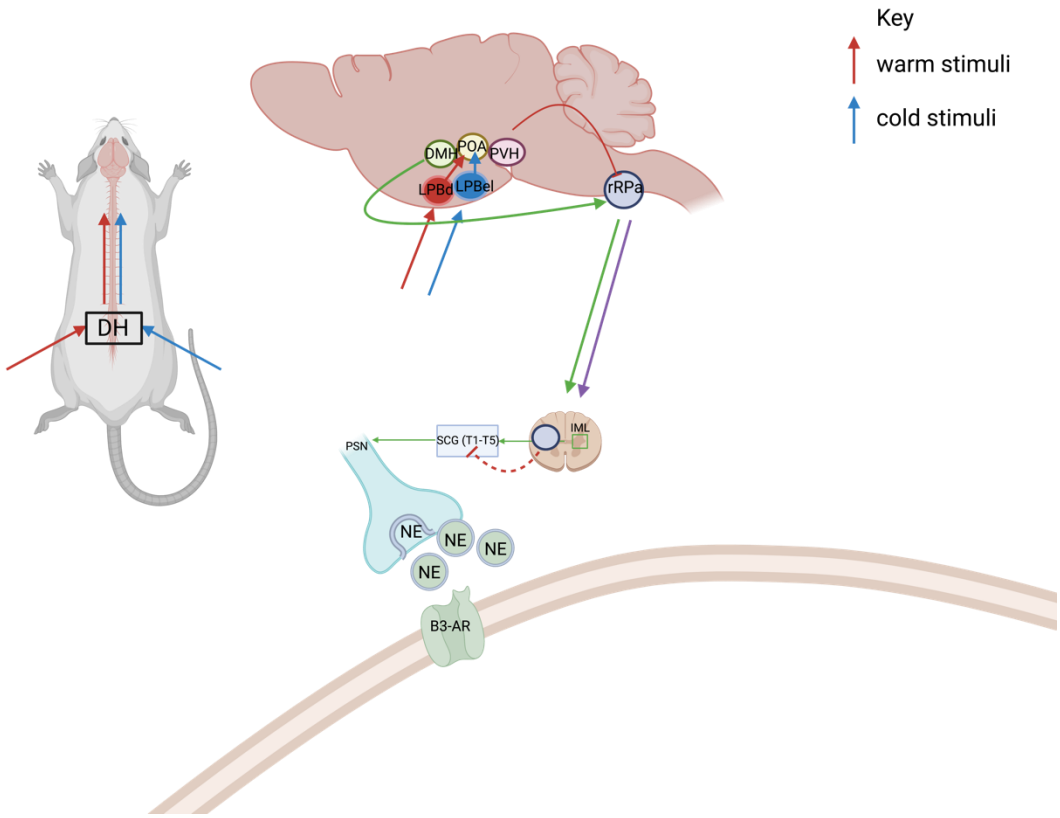

Figure 1.9: Thermal pathways of BAT activation in the hypothalamus. *Warm and cold sensation is transmitted to the respective primary sensory neurons in the dorsal root ganglia and relayed to second order neurons in the dorsal horn (DH) of the spinal cord. Cold sensation is transmitted via glutamatergic signalling and processed by third order neurons in the external lateral parabrachial nuclei (LPBel), whilst warm sensation is processed by the dorsal lateral parabrachial nuclei (LPBd). Thermosensory information in then transmitted to the preoptic area (POA), where a population of cold sensitive neurons mediate BAT thermogenesis by causing disinhibition of neurons in the dorsomedial hypothalamus (DMH), allowing excitation of BAT sympathetic premotor neurons in the ventral medulla, and specifically in the raphe pallidus nuclei (rRPa) (green arrow). The rRPa modulates BAT activity through activation of presympathetic neurons releasing glutamate onto sympathetic preganglionic neurons (SPNs) in the intermediolateral nucleus (IML) of the spinal cord to excite BAT (green arrow). Another population of premotor neurons from the rRPa can release serotonin (5-HT) (purple arrow) to suppress the activity of BAT inhibitory neurons in the IML (dotted red arrow) to increase BAT thermogenesis. The paraventricular hypothalamus (PVH) exerts an inhibitory action over the rRPa via GABAergic projections (red arrow) to inhibit BAT activity. Image created with Biorender.com.*

1.5.2 Brainstem

Whilst the hypothalamic circuits regulating energy homeostasis have been widely investigated, extra-hypothalamic circuits are far less understood. Early studies have shown that exposing rats to a cold environment resulted in c-Fos activation in the raphe magnus (RM), RPa and reticular nuclei of the medulla (Morrison, 1999; Morrison et al., 1999b; Martinez et al., 2001; Cano et al., 2003). Microinjections of bicuculline in these regions activate BAT (Morrison et al., 1999; Nason and Mason, 2004). Importantly, it is now established that these regions contain key BAT sympathetic premotor neurons, which are required to provide excitatory drive to BAT (Morrison et al., 2014). Warm-sensitive neurons in the POA regulate BAT thermogenesis by inhibiting BAT sympathoexcitatory neurons in the DMH and dorsal hypothalamic area (DA); these are synaptically connected to BAT via projections to the rostral ventromedial medulla (Morrison et al., 2014). During cold exposure, disinhibition of DMH/DA neurons excites BAT sympathetic premotor neurons in the rostral ventromedial medulla, including the rRPa, which in turn project to BAT sympathetic preganglionic neurons (SPNs) in the intermediolateral nucleus (IML) (Holstege and Kuypers, 1982; Bacon et al., 1990) of the thoracic-lumbar spinal cord (Figure 1.10). The SPNs in turn excite sympathetic ganglion cells innervating BAT to elicit thermogenesis. BAT premotor neurons can release glutamate to excite BAT SPNs and increase BAT sympathetic activation, whilst others can release serotonin (5-HT), which interacts with serotonin 1A receptor (5HT-1A), potentially located on inhibitory interneurons in the IML to increase BAT activity (Morrison et al., 2014) (Figure 1.10).

The RPa receives tonic inhibitory projections from warm-sensitive GABAergic neurons in the POA, and the disinhibition of RPa neurons increases BAT sympathetic activation and thermogenesis (Cao et al., 2004; Morrison et al., 1999b), whilst RPa inactivation blunts BAT thermogenesis (Morrison et al., 2001; Morrison 2002; Nakamura et al., 2002). Inhibitory GABAergic inputs to BAT also originate from the intermediate and parvicellular reticular nuclei to regulate BAT sympathetic activity during states of negative energy balance (Nakamura et al., 2017). Further, the activation of RVLM neurons can inhibit BAT sympathetic activity independently of GABA receptor activation in the rRPa (Cao et al., 2010), whilst

activation of neurons in the caudal ventrolateral medulla can reduce BAT sympathetic activity partially via activation of $\alpha 2$ adrenergic receptors in the rRPa (Madden et al., 2013).

Conversely, orexinergic projections from the perifornical LH can stimulate sympathetic premotor neurons in the rRPa to drive BAT thermogenesis (Tupone et al., 2011). Cholinergic neurotransmission also plays a role in the regulation of BAT thermogenesis (Conceição et al., 2017); for example, the activation of cholinergic neurons in the DMH suppresses BAT thermogenesis during skin warming by inhibiting serotoninergic neurons in the rRPa (Jeong et al., 2015). Additionally, a tonically active cholinergic input originating caudal to the hypothalamus and acting on muscarinic acetylcholine receptor (mAChR) in the rRPa inhibit BAT sympathetic activation in both warm and cold conditions (Conceição et al., 2017). Importantly, the inhibition of BAT sympathetic activity driven by mAChR activation in the rRPa is not dependent upon the activation of local GABAergic receptors (Conceição et al., 2017).

The NTS is also a key brainstem centre for the integration of metabolic cues and other physiological information received from a range of peripheral organs, including vagal-relayed signals from the gut and adipose tissues. Importantly, the NTS contains second-order sensory neurons innervated by glutamatergic vagal afferents, which relay metabolic cues to modulate satiety (Bednar et al., 1994) (Figure 1.5). The NTS, and in particular the intermediate NTS, also contains BAT sympathoinhibitory neurons that upon activation attenuate BAT sympathetic activation and thermogenesis (Figure 1.10); In fact, Cao et al. (2010) have shown that inhibition of BAT thermogenesis was also governed by the disinhibition of neurons in the VLM or the NTS of the brainstem; the authors demonstrated that injections of bicuculline in these regions suppress BAT sympathetic nervous activity and temperature elicited by cold defence and by activation of neurons in the DMH or rRPA (Cao et al., 2010); interestingly, synchronous inhibition of neurons in the VLM and NTS with muscimol increased BAT sympathetic nervous activity and temperature. This suggests that the NTS contains neurons that, when activated, inhibit BAT thermogenesis; and these neurons contribute to tonic inhibition of sympathetic premotor neurons in the rRPa. Moreover, it has been speculated that this activation is vagal-dependent (Madden et al., 2017). In particular, vagal-evoked inhibition of BAT sympathetic activation was prevented by blocking ionotropic glutamate receptors in vagal afferent

terminals in the NTS, as well as $GABA_A$ receptor antagonist in the rostral nucleus of the raphe pallidus (Madden et al., 2017). While the neuronal subpopulations within the NTS that are responsible for BAT inhibition are still unknown, it has been established that the NTS provides disinhibition to BAT sympathetic premotor neurons in rRPa via non-GABAergic inhibitory signalling or by activation of spinal inhibitory interneurons within the IML (Morrison and Madden, 2014) (Figure 1.10).

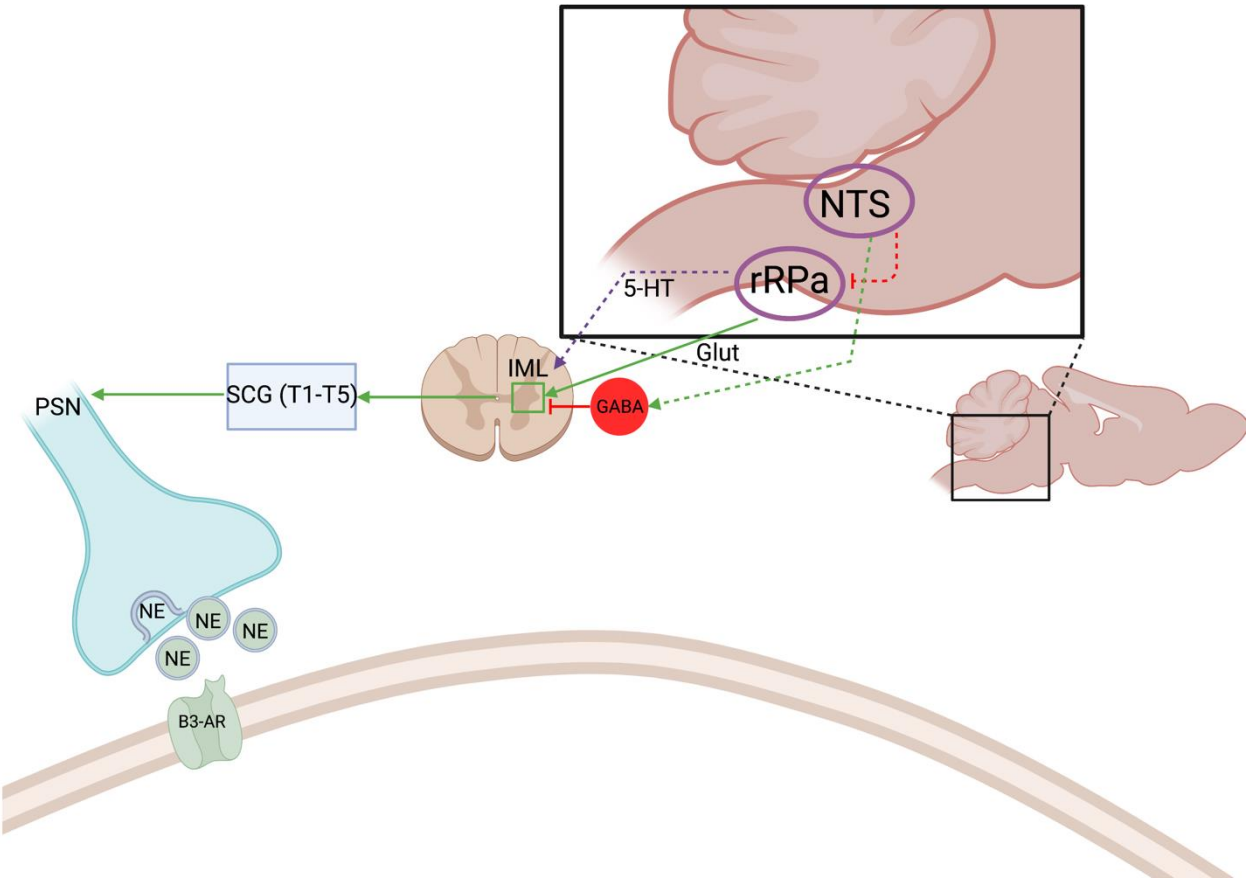

Figure 1.10: NTS role in the regulation of BAT activation. *The NTS contains unknown populations of BAT inhibitory neurons providing non-GABAergic disinhibition of BAT glutamatergic (Glut) (green arrow) or serotoninergic (5-HT) (purple arrow) premotor neurons in the rRPa or direct activation of spinal inhibitory interneurons in the IML. This results in blunting of the canonical UCP1-dependent pathway to thermogenesis. Image created with Biorender.com*

Vagal viscerosensory afferents terminating on second-order neurons in the NTS can control BAT activation (Székely, 2000); for example, upregulation of hepatic glucokinase- an enzyme

involved in the control of glucose disposal in the liver and glucose sensing for pancreatic insulin secretion- (Agius, 2009) inhibits BAT activation via the vagus (Tsukita et al., 2012). Additionally, the presence of lipids in the duodenum leads to NTS-mediated BAT activation via the vagus (Blouet and Schwartz, 2012). Leptin, thyrotropin-releasing hormone (Rogers et al., 2009), MC3/4R and Melanotan II (Williams et al., 2003) stimulate BAT activity when delivered to the 4th ventricle, and this action is potentially mediated via stimulation of NTS neurons.

1.5.3 Astrocyte involvement in the control of energy metabolism

Astrocytes are a type of glial cell critical for the control of energy balance and metabolism of the central nervous system as they are involved in the modulation of synaptic transmission, allowing functional neuronal communication. Interestingly, astrocytes have not only been associated with the control of a range of central mechanisms including memory (Martin-Fernandez et al., 2017) and addiction (Scofield and Kalivas, 2014), but have also been shown to exert significant functions in the regulation of systemic glucose metabolism, cardiovascular and respiratory functions and feeding behaviour (Grill and Hayes, 2012; Agulhon et al., 2013; Kim et al., 2014; Liang Yang et al., 2015a; MacDonald and Ellacott, 2020). Recently, astrocytes have started to be characterised as major regulators of feeding behaviour. For example, Yang et al. (2015) employed chemogenetic, electrophysiological and pharmacological approaches to show that astrocytes suppress ghrelin-evoked hyperphagia and facilitated leptin-dependent anorexia in mice. This feeding-suppressing role of astrocytes was found to be mediated by endogenous adenosine activation of adenosine A_1 receptors in the MBH (Yang et al., 2015). Furthermore, glial cells in the DVC respond to and influence food intake; in particular, DREADD-mediated activation of DVC astrocytes reduced dark phase feeding and refeeding after overnight fast in mice, without affecting locomotion (MacDonald et al., 2019). The authors also showed that activation of DVC astrocytes induced c-FOS in both neighbouring feeding circuits, including the parabrachial nucleus, as well as the recruitment of long-range neuronal circuits in the lateral parabrachial nucleus of the hypothalamus (MacDonald et al., 2019). Moreover, Patel et al (2020) found that HFD induced inducible nitric oxide (iNOS) in astrocytes of the DVC, and inhibition of iNOS in the DVC, or inhibition of

mitochondrial fission in astrocytes of the DVC protected rats from overeating, weight gain and increased abdominal adiposity, as well as preserving insulin sensitivity within the NTS.

Recent evidence has shown that astrocytes in the NTS are also involved in the regulation of BAT activity; for example, Manaserh et al. (2020) elegantly show that mice congenitally lacking insulin receptor in astrocytes ($IRKO^{GFAP}$) mice showed significantly lower energy expenditure and basal and fasting body temperature compared to wildtype controls; moreover, $IRKO^{GFAP}$ animals displayed bigger adipocytes within BAT, reduced innervation and lower levels of β3AR in BAT than controls, and more apoptosis was seen in the BAT of male $IRKO^{GFAP}$ mice. These findings identified a role for astrocytes in the regulation of BAT and body temperature control, suggesting that insulin signalling in these cells could be a novel target to increase energy expenditure. However, no further literature has investigated the role of astrocytes in the NTS in the control of BAT activation, therefore there is a need for deepening our understanding of these glial cells to identify potential new targets to ameliorate obesity by boosting BAT thermogenic capacity.

1.6 Mitochondrial dynamics

Mitochondria are membrane-bound organelles present in almost all eukaryotic cells, and largely conserved across all living organisms, from yeast to mammals. These organelles play a key role in the generation of chemical energy within cells, in the form of ATP via oxidative phosphorylation (OXPHOS). Further, these organelles exert other critical cellular functions, including synthesis of heme (Nilsson et al., 2009), calcium homeostasis (Gunter et al., 1998; Zenisek and Matthews, 2000; Trenker et al., 2007; Denton, 2009) and the activation calcium-dependent and calcium-independent apoptotic signalling and cell death (Danese et al., 2017.; Susin et al., 1999; Zou et al., 1999; Sattler et al., 2000; Li et al., 2001). Remarkably, mitochondria play an important role in the maintenance of cellular homeostasis and sustain energy production via the regulation of calcium concentration (Contreras et al., 2010). Mitochondrial calcium concentration is critical to cell homeostasis as it supports the production of energy (Contreras et al., 2010) and regulates neuronal and hormonal signalling

(Stark and Roden, 2007). This shows the importance of mitochondria in supporting endocrine functions within the CNS.

Importantly, ATP production rate within mitochondria is based on metabolic demand and the energy status of cells dictates mitochondrial size, shape and positioning within the cytoplasm (Collins et al., 2002). These rapid adaptations are known as mitochondrial dynamics. Here we will specifically focus on the remodelling of mitochondrial morphology and its significance in relation to energy status (Figure 1.11).

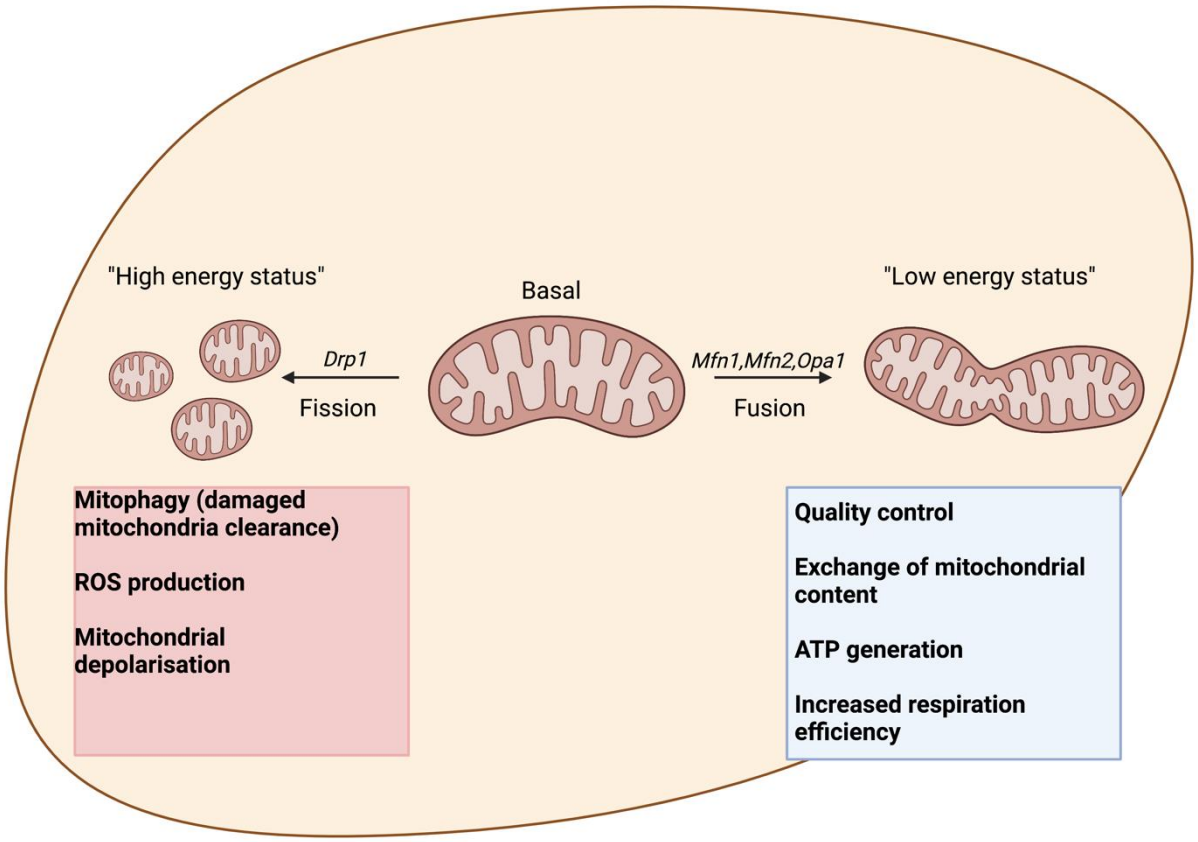

Figure 1.11: Mitochondrial dynamics are critical to cells' energy sensing. *Mitochondrial dynamics are regulated by a range of proteins; during low energy, state mitochondria favour a fused-state which is promoted by regulatory proteins Mfn1-2 and Opa1. In high energy status, mitochondria favour fission which is primarily regulated by Drp1. Image created with Biorender.com.*

1.6.1 Mitochondrial fusion

The two key mechanisms of mitochondrial dynamics are fusion and fission (division), and these two opposite processes are required to support physiological mitochondrial function and prevent disease (Yapa et al., 2021). Mitochondrial fusion is a survival mechanism that is triggered by several factors, including protein synthesis inhibition, autophagy and starvation (Tondera et al., 2009; Gomes et al., 2011; Rambold, Kostelecky, Elia, et al., 2011; Ramírez et al., 2017). Importantly, mitochondrial fusion allows the exchange of material between interconnected mitochondria to increase respiratory function and optimise cell energy production.

In mammals, fusion is regulated by three membrane nucleotide guanosine triphosphate (GTP)ases: two outer mitochondrial membrane (OMM) proteins, Mitofusin 1 (Mfn1) and Mitofusin2 (Mfn2) and one IMM protein, Optic Atrophy Protein 1 (Opa1) (Santel et al.,2001.; Chen et al., 2003; Eura et al., 2003; Yu et al., 2020). Whilst Mfn1 and Mfn2 are anchored on the outer mitochondrial membrane, only Mfn2 is also present on the endoplasmic reticulum (ER), and expression on this site is critical for mitochondrial tethering to ER to enable mitochondrial calcium uptake (De Brito et al., 2008). While the understanding of the exact mechanisms through which mitofusins induce mitochondrial fusion is still incomplete, studies have revealed that mitochondrial OMM is tethered via GTP hydrolysis and subsequent oligomerisation of GTPase binding domains (Brandt et al., 2016; Qi et al., 2016; Cao et al., 2017; Yan et al., 2018); this process facilitates fusion by docking two separate mitochondria and increase membrane contact sites (Figure 1.12).

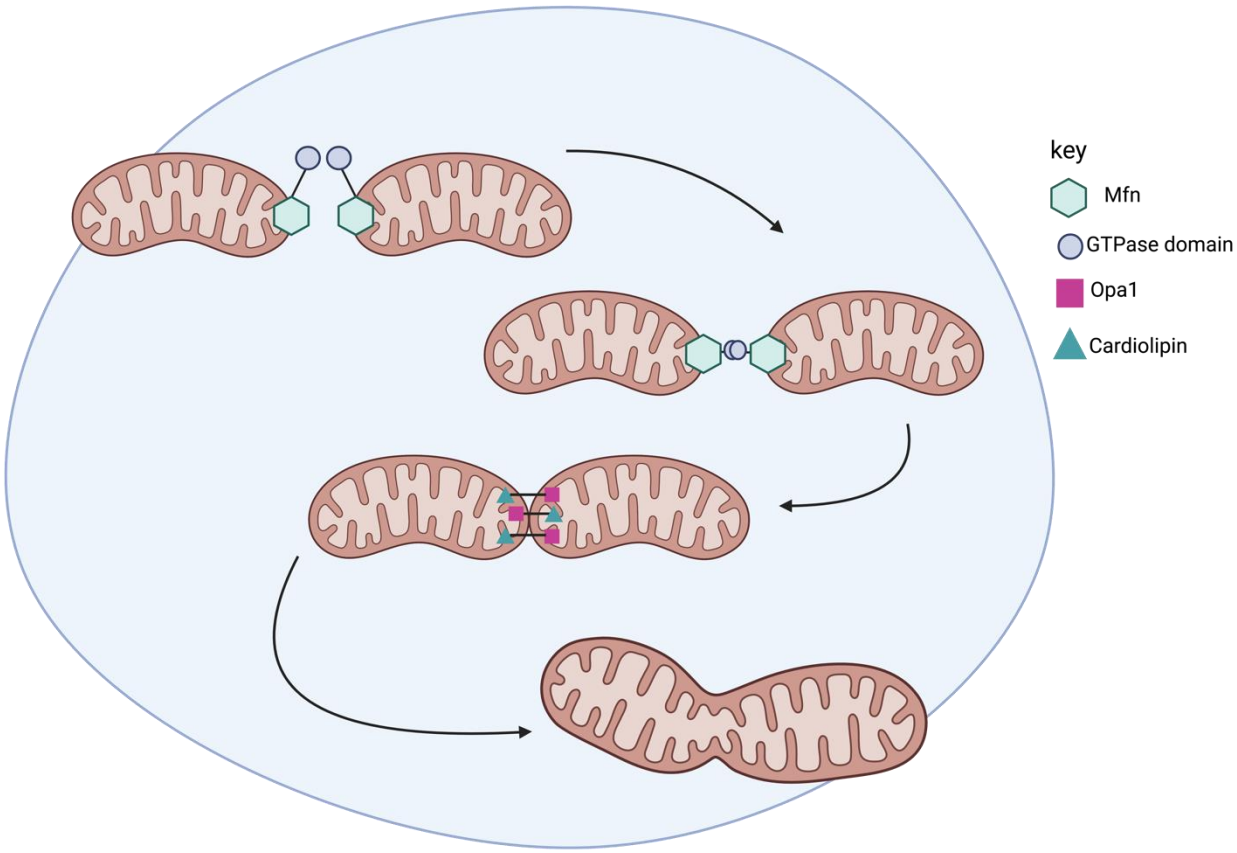

Figure 1. 12 Schematic representation of Mfn and Opa1 driven mitochondrial fusion. *Fusion is initiated by mitochondrial tethering governed by Mfn1-2 and GTP hydrolysis on the OMM and subsequent oligomerization of GTPase binding sites. The IMM fusion is mediated by Opa1 and CL, which fuse via Opa1-dependent GTP hydrolysis. Image created with Biorender.com*

The IMM fusion is mediated by Opa1 and by IMM lipids, including the phosphatidylglycerol lipid cardiolipin (CL). Similarly, to Mitofusin-mediated OMM fusion (Figure 1.12), IMM fusion is dependent upon GTP hydrolysis, however, this mechanism is only partially understood. It has been shown that several isoforms of Opa1 exist, and the co-expression of long and short isoforms appears to be critical for fusion activity (Del Dotto et al., 2017). Interestingly, contrasting data on the role of long isoforms have been produced, with some evidence showing that long isoforms alone have little to no fusion capacity (Song et al., 2007), whilst other authors suggest that long isoforms of Opa1 are required for stress-induced mitochondrial hyperfusion (Tondera et al., 2009). Notably, more recent *in vitro* studies, revealed that long isoforms of Opa1 are sufficient for membrane docking but the presence of both isoforms seems to be required to mediate membrane pore opening in a time-efficient manner (Ge et al., 2020). Interestingly, excess levels of short isoforms of Opa1 appear to inhibit fusion activity (Ge et al., 2020). This data suggests a complex interplay between the two forms of Opa1 and support the idea that both are equally important in different stages of IMM fusion and that the long isoform is associated with adaptive responses against stress.

1.6.2 Mitochondrial fission

Whilst mitochondrial fusion exerts critical functions in the regulation of respiration efficiency, mitochondrial fission (division) serves a critical role in the clearance of damaged mitochondria (mitophagy), reactive oxygen species (ROS) production and mitochondrial depolarisation, and it is mainly favoured by fed state and ageing-induced damage (Gao and Houtkooper, 2014; Rana et al., 2017). Mitochondrial fission is primarily driven by a single cytosolic protein, Dynamin-related protein 1 (Drp1) which belongs to the GTPase protein family. Only 3% of Drp1 is physiologically associated with OMM (Smirnova et al., 2001) and for this reason, Drp1 functionality is highly dependent on several mechanisms, including translocation, protein interaction, GTPase activity and higher-order assembly. Drp1 possesses four domains, including a GTPase domain, a middle domain, a variable domain and a GTPase effector domain (GED) (Figure 1.13). Importantly, GTP hydrolysis leads to Drp1 oligomeric conformational changes, generating the mechanical force required to perform mitochondrial division (Mears et al., 2011; Francy et al., 2015); the middle and GED domains are required to

promote Drp1 self-assembly to facilitate fission (Zhu et al., 2004; Chang and Blackstone, 2010), whilst the variable domain (VD) counteracts the function of middle and GED domain (Francy et al., 2015).

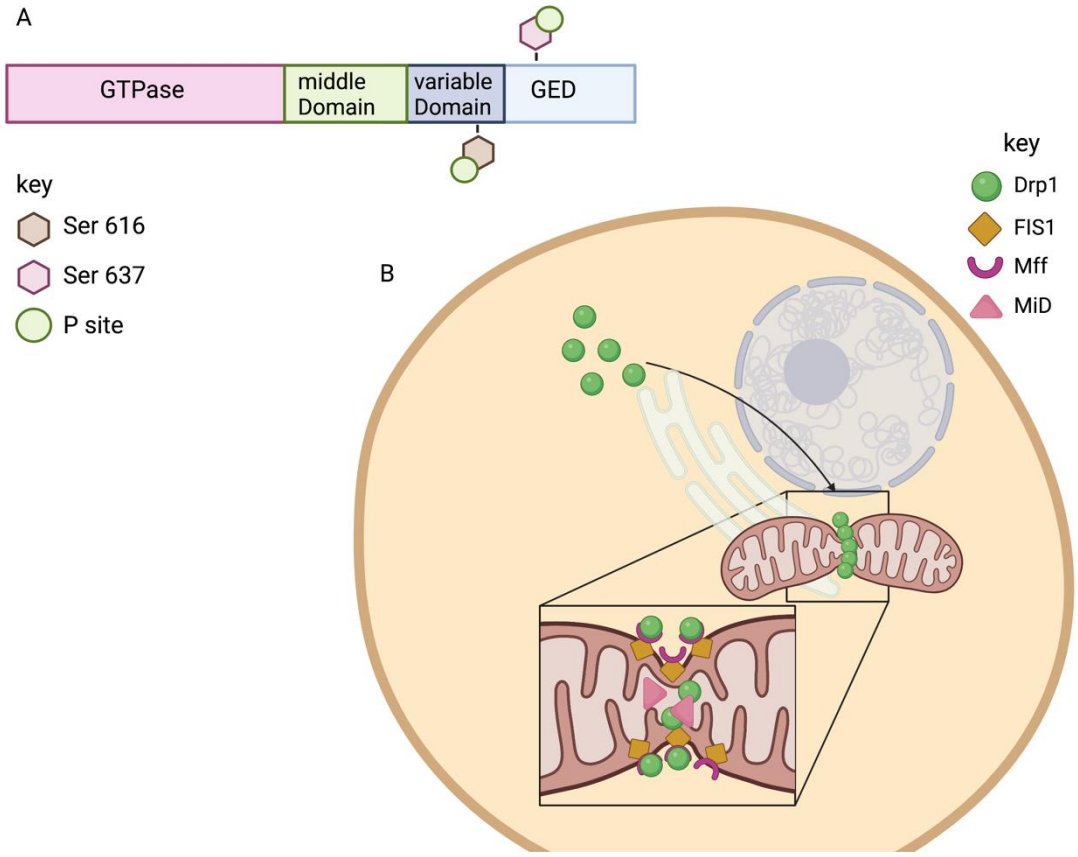

Figure 1.13: Structure of Drp1 and schematic representation of Drp1- driven mitochondrial fission. *Drp1 is composed of a G-domain, a middle and variable domain and a GTPase effector domain (GED). Mitochondrial fission is driven by the dephosphorylation of Ser637, which increases the recruitment of Drp1 to mitochondria. Following mtDNA replication, the ER is employed leading to the initiation of mitochondrial fission, where Drp1 and its adaptor proteins Mff and MiD form a ring-like structure surrounding the mitochondrion. Finally, GTP hydrolysis mediates mitochondrial division, leading to the release of two daughter mitochondria, and Drp1, mff and MiD are disassembled. Figure made with Biorender.com.*

Importantly, Drp1 is regulated by post-translational modifications which include ubiquitination, sumoylation, nitrosylation and phosphorylation. Phosphorylation and dephosphorylation processes are particularly important to drive fission; in fact, Drp1 must translocate to mitochondria to initiate fission, and this predominantly occurs via PKA-

mediated dephosphorylation of Ser637, whilst PKA-dependent Ser637 phosphorylation inhibits mitochondria fission by decreasing GTPase activity and Drp1 mitochondrial recruitment (Chang et al., 2010; Z. Zhang et al., 2016). Notably, Ser637 can be dephosphorylated by calcineurin in a calcium-dependent fashion to drive Drp1 translocation to mitochondria and mitochondria fission (Cereghetti et al., 2008). Phosphorylation of Ser616 can also activate mitochondrial fission by promoting the binding of Drp1 to other fission proteins, namely mitochondrial fission factor (Mff) and Fission 1 (Fis1) as well as to docking proteins mitochondrial dynamic proteins 49 (MiD49) and 51 (MiD51), which are adaptors that link Drp1 and Mff to form a trimeric complex.

Following Drp1 recruitment, the first step of fission occurs in the matrix, where replication of mitochondrial DNA (mtDNA) occurs, triggering the recruitment of the ER; in the second step, Mff and MiDs recruit Drp1 at the ER site (Lewis et al., 2016), where it is assembled into oligomers to envelop the mitochondrion to induce fission via mechanical constriction driven by its GTPase activity (Otera et al., 2013; Kraus and Ryan, 2017). This is evidence of a coordinated, multi-step process occurring in different sub-cellular compartments, to achieve mitochondrial fission. Interestingly, cryo-electron microscopy studies have revealed the mechanism through which Drp1 can exert mechanical constriction on the mitochondrion: (1) GTP binding to Drp1 prompts the formation of mitochondrial-bound linear polymers of Drp1 which are stabilised by continuous interaction with its receptors; (2) the hydrolysis of GTP associates with a reduction in polymers length leading to the formation of closed rings to drive mitochondrial constriction (Kalia et al., 2018) (Figure 1.13).

1.6.3 Mitochondrial dysfunction

Importantly, mitochondrial fusion and fission processes are not merely transient architectural states triggered by nutrients in the environment; in fact, they, are a fundamental part of the mitochondrial life cycle, allowing the execution of critical tasks including quality control mechanisms such as the elimination of damaged material (mitophagy) and reorganisation of mitochondrial content, but also ROS production and management of respiration efficiency, among others (Yapa et al., 2021). It then appears clear how changes in mitochondrial dynamics in response to nutrients can alter mitochondrial health by interfering with basic

mechanisms which are required to support critical quality control functions in these organelles. When the balance between fusion and fission becomes asymmetrical, for example, due to chronic alterations in nutrient availability, it results in mitochondrial dysfunction.

Mitochondrial dysfunction is characterised by alterations in several key mechanisms, namely loss of membrane potential to decrease the production of ATP and decrease respiration, leading to glycolysis-dependent ATP production, which, in turn, increases generation of mitochondrial ROS (Willems et al., 2015; Nagdas and Kashatus, 2017; Jezek et al., 2018). In particular, in presence of excess energy supplies, mitochondria become overloaded with glucose and fatty acids which increases Acetyl-CoA and NADH production, which ultimately drives an increase in electrons capable of crossing the IMM, resulting in excessive ROS and oxidative stress (Bournat and Brown, 2010; Alfadda and Sallam, 2012). Uncontrolled production of ROS has been implicated in mitochondrial membrane, DNA, lipid and protein damage (Glowacki et al., 2013), which could lead to the initiation of mitophagy-to promote cell survival- or apoptotic signalling cascades (Bordi et al., 2017; Martinez-Carreres et al., 2017). In this context, fusion and fission mechanisms are critical for mitochondrial quality control and survival.

For example, stressful conditions, such UV irradiation, and nutrient starvation trigger the stress-induced mitochondrial hyperfusion response. This pro-survival response to stress is associated with an increased ATP production (Tondera et al., 2009), and requires the synchronous recruitment of Mnf1 and Opa2. In fact, studies have shown that upon starvation, mitochondria that elongate were spared from degradation (Gomes et al., 2011 .; Rambold et al., 2011); conversely, Drp1 accumulation in mitochondria is associated with mitochondrial degradation via mitophagy (Pickles et al., 2018).

In obesity, excess nutrient supply generates alterations in the mitochondrial network leading to mitochondrial dysfunction. For example, in Zucker rats, a model of spontaneous obesity, the skeletal muscle exhibits reduced glucose uptake and oxygen consumption and insulin resistance which are associated with a reduced mitochondrial size and Mfn2 expression and a fragmented mitochondrial network (Bach et al., 2003). Moreover, an increase in

mitochondrial fission was observed in the skeletal muscle of *ob/ob* mice, a model of spontaneous genetic obesity, as well as in mice with HFD-induced obesity (Jheng et al., 2012). Mitochondrial dysfunction was also observed in the liver of *db/db* mice, a model of obesity and insulin resistance (Holmström et al., 2012). Interestingly, these data seem to indicate that a shift toward fission is involved in obesity. Moreover, excess nutrients without an increased demand for energy production are linked with higher oxidant production, leading to the development of insulin resistance (Fisher-Wellman and Neufer, 2012). Fission-driven mitophagy leads to increased mitochondrial ROS production, which activates inflammatory responses, resulting in further exacerbation of insulin resistance (Lebrun et al., 2009; Tanti et al., 2012).

1.6.4 Mitochondrial dysfunction in the brain

Maintenance of mitochondrial function is essential to sustain nutrient adaptation mechanisms to support whole-body energy homeostasis; as discussed, alterations in mitochondrial dynamics have been observed during the development of obesity and insulin resistance in several tissues, including the liver, the skeletal muscle, and the adipose tissue. However, the impact of metabolic disorders on mitochondrial dynamics is not limited to peripheral organs, but also extends to the central nervous system; in fact, neurons and glia are cells with high energy requirements, and for this reason, mitochondrial dynamics in these cells are particularly important to maintain adequate energy supplies to support their functions (Zhu et al., 2012; Rose et al., 2020). In the presence of excess energy supplies, mitochondria increase ROS production, leading to oxidative stress (Bournat and Brown, 2010; Alfadda and Sallam, 2012), and studies have shown that DIO results in increased oxidative stress and mitochondrial dysfunction in rat brain (Ma et al., 2014). Moreover, within the hypothalamus, POMC and AgRP neuron activity is profoundly modified by ROS; in particular, ROS alters POMC neuronal control of food intake via the mechanistic target of rapamycin complex 1 mTORC1 mediated mechanism (Haissaguerre et al., 2018).

Obesity is also associated with the development of ER stress, which consists of an imbalance between protein load and protein folding capacity, resulting in incorrectly folded (misfolded) proteins, and this interferes with normal cell function (Thangaraj et al., 2020). Importantly,

associations between increased ER stress and DIO have been described in the hypothalamus in relation to mitochondrial dysfunction (X. Zhang et al., 2008a; Ozcan et al., 2009). Mice with specific deletion of Mfn2 in POMC neurons exhibited alterations in mitochondria-ER contact sites, enhanced ROS production and ER stress which was accompanied by a distinct obese phenotype, due to increased food intake and reduced energy expenditure, associated with decreased BAT activity (Dietrich, Z.W. Liu, et al., 2013; Schneeberger, Marcelo O. Dietrich, et al., 2013). Strikingly, this effect was only present when Mfn2 was knocked out, as POMC Mfn1KO mice had no obvious alteration in body weight and feeding behaviour (Dietrich, Z.W. Liu, et al., 2013; Schneeberger, Marcelo O. Dietrich, et al., 2013). However, Mfn1 deletion in POMC neurons resulted in alterations of mitochondrial architecture and function which led to abnormal glucose homeostasis, due to impaired insulin secretion by the pancreas (Schneeberger et al., 2013), which was caused by enhanced central ROS production (Ramírez et al., 2017). Oppositely to Mfn2 deletion, Drp1KO in hypothalamic POMC neurons enhanced POMC neuronal activation and glucose and leptin sensing in mice; moreover, the deletion of Drp1 led to increased arcuate K_{ATP} channel expression mediated by PPARγ, suggesting that Drp1 KO enhanced glucoprivic responses in POMC neurons by activating PPAR-dependent counter-regulatory responses to hypoglycaemia (Santoro et al., 2017). Interestingly in orexigenic AgRP/NPY neurons fasting is associated with increased mitochondrial fission, whilst in presence of feeding and overnutrition, these cells exhibit a fused-like phenotype via expression of Mfn1/2 (Dietrich et al., 2013). In fact, in presence of HFD, AgRP-specific KO of Mfn1 or Mfn2 in mice is associated with smaller weight gain than control animals, due to reduced WAT accumulation Dietrich et al., 2013). Similarly, in female mice, Mfn1 KO in AgRP neurons had no effect on the metabolic phenotype of regular chow-fed animals, but significantly decreased food intake and body weight following HFD, and decreased AgRP firing rate in both male and female mice (Dietrich et al., 2013). Mfn2 deletion in AgRP neurons led to a decrease in body weight of regular chow-fed female mice, and similarly, HFD-fed mice with AgRP Mfn2 KO gained less weight compared to wild-type control. On a molecular level decreased AgRP firing rate was observed, as well as an increased number of mitochondria (Dietrich et al., 2013). Altogether these data suggest that mitochondrial fusion has opposite effects in anorexigenic POMC and orexigenic AgRP/NPY neurons, namely, Mfn1/2 deletion in POMC neurons is associated with an obese phenotype, whilst Mfn1/2 KO in AgRP neurons protects from DIO. Moreover, these data suggest that mitochondrial dynamics in the

hypothalamus critically regulate whole body energy homeostasis by regulating food intake, WAT accumulation and energy expenditure.

Alterations in mitochondrial dynamics in response to obesity and HFD have also been observed in the DVC. Three days of HFD-feeding were sufficient to induce insulin resistance in the DVC of rats via failure in activation of Erk 1/2 (Filippi et al., 2012), and this led to an inability to regulate food intake and HGP. Importantly, upon overnutrition, mitochondria undergo Drp1-driven mitochondrial fission in this brain region, which suggests a role for mitochondrial dynamics in the genesis of insulin resistance in the DVC (Filippi et al., 2017). In fact, chemical inhibition of Drp1 via DVC infusion of Mitochondrial division inhibitor 1 (MDIVI-1), a Drp1 translocation blocker, reversed the HFD-dependent shift towards mitochondrial fission in the DVC and prevented the development of insulin resistance (Filippi et al., 2017). Conversely, when Drp1 was molecularly activated via delivery of a constitutively active form of Drp1 (Drp1-S637-A) in the DVC of regular chow-fed rats, insulin resistance was induced (Filippi et al., 2017). This evidence revealed a bidirectional role of mitochondrial dynamics in controlling insulin sensitivity in the DVC and suggested that inducing mitochondrial fission in this brain region can recapitulate HFD-dependent insulin insensitivity. Importantly, further studies have demonstrated that HFD-induced Drp1-driven mitochondrial fission in the DVC results in ER stress, and similarly, molecular activation of Drp1 in this brain region also induces ER stress in regular chow-fed rats (Filippi et al., 2017). Moreover, the authors showed a concomitant rise in iNOS in the DVC of HFD-fed rats and regular chow fed animals expressing Drp1-S637-A in their DVC, which together with ER stress, contributes to the genesis of insulin resistance in this brain region (Filippi et al., 2017).

Mitochondrial dynamics in the DVC also control food intake, body weight and WAT abdominal depots in rats; the activation of Drp1 in the NTS increases weight gain and abdominal WAT depots as well as causing hyperphagia in regular chow-fed animals (Patel et al., 2021). Conversely, inhibition of HFD-dependent mitochondrial fission in the NTS of rats was sufficient to observe a decrease in food intake, body weight and abdominal fat depositions. iNOS KO using a ShiRNA (ShiNOS) vector in the DVC of HFD-fed rats prevented HFD-dependent insulin resistance and hyperphagia and led to a decrease in body weight and abdominal WAT compared to ShControl animals (Patel et al., 2021). iNOS is a key signalling molecule in

inflammation, and it associates with HFD and insulin resistance, and these results seem to indicate that iNOS mediates Drp1-driven effects on systemic metabolism and its suppression in the DVC is sufficient to prevent the detrimental systemic effects of HFD.

Interestingly, the authors also showed that the inhibition of mitochondrial fission restricted to GFAP+ astrocytes of the NTS is sufficient to decrease food intake, body weight and ependymal and total abdominal WAT deposition and prevent insulin resistance in this brain region, suggesting that these glial cells are critical in mediating Drp1 effects of systemic metabolic homeostasis (Patel et al., 2021). Whilst this body of evidence clearly shows the involvement of mitochondrial dynamics in the regulation of energy uptake, insulin sensitivity and abdominal WAT accumulation, very little is known about their role in controlling energy expenditure, and more specifically of the BAT.

1.6.5 Mitochondrial dynamics and dysfunction in the brain and the brown adipose tissue

BAT thermogenesis is a critical component of energy homeostasis and it is under the control of the CNS (Morrison et al., 2014). In the hypothalamus, overexpression of Mfn2 in the ARC of DIO mice increased intracapsular BAT surface temperature and expression of thermogenic marker UCP1, accompanied by increased anorexigenic output (Schneeberger et al., 2014b). Moreover, the authors showed that POMC Mfn2 deletion results in reduced energy expenditure, due to decreased BAT activity and reduced expression of the thermogenic gene marker UCP1 in BAT of mice. This evidence suggests that mitochondrial fusion in the hypothalamus controls BAT thermogenesis via anorexigenic POMC neurons. Mitochondrial dynamics in AgRP neurons also critically regulate BAT activation; in particular, Jin et al. (2021) have shown that *Drp1* KO in AgRP neurons in mice affects body temperature, and in particular BAT and rectal temperature were significantly increased in both female and male mice upon Drp1 deletion, compared to control mice. However, no previous studies have investigated the role of mitochondrial dynamics in the DVC in the control of BAT-mediated thermogenesis, for this reason, here we will investigate the role of mitochondrial dynamics in all cells, and specifically in astrocytes of the DVC in the control of BAT energy expenditure.

1.7 Aims and objectives

Obesity is growing at epidemic proportions, and the World Obesity Atlas (2022) has predicted that 1 billion people globally will be living with obesity by 2030, which will represent a significant burden on healthcare systems worldwide. In fact, being obese significantly increases the incidence of a range of non-communicable diseases, including cardiovascular disease, T2DM and cancer; moreover, obesity increases the severity and mortality of communicable diseases, including influenza and COVID-19 (Zhao et al., 2020). Whilst several lines of treatment are available, their success rates are highly variable, and no preventative options exist, showing a need for the development of new therapeutic approaches for the treatment and prevention of obesity. Chronic overnutrition is associated with low-grade chronic inflammation, increased levels of circulating glucose and insulin, increased levels of circulating FA and TG and decreased energy expenditure; all these factors can contribute to the development of insulin resistance, T2DM and liver disease.

The central nervous system is a key centre for the regulation of feeding behaviour and energy expenditure, as it receives metabolic cues from peripheral organs and uses this information to modulate whole-body energy uptake and consumption via peripheral efferents (Imai and Katagiri, 2022). Alterations in the crosstalk between the central nervous system and peripheral organs can lead to disruptions in the systemic metabolism of nutrients and energy expenditure, leading to metabolic disease; importantly, obesity is one such condition in which the whole-body energy metabolism, controlled by the brain-periphery axis, becomes disrupted.

Importantly, previous studies have determined the importance of the DVC in the brainstem in the regulation of metabolic functions, including feeding behaviour (Filippi et al., 2017; Patel et al., 2021), hepatic glucose production (Filippi et al., 2012) and energy expenditure (Cao et al., 2010; Madden and Morrison, 2016). Moreover, it has been shown that alterations in mitochondrial dynamics in the DVC affect the ability of the NTS to control feeding behaviour, abdominal adiposity and insulin sensitivity within this brain region (Filippi et al., 2017; Patel et al., 2021). In particular, three days of HFD were sufficient to induce Drp1-dependent mitochondrial fission and insulin resistance in the NTS of rats, whilst chemical inhibition of

Drp1 in this brain region reversed NTS insulin resistance in HFD-fed animals (Filippi et al., 2017). Moreover, two weeks of HFD induced ER stress and increased inflammation in the NTS of rats (Filippi et al., 2017), as well as hyperphagia and increased body weight and abdominal adiposity (Patel et al., 2021). The inhibition of mitochondrial fission in all cells, and then specifically in astrocytes of the NTS could reverse this process (Patel et al., 2021). Conversely, the activation of mitochondrial fission in the NTS of regular chow-fed rats using the constitutively active form of Drp1 S637-A led to insulin resistance in the NTS, increased body weight and food intake and increased abdominal adiposity in these animals. However, the effects of the modulation of mitochondrial dynamics in the NTS on energy expenditure are not known; in particular, no studies have previously investigated the role of BAT in this context. Here we aim to assess the contribution of BAT in animals expressing the dominant negative form of Drp1 in their NTS, which maintain a leaner phenotype than controls despite HFD. Moreover, we intend to assess whether activating mitochondrial fission in the NTS of regular chow-fed animals is sufficient to blunt the activity of brown adipose tissue. Notably, recent evidence has shown that insulin sensing in astrocytes of the NTS is important to control BAT thermogenesis (Manaserh et al., 2020), and HFD-dependent mitochondrial fission in the NTS leads to insulin resistance in this brain region (Filippi et al., 2017; Patel et al., 2021). Importantly, NTS insulin resistance in HFD-fed rats was prevented by inhibiting Drp1-dependent mitochondrial fission in all cells, and specifically in astrocytes of the NTS (Patel et al., 2021). For this reason, we decided to investigate the contribution of astrocytes in the NTS in the regulation of BAT activation. Lastly, given the involvement of the DVC in the regulation of hepatic glucose production and VLDL-TG secretion (Filippi et al., 2012; Li et al., 2021), we assessed the effect of altering mitochondrial dynamics in the astrocytes of the NTS in the control of hepatic metabolic health, and in particular, of lipid metabolism in this organ. The overarching hypothesis of this work is that inhibiting mitochondrial fission in the NTS of the DVC, and specifically in astrocytes, protects rats from HFD by increasing BAT glucose uptake and preventing hepatic lipid accumulation (Figure 1.14).

Considering these postulates, here we determined the aims to this project:

Aim 1: Investigate whether the inhibition of mitochondrial fission in the NTS of HFD-fed rats affects brown adipose tissue glucose uptake.

Aim 2: Determine whether astrocytes of the NTS are important in the control of brown adipose tissue glucose uptake.

Aim 3: Investigate the phenotypical and molecular changes in BAT related to the inhibition of mitochondrial fission in astrocytes of the NTS.

Aim 3: Investigate whether the activation of mitochondrial fission in the NTS of RC -fed rats affects brown adipose tissue glucose uptake.

Aim 4: Investigate the phenotypical and molecular changes in BAT related to the activation of mitochondrial fission in astrocytes of the NTS.

Aim 5: Assess the impact of mitochondrial dynamics in astrocytes of the NTS in the control of hepatic lipid metabolism.

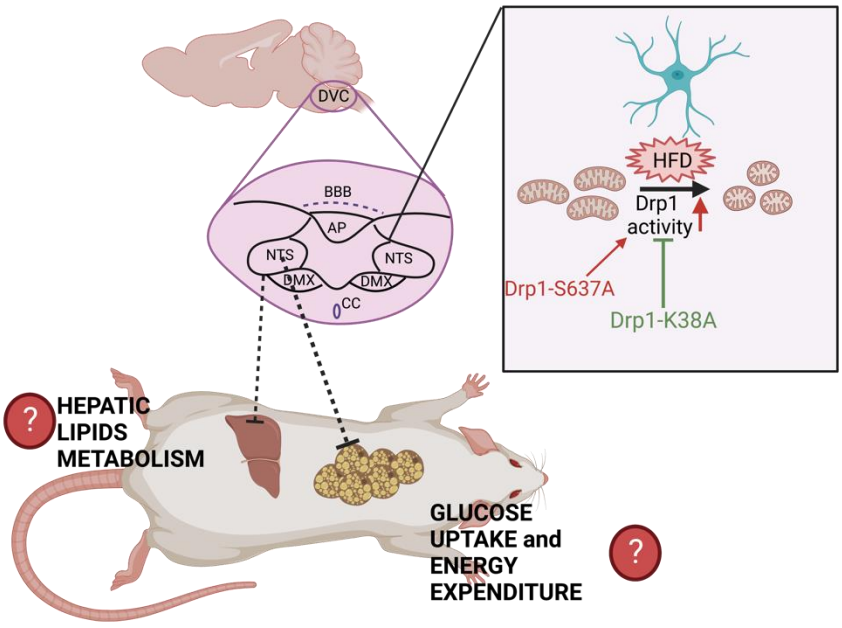

Figure 1.14: Working hypothesis for the thesis. *This work aims to determine whether Inhibiting Drp1-mediated mitochondrial fission in the NTS using the GFAP:Drp1-K38A (green) mutant to target astrocytes can improve BAT glucose uptake to improve energy expenditure and prevent insulin resistance in HFD-fed rats. Further, this study aims to investigate the effect of the mutant on hepatic lipids metabolism. Further, the study aimed to establish whether the activation of mitochondrial fission in astrocytes of the NTS of regular-chow-fed rats, using the constitutively active mutant GFAP:Drp1-S637A (red) can decrease BAT glucose uptake and energy consumption and increase hepatic lipid content.*

Chapter 2: General methods

2.1 Materials

2.1.1 Buffers and reagents

All reagents are prepared in 1 L batches unless specified otherwise.

10X Tris-buffered saline (TBS)

20 mM Tris Base (BP152-1) (w/v), 150 mM Sodium chloride (S/3160/62) (w/v) both (Fisher Bioreagents, ThermoFisher Scientific, Waltham, MA, USA) dissolved in distilled water and pH adjusted to 7.6.

10X Tris-buffered saline with 0.1% Tween20 (TBST)

20mM Tris Base (BP152-1) (w/v), 150 mM Sodium chloride (S/3160/62) (w/v) both (Fisher Bioreagents, ThermoFisher Scientific, Waltham, MA, USA) and 0.1% Tween20 (A1389) (v/v) dissolved in distilled water and pH adjusted to 7.6.

1X Resolving buffer

1.5 M Tris Base (BP152-1) (w/v) (Fisher Bioreagents, ThermoFisher Scientific, Waltham, MA, USA) pH adjusted to 8.6.

1X Stacking buffer

2 M Tris Base (BP152-1) (w/v) (Fisher Bioreagents, ThermoFisher Scientific, Waltham, MA, USA) pH adjusted to 6.8.

Sodium Dodecyl Sulphate -Poly Acrylamide Electrophoresis (SDS-PAGE) Gel

The gel was composed of a stacking portion and a resolving portion. The resolving portion was made up at 8%, 10% or 15% acrylamide according to the size (in kDa) of target proteins (Table 2.1). Both gels consisted of a mixture of 30% acrylamide/bis-acrylamide solution (1610154) (Bio-Rad, Hercules, CA, USA), a denaturant (10% sodium dodecyl sulphate (SDS)) (BP1311-200) (Fisher Bioreagents, ThermoFisher Scientific, Waltham, MA, USA), the respective resolving and stacking buffers (Section 2.1.1), catalyst ammonium persulfate (APS) (17874) (ThermoFisher Scientific, Waltham, MA, USA) and polymeriser tetramethylene diamine (TEMED) (443083G) (VWR, Lutterworth, UK) to allow gel polymerisation, all diluted in distilled water at different proportions (Table 2.1). To prepare the working gel, the resolving solution was made and poured into the glass cassettes and covered with methanol to remove air bubbles and prevent drying out during polymerisation. The stacking solution was then made, and poured on top of the resolving gel, after which methanol was carefully removed. Appropriate combs (Bio-Rad, Hercules, CA, USA) were inserted and the gel left polymerising for 30 minutes. After full polymerisation, the comb was removed, and light suction was applied inside wells with an aspirator to remove any air bubbles or gel debris.

Table 2.1:Composition of resolving and stacking SDS-PAGE gel

8% RESOLVING GEL	**10% RESOLVING GEL**	**15% RESOLVING GEL**	**STACKING GEL**
8% acrylamide 30% (v/v)	10% acrylamide 30% (v/v)	15% acrylamide 30% (v/v)	5% acrylamide 30% (v/v)
0.375 M Tris HCl pH 8.6	0.375 M Tris HCl pH 8.6	0.375 M Tris HCl pH 8.6	0.5 M Tris HCl pH 8.6
1% sodium dodecyl sulphate (SDS)	1% sodium dodecyl sulphate (SDS)	1% sodium dodecyl sulphate (SDS)	1% sodium dodecyl sulphate (SDS)
1% ammonium persulfate (APS)	1% ammonium persulfate (APS)	1% ammonium persulfate (APS)	0.5 % ammonium persulfate (APS)
0.25% tetramethylenediamine (TEMED)	0.25% tetramethylenediamine (TEMED)	0.25% tetramethylenediamine (TEMED)	0.1% tetramethylenediamine (TEMED)
Target size: 50-200 kDa	Target size: 15-100 kDa	Target size: 12-45 kDa	

10X Tris-Glycine SDS running buffer

25 mM Tris Base (BP152-1) (w/v) (Fisher Bioreagents, ThermoFisher Scientific, Waltham, MA, USA), 192 mM Glycine (G8790) (w/v), 0.1% (v/v) Sodium dodecyl sulphate (05030) both (Sigma-Aldrich, Steinheim, Germany).

10X Tris-Glycine SDS transfer buffer

48 mM Tris Base (BP152-1) (w/v) (Fisher Bioreagents, ThermoFisher Scientific, Waltham, MA, USA), 39 mM Glycine (G8790) (w/v) (Sigma-Aldrich, Steinheim, Germany).

5X Laemmli buffer

250 mM Tris hydrochloric acid (HCl) (BP152-1) (w/v) (Fisher Bioreagents, ThermoFisher Scientific, Waltham, MA, USA) pH adjusted to 6.8, 32.5% Glycerol (356350) (v/v) (VWR, Lutterworth, UK), 5% β- Mercaptoethanol (M6250) (v/v), 5% SDS (05030) (v/v) both (Sigma-Aldrich, Steinheim, Germany), 0.1% Bromophenol Blue (A18469) (v/v) (Alfa Aesar, Haverhill, MA, USA).

1X Lysis Buffer

50 mM Tris HCl (BP152-1) (w/v) (Fisher Bioreagents ThermoFisher Scientific, Waltham, MA, USA) pH 7.5, 1 mM Ethylene Glycol-Bis[β-Amino ether]N,N,'N',N -Tetra-Acetic Acid (EGTA) (428570500) (w/v), 1 mM Disodium Ethylene Diamine Tetra-Acetate (EDTA) (EDS) (w/v) both (Sigma-Aldrich, Steinheim, Germany) both pH to 8, 1% octyl phenoxypolethooxylethanol-40 (NP-40) (w/v) (LA60) (Bio basics Amherst, NY, USA), 1 mM Sodium Orthovanadate (S6508) (w/v), 50 mM sodium fluoride (PHR1408) (w/v), 5 mM sodium pyrophosphate (71501) (w/v), 0.27 M sucrose (S7903) (w/v) all (Sigma-Aldrich, Steinheim, Germany). To be added fresh before use 1 mM dithiothreitol (DTT) (R0861) (v/v) and Pierce protease inhibitor tablets as indicated by manufacturer (88266) both (ThermoFisher Scientific, Waltham, MA, USA).

Ponceau Red

Ponceau staining solution (59803S) was used as supplied from manufacturer (Cell Signalling Technology, Danvers, MA, USA).

5% Skimmed Milk Blocking solution

5% Skimmed milk powder (42590) (w/v) (Serva, Heidelberg, Germany) dissolved in 1X TBST.

1X Stripping solution

10X Nitrocellulose stripping buffer (v/v) (J62541) (Alfa Aesar, Ward Hill, MA, USA) diluted in distilled water to 1X concentration.

1% or 4% Agarose Gel with SYBR safe

1 g or 4 g of agarose powder (Fisher Bioreagents, ThermoFisher Scientific, Waltham, MA, USA) was dissolved in 1x commercial tris-borate-EDTA buffer (TBE buffer) (Merck Millipore, Darmstadt, Germany) and heated to fully dissolve the agarose. Once agarose was fully dissolved 0.004% SYBR safe DNA gel stain (Invitrogen, Waltham, MA, USA) was added to the mixture to allow DNA visualisation.

1X Phosphate-buffered saline (PBS)

1 Tablet Phosphate buffered saline (Dulbecco A) (BR0014G) (Oxoid Limited, Basingstoke, UK) per 100 ml of final product at 1X. Composition: sodium chloride (13.7 mM), potassium chloride (2.7 mM), disodium hydrogen phosphate (8.1 mM), potassium dihydrogen phosphate (1.4 mM). Alternatively, ready to use 1X PBS solution (SH30256) (Hyclone, Logan, UT, USA) was employed.

1X Phosphate buffered saline with Triton X (PBST)

1 Tablet Phosphate buffered saline (Dulbecco A) (BR0014G) (Oxoid Limited, Basingstoke, UK) per 100 ml of final product at 1X. Composition: sodium chloride (13.7 mM), potassium chloride (2.7 mM), disodium hydrogen phosphate (8.1 mM), potassium dihydrogen phosphate (1.4 mM) with 0.3% or 0.1% Triton X (X100) (v/v) (Sigma-Aldrich, Steinheim, Germany).

1X Phosphate buffered saline with Tween20 (PBST)

1 Tablet Phosphate buffered saline (Dulbecco A) (BR0014G) (Oxoid Limited, Basingstoke, UK) per 100 ml of final product at 1X. Composition: sodium chloride (13.7 mM), potassium chloride (2.7 mM), disodium hydrogen phosphate (8.1 mM), potassium dihydrogen phosphate (1.4 mM) with 0.5% Tween20 (v/v) (PanReach, AppliChem, Barcellona, Spain).

1% or 5% Bovine Albumin Serum Blocking solution

1% Bovine Albumin Serum pH 7 (A7906) (w/v) (Sigma-Aldrich, Steinheim, Germany) dissolved in 1X PBS.
5% Bovine Albumin Serum pH 7 (A7906) (w/v) (Sigma-Aldrich, Steinheim, Germany) dissolved in 1X TBST or 0.1% PBST (Tween20). Blocking solution prepared in 1X TBST was used for western blotting applications, blocking solution made in 1X PBS or 0.1% PBST for immunohistochemistry applications.

Glycine buffer

1 Tablet Phosphate buffered saline (Dulbecco A) (BR0014G) (Oxoid Limited, Basingstoke, UK) per 100 ml of final product at 1X. Composition: sodium chloride (13.7 mM), potassium chloride (2.7 mM), disodium hydrogen phosphate (8.1 mM), potassium dihydrogen phosphate (1.4 mM) with 0.1% Tween 20 (PanReach, AppliChem, Barcellona, Spain) and 0.3 M Glycine(G8790) (w/v) (Sigma-Aldrich, Steinheim, Germany).

0.4 M Phosphate buffer (PB) pH 7.4

0.31 M Disodium hydrogen orthophosphate anhydrous (w/v), 0.09 M Sodium dihydrogen orthophosphate hydrate (w/v), both (Sigma-Aldrich, Steinheim, Germany) dissolved in distilled water.

0.4 M Phosphate buffer (PB) pH 7.4

0.4 PB pH 7.4 diluted to concentration with distilled water.

4% Paraformaldehyde (PFA)

1.33 M Paraformaldehyde (w/v) (Sigma-Aldrich, Steinheim, Germany) dissolved in 0.1 M PB heated at 60°C and pH to 6.9.

Sucrose solution (15 or 30%)

15% or 30% sucrose (S7903) (w/v) (Sigma-Aldrich, Steinheim, Germany) dissolved in 1X PBS.

Cryoprotectant

30% ethylene glycol (102466) (w/v), 10% Polyvinylpyrrolidone (PVP 40) (w/v), 30% sucrose (S7903) (w/v) all (Sigma-Aldrich, Steinheim, Germany) in 0.1 M PB. Solid components were added in order as follows: PVP-40 dissolved in 0.1 M PB, followed by sucrose and ethylene glycol. 0.1 M PB was then added to final volume.

2.2 Methods

2.2.1 Adenoviral preparation

To allow the manipulation of mitochondria dynamics in the NTS of the brain, an adenoviral system (AV) was used. A plasmid under the cytomegalovirus (CMV), or a glial fibrillary acidic

protein (GFAP) promoter containing either the constitutively active (Drp1S637A) or catalytically inactive (Drp1K38A) forms of Drp1 was delivered to the NTS of male Sprague-Dawley (SD) adult rats. These promoters express either a FLAG-tagged constitutively active form of Dynamin-related protein 1 (Drp1) in the residue S637 to A (Drp1S637A), a FLAG-tagged dominant negative form of Drp1 in the residues K38 to A (Drp1K38A) or a control green fluorescent protein (GFP) (Filippi et al., 2017). Drp1S637A is a mutant phospho-deficient Drp1 which leads to increased Drp1 activity resulting in a shift to mitochondria fission (Chang and Blackstone, 2007); conversely, Drp1K38A lacks the guanosine triphosphate (GTP) binding site that is required for Drp1 to induce mitochondria fission, as Drp1 is a GTPase protein; This prevents mitochondria constriction upon GTPase hydrolysis, ultimately promoting mitochondrial fusion.

Importantly for this thesis, the use of both Drp1 mutants has been largely validated in *in vivo* and *in vitro* studies, confirming their efficacy in manipulating mitochondria dynamics in a range of tissues and cell types respectively- including the brain and its subcellular populations (Filippi et al., 2017; Patel et al., 2021). Drp1S637A was administered to regular chow-fed rats (RC), whilst Drp1K138-A was administered to high fat-fed rats (HFD). Dr Joanne Griffiths in the Filippi lab handled the viral production under specific promoters of interest, as well as amplification and purification steps as described.

2.2.2 Cell culture

HEK293AD cell line

To produce adenoviruses expressing Drp1S637A, Drp1K38A and GFP under the appropriate promoters, HEK293AD cell lines were used. The HEK293AD cell line is a derivative of the human embryonic kidney cell line HEK293, which has been specifically transformed by adenovirus type 5 DNA (Graham et al., 1977). This confers the cells the ability to express trans-acting genes encoded by adenoviral E1 region, allowing the replication of infectious viral particles when transfected with E1-deleted adenoviral vectors. Cells were cultured in the following conditions: 37°C , 5% CO2 in a Isotemp CO2 incubator (Fisher Brand, Loughborough, UK) in high glucose (25 mM) Dulbecco's modified eagle media (DMEM) with GlutaMAX and

Hepes supplements (10564011) (Gibco, ThermoFisher Scientific, Waltham, MA, USA), 10% Foetal Bovine Serum (FBS) (2024-01) (Gibco, ThermoFisher Scientific, Waltham, MA, USA), 1% Penicillin Streptavidin (P0781) (Sigma-Aldrich, Steinheim, Germany), 0.1 mM minimum essential medium (MEM) non-essential amino acids (NEAA) (11140-035) (Gibco, ThermoFisher Scientific, Waltham, MA, USA); this formulation is referred to as complete media.

2.2.3 Viral Amplification

HEK293AD cells were employed for amplification of the adenoviral constructs Drp1-K38A, Drp1-S637A and GFP under different promoters; Cytomegalovirus (CMV) to target all cells or glial fibrillary acidic protein (GFAP) to target astrocytes. On day 0 HEK293AD cells were seeded in 6 cm^3 plates (5 ml/plate) and the DNA prepared for transfection. 10 μg of pAcad59.2.100 backbone was digested with 2 μl of Pac1/10x Smart buffer at 37°C for 2 hours. DNA was purified using Zymo genomic DNA cleaner and concentrator (D4010) following the manufacturer's protocol. Next, 25 mg of pAcad5 shuttle vector containing the gene of interest with 2 μl of Pac1/10x Smart buffer were digested at 37°C for 2 hours and the DNA purified using Zymo genomic DNA cleaner and concentrator (D4010) following the manufacturer's protocol. Finally, the DNA concentration was determined using a Nanodrop (ThermoFisher Scientific, Waltham, MA, USA) and 2 μl of DNA was visualised by agarose gel electrophoresis using 1% agarose gel (section 2.1.1) and DNA products were mixed with 20 % 6x loading purple dye (New England Biolabs, Ipswich, MA, USA) and loaded onto gel alongside with equal volume of 1 kB Plus DNA ladder (New England Biolabs, Ipswich, MA, USA) and run at 100 V for 1h in 1x TBE buffer in a SubCell GT cell horizontal tank powdered by a Powerpack Basic (both Bio-Rad, Hercules, CA, USA) to check digestion.

Viral amplification stage 1

On Day 1 cells were checked and if around 70% confluent 3 ml of fresh media was added. Pac1 digested pAcad59.2.100 backbone vector and pac1 digested pAcad5 shuttle vector

containing the gene of interest (Tube B) and control were combined with Polyjet mixed with DMEM (Tube A) (Table 2.2) and left at room temperature for 10 minutes (Table 2.2). Next, the solution was added dropwise to the cells to perform co-transfection alongside with a Polyjet only control, and the plates were returned to the incubator and checked daily, and 2 ml of fresh media added on Day 3.

Between Day 7 and Day 12 ~ 50% of cells detached, which indicated that the cells were ready to be harvested; harvesting was performed in the media using a cell scraper (-) and the media was collected in a 15 ml falcon tube. The Poly Jet control was also harvested.

Table 2.2: Reagents for viral amplification

	Tube A		Tube B	
	DMEM (µl)	Polyjet (µl)	DMEM (µl)	DNA (µg)
Polyjet control	100	15	100	-
Co-transfection	100	15	100	1 pac1-pAcad59.2.100+ 4 pac1-pAcad5vector

Viral amplification step 2

On Day 0 HEK293AD cells were seeded in 24-wells plate (500 µl /well) and left for several hours to attach, and infected on the same day. Whilst cells were attaching, the virus from the transfected cells and media from the earlier amplification step was prepared for infection. First, 3 freeze-thaw cycles alternating dry ice and 37°C water bath were performed for 10 minutes each, including the polyjet control; next, the virus preps were spun at 3000 rpm at 4°C for 5 minutes in a centrifuge and filtered through a 0.4 µm cell strainer (stage 1-S1 virus). The viruses were then aliquoted in 50 µl into sterile Eppendorf tubes and stored at -80°C until use. When cells were fully attached their media was removed and 500 µl of S1 virus or polyjet control were added per well and the cells incubated at 37°C for 1 hour, and then the virus or polyjet were removed and replaced with 500 µl of fresh media. Cells were monitored daily and 500 µl of media was added on Day 3. On Day 5 or when more than 50% had detached cell

media was harvested, spun at 3000 rpm at 4°C for 5 minutes and filtered through a 0. 4 µm cell strainer (stage 2-S2 virus).

Viral amplification step 3

On Day 0, HEK293AD cells were seeded in 10 cm^3 plates (6 ml /plate) and left several hours to attach. When cells were attached, the media was removed and replaced with 2 ml of S2 virus and incubated for 1 hour at 37°C; the virus was then removed and replaced with 10 ml of fresh media and incubated at 37°C for additional 48-72 hours until all cells had detached. Next, the cell media was harvested, spun at 3000 rpm at 4°C for 5 minutes and filtered through a 0. 4 µm cell strainer (stage 3-S3 virus). This preparation was used for further working stocks and 3,3'-Diaminobenzidine (DAB) assay to determine the viral titre.

2.2.4 Viral Purification

Viruses were purified and concentrated via centrifugation through a 10% Sucrose/TENs solution at 4°C to minimise viral degradation. Falcon tubes were chilled in ice and 10 ml of 10% Sucrose/TENs solution added to each tube, followed by careful overlay of 40 ml of Stage 4 (S4) virus making sure that sucrose and media did not mix. Tubes were then transferred to a prechilled Centrifuge 5804-R (Eppendorf, Hamburg, Germany) (4°C) and spun at 10000 rpm for 4 hours at 4°C. Media and sucrose solution were then removed sequentially and a white pellet was left at the bottom of the tube and residual sucrose was eliminated by inverting the tube onto tissue. 400 µl of sterile PBS were overlayed onto pellets and left at 4°C overnight; the following day the PBS, containing pure virus (PV1) was carefully removed and the earlier passage repeated to collect residual pure virus (PV2). Viral preps were stored at -80°C in 50 µl aliquots until DAB assay titration. (Jiang et al, 2015).

2.2.5 DAB (3,3'-Diaminobenzidine) Assay to determine viral titre

DAB is a derivative of benzene which in immunohistochemical applications is oxidised by hydrogen peroxide in a reaction catalysed by horseradish peroxidase (HRP). When oxidised

DAB forms a brown precipitate corresponding to where HRP contained in the secondary antibody is localised, allowing staining detection under light microscopy. For this assay HEK293AD cells were seeded on the day of the assay in a 24-well plate in 500 µl of media.

Viral preparations were diluted with the viral solution in series ranging 10^{-2} to 10^{-7} VP (viral particles) /ml. To obtain the stock 10^{-2} dilution 5 µl of virus were added to a tube containing 495 µl of media and mixed well and diluted in series in tubes containing 900 µl of media. Cell media was then removed and 100 µl of the viral dilutions added in duplicates, alongside a negative cell control containing only cell media and the positive control containing 100 µl of ßgal virus at 10-4. Cells were incubated for 1 hour and 400 µl of fresh media were added to each well and left incubating for further 48 hours. Media was then replaced with 200µl/well of ice-cold methanol and the plate left at -20°C for 20 minutes to fix the cells, then methanol was removed, and cells washed three times with 200 µl of PBS/well for 5 minutes. Cells were then blocked in 200 µl/well 1% BSA in PBS for one hour at room temperature, followed by 200 µl/well primary Anti-Hexon antibody (1:500) in blocking solution for 1 hour at room temperature. Cells were washed three times with 200 µl of PBS/well for 5 minutes, followed by 200 µl/well secondary anti-mouse HRP (1:1000) in blocking solution for 1 hour at room temperature, followed by a final 5 washes with 200 µl of PBS/well for 5 minutes. Next, the DAB substrate was prepared by adding 2 drops of reagent 1, 4 drops of reagent 2 and 2 drops of reagent 3 from A DAB Substrate KIT (SK-4100) (Vector Labs, Burlingame, CA, USA) to 5 ml of H2O; 200 µl of the substrate were added to each well for 5 minutes, and immediately replaced with 200 µl of H2O. All washing and incubation steps were performed on a shaker (Mixer HC) (Starlab, Milton Keynes, UK). Staining was then visualised at 100x using an Evos imaging system (Invitrogen, Waltham, MA, USA). Positive stained cells (brown) were counted from 5 separate fields in the well with at least 5 positive cells per field. Average numbers of positive stained cells and viral titre (VP/ml) were calculated, and the viral titre was derived from the following formula:

*Viral titre= (average positive cells/field) * (fields/well) * (dilution factor)*

2.2.6 Animal preparation

All experiments were carried out in line with the UK Animals (Scientific Procedures) Act 1986, as well as ethical guidelines set by the University of Leeds Ethical Review Committee. Every effort was made to meet the 3Rs criteria to minimise the number of animals and suffering. Essential 10 ARRIVE guidelines (du Sert et al., 2020) were followed in the conception and execution of the experimental work, those that are relevant to the methods section are summarised in Table 2.3. Nine-week-old wild-type male Sprague-Dawley (SD) rats weighing 285±15 g (Margate, UK; Saint-Germane Nulles, France and Lodigiano, Italy) were used for the experiments. Animals were housed individually in clear cages to minimise isolation distress and kept at 22°C (standard range 20-24°C) on a 12-hour light/dark cycle (06:30-18.30) and either given *ad libitum* access to food and water or pair-fed.

Table 2.3: Criteria for animals used in the experimental designs according to ARRIVE guidelines

GUIDELINE	EXPLANATION AND ELABORATION
Study design • *Groups being compared* • *Experimental unit*	*CMV and GFAP K38-A HFD-fed animals were compared to GFAP:GFP HFD controls.* *GFAP GFP PF HFD-fed animals were compared to GFAP:K38-A HFD ad-libitum controls.* *CMV and GFAP S637A RC-fed animals were compared to GFAP:GFP RC controls.* *As the experimental results were dependent on food intake, animals were single housed to achieve precise measurement of food intake. To ensure animal welfare, transparent cages were used in order for animals to be able to see each other.*
Sample size • *Experimental units allocated to each group* • *Total number of animals used* • *Rationale for sample size*	*Feeding studies:Based on our previous studies we know that the effect size is 1.50, we consider an e power 1-b error probability of 0.8 and an error probability of 0.05. Based on this consideration our power calculation enables us to conclude that 6 rats per group will be enough to get a significant result.* *PET scans: No previous studies within the group were available to produce appropriate power calculations. Wider literature was used to obtain an appropriate sample size, which was set at n=4.*
Inclusion and exclusion criteria	*Exclusion criteria: Recovery after surgery, feeding pattern and experimental conditions are controllable variables. To ensure no evident deviation from the average we ensured that if a rat was not well recovered (at least 90% of his pre-surgical weight) or doesn't eat enough, it is humanely sacrificed and not used for the experiment. After sacrifice animals with no detectable viral expression were excluded from the study regardless of their experimental group.*
Randomisation • *Randomisation method used* • *Strategies used to minimize potential cofounders*	*Animals were allocated to the experimental conditions prior the surgical procedures; matching weight was the criteria used to randomize the animals to the experimental groups. The final aim was to have no significant differences in the mean animals' weight across the experimental groups.* *Experimental groups were divided into rows in the husbandry room to differentiate them and ensure each unit was receiving the correct viral injection and diet.*
Blinding • *Who was aware of group allocations at different stages of the experiment*	*All researchers involved in each of the study were aware of the animals' allocation group prior to surgery and throughout experiment conduction. Once samples were obtained, these were coded and analysed blindly, when possible, by two different members of staff (histology). Allocation was then revealed after the analysis stage of the study. This was not possible during the PET studies as tissues, with the exclusion of qPCR, were collected and analysed from one animal at the time, due to the nature of the study. Two overcome this, two members of the research team reviewed the results following collection.*
Experimental animals	*Male SD rats of 9 weeks of age were used.* *The animals were obtained by Charles Rivers (Margate, UK; Saint-Germane Nulles, France and Lodigiano, Italy).*

Animals were fed either standard laboratory rat diet or high-fat diet (HFD) or control diet. The diet composition for the (1) regular chow diet (3.91 kcal/g) was 8.68% protein, 4.73% fat, 3.48% fibre, 5.38% ash and 58.73% carbohydrate (BK001) (Special Diet Services, Witham, UK), (2) HFD (5.51 kcal/g) was 20.5% protein, 36% fat, 3,5% ash, 36.2% carbohydrate (F3282), (3) control diet (3.93 kcal/g) was 20.5% protein, 7.2% fat, 3.5% ash, 61.6 % carbohydrate (F4031), (Both Datesand group, Stockport, UK). As rodents put directly on HFD are less prone to recover well from surgeries, rats were allocated to the HFD condition 3 days post operatively and then put on HFD; this was also done to ease the transition from RC to HFD (consistency and taste).

2.2.7 Surgical procedures

Rodents were induced anaesthesia by inhalation of Isoflurane (5% v/v with oxygen) (Piramal Critical Care, London, UK) in an anaesthesia induction chamber. Animals were then transferred to an elevated U-stereotactic frame (75-1086) (Harvard Apparatus, Holliston, MA, USA) where anaesthesia was maintained with 1-3% isoflurane mixed with oxygen released from a nose cone. The skull was exposed to reveal the Lambda and Bregma hallmarks-which were measured to determine correct alignment of the skull, and level it, using vertical coordinates of the stereotactic frame if necessary. Once levelled, the occipital suture was measured, and the stereotactic apparatus aligned to implant each animal with a 26-gauge bilateral catheter (C235G-0.8-SPC) (PlasticsOnes, Anjou, Canada) to target the NTS of the DVC. The measurements used to implant the bilateral cannula were as follows: 0.0 mm on the occipital crest, 0.4 mm lateral to the midline and 7.9mm below the surface of the skull as previously described (Barraco et al., 1992; Filippi et al., 2017) (Figure 2.1). The cannula was secured to the skull with superglue followed by Unifast TRAD dental cement (0990607) and liquid buffer (4160803) (GC Europe, Leuven, Belgium). A dummy (C235DC-SPC) (Bilaney, Sevenoaks, UK) was inserted in the cannula to prevent blockages and backflow of injections during viral deliveries (described in section 2.2.4). Finally, to promote rehydration and improve post-operatory recovery, the animals were provided with bilateral intramuscular injections of 5ml saline solution (Hypaclens, SafetyFirstAid, London, UK) and Meloxicam 5mg/ml (Metacam) as analgesic (Boehringer Ingelheim, Bracknell, UK).

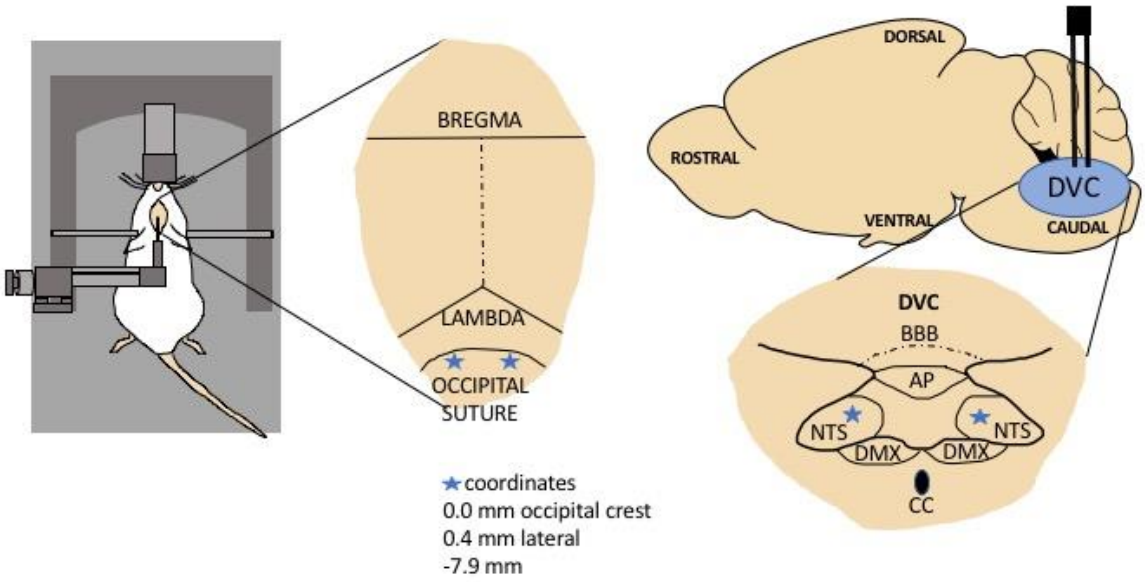

Figure 2.1: Schematic representation of the surgical set-up. *DVC= dorsal vagal complex; BBB= blood brain barrier; AP= area postrema; NTS= nucleus tractus solitarius; DMX= dorsal motor nucleus of the vagus; CC= central canal.*

2.2.8 Injection of adenoviral systems

The viral injections were performed the afternoon following the surgeries, using a 50 μl Hamilton syringe (Hamilton UK LTD, Birmingham UK) attached to polythene lines (0.58 mm inner Ø) with a bilateral cannula inserted onto the other end (C2351-SPC) (Bilaney, Sevenoaks, UK). After this system was assembled it was flushed with double distilled water to eliminate any air bubble from the lines. To prevent the dilution of the viral solution with the water used in the preparatory phase, syringes were pushed to 5 μl and pulled back to 10 μl to create a small air bubble. Subsequently, the virus was loaded into the cannula and pushed out until a small drop formed at the tip of the cannula to ensure the absence of air bubbles which can result in adverse neurological outcomes in the animals. Finally, the dummy cannula was removed, and the cannula attached to the lines inserted to deliver 2.5 μl of virus in each side of the NTS. The lines and the cannula were left attached to the animal for ~ 5 minutes whilst

rats were freely moving in the cage, to prevent backflow and ensure correct delivery of the virus. All throughout this process, animals were monitored to prevent any adverse reaction, such as seizures or strokes. To confirm correct targeting of the NTS, immunofluorescence was performed in 4% PFA fixed brain or western blot analysis was conducted using FLAG or GFP antibodies at the end of the experimental procedures. The FLAG epitope is a hydrophilic short polypeptide chain that fuses to the recombinant proteins of interest, which in our case consisted of either DrpK138A or Drp1-S637A expressed under the respective promoter of interest. By using an antibody against FLAG, we could probe for presence of our mutant proteins in the rat NTS following injection. An anti-GFP antibody was used for the same purpose in control animals.

2.2.9 Feeding studies

Chronic feeding studies

Animals were implanted with bilateral cannulas targeting the NTS via stereotactic surgery on day 0, as described in section 2.2.7. The same day (day 0) or following day (day 1) viral injections containing Drp1S637A, Drp1K38A or GFP control, expressed under CMV or GFAP promoters, were administered. Animals used for section 3.2 and 3.3 received viral injection on day 1, for all other results chapters, animals received injection on day 0. Animals that received the constitutively active form of Drp1 Drp1S637A and matching GFP controls were fed regular chow from day 1 to 15; Animals that received the dominant negative Drp1K38A form of Drp1 and respective GFP controls received regular chow up to day 3 of the study and were then transferred to HFD until the end of the study (day 15 or 17) (Figure 2.2). This transition was necessary as animals subjected to anaesthesia and surgery do not recover as well if directly fed an HFD, and this helps reducing the chances of spurious variables connected to the experimental design. The cumulative weight gain and food intake of the animals was monitored daily at the same time in the second quarter of the light phase (9am-12pm) to obtain consistent data. Rats were sacrificed on day 17 and brain, liver, brown adipose tissue and epididymal, retroperitoneal and visceral white adipose tissues were weighted and collected.

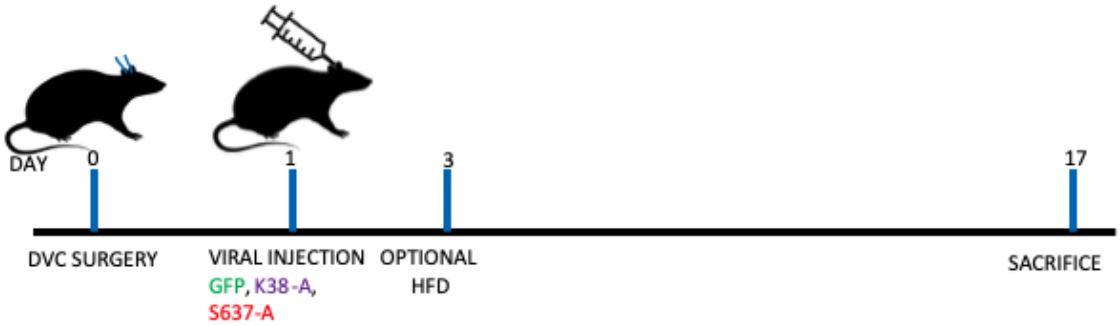

Figure 2.2: Schematic representation of the experimental design for the chronic feeding studies*. On day 0 animals underwent stereotactic surgery to implant a bilateral cannula in the NTS. On day 1 animals received an injection of either GFP control protein, K38A or S637A under CMV or GFAP promoters. K38A animals and GFP controls were fed high-fat diet for 2 weeks starting on day 3. S637A and GFP controls were fed regular chow through the experiment. On day 17 animals were sacrificed and tissues collected.*

Acute feeding studies

At day 9 and 14 of the chronic feeding study the same animals were subjected to acute feeding studies, which consisted of bilateral infusion of 2mU/μl insulin or 0.9% saline VEHICLE in the NTS. Importantly, insulin infusion in the NTS of the brain decreases food intake in animals with conserved NTS insulin sensitivity (Filippi et al., 2017); conversely, HFD is characterised by insulin insensitivity within the NTS, and animals completely lose the ability to reduce food intake in response to insulin infusions to the NTS (Filippi et al., 2017; Patel et al., 2021). On the days of the study, body weight and food intake (to two decimal points) were measured at 10 am, and then animals were fasted whilst access to water was maintained (Figure 2.3). At 4pm the rats were bilaterally infused with 2mU/μl insulin (I-5523) (Sigma-Aldrich, Steinheim, Germany) or 0.9% saline vehicle into the NTS for a total volume of 0.2 μl over 5 minutes, which results in an infusion rate of 0.04μl/minute. Food was returned immediately after infusion, and food intake measured as above, every half an hour for four hours and then at 12, 24 and 36 hours. Body weight was also monitored prior to infusion and post-infusion at four hours then at 12, 24 and 36 hours. To reduce the number of animals employed in this study and provide internal controls for the treatment, we used a within-

subject (repeated measures) experimental design, in which the same animal was subjected to both insulin and vehicle treatment at two different time points -day 9 and day 14. Due to the length of the study, in some cases we observed loss of the cap containing the bilateral cannula; these animals were only used as controls for the acute feeding study as no differences in feeding behaviour could be detected in animals that lost their cap when compared to those that still had it. However, to ensure that these animals would undergo the same levels of stress as those who got the infusion, a mild stress-consisting of handling and mimicking of infusion procedure- was applied.

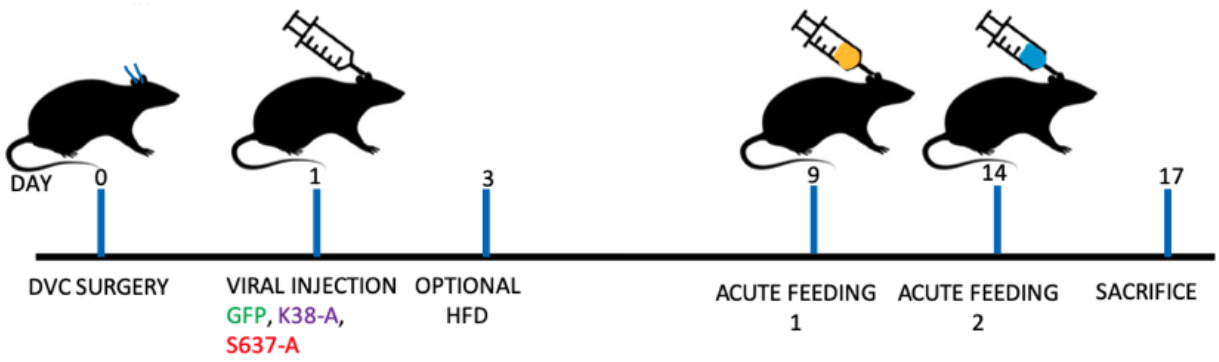

Figure 2.3: Schematic representation of the experimental design for the acute feeding studies. *On day 0 animals underwent stereotactic surgery to implant a bilateral cannula in the NTS. On day 1 animals received an injection of either GFP control protein, K38A or S637A under CMV or GFAP promoters. K38A animals and GFP controls were fed high-fat diet for 2 weeks starting on day 3. S637A and GFP controls were fed regular chow through the experiment. On day 9 and 14 animals were infused in the NTS with 0.2µl of 2 mU/µl of insulin or saline vehicle. Each animal received both infusions, using a within-subjects experimental design. On day 17 animals were sacrificed and tissues collected.*

Pair feeding studies

To determine whether the changes observed in body weight, adipose tissues deposition and insulin sensitivity in the NTS- in response to astrocyte-specific inhibition of mitochondria fission in the NTS- are due to changes in feeding behaviour or sympathetically driven energy expenditure, a pair feeding paradigm was employed.

Animals were implanted with bilateral cannulas targeting the NTS via stereotactic surgery on day 0, as described in section 2.2.7. The same day as surgery (day 0) viral injections containing Drp1K38A or GFP expressed under the GFAP promoter were delivered to the NTS. Animals were put on regular chow up to day 3 (control diet for HFD- F4031 (Datesand group, Stockport, UK) and were then transferred to HFD until the end of the study (day 17).

Control animals (GFAP:K38A) were provided with excess food in the cage hopper at all times. Pair-fed GFAP: GFP rats were given at a fixed time a day (1 hour prior to the beginning of the dark phase) the amount of food that the GFAP:K38A group consumed during the previous experimental day. The cumulative weight gain and food intake of the animals were monitored daily at the same time in the second quarter of the light phase (9am-12pm) to obtain consistent data. Rats were sacrificed on day 17 and brain, liver, brown adipose tissue, plasma and epididymal, retroperitoneal and visceral white adipose tissues were weighted and collected.

2.2.10 Western Blot

Sample collection

To collect tissues of interest, animals were anaesthetised with intraperitoneal (IP) (60mg/kg) Pentobarbital injection to induce terminal anaesthesia. When pedal and pupillary reflexes were completely lost, intrascapular BAT pads were quickly exposed by making a 2-3 cm lateral incision at the base of the neck followed by a 2-3 cm vertical incision along the line of the spinal cord; once the subcutaneous intrascapular WAT pad was exposed a further incision was

performed down to the level of the trapezius muscle and the two BAT pads lifted towards the sides. These were then carefully dissected using a scalpel and Noyes scissors and weighed along with intrascapular subcutaneous white adipose tissue (SCiWAT), epididymal white adipose tissue (epiWAT), intraperitoneal white adipose tissue (ipWAT), visceral (vWAT) and liver and immediately snap frozen in liquid nitrogen. Whole blood was also collected in heparinised eppendorfs, and plasma extracted for further biochemical analysis. In some animals the DVC region was identified using two anatomical hallmarks, (1) the fourth ventricle (2) the fasciculus gracilis and collected following decapitation and immediately snap frozen for immunoblotting or immunohistochemistry analysis to confirm viral expression.

Sample preparation for protein analysis

To harvest tissues, cryopreserved samples were weighed, transferred to 1.5 mL Eppendorf, and immediately placed in dry ice. Lysis buffer was then added to the tube, and the quantity in μl was determined by multiplying the tissue weight by the factor 7.5. The lysis buffer solution contains protease and phosphatase inhibitors allowing both the exposure of membrane and cytoskeleton- bound proteins from other non-soluble parts of the cell, and preservation of proteins at their phosphorylated state. Tissues were homogenised in ice using a handheld homogeniser (Appleton Woods Ltd, Birmingham UK) or a Kimble pellet pestle mortar (DWK Life Sciences, Mainz, Germany) for 30 seconds until the tissue was completely disrupted. Following, samples were centrifuged at 12000 g for 15 minutes at 4°C using a Centrifuge 5804-R (Eppendorf, Hamburg, Germany). Finally, the supernatant was collected using either a 100 μl pipette or a 25-gauge needle when protein extraction was performed on adipose tissues, and the precipitate discarded.

Determining protein concentration using Bradford assay

The Bradford assay is a quantitative technique used to determine the amount of protein present in a sample. This method exploits the binding of a dye-metal complex to proteins kept in acidic conditions in a sample, resulting in dye deprotonation; this interaction causes a stable colorimetric reaction transitioning from brown to green upon protein binding, accompanied by a shift in dye maximum absorbance measured at 660 nm. To perform

Bradford Assay, 10 μl of eight protein standards at concentration ranging 0 μg/ul to 2 μg/ul were loaded in duplicates in a sterile 96-wells plate alongside triplicates of 1:10 dilution of samples of interest; 150 μl of Bradford 660nm protein assay solution (22660) (ThermoFisher Scientific, Waltham, MA, USA) was then added in each well. The plate was then run in a Hidex Sense microplate reader (Hidex, Turku, Finland) to determine protein concentration. Real concentration was then calculated using a standard curve (Table 2.4) and samples were made up to 1 µg/ul with sterile ddH2O and 1 in 5 parts of 5x sample buffer was added to samples and boiled at 90°C for 2-5 minutes to ensure protein denaturation. This is a crucial step as the epitope of interest may be localised within the tri-dimensional conformation of the protein, and denaturation allows the unfolding of the protein and exposure of the protein of interest for antibody detection.

Table 2.3: BSA standards for Bradford protein assay

BSA STANDARDS (μg/ul)
2
1.5
1
0.75
0.5
0.25
0.125
0

Sodium dodecyl sulphate- polyacrylamide gel electrophoresis (SDS-PAGE)

Electrophoresis refers to the migration of charged proteins, when subjected to an electric field of opposite charge, which results in the separation of proteins according to size. The stacking gel has a lower concentration of acrylamide and lower pH to allow proteins to be tightly concentrated before entering the resolving portion of the gel, in which proteins migrate and separate according to their size; this is due to the porous structure of the gel,

which allows small proteins to travel more rapidly than larger proteins. In our experiments, samples were run on an SDS-polyacrylamide gel prepared in 1.0 mm or 1.5 mm hand cast glass cassettes (Bio-Rad, Hercules, CA, USA), with the SDS-PAGE gel composed of a resolving layer pH 8.6, and a stacking layer pH 6.6 (Table 2.1).

After preparation, gels were placed into a Mini-PROTEAN Tetra Cell both (Bio-Rad, Hercules, CA, USA) and 1X running buffer (Section 2.1.1) was added. 1 to 2 µg/µl of proteins per sample were then loaded onto gels together with extra 5µl 2x Laemmli buffer to balance the pH. 5µl of molecular weight marker (Page Ruler Plus) (ThermoFisher Scientific, Waltham, MA, USA) were also loaded onto each gel. Gels were electrophoresed in 1x running buffer (Section 2.1.1) for 30 minutes at 100 V followed by 60 minutes at 130 V (Figure 2.4).

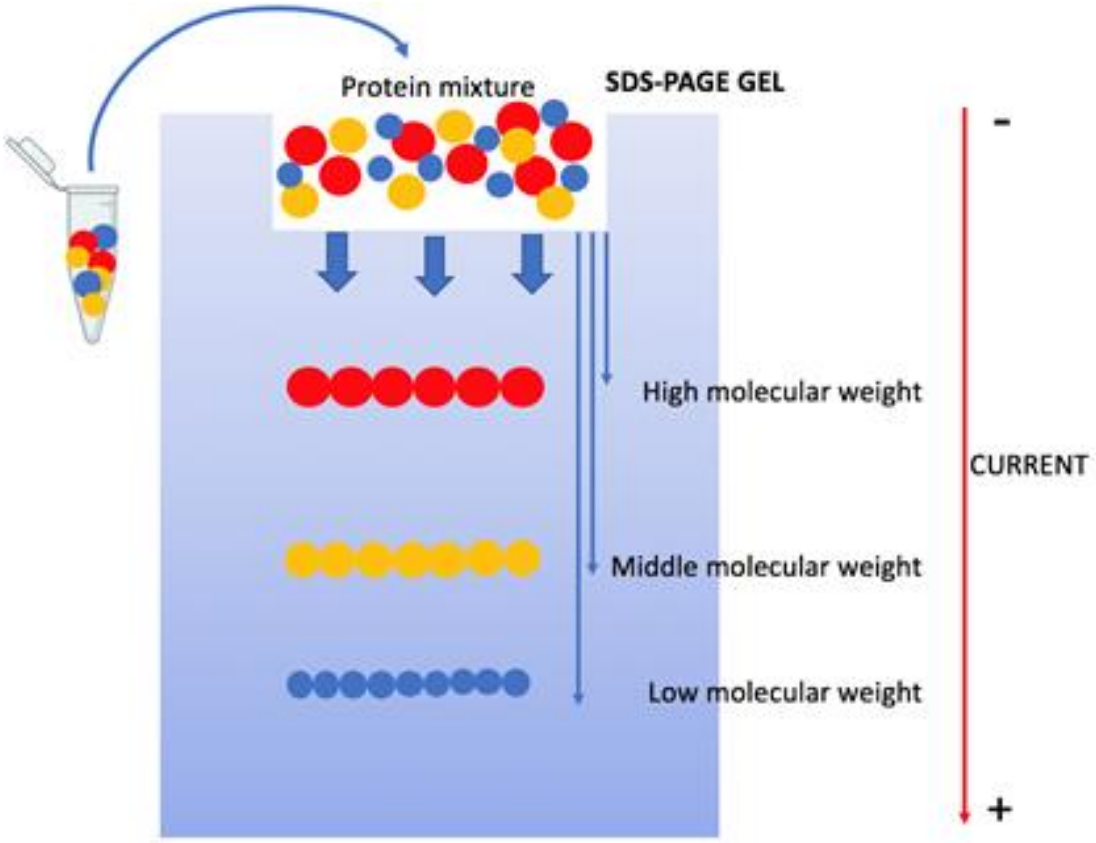

***Figure 2.4: Physical principles of western blotting**. Proteins are charged molecules and electrophoresis separation exploits this property to allow their movement under the influence of an electric field. In a sodium dodecyl sulfate-polyacrylamide gel electrophoresis (SDS-PAGE) proteins are resolved and separated according to their electric properties, which depend on their charge, size, and structure.*

Antibodies

Table 2.4: Primary antibodies for western blotting

Antibody	Application	Blocking	Dilution	Species	Catalogue reference
Anti-FLAG M2	WB	5% BSA	1:3000	Mouse	Sigma F7425-2MG
Anti-GFP	WB	5% BSA	1:20000	Mouse	Aviva Systems Biology OAEA00007

Primary antibodies for Western blotting (WB) were made in 5% BSA (Section 2.1.1) unless otherwise stated in table 2.5.

Table 2.5: Secondary antibodies for western blotting

Donkey Anti-Mouse IgG HRP	WB	1:5000	Donkey	Invitrogen A16011
Donkey Anti-Rabbit IgG HRP	WB	1:5000	Donkey	Invitrogen A16029

Secondary antibodies for WB were made in 5% skimmed milk blocking (Section 2.1.1) solution.

Table 2.6: Total protein labelling reagent

Product	Application	Catalogue reference
No-stain protein labelling reagent	WB (loading control)	Invitrogen A44717

Immunoblotting and analysis

Proteins contained in the gels were transferred onto 0.2µm nitrocellulose membranes (GE Healthcare life Sciences, Marlborough, MA, USA) in a Trans-Blot transfer cell (Bio-Rad, Hercules, CA, USA) in 1x transfer buffer (Section 2.1.1) and proteins transferred at 0.75A for 2h at 4°C. Membranes were then washed twice in distilled water and incubated for 10 minutes in No-Stain working solution (ThermoFisher Scientific, Waltham, MA, USA) then washed three times in distilled water (all at 60 rpm). No-Stain is a protein labelling reagent that allows protein visualization and normalization. After staining, membranes were immediately imaged, and data normalized with an in-built function of the iBright Western Blot Imaging System (ThermoFisher Scientific, Waltham, MA, USA). This approach substituted the use of traditional housekeeping proteins such as GADH or β-Tubulin as it is considered more reliable.

Membranes were then blocked in 5% BSA or 5% milk in TBST for 1h at room temperature. Primary antibodies (Table 2.5) were prepared in blocking solution and incubated either at room temperature for 1h or overnight at 4°C. Membranes were then washed three times in TBST (10min/wash) and incubated for 1h in horse-radish peroxidase (HRP)-conjugated secondary antibodies (table 2.6) at room temperature, followed by five washes in PBST (5min/wash). Proteins were then detected by enhanced chemiluminescence; Clarity Western ECL Substrate Kit (Bio-Rad) was prepared using 1:1 ratio of Peroxide Reagent and Luminol/Enhancer Reagent. The HRP contained in the secondary antibody catalyses luminol oxidation when interacting with the peroxide solution; this moves luminol into an excitatory state, in which light is the emitted as a product of it decaying, allowing protein detection (Figure 2.5). Membranes were imaged within 15 minutes using an iBright Western Blot Imaging System for acquisition and iBright Analysis Software for analysis, both (ThermoFisher Scientific, Waltham, MA, USA.

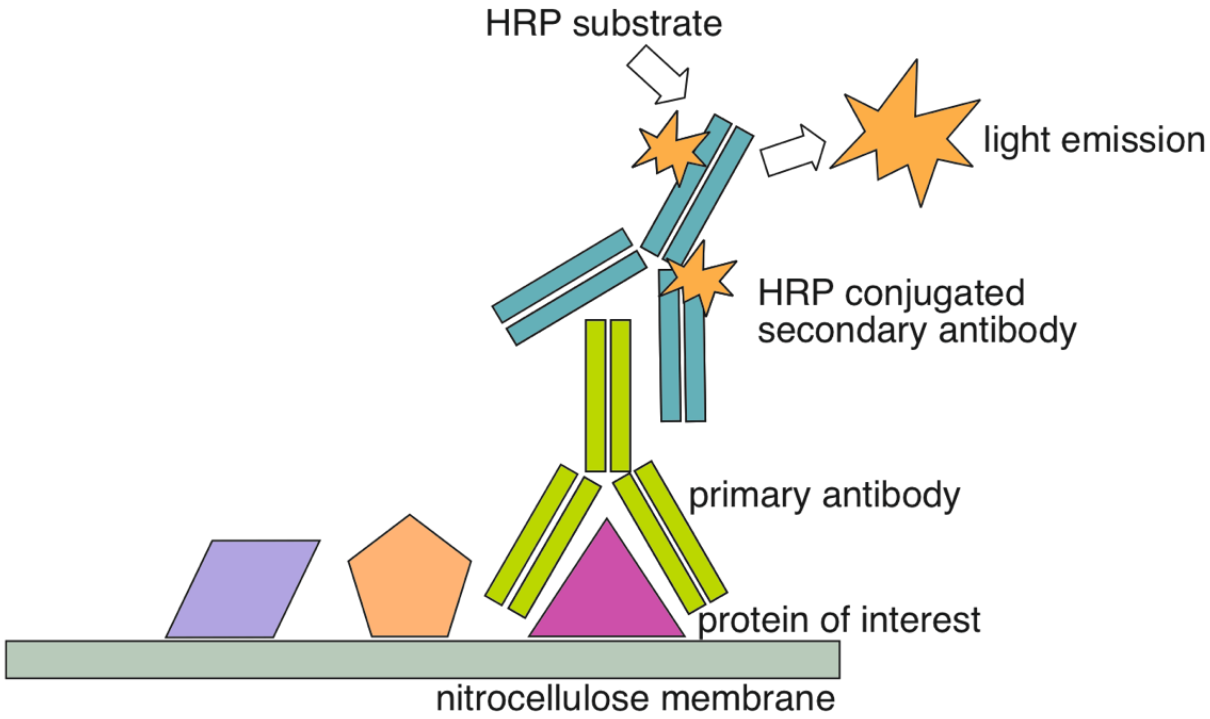

Figure 2.5: Western blot is a technique that allows immobilization of a protein sample on a nitrocellulose or polyvinylidene membranes*. After blocking, the membrane is probed with a primary antibody raised against the target of interest. A horseradish peroxidase (HRP) conjugated secondary antibody is then added to react with the primary antibody. Enhanced chemiluminescent (ECL) reagent is then added. ECL is a luminol-based chemiluminescent substrate that interacts with HRP conjugated to the secondary antibody. HRP catalyses luminol oxidation when interacting with hydrogen peroxide. This results in luminol going into an excitatory state that produces light emission during decay. This signal can then be detected by imaging systems.*

Image analysis

Total protein expression or phosphorylated protein levels were analysed using iBright Analysis Software (ThermoFisher Scientific, Waltham, MA, USA). Briefly, files were exported from the iBright imaging system as G2i files, opened with the iBright Software and ladders were overlapped to ensure correct localisation of the protein bands. Next, protein expression was determined by using a standardised rectangle selection tool which allowed the signal to be obtained from each sample; expression of phosphorylated proteins was normalised to the total protein from the control group. Total proteins were standardised against normalised total protein content detected with the No-Stain (Table 2.7). To be used for quantification, images were required not to be over-saturated. Volumetric data obtained from the analysis were exported to Excel for data management and analysed using GraphPad Prism 9 (GraphPad, San Diego, CA, USA).

2.2.11 RNA extraction

Cryopreserved samples were weighed, and total RNA was extracted from 30 ~50 mg of tissue. Each sample was disrupted and homogenised in a 1.5 ml Eppendorf in 1 ml QIAzol Lysis Reagent (Qiagen, Hilden, Germany) using a handheld tissue homogeniser (Appleton Woods Ltd, Birmingham, UK) for 30s at speeds of 4-5 and the homogenised samples were incubated at room temperature for 5 min to allow full dissociation of nucleoprotein complexes. Next, 200 μl of chloroform was added, and the Eppendorf was vigorously shaken and then left for 2-3 minutes at room temperature for further RNA separation, before being centrifuged at 12,000 g at 4°C for 15 min. Following centrifugation, the sample was separated in aqueous phase (clear), interphase (white) and phenol-chloroform phase (pink). The aqueous phase was collected and transferred to a new 1.5 ml Eppendorf and one volume of 70% ethanol was added and the mixture briefly vortexed. Using a RNeasy Lipid Tissue Mini Kit (Qiagen, Hilden, Germany), up to 700 μl of the prepared sample was transferred to a RNeasy Mini spin column in 2 ml collection tubes, followed by centrifugation at room temperature for 15s at 8000 g and the flow-through discarded. If required, the step was repeated until all the sample was processed. Following this, a DNA digest step was performed, to ensure full digestion of DNA during RNA purification and efficient removal of contaminating genomic DNA; this step is

particularly important as further applications such as q-PCR are highly sensitive to exceedingly small amounts of residual DNA. All buffers described are part of the RNAeasy Lipid Tissue Mini Kit (Qiagen, Hilden, Germany) and their composition is classified. Briefly, 350 μl of RW1 buffer were added to each column, centrifuged for 15s at 8000 g to wash the membrane, and flow-through discarded: following this, 10 μl of DNase I in 70 μl of RDD buffer were added to each column and incubated at room temperature for 15 min, followed by a further wash with RW1 buffer. After DNase digest step 500 μl of RPE buffer was added, centrifuged for 15s at 8000 g two consecutive times; RPE is a mild washing buffer used to remove traces of salt from previous steps. Finally, membranes were further dried by placing the column in a new tube and centrifuged at 14000 g for 1 min, then the column was transferred to a 1.5 collection Eppendorf, 40 μl of RNase-free water was added and centrifuged for 1 min at 8000 g.

Assessment of RNA quality and integrity

RNA integrity analysis was performed using an RNA 6000 Nano Kit and run on a 2100 Bioanalyser, both (Agilent, Santa Clara, CA, USA). This technique determines RNA quality and integrity by electrophoretic separation of the RNA sample. This allows measurement of concentration and eukaryotic ribosomal bands 28S and 18S to assess for potential contamination and degradation of RNA. The bands should appear sharp and free of smears and the 28S band should be approximately twice the intensity of 18S (Figure 2.6); 18S and 28S bands of similar size suggest that degradation has occurred. To perform this assay, all reagents for chip preparation were allowed to equilibrate at room temperature for approximately 30 minutes prior to use. RNA ladder and samples were then heated and denatured in a thermocycler for 2 min at 70°C and immediately cooled in ice. Next, the gel matrix was prepared by adding 550 µl of RNA gel matrix into a spin filter and centrifuged at 1500g for 10 min at room temperature and 1 µl of RNA dye was added to 65 µl of filtered gel, and the mix vortexed and spun at 13000 g for another 10 minutes at room temperature. The RNA chip was then assembled on a chip priming station, both (Agilent, Santa Clara, CA, USA); briefly, 9 µl of gel-dye mix was added in the well marked as ⓖ, the syringe plunger positioned at 1 mL and the chip priming station closed. The plunger was then pressed until held by the clip and after 30 s it was released and plunger brought back to 1 ml. 9 µl of gel-dye mix were

then added in the wells marked G, whilst 5 µl of RNA marker were added in all the other wells. Finally, 1 µl of ladder was added in the ladder well and 1 µl of each RNA sample was added to the sample slots numbered 1 to 12. The chip was then vortexed for 30 s at 2400 rpm and run in the Bioanalyser. Finally, an inbuilt algorithm in the Bioanalyser software (Agilent, Santa Clara, CA, USA) calculated the ribosomal ratio and RNA Integrity Number (RIN) which considers the full electrophoretic trace and scored the RNA quality based on a 1 to 10 scoring system, with 1 being completely degraded and 10 being mostly intact. In our experiments, in accordance with pre-existing literature we imposed a cut off RIN of 8, below which samples were not considered for further gene expression analysis.

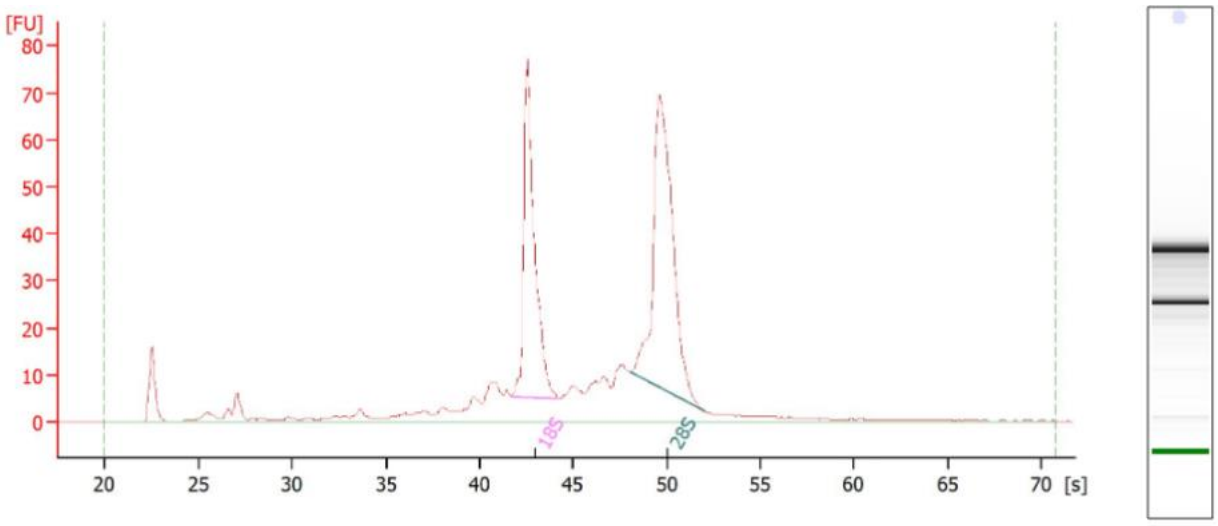

Overall Results for sample 1 : rc1 gfp

RNA Area:	517.3	RNA Integrity Number (RIN):	9 (B.02.07)
RNA Concentration:	1,037 ng/µl	Result Flagging Color:	
rRNA Ratio [28s / 18s]:	1.4	Result Flagging Label:	RIN:9

Fragment table for sample 1 : rc1 gfp

Name	Start Time [s]	End Time [s]	Area	% of total Area
18S	41.72	44.23	108.2	20.9
28S	48.02	52.02	151.4	29.3

***Figure 2.6: Representative output of a sample run on a bioanalyser**. The concentration of eukaryotic ribosomal bands 28S and 18S are measured to assess potential RNA contamination and degradation. The 28S band should appear double the size of the 18S band. The bands should be sharp and free of smears and the RNA integrity score (RIN).*

Assessment of RNA purity

After performing RNA purification and integrity analysis, the concentration of RNA was determined using a Nanodrop 2000C and NanoDrop1000 software (both, ThermoFisher Scientific, Waltham, MA, USA) and the method selected for the analysis was nucleic acid absorbance. Briefly the emission of nucleic acids absorbance maxima at 260 nm and further absorbances at 280 nm and 230 nm were measured, with the latter two being a control for proteins and organic compound contamination, respectively. RNA purity was calculated by determining the ratio of absorbance at 260 nm and 280 nm (260/280), with a ratio of ~2.0 defined as 'pure' RNA. Furthermore, the ratio of absorbance at 260 nm and 230 nm (260/230) was calculated as a second measurement for nucleic acid purity, with acceptable values falling in the range of 2.0-2.2. To perform this step, 1 µl of DNase free water was pipetted onto the Nanodrop pedestal to blank the background, then 1 µl of RNA sample was pipetted for measurement. The values returned were RNA concentration expressed in ng/µl, and RNA purity, assessed by 260/280 and 260/230 ratios. Our cut-off points were imposed at >100 ng/µl, ~ 2 for 260/280 and between 2.0-2.2 for 260/230; the samples failing to show such characteristics were re-purified using RNaeasy MiniElute Clean up Kit (Qiagen, Hilden, Germany) to increase both yield and purity of the RNA (Figure 2.7).

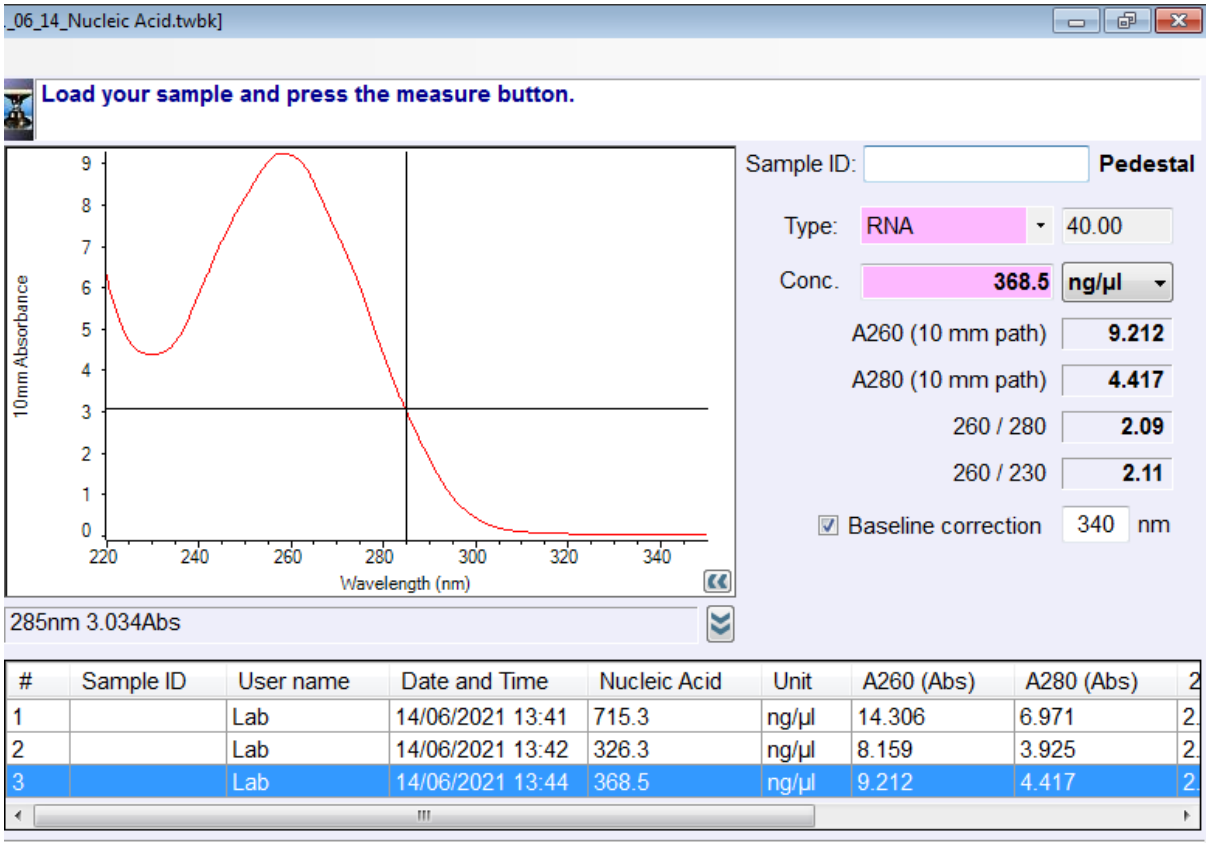

***Figure 2.7**: **Representative spectrophotometric results produced when measuring RNA with a Nanodrop.** The RNA absorbance spectrum indicates high purity as confirmed by the 260/280 ratio, confirming the absence of protein contaminants and the 260/230 ratio, showing the absence of organic contaminants. The RNA concentration is also shown in ng/µl. These results show an example of a sample suitable for downstream applications.*

2.2.12 Reverse transcription polymerase chain reaction

Reverse transcription polymerase chain reaction uses reverse transcriptase enzymes to drive the synthesis of complementary DNA (cDNA) from an RNA template, with the cDNA fragments produced being representative of gene populations in the tissue from which RNA was extracted. The selective amplification of messenger RNA (mRNA), hence isolation of coding regions, was achieved by introducing Oligo-(dT)20 to the reverse transcription reaction, allowing hybridisation to the poly-adenylated (Poly(A) tail found on the 3' terminus of eukaryotic mRNAs; as a result, the synthesised cDNA could be used to study the transcripts of protein-coding genes of a given tissue.

All the reagents stated were obtained from Applied Biosystems (ThermoFisher Scientific, Waltham, MA, USA). Following total RNA extraction, specific amplification of mRNA and first-strand cDNA synthesis was achieved using the Superscript III First-Strand Synthesis System using a PRC-200 Peltier thermal cycler (MJ Research, Reno, Nevada). The first reaction contained 1µl Oligo-(dT)20 (50µM), 1µl dNTPs (10mM) and 11 µl RNA (100ng/µl) for a total volume of 13 µl. The samples were incubated at 65°C for 5 minutes to allow the primer to anneal to the RNA strand and immediately cooled in ice or at 4°C for 1 minute. The second reaction mix containing cDNA synthesis mix consisting of 4µl 5X First-strand buffer, 1µl DTT (0.1M), 1µl RNasin Plus (40 units/µl), 1µl Superscript III (200 units/µl) was added to the RNA/primers mixture and the reaction was performed at 55°C degree for 45 minutes to extend the RT reaction to allow transcription, followed by 70°C for 15 minutes to inactivate the reverse transcriptase enzyme; at the end of the reaction cDNA samples were immediately placed on ice and diluted 1:50 for Real Time Quantitative PCR (RT-qPCR) or stored at -80°C until use.

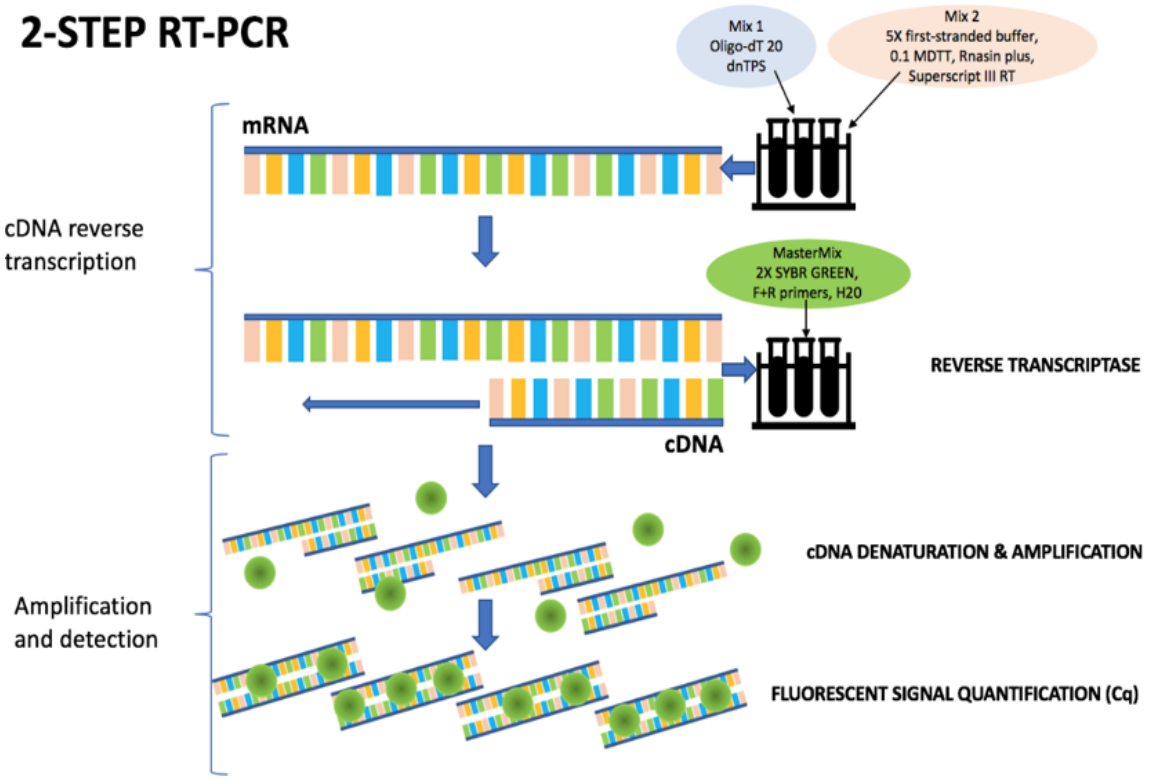

Figure 2.8: Schematic showing a two-step real time quantitative PCR (RT-qPCR). *In a two-steps RT-qPCR, the reverse transcription and PCR steps are carried out as two separate reactions. In the first step cDNA is synthetised from mRNA using oligo-dT_{20} primers by reverse transcription. In the second step the cDNA is denatured, the primers bind to the cDNA template and the resulting cDNA is amplified and detected via fluorescent signal quantification.*

Oligonucleotide primers

Table 2.7: Quantitative polymerase chain reaction (qPCR) primers

Gene ID	NCBI reference	5' to 3' sequence	3' to 5' sequence	Size (bp)
Housekeeping gene				
36B4	NM_022402.2	CGACCTGGAAGTCCAACTAC	ATCTGCTGCATCTGCTTG	109
RPLP0	NM_022402.2	CCCTTCTCCTTCGGGCTGAT	TGAGGCAACAGTCGGGTAGC	165
Target genes				
ACACA	NM_022193.1	AGGAAGATGGTGTCCGCTCTG	GGGGAGATGTGCTGGGTCAT	145
ACADL	NM_012819.2	CCCGATTGCAAAAGCCTACG	ACTGACGATCTGTCTTGCGA	97
ADRB3	NM_013108.2	CCTTCCCAGCTAGCCCTGTT	TGCTAGATCTCCATGGTCCTTCA	109
CD36	NM_031561.2	CAGTGCAGAAACAGTGGTTGTCT	TGACATTTGCAGGTCCATCTATG	137
CD68	NM_001031638.1	TACCTGACCCAGGGTGGAAA	GCTCTGATGTCGGTCCTGTT	159
CIDEA	NM_001170467.1	ACCATCTGTTACAGGCTGTGGGAT	AAAGCTCTTGAAAGGCCCATCTGC	124
CRP	NM_017096.4	TTTGTGCTATCTCCAGAACAGATCA	GCCCGCCAGTTCAAAACAT	77
DDIT3	NM_001109986.1	GAAAGCAGAAACCGGTCCAAT	GGATGAGATATAGGTGCCCCC	151
DGAT 1	NM_053437.2	AAGTATGGCATCCTGGTGGA	CAGGCGCTTCTCAATCTGAA	135

DGAT 2	NM_001012345.1	CCTGGCAAGAACGCAGTCAC	GAGCCCTCCTCAAAGATCACC	137
DNML1	NM_053655.3	GGTGGAATTGGAGATGGTGGTCGA	TTCGTGCAACTGGAACTGGCACA	199
FAS	NM_139194.3	GCAGCTGTTGGTTTGTCCTG	ATTCACTGCAGCCTGAGGTC	117
INSR	NM_017071.2	GGATTATTGTCTCAAAGGGCTGAA	CGTCATACTCACTCTGATTGTGCTT	98
PNPLA2	NM_001108509.2	AGACTGTCTGAGCAGGTGGA	AGTAGCTGACGCTGGCATTC	158
HSL	NM_012859.1	ATGGCAGCCTACCCAGTTAC	TTGGAGAGTACGCTCAGTGG	98
MFN2	NM_130894.4	GGGGCCTACATCCAAGAGA	AAAAAGCCACCTTCATGTGC	166
NFKβ	NM_001276711.1	AATTGCCCCGGCAT	TCCCGTAACCGCGTA	130
PPARG	NM_013124.3	CCTGAAGCTCCAAGAATACC	GATGCTTTATCCCCACAGAC	153
PPARGC1A	NM_031347.1	CAATGAGCCCGCGAACATAT	CAATCCGTCTTCATCCACCG	109
SLC2A1	NM_138827.1	TGGCCAAGGACACACGAATACTGA	TGGAAGAGACAGGAATGGGCGAAT	144
SLC2A4	NM_012751.1	AGGCACCCTCACTACCCTTT	TTTCCTTCCCAACCATTGAG	106
TNFα	NM_012675.3	TCCCAGGTTCTCTTCAAGGGA	GGTGAGGAGCACGTAGTCGG	52
UCP1	NM_012682.2	GCCTCTACGATACGGTCCAA	TGCATTCTGACCTTCACCAC	145

Oligonucleotide primers validation

Primers used for qPCR are presented in Table 2.8. Primers were synthesised by Integrated DNA Technologies (Coralville, IA, USA) based on designed sequences using Primer3 design Package (http://frodo.wi.mit.edu/primer3/.) or sequences obtained from previously designed and published primers in peer-reviewed journals (Appendix 9.2). Primers arrived lyophilised and were reconstituted according to manufacturer instructions at a stock concentration of 100µM. The working dilution, consisting of forward (F) and reverse (R) primers was prepared to a final concentration of 3-5 µM in RNAse-free water.

Primers were selected based on the following parameters: length between 17-22 bp, melting point between 59°C and 65°C and less than 2°C difference in melting temperature between the forward (F) and reverse (R) primers and GC content 45-55%. Further criteria for selection concerned the absence of hairpin loops, dimers, cross-dimers, and repeats. Moreover, primers were verified in silico using PRIMER BLAST (https://www.ncbi.nlm.nih.gov/tools/primer-blast/) to confirm primer specificity and assay optimized using a range of cDNA dilutions (1:50, 1:100, 1:200) obtained from a pool of all samples used in each study. Finally, products of assay optimisation were run on an agarose gel to confirm in silico predicted primer size and absence of products in non-template controls.

Agarose Gel Electrophoresis

PCR products were visualised by agarose gel electrophoresis using 4% agarose gels as described in section 2.1.1. The DNA products were mixed with 20% 6x loading buffer (ThermoFisher Scientific, Waltham, MA, USA) and loaded onto the gel alongside with equal volume of 10-300 bp Ultralow Range DNA ladder (ThermoFisher Scientific, Waltham, MA, USA) and run at 100 V for approximately 1h in 1x TBE buffer in a SubCell GT cell horizontal tank powdered by a Powerpack Basic (both Bio-Rad, Hercules, CA, USA). Once the run was complete, the SYBRSafe-DNA complexes were visualised under UV transilluminator and the relative distances of migration of the DNA products could be determined to confirm primer specificity.

2.2.13 Real Time Quantitative Polymerase Chain Reaction (RT-qPCR)

All the reagents used were obtained from Applied Biosystems (ThermoFisher Scientific, Waltham, MA, USA). The qPCR was performed using SYBR Select Master Mix in clear Microamp optical 96-well reaction plates (ThermoFisher Scientific, Waltham, MA, USA) and the template DNA was amplified in a reaction volume of 12.5 µl using a QuantStudio3 PCR system (ThermoFisher Scientific, Waltham, MA, USA). Reactions contained 1.25 µl of forward+reverse (F+R) oligonucleotide primer mix (10µM) 6.25 µl of 2x SYBR Select Master Mix, 1µl H2O, and 4µl of 1:50 cDNA per sample. Cycling conditions were as follows: 95°C for 10 minutes followed by 39x cycles at 95°C for 15s followed by 55-65°C for 1 minute; the 95°C steps allow the denaturation of the two DNA strands, whilst 55-65°C is the calculated interval of annealing temperature for the primers according to in silico analysis- which allows both F and R primers to bind to the DNA template. Before plate reading, melting curves were analysed by increasing temperature from 65°C to 95°C by 0.5°C at the time for 0.05s; SYBR-based qPCR binds to double-stranded DNA, and melting curves measure the dissociation of dsDNA at high temperatures. Distinct DNA species- resulting from primer binding should result in a single melting curve peak, associated with the production of a single product. If multiple peaks are present this may indicate that the primer is not specific or that primer dimers-the hybridisation of two primer molecules- were formed, which may require adjustments to the annealing temperature (Figure 2.8).

Data quantification- 2ΔΔt method

The Delta Delta Ct method (2ΔΔCt) is a standard method used to calculate the relative fold gene expression of samples after performing real time qPCR (Schmittgen and Livak, 2008). The first step consisted of averaging the triplicate Ct values of replicates from each sample; samples with Ct value triplicates spanning more than 0.5 Ct values from one another, or with reaction efficiency below 95% were excluded from quantification. The next step consisted of calculating the delta Ct value (ΔCt) for each sample using the average CT values previously calculated, using the following formula:

$$\Delta Ct = Ct\ (gene\ of\ interest) - Ct\ (housekeeping\ gene)$$

Next, the control group of samples was used as a calibrator to calculate the delta delta Ct values ($\Delta\Delta$Ct) using the following formula:

$$\Delta\Delta Ct = \Delta Ct \text{ (experimental group)} - \text{average } \Delta Ct \text{ (control group)}$$

Finally, the fold gene expression values were calculated using the following formula:

$$\text{Fold gene expression} = 2^{-\Delta\Delta Ct}$$

Data were processed and stored in Excel and statistical tests conducted as described in the statistical analysis section.

2.2.14 Histochemistry (HC) and Immunohistochemistry (IHC) analyses

Upon termination of studies, non-recovery anaesthesia was induced in the animals with Pentobarbitone Sodium (Pentojet, Animalcare, York, UK) (60mg/kg) and pedal and ocular reflexes checked to ensure surgical plane anaesthesia was reached. The intrascapular BAT pads were then quickly exposed by making a 2-3 cm lateral incision at the base of the neck followed by a 5-6 cm vertical incision along the line of the spinal cord; once the subcutaneous intrascapular WAT pad was exposed, a further incision was performed down to the level of the trapezius muscle and the two BAT pads lifted towards the sides. These were then carefully dissected and weighed alongside with SCiWAT and post fixed with 4% PFA or snap frozen for further investigations. Next, a 5-6 cm lateral incision was made through the abdominal wall just below the level of the rib cage, and the liver collected. Finally, the rib cage was cut on the sides and lifted to expose the heart. A small incision was then performed on the left ventricle of the hearth and a perfusion needle inserted through the cut into the ascending aorta. The heart and the needle were then clamped to prevent leakages and a cut in the right atrium was made to allow and outlet for the saline and 4% PFA solutions during perfusion. The circulatory system was flushed using 0.1 M PB followed by 4% PFA to allow tissue fixation. After approximately 30 minutes, the animal was fully fixed, and brain carefully dissected and left in 4% PFA for 48 hours for post fixation.

Haematoxylin & Eosin Histochemistry (HC) for Brown adipose tissue and liver

Tissues used for routine histochemistry were fixed for 24 h in 4% PFA, washed in PBS and stored in 70% ethanol in distilled water for 48 hours prior to paraffin-embedding. Paraffin embedding, cutting and haematoxylin and eosin (H&E) staining steps were performed by the Division of Pathology at St James University Hospital (Leeds University Teaching Hospitals, UK). Mounted sections were examined in situ by light microscopy using an Evos imaging system (Invitrogen, Waltham, MA, USA) and analysed using an automated cell counting protocol in Image J (National Institute of Health, Bethesda, MD, USA). For brown adipose tissue, the aim of the analysis was to determine the number and size of lipid droplets in a field of view of standardised size by assuming circularity of the droplets. Since white or white-like adipocytes are unilocular and have an average size of 20-150 µm, while brown adipocytes have a total average size of 10-25 µm, 20 µm was set as maximum acceptable size for multilocular brown adipocyte droplets. This value was used, assuming circularity of the droplets, to calculate their maximum area using the classical formula A=$\pi * r^2$ which returned a maximum acceptable value of 17.671 µm^2. Next, images were converted to 16-bit and scale set to µm, after determining the conversion factor (based on magnification and microscope used, images were calibrated to a known distance, for an Evos microscope at 40x 1 µm= 4.55 px); images were then segmented by threshold filtration (32±1%) and made binary using the in-built watershed algorithm- which allowed reconstruction of image details using a 0.25 µm line in regions where information was missing due to droplets with visible lacerations in their membranes. Please note that this process does not distort nor affect the attributes of the images. Finally, the in-built function particle analysis was used with the following factors considered: (1) maximum acceptable area set at 17.671 µm^2, (2) shape factor of 0.25-1 (with 0 indicating a straight line and 1 a perfect circle and (3) no adipocyte was bordering the image frame. From this, two sets of information were returned: (a) average size of adipocytes and (b) number of adipocytes counted. The liver samples were scored using the method described by (Liang et al., 2014) for hepatic lipid infiltration, and anatomical features compared with liver TG levels for quantitative analysis. Image analysis was carried out for a minimum of five separate images for 4-7 animals per experimental group, and the data obtained exported to an excel spread sheet for storage.

Fluorescent Immunohistochemistry (FIHC)

Table 2.8: Primary antibodies for fluorescent immunohistochemistry (FIHC)

Antibody	Application	Blocking	Dilution	Species	Catalogue reference
Anti-FLAG M2	FIHC	% BSA	1:500	Mouse	Sigma F7425-2MG
Anti-glial fibrillary acidic protein (GFAP)	FIHC	% BSA	1:1000	Rabbit	Abcam ab7260
Anti-green fluorescent protein (GFP)	FIHC	% BSA	1:1000	Mouse	Protein Tech 66002-1-lg
Anti-Hex ribonucleotide binding protein-3 (NeuN)	FIHC	% BSA	1:3000	Guinea Pig	Millipore ABN90
Anti-Tyrosine Hydroxylase (TH)	FIHC	% BSA	1:250	Sheep	Abcam ab113

Immunohistochemistry Primary antibodies for fluorescent immunohistochemistry on brain and brown adipose tissue were made in glycine buffer (Section 2.1.1) to reduce background.

Table 2.9: Secondary Antibodies

Antibody	Application	Dilution	Species	Catalogue reference
Donkey Anti-Mouse IgG (H+L) Biotin Conjugate	IF	1:250	Donkey	Invitrogen 16021
Donkey Anti-Rabbit IgG (H+L) Biotin Conjugate	IF	1:250	Donkey	Invitrogen A16039
Donkey Anti-Sheep IgG (H+L) Biotin Conjugate	IF	1:250	Donkey	Invitrogen A16045
Donkey Anti-Guinea Pig IgG (H+L) Biotin Conjugate	IF	1:250	Donkey	Fitzgerald 43R-ID014bt

Alexa Fluor Donkey Anti-Goat IgG |(H+L) 488	IF	1:1000	Donkey	Invitrogen A11055
Alexa Fluor Goat Anti-Guinea Pig IgG |(H+L) 488	IF	1:1000	Donkey	Invitrogen A11073
Alexa Fluor Donkey Anti-Mouse IgG |(H+L) 488	IF	1:1000	Donkey	Biotium CF488A
Alexa Fluor Donkey Anti-Mouse IgG |(H+L) 555	IF	1:1000	Donkey	Invitrogen A32773
Alexa Fluor Donkey Anti-Rabbit IgG |(H+L) 555	IF	1:1000	Donkey	Invitrogen A31572
Alexa Fluor Donkey Anti-Sheep IgG |(H+L) 488	IF	1:1000	Donkey	Invitrogen A11015
Alexa Fluor Donkey Anti-Sheep IgG |(H+L) 555	IF	1:1000	Donkey	Invitrogen A21436
Streptavidin Alexa Fluor Donkey conjugate 555	IF	1:1000	Donkey	Invitrogen S21381
Streptavidin Alexa Fluor Donkey conjugate 647	IF	1:1000	Donkey	Invitrogen S21374

Immunohistochemistry Secondary antibodies for fluorescent immunohistochemistry on brain and brown adipose tissue were made in 1X PBS (Section 2.1.1).

Fluorescent Immunohistochemistry (FIHC) for viral confirmation and cell characterisation

Immunohistochemistry is a technique used to detect antigens of interest in a tissue section via antigen-specific antibody binding which is then visualised by light or fluorescent microscopy. As previously described, after terminal anaesthesia animals were fixed with 4% PFA and brains were dissected and left in 4% PFA for 48 hours to fix to prevent cellular protein breakdown and to preserve the tissue cytoarchitecture via aldehyde protein cross-link formation. Next, tissues were placed in 15% sucrose and 30% sucrose for at least 3 days in

each solution (or until the tissue sunk to the bottom of the falcon tube) to preserve the tissue integrity prior to cryoembedding.

Following, the brainstem was isolated, while single use plastic moulds were placed in dry ice and half-filled with frozen section compound FSC22 Clear (Leica Biosystems, Richmond, IL, USA). Once the compound started to solidify, the tissue specimen was placed in the mould in the desired orientation and covered with FSC22 Clear. After overnight freezing at -80 °C, samples were transferred to the pre-chilled chamber (-25°C) of a cryostat CM1800 (Leica Biosystems, Richmond, IL, USA), then sections cut at 40 µm and transferred in a 24-well plate containing cryoprotectant. The appropriate anatomical sections containing the DVC were selected and prepared for fluorescent immunohistochemistry. Sections were blocked in 10% donkey serum in 0.1% PBST for 1 hour at room temperature, following by appropriate primary antibody (FLAG or GFP) at working concentration (Table 2.9) made in 0.1% PBST to allow tissue permabilisation, and incubated overnight at 4°C on an orbital shaker. After primary incubation, sections were washed three times in PBS and appropriate secondary antibody was added (Table 2.10) and incubation occurred on a shaker for 2 hours in the dark at room temperature. Sections were then washed five times at room temperature and the protocol repeated to label neurons (NeuN) or astrocytes (GFAP). Finally, sections were mounted on glass slides using a fine paint brush and left to air dry then sealed with coverslips using Vectashield plus 4'6-diamidino-2-phenylindole (DAPI) (H-1200) (Vector laboratories, Burlingame, CA, USA) and nail polish around the edges.

Sections were then imaged using a Zeiss LSM880 upright confocal microscope (Carl Zeiss, Oberkochen, Germany) at 40x and 63x magnification for representative images. The Zen software (Carl Zeiss, Oberkochen, Germany) tile scan function was used to image the entire DVC area and processed as a single plane image.

Tyrosine Hydroxylase Fluorescent Immunohistochemistry

Brown adipose tissue samples for FIHC were quickly dissected as previously described and placed in 4% PFA for 24 hours and prepared for cryoembedding as described in the previous paragraph. When the cryomatrix was completely solidified, samples were transferred to the

pre-chilled chamber (-25°C) of a cryostat CM1800 (Leica Biosystems, Richmond, IL, USA), with sections cut at 5 µm and collected in sets of 4-5 onto Superfrost Plus microscope slides (ThermoFisher Scientific, Waltham, MA, USA). Once cut, they were either stored at -80°C or equilibrated at room temperature for 10-15 minutes to increase adherence and prepare for FIHC. As tyrosine hydroxylase (TH) is mainly present in the cytosol, sections were subjected to a permeabilisation step to improve antibody access to cytosolic antigens via a 10 min incubation in PBS with 0.5% Tween20. Next, to prevent unspecific binding, sections were blocked in 1% BSA in 0.3 M glycine buffer with 10% Donkey Serum (D9663) (Sigma-Aldrich, Steinheim, Germany) for 1 hour at room temperature. Blocking solution was then gently aspirated, and TH antibody (1:250) (table 2.9) in 0.1% PBST was added. Sections were statically incubated overnight at 4°C to allow antibody binding. After primary antibody incubation, sections were washed three times in PBS to remove excess primary antibody and statically incubated with donkey-anti-sheep 555 secondary antibody (1:1000) (Invitrogen A21436) (table 2.10) made up in PBS for 2 hours at room temperature in the dark. Sections were then washed 5 times, coverslipped using Vectashield plus 4'6-diamidino-2-phenylindole (DAPI) (H-1200) (Vector laboratories, Burlingame, CA, USA) and sealed with nail polish around the edges. Sections were visualised at 20x magnification with an Evos imaging system (Invitrogen, Waltham, MA, USA) for quantification purposes. Representative images were obtained at 20x magnification using a Zeiss LSM880 upright confocal microscope (Carl Zeiss, Oberkochen, Germany). For analysis purposes 4-5 images from n=4 animals per group were selected and TH quantified using a threshold function, and further confirmed with particle analysis to isolate TH pools in nerve terminals within BAT. Both analyses were carried out using Image J (National Institute of Health, Bethesda, MD, USA).

2.2.15 Triglyceride assay

TG are neutral esters formed by one molecule of glycerol and three fatty acids (which are synthesised in the adipose tissue and liver) and can be secreted in the form of VLDL in the blood. TG can be broken down in fatty acids and glycerol to act as energy substrates- high levels of TG in the liver and plasma, however, can result in steatosis and fatty liver disease and hypertriglyceridemia, respectively, both of which are associated with HFD and obesity.

To measure plasma and liver TG, an enzymatic technique was used to covert TG in FA and glycerol, with glycerol being subsequently oxidised to generate a colorimetric reaction, which could be detected at λ=570 nm.

All reagents were included in a commercial TG assay kit (Ab65336) (Abcam, Cambridge, UK) and after brief centrifugation and equilibration at room temperature were prepared for use in accordance with supplier indications.TG standard at 0.2 mM was prepared fresh before use and standard curve dilutions prepared as described in Table 2.11.

Table 2.10: Triglyceride standards prepared at 0.2mM

Standard	Volume of TG standard (µl)	Assay buffer	Final volume of standard in well (µl)	End TG concentration in well (nmol/well)
1	0	150	50	0
2	30	120	50	2
3	60	90	50	4
4	90	60	50	6
5	120	30	50	8
6	150	0	50	10

Liver samples were processed prior to testing; liver was harvested and approximately 100 mg dissected and washed in cold 1x PBS. Samples were then re-suspended and homogenised in 5% NP-40 buffer and homogenised using a handheld homogeniser (Appleton Woods Ltd, Birmingham UK). Samples were slowly heated to 80°C in a water bath for 5 minutes or until the NP-40 solution became cloudy and brought back to room temperature prior to a further heating passage to ensure maximum TG solubilisation. Samples were then centrifuged for 2 minutes at 14000g to remove any insoluble material, and the supernatant collected and diluted 30-fold with distilled water. Plasma samples were tested directly.

Reaction was set up in a clear 96-well plate and each reaction well contained 50 µl of standard dilutions or sample (1/20 plasma, 1/30 liver) adjusted to volume with supplied assay buffer. Next, 2 µl of lipase enzyme were added into all standard and sample wells, mixed and the reaction incubated for 20 minutes at room temperature in constant agitation. This step is to promote the conversion of TG in FA and glycerol. Reaction mix was then prepared (Table 2.12) using the following calculation:

*Reaction mix volume=X µl component * (number reactions+1)*

Table 2.11:Triglyceride assay reaction mix

Component	Reaction mix (µl)
Assay Buffer	46
TG Probe	2
Enzyme Mix	2

50 µl of reaction mix were added to each reaction and incubated at room temperature in the dark for 60 minutes. Output was immediately measured using a microplate reader at λ=570 nm.

Calculations to obtain triglyceride concentration

To calculate the TG concentration, the duplicates for each standard and samples were averaged and the mean absorbance value of the blank (standard 1) was subtracted from all standard and sample readings to correct absorbance. Corrected absorbance values of standards were then plotted on Excel (Microsoft, Redmond, WA, USA) and the best fit curve was drawn to construct the standard curve and the trend-line equation was calculated. Finally, *TG concentrations* in samples were calculated using the following formula:

$$TG\ Concentration = \left(\frac{B}{V}\right) * D$$

Where *B* is the amount of TG in the sample calculated from the standard curve in nmol, *V* is the amount of sample volume added in the sample well in µl and *D* is the sample dilution factor.

2.2.16 Fatty Acid Assay

Background and Assay

FA are a main source of lipids in plasma after being hydrolysed from TG stores in white adipocytes and transported in the circulation by plasmatic albumin to provide energy during fasting periods (Lafontan and Langin, 2009). Importantly, elevated plasma FA have been implicated in obesity, insulin resistance and systemic low-grade inflammation (Boden, 2008). To measure plasma FA, an enzyme method is used to convert FA into their Coenzyme A (CoA) derivatives, which after oxidation can be quantified in a colorimetric reaction at λ=570 nm. All reagents were included in a commercial free fatty acid assay kit (Ab65341) (Abcam, Cambridge, UK) and after brief centrifugation and equilibration at room temperature, were prepared for use in accordance with supplier indications. Palmitic acid standard at 1 nmol/µl was prepared fresh before use and standard curve dilutions prepared as described in Table 2.13.

Table 2.12: Palmitic Acid standards prepared at 1 nmol/ µl

Standard	Volume of palmitic acid standard (µl)	Assay buffer	Final volume of standard in well (µl)	End palmitic acid concentration in well (nmol/well)
1	0	150	50	0
2	6	144	50	2
3	12	138	50	4
4	18	132	50	6
5	24	126	50	8
6	30	120	50	10

Reaction was set up in a clear 96-well plate and each reaction well contained 50 µl of standard dilutions or sample (1/2) adjusted to volume with supplied Assay buffer. Next, 2 µl of ACS reagent were added into all standard and sample wells, mixed and the reaction incubated for 30 minutes at 37°C. Reaction mix was then prepared (Table 2.14) using the following calculation:

*Reaction mix volume=X µl component * (number reactions+1)*

Table 2.13: FA assay reaction mix

Component	Reaction mix (µl)
Assay Buffer	44
Fatty Acid Probe	2
Enzyme Mix	2
Enhancer	2

50 µl of reaction mix were added to each reaction and incubated at 37°C in the dark for 30 minutes. Output was immediately measured using a microplate reader at λ=570 nm.

Calculations to obtain FA concentration

To calculate FA concentration, the duplicates for each standard and samples were averaged and the mean absorbance value of the blank (standard 1) was subtracted from all standard and sample readings to correct absorbance. Corrected absorbance values of standards were then plotted on Excel (Microsoft, Redmond, WA, USA) and the best fit curve was drawn to construct the standard curve and the trendline equation was calculated. Finally, FA concentrations in samples were calculated using the following formula:

$$Fatty\ Acid\ Concentration = \left(\frac{Fa}{Sv}\right) * D$$

Where *Fa* is the amount of fatty acids in the sample calculated from the standard curve in nmol, *Sv* is the amount of sample volume added in the sample well in µl and *D* is the sample dilution factor.

2.2.17 Plasma Insulin Sandwich Enzyme-linked Immunosorbent Low Range Assay (ELISA) (0.1-6.4 ng/ml)

Enzyme-Linked Immunosorbent Assay (ELISA) is a method to detect the presence of specific target antigens or antibodies in a sample. ELISA is an immunoassay and relies on antibodies to detect targets via highly specific antibody-antigen interactions; to achieve this the antigen was immobilised on a solid surface (e.g., using capture antibodies coated plates) and then complexed with a specific enzyme-conjugated antibody to allow detection (Figure 2.9).

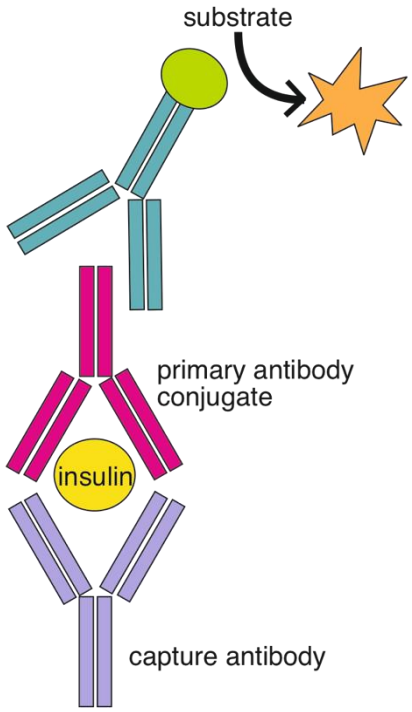

***Figure 2.9: Principles of sandwich ELISA**. Enzyme-linked immunosorbent assay (ELISA) is a plate-based assay technique used to detect specific antigens from a sample. In a sandwich ELISA, the antibody is immobilized on the solid surface of the plate. After being incubated with a specific antigen, a primary conjugated antibody is added to the reaction. For detection, the reaction is incubated with a substrate that interacts with the primary conjugate to release a product measured in a plate reader.*

To measure plasma insulin a commercial Ultrasensitive Rat Insulin ELISA Kit low range assay (0.1-6.4 ng/ml) (Crystal Chem, Elk Grove, IL, USA) was used. All supplied reagents were equilibrated at room temperature before use and rat insulin standard reconstituted with 100 µl of distilled H2O to the final stock concentration of 25.6 ng/ml of rat insulin and carefully inverted until fully dissolved.

To prepare the insulin standards, 50 µl of the 25.6 ng/ml stock rat insulin were diluted with 150 µl of supplied sample diluent to 6.4 ng/ml. Next, 50 µl of sample diluent was added to 6 Eppendorfs labelled 0.1, 0.2, 0.4, 0.8, 1.6, 3.2 ng/ml and a serial dilution was performed by dispensing 50 µl of 6.4 ng/ml standard into the 3.2 ng/ml tube and repeating the dilution scheme for the rest of the tubes. For the blank standard 50 µl of sample diluent was added to the tube labelled 0 ng/ml (Figure 2.10).

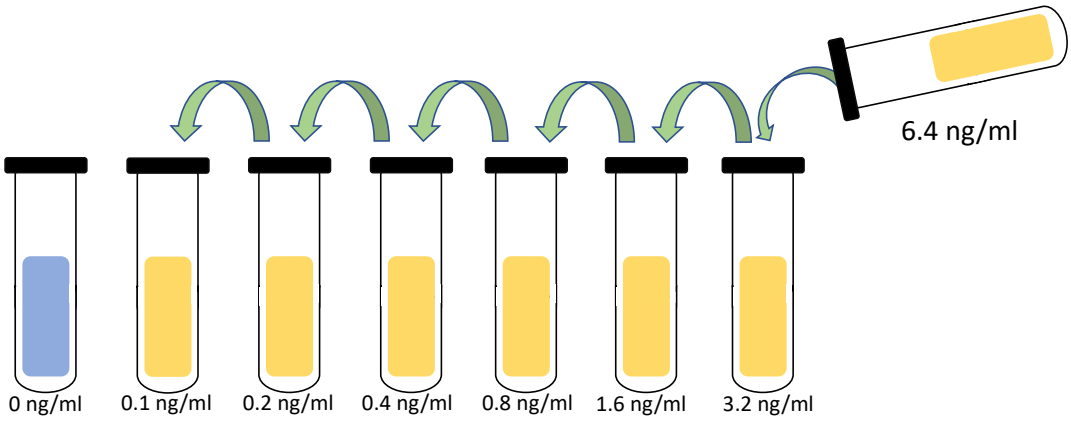

Figure 2.10: Serial dilutions performed to prepare the insulin standards for Enzyme-linked Immunosorbent Low Range Assay (ELISA).

To perform the assay, three separate reactions were carried out. In the first reaction, the antibody-coated microplate was equilibrated at room temperature, and 95 µl of sample diluent was pipetted into each well, followed by duplicates of 5 µl insulin standards. The microplate was then covered and incubated at 4°C for 2 hours. In the second reaction, the well content was aspirated, and each well washed five times using 300 µl of wash buffer per well; any remaining solution was removed by inverting and tapping the plate on paper towel.

Next, anti-insulin enzyme conjugate was prepared to the required volume of 5 ml for a full 96-well plate, by mixing 3.6 ml of anti-insulin enzyme conjugate stock solution with 1.8 ml of enzyme conjugate diluent and inverted until a homogenous clear solution was obtained.

100 µl of the kit anti-insulin antibody was added into each well, and microplate covered and incubated at room temperature for 30 minutes. In the third and final reaction well, content was aspirated, and wells washed 7 times as previously described. 100 µl of enzyme substrate solution was immediately dispensed into each well and microplate incubated at 40 minutes in the dark at room temperature. Finally, the enzyme reaction was stopped by adding 100 µl of enzyme reaction stop solution and absorbance measured within 30 minutes using λ=450 nm/630 nm. To determine the absorbance of standards and samples insulin standard curve was constructed by plotting values of standards on Excel (Microsoft, Redmond, WA, USA) and the best fit curve was drawn to construct the standard curve and the trendline equation was calculated and used to determine samples insulin concentration.

2.2.18 Coenzyme Q Competitive Enzyme-linked Immunosorbent Assay (ELISA)

A competitive ELISA measures the concentration of an antigen of interest by detecting signal interference, namely the competitive binding to the primary antibody of the antigen of interest present in a sample and the antigen present on the coated plate (reference antigen). Depending on the amount of antigen present in a sample, a smaller or bigger amount of free antibodies will be available to bind the reference antigen; the greatest the amount of antigen in the sample the weaker will be the detected signal from the reference antigen.

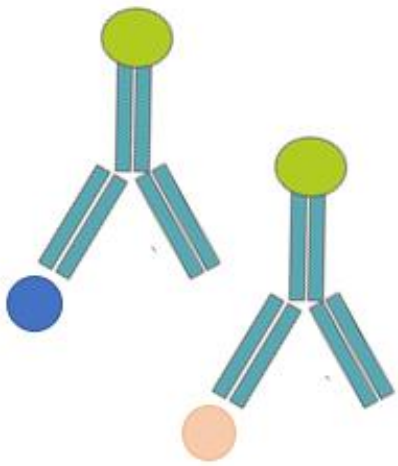

Figure 2.11: Principles of competitive ELISA. *Enzyme-linked immunosorbent assay (ELISA) is a plate-based assay technique used to detect specific antigens from a sample. In a competitive ELISA, the antigen presents in the sample (blue) and that immobilised to surface of the plate (pink) will compete to bind to the primary antibody. The greatest is the amount of antigen in the sample the lower will be the signal detected from the assay. For detection, the reaction is incubated with an HRP substrate that interacts with the primary conjugate to release a product measured in a plate reader at 450 nm.*

To measure Coenzyme Q levels in BAT a commercial Rat Coenzyme Q10 ELISA kit (competitive ELISA) – (MBS7241152) (MyBioSource, San Diego, CA, USA) was used. All reagents were supplied and equilibrated at room temperature before use; the supplied wash solution concentrate (10x) was diluted 1x in water as per instructions and stored at 2-8°C up to two weeks. 70-80 mg of samples were used for this assay and rinsed in ice cold PBS to remove excess blood. Tissues were then homogenised, ultrasonicated (10 pulses x 3s each) and centrifuged at 5000 rpm at 4°C for 15 minutes. Supernatant was then immediately collected with a syringe and a 25G needle to prevent the accidental collection of the fatty interphase. A test-run was performed to determine the ideal concentration for the assay, and it was determined that the neat samples should be used. 100 µl of samples and standards (Table 2.15) were assayed in duplicates, alongside with a blank control (100 µl PBS). To perform the assay two separate reactions were carried out. In the first reaction 10 µl of balance solution was added to all sample wells, followed by 50 µl of conjugate to each standard and sample well and mixed well. Plate was then covered with plastic film and incubated at 37°C for 1 hour. Plate was then washed 5x times with washing buffer and inverted to blot dry on to absorbent paper towel until fully dry.

Table 2.14: Coenzyme Q standards (ng/mL) as supplied.

Standard	CoQ(ng/mL)	Final volume of standard in well (µl)
1	0	100
2	10	100
3	25	100
4	50	100
5	100	100
6	250	100

In the second reaction 50 µl Substrate A and 50 µl Substrate B were added to each well, including the blank control. The plate was then covered and incubated in the dark for 15-20 minutes at 37°C; at the end of the incubation 50 µl of stop solution was added to each well and absorbance measured within 30 minutes using λ=450 nm.

Calculations to obtain CoQ concentration

To calculate CoQ concentration, the duplicates for each standard and samples were averaged, and the mean absorbance value of the blank was subtracted from all standard and sample readings to correct absorbance. Corrected absorbance values of standards were then plotted on Excel (Microsoft, Redmond, WA, USA) and the four-parameter logistic (4-PL) curve fit was obtained. Samples concentration corresponding to the mean absorbance from the standard curve were calculated using the following formula:

$$x = c\left(\frac{a-d}{y-d} - 1\right)^{\frac{1}{b}}$$

Where *a* is the minimum value that can be obtain, *d* is the maximum value, *c* is the point of inflection of the sigmoid (mid-point between a and d) and *b* is the Hill's slope of the curve at point *c*.

2.2.19 Fluorodeoxyglucose Positron Emission Tomography- Computerised Tomography (^{18}FDG-PET/CT)

Background

Positron Emission Tomography (PET) is a nuclear medicine technique that enables non-invasive imaging of the molecular characteristics of tissues in vivo by employing specific radiotracers.

2-deoxy-2-18F-fluoro-β-D-glucose (^{18}F-FDG) is a biologically active radiolabelled glucose analogue commonly used as a radiotracer for PET scans; as the ^{18}F isotope undergoes radioactive decay within tissues, a proton is transformed into a neutron and a positron is

released from the nucleus via beta emission. As positrons travel throughout the tissue, they interact with nearby electrons once they have exhausted their kinetic energy; next, the newly formed pair of particles quickly undergo annihilation and are ultimately converted into gamma rays. The PET camera is then able to record the emission sonogram, which is the reconstruction of all photons absorbed by the PET scan photodetectors. Namely, the use of ^{18}F isotope allows a semi-quantitative estimation of glucose uptake, hence, metabolic activity, within tissues of interest, as the isotope is accumulated but not metabolised by body tissues. It is possible to combine this technique with Computerised Tomography (CT) which employs high exergy x-ray emission to produce high resolution structural images of bones, soft tissues, and blood vessels. This allows a combination of the glucose absorption data obtained from PET with fine structural reconstructions (Figure 2.12).

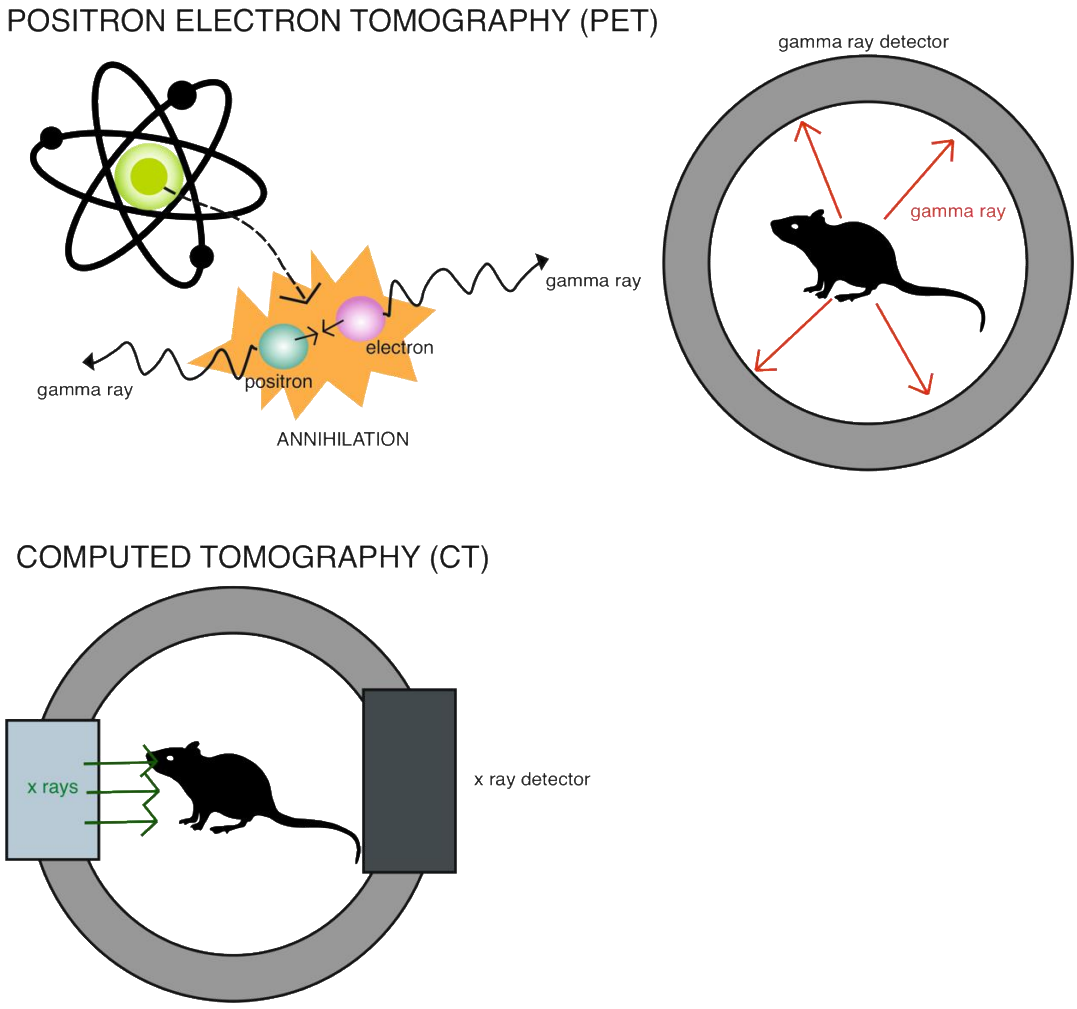

Figure 2.12: Schematic representation of a positron electron tomography/ computed tomography (PET/CT) scan. *After injection of radiolabeled glucose analogue 2-deoxy-2-^{18}F-fluoro-β-D-glucose (^{18}F-FDG) the ^{18}F undergoes radioactive decay and the PET scan absorbs the gamma ray generated during the decay and records the emission sonogram. The CT employs high energy x-rays to reconstruct tissues structures based on their density.*

.

Drug and vehicle preparation

Desiccated 5-[(2R)-2-[[(2R)-2-(3-Chlorophenyl)-2-hydroxyethyl] amino] propyl]-1,3-benzodioxole-2,2-dicarboxylic acid disodium salt (CL 316,243) (Tocris, Bristol, UK) was reconstituted at 1 mg/ml with 0.9 % saline solution for injection and 2 ml aliquotes stored at -20°C until use. Prior to use, the drug was thawed in a commercial fridge and administered via intraperitoneal route at 1 mg/kg. 0.9% Saline solution for injection used to prepare drugs was injected in the same volume as the experimental drugs via intraperitoneal route as control vehicle.

Animal preparation

Animals were implanted with bilateral cannulae targeting the NTS via stereotactic surgery on day 0, as described in section 2.2.7. The same day (day 0) viral injections containing Drp1S637A, Drp1K38A or GFP control, expressed under CMV or GFAP promoters, were administered as described in section 2.2.8.

Prior to experimental procedures, animals were maintained at standard rat housing temperature of 22°C. 48 hours prior to scans, animals were transferred to the Experimental and Preclinical Imaging Centre (ePIC) housing facility and randomly allocated to either vehicle (control) or CL 316,243 injected conditions. All animals were maintained at thermoneutrality during imaging. Thermoneutrality is classically defined as “ambient temperature over which metabolic rate is minimum and constant” (Poole and Stephenson, 1977); in this condition, core temperature (T°CORE) is solely maintained by alterations in cutaneous vasoconstriction sympathetic outflow, in rodents this equals to 28-30°C. Conversely, in conditions of sub thermoneutrality, or selective β3 adrenoreceptor stimulation, brown adipose tissue is activated, and its stimulation maintained by competent neuronal subpopulations in the hypothalamus, brainstem and spinal cord (Morrison and Nakamura, 2011b).

All scans were performed in accordance with the UK Animals (Scientific Procedures) Act 1986, as well as ethical guidelines set by the University of Leeds Ethical Review Committee. Every effort was made to meet the 3Rs criteria to minimise the number of animals and suffering.

Scans were performed at the Experimental and Preclinical Imaging Centre (ePIC) at the Leeds Institute of Cardiovascular and Metabolic Medicine (LICAMM).
Animals were injected intraperitoneally with 1mg/kg of CL 316,243 in 0.9% saline or 0.9% saline vehicle 30 minutes prior to scan, to allow the selective β3 adrenergic stimulation to take place and thus the effect of this to be detectable during the scans.

Tail vein cannulation

For injection of ^{18}F-FDG, animals were induced into surgical plane anaesthesia 10 minutes prior to the scan with 5% isoflurane in a 2L/min oxygen flow; A 23G needle attached to a bespoke line was inserted in the lateral tail vein of the animal and held in place using tissue adhesive and tissue tape.

Tracer preparation and administration and PET/CT scan

The fluorine isotope ^{18}F has a half-life of 109.8 minutes and because of its short half-life, radioactivity levels expressed in Megabecquerel (MBq) need to be calculated at several time points prior to the experiment using the Rad Pro Calculator (Ludlum Measurement, Sweetwater, TX, USA) (hhtp://www.radprocalculator.com/) to ensure that the injected dose at a specific time point is known. Namely, the syringe activity was recorded prior and post injection and at the end of the scan the catheter was removed, and its activity also measured and corrected to time of injection to calculate the final injected activity.

PET/CT scans were acquired on an Albira Si PET-CT system (Bruker, Billerica, MA, USA) using a 90-minute dynamic imaging sequence. Briefly, the animal was placed prone in the scan bed, with field of view centred on the intrascapular brown adipose tissue; next, ^{18}F-FDG activity (Royal Preston Hospital, Preston, UK) was injected with the following means ± standard deviations (SDs) of activity in 500 μl of 0.9% saline solution (AquaPharm, Animalcare Ltd, York, UK) through the line inserted in the tail vain at the beginning of the PET scan: 21.86±0.73 (n=27), simultaneously to the initiation of the dynamic scan. Rats were maintained at 2.5% isofluorane (v/v with oxygen) throughout the duration of the scan. The bed was supplemented with an and electrode to track respiratory rhythm throughout the scan (Bruker, Billerica, MA, USA).

Following the PET scan, CT images were acquired for anatomic co registration (x-ray energy 40 kVp, resolution 90 µm, 360 projections, 8 shots) and reconstructed using the three-dimensional ordered subset expectation maximisation algorithm.

Image Reconstruction and analysis

Animals that failed to show viral expression in the NTS of the DVC or did not recover at least 90% of their presurgical weight were excluded from the analysis (n=1-2 per experimental group). The PET and CT scans of all animals included in the study were reconstructed according to the following characteristics: using the in-built Albira software (Bruker, Billerica, MA, USA) (1) CT scan was reconstructed using the Filtered Back Projection (FBP) algorithm set on high (2) PET scan was reconstructed using the Maximum Likelihood Estimation Method (MLEM) set at 0.25 mm and scatter, randoms and decay corrections combined with partial volume correction and attenuation using the following frames: 15 frames at 2 s, 2 frames at 15 s, 4 frames at 60 s, 1 frame at 300 s, 6 frames at 600s and 1 frame at 1200 s (total 4800 s). Reconstructed images were fused using pmod software (pmod technologies, Zurich, Switzerland); the PET image information was modified to included weight and actual injected dose to visualise metabolic activity in tissues at standardised uptake value (SUV)=3. PET images were overlapped with CT images to ensure correct alignment and PET images smoothed using a Gaussian filter set at 1 mm. The same software was used to analyse images using the view mode; Three-dimensional volume of interest (VOI) for BAT was generated and saved to be utilised for each scan to ensure consistency in the measurement. The VOI for BAT was constructed between the scapular region, above the thoracic spinal cord, based on CT images and the most prominent PET scan recorded in the last sequence. These VOIs were compared using an in-built VOI statistics function so BAT glucose uptake, and from this ratio time-activity curves for the ROIs were generated.

CT scans were also analysed to quantify the total white adipose tissue mass, to obtain volumetric information on the visceral and subcutaneous fat in the animals. To do so, a fat segmentation method as described in (Sasser et al., 2012) was used. Differences in tissue density were exploited to calculate total amount of fat volume, as a specific density

corresponds to each tissue and this density can be filtered out using Hounsfield units. Briefly, bed and nose cone components were excluded from the CT images by drawing vertices and applying a masking tool; a first segmentation using parameters –300 HU, +3500 HU was used to segment the whole body and the volume calculated using inbuilt VOI statistics function. The same operation was repeated to selectively segment out white adipose tissue using the parameters –190 HU, -60 HU and the volume calculated using inbuilt VOI statistics function. The ratio of these two values was then calculated to obtain the total percentage of fat volume mass from each animal.

2.2.20 Scintillation (Gamma) Counting

Following the scan, the catheter was removed and measured with a dose calibrator to correct for potential fractions of activity that did not enter the animal circulation, and this value was subtracted from the total injected activity to recalculate the corrected injected dose. Before animals could regain consciousness, they were sacrificed by decapitation to quickly collect brain regions of interest, followed by collection of liver, BAT, WAT, and muscle for scintillation counting and further investigations. The remaining portions of tissues were immediately snap frozen in liquid nitrogen and stored for further investigations.

For the gamma counting, empty tubes were tared, and fresh tissues were placed into the tubes and positioned in an automated gamma counter (Hidex, Turku, Finland). ^{18}F spectrum was quantified and analysed for each tissue for 1 minute. Next, counts per minute (CPM) normalised to the starting time of the analysis, were corrected to time of injection using the Rad Pro Calculator (Ludlum Measurement, Sweetwater, TX, USA). The CPM counts were then converted in MBq using a standard curve generated with triplicates ranging 0-0.005 MBq; this value was divided by total injected dose and multiplied by 100 to obtain total injected dose. Finally, the total injected dose was divided by the mass of the tissue to calculate the percentage of injected dose per gram of tissue.

2.2.21 Statistical Analysis

All data presented are expressed as mean±SEM and single data point highlighted. Data were summarized and stored in Excel (Microsoft, Redmond, WA, USA) files. Prior to analysis, all data collected was tested for normality using the Shapiro-Wilk normality test function of Prism 9 (GraphPad, San Diego, CA, US). All data was analysed using Prism 9 (GraphPad, San Diego, CA, USA). Significant differences were determined using t-test, Nested unpaired t-test, paired t-test, One-way ANOVA (post-hoc test: Tukey) or Two-way ANOVA (post-hoc test: Tukey) accordingly. Unpaired t-test was used for tissue mass, plasma analysis and qPCR. Nested unpaired t-test or unpaired t-test were used for histochemistry and immunohistochemistry. One-way ANOVA for tissue mass, gamma counting and plasma/liver analysis and Two-way ANOVA for PET/CT scans and some qPCR. Paired t-test was used for acute feeding studies. Repeated measures ANOVA was used for cumulative chronic feeding studies and PET scan data over time. Prism Outlier Calculator (GraphPad, San Diego, CA, USA) was used to identify and exclude data from statistical analysis where appropriate. In figures and legends n refers to the number of biological replicates, and when appropriate the number of technical replicates was also indicated. $P< 0.05$ was statistically significant. Significance was defined as following: (*) $p<0.05$, (**) $p<0.01$, (***) $p<0.001$, (****) $p<0.0001$.

Chapter 3

Chronic inhibition of mitochondrial fission in the NTS improves BAT glucose uptake in HFD- fed rats

3.1 Chronic inhibition of mitochondrial fission in the NTS is associated with higher in vivo dynamic glucose uptake in HFD-fed rats in BAT measured with Fluorodeoxyglucose Positron Electron Tomography (^{18}FDG PET)/ Computed tomography (CT) (PET/CT) scans

3.1 Introduction and rationale

3.1.1 The brown adipose tissue

One of the major physiological events in small mammals in the regulation of energy expenditure is adaptive heat production, or thermogenesis, which is critical to maintain body temperature in conditions of sub-thermoneutral environments. While in mammals, thermogenesis occurs at different magnitudes in all body tissues, the BAT is the major thermogenic organ responding to cold and sympathetic stimulation via the noradrenergic system (Smith and Horwitz, 1969a; Nicholls and Locke, 1984). Brown adipocytes possess elevated levels of mitochondria, which express UCP1 that is capable of uncoupling electron transport from the Mitochondria Oxidative Phosphorylation System OXPHOS, to generate heat (Ricquier and Kader, 1976). UCP1 transcription and regulation are driven by sympathetic activation, and in particular, via β3 Adrenergic stimulation (Cypess et al., 2015a), which generates an increase afflux of glucose which is uptaken from the circulation, to drive thermogenesis in BAT.

Interestingly, BAT had been deemed to be non-existent or non-functional in adult humans until the early 2000's, when nuclear medicine started playing a critical role in the discovery of active brown adipose tissue present in humans. ^{18}FDG-PET/CT is a powerful imaging tool, traditionally used for the detection of solid cancers (Castell and Cook, 2008), that measures the accumulation of radiolabelled glucose in tissues with a high metabolic rate. As BAT presents a high metabolism fuelled by glucose, this technique is particularly valuable to study the contribution of BAT in whole body glucose clearance and thermogenesis. Importantly, a fundamental study from 2002 by Hany et al. reported, for the first time, an increase in uptake of radiolabelled ^{18}FDG in BAT of adult humans, using a combined PET/CT scanner. Moreover, in 2009 three independent studies reported unequivocal evidence of metabolically active BAT

in adult humans (Cypess et al., 2009a; Saito et al., 2009b; Au-Yong et al., 2009). Importantly, several studies conducted in rodent models of obesity and diabetes show that these conditions are associated with reduced non-shivering thermogenesis capacity and BAT activity (Trayhurn, 1979; Mercer and Trayhurn, 1984; Yoshioka et al., 1989). Interestingly, a single day of HFD was able to induce an increase in lipid content and a rapid reduction of insulin-dependent glucose uptake in BAT of wild-type mice, whereas three days of HFD induced alterations in BAT mitochondrial networks and promoted the expression of macrophage markers in these animals (Kuipers, Held, in het Panhuis, et al., 2019). Similarly, long term HFD induced insulin resistance (Cypess et al., 2015a) and BAT whitening (Shimizu et al., 2014), and increased lipid content and dysfunctional mitochondria, as well as reduce fat oxidation in mice (Cinti, 2009; Shimizu and Walsh, 2015).

It is known that brown adipose tissue (BAT) is under the direct control of the CNS via its sympathetic branch, which is governed by heterogenous populations of neurons located in diverse brain regions, including the hypothalamus and the brainstem (Morrison et al., 2014; Labbé et al., 2015). Studies have shown that the NTS exerts inhibitory control of BAT sympathetic outflow; in particular a 2017 study has demonstrated that the inhibition of BAT via vagal stimulation could be prevented by blocking ionotropic glutamate receptors in vagal afferent terminals in this brain region (Madden et al., 2017). Moreover, Madden et al. (2017) have concluded that the activation of glutamatergic second-order neurons in the NTS and the inhibition of sympathetic GABAergic premotor neurons in the rostral raphe nucleus are responsible for the vagal-mediated inhibition of BAT.

Interestingly, tracing studies using isolectin B4 have shown that glutamatergic vagal afferents terminating on NTS neurons are unmyelinated and express TRPV1 channels (Hermes et al., 2016). Importantly, Conceição et al. (2021) have revealed that TRPV1 expressing neurons in the mNTS excite dynorphinergic expressing neurons in the dorsal lateral parabrachial nucleus (LPBd), which inhibit sympathoexcitatory neurons in the median preoptic nucleus (MnPO) to inhibit BAT thermogenesis and energy expenditure in a rat model of diet-induced obesity.

3.1.2 The importance of mitochondrial dynamics

Mitochondria are highly dynamic organelles that continuously undergo fission and fusion processes- known as mitochondrial dynamics- to ensure that their shape, distribution and size, and appropriate energy levels are maintained throughout the cell. Mitochondrial fusion is under control of Mfn1, Mfn2 and Opa1 in a 2-step reaction. Mitochondrial fission is driven by the recruitment of the GTPase Drp1, which performs mechanical constriction on the mitochondria, resulting in their fragmentation (Helle et al., 2017). These processes are transient and alterations in mitochondrial dynamics have been associated with obesity and insulin resistance in several tissues and organs, including the muscle (Jheng et al., 2012), the hypothalamus (Schneeberger et al., 2014; Ramírez et al., 2017) and the DVC (Filippi et al., 2017; Patel et al., 2021).

Mitochondrial dysfunction in the brain, and in particular in hypothalamus and in the brainstem, has been reported in association with obesity and insulin resistance. In particular, Mfn1 knockout in hypothalamic POMC neurons altered central glucose sensing and defective pancreatic insulin secretion, via enhanced reactive oxygen species production in this brain region; while Opa1 knockout was associated with obesity from 7 weeks of age in mice (Ramírez et al., 2017).

Moreover, a shift towards mitochondrial fission in the NTS of the DVC was observed in animals fed with HFD (Filippi et al., 2017). This effect was dependent upon Drp1 over-expression, as chemical inhibition of mitochondrial fission using MDIVI-1 reversed the impact of HFD on mitochondrial morphology (Filippi et al., 2017). Increased mitochondrial fission in the NTS of HFD-fed animals was also associated with increased body weight, food intake, iNOS and insulin resistance in the NTS as demonstrated in Patel et al. (2021).

Interestingly, the inhibition of mitochondrial fission in the NTS, via delivery of an adenoviral vector containing the dominant-negative form of Drp1 K38A (CMV:K38A), to target all cells within the NTS, in HFD-fed rats reduced body weight and food intake, decreased visceral adiposity, and prevented insulin resistance in the NTS of these animals (Patel et al., 2021). Moreover, the authors reported that the effects induced by HFD were recapitulated by

adenoviral expression of the constitutively active form of Drp1 S637-A (CMV:S637A) in the NTS of animals fed regular chow, suggesting that mitochondrial dynamics in the NTS are critical for the maintenance of energy homeostasis and insulin sensitivity.

Surprisingly, when the dominant-negative form of Drp1 K38A was designed to specifically target astrocytes in the NTS using a GFAP promoter (GFAP:K38A), a significant reduction of body weight, food intake and visceral adiposity was also observed, along with restored insulin sensitivity in the NTS (Patel et al., 2021). This indicated that astrocytic mitochondrial dynamics play a significant role in the regulation of whole-body energy metabolism and local insulin sensitivity in the DVC.

3.1.3 The white adipose tissue

White adipose tissue (WAT) exerts an antagonistic function to BAT, namely, it stores excess energy in form of TG. Its cellular structure is also profoundly different from that of BAT since it is characterised by unilocular, TG-rich lipid droplets and mitochondria in a fused-like state. WAT is also innervated by noradrenergic nerve fibres, and WAT denervation increases WAT volume to impair centrally driven lipolysis (Demas and Bartness, 2001; Bartness et al., 2010). Importantly, studies have shown that cold exposure increased tyrosine hydroxylase levels, the enzyme involved in synthesis of noradrenaline and adrenaline, in WAT, which was concomitant with the appearance of brown-like adipocytes in WAT (Vitali et al., 2012). AMP-activated protein kinase signalling in the hypothalamus is a central regulator of WAT browning (Nguyen et al., 2017). Moreover, reduction of HFD-induced endoplasmic reticulum stress in the hypothalamus was associated with browning of WAT and amelioration of obesity via the chaperone protein unfolded protein response regulator GRP78/BiP within the ventromedial hypothalamus in wild-type rats (Contreras et al., 2017). Here we hypothesised that concomitantly with increased BAT thermogenesis, the inhibition of mitochondrial fission in the NTS may also increase WAT browning in HFD-fed animals.

3.1.4 Study rationale

In this study we therefore aimed to assess whether the inhibition of mitochondrial fission in the NTS, and then specifically in astrocytes of the NTS, is capable of increasing glucose uptake in BAT *in vivo*, which is a marker for glucose clearance from the circulation and thermogenesis. Here we hypothesise that short-term HFD decreases glucose uptake in BAT, and that the inhibition of mitochondrial dynamics in the NTS restores glucose uptake in BAT compared to HFD controls. Moreover, we postulate that targeting specifically astrocytes, which according to (Patel et al., 2021) is sufficient to ameliorate the metabolic profile of HFD-fed rats, will preserve the capacity of BAT to appropriately uptake glucose from the circulation compared to HFD controls. Finally, we hypothesise that the higher BAT glucose uptake capacity in animals where mitochondrial fission was inhibited in the NTS, could be partially due to BAT expansion or WAT browning. To this aim, we measured BAT and WAT glucose uptake and overall, WAT visceral and subcutaneous volume.

3.2 Aims

Aim 1: To determine using a combined PET/CT scanner whether short-term HFD is sufficient to induce lower levels of BAT activation compared to regular chow-fed controls at basal level and upon selective adrenergic stimulation.

Aim 2: To determine using a combined PET/CT scanner whether inhibition of HFD-mediated increase of mitochondrial fission in all cells of the NTS can lead to elevated BAT activation compared to HFD controls upon selective adrenergic stimulation.

Aim 3: To determine using a combined PET/CT scanner whether inhibition of HFD-mediated increase of mitochondrial fission in astrocytes of the NTS is sufficient to cause higher levels of BAT activation compared to HFD controls upon selective adrenergic stimulation.

Aim 4: To measure WAT glucose uptake as a marker of browning and subcutaneous and visceral WAT volume to determine if the inhibition of mitochondrial dynamics affects the WAT.

3.3 Targeting all cells and specifically astrocytes in the NTS using an adenoviral system expressed under CMV and GFAP promoters

To manipulate mitochondrial dynamics of all cells in the NTS, an adenoviral system was generated under the CMV promoter to target all cells in the NTS.To manipulate mitochondrial dynamics of astrocytes in the NTS, an adenoviral system was generated under the GFAP promoter to target all GFAP positive astrocytes in the NTS. A control adenovirus expressing GFP, and an adenovirus expressing the dominant negative form of Drp1 mutated in residues K38 to A (Drp1-K38A) to induce defective GTPase binding site and Drp1 functionality, were generated under both promoters. The dominant negative K38-A adenovirus was tagged with a FLAG epitope, which allowed recognition and detection of the virus in the NTS via immunohistochemistry (Section 2.2.14).

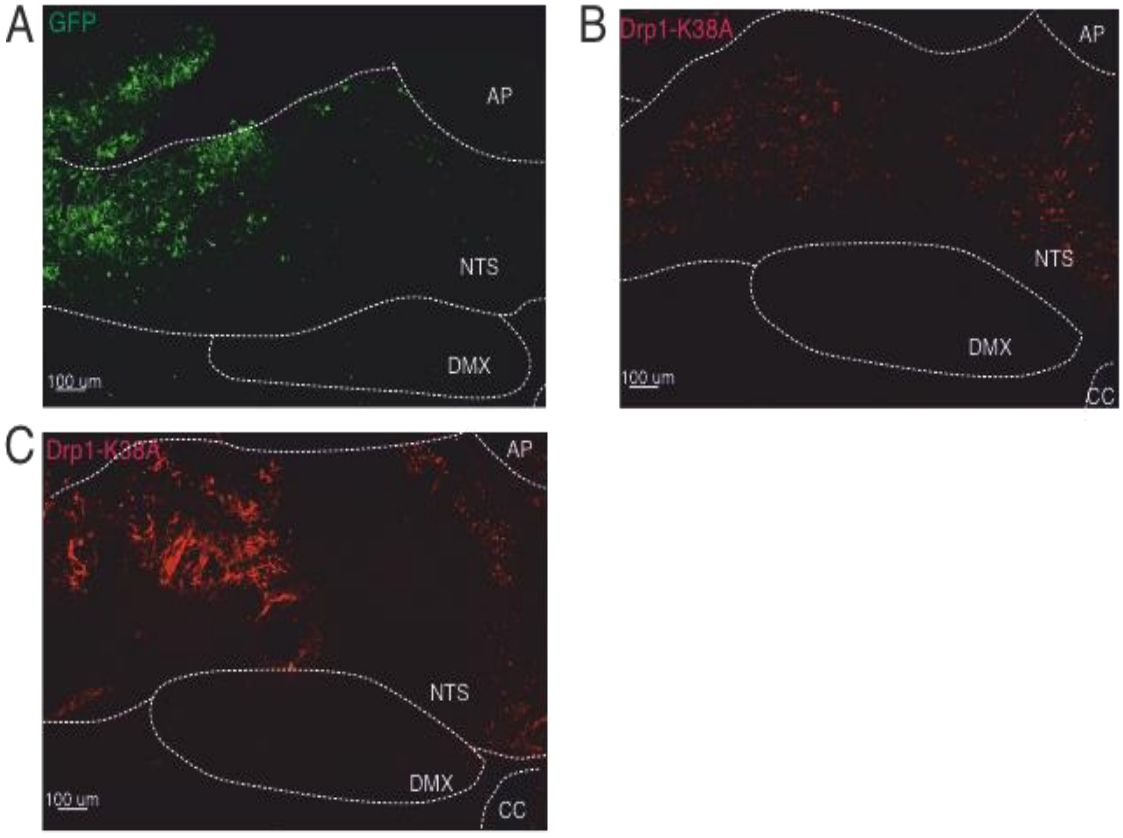

Figure 3.1: Representative confocal image of the DVC showing correct localisation of our viral systems within the NTS. *(A) GFP (CMV-GFP) and FLAG-tagged dominant negative Drp1 mutants (B) CMV:Drp1-K38A and (C) GFAP:Drp1-K38A in the NTS of the DVC. NTS= nucleus tractus solitarius; AP= area postrema; CC= central canal; DMX=dorsal motor nucleus of the vagus.*

IHC was used to confirm correct viral delivery to the animals' NTS and was used as a criterion for inclusion/exclusion of animals in the data analysis. Surgeries, viral injections and feeding studies were conducted as previously described (Sections 2.2.6 to 2.2.8). After sacrifice, NTS anatomical sections obtained from the animals were used to confirm correct viral delivery in the NTS (Figure 3.1) and co-localisation with GFAP to ensure astrocytes were specifically targeted (Figure 3.1C and 3.2). The IHC images confirm correct execution of the surgery and viral delivery of the adenoviral systems in the NTS (Figure 3.1 A-C), and adenoviral distribution restricted to GFAP+ astrocytes (Figure 3.1C and 3.1). This is accordance with previously published work within the Filippi group (Patel et al., 2021).

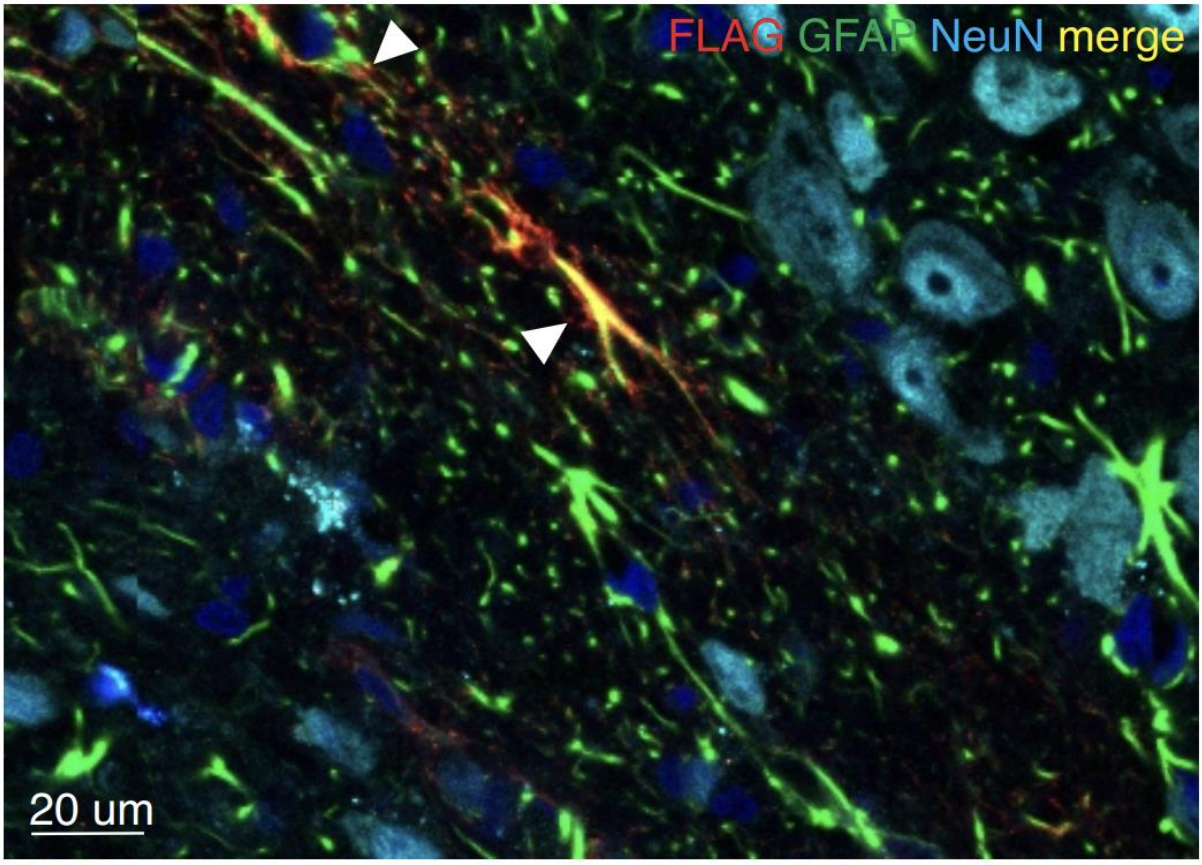

Figure 3.2: Representative x40 confocal image of GFAP-Drp1-K38A in the NTS of the DVC, showing that this virus exclusively colocalises with GFAP+ astrocytes. *White arrows indicate regions of colocalisation.*

3.4 In dynamic ^{18}FDG -PET/CT scans at thermoneutrality, there are no differences in glucose uptake in BAT of regular chow vs HFD animals

The first set of questions aimed to determine whether there are differences in BAT glucose uptake in control regular chow and HFD-fed animals at thermoneutrality. Animals underwent stereotactic surgery to insert a bilateral cannula in the NTS and were injected the same day with an adenovirus expressing control GFP under a CMV promoter (Ad-CMV-GFP) (Sections 2.2.7, 2.2.8). Next, animals were maintained on regular chow control diet or HFD for 2 weeks and housed at 22 °C, and prior to scans they were anesthetised, and their tail vein cannulated, and then placed into the PET/CT scan. An injection of 65±5 MBq/kg of ^{18}FDG was given in the lateral tail vein at the initiation of the scan and data acquisition run for 4800 s (section 2.2.20). The internal scan temperature was kept at 28°C throughout the duration of the dynamic scan to achieve thermoneutrality. At the end of the scan, the animals were sacrificed, and a fraction of BAT dissected then gamma counting was performed on the tissue to detect the amount of uptake of ^{18}FDG. ^{18}FDG uptake was calculated as percentage of injected dose (MBq) per gram of collected tissue (Section 2.2.21); gamma counting revealed that no significant differences could be detected between the BAT of CMV:GFP RC 0.144±0.0518 (n=5) and CMV:GFP HFD 0.0679±0.0145 (n=5) (p=0.19) (Figure 3.3).

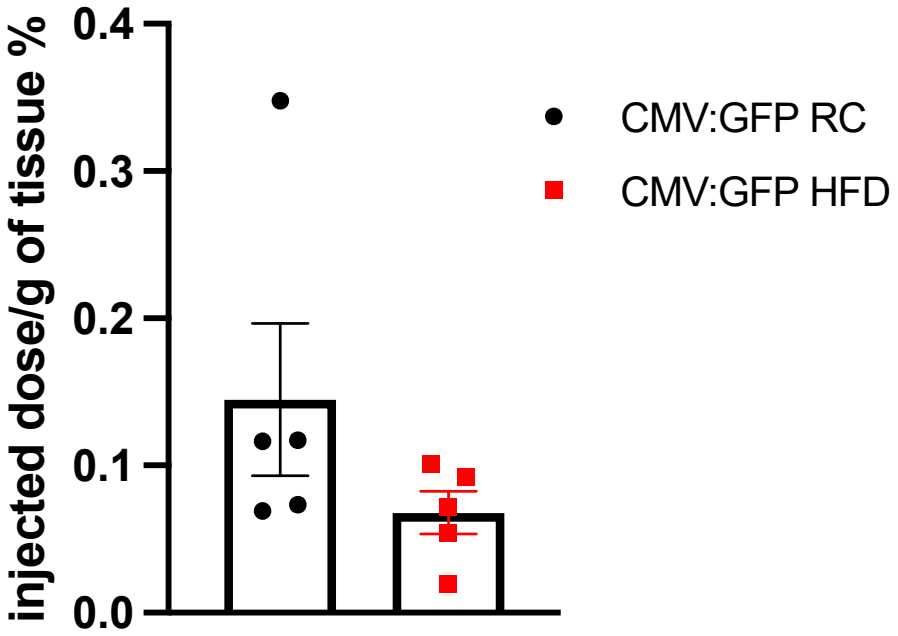

Figure 3.3: BAT uptake of ^{18}FDG is similar in regular chow and HFD-fed animals assessed at thermoneutrality with gamma counting. *Data are representative of n = 5 rats for both CMV:GFP regular chow and CMV: GFP HFD. All data was tested for normality prior statistical tests using the Shapiro-Wilk normality test. Values are shown as mean ± SEM and single data points are highlighted. Statistical test: unpaired t-test.*

Next, to assess the uptake of ^{18}FDG in BAT, PET scan images, reconstructed as described in Section 2.2.20 were analysed. Scans were visualised at SUV=3 and standardised VOIs were used to isolate the BAT as described in section 2.2.20. Representative FDG/PET images of GFP regular chow (A) and GFP HFD (B)-fed rats are shown in Figure 3.4 (n=5 animals per group).

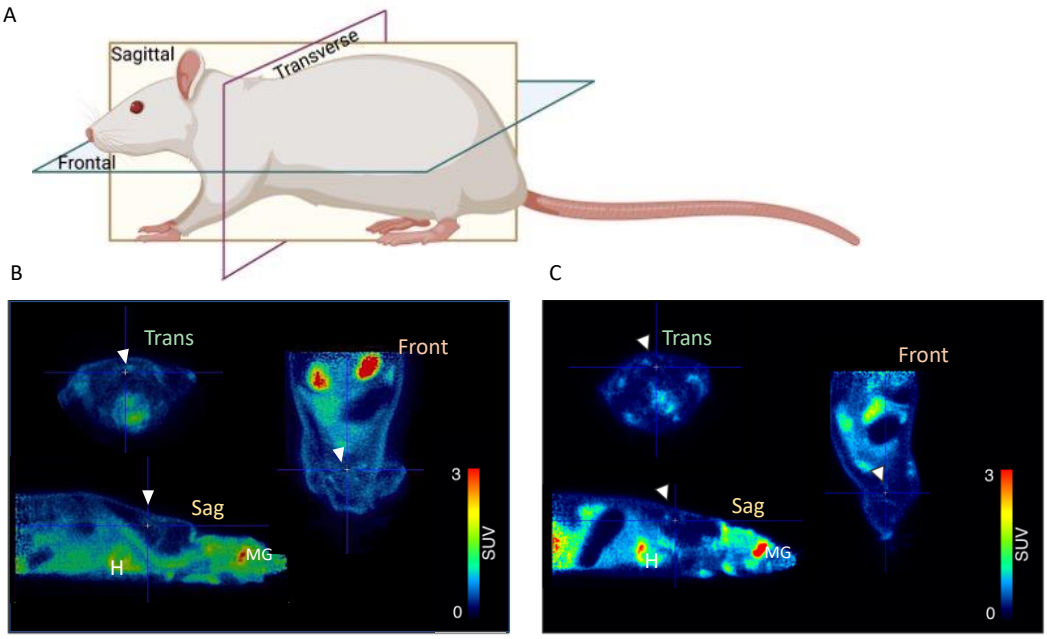

Figure 3.4: Representative PET/CT scan reconstructions of regular chow and HFD animals at thermoneutrality*. Images are presented in standardised uptake value (SUV) for each group following a dynamic PET/CT scan. (A) Illustration of the anatomical plans showed in the ^{18}FDG PET reconstructions. (B) Representative transverse, frontal and sagittal ^{18}FDG PET scan of a regular chow animal (C) Representative transverse, frontal and sagittal ^{18}FDG PET scan of an HFD animal. The scale bar represents SUV. The white arrow points toward BAT. Abbreviations: H, heart; MG, meibomian gland; Trans, transverse; Front, frontal; Sag, sagittal; SUV, standard uptake value.*

PET scan data were expressed as mean standard uptake value (SUV) ratio in BAT (SUV_{BAT}) in function of time (Figure 3.5). A two-way ANOVA was performed to analyse the effect of diet and viral construct on BAT glucose uptake. At the scan end point (t=4800 s), no detectable difference in BAT glucose uptake could be observed between CMV:GFP regular chow diet (0.581±0.0538) and the CMV:GFP HFD groups (0.569±0.0546) (p=0.80) (n=5 animals per group). These results corroborate the evidence from the gamma counting analysis, confirming that at thermoneutrality, BAT glucose uptake is similar in regular chow and HFD animals.

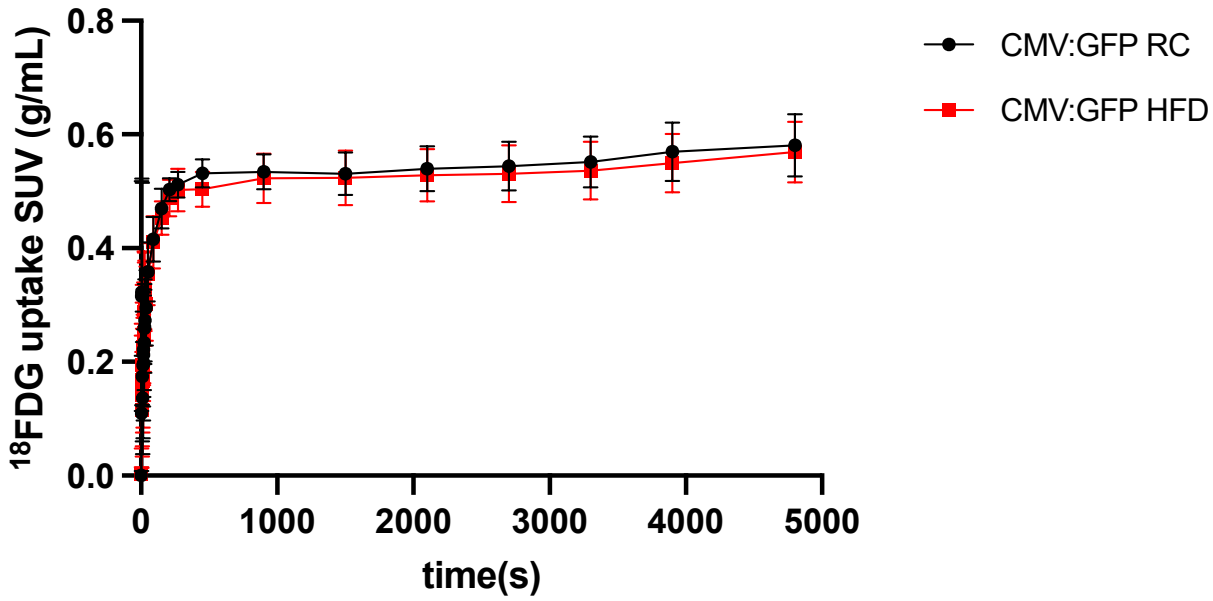

Figure 3.5: BAT ^{18}FDG glucose uptake expressed in SUV (g/mL) is similar in regular chow and HFD animals exposed to thermoneutrality. *Data are representative of n = 5 rats for both CMV:GFP regular chow and CMV:GFP HFD. All data was tested for normality prior statistical tests using the Shapiro-Wilk normality test. Data are shown as mean ± SEM Statistical test: Two-Way ANOVA with repeated measures. Post hoc test: Tukey.*

3.5 In HFD rats, there was lower glucose uptake in BAT compared to RC fed animals in dynamic ^{18}FDG-PET/CT scans upon selective β3 adrenergic activation using the compound CL 316,243

Our results demonstrate that at thermoneutrality, the BAT of regular chow and HFD-fed rats show no significant differences in glucose uptake and activation. Therefore, we decided to test whether it is possible to observe differences in BAT glucose uptake upon adrenergic stimulation in regular chow vs HFD-fed animals. This is important to study how responsive BAT is to adrenergic stimulation, which is the main drive to BAT thermogenesis in vivo (Cypess et al., 2015; Tabuchi and Sul, 2021). The selective β3 adrenergic agonist, CL 316,243 was used to achieve this. Briefly, animals underwent surgery as described in section 2.7 and on the same day, they received an injection of Ad-CMV-GFP into the NTS under a CMV promoter. They were then maintained on regular chow control diet or HFD for 2 weeks and housed at 22 °C until the day of the scan. 30 minutes prior to the scan CL 316,243 at 1 mg/kg in 0.9% saline was injected (Park et al., 2015). The animal was then anaesthetised, and the lateral tail

vein cannulated (section 2.2.20). Animals were placed in the scanner and 65±5 MBq/kg of ^{18}FDG were injected in the lateral tail vein, before running the scan for 4800 s. At the end of the scan, the animals were sacrificed, BAT and WAT dissected and ^{18}FDG measured in a gamma counter. As described in section 3.2 ^{18}FDG uptake was calculated as percentage of injected dose (MBq) per gram of collected tissue. Gamma counting analysis revealed a significantly higher uptake in ^{18}FDG in the BAT of CMV:GFP regular chow animals injected with β3 adrenergic agonist CL 316,243 (7.29±1.44 % injected dose/g) compared to that of CMV:GFP HFD-fed animals injected with β3 adrenergic agonist CL 316,243 (0.371±0.0874 % injected dose/g) (**p<0.01) (n=4 for each group) (Figure 3.6).

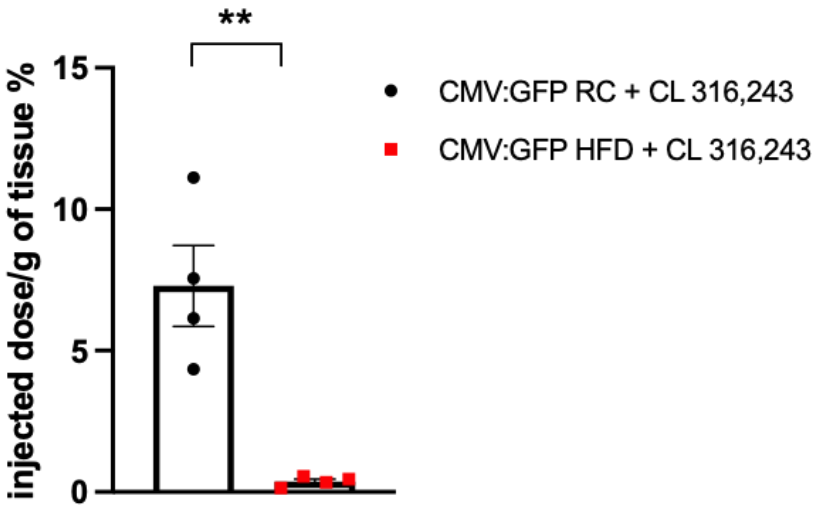

Figure 3.6: BAT uptake of ^{18}FDG is lower in HFD animals compared to RC controls after IP injections of CL 316,243 as measured with gamma counting. *30 minutes prior to scan, rats were injected with 1 mg/kg of selective β3 adrenergic agonist CL 316,243 to activate BAT. Data are shown as mean ± SEM, with each single point highlighted. Data are representative of n = 4 rats for both CMV:GFP regular chow and CMV:GFP HFD. All data was tested for normality prior statistical tests using the Shapiro-Wilk normality test. Values are shown as mean ± SEM and single data points are highlighted. .∗∗p < 0.01. Statistical test: unpaired t-test.*

We then examined potential differences in ^{18}FDG uptake in the BAT of regular chow and HFD animals injected with 0.9% saline vehicle and 1 mg/kg CL 316,243 with gamma counting analysis. A two-way ANOVA was performed to analyse the effect of diet and β3 adrenergic stimulation on BAT glucose uptake. Data revealed that regular chow animals injected with 0.9% saline vehicle behave similarly to thermoneutral regular chow animals (Figure 3.6), however when injected with CL 316,243 their BAT was strongly responsive to β3 adrenergic stimulation (saline 0.145±0.0518 % injected dose/g) (n=5) (+CL 316,243 6.22±1.57 % injected dose/g) (n=4)(**p<0.01). In contrast, no significant differences were found between BAT ^{18}FDG uptake of HFD control animals injected with saline (0.0679±0.0145 % injected dose/g) (n=5) and CL 316,243 injected HFD animals (0.371±0.0874 % injected dose/g) (n=4) (p=0.934) (Figure 3.7). When we compared saline injected RC and HFD controls no significant differences in BAT ^{18}FDG were observed (saline RC 0.0690±0.0518%; saline HFD 0.0200±0.0145% injected dose/g) (n=5) (p=0.999); however, a significantly higher ^{18}FDG BAT uptake was seen in RC animals (6.22±1.57% injected dose/g) compared to HFD animals (0.371±0.0874% injected dose/g) (n=4) (**p<0.01) following injection of CL 316,243. Thus, according to our data, BAT loses the ability to respond appropriately to adrenergic stimulation to drive glucose uptake and thermogenesis upon 2 weeks of HFD.

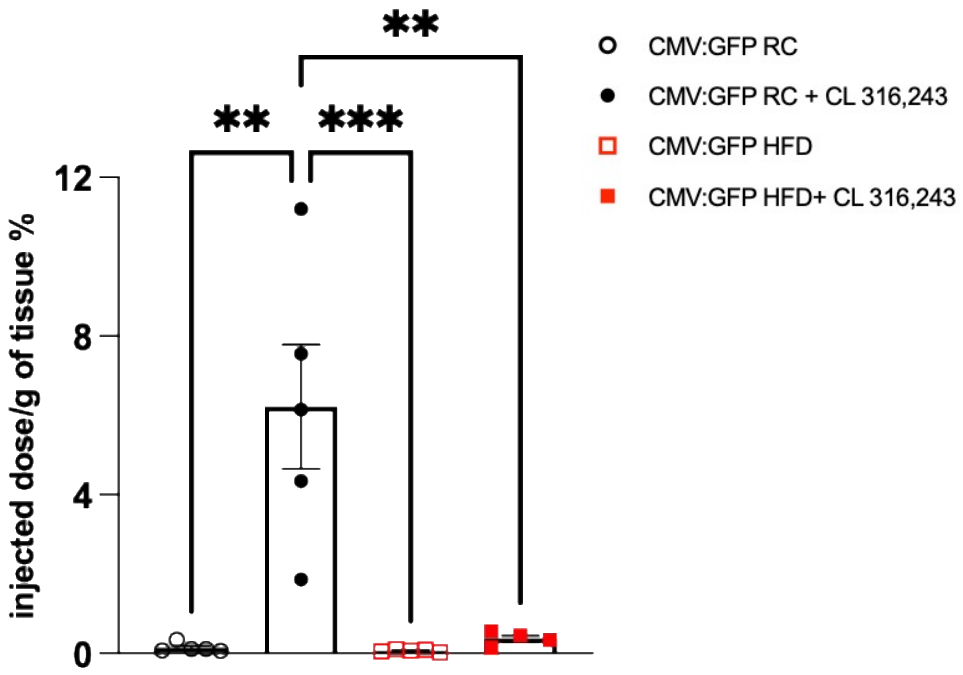

Figure 3.7: BAT uptake of ^{18}FDG is increased after stimulation with CL 316,243 in RC but not HFD animals as measured with gamma counting*. 30 minutes prior to scan, rats were injected with either 0.9% saline vehicle or 1 mg/kg of selective β3 adrenergic agonist CL 316,243 to activate BAT. Data are representative of n = 5 rats for saline controls CMV:GFP regular chow and CMV:GFP HFD and of n = 4 rats for CL 316,243 injected CMV:GFP regular chow and CMV:GFP HFD. All data was tested for normality prior statistical tests using the Shapiro-Wilk normality test. Values are shown as mean ± SEM and single data points are highlighted. ***p < 0.001. Statistical test: Two-Way ANOVA with repeated measures. Post hoc test: Tukey.*

Next, we examined ^{18}FDG uptake in BAT by analysing PET scans images, reconstructed as described in section 2.2.20. Scans were visualised at SUV=3 and analysed as described in section 3.1.4. Representative FDG/PET scans of CMV:GFP regular chow (A) and HFD (B)-fed rats after injection of CL 316,243 (n=4 and n=5 animals per group, respectively) are shown in Figure 3.8.

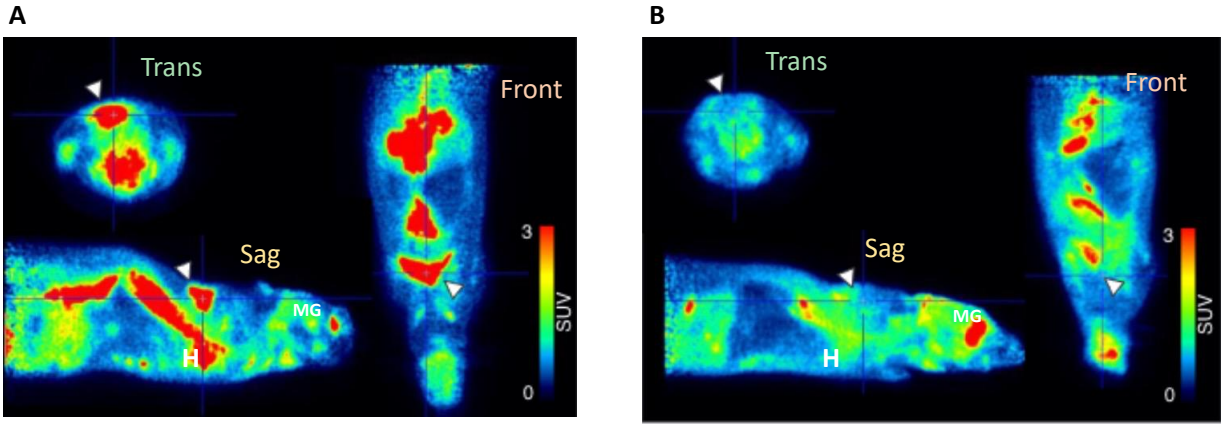

Figure 3.8: Representative PET/CT scan reconstructions of animals injected with 1mg/kg of selective β3 adrenergic agonist CL 316,243 to activate BAT. *Images are presented in standardised uptake value (SUV) for each group following a dynamic PET/CT scan. (A) Representative transverse, frontal and sagittal ^{18}FDG PET scan of a CMV:GFP regular chow animal. (B) Representative transverse, frontal and sagittal ^{18}FDG PET scan of a CMV:GFP HFD animal. The scale bar represents SUV. The white arrow points toward BAT. Abbreviations: H, heart; MG, meibomian gland.*

Scans were then analysed using a ratio of SUV_{BAT} in function of time (Figure 3.9). A two-way ANOVA was performed to analyse the effect of diet and β3 adrenergic stimulation on BAT glucose uptake. A higher BAT glucose uptake in RC fed animals could be observed from frame 23 (approximately t=900 s post commencement of the scan) until the end point (t=4800 s). At end point, BAT glucose uptake was 3.51±0.418 for the CMV:GFP regular chow diet and 0.797±0.0105 (n=4) for the CMV:GFP HFD group (n=5) (****p<0.0001).

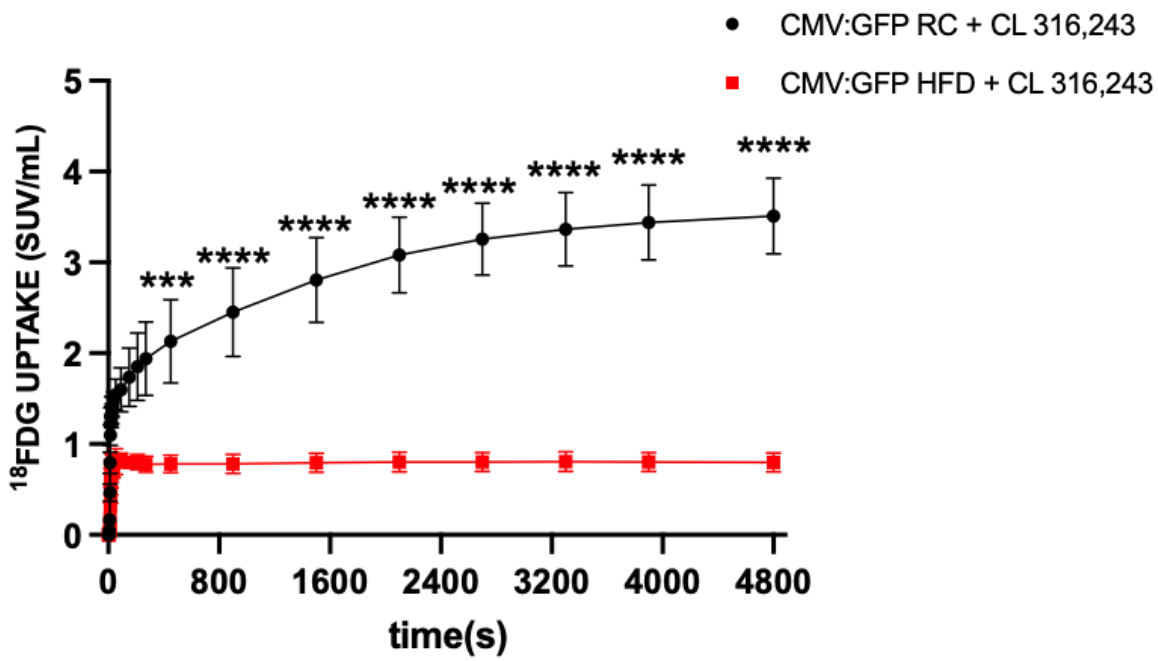

Figure 3.9: BAT ^{18}FDG glucose uptake for each group expressed in SUV (g/mL). *Data are representative of n = 4 rats for CMV:GFP regular chow and n = 5 rats CMV:GFP HFD, all treated with CL 316,243. All data was tested for normality prior statistical tests using the Shapiro-Wilk normality test. Data are shown as mean ± SEM. ***p<0.001; ****p < 0.0001. Statistical test: Two-Way ANOVA with repeated measures. Post hoc test: Tukey.*

To conclude, the results, as shown in Figure 3.6, 3.7 and 3.9, indicate that upon selective adrenergic stimulation, CMV:GFP regular chow animals have a significantly higher BAT glucose uptake than the CMV:GFP HFD group. Altogether, this evidence supports the notion that our HFD model is effective and that 2 weeks of HFD are sufficient to induce detrimental effects on BAT glucose uptake. Whilst evidence exists regarding the effects of long term HFD and obesity on glucose uptake and BAT activation in vivo using PET/CT scans, here we have demonstrated, for the first time, that detrimental changes in BAT activation occur much earlier than reported in existing literature (Wu et al., 2014; Schade et al., 2015).

3.6 Chronic inhibition of mitochondrial fission in all cells and specifically astrocytes in the NTS of HFD-fed rats partially rescues glucose uptake in BAT in dynamic ^{18}FDG -PET/CT scans upon selective β3 adrenergic activation using the compound CL 316,243

Next, we aimed to determine whether inhibition of HFD- mediated increase of mitochondrial fission in the NTS, and then in particular in astrocytes of the NTS, is sufficient to induce higher BAT activation compared to HFD controls upon selective adrenergic stimulation using PET/CT scans. As previously shown in Figure 3.3, in the absence of adrenergic stimulation, BAT glucose uptake is minimal, and it is not possible to observe any significant differences in regular chow versus HFD animals. For this reason, to limit the number of animals used in the study and meet the 3Rs criteria for animal use in research, in this experiment we only performed PET/CT scans in CL 316,243 injected animals.

Animals underwent stereotactic surgery to insert a bilateral cannula in the NTS and were injected the same day with an adenovirus containing the catalytically inactive form of Drp1 K38A to inhibit mitochondrial fission in the NTS, under a CMV-to target all cells (Patel et al., 2021) or GFAP, to target GFAP-expressing astrocytes (Patel et al., 2021), promoter (Sections 2.2.7 and 2.2.8). Animals then underwent the same procedures as animals described in paragraph 3.4. Please note that n=4 animals were injected with GFAP:GFP and we confirmed that they behaved like CMV:GFP animals, namely there was no significant differences in BAT ^{18}FDG uptake across the two groups (data not shown); for this reason, we decided not to repeat this experiment in a GFAP:GFP cohort to meet the reduce principle of the 3Rs for use of animals in research.

At the end of the scan, the animals were sacrificed, and BAT collected and ^{18}FDG measured in a gamma counter. As described in Section 3.2 ^{18}FDG uptake was calculated as percentage of injected dose (MBq) per gram of collected tissue. A two-way ANOVA was performed to analyse the effect of the viral construct and β3 adrenergic stimulation on BAT glucose uptake. The % of injected dose per gram of tissue in CL 316,243 injected CMV:K38A HFD (1.250±0.121 % injected dose/g) (n=5) and GFAP:K38A HFD (1.080±0.199 % injected dose/g) (n=4) animals were significantly higher than that of CMV:GFP HFD-fed animals injected with β3 adrenergic agonist CL 316,243 (0.371±0.0874 % injected dose/g) (n=4) (**p<0.01 and *p<0.05) (Figure

3.10). This data show that inhibiting mitochondrial fission in all cells, and specifically in astrocytes in the NTS of the animals prior to administration of short-term HFD can prevent the lower glucose uptake and thermogenesis in BAT associated with HFD.

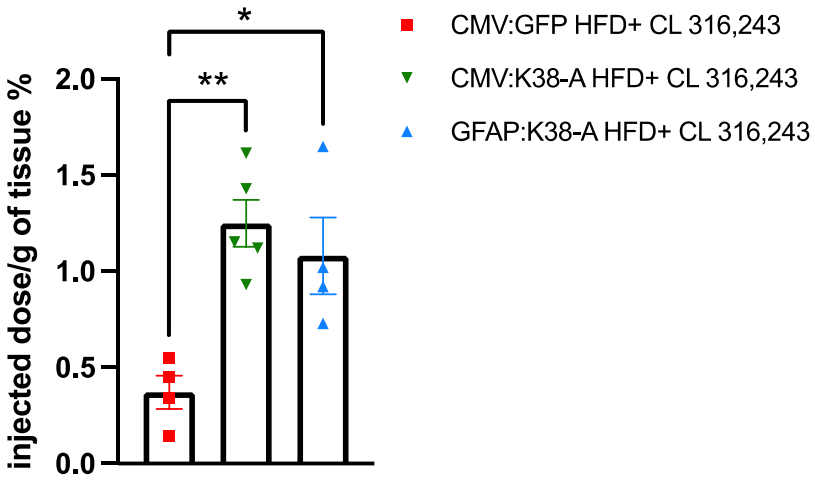

Figure 3.10: BAT uptake of ^{18}FDG is increased upon inhibition of mitochondrial fission in all cells and specifically in astrocytes of the NTS of HFD-fed animals upon CL 316,243 as measured with gamma counting. *30 minutes prior to scan, rats were injected with 1 mg/kg of selective β3 adrenergic agonist CL 316,243 to activate BAT. All data was tested for normality prior statistical tests using the Shapiro-Wilk normality test. Data are shown as mean ± SEM, with each single point highlighted. Data are representative of n = 4 rats for CMV: GFP HFD, n=5 for CMV:K38-A HFD and n=4 for GFAP:K38-A HFD. ∗p < 0.05, ∗∗p < 0.01. Statistical test: Two-Way ANOVA. Post hoc test: Tukey.*

Next, the ^{18}FDG uptake in BAT was analysed using reconstructed PET scans images as described in Section 2.2.20. Scans were visualised at SUV=3 and analysed as described in Section 3.4. Representative FDG/PET images of CMV:GFP HFD (A), CMV:K38A HFD (B) and GFAP:K38A HFD (C) show glucose uptake in BAT after injection of CL 316,243 (n=4 animals for CMV:GFP HFD, CMV:K38A HFD and GFAP K38A HFD) (Figure 3.11).

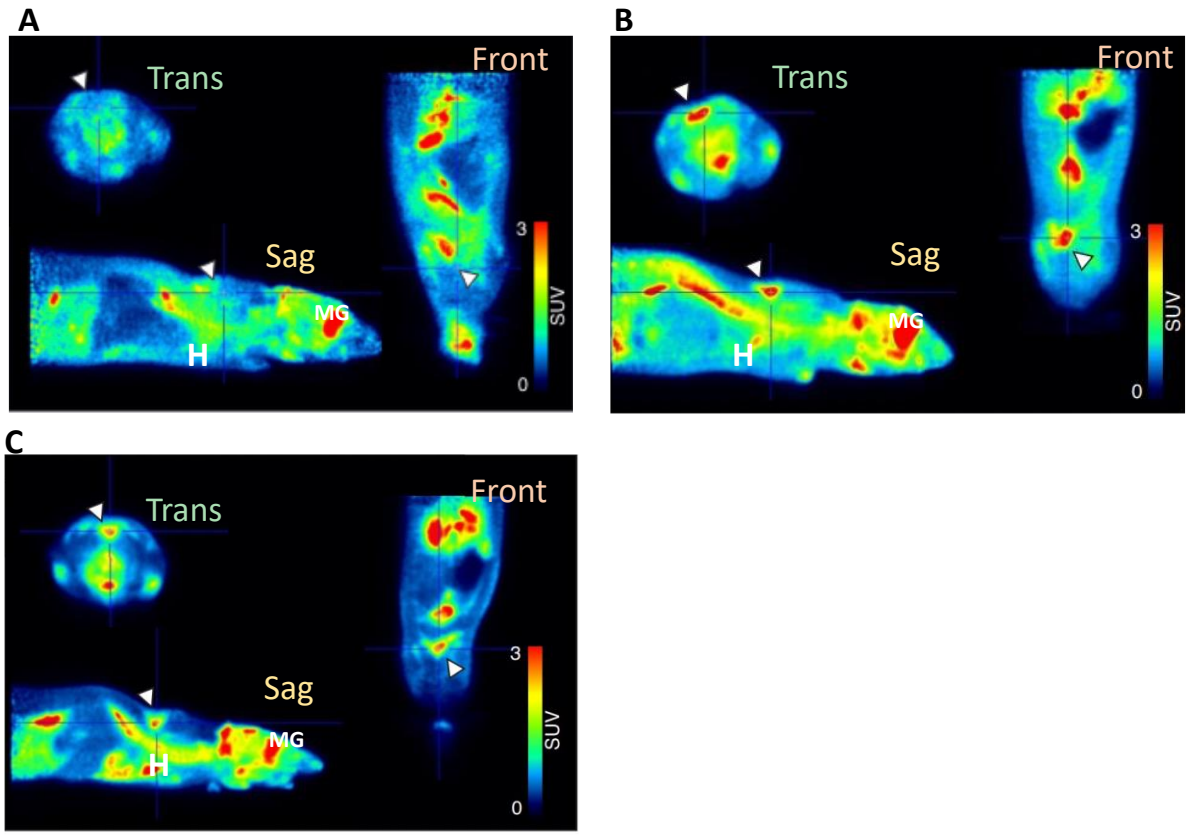

Figure 3.11: Representative PET/CT scan reconstructions of animals injected with 1mg/kg of selective β3 adrenergic agonist CL 316,243 to activate BAT. *Images are presented in standardised uptake value (SUV) for each group following a dynamic PET/CT scan. (A) Representative transverse, frontal and sagittal ^{18}FDG PET scan of a CMV: GFP HFD animal. (B) Representative transverse, frontal and sagittal ^{18}FDG PET scan of a CMV:K38-A animal. (C) Representative transverse, frontal and sagittal ^{18}FDG PET scan of a GFAP:K38-A animal. The scale bar represents SUV. The white arrow points towards BAT. Abbreviations: H, heart; MG, meibomian gland.*

PET scans analysis is presented as SUV_{BAT} in function of time. A two-way ANOVA was performed to analyse the effect of the viral construct and β3 adrenergic stimulation on BAT glucose uptake Interestingly, at the scan end point(t=4800), BAT glucose uptake was significantly higher in the CMV:K38A HFD, (1.77±0.472) (n=5) and in the GFAP:K38A HFD(1.345±0.264) (n=4) groups, when compared to CMV:GFP HFD control (0.797±0.0183) (n=5) of animals injected with CL 316,243 (***p<0.001 and $=*p<0.05, respectively).

In summary, it appears evident that HFD is associated with dramatically lower BAT glucose uptake and activation compared to regular chow-fed GFAP:GFP controls, as measured by gamma counting (Figure 3.10) and PET/CT scans (Figure 3.11), in as little as 2-weeks. Importantly, the inhibition of mitochondrial fission in all cells of the NTS (Figure 3.10, 3.11B, Figure 3.12) and then specifically in astrocytes of the NTS (Figure 3.10, 3.11C, Figure 3.12), of HFD animals injected with CL 316,243, can prevent the detrimental reduction of glucose uptake and activation of BAT occurring in short-term HFD fed animals.

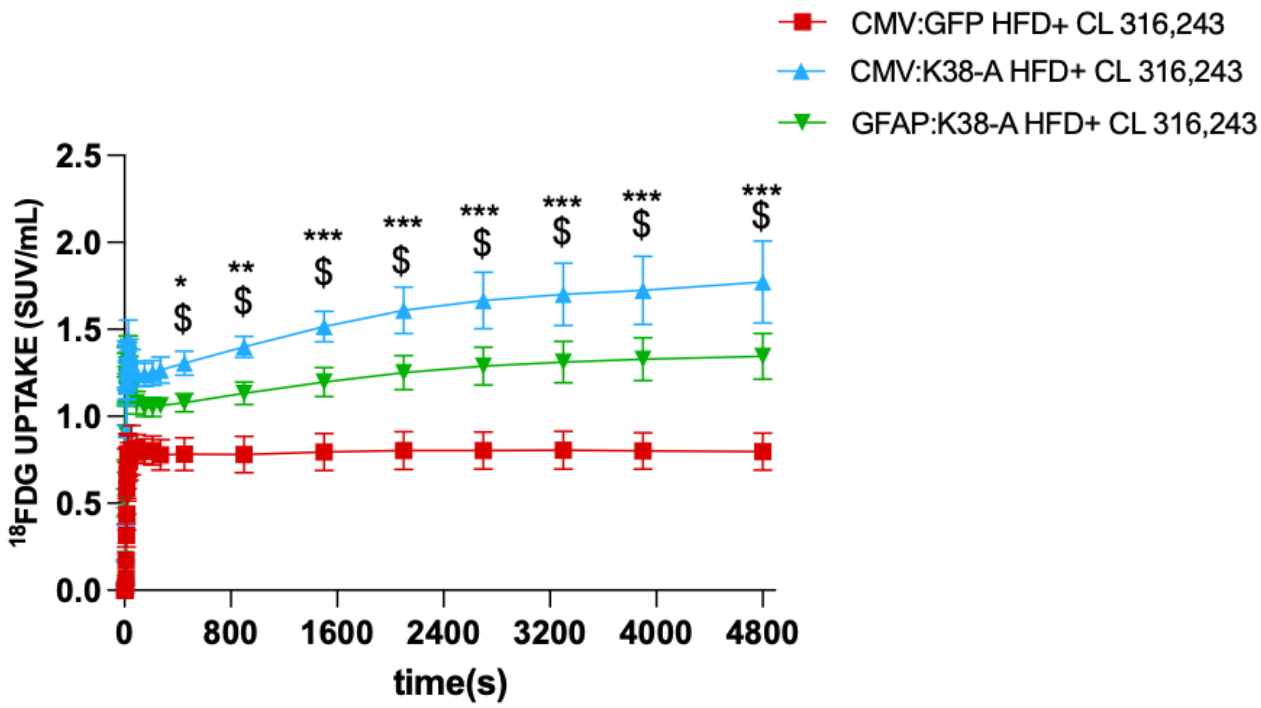

Figure 3.12: BAT ^{18}FDG glucose uptake is higher in CMV:K38-A HFD and GFAP:K38-A HFD animals compared to CMV:GFP HFD controls in SUV (g/mL). *Data are representative of n =5 rats for CMV:GFP HFD, n=5 rats for CMV:K38-A HFD and n=4 for GFAP:K38-A HFD. All data was tested for normality prior statistical tests using the Shapiro-Wilk normality test Data are shown as mean ± SEM. $=p < 0.05, *p<0.05; ** p<0.01; ***p< 0.001. Statistical test: Two-Way ANOVA with repeated measures. Post hoc test: Tukey.*

3.7 CT scans reveal differences in visceral and subcutaneous adiposity in regular-chow and HFD fed rats

The last objective of the chapter was to measure WAT glucose uptake as a marker of browning and subcutaneous and visceral WAT volume to determine if the inhibition of mitochondrial dynamics affects the WAT. These measurements were taken from the same animals used in the PET/CT scan experiments for BAT ^{18}FDG uptake measurement.

^{18}FDG uptake in WAT was assessed, as browning- which is defined by the appearance of brown-like adipocytes in the WAT- is associated with elevated glucose uptake by WAT; in particular, WAT browning is associated with the induction of GLUT1 expression in this tissue (Mössenböck et al., 2014). However, at thermoneutrality, no significant differences between the WAT of regular chow-fed (0.0816±0.0265) (n=5) and HFD-fed animals (0.0450±0.0134) n=5) could be observed (p=0.253) (Figure 3.13), suggesting that adrenergic stimulation may be required.

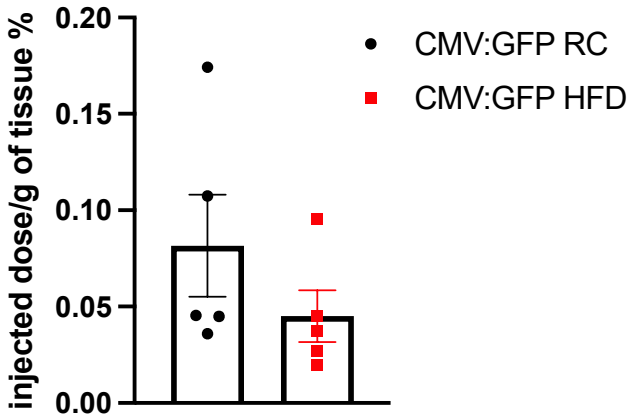

Figure 3.13: WAT uptake of ^{18}FDG is not affected by diet at thermoneutrality as measured with gamma counting*. Data are representative of n = 5 rats for both CMV:GFP regular chow and CMV: GFP HFD. All data was tested for normality prior statistical tests using the Shapiro-Wilk normality test. Data are shown as mean ± SEM, with each single point highlighted. Statistical test: unpaired t-test.*

^{18}FDG uptake in WAT was then assessed upon adrenergic stimulation, and a significantly higher uptake in WAT of regular chow-fed (0.638±0.214) (n=5) was observed when compared to HFD-fed animals (0.134±0.0181) (n=5), (*p<0.05) (Figure 3.14). This could mean that upon in RC animals, there is a higher level of brown-like adipocytes in WAT, which in literature has been associated with increased branching and activation of sympathetic nerve fibres in this tissue (Garofalo et al., 1996). However, H&E staining and brown adipocyte quantification would be needed to prove this.

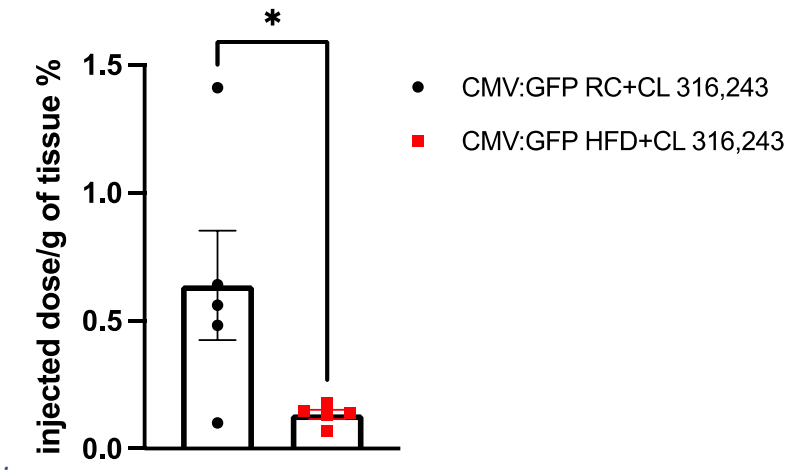

Figure 3.14: WAT uptake of ^{18}FDG is lower in HFD compared to regular-chow controls upon IP administration of CL 316,243 as measured with gamma counting. *30 minutes prior to scan, rats were injected with 1 mg/kg of selective β3 adrenergic agonist CL 316,243 to activate BAT. Data is representative of n = 4 rats for both CMV:GFP regular chow and CMV:GFP HFD. All data was tested for normality prior statistical tests using the Shapiro-Wilk normality test. Data are shown as mean ± SEM, with each single point highlighted. ∗p < 0.05. Statistical test: unpaired t-test.*

Next, ^{18}FDG uptake in WAT was assessed across the HFD groups, control and with inhibition of mitochondrial fission in the NTS. A two-way ANOVA was performed to analyse the effect of the viral construct and β3 adrenergic stimulation on WAT glucose uptake. Upon adrenergic stimulation, no significant differences were observed in WAT of CMV:K38A HFD (0.311±0.0926) (n=5) and GFAP:K38A HFD(0.228±0.0581) (n=4) animals compared to HFD

controls (0.134±0.0181) (n=5) (p=0.198 and p=0.665, respectively) (Figure 3.15) suggesting that our treatments do not increase browning capacity in WAT of HFD-fed animals.

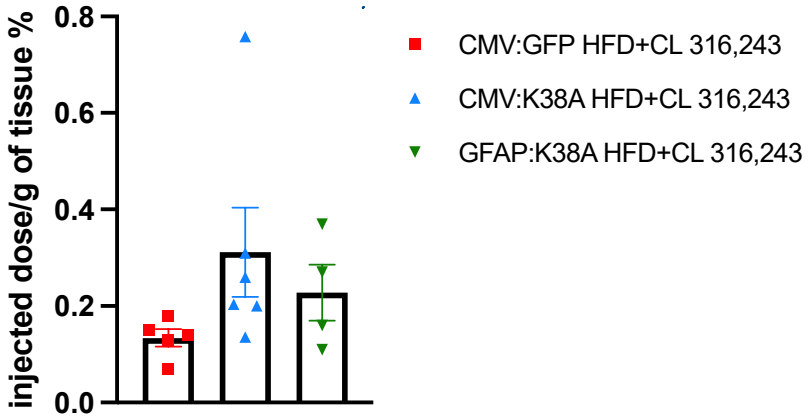

Figure 3.15: WAT uptake of ^{18}FDG is not affected by inhibition of mitochondrial dynamics in the NTS of HFD-fed animals. *30 minutes prior to scan, rats were injected with 1 mg/kg of selective β3 adrenergic agonist CL 316,243 to activate BAT. All data was tested for normality prior statistical tests using the Shapiro-Wilk normality test. Data are shown as mean ± SEM, with each single point highlighted. Data are representative of n = 5 rats for both CMV:GFP HFD and CMV:K38A HFD, and n=4 for GFAP:K38A HFD. Statistical test: Two-Way ANOVA. Post-hoc: Tukey*

Finally, the visceral and subcutaneous fat mass of rats from the cohorts previously described were assessed by whole body CT scans. Volumetric information of visceral and subcutaneous fat was segmented using the method described by Sasser et al., 2012. By exploiting differences in tissue density, total body volume and adipose tissue volumes were filtered out and ratio calculated (Section 2.2.20). Figure 3.15 shows visceral and subcutaneous adipose depots (red) in regular chow (Figure 3.16, A) and HFD- fed (Figure 3.16, B) animals.

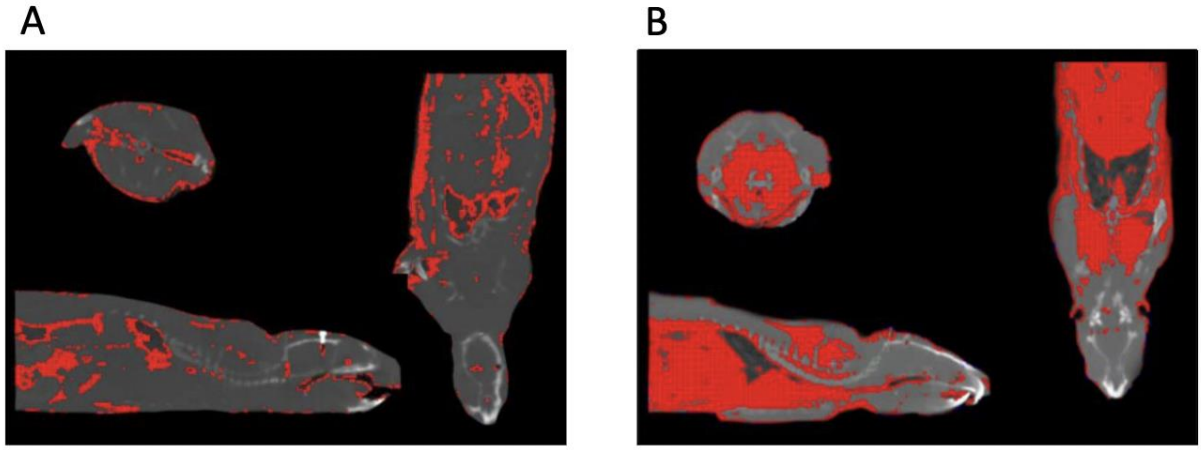

Figure 3.16: Representative CT scan images showing the presence, distribution, and abundance of visceral and subcutaneous adipose tissue. *(A) Representative transverse, frontal and sagittal CT scan of a CMV: GFP RC animal. (B) Representative transverse, frontal and sagittal ^{18}FDG PET scan of a CMV:GFP HFD animal. The red mask superimposed on the CT image represents visceral and subcutaneous adipose tissue.*

After obtaining information on individual total body volume and adipose mass volume the ratio of adipose tissue over total body volume was calculated as described in table 3.1.

Table 3.15: Total volumes, adipose volumes and calculated adipose tissue/total volume ratios at three significant figures for RC group CMV:GFP RC and HFD group CMV:GFP HFD.

Regular chow	Tot vol (cm^3)	Fat vol (cm^3)	Fat/tot ratio	HFD	Tot vol (cm^3)	Fat vol (cm^3)	Fat/tot ratio
Animal 1	185	26.3	0.125	Animal 1	202	26.1	0.129
Animal 2	160	9.05	0.0566	Animal 2	153	61.6	0.402
Animal 3	177	19.2	0.108	Animal 3	161	71.7	0.445
Animal 4	228	23.1	0.101	Animal 4	251	30.7	0.12
-	-	-	-	Animal 5	190	74.8	0.394
mean± SEM			0.977±0.0146	mean± SEM			0.298±0.0714

Ratios calculated in table 3.1 were then plotted as individual values and statistical analysis was performed. The results obtained from CT scans from regular chow and HFD fed animals revealed that after 2 weeks from the beginning of the study, regular chow animals have significantly less visceral and subcutaneous adiposity than HFD- fed animals, expressed as percentage of total body volume (Figure 3.17) (9.77±1.46 % and 29.8±7.14 % fat volume, respectively) (n=4 and n=4, respectively) (*p<0.05). This suggests that 2-weeks of HFD are sufficient to induce profound changes in visceral and subcutaneous adiposity in adult male rats.

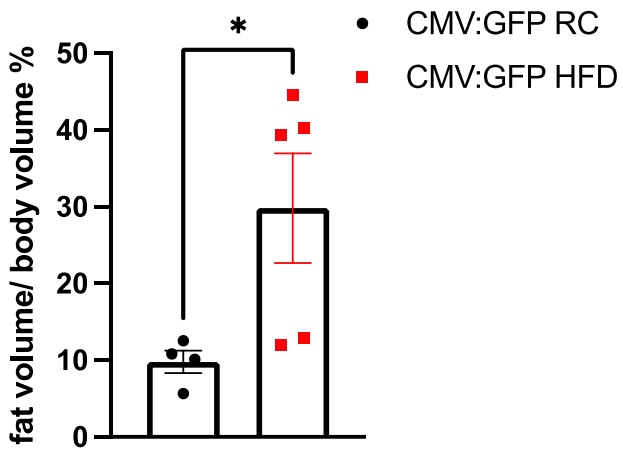

Figure 3.17: HFD-fed animals have higher fat volume over total body volume (cm^3) than regular-chow fed controls. *Data are representative of n =4 rats for CMV:GFP RC and n=5 for CMV:GFP HFD. All data was tested for normality prior statistical tests using the Shapiro-Wilk normality test. Data are shown as mean ± SEM, with each single point highlighted. ⁎p < 0.05. Statistical test: unpaired t-test.*

Next, the visceral and subcutaneous depots of CMV:GFP HFD, CMV:K38A HFD and GFAP:K38A HFD were analysed. Figure 3.18 shows visceral and subcutaneous adipose depots (red) of CMV:GFP HFD (Figure 3.18A), CMV:K38A HFD (Figure 3.18B) and GFAP:K38A HFD (Figure 3.18C).

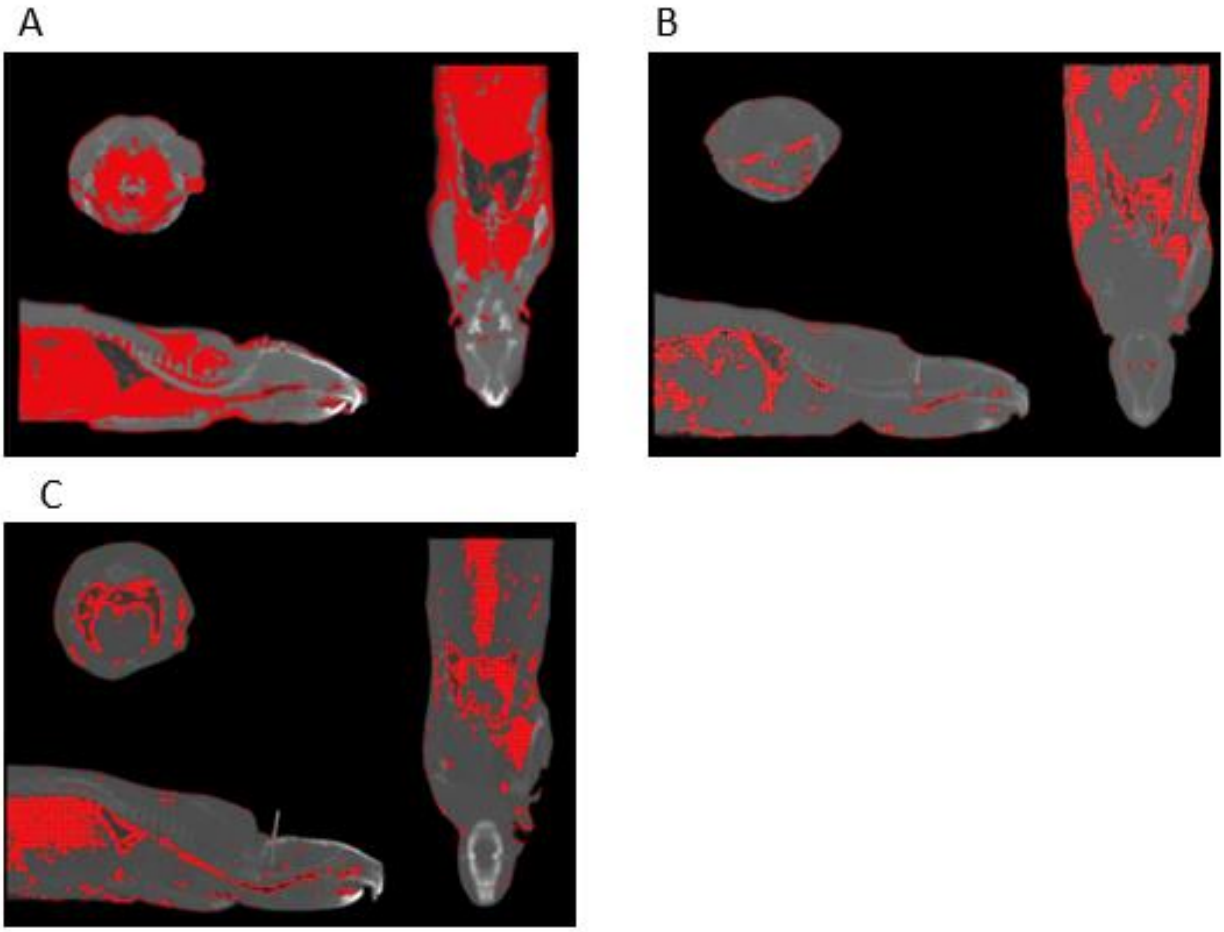

Figure 3.18: Representative CT scan images showing the presence, distribution, and abundance of visceral and subcutaneous adipose tissue. *(A) Representative transverse, frontal and sagittal CT scan of a CMV: GFP HFD animal. (B Representative transverse, frontal and sagittal ^{18}FDG PET scan of a CMV:K38A HFD animal. (C) Representative transverse, frontal and sagittal ^{18}FDG PET scan of a GFAP:K38A HFD animal. The red mask superimposed on the CT image represents visceral and subcutaneous adipose tissue.*

After obtaining information on individual total body volume and adipose tissue volume, the ratio of adipose tissue volume over total body volume was calculated as described in table 3.2.

Table 3.16: Total volumes, adipose volumes and calculated adipose tissue/total volume ratios at three significant figures for HFD groups CMV:GFP HFD, CMV:K38A HFD and GFAP:K38A HFD.

HFD	Tot vol (cm^3)	Fat vol (cm^3)	Fat/ Tot ratio	CMV: K38A	Tot vol (cm^3)	Fat vol (cm^3)	Fat/ Tot ratio	GFAP: K38A	Tot vol (cm^3)	Fat vol (cm^3)	Fat/ tot ratio
Animal 1	202	26.1	0.129	Animal 1	159	15.6	0.0981	Animal 1	170	33.9	0.199
Animal 2	153	61.6	0.402	Animal 2	178	39.7	0.223	Animal 2	166	8.43	0.0507
Animal 3	161	71.7	0.445	Animal 3	187	19.5	0.104	Animal 3	162	33.4	0.206
Animal 4	251	30.7	0.122	Animal 4	208	11.8	0.0567	Animal 4	141	30.9	0.219
Animal 5	190	74.8	0.394	Animal 5	176	33.4	0.189	-	-	-	-
mean± SEM			0.298± 0.0714	mean±SEM			0.134± 0.309	mean± SEM			0.168± 0.0395

Ratios calculated in table 3.2 were then plotted as individual values and statistical analysis was performed.

The results obtained from CT scans from CMV:K38A HFD (13.4±3.09 % fat volume) (n=5) revealed a trend towards lower visceral and subcutaneous adiposity after 2 weeks of HFD when compared to CMV:GFP HFD control (29.8±7.14 % fat volume) (n=5) (p=0.131). By contrast, GFAP:K38A HFD (16.8±3.95 % fat volume) (n=4) visceral and subcutaneous adiposity is not different from that of CMV:GFP HFD controls (29.8±7.14% fat volume) (n=5) (p=0.397) (Figure 3.19). These results partially reflect those Patel et al. (2021) who, upon post-mortem collection and weighing of visceral adipose depots, found significantly lower total visceral fat in CMV:K38A HFD animals compared to GFP HFD controls, and no significant differences between GFAP:K38A HFD and GFP HFD animals. This partial discrepancy could be attributed to the fact that in this present study the total body fat, and not just the visceral fat was measured. It is also possible that our treatment only affects visceral adiposity but not whole-

body adiposity, and that when the whole fat volume is examined, it is not possible to discern regional differences and the contribution of each fat depot in the analysis.

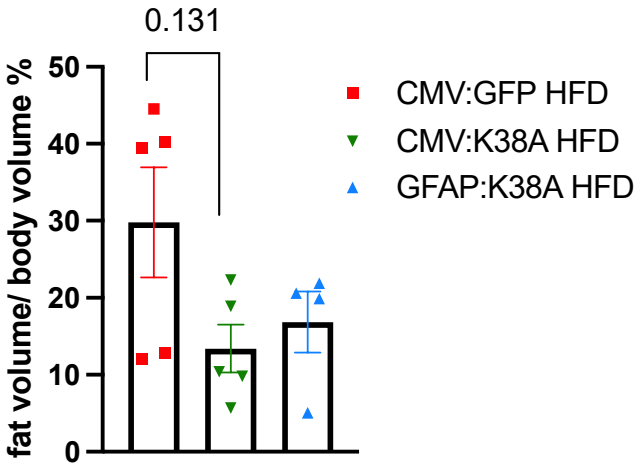

Figure 3.19: Inhibition of mitochondrial fission in the NTS of HFD-fed rats does not affect global WAT accumulation*. Data are representative of n =5 rats for CMV:GFP HFD and CMV:K38A HFD, and n=4 for GFAP:K38A HFD. All data was tested for normality prior statistical tests using the Shapiro-Wilk normality test. Data are shown as mean ± SEM, with each single point highlighted. Statistical test: Two-way ANOVA with repeated measures. Post hoc test: Tukey.*

3.8 Discussion

3.8.1 General considerations

A very limited body of literature has reported the effects of HFD on brown adipose tissue glucose uptake and activation in vivo. One such study (Saeed et al. 2019) reported that upon 12 weeks of HFD, no detectable difference in BAT ^{18}FDG uptake was observed in wild-type mice at thermoneutrality when compared to matched regular chow controls. Conversely, long term HFD (8-weeks) and Streptozocin-induced diabetes mellitus mice models exhibit a significantly lower ^{18}FDG uptake in BAT (Wu et al., 2014) when compared to regular chow controls, upon selective adrenergic stimulation using β3 adrenergic agonist BRL37344. Our findings support the existing literature on selective β3 adrenergic stimulation being the initiator of an intracellular signalling cascade leading to BAT activation. Moreover, we found

that BAT ^{18}FDG uptake in regular chow animals was 13.4-fold higher than that of animals fed HFD for 2 weeks.

It is well established that short-term HFD is associated with rapid changes in many organs and tissues in rodents. For example, short-term HFD suppresses insulin signalling and activates p70 S6 kinase in the mediobasal hypothalamus to blunt insulin-dependent suppression of hepatic glucose production (Ono et al., 2008). Moreover, three days of HFD were sufficient to stop activation of Erk1/2 insulin pathway in the DVC, leading to an inability of the DVC to increase glucose infusion rate and lower glucose production upon insulin infusion in the DVC, as measured by euglycemic clamps (Filippi et al., 2012).

The consumption of HFD over a short-term is also sufficient to induce inflammatory, ER stress and apoptotic signs in young mice hippocampi (Nakandakari et al., 2019). In the NTS of the DVC, short-term HFD has also been associated with alterations in circadian phasing in the DVC, and disturbances in the 24-hour feeding pattern in rats (Chrobok et al., 2022); moreover, these changes preceded the effects on body weight, suggesting the rapid impact of HFD on this brain region. In the liver, short-term HFD induces oxidative stress, resulting from a combination of an overabundance of FAs and increased FA oxidation in rats (Ciapaite et al., 2011). Furthermore, muscle tissue shows alterations in its integrity after only 3 days of HFD, and this appears to be associated with alterations in the gut microbiota and systemic low-grade inflammation in male rats (Collins et al., 2016). The BAT is also affected by short-term HFD; a study from 2019 showed that 72 hours consumption of HFD induced upregulation of genes involved in insulin signalling and lipid metabolism, as well as an effect on glucagon and peroxisome proliferator-activated receptor (PPAR) signalling pathways in adult rats (Aldiss et al., 2019). Similarly, in mice within 1 day of HFD BAT lipid content was increased, and upon 3 days of HFD, BAT mitochondria had reorganised into a more fused network and an increase in macrophage markers was revealed (Kuipers, Held, in het Panhuis, et al., 2019).

Here we have demonstrated for the first time that short-term HFD is associated with lower glucose uptake and activation of BAT when compared to lean controls, upon selective adrenergic stimulation in adult rats. WAT glucose uptake was also significantly lower in HFD animals, when compared to matching regular chow controls, suggesting that during HFD WAT

glucose metabolism is impaired. This could potentially be explained by an increase in brown adipocytes within the tissue (browning) or higher insulin sensitivity in RC vs HFD animals, which could translate in a higher expression of insulin-dependent glucose transporters, facilitating the uptake of glucose in the tissue. To probe this, histological analysis of BAT (browning) and qPCR or *in situ* hybridisation (glucose transporters) would be useful. This evidence suggests that animals fed HFD not only consume more calories, but also lose the ability to eliminate excessive nutrients via uncoupling respiration in the BAT and recruiting thermogenesis-capable brown adipocytes in WAT. Moreover, the reduction in glucose uptake in HFD-fed animals may be indicative of BAT insulin resistance in these animals.

The next scope of our experiment was to determine whether the inhibition of Drp1-dependent mitochondrial fission in the NTS of HFD-fed rats is sufficient to prevent the detrimental loss of activity of BAT. Filippi et al., (2017) have shown that upon short-term HFD, animals exhibit higher levels of mitochondrial fission in the NTS when compared to matched lean controls. Moreover, Patel et al. (2021) have demonstrated that inhibiting mitochondrial fission in the NTS of HFD-fed rats could prevent inflammation and insulin resistance in the NTS, and decrease food intake, body weight and visceral adiposity. Additionally, the authors showed that the inhibition of Drp1- dependent mitochondrial fission specifically in astrocytes in the NTS of HFD-fed rats was sufficient to reduce body weight and food intake and could prevent inflammation and insulin resistance in the NTS. Here we showed that inhibiting Drp1-dependent mitochondrial fission in the NTS of HFD-fed rats in all NTS cells and then specifically in astrocytes can cause significantly higher levels of BAT glucose uptake compared to HFD controls upon adrenergic stimulation.

3.8.2 Brain regions important in energy expenditure and BAT activation

A large body of evidence has reported that the brain is a key site for the monitoring of body energy state as it can sense alterations in plasma levels of nutrients and key hormones and metabolites. Moreover, mitochondria play a critical role in nutrient adaptation, and the bioenergetics of mitochondria reflect on their architecture. Specifically, it has been demonstrated that an overabundance of nutrients is associated with mitochondrial fragmentation, whilst fasting is associated with a fused-like mitochondria state. Indeed this

has been observed in several different body tissues, including skeletal muscle (Jheng et al., 2012), pancreatic beta cells (Molina et al., 2009) and the brain (Schneeberger et al., 2014; Filippi et al., 2017; Ramírez et al., 2017; Patel et al., 2021).

The hypothalamus plays a key role in energy expenditure, including the activation of BAT. The DMH contains sympathoexcitatory neurons that regulate BAT activity (Zhang et al., 2011), whilst the melanocortin system of the ARC nucleus of the hypothalamus promotes α-MSH-mediated activation of BAT (Brito et al., 2007). Moreover, central administration of glucagon and GLP1 stimulate BAT activity (Lockie et al., 2012) and inhibition of MAPK in the hypothalamus blocked insulin-induced sympathetic activation to the BAT (Rahmouni et al., 2004). Nutritional excess has been shown to cause ER stress in the hypothalamus, leading to systemic leptin and insulin resistance, glucose intolerance and decreased sympathetic tone and BAT activation (Contreras et al., 2017). Importantly the ER has been shown to regulate Drp1-driven mitochondrial fission via associated C1q/TNF-related protein 1 (Sonn et al., 2021). Moreover, HFD induces mitochondrial fission in POMC neurons in the ARC nucleus of the hypothalamus, leading to increased food intake (Schneeberger et al., 2014; Ramírez et al., 2017).

The NTS is an equally important, but far less studied brain region that is involved in energy metabolism and BAT activation; importantly, the NTS contains GABAergic neurons whose activation inhibits BAT thermogenesis via tonic inhibition of sympathetic premotor neurons in the rRPa (Cao et al., 2010). This is a physiological mechanism in thermoneutral conditions, however, HFD appears to induce a sustained suppression of BAT thermogenesis. In fact, evidence has shown that during cooling, rats maintained on HFD fail to activate BAT and cervical vagotomy, or blockade of glutamate receptors in the NTS reversed this (Madden and Morrison, 2016). Interestingly, the NTS is the termination site of glutamatergic vagal afferents, and HFD does not prevent a robust central activation of BAT, but rather acts via vagal activation of sympathoinhibitory neurons involved in the circuits controlling BAT (Madden and Morrison, 2016).

It has now been established that HFD increases mitochondrial fission in the NTS (Filippi et al., 2017), which is associated with increased levels of inflammation driven by iNOS, insulin

resistance in the NTS and increased body weight and visceral adiposity in rats compared to lean controls (Patel et al 2021). Moreover, the inhibition of mitochondrial fission in HFD-fed rats prevents these detrimental effects (Patel et al., 2021). Of particular note, these effects have been recapitulated by specifically targeting astrocytes in this brain region (Patel et al., 2021). This is interesting since while it is known that astrocytes are involved in circuits controlling feeding behaviour (MacDonald et al., 2020), but they have only recently been implicated in the maintenance of normal thermogenesis and regulation of body temperature. Specifically, astrocytic insulin signalling seems to be critical in regulating the signals that control the body temperature and BAT activation (Manaserh et al., 2020), and given that thermogenesis is an important component of the body energy expenditure it is possible that astrocytic insulin resistance may exacerbate or contribute to the development of obesity and diabetes by disrupting BAT function. However, the connection between mitochondrial dynamics in the NTS, and specifically in astrocytes in the NTS and brown adipose tissue activation is not clear.

Astrocytes do not require mitochondria to meet their energy demands, however, it has been demonstrated that mitochondrial metabolism in astrocytes is critical to the regulation of brain bioenergetics, the homeostasis of neurotransmitters and redox equilibrium (Rose et al., 2020).

The regulation and metabolism of glutamate is a pivotal process occurring in astrocytes (Parpura and Verkhratsky, 2012), and the maintenance of this neurotransmitter is strictly dependent upon *de novo* glutamine synthesis in astrocytes. Moreover, their finely-tuned response to subtle changes in nearby neuronal glutamate levels is fundamental to adjust glutamate oxidation for energy glutamine production to meet neurotransmission demand (Mahmoud et al., 2019).

Importantly, obesity and HFD impair this mechanism, leading to increased brain glutamate levels, dysfunction in extra-synaptic NMDA levels and mitochondrial dysregulation (Labban et al., 2020). As previously discussed, HFD is associated with suppression of BAT driven by glutamatergic afferents to the NTS, and blockade of glutamate receptors, or cervical vagotomy reversed this (Madden and Morrison, 2016). Glutamate has been shown to induce

iNOS in the brain, and obesity and HFD have been associated with increased iNOS levels in the NTS, and the staining pattern was mainly localised on astrocytes (Patel et al., 2021); astrocytes express iNOS and inhibiting mitochondrial fission in the NTS decreased expression of iNOS in this brain region (Patel et al., 2021). Whilst the causality is not clear, HFD is known to cause mitochondrial fission in the NTS. A potential mechanism that could explain the link between mitochondrial dynamics in astrocytes in the NTS and BAT activation is that increased mitochondrial fission in the NTS could drive an increase in inflammation via increased iNOS expression in astrocytes, which is exacerbated by glutamatergic afferents discharge to the NTS. Dysfunctional astrocytic mitochondrial dynamics may have a reduced capacity to uptake glutamate and clear it from the extracellular space, causing alterations in neurotransmission. This could eventually lead to alterations in the sympathetic innervation to BAT and consequent activation and thermogenesis.

The experiments presented in this chapter have shown that short-term HFD is sufficient to impair BAT glucose uptake and activation. Moreover, mitochondrial fission in the NTS of the DVC plays a key role in this process, as inhibition of mitochondrial fission protects glucose uptake and BAT activation in HFD-fed rats. In summary, an increase in mitochondrial fission in the NTS of rats decreases BAT glucose uptake and activity in vivo, and the inhibition of mitochondrial fission rescues BAT glucose uptake and activation in HFD animals. However, the molecular mechanisms that link mitochondrial dynamics in the NTS of the DVC and BAT activation are still unclear. Evidence from literature show the importance of astrocytes in the maintenance of whole-body energy homeostasis (MacDonald et al., 2020; MacDonald and Ellacott, 2020; Manaserh et al., 2020; Patel et al., 2021); moreover, we presented evidence on the role of inhibition of mitochondrial fission in astrocytes of the NTS in BAT activation *in vivo*. For these reasons, in the following chapter we performed molecular analysis of BAT in HFD animals in which mitochondrial fission was inhibited in the astrocytes of the NTS. The scope of this analysis will be to identify the molecular changes occurring with inhibition of mitochondrial fission that enable BAT to preserve its thermogenic capacity during HFD.

Chapter 4

Chronic inhibition of mitochondrial fission in astrocytes of the NTS of HFD-fed rats prevents BAT hypertrophy, preserves BAT sympathetic innervation, and induce changes in BAT gene expression

4.1 Chronic inhibition of mitochondrial fission in astrocytes in the NTS prevents HFD-dependent morphological and molecular alterations in BAT

4.1.1 Introduction and rationale

Inhibition of Drp1 in the NTS increased *in vivo* dynamic glucose uptake in BAT in rats fed short-term high-fat diet compared to matching HFD controls. In addition to this, the inhibition of Drp1 in GFAP+ astrocytes of the NTS was sufficient to maintain this effect, suggesting that these cells are critical in the maintenance of brown adipose tissue activity during HFD.

It is well established that astrocytes do not merely serve the function of support cells to the surrounding neurons, but they communicate with neurons and respond to their synaptic activity as well as regulate synaptic transmission via release of gliotransmitters, scaling of synaptic strength and direct modulation of neuronal circuits (Perea et al., 2009; Sasaki et al., 2012; Allen and Eroglu, 2017).

As well as regulating neuronal circuits, astrocytes serve a critical role in the control of feeding behaviour and systemic metabolism, and this has been widely reported in literature. For example, chemogenetic activation of astrocytes in the DVC suppressed food intake in mice (MacDonald et al., 2019); importantly, the authors showed that the activation of DVC astrocytes resulted in induction of c-FOS expression in the NTS, AP and in the lateral parabrachial nucleus, a downstream target of NTS neurons (MacDonald et al., 2019), suggesting activation of both local neurons and the recruitment of a long-range neuronal network in response to astrocytic activation in the DVC. Genetic loss of leptin receptors in mature astrocytes leads to dysregulation of leptin-dependent feeding behaviour in genetic *Gfap-Lepr-/-* mice models (Kim et al., 2014), while chemogenetic inhibition of astrocytes in the medial basal hypothalamus of mice enhanced and prolonged ghrelin-evoked feeding (Liang Yang et al., 2015). In contrast, chemogenetic activation of astrocytes in the same region induced leptin-mediated suppression of food intake, and their subsequent reactivation stopped leptin-induced anorexia via modulation of Adenosine A1 receptor in AGRP neurons in ARC a dose-dependent fashion (Liang Yang et al., 2015).

Notably, a recent study has reported that consumption of HFD impairs astrocytic glutamate clearance, and consequentially heterosynaptic depression of inhibitory GABAergic transmission on pyramidal neurons in the orbitofrontal cortex, a key brain region for the evaluation of reward upon food ingestion in rats (Lau et al., 2021), showing the importance of astrocytic integration of nutritional cues to modulate neuronal activity and behaviour. Moreover, in the hypothalamus, positive chemogenetic manipulation of astrocytes Ca^{2+} signalling in PVN neurons worsened metabolic status in diet-induced obese mice, whilst decrease of Ca^{2+} signalling in these cells, via negative chemogenetic manipulation, improves the metabolic condition of obese mice (Herrera et al., 2022).

4.1.2 Mitochondrial dynamics in astrocytes control metabolism

Mitochondrial dynamics are critical to the functionality of all cells, and alterations of mitochondrial function in the brain, and in particular in glia, are associated with HFD feeding and obesity (Kim et al., 2019; Patel et al., 2021). For example, a fragmented mitochondrial pattern has been observed in isolated oligodendrocytes grown under HFD conditions, and this effect was recapitulated in the spinal cord of a mice model consuming HFD for 12 weeks (Langley et al., 2020). Moreover, HFD induced mitochondrial fission in the NTS and increased iNOS levels in astrocytes in this brain region (Patel et al., 2021) in adult male rats; this led to increased body weight, food intake and visceral adiposity. Importantly, these events were prevented by inhibiting mitochondrial fission in NTS astrocytes of HFD-fed rats (Patel et al., 2021), suggesting a connection between astrocytic mitochondrial fission, inflammation and whole body energy metabolism; however, the causality of such events has not yet been elucidated.

Inflammation, defective insulin signalling and alterations in mitochondrial metabolism are common denominators of metabolic disorders such as obesity and T2DM. Astrocytes, alongside microglia, produce inflammatory cytokines and drive inflammation in the brain in response to HFD while inflammation itself can alter mitochondrial dynamics in astrocytes via Drp1-mediated increase in fission, ROS production and reduced respiratory capacity (Motori et al., 2013). This suggests that chronic, low-grade inflammation observed in obesity and HFD is at least partially mediated by astrocytes. Importantly, Patel et al. (2021) demonstrated that

mitochondrial fission in the NTS of HFD-fed rats drives inflammation by increasing iNOS, and lentiviral suppression of iNOS could protect these animals from developing insulin resistance. Moreover, inflammatory recruitment of astrocytes in the hypothalamus via IKKB/NFKB signalling pathway is associated with insulin resistance, and astrocytic deletion of IKKB after exposure to HFD in mice reduces glucose intolerance and insulin resistance, potentially via a mechanism mediated by the adipose tissue (Douglass et al., 2017). Additionally, in a mouse model of postnatal KO of insulin receptors in astrocytes, mitochondria presented a reduced mitochondrial aspect/ratio- defined as the ratio between centreline length and average width- and higher basal mitochondrial respiration rate in response to elevated blood glucose (Herrera et al., 2022).

The NTS is a critical area for the control of systemic energy expenditure via sympathetic activation of the BAT. Moreover, the role of astrocytes in the control of central and peripheral energy metabolism and glucose homeostasis has been recently recognised, and there are indications that normal thermogenesis and body temperature are regulated via insulin sensing by astrocytes (Manaserh et al., 2020). Importantly, increased mitochondrial fission in astrocytes in the NTS is linked to insulin insensitivity in this region (Patel et al., 2021) and insulin and insulin-like growth factor decreased mitochondrial fission in vitro (Ribeiro et al., 2014). Therefore, HFD-mediated disruption of insulin sensitivity in the NTS could also be linked to an alteration of mitochondrial dynamics in astrocytes in this region.

If we consider this body of evidence, it is reasonable to speculate that HFD-induced inflammation and insulin insensitivity may contribute to causing and/or exacerbating HFD-dependent mitochondrial fission in NTS astrocytes. This could lead to alterations in energy sensing in astrocytes and induce changes in the firing of nearby neurons to influence BAT adrenergic discharge and metabolic profile. Further, as it was previously observed by Patel et al. (2021), inhibition of mitochondrial fission in the NTS significantly reduces body weight and visceral adiposity, and we could speculate that this may be partially due to an increase in energy expenditure. In fact, we previously showed (Chapter 3) that the inhibition of mitochondrial dynamics in astrocytes in the NTS is sufficient to increase FDG-18 uptake in brown adipose tissue HFD-fed animals when compared to control HFD GFP animals, and in literature increased glucose uptake in BAT is a typical indirect marker of increased metabolic

activity and thermogenesis of BAT *in vitro* and *in vivo* (Cypess et al., 2013; Cypess et al., 2015c). This is evidence that astrocytes in the NTS play an important role in the activation of BAT *in vivo*.

4.1.3 Study rationale

We showed that inhibiting Drp1 function in astrocytes of the NTS increases the energy expenditure and glucose uptake of BAT in vivo (Chapter 3); here we aim to investigate the histological and molecular correlates to these observations in the BAT of animals exposed to standard laboratory temperature, and in absence of exogenous noradrenergic stimulation. For the molecular analysis we selected five different classes of genes to interrogate the overall metabolic health of BAT during HFD and in response to inhibition of mitochondrial dynamics in the astrocytes of the NTS, which will be described and discussed in their dedicated result section.

Our objective is to understand what is different, on a molecular and histological level, in the BAT from animals that express GFAP:K38-A in their NTS compared to control GFP animals. Specifically, we are interested in establishing why the BAT from these animals can respond to noradrenergic stimulation, while control HFD animals have lost this capacity.

The hypothesis for this chapter is that in HFD-fed animals, BAT will present a "white-like" appearance and lower levels of noradrenergic innervation measured with TH immunolabelling compared to RC control animals. These would be signs of alterations in the brain-BAT axis, and in particular, of decreased postganglionic noradrenergic discharge onto BAT. Moreover, we are expecting that inhibition of mitochondrial fission in the NTS of HFD-fed rats will result in higher noradrenergic discharge and a multilocular appearance of BAT, associated with a metabolically healthy phenotype compared to GFP control HFD fed animals. We also expect to see changes in genes associated with active BAT and lower levels of stress and inflammation of the tissue in HFD fed animals with inhibited mitochondrial fission in their NTS compared to HFD matching controls.

We will also assess the contribution of food intake in the effects we will observe in the *ad libitum* cohorts by employing a pair-fed paradigm (Section 2.2.9); Patel et al. (2021) has revealed that inhibiting mitochondrial fission in astrocytes of the NTS of HFD-fed rats decreases food intake compared to control HFD animals, therefore if we eliminate the differences in feeding behaviour by adopting a pair-fed paradigm we can assess to what extent food intake is responsible for the metabolic health of BAT.

To probe this hypothesis, adenoviruses expressing either GFP or K38-A under the control of a GFAP promoter (GFAP:GFP, GFAP:K38-A) were generated and delivered to the NTS of male Sprague-Dawley rats (Section 2.2.8). After 2-weeks of HFD from the day of the brain injection BAT morphology, adrenergic innervation and genes were investigated.

4.2 Aims

Aim 1: To determine whether 2-weeks of HFD are sufficient to affect brown adipose tissue morphology and noradrenergic innervation of BAT compared to RC animals.

Aim 2: To determine whether the inhibition of HFD-mediated increase of mitochondrial fission in the NTS astrocytes of HFD-fed rats is affecting brown adipose tissue morphology and noradrenergic innervation of BAT.

Aim 3: To determine whether inhibition of HFD-mediated increase of mitochondrial fission in the NTS astrocytes is sufficient to induce changes in key genes associated with an active metabolic profile of BAT.

Aim 4: To understand the contribution of food intake on BAT morphology and genes associated with an active metabolic profile of BAT employing a pair-feeding paradigm.

4.3 2-weeks HFD is sufficient to induce BAT hypertrophy and disrupt adrenergic terminals in BAT

Please note that some of the tissues analysed and discussed in this chapter are from the animals from the published study by Patel et al. (2021), which confirmed changes in body weight, food intake, visceral adiposity and insulin sensitivity in this cohort. Moreover, confirmation of viral expression in the NTS is also presented in Patel et al. (2021), alongside with confirmation of astrocytic specificity for the GFAP viruses. Three separate cohorts were employed; the first cohort is that described in Patel et al. (2021) and was used to conduct all histological and molecular analysis on BAT. The second cohort was used for the pair-fed studies to observe the contribution of feeding, and this was used for the feeding study data and for histological and molecular analysis on BAT. Finally, the last cohort was used for ^{18}FDG PET/CT scans both at thermoneutrality and upon adrenergic stimulation.

Before looking at the potential role of mitochondrial fission in the astrocytes of the NTS in the control of BAT metabolic health, we aimed to assess whether 2-weeks of HFD was sufficient to induce changes in BAT anatomical features and noradrenergic innervation, measured as TH fibre innervation, compared to RC-fed controls. In Chapter 3 we confirmed we can effectively deliver control virus GFP to the NTS, as demonstrated via IHC. To investigate morphological changes in BAT, after 2 weeks of HFD or RC, BAT pads were accurately dissected from the animals and immediately weighed to measure whether there were any differences in BAT mass. No significant differences were observed when comparing BAT of RC GFAP:GFP HFD (0.755$\pm$0.0537 g/kg) (n=5) to that of GFAP:K38-A HFD (0.844$\pm$0.0581 g/kg) (n=14) after normalization to body weight (p=0.403)(Fig 4.1).

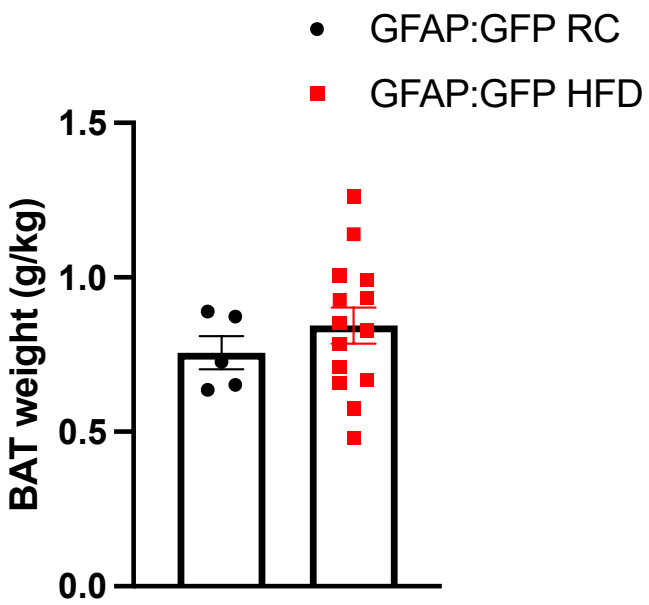

Figure 4.1: BAT weight is not affected by HFD. *BAT weight normalised to body weight (g/kg) in GFAP:GFP RC (n=5) and GFAP:GFP HFD (n=14) animals from Patel et al (2021). All data was tested for normality prior to statistical tests using the Shapiro-Wilk normality test. Values are shown as mean ± SEM and single data points highlighted. Statistical test:unpaired t-test.*

Next, samples were then snap frozen and post fixed for 2 hours in 4% PFA followed by 70% EtoH for long-term storage. Tissue samples were submitted to St. James's Teaching Hospital (Leeds, UK) for paraffin embedding and microtome cutting. Sequential sections were cut at 5 μm and stained for hematoxylin and eosin (H&E), which is a classical histological staining used to investigate microscopic anatomy of organs and tissues (Section 2.2.14).

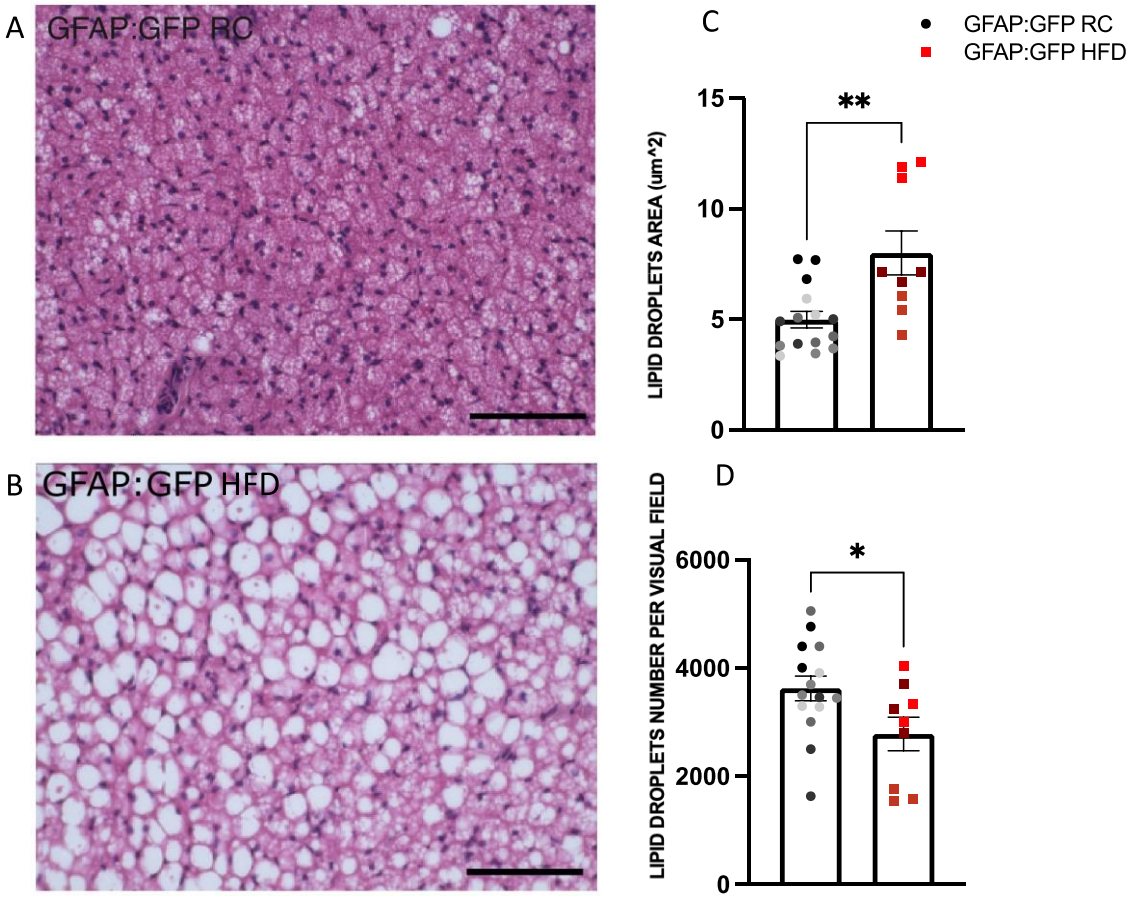

Figure 4.2: 2- weeks of HFD are sufficient to induce BAT lipid droplets enlargement. *(A-B) representative images of H&E staining on serial BAT sections cut at 5 µm. (A) is representative for GFAP:GFP RC and (B) is representative for GFAP:GFP HFD. (C) Lipid droplets area quantification for GFAP:GFP RC (n=5, 3 technical repeats.) and GFAP:GFP HFD (n=3, 3 technical repeats). (D) Lipid droplets number per visual field for GFAP:GFP RC (n=5, 3 technical repeats) and GFAP:GFP HFD (n=3, 3 technical repeats). Scale bar=50 µm. All data was tested for normality prior statistical tests using the Shapiro-Wilk normality test. Values are shown as mean ± SEM and individual technical replicates shown and grouped by biological replicate. Statistical testing was performed on the averages of each technical replicate:unpaired t-test.* $**p < 0.01$.*

H&E staining showed that white-like infiltration and hypertrophy were present in the BAT of GFAP:GFP HFD animals (Fig 4.2B) when compared to GFAP:GFP RC controls, which conversely present a uniform multilocular appearance typical of healthy brown adipocyte (Fig 4.2A).

Lipid droplet size was measured by obtaining their area from three random regions of interest for 3-4 animals per group, assuming lipid droplet circularity (Section 2.2.14). We found that in GFAP:GFP HFD animals, brown adipocytes were significantly bigger (7.99±0.992 μm^2)(n=3, 3 technical repeats) than those of GFAP:GFP RC animals, (4.98±0.377 μm^2) (n=5, 3 technical repeats) (**p<0.01) (Figure 4.2C). Next, we looked at the number of lipid droplets as an indirect marker of tissue expansion; we observed a significantly higher number of brown adipocytes per visual field in GFAP:GFP RC animals (3600±217 droplets) when compared to GFAP:GFP HFD fed animals (2453±279 droplets). (** p<0.01) (Figure 4.2D). This data confirms that 2-weeks of HFD are sufficient to dramatically change the anatomical structure of BAT and induce hypertrophy and unilocular appearance of BAT, suggesting that the tissue is being converted into WAT-like tissue and stores excessive lipids instead of consuming them via β oxidation to fuel thermogenesis.

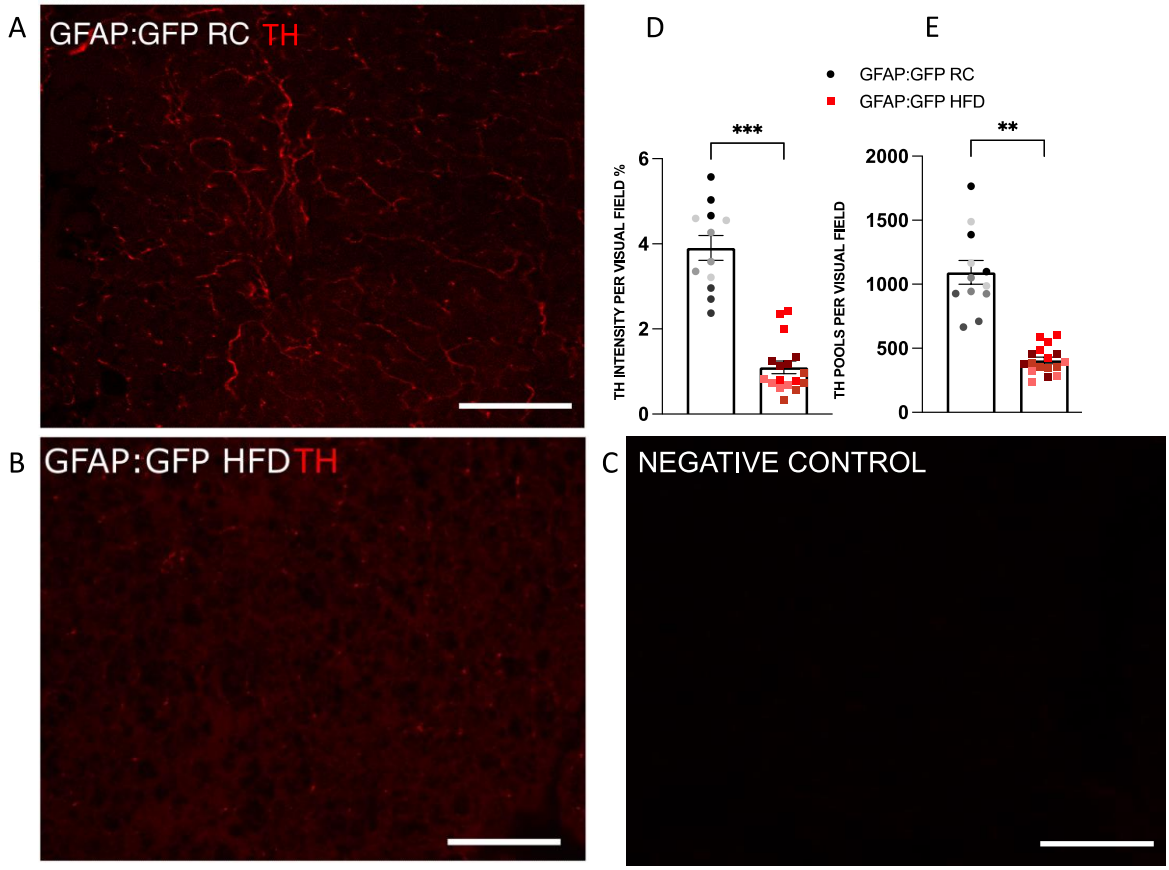

Figure 4.3: 2- weeks of HFD are sufficient to blunt noradrenergic innervation to BAT. *Representative confocal images of tyrosine hydroxylase (TH) immunoreactivity, a marker of noradrenergic innervation on serial BAT sections cut at 5 µm. (A) Representative image for GFAP:GFP RC group. (B) Representative image for GFAP:GFP HFD group. (C) Representative negative control (- primary antibody). (D) TH intensity quantification per visual field for GFAP:GFP RC (n=4, 3 technical repeats) and GFAP:GFP HFD animals (n=4, 4 technical repeats). (E) Shows the number of TH pools per visual field for GFAP:GFP RC animals (n=4, 3 technical repeats) and GFAP:GFP HFD animals (n=4, 4 technical repeats). Scale bar=50 µm. All data were tested for normality prior statistical tests using the Shapiro-Wilk normality test. Values are shown as mean ± SEM and individual technical replicates shown and grouped by biological replicate. Statistical testing was performed on the averages of each technical replicate:unpaired t-test. ****p < 0.0001.*

Next, a portion of cryopreserved BAT pads was post-fixed in 4% PFA for 2 hours and cryoembedded in OCT in preparation for cryosectioning. Sections were cut at 8 µm, directly mounted on charged slides and IHC for TH was performed (Section 2.2.14). TH catalysis is the

first step of the synthesis of catecholamines, and it is used as a classical marker for noradrenergic innervation of BAT; in particular, TH immunoreactivity is used as an estimation of the ability of the nerve terminals to synthesise catecholamines.

Here we aimed to determine whether 2 weeks of HFD are sufficient to reduce TH availability in BAT, which would suggest a decrease in sympathetic noradrenergic discharge to BAT.
First, we aimed to determine whether we could establish a protocol with which we could observe TH immunoreactivity in BAT. Immunoreactivity was present in both HFD-fed and regular-chow GFAP:GFP animals (Fig 4.3A-B). No expression was detected in the negative control, in which the primary antibody was omitted, confirming that the secondary antibody is not binding non-specifically to the tissue samples (Fig 4.3C).

We measured the impact of HFD on noradrenergic innervation of BAT and quantified two parameters: overall TH intensity and number of TH pools- which are defined as the accumulation of TH within the nerve terminals within BAT. These were quantified by randomly selecting 4 regions per animal, 4 animals per group. We found that TH intensity per visual field was significantly higher in GFAP:GFP RC animals (3.90±0.292%) (n=4, 4 technical repeats) when compared to GFAP:GFP HFD controls (1.10±0.150%) (n=4, 4 technical repeats) (****$p<0.0001$) (Fig 4.3A-B,D); TH pool numbers were also significantly higher in GFAP:GFP RC (1093±92.2) (n=4, 4 technical repeats) animals when compared to GFAP:GFP HFD controls (405±25.8) (n=4,4 technical repeats) (****$p<0.0001$) (Fig 4.3A-B,E).

4.4 Inhibition of mitochondrial fission in astrocytes in the NTS of the brain prevents BAT hypertrophy and preserves noradrenergic terminals in BAT

After validating efficacy and specificity of our adenoviral systems (Chapter 3), we wanted to investigate whether the inhibition of Drp1-dependent mitochondrial fission in the NTS can prevent HFD-linked BAT hypertrophy and increase noradrenergic innervation- measured as TH intensity and pool number- in BAT in HFD-fed rats.

To investigate changes in BAT, after 2 weeks of HFD, BAT pads were accurately dissected from the animals and immediately weighed to measure whether any differences could be seen in

BAT mass. A trend towards increase was observed when comparing BAT of GFAP:K38-A HFD (1.068±0.120 g/kg) (n=12) to that of GFAP:GFP HFD (0.843±0.0581 g/kg) (n=14) after normalization to body weight (p=0.0923)(Fig 4.4).

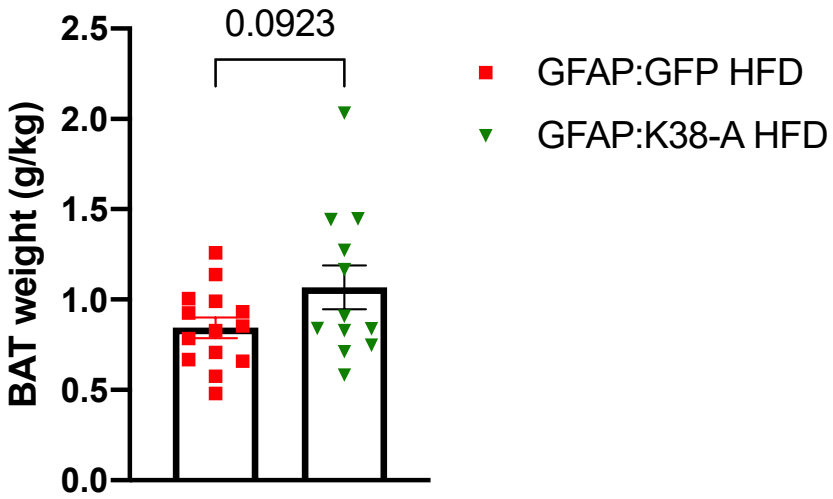

Figure 4.4: BAT weight is not affected by inhibition of mitochondrial fission in the astrocytes of the NTS of HFD-fed rats. *BAT weight normalised to body weight (g/kg) in GFAP:GFP HFD (n=14) and GFAP:K38-A (n=12) animals. All data was tested for normality prior statistical tests using the Shapiro-Wilk normality test. Values are shown as mean ± SEM and single data point highlighted. Statistical test: unpaired t-test.*

Next, H&E staining was performed and revealed a hypertrophic appearance of brown adipocytes in GFAP:GFP HFD fed animals (Fig 4.5A), accompanied by a clear shift to unilocular like appearance of individual cells. Healthy brown adipocytes are typically multilocular, as each adipocyte stores several small lipid droplets, and remarkably, this feature is observed in the GFAP:K38-A HFD fed animals (Fig 4.5B). Lipid droplet size was measured by obtaining their area from three random regions of interest for 3-4 animals per group, assuming lipid droplet circularity (Section 2.2.14). We found that in GFAP:GFP HFD fed animals, brown adipocytes were significantly bigger (7.99±0.992 μm^2)(n=3, 3 technical repeats) than those of GFAP:K38-A HFD fed animals, (5.57±0.18 μm^2) (n=4, 3 technical repeats) (*$p<0.05$) (Figure 4.5C). Next, we looked at the number of lipid droplets as an indirect marker of tissue expansion; we observed no significant differences in the numbers of brown adipocytes per visual field in

GFAP:K38-A HFD fed animals (3000±87) when compared to GFAP:GFP HFD fed animals (2453±279). (p=0.356) (Figure 4.5D).

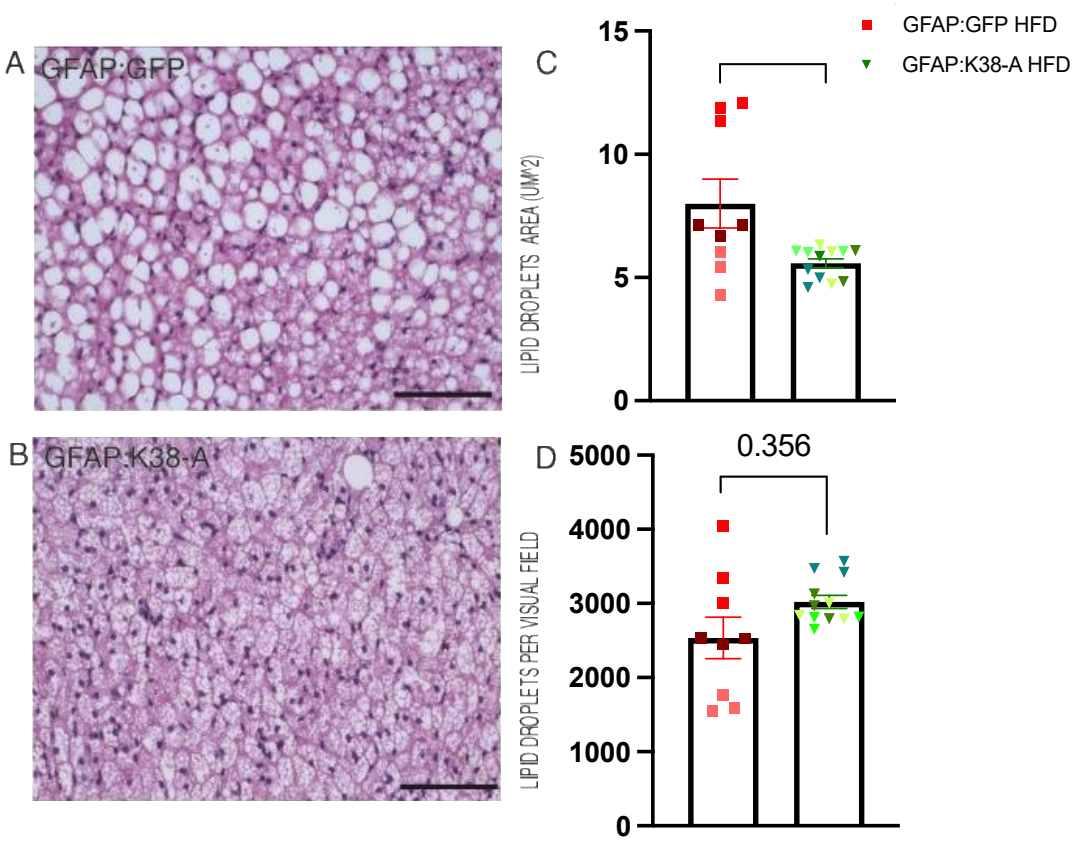

Figure 4.5: Inhibition of mitochondrial fission in the astrocytes of the NTS of HFD-fed rats prevents BAT lipid droplets enlargement. *Representative images of H&E staining on serial BAT sections cut at 5 µm. (A) GFAP:GFP HFD PF and (B) GFAP:K38- A HFD (C) Lipid droplet area quantification for GFAP:GFP HFD (n=3, 3 technical repeats.) and GFAP:K38-A HFD (n=4, 3 technical repeats).(D) Lipid droplets number per visual field for GFAP:GFP HFD (n=3, 3 technical repeats) and GFAP:K38-A HFD (n=4, 3 technical repeats). Scale bar=50 µm. Each data point is representative of one technical replicate. All data was tested for normality prior statistical tests using the Shapiro-Wilk normality test. Values are shown as mean ± SEM and individual technical replicates shown and grouped by biological replicate. Statistical testing was performed on the averages of each technical replicate:unpaired t-test. $*p < 0.05$.*

Next, post-fixed BAT was embedded in OCT and cut at 8 µm, directly mounted on charged slides and IHC for TH was performed (Section 2.2.14). Here we aimed to determine whether

the increase in dynamic glucose uptake in BAT (Chapter 3), and preserved BAT morphology we observed in GFAP:K38-A HFD animals (Figure 4.5), is associated with an increase in TH availability to BAT, which could suggest an increase in sympathetic noradrenergic discharge to BAT, potentially mediated by the NTS, despite HFD.

We measured two separate parameters, namely overall TH fluorescent intensity and number of TH pools in BAT. TH quantifications were carried out by randomly selecting 4 regions per animal, 4 animals per group. We found that TH fluorescent intensity per visual field was significantly higher in GFAP K38-A HFD fed animals (2.07±0.20%) (n=4, 4 technical repeats) when compared to GFAP:GFP HFD fed controls (1.09±0.14%) (n=4, 4 technical repeats) (*$p<0.05$) (Fig 4.6A-B,D); TH pool numbers were also significantly higher in GFAP:K38-A HFD fed (636±55) (n=4, 4 technical repeats) animals when compared to GFAP:GFP HFD fed controls (405±25) (n=4, 4 technical repeats) (*$p<0.05$) (Fig 4.6A-B,E).

It is known that in HFD-fed mice, TH availability in the brain (Li et al., 2009) and BAT (Fischer et al., 2019) is reduced, and that BAT transplant is able to enhance sympathetic drive to endogenous BAT in mice (Zhu et al., 2014). However, this is the first evidence that characterises the role of the NTS in maintaining TH levels in BAT during HFD. Moreover, this is the first evidence that suggests that inhibition of mitochondrial fission in the astrocytes of the NTS preserves BAT ability to adequately synthesise catecholamines to preserve its morphology and metabolic activity (Chapter 3) during HFD.

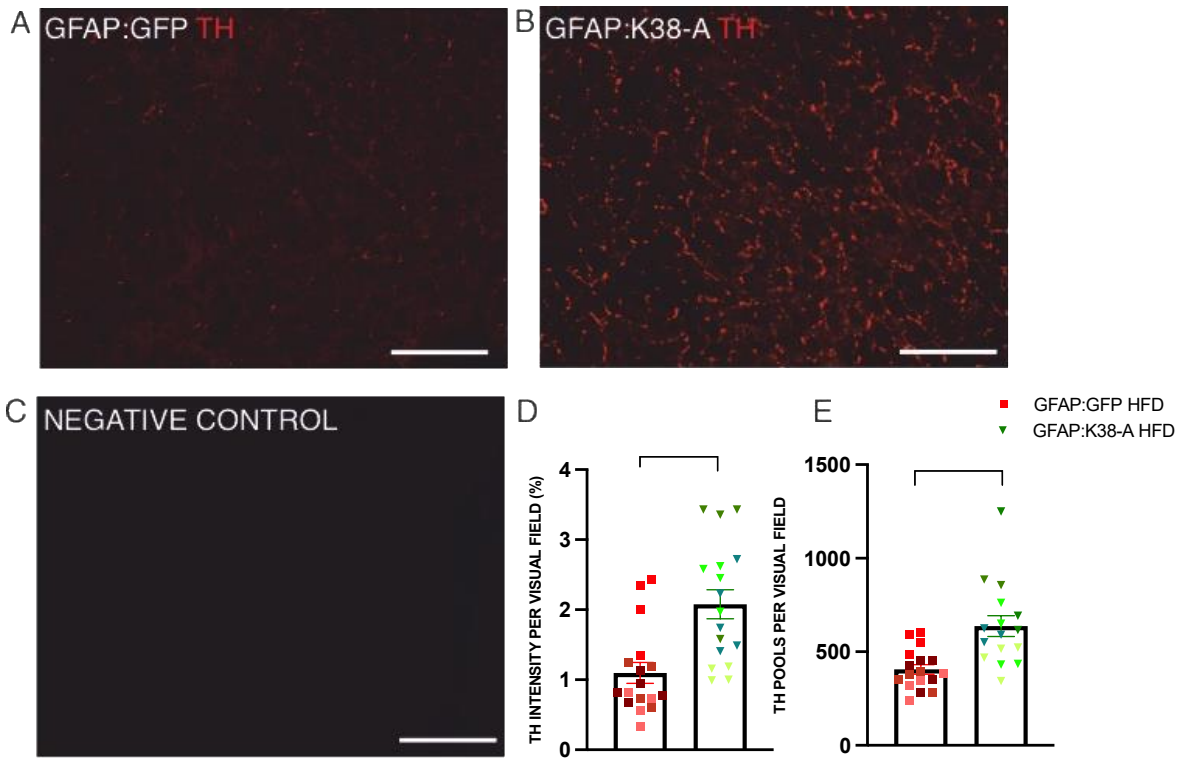

Figure 4.6: Inhibition of mitochondrial fission in the astrocytes of the NTS of HFD-fed rats prevents loss of noradrenergic innervation to BAT. *Representative confocal images of tyrosine hydroxylase (TH) immunoreactivity, a marker of noradrenergic innervation on serial BAT sections cut at 5 µm. (A) Is representative for GFAP:GFP HFD group. (B) Is representative for GFAP:K38-A HFD group. (C) Representative negative control (Primary antibody). (D) TH intensity quantification per visual field for GFAP:GFP HFD animals (n=4, 4 technical repeats) and GFAP:K38-A HFD animals (n=4, 4 technical repeats). (E) Number of TH pools per visual field for GFAP:GFP HFD animals (n=4, 4 technical repeats) and GFAP:K38-A HFD animals (n=4, 4 technical repeats).Scale bars=50 µm. Each data point is representative of one technical replicate. All data was tested for normality prior statistical tests using the Shapiro-Wilk normality test. Values are shown as mean ± SEM and individual technical replicates shown and grouped by biological replicate. Statistical testing was performed on the averages of each technical replicate:unpaired t-test. $*p < 0.05$.*

4.5 Chronic inhibition of mitochondrial fission in astrocytes in the NTS of the brain can induce changes in gene expression in the brown adipose tissue of high-fat diet-fed rats

4.5.1 Validation of housekeeping genes and primers

Following histological investigations, we proceeded to determine if the inhibition of mitochondrial fission in the astrocytes of the NTS can induce changes in mRNA transcript of BAT which are associated with metabolic activity, ER stress and inflammation and mitochondrial dynamics.

On the day of sacrifice the BAT was quickly collected, weighed and snap frozen and lysated to extract RNA (Section 2.2.11). To determine how BAT from GFAP:K38-A HFD-fed animals responds to inhibition of mitochondrial fission in astrocytes of the NTS of the brain, we examined changes in BAT gene expression compared to GFAP:GFP HFD control using reverse transcription followed by qPCR. Based on a literature search we selected a panel of genes whose expression has been found to be altered by exposure to HFD, both long and short-term. These genes were grouped into clusters of interest, namely: (1) glucose-insulin group, (2) BAT-specific group, (3) fatty acid oxidation group, (4) lipolysis group, (5) inflammation and ER stress group and (6) mitochondrial dynamics group (Table 4.1).

Table 4.17: Primers utilised for qPCR assays to investigate clusters of genes of interest. *Glucose transporter 1 (Slc2a1, Glucose Transporter 4 (Slc2a4), Insulin receptor (INSR) Adrenoreceptor Beta 3 (ADRB3), Uncoupling protein 1 (UCP1), Peroxisome proliferator-activated receptor gamma coactivator 1-alpha (PPARGC1A), Peroxisome proliferator-activated receptor gamma PPARG, Acyl-CoA Dehydrogenase Long Chain (ACADL), Cluster of Differentiation 36 (CD36), Cell Death Inducing DFFA Like Effector A (CIDEA), Patatin Like Phospholipase Domain Containing 2 (PNPLA2), Hormone Sensitive Lipase (HSL) (98 bp), DNA Damage Inducible Transcript 3 (DDIT3), Nuclear Factor Kappa B Subunit 1 (NFKB1), Tumor Necrosis Factor Alpha (TNFA), Dynamin like Protein 1 (DNML1), Mitofusin 2 (Mfn2).*

Glucose-insulin	BAT-specific	Fatty acid oxidation	Lipolysis	Inflammation/ ER stress	Mitochondrial dynamics
Slc2a1	ADRB3	ACADL	PNPL2A	DDIT3	DNML1
Slc2a4	UCP1	CD36	HSL	NFKB	Mfn2
INSR	PPARGC1A			TNFA	
	PPARG				
	CIDEA				

The *36b4* gene, encoding for acidic ribosomal phosphoprotein P0, was selected as housekeeping control as previous literature established its high degree of stability in adipose tissue of rats (Zhang et al., 2016). Prior to the experiment, we validated the expression of housekeeping gene 36b4 and we tested whether the size of our PCR products matched that of predictive in silico analysis.

The cycle threshold (Ct) value for the reference gene was obtained and no significant differences could be found between the control regular chow and HFD groups; the mean Ct value of the reference gene for the regular chow group was 19.97±0.1431 and that of the HFD group was 19.62±0.0914, (p=0.5356) exhibiting high and stable transcript levels (Figure 4.7).

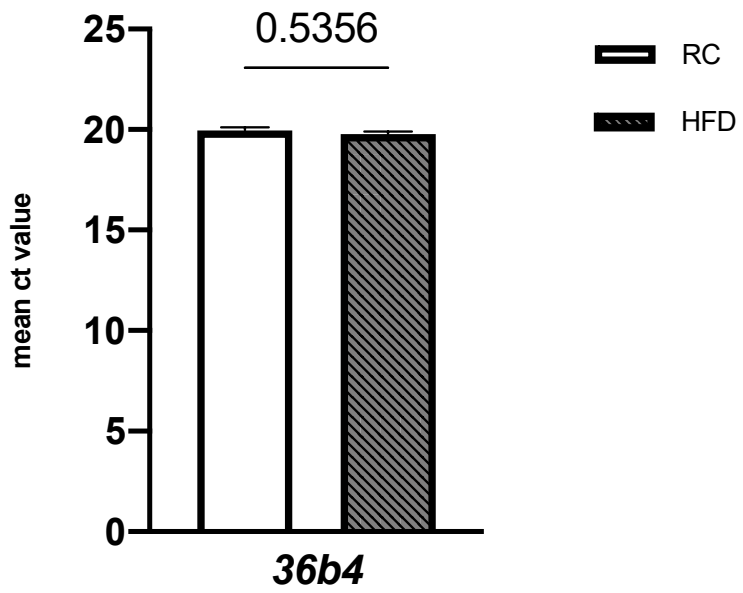

Figure 4.7: Expression of 36b4 in regular-chow and HFD-fed animals to prove that the expression of the gene is stable regardless of the diet. *Values are shown as mean ± SEM. Statistical test:unpaired t-test.*

This indicates that the house keeping is not itself affected by HFD. Altogether these results are in accordance with previous literature (Zhang et al., 2016) and we can therefore confirm *36b4* stability as housekeeping gene in BAT for our experiments.

Next, qPCR reactions containing primers for genes of interest and a serial cDNA dilution of sample pool (1:50,1:100,1:200) were performed using a combined comparative Ct and melting curves program to ensure primer quality and test optimal cDNA dilution. qPCR data are expressed on a logarithmic scale in which 10x serial cDNA dilution corresponds to ~ 3.3 cycles difference between dilutions in optimal reactions. We used 2x cDNA serial dilution that theoretically corresponds to ~ 1 cycle difference between dilutions for optimal reaction; this was confirmed by qPCR reactions for primer testing confirming the high quality of the primers employed for our study (average difference=1.1 cycles), as shown in a representative amplification plot (Figure 4.8). Moreover, this trial determined that 1:50 was the optimal dilution for our sample as it allowed optimal qPCR reactions across all primers.

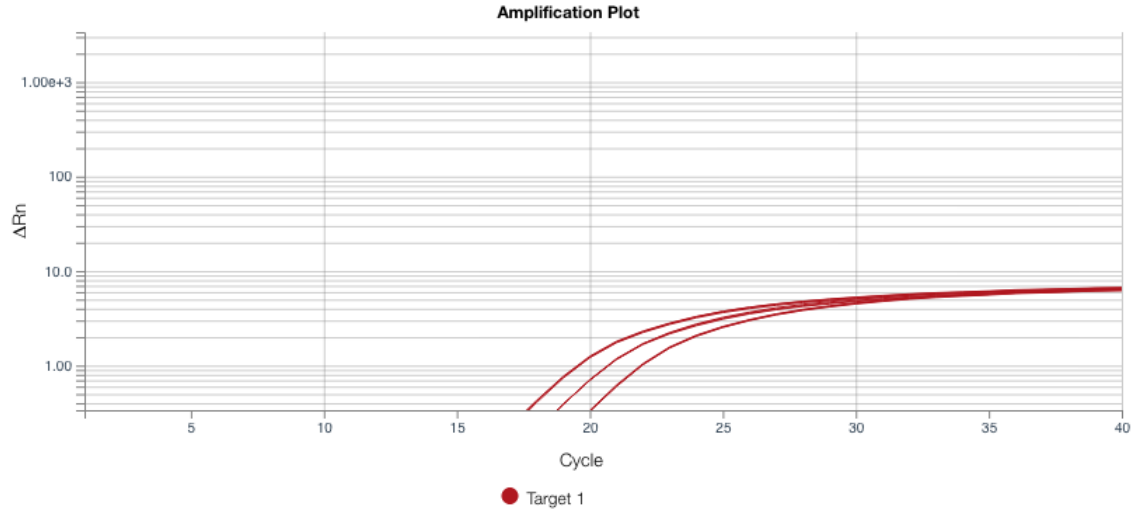

Figure 4.8: Representative image of an amplification plot confirming the quality of the primers upon serial dilution of the cDNA at 1:50, 1:100 and 1:200. *2x cDNA serial dilution corresponds at roughly 1.1 cycle difference between dilutions which is confirmed by our trial.*

Following this, the products of the qPCR reactions for primers testing were collected and electrophoresed on a 4% agarose gel (Section 2.2.13) and analysed to obtain several pieces of information. These were: (1) visualise the cDNA products and ensure their integrity, (2) confirm the predicted product size and (3) screen for potential primers-dimers formation and genomic DNA contamination, which could affect the validity of our results. All reactions produced a single product of the size predicted by in silico analysis confirming primer validity and specificity (Figure 4.9); moreover, DNA products appeared free of smears suggesting preserved integrity of the genomic material and bands appearing over a range of intensity, suggesting differences in expression levels of each gene in BAT. Primers are presented starting from the left-hand side in the following order:*36b4* (109 bp), *Slc2a1* (145 bp), *Slc2a4* (90 bp), *INSR* (98 bp), *ADRB3* (109 bp), *UCP1* (145 bp), *PPARGC1A* (109bp), *PPARG* (153 bp), *ACADL* (97 bp), *CD36* (137 bp), *CIDEA* (124 bp), *PNPLA2* (158bp), *HSL* (98 bp), *DDIT3* (151 bp), *NFKB* (130 bp), *TNFA* (52 bp), *DNML1* (199 bp), *Mfn2* (166 bp) (Figure 4.9).

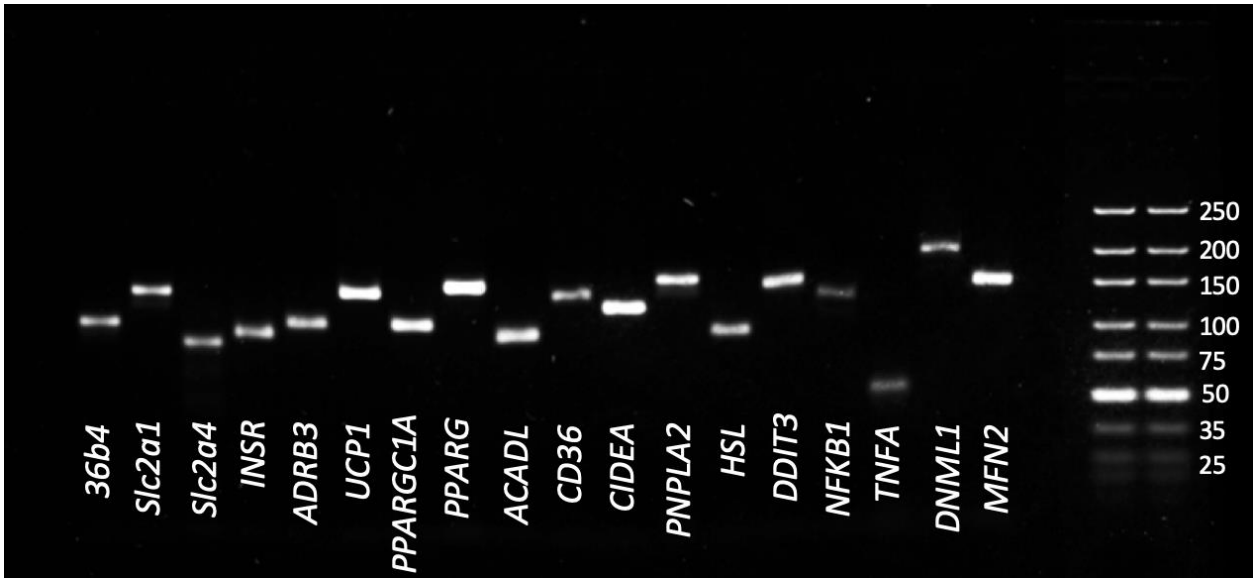

Figure 4.9: Representative agarose gel showing that the size of the primers employed in this study correspond to the in silico predicted size and that they produce a single clean product free of smears or primer-dimer formations.

4.6 Effect on glucose-insulin cluster mRNA levels

The brown adipose tissue has the capacity to clear glucose from the circulation and this mechanism is stimulated by two separated metabolic states: (1) insulin-driven glucose uptake during active anabolism (2) thermogenesis driven by sympathetic stimulation from the central nervous system.

Insulin-mediated glucose uptake in BAT occurs via a well-characterized pathway, in which the binding of insulin to the extracellular ∝ subunit of its receptor on the cell surface triggers phosphorylation of tyrosine residues of the β subunit and initiates insulin signalling transduction via the metabolic pathway PI3K-Akt (Hemmings and Restuccia, 2012).The activation of this pathway results in GLUT4 (encoded by gene *Slc2a4*) translocation and fusion of perinuclear GLUT4 vesicles to the cellular membrane, ultimately increasing glucose uptake in the cell. Another less characterized mechanism is that driven by noradrenergic mediated

glucose uptake, which in BAT occurs via activation of $\beta 3$ adrenergic receptors. Interestingly this process seems to be mediated by synergistic action of cyclic adenosine monophosphate (cAMP) and rapamycin complex 2 (mTORC2) leading to *de novo* synthesis and translocation of GLUT1 (encoded by gene *Slc2a1*) vesicles to the plasma membrane to increase glucose uptake (Olsen et al., 2014; Olsen et al., 2017). Importantly, in mature primary brown adipocytes, noradrenergic stimulation induces a potent upregulation of GLUT1 encoding mRNA and a decrease of GLUT4 encoding transcripts (Dallner et al., 2006). Moreover, it appears that glucose uptake in these cells involves *de novo* GLUT1 synthesis instead of GLUT1 and GLUT4 translocation (Dallner et al., 2006).

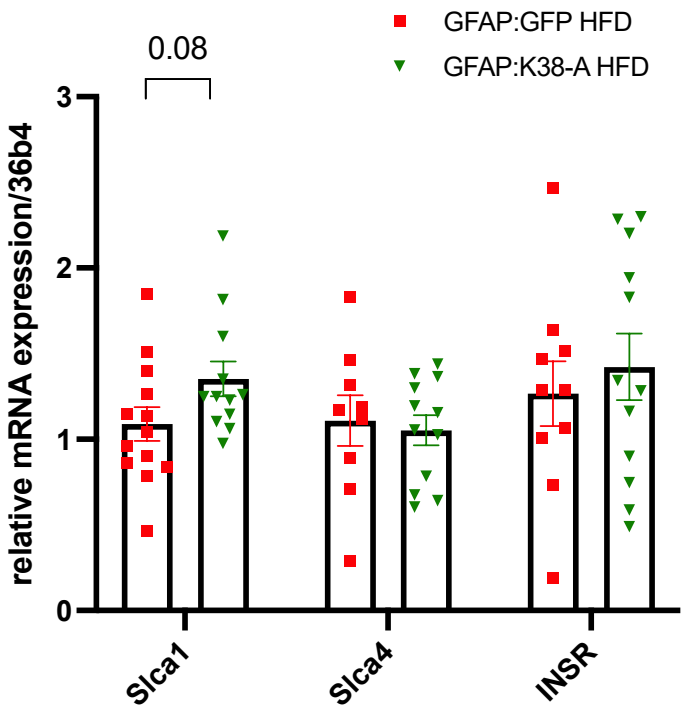

Figure 4.10: Genes involved in insulin and glucose metabolism are not affected by inhibition of mitochondrial fission in astrocytes of the NTS in HFD-fed animals. *Relative expression of genes of interest in GFAP:GFP HFD (n=11) versus GFAP:K38-A HFD (n=11) animals fed ad libitum. Primers were run at separate times with internal controls to ensure gene expression consistency. All data was tested for normality prior statistical tests using the Shapiro-Wilk normality test. Values are shown as mean ± SEM and single data point highlighted. Statistical test:unpaired t-test.*

Here we examined whether inhibition of mitochondrial fission in GFAP positive astrocytes was sufficient to induce changes in the expression of mRNA transcripts of genes involved in insulin sensitivity and glucose uptake in BAT at basal level. The relative mRNA expression in BAT of *Slc2a1, Slc2a4* and *INSR* genes was investigated for this purpose and GFAP:GFP HFD group was used as control. qPCR analysis showed that these genes were not affected by our treatment, as measured by gene fold-change (Figure 4.10). *INSR* expression levels were unchanged in GFAP:K38-A HFD animals (1.26±0.212) (n=12) when compared to GFAP:GFP HFD controls (1.42±0.194) (n=13) (p=0.589). *Slc2a4* transcripts were also unaffected, GFAP:K38-A HFD (1.11±0.148) (n=12) and GFAP:GFP HFD controls (1.05±0.0884)(n=13) (p=0.735). A trend towards increase was observed for *Slc2a1*, with GFAP:K38-A HFD animals (1.09±0.107) (n=12) showing a 1.36-fold higher value when compared to GFAP:GFP HFD controls (1.36±0.110) (n=12) (p=0.0864).

While the inhibition of mitochondrial dynamics in the astrocytes of the NTS is capable of increasing glucose uptake in brown adipose tissue in vivo (Chapter 3) upon noradrenergic stimulation, it is not able to induce changes in mRNA transcript for INSR, GLUT4-encoding gene *Slc2a4* and GLUT1-encoding gene *Slc2a1* at basal level after 2 weeks of HFD. Reasons for this could be that (1) 2-weeks HFD is not sufficient to promote mRNA transcript changes at basal level, or (2) noradrenergic activation via use of β3 adrenergic agonists and/or cold exposure (single or continuous) may be required by BAT to observe an effect on mRNA transcripts related to insulin-glucose metabolism in this tissue.

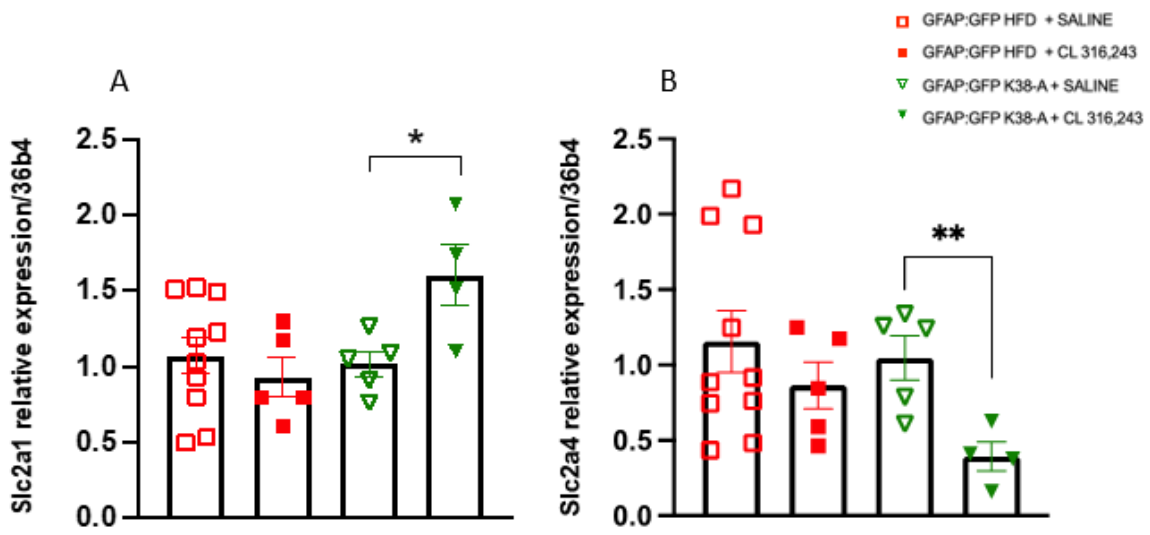

Figure 4.11: Relative expression of Slc2a1 is higher and Slc2a4 is lower in HFD-fed animals with inhibition of mitochondrial fission in astrocytes of the NTS upon IP administration of 1 mg/kg CL 316,243. *(A) Slc2a1 relative expression in non-injected GFAP:GFP HFD (n=10) and GFAP:K38-A HFD fed (n=5) animals and GFAP:GFP HFD (n=5) and GFAP:K38-A HFD (n=4) injected with CL 316,243 . (B) Slc2a1 relative expression in non-injected GFAP:GFP HFD (n=10) and GFAP:K38-A HFD fed (n=5) animals and GFAP:GFP HFD (n=5) and GFAP:K38-A HFD (n=4) injected with CL 316,243 All data was tested for normality prior statistical tests using the Shapiro-Wilk normality test. Values are shown as mean ± SEM and single data point highlighted. . ∗∗p < 0.01; ∗∗∗p < 0.001. Statistical test: Two-way ANOVA, corrected for multiple comparisons post-hoc: Tukey.*

As we could not detect any differences in gene expression of GLUT1 and GLUT4 transporters encoding genes *Slc2a1* and *Slc2a4* at basal level, we analysed the BAT of the CL 316,243-stimulated HFD cohorts from the PET scan study (Chapter 3). Strikingly, we were able to recapitulate the observations of Dallner et al. (2006), namely that CL 316,243 mimics noradrenaline and induces a potent increase in *Slc2a1* mRNA and a decrease in *Slc2a4* mRNA in mature brown adipocytes compared to unstimulated controls. Remarkably, this was only observed in GFAP:K38-A HFD fed animals (*Slc2a1* saline: 1.015± 0.0852, CL 316,243: 1.606± 0.205) (*Slc2a4* saline :1.046± 0.146 , CL316,243: 0.393± 0.0953) (*p<0.05, **p=0.001, respectively) but not in control GFAP:GFP HFD animals (*Slc2a1* saline: 1.072± 0.122, CL 316,243: 0.930± 0.130) (*Slc2a4* saline: 1.16± 0.204 , CL 316,243: 0.865± 0.155), (p=0.483, p=0.368, respectively) (Figure 4.11). This suggests that the BAT of HFD-fed animals, in which

mitochondrial fission in the astrocytes of the NTS is inhibited, responds to noradrenergic stimulation appropriately, via upregulation of *Slc2a1* mRNA and a decrease in *Slc2a4* mRNA levels, but this ability is lost after only 2-weeks of HFD in control animals. Short-term HFD could be sufficient to induce changes in tissue glucose sensitivity or initiate the development of insulin resistance; importantly, insulin resistance does not necessarily associate with decreased *INSR* mRNA levels, but could manifest via alterations of insulin binding kinetics or reduced tyrosine kinase activity (Boucher et al., 2014). Inhibition of mitochondrial fission in the astrocytes of the NTS on the other hand could prevent these phenomena by maintaining glucose uptake in BAT via correct recruitment and activation of glucose transporters GLUT 1-4.

4.7 Effect on BAT specific cluster mRNA levels

The thermogenic activation of BAT is largely driven by the sympathetic nervous system via noradrenergic signalling. ADRB3 activation triggers a signalling cascade resulting in PGC1α activation, a key transcription factor for UCP1. UCP1 activation induces uncoupling of OXPHOS complexes I-IV to generate heat instead of ATP to release energy and consume excess calories. Importantly, in this process, several genes are involved in the transcriptional regulation of *UCP1*; here we analysed the relative mRNA expression in BAT of *ADRB3, PPARGC1A, PPARG, UCP1, CIDEA*-a group of BAT-specific genes, all of which directly or indirectly regulate thermogenesis, BAT proliferation and expansion, and importantly, can be affected by HFD. For example, *ADRB3*, which encodes for the β adrenergic 3 receptor on the surface of brown adipocytes, has been shown to be downregulated by HFD, concurrently with catecholamine resistance and elevated levels of inflammation (Valentine et al., 2022). PGC1α is a transcriptional factor which is critical in the regulation of adaptive thermogenesis by mediating cold and noradrenergic stimulations to induce UCP1 and other genes involved in mitochondrial OXPHOS (Puigserver et al., 1998; Wu et al., 1999). Importantly, loss of PGC1α in mature brown adipocytes in vitro did not alter differentiation but severely inhibited the induction of thermogenic genes in these cells (Uldry et al., 2006). Furthermore, PGC1α suppression has been associated with HFD in a range of tissues, including the liver (Barroso et al., 2018) and the skeletal muscle (Koves et al., 2005). PPARγ is critical for BAT recruitment

that is not dependent upon noradrenergic stimulation (Nedergaard et al., 2005), and importantly PPARγ ligands can induce browning of white adipose tissue, which associates with protection against HFD and obesity in rodents (Cederberg et al., 2001;Seale et al., 2011).

UCP1 expression level is classically measured as it represents the central mechanism for energy expenditure in BAT. However, literature shows contradictory results on the effect of HFD on *UCP1* mRNA transcripts; for example, in a study conducted in obese *ob/ob* mice showed a lower level of UCP1 mRNA when compared to animals fed regular chow (Commins et al., 1999). Oppositely, evidence has shown that obese animals fed HFD had higher level of expression than the low-fat diet control mice (Fromme and Klingenspor, 2011), while (Ohtomo et al., 2017) showed that *UCP1* transcripts are significantly higher in BAT of mice on short-term HFD. In other instances, no effects were observed; this suggests that the duration and nutritional composition of HFD play a critical role in the regulation of UCP1 transcripts. Finally, CIDEA is highly expressed in thermogenic tissues and molecularly it has been shown to act as a direct inhibitor of thermogenesis by suppressing UCP1 activity via an indirect inhibitory effect (Fischer et al., 2017). However, it is not clear whether it can be affected by HFD.

Here we aimed to examine whether inhibition of mitochondrial dynamics in GFAP+ astrocytes was sufficient to induce changes in the expression of mRNA transcripts of these BAT specific genes in unstimulated animals.

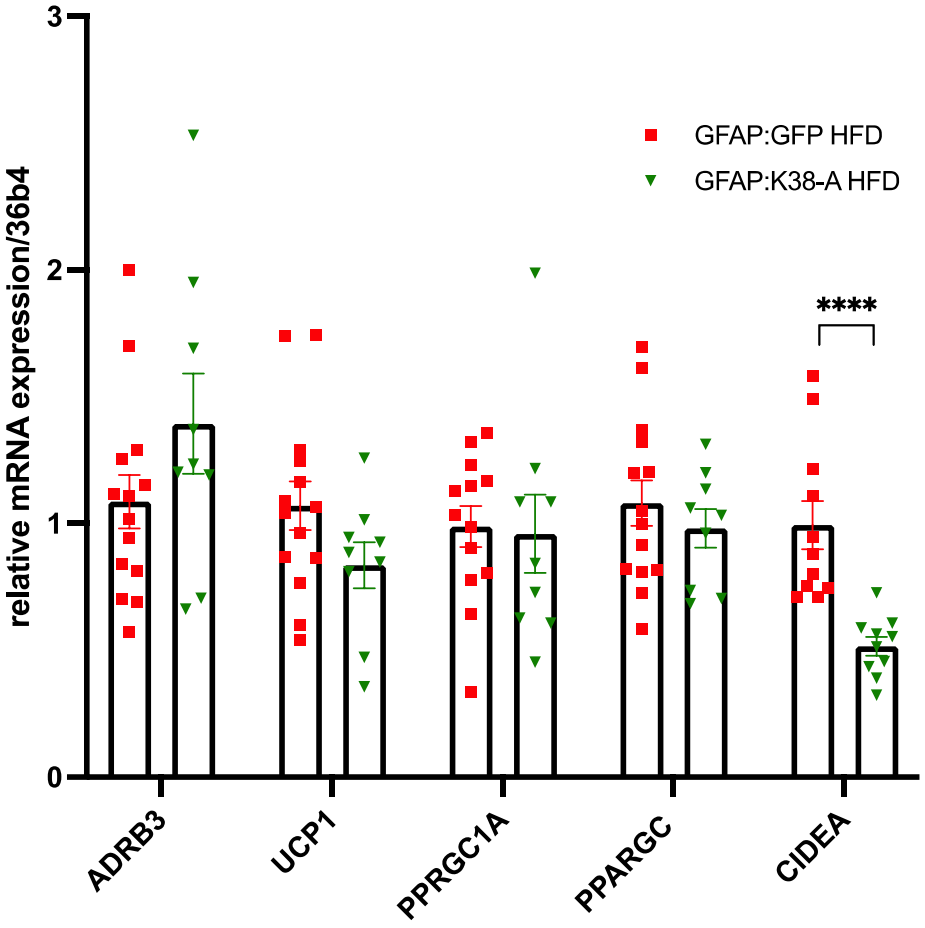

Figure 4.12: CIDEA mRNA level in BAT is lower in HFD-fed animals with inhibition of mitochondrial fission in astrocytes of the NTS. *Relative expression of genes of interest in GFAP:GFP HFD (n=11) versus GFAP:K38-A HFD (n=11) animals fed ad libitum. Primers were run at separate times with internal controls to ensure gene expression consistency. All data was tested for normality prior statistical tests using the Shapiro-Wilk normality test. Values are shown as mean ± SEM and single data point highlighted. ****p < 0.0001. Statistical test: unpaired t-test.*

When observing the mRNA transcripts of BAT-specific genes, *CIDEA* was significantly lower in GFAP:K38-A HFD animals (0.496±0.0393) (n=12) when compared to matching GFAP:GFP HFD controls (1.023±0.100) (**** p<0.0001), whilst all other markers were not affected: *ADRB3* GFAP:GFP HFD (0.871±0.0998) and GFAP:K38-A HFD (1.109±0.132), (p=0.1601), *UCP1* GFAP:GFP HFD (1.597±0.0998) and GFAP:K38-A HFD (1.338±0.0128),(p=0.2354), *PPARGC1A* GFAP:GFP HFD (0.986±0.0830) and GFAP:K38-A HFD (0.967±0.0134) , (p=0.905), *PPARG* GFAP:GFP HFD (0.835±0.0810) and GFAP:K38-A HFD (0.820±0.0563), (p=0.885) (Figure 4.12).

We speculated that noradrenergic stimulation would have been necessary to observe any change in thermogenesis related markers in the BAT, therefore we decided to look at the ADRB3- PGC1α -UCP1 pathway upon administration of CL 316,243 by analysing tissue samples from the PET scan cohort. Remarkably, upon noradrenergic stimulation with 1mg/kg of CL316,243 *PPARGC1A* transcripts were significantly higher in both GFAP:GFP HFD fed (CL316,243: 23.2±5.52) and GFAP:K38-A HFD fed (CL 316,243: 22.4±6. 39) when compared to non-injected controls (saline:1.060±0.355) (saline:1.042±0.0830), respectively (***p<0.0001 and **p<0.001, respectively) (Figure 4.13A). However *UCP1* transcripts were only higher in CL 316,243 stimulated GFAP:K38-A HFD fed (2.121±0.435) when compared to saline GFAP:K38-A HFD animals (1.021±0.105), whilst GFAP:GFP HFD fed animals did not respond to the treatment suggesting that the recruitment of UCP1 in these animals is blunted (saline: 1.019±0.0648, CL 316,243: 1.583±0.0823) (* p<0.05 and p=0.672, respectively)(Figure 4.13B). Unexpectedly, *ADRB3* mRNA was significantly lower upon noradrenergic stimulation in GFAP:K38-A HFD fed (saline:1.05±0.146 CL 316,243:0.393±0.0956) but not in GFAP:GFP HFD fed (saline: 1.589±0.510, CL316,243: 1.67±0.299) (**p<0.001) and (p=0.922), respectively (Figure 4.13C). This phenomenon could be explained by the fact that BAT of GFAP:K38-A HFD animals preserve noradrenergic stimulation at levels that are not dissimilar to those of regular chow fed animals, therefore, further stimulation with adrenergic receptor agonist CL 316,243 could have led to homologous receptor desensitisation, which is a critical biological mechanism to allow an organism to maintain homeostasis (Okeke et al., 2019; Valentine et al., 2022). This was not observed in HFD-fed GFAP:GFP HFD animals that have suppressed the physiological noradrenergic discharge from the sympathetic nervous system, and therefore exogenous stimulation was needed to counteract the detrimental effects of HFD to try and restore physiological noradrenergic signalling to BAT, which, however, was insufficient to stimulate *UCP1* mRNA translation.

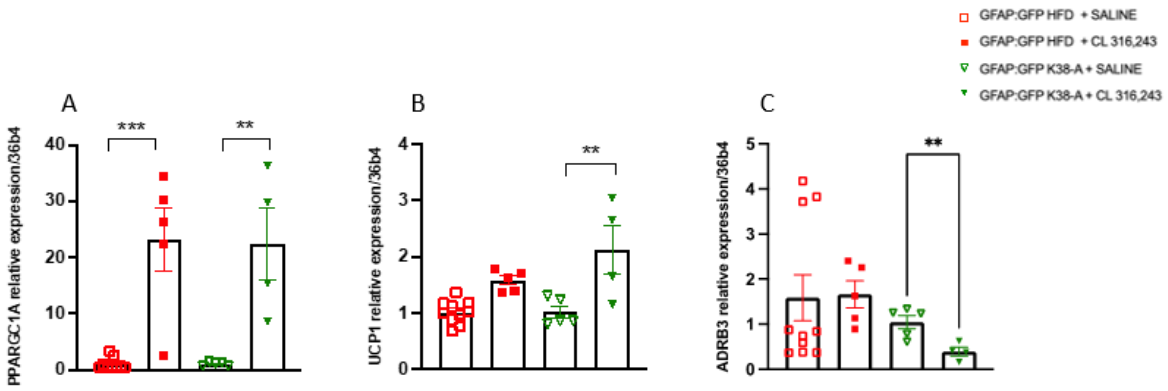

Figure 4.13: Relative expression of genes involved in thermogenesis is altered in HFD-fed animals with inhibition of mitochondrial fission in astrocytes of the NTS following IP administration of 1 mg/kg CL 316,243. *(A) PPARGC1A relative expression in non-injected GFAP:GFP HFD (n=10) and GFAP:K38-A HFD fed (n=5) animals and GFAP:GFP HFD (n=5) and GFAP:K38-A HFD (n=4) injected with CL 316,243 . (B) UCP1 relative expression in non-injected GFAP:GFP HFD (n=10) and GFAP:K38-A HFD fed (n=5) animals and GFAP:GFP HFD (n=5) and GFAP:K38-A HFD (n=4) injected with CL 316,243. (C) ADRB3 relative expression in non-injected GFAP:GFP HFD (n=10) and GFAP:K38-A HFD fed (n=5) animals and GFAP:GFP HFD (n=5) and GFAP:K38-A HFD (n=4) injected with CL 316,243. All data was tested for normality prior statistical tests using the Shapiro-Wilk normality test. Values are shown as mean ± SEM and single data point highlighted. $**p < 0.01$; $***p < 0.001$. Statistical test: Two-way ANOVA, corrected for multiple comparisons. Post-hoc: Tukey.*

4.8 Effect on genes involved in fatty acid uptake and β oxidation

Next, we analysed the gene expression of *CD36* and *ACADL*, which are involved in fatty acid uptake and oxidation, respectively. CD36 is an integral membrane protein that carries out the first two steps of FA transport, acting as a docking site for the associated fatty acid binding protein (FABP) and the fatty acid transport proteins (FATPs) to facilitate FA absorption and maintain concentration of unbound FA across the plasma membrane, and shuttle FA to mitochondria for β oxidation (Xu et al., 2013). Moreover, CD36 enhances the transport of long-chain FA across the plasma membrane via intracellular esterification (Xu et al., 2013). The expression of CD36 is increased upon cold exposure and this enhances the uptake of TG-

rich proteins (TRL) and albumin-bound FA in BAT, which is followed by increased activity of LPL to increase the rate of TG hydrolysis in BAT. Studies have shown that CD36 KO mice have reduced FA uptake, which is compensated by a significant increase in glucose uptake, however they are cold intolerant and present TG build up in their BAT (Yamashita et al., 2007; Bartelt et al., 2011). Further, CD36 KO mice have higher levels of circulating lipoproteins and FA-bound albumin in their plasma (Bartelt et al., 2011b). Interestingly, CD36 drives the uptake of coenzyme Q (CoQ)-an essential component of mitochondrial OXPHOS- in BAT and it is required to maintain normal BAT function in mice (Anderson et al., 2015). CD36 KO mice display CoQ deficiency and impaired uptake as well as alterations in BAT, encompassing hypertrophy, alterations in lipid metabolism, mitochondrial dysfunction and defective thermogenesis (Courtney M. Anderson et al., 2015). Importantly, our experiments revealed BAT hypertrophy and blunted thermogenesis in fed HFD rats for 2-weeks, and these effects were prevented by inhibiting mitochondrial fission in astrocytes of the NTS. Strikingly GFAP:K38-A HFD animals had significantly higher expression of *CD36* in BAT (2.027±0.148) compared to GFAP:GFP HFD animals (1.05±0.0982) (****$p<0.0001$) (Figure 4.14). *ACADL* mRNA was also analysed as this gene encodes for the homonymous key enzyme responsible for β oxidation of FA in mitochondria (Le et al., 2000). No significant differences could be observed across the two groups, GFAP:K38-A HFD, (0.756±0.0699) and GFAP:GFP HFD (0.913±0.0937) ($p=0.186$) (Figure 4.14), suggesting that β oxidation is not critical to the differences in lipid accumulation in BAT that we observed (Figure 4.5).

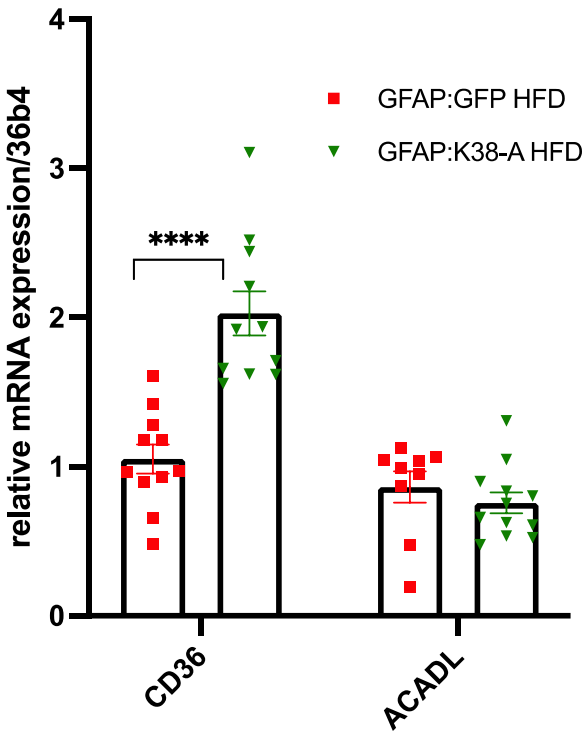

Figure 4.14: CD36 mRNA level in BAT is lower in HFD-fed animals with inhibition of mitochondrial fission in astrocytes of the NTS*. Relative expression of genes of interest in GFAP:GFP HFD (n=11) versus GFAP:K38-A HFD (n=11) animals fed ad libitum. Primers were run at separate times with internal controls to ensure gene expression consistency. All data was tested for normality prior statistical tests using the Shapiro-Wilk normality test. Values are shown as mean ± SEM and single data point highlighted. ****p < 0.0001. Statistical test:unpaired t-test.*

4.9 Effect on lipolysis cluster mRNA levels

Lipolysis is the catabolic process through which triacyclglycerols are broken down into glycerol and FA via hydrolysis. Whilst the glycerol produced by lipolysis is used for hepatic gluconeogenesis, albumin-bound FA are transported through the circulation and are oxidized in tissues via β oxidation or converted to ketone bodies. Lipolysis is a three-steps reaction catalysed by ATGL, HSL and monoacylglycerol lipase (MGL), which are preferentially activated by TG, diacylglycerol and monoacylglycerol, respectively (Zechner et al., 2009). In BAT lipolysis is activated by the release of noradrenaline via sympathetic innervation, mediated by the activation of $\beta 3$ adrenergic receptors. This in turn, increase intracellular cAMP PKA, which

stimulates lipid droplet lipolysis in the cytosol by increasing HSL phosphorylation. This process is deemed to provide FA for heat production during BAT thermogenesis. Here we analysed the expression of *PNPLA2*-encoding for ATGL protein- and *HSL,* which are main contributors of the intracellular degradation of TG (Morak et al., 2012) in BAT. Interestingly, we observed significantly lower *PNPLA2* and *HSL* in GFAP:K38-A HFD animals (0.829±0.0718 and 0.647±0.0338 respectively) compared to GFAP:GFP HFD controls, (1.02±0.0539 and 1.02±0.0644 respectively) (*$p<0.05$ and ****$p<0.0001$) (Figure 4.15).

Surprisingly, recent work employing a lipolysis-deficient mouse model showed that lipolysis is not required to maintain thermogenesis during cold exposure (Shin et al., 2017); moreover, lipolysis deficiency in BAT induces WAT browning, and WAT lipolysis is essential for the release of FA during fasting to maintain thermogenesis (Shin et al., 2017). Moreover, FA are likely to be derived from WAT lipolysis after a meal via hydrolysis of chylomicron by lipoprotein lipase (Bartelt et al., 2011). FA liberated from the lipolysis of WAT promotes hepatic acylcarnitine production, which can in turn enter the circulation to fuel BAT thermogenesis (Simcox et al., 2017). As we did not analyse the WAT from these animals, we cannot make further comments on the role of WAT in driving lipolysis to sustain thermogenesis in our model, but it would be interesting to analyse this tissue to understand its contribution in BAT thermogenesis.

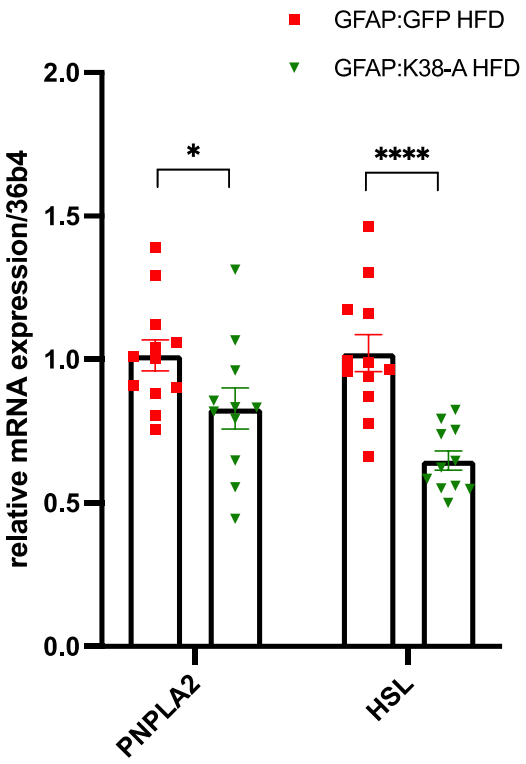

Figure 4.15: Lipolysis markers PNPLA2 and HSL are lower in HFD-fed animals with inhibition of mitochondrial fission in astrocytes of the NTS*. Relative expression of genes of interest in GFAP:GFP HFD (n=11) versus GFAP:K38-A HFD (n=11) animals fed ad libitum. Primers were run at separate times with internal controls to ensure gene expression consistency. All data was tested for normality prior statistical tests using the Shapiro-Wilk normality test. Values are shown as mean ± SEM and single data point highlighted *p<0.05 ****p < 0.0001. Statistical test: unpaired t-test.*

4.10 Effect on inflammation-endoplasmic reticulum (ER) stress cluster mRNA levels

Obesity and chronic overnutrition are associated with systemic low-grade inflammation; for example inflammation can impact BAT thermogenic function mainly via TNFα-driven insulin resistance and recruitment of macrophagic pro-inflammatory cytokines (Valverde et al., 1998; Sakamoto et al., 2013). Moreover, the pharmacological inhibition of Nuclear factor kappa-light-chain-enhancer of activated B cells (NF-Kβ) pathway attenuates the expression of proinflammatory markers in brown adipocytes in vitro (Bae et al., 2014); further, HFD can increase NF-Kβ expression in mice via an Inhibitor of nuclear factor kappa-B kinase subunit

epsilon (IKKβ) dependent mechanism in liver and adipose tissues. Indeed genetic models of IKKβ KO are protected against HFD-induced obesity and insulin resistance and show higher expression of UCP1 and energy expenditure (Chiang et al., 2009). My data show that inhibiting mitochondrial fission in astrocytes of the NTS of HFD-fed rats led to significantly lowers levels of BAT expression of *NFKB* (0.455±0.0612 and *TNFA* (0.347±0.0682) mRNA, when compared to GFAP:GFP HFD controls (1.12±0.141 and 0.996±0.215, respectively) (*** $p<0.001$ and ** $p<0.01$) (Figure 4.16).

ER stress is also a common hallmark of metabolic disease and overnutrition and activates UPR to suspend protein synthesis and promote protein folding. It is established that ER stress has detrimental effects on BAT, namely ER stress can inhibit adaptive thermogenesis by downregulating mitochondrial DNA in BAT (Okla et al., 2015). For this reason, we investigated the expression of *DDIT3*, which encodes for C/EBP homologous protein (Chop), which is a key marker of severe ER stress, and upregulation of which is indicative of increased UPR and apoptotic processes.

We observed lower mRNA levels of *DDIT3* in GFAP:K38-A HFD animals (0.733±0.0702) compared to GFAP:GFP HFD (1.02±0.0511) controls (** $p<0.01$) (Figure 4.16). We can conclude that inhibiting mitochondrial dynamics in astrocytes of the NTS reduces inflammatory and ER-stress markers in BAT.

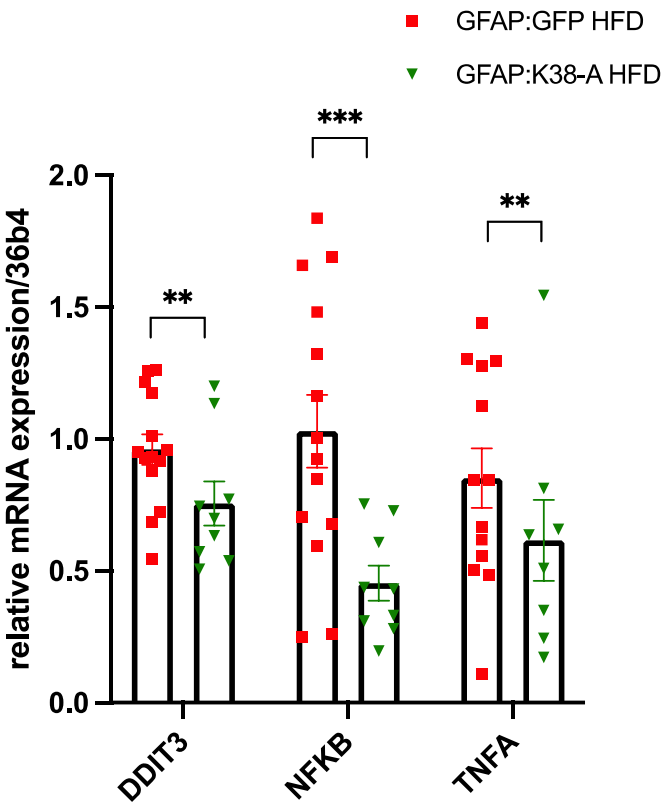

Figure 4.16: Markers for inflammation and ER stress in BAT are lower in HFD-fed animals with inhibition of mitochondrial fission in astrocytes of the NTS*. Relative expression of genes of interest in GFAP:GFP HFD (n=11) versus GFAP:K38-A HFD (n=11) animals fed ad libitum. Primers were run at separate times with internal controls to ensure gene expression consistency. All data was tested for normality prior statistical tests using the Shapiro-Wilk normality test. Values are shown as mean ± SEM and single data point highlighted. *p<0.01 ***p < 0.001. Statistical test:unpaired t-test.*

4.11 Effect on mitochondrial dynamics cluster mRNA levels

Finally, we aimed to investigate the expression of genes involved in mitochondrial dynamics in BAT, namely Mfn2, which is involved in mitochondrial fusion and DRP1, which as extensively discussed in this work, is critical for mitochondrial fission. Existing literature has shown that Mfn2, but not Mfn1 deficiency in BAT of mice is associated with decreased BAT activation upon noradrenergic stimulation, decreased respiratory capacity and BAT dysfunction (Boutant et al., 2017). In contrast, Mfn2-deletion in mice was associated with protection from HFD-induced insulin resistance and hepatic steatosis (Boutant et al., 2017).

In our study we did not observe differences in *Mfn2* mRNA transcripts across the two groups, GFAP:K38-A HFD (1.30±0.149), GFAP:GFP HFD controls (1.17±0.0681) (p=0.419) (Figure 4.17). Drp1-mediated mitochondrial fission also exerts an important role in BAT, in particular noradrenergic stimulation of BAT induces reversible mitochondrial fragmentation in these cells to support uncoupled respiration and increase energy expenditure (Wikstrom et al., 2014). Surprisingly, we found significantly lower levels of *Drp1* mRNA in GFAP:K38-A HFD animals (0.602±0.0484) compared to GFAP:GFP (0.872±0.0528) (** p<0.01) (Figure 4.17).

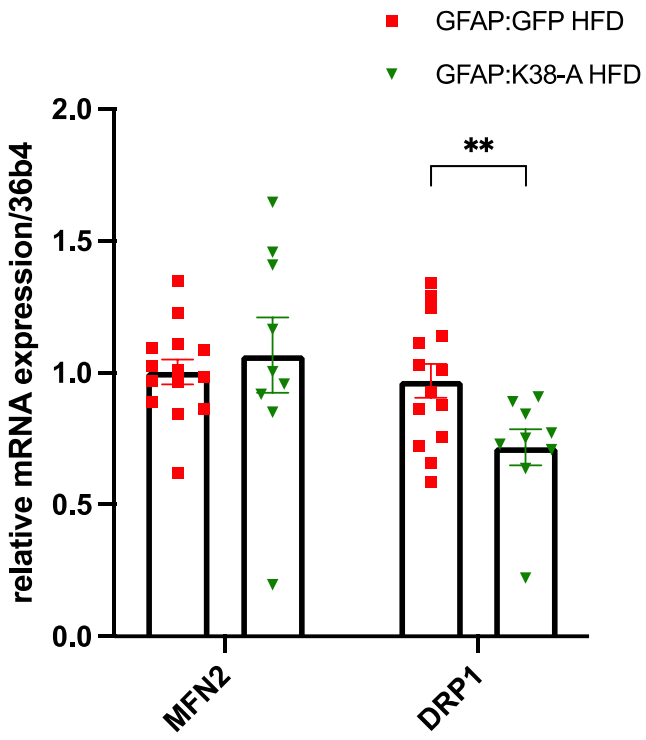

Figure 4.17: Drp1 mRNA transcripts are lower in HFD-fed animals with inhibition of mitochondrial fission in astrocytes of the NTS. *Relative expression of genes of interest in GFAP:GFP HFD (n=11) versus GFAP: K38-A HFD (n=11) animals fed ad libitum. Primers were run at separate times with internal controls to ensure gene expression consistency. All data was tested for normality prior statistical tests using the Shapiro-Wilk normality test. Values are shown as mean ± SEM and single data point highlighted. **p<0.01. Statistical test unpaired :t-test.*

4.12 Chronic inhibition of mitochondrial fission in the NTS reduces abdominal adiposity and increases BAT mass regardless of food intake

The inhibition of mitochondrial fission in the astrocytes of the NTS decreases food intake, body weight and WAT depositions in HFD-fed animals (Patel et al., 2021). To determine whether part of all the effects we have observed on BAT are due to changes in body weight, or to a direct effect of the mitochondrial manipulation in the astrocytes of the NTS we employed a pair-feeding paradigm.

In this study GFAP:K38-A HFD fed animals acted as a control, and GFAP:GFP HFD pair-fed (PF) animals were given each day the average of what the GFAP:K38-A HFD group had eaten on the previous day (Figure 4.18A). Animals were fed prior to the nocturnal phase and food intake monitored in the morning (Section 2.2.9). A two-way ANOVA was performed to analyse the effect of the viral construct and food intake on weight. After two weeks no significant differences could be observed in body weight increase across the two cohorts, GFAP:GFP HFD PF (47.9±2.54 g) (n=10) and GFAP:K38-A HFD (41.8±8.39 g)(n=6) ($p=0.451$) (Figure 4.18B). This result suggests that the inhibition of mitochondrial fission in astrocytes of the NTS is associated with lower body weight in HFD-fed animals via a strictly feeding-dependent mechanism. A further control group of *ad libitum* GFAP:GFP HFD could have been included to strengthen these results.

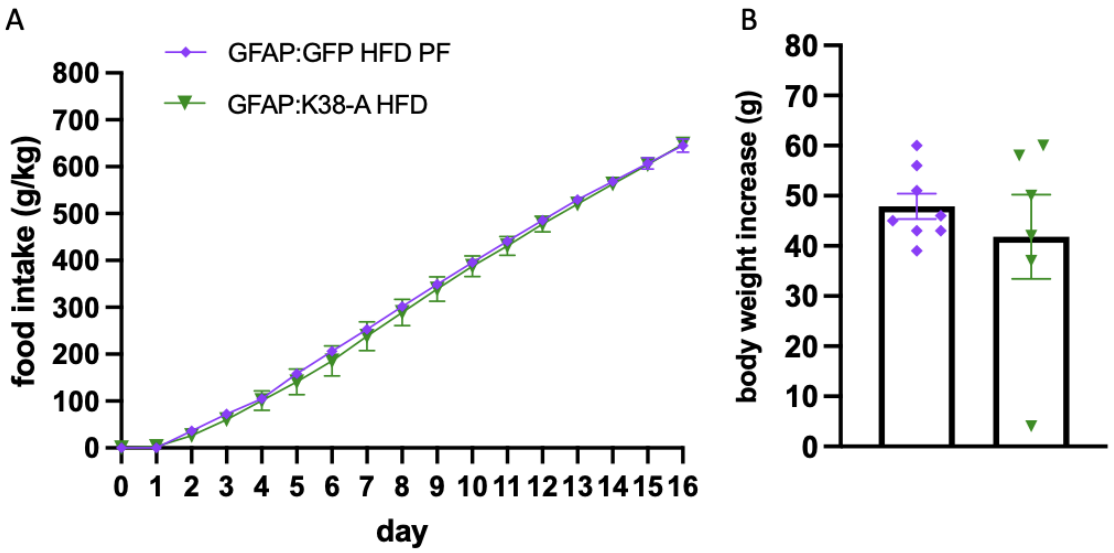

Figure 4.18: Cumulative food intake and body weight is similar during the 2-week feeding study in GFAP:GFP HFD PF and GFAP:K38-A HFD animals*. (A) Cumulative food intake in GFAP:GFP HFD PF (n=9) and GFAP:K38-A HFD (n=6) expressing rats from the day following viral injection (day 1). (B) Body weight increase in GFAP:GFP HFD PF (n=9) and GFAP:K38-A HFD (n=6) expressing rats from the day following viral injection (day 1). All data was tested for normality prior statistical tests using the Shapiro-Wilk normality test. Values are shown as mean ± SEM and single data point highlighted. Statistical test for A: 2-way ANOVA with repeated measures, (post-hoc test Tukey) Statistical test for B: unpaired t-test.*

Upon termination of the feeding study, animals were sacrificed, and abdominal WAT and BAT were collected as previously described (Section 2.2.9). Abdominal WAT was obtained from three depots, namely the epididymal depot from the groin region, retroperitoneal fat surrounding the kidneys and visceral fat adjoining the intestinal tract. The total abdominal WAT was defined as the sum of the three depots. Strikingly, a significantly lower amount of retroperitoneal (7.84±1.07 g/kg) and visceral (14.5±0.970 g/kg) depots was observed in GFAP:K38-A HFD animals (n=6) when compared to those of GFAP:GFP HFD PF (n=9), (16.1±1.05 g/kg) (25.3±1.37 g/kg), respectively (*p<0.05 and **p<0.01, respectively) (Figure 4.19). No significant differences were observed in the epididymal fat pad, GFAP:GFP HFD PF (12.9±1.37 g/kg) (n=9) and GFAP:K38-A HFD (9.66±1.03 g/kg)(n=6). Overall, GFAP:K38-A HFD animals (32.03±2.89 g/kg) (n=6) had significantly less abdominal fat than GFAP:GFP HFD PF

(54.41±3.27 g/kg) (n=9) (****p<0.0001) (Figure 4.19). Interestingly, Patel et al. (2021) observed significantly lower levels of epididymal and total WAT but no differences in retroperitoneal and visceral fat pads in HFD- fed rats expressing Drp1 K38-A in the NTS astrocytes when compared with HFD-fed control rats. This evidence suggests differences in abdominal adiposity storage during *ad libitum* and pair-fed HFD, and that the inhibition of mitochondrial dynamics in the astrocytes of the NTS can reduce abdominal WAT accumulation regardless of differences in food intake and body weight.

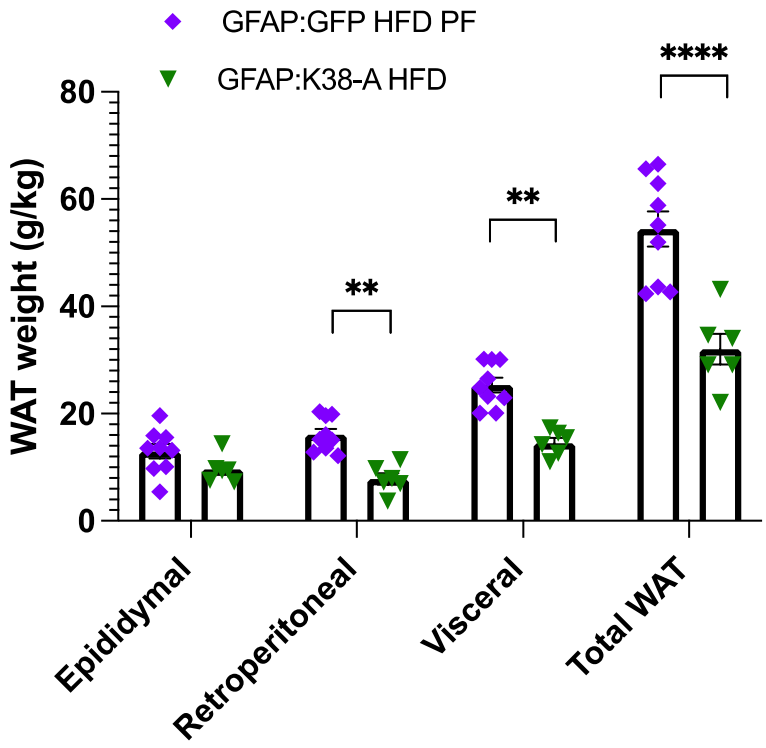

Figure 4.19: Inhibition of mitochondrial fission in astrocytes of the NTS lowers retroperitoneal and visceral WAT depots independently of food intake*. WAT weight normalised to body weight (g/kg) in GFAP:GFP HFD PF (n=9) and GFAP:K38-A HFD (n=6) animals. WAT is divided into three depots: epididymal, retroperitoneal and visceral. Total WAT is defined as the sum of the three depots. All data was tested for normality prior statistical tests using the Shapiro-Wilk normality test. Values are shown as mean ± SEM and single data point highlighted. **P<0.01. Statistical test:unpaired t-test.*

Next, we aimed to investigate potential changes in BAT after 2 weeks of HFD using PF animals. BAT pads were dissected from the animals and immediately weighted to measure BAT mass. A significantly higher BAT weight was observed when comparing GFAP:K38-A HFD (0.675±0.0456 g/kg) (n=6) to that of GFAP:GFP HFD PF (0.511±0.0403 g/kg) (n=9) after normalization to body weight (* p<0.05) (Fig 4.20).

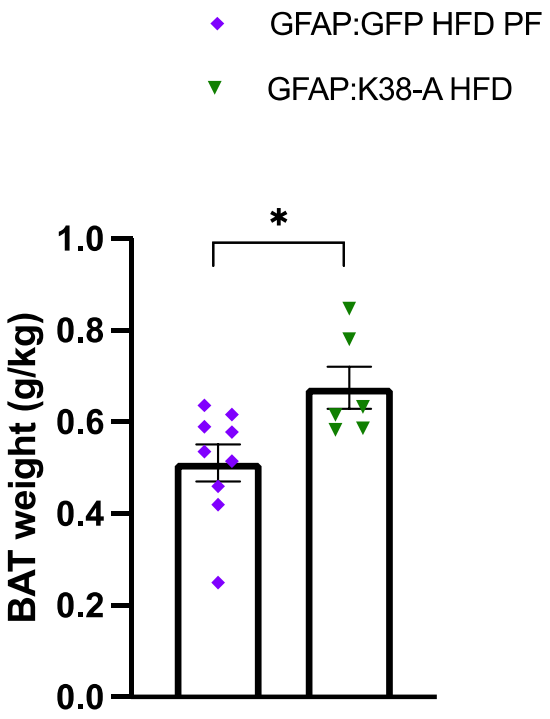

Figure 4.20: Inhibition of mitochondrial fission in the NTS of the DVC increases BAT mass regardless of food intake. *HFD animals have more BAT compared to GFAP:GFP HFD PF controls after normalisation to body weight (g/kg). GFAP:GFP HFD PF (n=9) and GFAP:K38-A HFD (n=6) animals. All data was tested for normality prior statistical tests using the Shapiro-Wilk normality test. Values are shown as mean ± SEM and single data point highlighted.*p<0.05. Statistical test: unpaired t-test.*

4.13 Chronic inhibition of mitochondrial fission in astrocytes of the NTS prevents BAT hypertrophy and preserves noradrenergic terminals in BAT regardless of food intake

With H&E staining we could observe BAT hypertrophy and enlarged unilocular droplets in the BAT of GFAP:GFP HFD PF animals (Fig 4.21A) compared to BAT of GFAP:K38-A HFD animals, which appeared normal (Fig 4.21B). Lipid droplet size was measured as previously reported (Section 2.2.14) and the analysis revealed that GFAP:GFP HFD PF animals' brown adipocytes were significantly larger (7.57±0.432 μm^2)(n=3, 4 technical repeats) than those of GFAP:K38-A HFD animals, (5.58±0.183 μm^2) (n=3, 4 technical repeats) (*p<0.05) (Figure 4.21C). Similarly, the number of lipid droplets were significantly higher in number of brown adipocytes per visual field in GFAP:K38-A HFD animals (3021±88.64) when compared to GFAP:GFP HFD PF animals (2240±147.3). (*p<0.05) (Figure 4.21D).

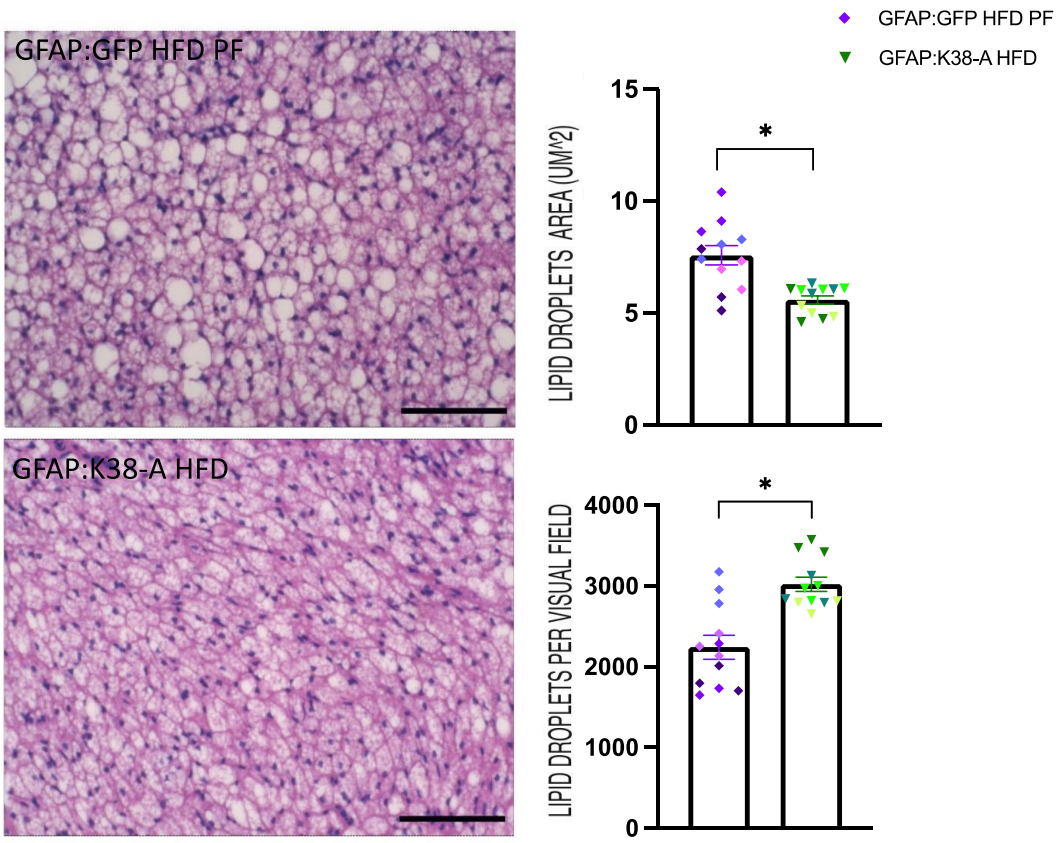

Figure 4.21: Inhibition of mitochondrial dynamics in astrocytes of the NTS of HFD-fed animals prevent lipid droplets enlargement in BAT*. Serial BAT sections (5 µm) were stained for H&E and (A) is representative for GFAP:GFP HFD PF and (B) is representative for GFAP:K38-A HFD.:-K38-A. (C) lipid droplets area quantification for GFAP:GFP HFD (n=3, 3 technical repeats) and GFAP:K38-A HFD (n=4, 3 technical repeats).(D) lipid droplets number per visual field for GFAP:GFP HFD (n=3, 3 technical repeats) and GFAP:K38-A HFD (n=4, 3 technical repeats). Scale bars=50 µm. All data was tested for normality prior statistical tests using the Shapiro-Wilk normality test. Values are shown as mean ± SEM and individual technical replicates shown and grouped by biological replicate. Statistical testing was performed on the averages of each technical replicate:unpaired t-test. $*p < 0.05$.*

Altogether this data suggests that differences in BAT morphology and expansion in HFD-fed animals expressing GFAP:K38-A HFD, to inhibit mitochondrial fission in the astrocytes of the NTS, is independent of feeding. This result could be due to differences in noradrenergic innervation from the sympathetic nervous system in the two cohorts, so we next examined this possibility.

TH fluorescent intensity per visual field was significantly lower in GFAP:GFP HFD PF animals (1.10±0.150%) (n=4, 4 technical repeats) when compared to GFAP:K38-A HFD controls (2.08±0.206%) (n=4, 4 technical repeats) (*$p<0.05$) (Fig 4.22A-B,D). TH pool numbers showed a trend towards lower values in GFAP:GFP HFD PF (405±25.8) (n=4, 4 technical repeats) animals when compared to GFAP:K38-A HFD controls (636±55.5) (n=4,4 technical repeats) ($p=0.0233$) (Fig 4.22A-B,E). This data corroborates the idea that GFAP:GFP HFD PF animals present altered BAT morphology because of lower noradrenergic innervation in the tissue. Importantly, this evidence shows, for the first time, that the inhibition of mitochondrial dynamics in the NTS of astrocytes can preserve noradrenergic innervation of BAT in HFD fed animals regardless of food intake.

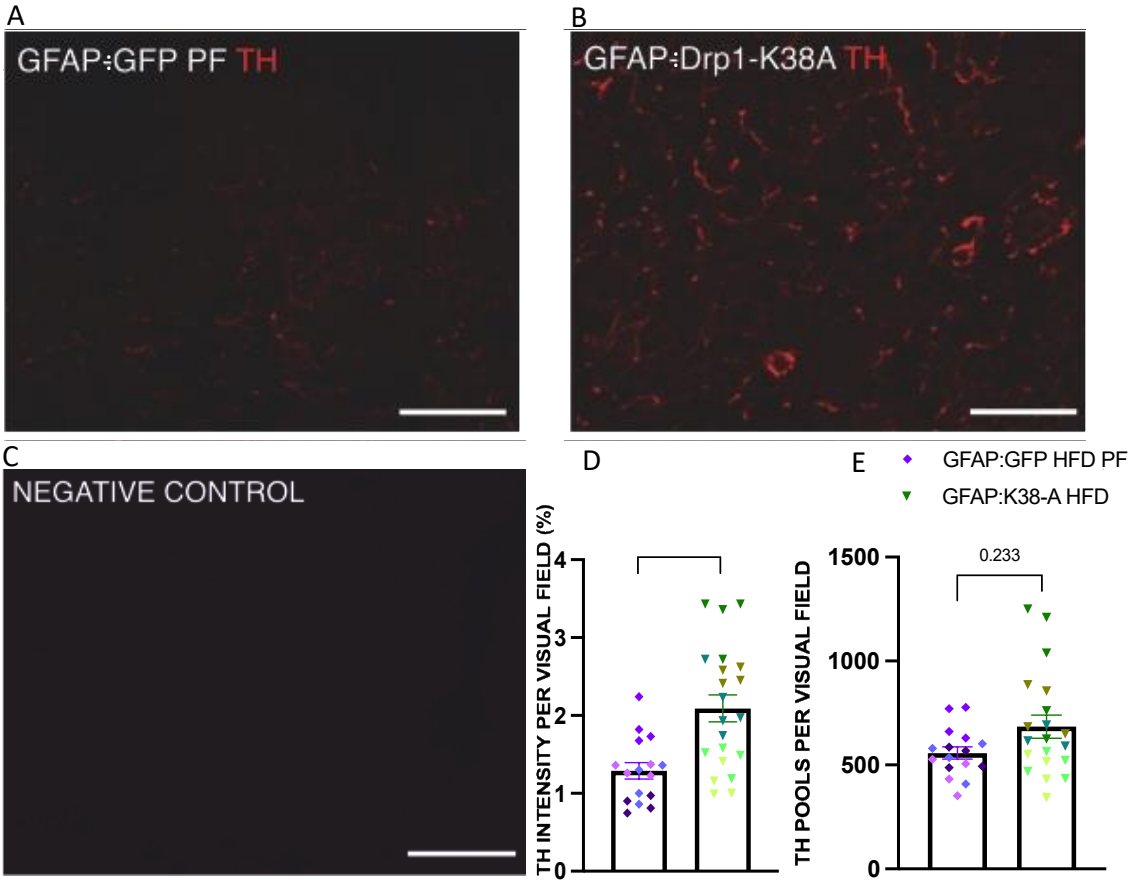

Figure 4.22: Inhibition of mitochondrial fission in astrocytes of the NTS of HFD-fed rats preserves noradrenergic innervation to BAT compared to GFAP:GFP HFD PF controls. *Representative confocal images of tyrosine hydroxylase (TH) immunoreactivity, a marker of noradrenergic innervation on serial BAT sections cut at 5 µm. (A) GFAP:GFP HFD PF group. (B) GFAP:K38-A HFD group. (C) Representative negative control (- 1ary antibody). (D) TH intensity quantification per visual field for GFAP:GFP HFD PF animals (n=4, 4 technical repeats) and GFAP:K38-A HFD animals (n=4, 4 technical repeats). (E) Number of TH pools per visual field for GFAP:GFP HFD PF animals (n=4, 4 technical repeats) and GFAP:K38-A HFD animals (n=4, 4 technical repeats).Scale bars=50 µm. All data was tested for normality prior statistical tests using the Shapiro-Wilk normality test. Values are shown as mean ± SEM and individual technical replicates shown and grouped by biological replicate. Statistical testing was performed on the averages of each technical replicate:unpaired t-test. $*p < 0.05$.*

4.14 Gene expression changes in BAT of HFD animals expressing Drp1 dominant negative form in astrocytes of the NTS are largely associated with lower food intake

Following the changes observed in mRNA transcript levels of several genes associated with BAT metabolism and inflammation/ER stress (Section 4.10) we aimed to determine the contribution of food intake in these results. Inhibiting mitochondrial fission in the astrocytes of the NTS is associated with lower food intake in HFD-fed rats compared to matching controls (Patel et al., 2021), and nutritional intake is important in BAT biology, and a key driver of thermogenesis (Cannon and Nedergaard, 2004). For these reasons, we used pair fed animals to assess the levels of genes associated with BAT metabolism and Inflammation /ER stress. On the day of sacrifice, BAT was collected, and RNA extracted as previously described (Section 2.2.13). Only three genes were found to be significantly modified by the inhibition of mitochondrial dynamics in the astrocytes of the NTS, namely *INSR* (GFAP:K38-A HFD (1.42±0.194), GFAP:GFP HFD PF (0.567±0.0996), (**p<0.01), *PPARGC1A* (GFAP:K38-A HFD(1.093±0.219), GFAP:GFP HFD PF (0.594±0.0967), (*p<0.05), and *CIDEA* (GFAP:K38-A HFD (1.069±0.167), GFAP:GFP HFD PF (1.61±0.107), (*p<0.05) (Figure 4.23).

In regards to our findings on *INSR*, it has previously been shown that 40 hours of fasting increased BAT *INSR* transcripts 8-fold in rats, and *INSR* levels declined rapidly upon refeeding for 4 hours (Knott et al., 1992). Our pair-fed model was also subjected to prolonged period of fasting, as animals were fed prior to the night phase due to the lack of an automated feeder system to guarantee 24-hours food availability. Therefore, it seems reasonable to speculate that the effect on *INSR* mRNA transcript we observed could be due to the nature of our experimental design rather than effects driven by mitochondrial dynamics in the NTS.

Importantly, only *CIDEA* mRNA transcripts were found to be upregulated in GFAP:GFP HFD of pair-fed cohorts. CIDEA promotes lipid droplet enlargement to facilitate lipolysis and lipogenesis coupling in active BAT to prepare for thermogenesis (Barneda et al., 2015) and enhanced expression of CIDEA proteins has been linked to conditions characterised by the accumulation of enlarged lipid droplets, such as hepatic steatosis (Zhou et al., 2012). Moreover, a trend towards an increase was observed in the mRNA transcripts of *CD36* in

GFAP:K38-A HFD animals (1.74±0.188) when compared to GFAP:GFP HFD PF (1.26±0.261) controls (p=0.139) (Figure 4.23).

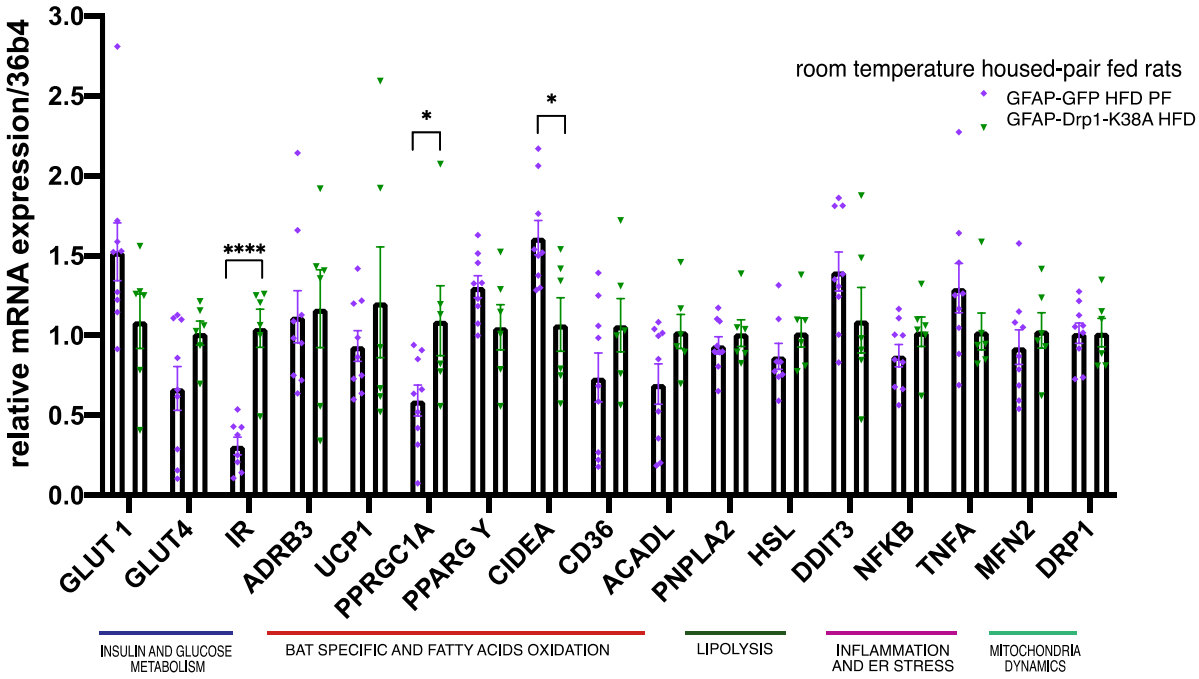

Figure 4.23: IR, PPARGC1A and CIDEA mRNA transcripts are affected by the inhibition of mitochondrial fission in astrocytes of the NTS of HFD-fed animals independently of food intake. *Genes of interest are relative to the expression of housekeeping gene 36b4. Relative expression of genes of interest in GFAP:GFP HFD pair-fed (n=9) versus GFAP:K38-A HFD (n=6) animals. Primers were run at separate times with internal controls to ensure gene expression consistency. All data was tested for normality prior statistical tests using the Shapiro-Wilk normality test. Values are shown as mean ± SEM and single data point highlighted. *p < 0.05, ****p< 0.0001. Statistical test: unpaired t-test.*

4.15 Chronic inhibition of mitochondrial fission in astrocytes in the NTS does not affect CoQ levels in the BAT

As we previously discussed, CD36 plays a critical role in the transport of FA across the plasma membrane towards mitochondria to fuel β oxidation. The lipid Coenzyme Q (CoQ or ubiquinone) is a critical component of the ETC, where it transports electrons from Complex I

and Complex II to Complex III of the ETC to allow proton translocation to the intermembrane environment.

CoQ is also known as a potent antioxidant of the cellular membranes, with its protective effect extending to lipids, proteins, and DNA (Crane et al., 2001). Low levels of CoQ are linked with age-related disorders, cardiomyopathies, and myopathies (Bentinger et al., 2010). Moreover, CoQ deficiency has been linked with insulin resistance, in particular insulin resistance in the WAT and muscle of mice is associated with selective mitochondrial CoQ deficiency (Fazakerley et al., 2018). For these reasons, it has been speculated that increased levels of CoQ could have a therapeutic effect in the treatment of metabolic disorders. In 2015, Anderson et al. speculated that a link may exist between normal CD36 function and CoQ levels within the BAT. They suggested that, given the ability of CD36 to mediate the uptake hydrophobic molecules across the cellular membrane, it may also be required by BAT to uptake CoQ, which is a lipid molecule. They generated a CD36 deficient mouse and observed that CoQ uptake in BAT was greatly impaired, whilst fatty acid uptake rate remained unchanged (Anderson et al., 2015). Here we investigated whether CoQ levels are affected by CD36 upregulation in GFAP:K38-A HFD animals, with the aim of understanding the potential molecular mechanisms behind the results we have observed in regard to CD36 transcripts.

To resolve this question, we used a competitive ELISA technique (Section 2.2.19) and we determined the amount of CoQ present in the BAT of animals from the cohorts previously presented in this chapter, namely: GFAP:GFP HFD *ad libitum*, GFAP:GFP HFD pair-fed and GFAP:K38-A HFD animals. GFAP:GFP HFD *ad libitum* animals were used as control.

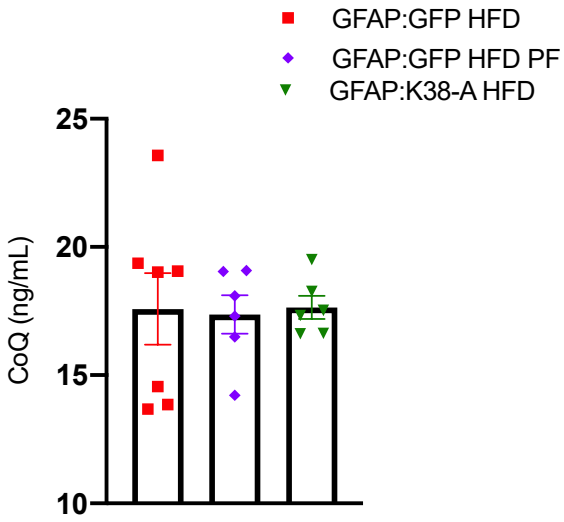

Figure 4.24: CoQ levels in the BAT were unchanged in response to the chronic inhibition of mitochondrial fission in astrocytes of the NTS. *CoQ levels in ng/mL measured in GFAP:GFP HFD (n=7), GFAP:GFP HFD PF (n=6) and GFAP:K38-A HFD (n=7) .All data was tested for normality prior statistical tests using the Shapiro-Wilk normality test. Values are shown as mean ± SEM and single data point highlighted .Statistical test: One-way ANOVA, post-hoc: Tukey.*

To analyse the data, we employed a one-way ANOVA analysis and GFAP:GFP HFD *ad libitum* cohort was used as reference group. The results show no significant changes in CoQ levels, expressed in ng/mL, in GFAP:GFP HFD PF (17.4±0.752) and GFAP:K38-A HFD (19.7±2.05) when compared to GFAP:GFP HFD (17.6±1.39) (p=0.993 and p=0.539, respectively) (Figure 4.24). We conclude that the increase in CD36 mRNA transcript levels we observed in the BAT of GFAP:K38-A HFD animals is not associated with the protective action of increased CoQ levels within the tissue.

4.16 Discussion

We have previously shown that short-term HFD blunts BAT glucose uptake (Chapter 3), and here we provided the molecular and histological bases to this finding, showing that upon 2-weeks of HFD, BAT adipocytes become enlarged and hypertrophic and lose noradrenergic innervation from the sympathetic nervous system. When we compared the GFAP: GFP HFD pair-fed group to the GFAP:K38-A HFD we also observed hypertrophic BAT with lower levels of noradrenergic innervation, which suggests that these effects are independent of food intake. Moreover, the inhibition of mitochondrial fission in astrocytes of the NTS reduces the expression of markers related to inflammation and ER stress, and increases the expression of fatty acid transporter CD36, but this effect is feeding dependent.

It is well established that the NTS is a key brainstem centre for the integration of metabolic cues received from peripheral organs, including vagal-relayed information from the adipose tissues. Moreover, astrocytes are critical in the control of synaptic transmission, and they are integrally associated with vagal afferents to the NTS and NTS neurons. In particular, the activation of vagal afferents inhibited BAT thermogenic response to cold, and vagal afferent-dependent inhibition of BAT was prevented by antagonism of ionotropic glutamate receptors postsynaptic to vagal afferent terminals in the NTS (Madden et al., 2017). Moreover, activation of BAT sympathoinhibitory neurons in the intermediate NTS, suppressed BAT sympathetic activation and thermogenesis (Morrison et al., 2014).Importantly, this evidence supports our hypothesis that the NTS is important in the regulation of BAT thermogenesis, however the mechanisms behind this remain largely unknown.

Here we aimed to assess the consequences of manipulating mitochondrial dynamics in astrocytes of the NTS on the control of BAT thermogenesis. It has been suggested that mitochondria support several astrocytic functions, including ATP production via the ETC, and the regulation of the glutamate-glutamine cycle, which allows the maintenance of adequate supplies of the neurotransmitter glutamate (Dienel, 2013). Furthermore in HFD, glutamate levels from vagal afferents within the NTS are increased (Madden and Morrison, 2016; Madden et al., 2017).

In our study we investigated the role of astrocytes in the NTS in the regulation of BAT innervation and glucose uptake. Remarkably, astrocytes are integrally associated with vagal afferents and NTS neurons, and vagal stimulation activates NTS astrocytes by inducing the release of gliotransmitters and activation of nearby neurons (McDougal et al., 2011).Moreover, astrocytes in this region regulate tonic and phasic glutamate levels in the NTS to control sympathetic functions (McDougal et al., 2011).

Here, we show that the inhibition of mitochondrial dynamics in astrocytes of the NTS prevents HFD-induced loss of sympathetic innervation-measured with the marker TH-and morphological alterations in BAT. Interestingly, literature reports conflicting results regarding the ability of HFD to induce changes in TH availability in body organs, including BAT. For example, Fischer et al. (2019) showed that in 12-weeks HFD-fed mice no differences could be detected in TH levels when compared to control RC animals, and TH reduction in both groups was only achieved via an intrascapular BAT denervation procedure. Whilst these results conflict with our data, the study by Fisher et al. (2019) employed the same HFD diet used our work, and this may provide interesting insights into the differences between mice and rat physiology. Further, it could be suggestive of differences between acute and chronic exposure to HFD and how these relate to BAT innervation and activation. A 2020 metanalysis revealed profound differences in metabolic events occurring in a range of mouse and rat models of HFD, suggesting that the choice of experimental model is important when investigating metabolism (Preguiça et al., 2020). Remarkably, here we show the first evidence suggesting that 2-weeks of HFD are sufficient for TH levels in BAT to reduce in adult rats; moreover, our evidence seems to support the hypothesis we propose, namely that astrocytic mitochondrial dynamics within the NTS are important to maintain BAT innervation and morphology to sustain thermogenesis.

Importantly, HFD-dependent increase of mitochondrial fission in the NTS is associated with inflammation in this brain region, and in particular with increased levels of iNOS in NTS astrocytes (Patel et al., 2021). Importantly, glutamate can also increase levels of iNOS in the brain. It could then be speculated that during obesity and HFD, which associates with increased levels of low-grade chronic inflammation, including in the brain (Patel et al., 2021), ATP production in astrocytes may be compromised, ultimately affecting neurotransmitter

glutamate clearance and availability (Clyburn and Browning, 2019). This would lead to elevated tonic activation of glutamate afferents within the NTS, potentially resulting in blunted activation of BAT. Remarkably, (Patel et al., 2021) showed that when mitochondrial fission is inhibited in the astrocytes of the NTS, the marker of inflammation iNOS within this brain region decreases. Moreover, we showed that when we inhibit mitochondrial fission in the astrocytes of the NTS we are able preserve BAT morphology and innervation in presence of HFD. Whilst the mechanism behind these effects remains unknown, we propose that the role of astrocytes in the regulation of glutamate availability within the NTS would represent a good model to explain our observations, but further studies would be required to prove this hypothesis.

Insulin sensitivity in astrocytes is also an important factor to consider when we think about regulation of systemic metabolism. Importantly, insulin sensitivity and mitochondrial dynamics in astrocytes are tightly related; in fact, Patel et al. (2021) showed that HFD induces insulin resistance in the NTS via increased mitochondrial fission, and the authors demonstrated that inhibiting mitochondrial fission in astrocytes within the NTS is sufficient to prevent insulin resistance. Moreover, Manaserh et al. (2020) observed reduced noradrenergic innervation and lower ADRB3 expression levels in BAT of mice with IR KO in astrocytes. This suggests that BAT innervation and activity may not only be regulated by HFD-induced and astrocytic-dependent alterations in glutamate availability within the NTS but also by astrocytic insulin sensitivity within this region.

Here we showed for the first time that two weeks of HFD are sufficient to profoundly change the morphology and noradrenergic innervation of BAT; moreover, we discovered that inhibiting mitochondrial fission in astrocytes of the NTS of HFD-fed rats prevents a decrease of noradrenergic innervation of BAT and preserves BAT multilocular morphology regardless of HFD. Strikingly, this effect was maintained when controlling food intake as a variable, as observed in the pair-fed experiment, whilst these animals consumed the same amount of calories as the GFAP:K38-A HFD group, only the GFAP:GFP HFD animals proceeded to develop enlarged, hypertrophic and unilocular BAT with reduced noradrenergic innervation.

Whilst we know that the inhibition of mitochondrial fission in astrocytes of the NTS reduces food intake in HFD-fed animals when compared to matching HFD controls (Patel et al., 2021), this intervention does not appear to act on BAT morphology and innervation via a mechanism mediated by feeding, as shown in our PF model. This could indicate central alterations that influence the rate of noradrenergic discharge on BAT, and adequate noradrenergic innervation may be necessary to maintain the typical multilocular appearance of BAT in rats. A significant increase in the retroperitoneal and visceral WAT depots was also observed in GFAP:GFP HFD PF animals, when compared to the GFAP:K38-A HFD group, suggesting that mitochondrial dynamics in the astrocytes of the NTS play an important role in the accumulation of visceral fat, regardless of food intake; however, the mechanism behind this observation is not clear. However, it is important to note that the pair feeding paradigm has some limitations as the nature of experiment implies periods of intermitting fasting, namely, the rats are fed prior to the nocturnal phase (4 PM) and are not refed until 24 hours later. In our study we observed that almost all animals finished their food by the morning food intake monitoring (10 AM), meaning they underwent periods of prolonged fasting (10 AM-4 PM). Interestingly, a literature search has revealed that intermittent fasting in rodents is linked with dramatic changes in visceral fat, and in particular with significant reduction of fatty acid release rate to preserve energy storage upon prolonged fasting (Harney et al., 2021), so our findings could be a reflection of such mechanism. Finally, an increase in retroperitoneal fat is typically associated with HFD in rodents, however it is not understood what the contribution of the pair-feeding paradigm may be to explain the differences between the findings on WAT in this study and those observed in Patel et al. (2021).

Finally, the inhibition of mitochondrial fission in HFD-fed rats is associated with significantly lower levels of inflammatory markers in BAT and higher expression of the fatty acid transporter CD36 in a feeding-dependent manner, however the effects on CD36 expression was not associated with an increase of mitochondrial CoQ in this tissue, suggesting that the effects we observed in mitochondrial morphology and lower inflammation are not associated with the protective action of CoQ in this tissue. Lastly, given the role of CIDEA in lipid droplets enlargement, and the observation we presented on BAT morphology and *CIDEA* mRNA transcripts in GFAP:K38-A HFD animals compared to GFAP:GFP HFD and GFAP:GFP HFD PF

animals, it would be interesting to study the contribution of this gene/protein to the prevention of BAT lipid droplet accumulation and enlargement in GFAP:K38-A HFD animals.

Chapter 5

Chronic activation of mitochondrial fission in astrocytes of the NTS of RC-fed rats affects body weight, food intake and NTS insulin sensitivity, decreases BAT sympathetic innervation and induces changes in BAT gene expression

5.1 Activation of mitochondrial fission in astrocytes of the NTS decreases BAT dynamic glucose uptake and alters key parameters associated with thermogenesis in BAT in regular chow-fed rats

5.1.1 Mitochondrial dynamics in the brain: a bidirectional relationship to control systemic metabolism

The brain is responsible for regulating whole-body energy homeostasis and it is highly sensitive to changes in energy availability. Whilst the hypothalamus is a well-known region of the brain involved in energy sensing, more recently, the role of the DVC of the brainstem has become more characterized (Filippi et al., 2012; Filippi et al., 2017; Madden et al., 2017; MacDonald et al., 2019; Patel et al., 2021; Ludwig et al., 2021). Mitochondria respond to energy availability by dynamically changing their morphology between fused and fragmented state to meet energy demand, and mitochondria dynamics in the NTS are critical for the maintenance of energy homeostasis (Section 1.6).

High-fat diet and obesity are associated with alterations in mitochondrial dynamics, in particular with a shift towards Drp1-dependent mitochondrial fission, which affects the rate of mitochondrial oxidative metabolism in several tissues. For example, HFD-dependent mitochondrial fission has been reported in the muscle, leading to a decrease in insulin-mediated glucose uptake in humans (Jheng et al., 2012); whilst Drp1 activation is induced in pancreatic β cells in response to hyperglycaemia, which is followed by the activation of proapoptotic signalling cascades in these cells (Liu et al., 2013).

Moreover, in the NTS, where Drp1-driven mitochondrial fission is associated with insulin resistance in this brain region, increased levels of inflammation, and increased body weight gain, food intake and visceral adiposity in rats are seen (Filippi et al., 2017; Patel et al., 2021). Strikingly, 3 days of HFD were sufficient to induce a shift towards Drp1-driven mitochondrial fission in the NTS of rats, and this effect was reversed upon chemical inhibition of mitochondrial fission using the Drp1 inhibitor MDIVI-1 and molecular inhibition of Drp1, using the dominant negative form of the protein Drp1-K38-A. which alongside with the effects on

mitochondrial morphology also reversed insulin resistance in the NTS (Filippi et al., 2012; Filippi et al., 2017; Patel et al., 2021). Importantly, Patel et al. (2021) reported that the inhibition of mitochondrial fission in the NTS of the DVC, and in particular in astrocytes is sufficient to decrease food intake, body weight gain and visceral adiposity and restore insulin sensitivity in the DVC in HFD-fed animals. Moreover, in Chapters 3 and 4, we reported that the inhibition of mitochondrial fission in all cells, and then specifically in astrocytes of the NTS is associated with higher BAT glucose uptake in vivo. Furthermore, selective targeting of NTS astrocytes with the dominant negative form of Drp1 preserved BAT morphology and prevented loss of noradrenergic innervation to this organ compared to matching HFD controls, regardless of food intake. Associated with this, qPCR data revealed lower levels of inflammatory markers and higher level of CD36-fatty acids transporter encoding gene, however this effect was lost when rats were pair-fed, suggesting that these effects are feeding-dependent.

Altogether this data suggested that mitochondrial dynamics play an important role in BAT thermogenesis, and that inhibiting mitochondrial fission in astrocytes of the NTS can prevent the detrimental effects of HFD on BAT thermogenesis.

Patel et al. (2021) has demonstrated that the chronic activation of Drp1 in the NTS using a constitutively active form of Drp1 (Drp1-S637-A), under a CMV promoter (CMV:S637-A), to target the NTS was sufficient to induce hyperphagia, induce higher body weight gain and visceral fat and induce brain insulin resistance in regular chow-fed rats. A range of cell types are understood to be involved in the pathophysiology of Drp1-driven mitochondrial fission, and Patel et al. (2021) showed that the majority of cells that become infected with the CMV:GFP, CMV:K38-A and CMV:S637-A viruses in the NTS are glial cells, and in particular astrocytes. Astrocytes play a key role in energy balance; for example, their activation in the DVC using a chemogenetic approach resulted in decreased food intake in mice due to activation of local and distal neurons to control energy balance (MacDonald et al., 2019). Moreover, insulin sensing by astrocytes in this brain region is critical for BAT-driven thermogenesis and maintenance of body temperature in mice (Manaserh et al., 2020). In Chapter 3 and 4 we proved the importance of mitochondrial dynamics in regulating BAT glucose uptake and maintain and healthy metabolic profile of this tissue in HFD-fed animals.

However, it has not been proven whether the selective targeting of astrocytes to increase mitochondrial fission in the NTS of regular chow-fed animals, is sufficient to recapitulate the effects observed by (Patel et al., 2021) in regular chow animals. Further, it is not known whether increasing mitochondrial fission in the NTS of regular-chow fed rats can mimic the effects on glucose uptake of BAT in vivo or on BAT molecular and histological markers that we observed in HFD-fed animals (Chapter 3 and 4).

5.1.2 Study rationale

In this study we aimed to assess whether the activation of mitochondrial fission in all cells and specifically in astrocytes of the NTS using a constitutively active form of Drp1 is sufficient to decrease glucose uptake in BAT *in vivo*, to reduce its thermogenic and glucose clearance capacities. Further, we hypothesised that inducing mitochondrial fission specifically in astrocytes of the NTS could affect body weight, food intake, visceral adiposity and insulin sensitivity in the NTS, at a similar level to what observed by Patel et al. (2021), where all cells within the NTS were targeted. To this aim, two separate cohorts were employed; the first cohort was used to perform feeding studies and molecular analysis and to measure BAT and WAT adipose tissue pads. The second cohort was used for FDG-18 PET studies and gamma counting.

5.2 Aims

Aim 1: To determine whether promoting mitochondrial fission in astrocytes of the NTS is sufficient to induce higher body weight, food intake and visceral adiposity and induce insulin resistance in the NTS in regular chow fed animals.

Aim 2: To determine whether promoting mitochondrial fission in all cells and specifically in astrocytes of the NTS is sufficient to reduce the activation and dynamic glucose uptake in BAT of regular chow-fed rats upon selective noradrenergic stimulation using a combined PET/CT scanner.

Aim 3: To determine whether promoting mitochondrial fission in astrocytes of the NTS of regular chow fed animals is affecting brown adipose tissue morphology and noradrenergic innervation and key genes associated with an impaired metabolic profile of BAT.

5.3 The GFAP:S637-A AV system specifically targets GFAP+ astrocytes in the NTS

In this study we employed the GFAP:S637-A virus for the first time and we wanted to confirm that is the correct molecular weight via western blotting and that it selectively targets GFAP+ astrocytes within the NTS. After sacrifice, the DVC area was immediately collected and snap frozen for western blot analysis (Section 2.2.10). This confirmed that FLAG-tagged GFAP:S637-A is ~70 kDa, which is the correct size according to previous literature (Filippi et al., 2017; Patel et al., 2021) (Figure 5.1A). Alongside S376-A, we also ran a western blot to check GFP control virus, and we observed a ~33 kDa product, which confirmed that our control protein was also the correct size (Filippi et al., 2017; Patel et al., 2021) (Figure 5.1B).

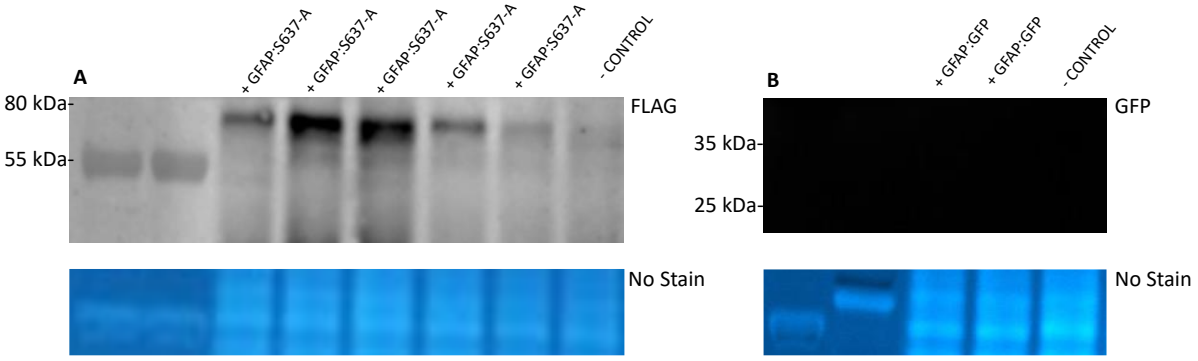

Figure 5.1: Viral expression of GFAP:S637-A and GFAP:GFP in the NTS of regular chow-fed rats. *Representative western blots showing (A) levels of expression of FLAG-tagged GFAP:S637-A in the NTS of rodents and (B) levels of expression of GFP in the NTS of GFAP:GFP control rodents.*

Next, we tested whether the novel adenovirus system GFAP:S637-A, a constitutively active form of Drp1, specifically targets GFAP+ astrocytes in the NTS. Our histological data confirm that GFAP:S637-A expression is restricted to GFAP+ astrocytes, and the viral expression pattern in restricted to the NTS (Figure 5.2) Interestingly, GFAP:S637-A appears as a diffuse staining, compartmentalised in the astrocytic processes (Figure 5.2, yellow).

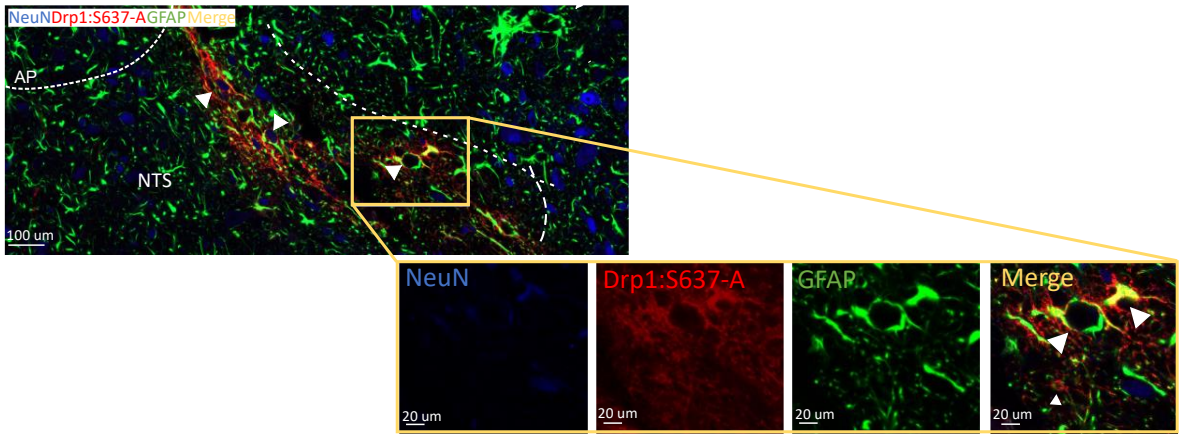

Figure 5.2: Viral expression of GFAP:S637-A confirms expression restricted to GFAP positive astrocytes in the NTS of regular chow-fed rats*. White arrows indicate colocalisation of FLAG-tagged GFAP:S637-A virus with GFAP immunoreactivity, but not with NeuN, demonstrating that GFAP+ astrocytes are specifically targeted. AP= area postrema; NTS= nucleus of the solitary tract.*

5.4 Chronic activation of mitochondrial fission in astrocytes in the NTS of regular chow fed rats elicits higher food intake and body weight gain without affecting abdominal adiposity

We aimed to assess if chronic activation of Drp1 in astrocytes can affect body weight and food intake, as observed by Patel et al. (2021) with the CMV:S637-A AV system; the authors observed that targeting all cells of the NTS significantly is associated with higher body weight and food intake in regular chow-fed animals.

In this experiment, food intake and body weight of animals were monitored daily, at the same time in the second quarter of the light phase (9am-12pm) to obtain consistent data (Section 2.2.9). A two-way ANOVA was performed to analyse the effect of the viral construct and food intake on body weight. Rats expressing GFAP:S637-A RC showed a significantly higher levels of cumulative food intake-normalised to body weight- only as they approached the last day of the study (GFAP:GFP RC 1031±46.7; GFAP:S637-A RC 1159±16.0 g/kg) (n=5 and n=6, respectively) ($p<0.05$) (Figure 5.3A) compared to GFAP:GFP RC matching controls. Moreover, a significantly higher body weight gain was observed in GFAP:S637-A RC animals (77.0±6.35 g) (n=6) when compared to GFAP:GFP RC matching controls (45.4±7.85 g) (n=5) ($p<0.05$) (Figure 5.3B). In summary, the activation of mitochondrial fission in astrocytes of the NTS is

associated with higher food intake and body weight gain in regular chow-fed rats, however, the effect is not as prominent as that observed delivering Drp1-S637-A to the NTS under the CMV promoter. In fact, compared to the CMV:GFP RC control group, CMV:S637-A animals exhibited significantly higher body weight and food intake at day 7 and day 10 of the feeding study, respectively (Patel et al., 2021). This may suggest that activating mitochondrial fission in astrocytes of regular chow-fed animals is sufficient to induce changes in food intake and body weight gain but other types of glial or non-glial cells contribute to the stronger effect on food intake and body weight observed by Patel et al. (2021).

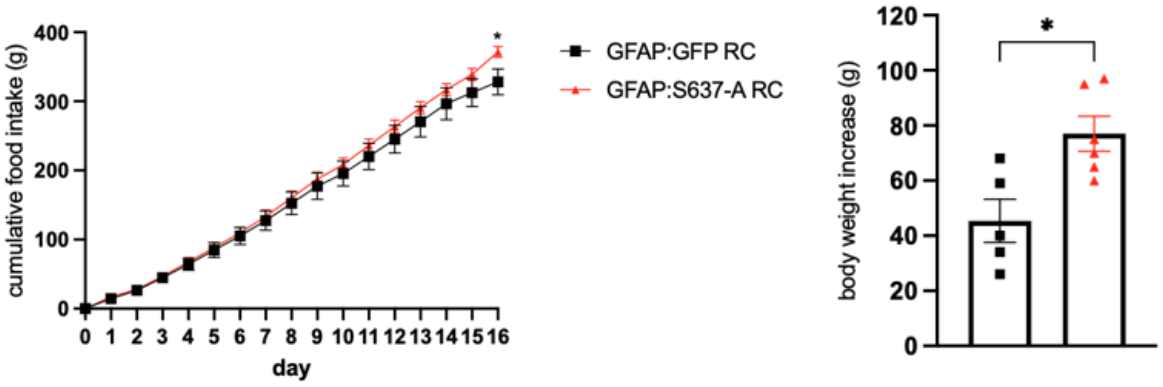

Figure 5.3: GFAP:S637A is associated with higher body weight and food intake in regular chow fed animals. *(a) Food intake of GFAP:S637A RC (n=6) and GFAP:GFP RC (n=5) normalised to body weight in kg. (b) Body weight increase of GFAP:S637A RC (n=6) and GFAP:GFP RC (n=5) animals at day 16 of the feeding study. All data were tested for normality prior statistical tests using the Shapiro-Wilk normality test. Values are shown as mean ± SEM and single data points are highlighted. ∗p< 0.05. Statistical test: Two-way ANOVA eith repeated measures and post-hoc Tukey, (a),unpaired t-test (b).*

As we observed higher body weight in GFAP:S637-A RC animals, the next objective was to investigate the effects of chronic activation of Drp1 on abdominal adiposity, to determine if abdominal adipose tissue expansion is responsible for the higher body weight we observed. On the last day of the study, animals were sacrificed, and tissues quickly dissected; three separate white adipose tissue depots were collected, namely the epididymal depot from the groin region, retroperitoneal fat surrounding the kidneys and mesenteric fat adjoining the intestinal tract. Total abdominal fat was defined as the sum of the three depots. Rats expressing GFAP:S637-A had the same amount of abdominal white adipose tissue as

GFAP:GFP RC animals across the three depots-GFAP:S637-A RC epididymal (8.13±0.517 g/kg), retro (26.1±2.67 g/kg, vis (16.5±1.33 g/kg) and GFAP:GFP RC epididymal (8.33±0.859 g/kg), retro (26.9± 2.53 g/kg), vis (16.8±1.06 g/kg) after normalization to body weight (p>0.999, p=0.999, p>0.999, respectively) (GFAP:GFP RC n=5, GFAP:S637-A RC n=6) (Figure 5.4).

This suggests that the observed higher body weight gain in GFAP:S637-A RC animals is not due to the expansion of abdominal fat; however, this could be due to other factors such as higher subcutaneous adiposity in these animals.

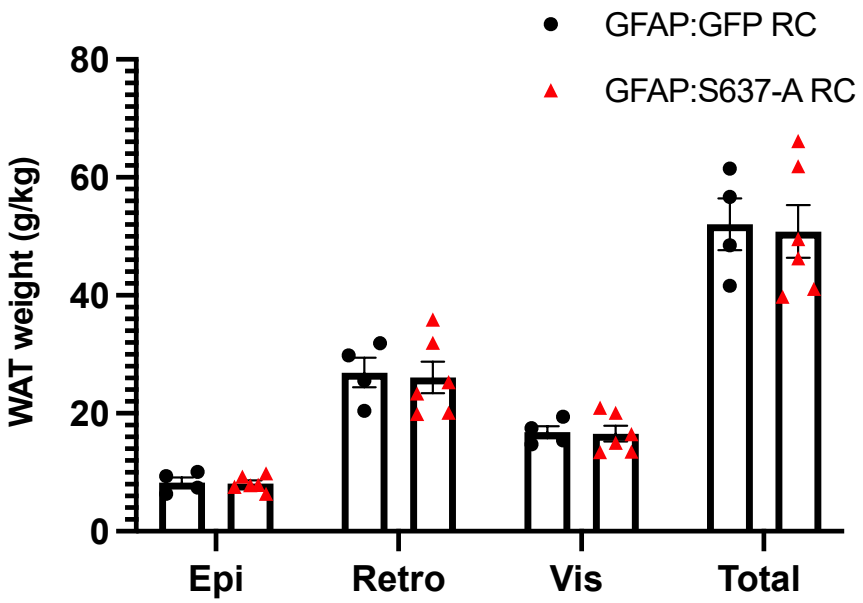

Figure 5.4: Activation of mitochondrial fission in the NTS of RC-fed rats does not affect WAT abdominal WAT depositions*. WAT weight normalised to body weight (g/kg) in GFAP-GFP RC (n=4) and GFAP:S637-A RC (n=6) animals. WAT is divided into three depots: Epididymal (Epi), retroperitoneal (Retro) and viscera (Vis)l. Total WAT is defined as the sum of the three depots. All data was tested for normality prior statistical tests using the Shapiro-Wilk normality test. Statistical test: unpaired t-test. Values are shown as mean ± SEM and individual data point highlighted.*

5.5 Chronic activation of mitochondrial fission in astrocytes in the NTS of regular chow fed rats induces insulin resistance in the NTS

Patel et al., (2021) has demonstrated that the activation of Drp1-dependent mitochondrial fission in all cells of the NTS did not only affect body weight, food intake and visceral adiposity but also induced insulin resistance within this brain region. This effect was observed in the first 4-hours following infusion of insulin and was still visible after 12 hours (Patel., 2021, unpublished data). Here we aimed to recapitulate this effect by activating mitochondrial fission specifically in the astrocytes of the NTS. On days 9 and 15, animals were fasted from 10 am to 4 pm. At 4 pm acute feeding studies commenced (Section 2.2.9), and 2 mU of insulin or saline vehicle at 6.6x 10-4 µl/s for a total volume of 0.2 µl were infused in the rats NTS. Food was then returned, and food intake measured every 30 minutes for 4 hours and then again after 12 hours. Unexpectedly, when infused with insulin, neither GFAP: GFP RC (n=2) and GFAP:S637-A RC (n=3-4) animals lowered their food intake GFAP:GFP RC (saline=2.66±0.343 g; insulin=1.95±0.217 g) (p=0.222) and GFAP:S637-A RC (saline=5.62±1.22 g; insulin=4.04±1.49 g) (p=0.354) at the 4 hour time period (Figure 5.5A). However at the 12-hour time point, GFAP:GFP RC animals had consumed significantly less food than the saline-infused group (saline=23.5±1.08; insulin=9.50±3.87 g) (*p<0.05) whilst GFAP:S637-A RC (saline=22.6±3.12; insulin=23.3±1.92 g) (p=0.792) animals consumed the same amount when infused with either saline or insulin (Figure 5.5B).

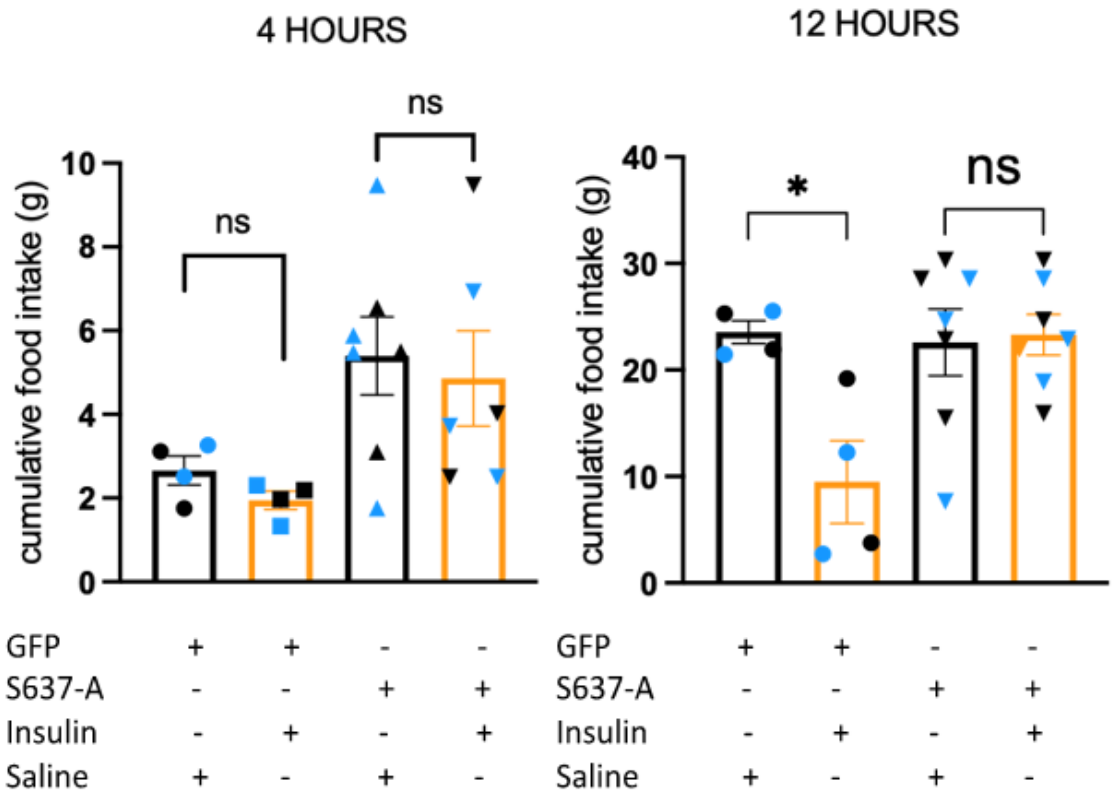

Figure 5.5: Insulin infusion in the NTS decreases food intake at 12-hour time point during acute feeding in GFAP:GFP RC fed rats but not in GFAP:S637-A RC expressing rats. *(A) Total food intake at the 4-hour time point, showing no difference in food intake of GFAP:GFP RC and GFAP:S637-A RC infused with insulin and vehicle. (B) Total food intake taken at the 12-hour time point, showing a response to insulin in GFAP:GFP RC animals but not in GFAP:S637-A RC animals. n=2 for GFAP:GFP RC vehicle, n=2 GFAP:GFP RC insulin (technical replicates n=2), n=4 for GFAP:S637-A RC vehicle, n=3-4 for GFAP:S637-A RC (technical replicates n=2). Black dots are representative of data obtained from technical replicates on day 9, blue dots represent data obtained from technical replicates on day 15. Each animal acted as internal control and therefore allocated to the saline group on day 9 and insulin group on day 15 or vice versa. All data were tested for normality prior statistical tests using the Shapiro-Wilk normality test. *p <0.05. Data are expressed as a mean ± SEM with each single data point highlighted. Statistical test:paired t-test.*

Altogether these results suggest that compared to the findings of Patel et al. (2021), the effect of insulin on feeding behaviour was delayed in GFAP:GFP RC animals, since they only significantly reduced their food intake at the 12-hour time point following infusion. This could be due to the small sample size of our study (n=2, 2 technical replicates) compared to Patel

et al. (2021) (n=12). Moreover, seasonal differences could play a role in these results, which will be examined in the discussion to the chapter. Conversely, GFAP:S637-A RC failed to show a response to insulin infusion in the NTS at both time points. Here we showed, for the first time, that activating mitochondrial fission in the NTS of regular chow-fed rats blunts the anorexigenic effects of insulin on a 12-hour time point, suggestive of insulin insensitivity in this brain region.

5.6 Chronic activation of mitochondrial fission in all cells and specifically in astrocytes in the NTS of regular-chow fed rats results in blunted glucose uptake in BAT in dynamic ^{18}FDG -PET/CT scans upon selective β3 adrenergic activation using the compound CL 316,243

We previously established that we can correctly deliver the AV systems to the NTS to activate mitochondrial fission specifically in GFAP+ astrocytes in the NTS. Moreover, we have observed that the activation of mitochondrial fission in astrocytes of the NTS affects feeding behaviour, body weight and insulin sensitivity in the NTS, but not abdominal adiposity. Here we aimed to assess the impact of our treatment on BAT. In particular, we determined whether promoting mitochondrial fission in all cells of the NTS, and then specifically in astrocytes of the NTS, can affect BAT glucose uptake *in vivo*. Animals underwent stereotactic surgery to insert a bilateral cannula in the NTS and were injected the same day with an adenovirus expressing GFP under a CMV promoter (Ad-CMV-GFP) or the constitutively active form of Drp1 (Drp1-S637-A) under a CMV (Ad-CMV:S637-A) or a GFAP (Ad-GFAP:S637-A) promoters (Sections 2.2.7, 2.2.8). Please note that n=2 RC animals were injected with GFAP:GFP and we confirmed that they were comparable to CMV:GFP RC animals; for this reason, we decided not to repeat this experiment in a GFAP:GFP RC cohort to meet the reduce principle of the 3Rs for use of animals in research. The animals were prepared for the scan as described in Section 3.4, and an injection of 65±5 MBq/kg of ^{18}FDG was given in the lateral tail vein at the initiation of the scan (t=0) and data were acquired for 4800 s (Section 2.2.20). At the end of the scan, the animals were sacrificed, and a fraction of BAT and WAT were dissected, and ^{18}FDG counted using a gamma counter. ^{18}FDG uptake was calculated as percentage of injected dose (MBq) per gram of collected tissue (Section 2.2.21). A two-way ANOVA was performed to analyse the effect of viral construct and β3 adrenergic stimulation on BAT glucose uptake.

The % of injected dose per gram of BAT of CMV:S637-A RC (1.86±0.410% injected dose/g) (n=4) and GFAP:S637-A RC (2.27±0.552% injected dose/g) (n=5) animals was significantly lower than that of CMV:GFP RC controls after CL 316,243 injection (6.20±1.55% injected dose/g) (n=5) (**p<0.01 and **p<0.01, respectively) (Figure 5.6). These data show, for the first time, that promoting mitochondrial fission in all cells, and specifically in astrocytes in the NTS is associated with lower glucose uptake in BAT of regular chow-fed animals, suggesting that mitochondrial dynamics, and in particular mitochondrial fission alone can mimic the effects of HFD on BAT glucose metabolism.

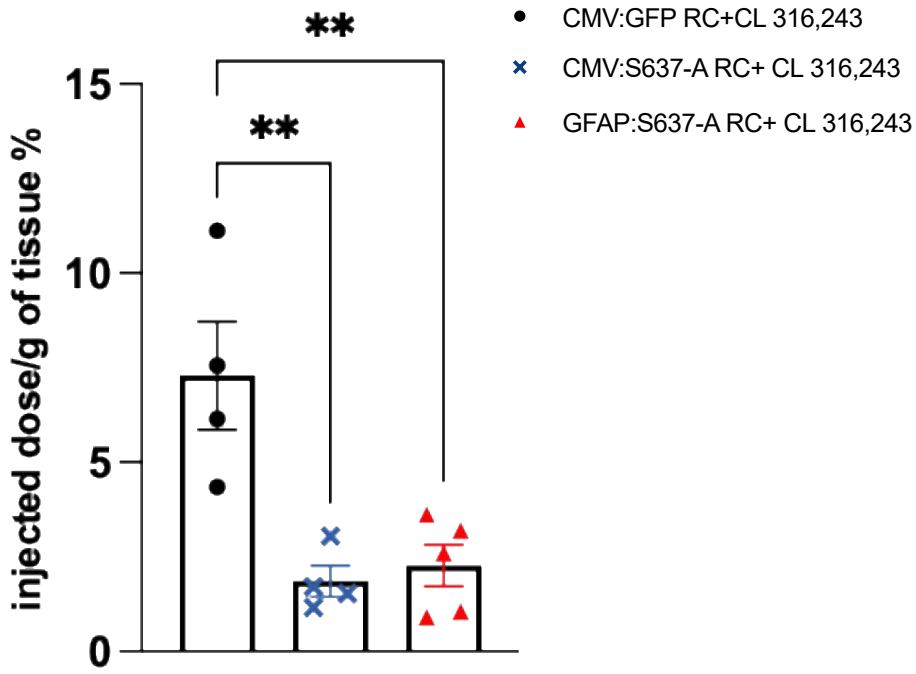

Figure 5.6: BAT uptake of ^{18}FDG as measured with gamma counting is lower when mitochondrial fission is activated in the NTS of RC fed rats*. Data are shown as mean ± SEM, with each single point highlighted. Data are representative of n= 5 rats for CMV:GFP RC and GFAP:S637-A RC, and n=4 rats for CMV:S637-A RC. **p<0.01. Statistical test: Two-way ANOVA. Post hoc test: Tukey.*

Next, we measured the % of injected dose per gram of WAT of CMV:S637-A RC (0.132±0.023%) injected dose/g) (n=4) and GFAP:S637-A RC (0.310±0.0802% injected dose/g) (n=5) animals and we found no significant differences from CMV:GFP RC control animals after CL 316,243 injection (0.554±0.229% injected dose/g) (n=5) (p=0.144 and p=0.425, respectively) (Figure 5.7).

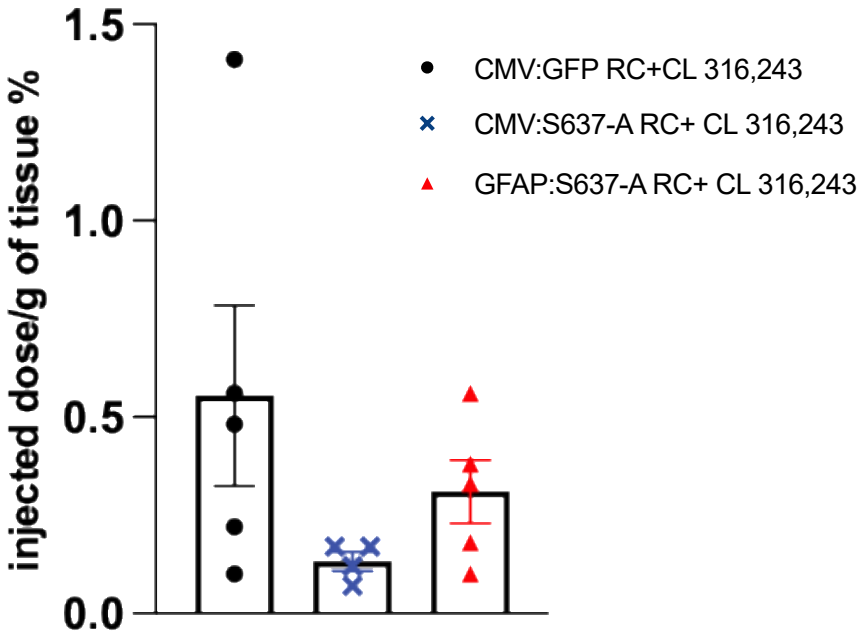

Figure 5.7: WAT uptake of ^{18}FDG is not affected by activation of mitochondrial fission in the NTS of RC fed rats*. Data are representative of n= 5 rats for CMV:GFP RC and GFAP:S637-A RC, and n=4 rats for CMV:S637-A RC. Data are shown as mean ± SEM, with each single point highlighted. Statistical test: Two-way ANOVA. Post hoc test: Tukey.*

^{18}FDG uptake in BAT was then analysed using reconstructed PET scans images (Section 2.2.20). Scans were visualised at SUV=3 and analysed as described in Section 3.4. Representative FDG/PET images of CMV:GFP RC (A), CMV:S637-A RC (B) and GFAP:S637-A RC (C) show glucose uptake in BAT after injection of CL 316,243 (n= animals for each group) (Figure 5.8).

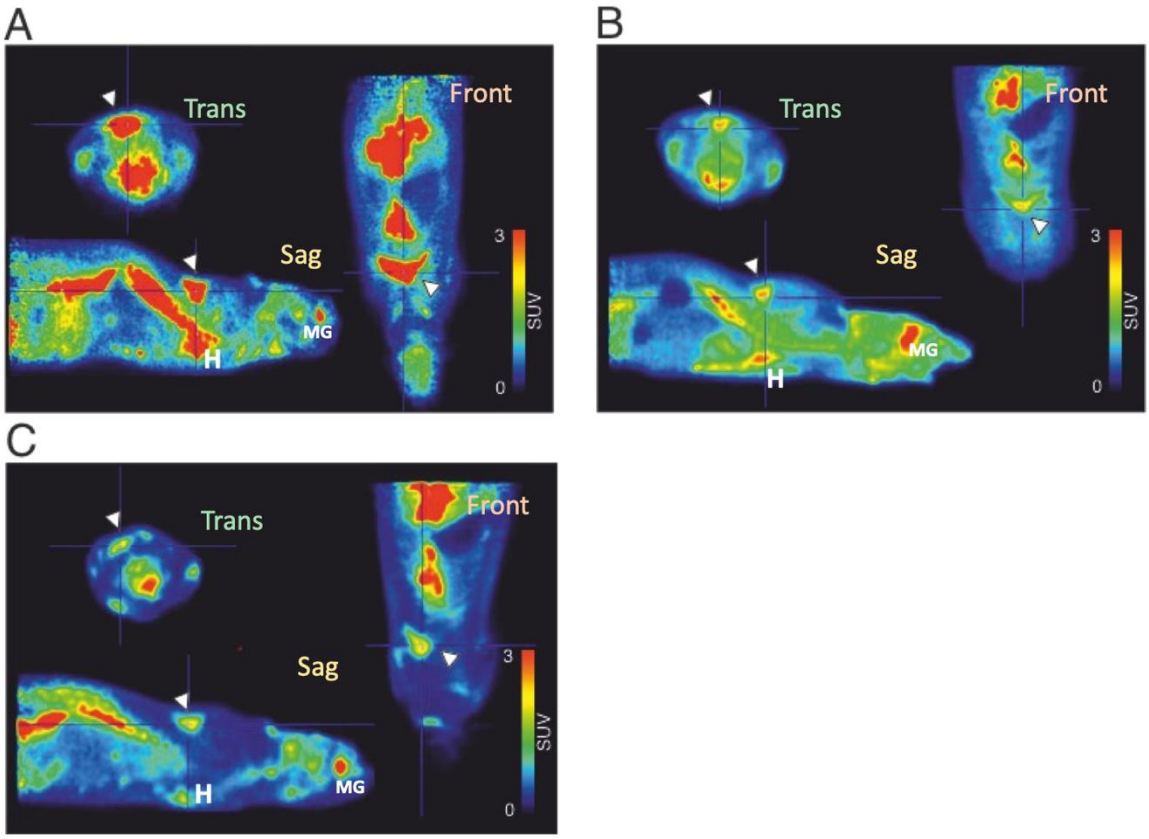

Figure 5.8: Representative PET/CT scan reconstructions of animals injected with 1mg/kg of selective β3 adrenergic agonist CL 316,243 to activate BAT*. Images are presented in standardised uptake value (SUV) for each group following a dynamic PET/CT scan. (A) Representative coronal, axial and sagittal ^{18}FDG PET scan of a CMV:GFP RC animal. (B) Representative coronal, axial and sagittal ^{18}FDG PET scan of a CMV:S637-A RC animal and (C) Representative coronal, axial and sagittal ^{18}FDG PET scan of a GFAP:S637-A RC animal. The scale bar represents SUV. The white arrow points toward BAT. Abbreviations: H, heart; MG, meibomian gland.*

PET scans analysis is presented as SUV_{BAT} in function of time. A two-way ANOVA was performed to analyse the effect of viral construct and β3 adrenergic stimulation on BAT glucose uptake. Strikingly, BAT glucose uptake was significantly lower at the end of the dynamic PET scan (t=4800) in CMV:S637-A RC (2.01±0.398 g/mL) and GFAP:S637-A RC (1.79±0.551 g/mL) animals when compared to CMV:GFP RC controls (3.32±0.352 g/mL), following CL 316,243 injection ($$$=p<0.001 and ****p<0.0001, respectively) (n=4 for all groups) (Figure 5.9).

To summarise, here we have shown, for the first time, that the promotion of mitochondrial fission in the NTS of regular chow-fed rats can significantly reduce BAT glucose uptake and activation as measured with gamma counting (Figure 5.6) and PET/CT scan (Figure 5.9).

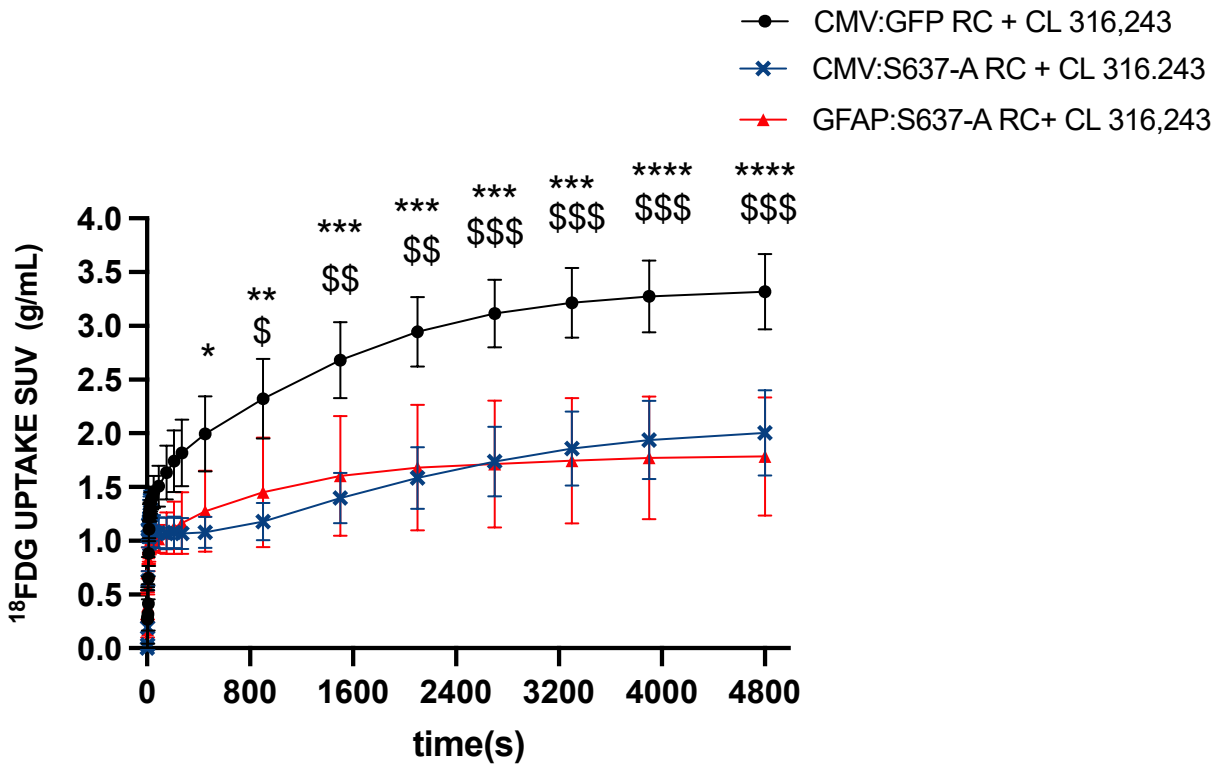

Figure 5.9: BAT ^{18}FDG glucose uptake expressed in SUV in lower in CMV:S637-A RC and GFAP:S637-A RC animals compared to GFAP:GFP RC controls in(g/mL). *Data are shown as mean ± SEM. Data are representative of n = 4 rats for CMV:GFP RC, CMV:S637-A RC and GFAP:S637-A RC, all treated with CL 316,243. $= p < 0.05; $$= p < 0.01; $$$= p < 0.001;*p < 0.05; **p < 0.01; ***p < 0.001 ****p < 0.0001. Statistical test: 2-way ANOVA with repeated measures. Post hoc test: Tukey.*

These data suggest an important role for mitochondrial dynamics in the control of BAT glucose uptake in rodents; further, we have shown that promoting mitochondrial fission in the NTS of regular chow-fed animals produced a diametrically opposite effect on BAT to what was observed when mitochondria fission in the NTS was inhibited. Moreover, this is effect is conserved when astrocytes are selectively targeted.

5.7 Chronic activation of mitochondrial fission in astrocytes of the NTS of regular chow-fed rats lowers BAT mass without altering its morphology and decreases noradrenergic terminals in BAT

On the day of sacrifice, BAT pads were collected and weighed from both cohorts, to measure differences in BAT mass. Interestingly, a significantly lower mass was observed in the BAT of GFAP:S637-A RC (0.533±0.0414) (n=6) animals when compared to GFAP:GFP RC (0.762±0.0687) (n=5) controls after normalization to body weight (* p<0.05) (Fig 5.10).

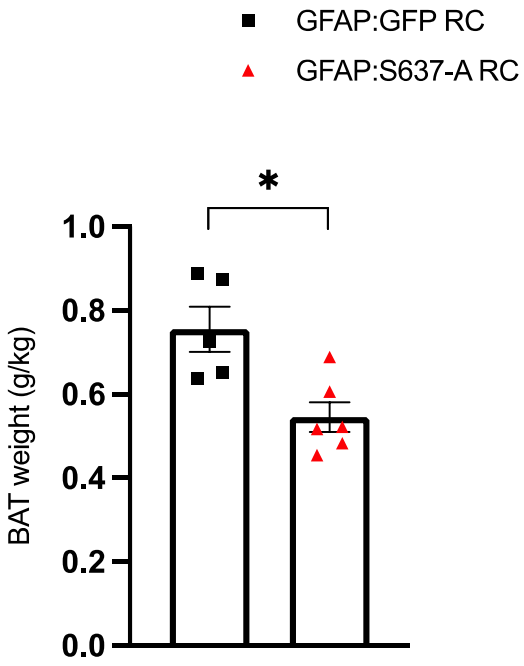

Figure 5.10: GFAP:S637-A RC animals have less BAT compared to GFAP:GFP RC controls after normalisation to body weight (g/kg). *GFAP-GFP RC (n=5) and GFAP:S637-A RC (n=6) animals. All data were tested for normality prior statistical tests using the Shapiro-Wilk normality test. Values are shown as mean ± SEM and single data point highlighted.* p<0.05.Statistical test: unpaired t-test.*

Next, BAT samples for H&E were prepared as previously described (Section 2.2.14) and we analysed the anatomical features of BAT across the two groups, however no notable differences in BAT morphology could be observed. In both groups, the tissue appeared normal, with the classical multilocular distribution of lipid droplets in the intracellular space of individual brown adipocytes and free from regions of hypertrophy (Figure 5.11A and B).

Quantitative analysis of the lipid droplet area (GFAP:GFP RC 4.98±0.378 μm^2, GFAP:S637-A RC 4.68±0.353 μm^2) (n=4, 4-5 technical replicates each) and lipid droplets number per visual field (GFAP:GFP RC 3600±217, GFAP:S637-A RC 3982±175) (n=4, 4-5 technical replicates each) corroborated this observations, revealing that there are no differences in these parameters across the two groups (p=0.562 and p=0.186, respectively) (Figure 5.11C and D).

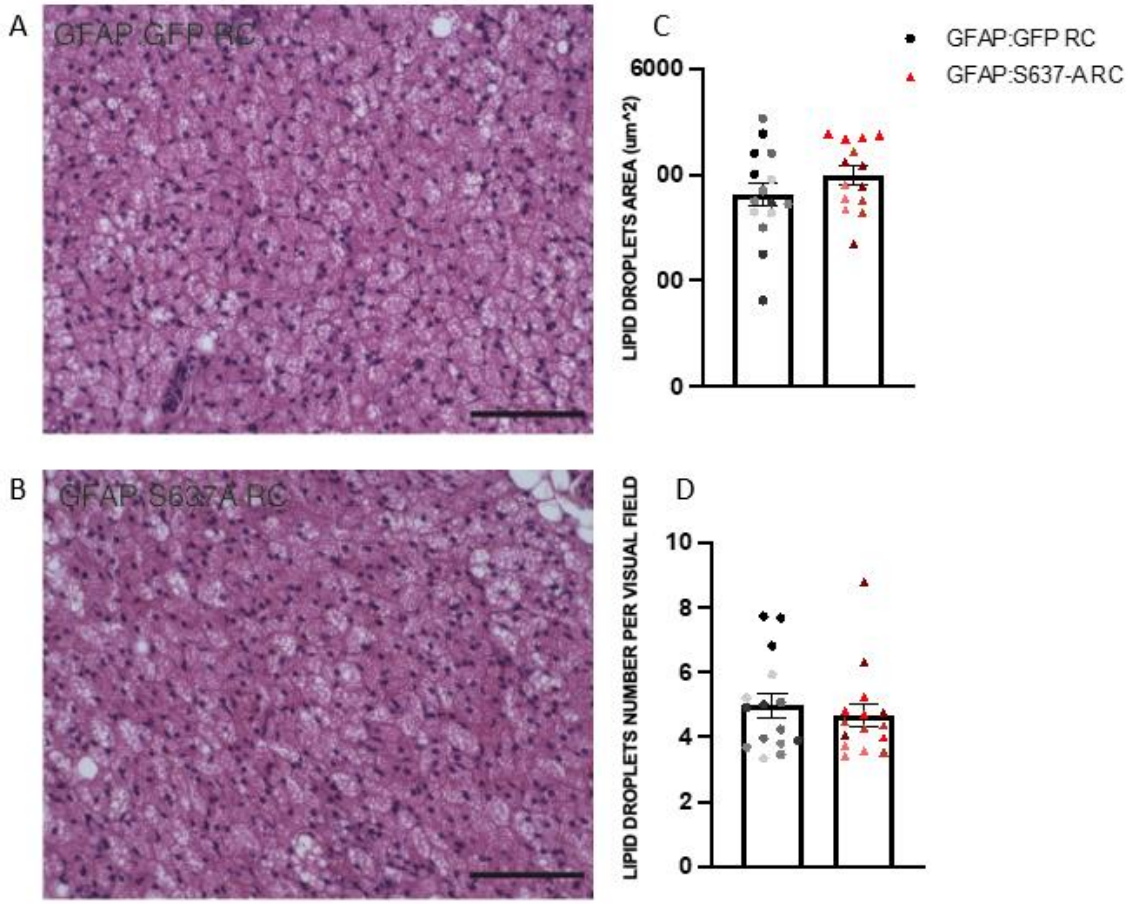

Figure 5.11: Activation of mitochondrial dynamics in astrocytes of the NTS of RC-fed animals does not affect lipid droplet size or number in BAT. *Representative images of H&E staining on serial BAT sections cut at 5 μm. (A) is representative for GFAP:GFP RC and (B) is representative for GFAP:S367-A RC. (C) shows lipid droplet area quantification for GFAP:GFP RC (n=3, 3 technical repeats) and GFAP:S367-A RC (n=4, 3 technical repeats).(D) shows lipid droplets number per visual field for GFAP:GFP RC (n=3, 3 technical repeats) and GFAP:S367-A RC (n=4, 3 technical repeats). Scale bars=50 μm. All data were tested for normality prior statistical tests using the Shapiro-Wilk normality test. Values are shown as mean ± SEM and individual technical replicates shown and grouped by biological replicate. Statistical testing was performed on the averages of each technical replicate:unpaired t-test.*

Next, a portion of cryopreserved BAT pads was prepared for TH immunoreactivity as previously described (Section 2.2.14). Here we aimed to determine if the activation of mitochondrial fission in the NTS of astrocytes was sufficient to decrease the sympathetic noradrenergic innervation of BAT, mimicking what we observed in the control HFD group in Chapter 4. We determined the level of expression of TH in GFAP:GFP RC animals and in GFAP:S637-A RC animals, and surprisingly, despite no significant changes in tissue morphology, we observed a lower TH intensity per visual field in GFAP:S637-A RC animals (2.19$\pm$0.164 %) (n=4, 4-5 technical repeats) compared to the GFAP:GFP RC controls (3.90$\pm$0.292 %) (n=4, 4-5 technical repeats) (*p<0.05)(Fig 5.12A-B,D). Moreover, the numbers of TH pools per visual fields were significantly lower in the GFAP:S637-A RC group (721$\pm$61.3) (n=4, 4-5 technical repeats), compared to the matching GFAP:GFP RC controls (1093$\pm$92.2) (n=4, 4-5 technical repeats). (*p<0.05) (Fig 5.12A-B,E).

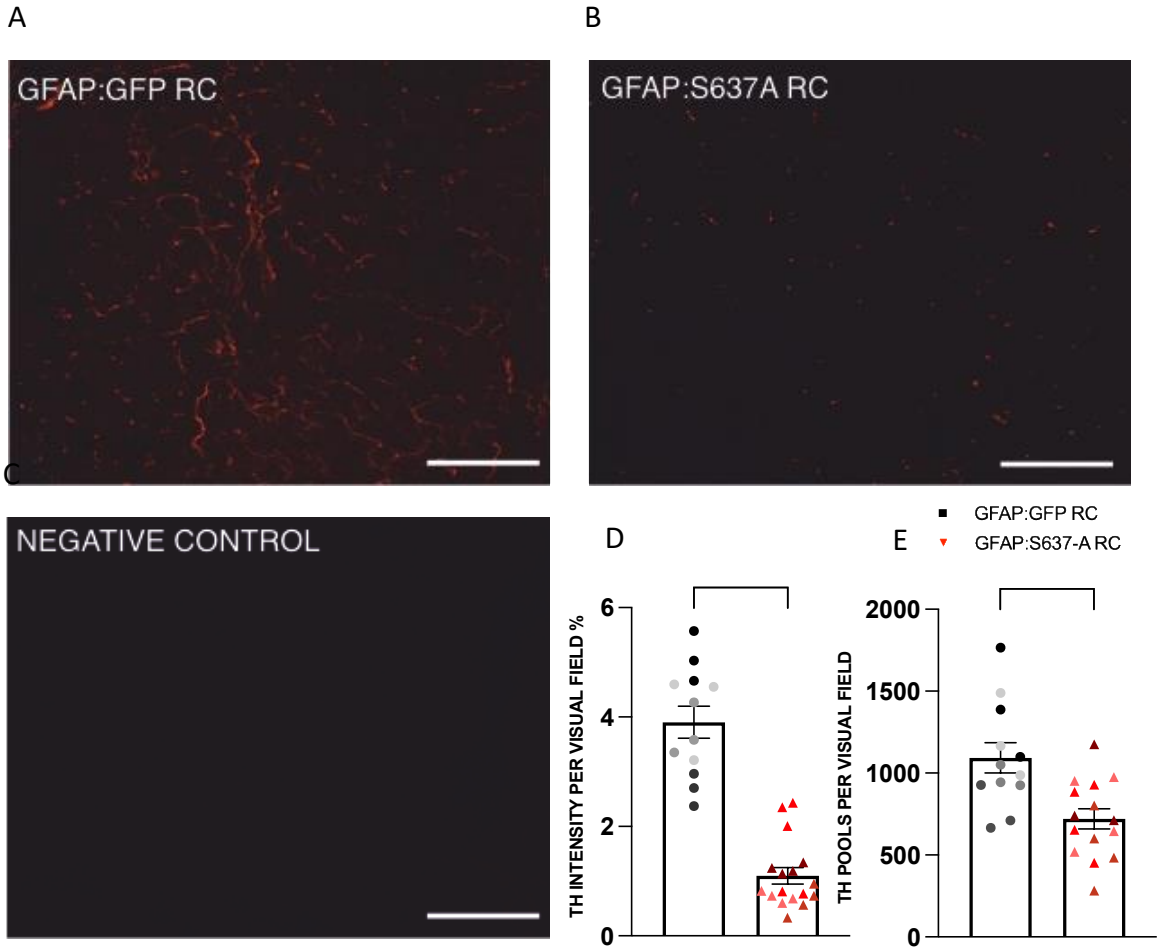

Figure 5.12: Activation of mitochondrial fission in astrocytes of the NTS of RC-fed rats blunts noradrenergic innervation of BAT compared to GFAP:GFP RC controls. *Representative confocal images of tyrosine hydroxylase (TH) immunoreactivity, a marker of noradrenergic innervation on serial BAT sections cut at 5 µm. (A) Is representative for GFAP:GFP RC group. (B) Is representative for GFAP:S637-A RC group. (C) Shows a representative negative control (- 1ary antibody). (D) TH intensity quantification per visual field for GFAP:GFP RC animals (n=3, 4 technical repeats) and GFAP:S637-A RC animals (n=4, 3- 4 technical repeats). (E) Number of TH pools per visual field for GFAP:GFP RC animals (n=3, 4 technical repeats) and GFAP:S637-A RC animals (n=4, 3-4 technical repeats).Scale bars=50 µm .All data was tested for normality prior statistical tests using the Shapiro-Wilk normality test. Values are shown as mean ± SEM and individual technical replicates shown and grouped by biological replicate. Statistical testing was performed on the averages of each technical replicate:unpaired t-test. ⁎p < 0.01.*

5.8 Chronic activation of mitochondrial fission in astrocytes in the NTS of the brain can induce changes in key genes expression in the brown adipose tissue of regular chow-fed rats.

The final aim of this chapter was to examine whether activation of mitochondrial fission in GFAP positive astrocytes was sufficient to induce changes in the expression of mRNA transcripts of genes involved in BAT metabolic health at basal level. First, we analysed the expression of genes related to BAT insulin sensitivity and glucose uptake, namely *Slc2a1*, *Slc2a4* and *INSR* (Section 4.6). GFAP:GFP RC group was used as control. qPCR analysis showed that these genes were mostly unaffected by the activation of mitochondrial fission in astrocytes of the NTS, as measured by gene fold-change (Figure 5.13). *Slc2a1* expression levels were unchanged in GFAP:S637-A RC animals (0.858±0.124) (n=6) when compared to GFAP:GFP RC controls (1.05±0.111) (n=9) (p=0.281); similarly, *Slc2a4* transcripts were also unaffected, GFAP:S37-A RC (1.14±0.0839) (n=6) and GFAP:GFP RC controls (1.30± 0.263)(n=9) (p=0.648). Interestingly, *INSR* transcripts were lower in GFAP:S637-A RC animals (1.91±0.231) (n=6) when compared to GFAP:GFP RC controls (1.19±0.227) (n=9) (p=0.0512) (Figure 5.13).

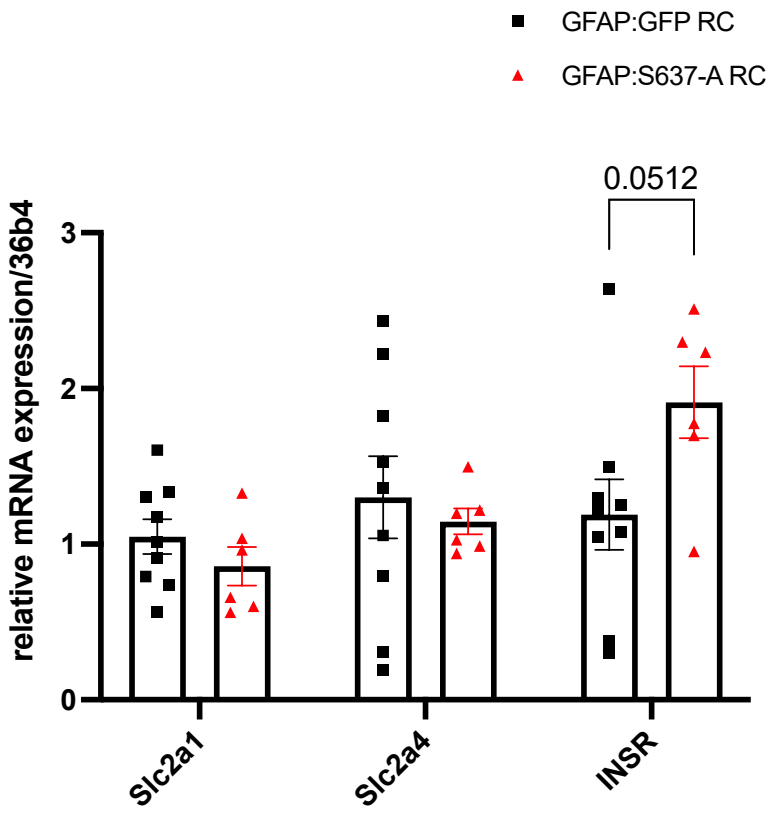

Figure 5.13: INSR mRNA transcripts in BAT show a trend towards increase upon activation of mitochondrial fission in astrocytes of the NTS of RC-fed animals. *Genes of interest are relative to the expression of housekeeping gene 36b4. Relative expression of genes of interest in GFAP:GFP RC (n=9) versus GFAP:S637-A RC (n=6) animals. Primers were run at separate times with internal controls to ensure gene expression consistency. All data was tested for normality prior statistical tests using the Shapiro-Wilk normality test. Values are shown as mean ± SEM and single data point highlighted. Statistical test: unpaired t-test.*

Next, we analysed the expression of genes specific to BAT thermogenesis, namely *ADRB3, UCP1,PPARGC1A, PPARG* and *CIDEA* (Section 4.7). Here we found that mRNA transcripts for *ADRB3* and *UCP1* were significantly lower in GFAP:S637-A RC animals (0.568±0.0443; 0.649±0.0854) compared to GFAP:GFP RC controls (1.11±0.156; 1.05±0.104) (*p<0.05 and *p<0.05, respectively) (Figure 5.14). This suggests that in absence of HFD, the activation of mitochondrial fission in astrocytes of the NTS alone is sufficient to reduce the expression of UCP1- a classic marker of thermogenesis in BAT (Section 5.7); similarly, *ADRB3* transcripts correlate with lower noradrenergic innervation of BAT we previously observed (Section 5.7). Moreover, *PPARG* and *CIDEA* levels are also significantly lower in GFAP-S637-A animals (0.712±0.0648;0.454±0.0732) compared to GFAP:GFP RC controls (1.03±0.0773;1.14±0.201)

(*p<0.05 and *p<0.05, respectively) (Figure 5.14). Lastly, *PPARGC1A* transcripts were not affected, GFAP:S637-A RC (1.06±0.242) and GFAP:GFP RC (1.09±0.159), (p=0.911) (Figure 5.14).

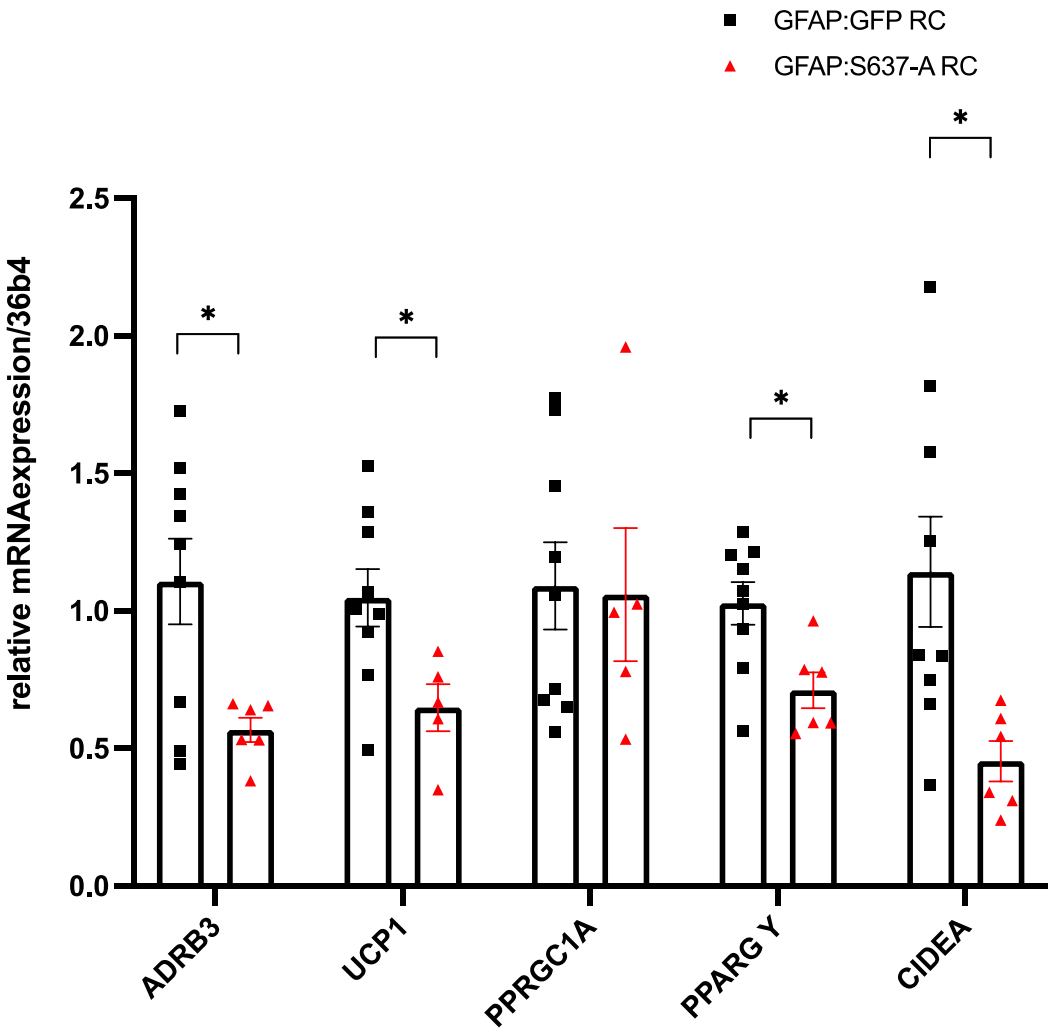

Figure 5.14: ADRB3 and UCP1 mRNA transcripts in BAT are lower upon activation of mitochondrial fission in astrocytes of the NTS of RC-fed animals*. Genes of interest are relative to the expression of housekeeping gene 36b4. Relative expression of genes of interest in GFAP:GFP RC (n=9) versus GFAP:S637-A RC (n=6) animals. Primers were run at separate times with internal controls to ensure gene expression consistency. All data was tested for normality prior statistical tests using the Shapiro-Wilk normality test. Values are shown as mean ± SEM and single data point highlighted. * p<0.05. Statistical test:unpaired t-test.*

We then looked at genes related to fatty acid uptake and oxidation (Section 4.8), and there were significantly lower levels of mRNA transcripts for both *CD36* (0.657±0.0775) and *ACADL* (0.713±0.0950) in the BAT of GFAP:S637-A RC animals when compared to GFAP:GFP RC controls- *CD36* (1.007±0.0425) and *ACADL* (1.003±0.02946) (***p<0.001 and *p<0.05,respectively) (Figure 5.15).

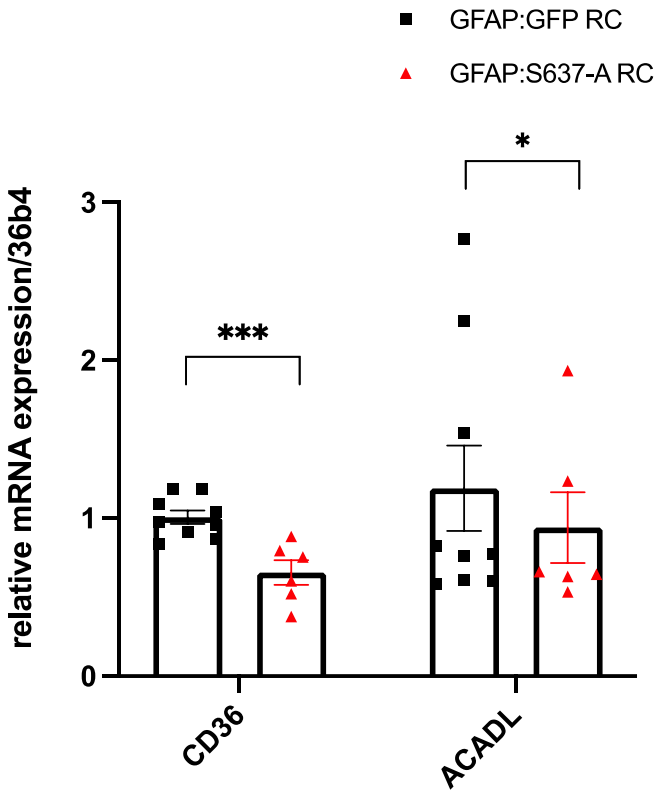

Figure 5.15: CD36 and ACADL mRNA transcripts in BAT are lower upon activation of mitochondrial fission in astrocytes of the NTS of RC-fed animals*. Genes of interest are relative to the expression of housekeeping gene 36b4. Relative expression of genes of interest in GFAP:GFP RC (n=9) versus GFAP:S637-A RC (n=6) animals. Primers were run at separate times with internal controls to ensure gene expression consistency. All data was tested for normality prior statistical tests using the Shapiro-Wilk normality test. Values are shown as mean ± SEM and single data point highlighted. * p<0.05: *** P<0.001. Statistical test: unpaired t-test.*

We then analysed the expression of markers related to lipolysis. No significant different in the expression of *PNPL2A* and *HSL* was observed across the two groups (Section 4.9). *PNPLA2* and *HSL* in GFAP:S637-A RC animals (1.19±0.217 and 1.786±0.257, respectively) compared to

GFAP:GFP RC controls, (0.763±0.164 and 1.14±0.187, respectively) (p=0.170, p=0.0585) (Figure 5.16).

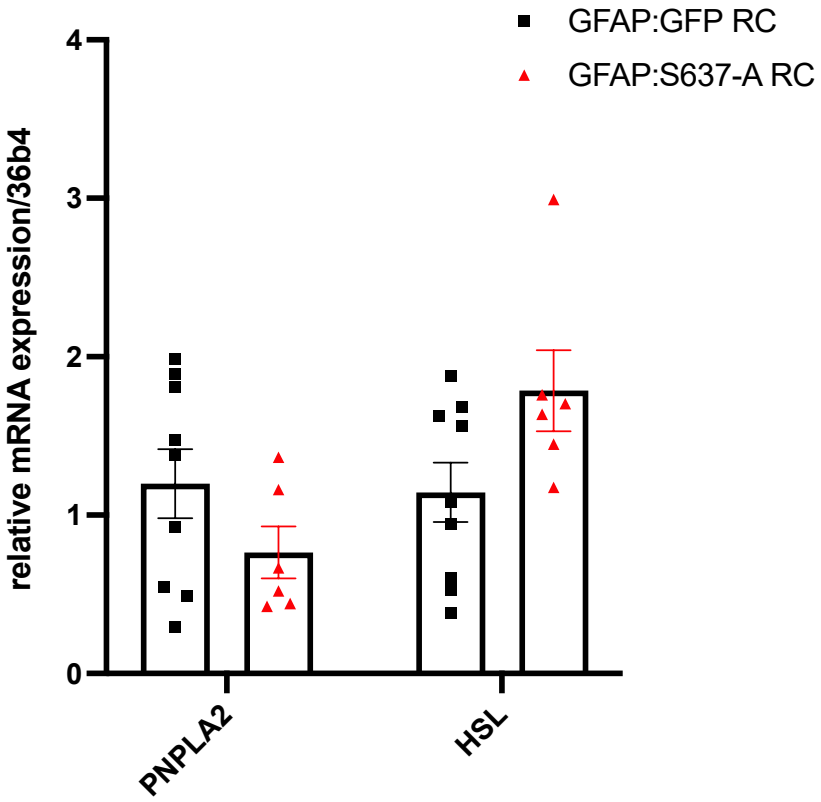

Figure 5.16: Genes involved in lipolysis in BAT are not affected by the activation of mitochondrial fission in astrocytes of the NTS of RC-fed animals. *Genes of interest are relative to the expression of housekeeping gene 36b4. Relative expression of genes of interest in GFAP:GFP RC (n=9) versus GFAP:S637-A RC (n=6) animals. Primers were run at separate times with internal controls to ensure gene expression consistency. All data was tested for normality prior statistical tests using the Shapiro-Wilk normality test. Values are shown as mean ± SEM and single data point highlighted. Statistical test:unpaired t-test.*

Next, we aimed to assess if, similarly to HFD, the activation of mitochondrial fission in astrocytes of the NTS could drive the expression of genes related to ER stress (*DDIT3*) and inflammation (*NFKB, TNFA*) (Section 4.10). Remarkably, we observed a significantly higher value in *TNFA* transcripts in the BAT of GFAP:S637-A RC animals (1.51±0.233) when compared to matching GFAP:GFP RC controls (0.924±0.0947) (*p<0.05). However, *DDIT3* and *NFKB* were not affected; *DDIT3* and *NFKB* in GFAP:S637A RC animals (1.057±0.131 and 0.922±0.133, respectively) compared to GFAP:GFP RC controls, (0.868±0.144 and 0.877±0.293, respectively) (p=0.360, p=0.881) (Figure 5.17).

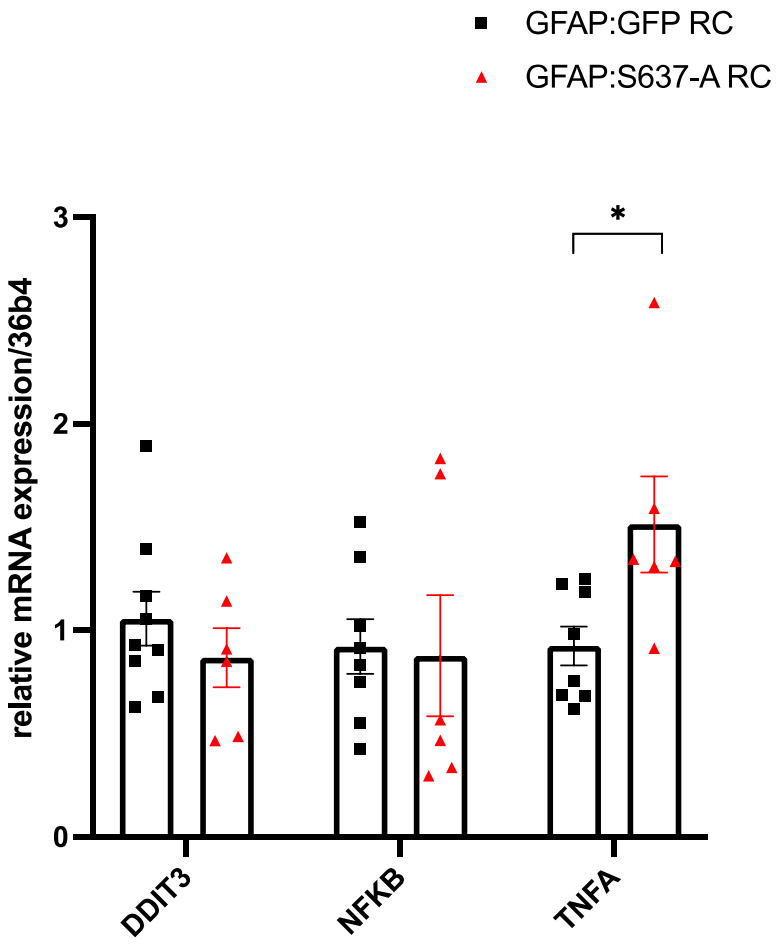

Figure 5.17: TNFA mRNA transcripts in BAT are higher upon activation of mitochondrial fission in astrocytes of the NTS of RC-fed animals *Genes of interest are relative to the expression of housekeeping gene 36b4. Relative expression of genes of interest in GFAP:GFP RC (n=9) versus GFAP:S637-A RC (n=6) animals. Primers were run at separate times with internal controls to ensure gene expression consistency. All data was tested for normality prior statistical tests using the Shapiro-Wilk normality test. Values are shown as mean ± SEM and single data point highlighted. * p<0.05. Statistical test:unpaired t-test.*

Finally, we investigated the expression of genes involved in mitochondrial dynamics in BAT (Section 4.11). Whilst *MFN2* expression was unchanged across the two groups, GFAP:S637-A RC (2.404±0.498) and GFAP: GFP RC (1.89±0.307) (p=0.374), *DRP1* transcripts were significantly down regulated in GFAP:S637-A RC animals (0.554±0.118) when compared to the GFAP: GFP RC controls (0.899±0.0853) (*p<0.05) (Figure 5.18).

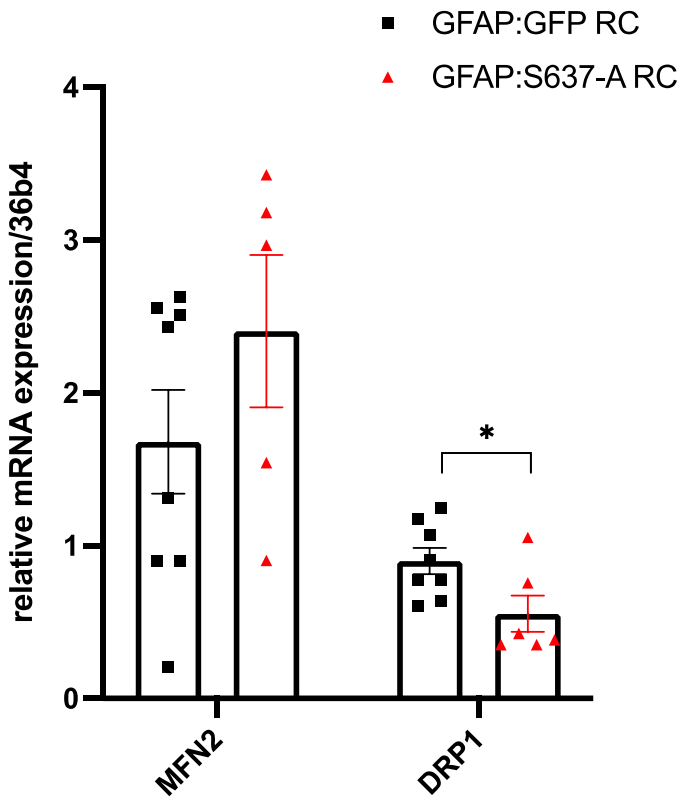

Figure 5.18: Drp1 mRNA transcripts in BAT are lower upon activation of mitochondrial fission in astrocytes of the NTS of RC-fed animals. *Genes of interest are relative to the expression of housekeeping gene 36b4. Relative expression of genes of interest in GFAP:GFP RC (n=9) versus GFAP:S637-A RC (n=6) animals. Primers were run at separate times with internal controls to ensure gene expression consistency. All data was tested for normality prior statistical tests using the Shapiro-Wilk normality test. Values are shown as mean ± SEM and single data point highlighted. * p<0.05. Statistical test:unpaired t-test.*

As we discussed in Section 4.15 CD36 is critical to the transport of FA from the plasma membrane to mitochondria to sustain β oxidation, and CD36 drives the uptake of CoQ within BAT to support normal BAT thermogenic function (Anderson et al., 2015). Here we determined whether CoQ levels are affected by CD36 downregulation in GFAP:S637-A RC animals. To resolve this question, we used a competitive ELISA technique (Section 2.2.19) and we determined the amount of CoQ in the BAT of control GFAP:GFP RC animals fed and GFAP:S637-A RC animals.

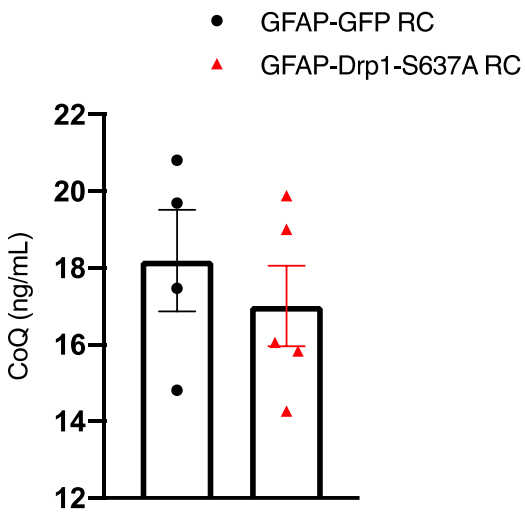

Figure 5.19: Activation of mitochondrial dynamics in astrocytes of the NTS does not affect CoQ levels in BAT. *CoQ level in ng/mL measured in GFAP:GFP RC (n=4), GFAP:S637-A RC (n=5).All data was tested for normality prior statistical tests using the Shapiro-Wilk normality test. Values are shown as mean ± SEM and single data point highlighted. Statistical test:unpaired t-test.*

The results revealed no significant changes in levels of CoQ, expressed in ng/mL in the BAT of GFAP:S637-A RC animals (17.0±1.05) when compared to GFAP:GFP RC controls (18.2±1.33) (p=0.501) (Figure 5.19). This suggests that the decrease in *CD36* transcripts we observed in the BAT of our model is not associated with CoQ deficiency in this tissue.

5.9 Discussion

The data we presented has demonstrated that the activation of Drp1- dependent mitochondrial fission in the astrocytes of the NTS leads to higher body weight and food intake in RC-fed rats. This is analogous to what observed by Patel et al. (2021), where the authors increased mitochondrial fission in all cells of the NTS using the CMV:S637-A system and observed higher body weight and food intake in RC-fed animals over 2-weeks when compared to control CMV:GFP RC group. We also showed that increasing mitochondrial fission specifically in astrocytes of the NTS is sufficient to induce higher body weight and food intake in RC-fed animals when compared to GFAP:GFP RC controls. Importantly, previous studies have determined that astrocytes play an important role in the regulation of food intake; for example, 24 hours of HFD resulted in hyperphagia in wild-type mice, and this

increase in caloric intake was accompanied by increased astrocytic activation in the MBH while their activation was suppressed by inducing the expression of a dominant negative form of the transcription factor NFKβ in these cells (Buckman et al., 2015). Similarly, in the NTS of HFD-fed mice, excessive caloric intake induces GFAP expression upregulation and increases astrocytic morphological complexity and number of processes compared to regular chow control animals (MacDonald et al., 2020). Moreover, the authors show that chemogenetic activation of astrocytes in DVC:GFAPhM3Dq mice reduces food intake and induces c-FOS expression in neighbouring neurons in the NTS, AP, and distal neurons in the lateral parabrachial nucleus (IPBN) (MacDonald et al., 2020). This data suggests that similarly to the hypothalamus, astrocytes in the NTS are acutely recruited and activated by nutritional excess and could recruit short and long-range neurons in the brainstem to control feeding.

Importantly, the activation of Drp1-dependent mitochondrial fission increases iNOS levels and leads to elevated ER stress in the NTS and delivering shRNA to KO iNOS in the NTS of HFD-fed rats reduced body weight, food intake and abdominal adiposity compared to scramble ShRNA controls (Patel et al., 2021). Interestingly, iNOS is induced in the brain via a NFKβ-dependent mechanisms in response to stress, and NMDA receptor antagonism inhibits the NFKβ activation induced by stress response as well as the increase in iNOS in the brain cortex of rats (Madrigal et al., 2001). Similarly, the pro-inflammatory stimulus of lipopolysaccharides induced NFKβ-dependent iNOS expression and subsequent NO production in murine cerebellar granule neurons (Arias-Salvatierra et al., 2011); moreover, overnutrition atypically activates IKKβ/NFKβ in the hypothalamus, through elevated levels of ER stress in this brain region (Zhang et al., 2008).

NFKβ in astrocytes is implicated in feeding behaviour (Buckman et al., 2015) and energy imbalance during obesity (Zhang et al., 2008) and iNOS can be induced in a NFKβ dependent mechanism in other regions of the brain (Madrigal et al., 2001; Arias-Salvatierra et al., 2011). For these reasons, it would be interesting to investigate if iNOS overexpression in the NTS in response to HFD is also modulated by NFKβ. Moreover, the NTS receives glutamatergic vagal afferent, and in HFD, glutamate levels from vagal inputs within the NTS are increased (Madden and Morrison, 2016; Madden et al., 2017). It would then be noteworthy to investigate whether HFD- dependent increase in glutamate in the NTS activates NFKβ, and

whether similarly to what observed in the brain cortex (Madrigal et al., 2001), the antagonism of glutamatergic NMDA receptors would be sufficient to inhibit NFKβ activation and iNOS expression in the NTS during HFD.

Our data also revealed that infusion of insulin in the NTS of GFAP:GFP RC control animals significantly decreased food intake within 12 hours, but this was not observed in GFAP:S637-A RC animals, which is suggestive of insulin resistance within the NTS. One possible explanation for this discrepancy is that while Patel et al. (2021) targeted all cells of the NTS with the constitutively active form of Drp1, we specifically targeted astrocytes, and this could potentially account for the delayed effect of insulin in the control of feeding behaviour in regular chow-fed rats. Interestingly, Patel et al. (2021) showed that CMV:GFP RC animals decreased food intake 4 hours after the infusion of insulin in their NTS, and a trend towards decrease in their food intake was still present after 12 hours from the insulin infusion in the NTS (Patel., 2020 unpublished data). Moreover, Patel et al. (2021) revealed that CMV:S637-A RC failed to decrease food intake at both the 4 and 12 hours-time point. Remarkably, in our study we did not observe a feeding response to insulin infusion in the NTS until 12 hours after infusion in control GFAP:GFP RC; therefore, we speculate that difference in sample sizes could account for this difference; in our study we only had n=4 animals in the control group, whilst Patel et al., 2021 reported a sample size of n=12. Moreover, changes in seasonality could bring an interesting justification to these observations; in fact, studies on marmots have shown seasonal changes in CSF insulin and a decreased efficiency of insulin in transmitting satiety signalling during colder months (Florant et al., 1991). Moreover human studies have shown that insulin sensitivity shows seasonal variations, and similarly to the marmots, a decrease in insulin sensitivity occurred in colder season (Berglund et al., 2012). Similarly, our experiment was conducted in late winter (February). Whilst in a laboratory context temperature, humidity and day/lights cycles are constantly maintained throughout the year, the existence of seasonal effects on laboratory rodent behaviour has been widely discussed, and it is known that some laboratory animals retain characteristics of their “wild” counterpart. While this could not be explored, it could be an interesting topic for debates about reliability in science employing animal models in metabolic studies and beyond.

We then demonstrated that the activation of mitochondrial fission in all cells, and then specifically in astrocytes of the NTS decreased BAT glucose uptake, suggestive of lower thermogenic capacity of this tissue in regular chow-fed animals. Importantly, in Chapter 3 we reported that inhibiting mitochondrial fission in all cells, and then specifically in astrocytes of the NTS is associated with higher glucose uptake in BAT of HFD-fed animals. These results show, for the first time, evidence of the bidirectional role of mitochondrial dynamics in controlling BAT glucose uptake, which is a marker of metabolic capacity of this tissue to perform thermogenesis. Whilst the connection between mitochondrial dynamics in astrocytes and BAT thermogenesis is still unknown, insulin sensing in astrocytes could be a mechanism of interest in the central control of thermogenesis. In fact, Manaserh et al. (2020) showed that insulin resistance in astrocytes alters sympathetic outflow to BAT, which resulted in reduced energy expenditure and lower basal and fasting body temperature in mice congenitally lacking IR in astrocytes ($IRKO^{GFAP}$ mice), when compared to IRloxp animals. Moreover, increasing Drp1-dependent mitochondrial fission in all cells (Patel et al., 2021), and specifically in astrocytes of the NTS, induced insulin resistance in this brain region in wild type, regular chow-fed rats. In contrast, inhibiting Drp1-dependent mitochondrial fission in all cells, and then specifically in astrocytes of the NTS of HFD-fed rats prevented insulin resistance in this brain region, independently of HFD (Filippi et al., 2017; Patel et al., 2021). Similarly, inhibition of Drp1 in the NTS via MDIVI-1 infusion, which prevents Drp1 translocation to the mitochondria (Cassidy-Stone et al., 2008) reversed HFD-induced insulin resistance in this brain region (Filippi et al., 2017). It is therefore reasonable to speculate that the activation of mitochondrial fission in all cells, and specifically in astrocytes of the NTS, triggers insulin resistance in this brain region, which in turn influences sympathetic stimulation to BAT to support thermogenesis. Importantly, Manaserh et al. (2020) also showed that TH immunoreactivity in BAT of $IRKO^{GFAP}$ mice were significantly reduced when compared to controls to IRloxp; similarly, we observed a significant decrease in TH abundance in GFAP:S637-A RC animals when compared to GFAP:GFP RC control group. This evidence supports the hypothesis that insulin sensing in astrocytes may be important in supporting sympathetic innervation to BAT and sustain thermogenesis in this tissue by favouring glucose uptake. Moreover, it could be speculated that mitochondrial dynamics in astrocytes could contribute to BAT stimulation via modulation of insulin sensing in astrocytes.

Unexpectedly, whilst GFAP:S637-A RC animals presented smaller BAT depots than GFAP:GFP RC controls, the decrease in TH abundance we have observed in the GFAP:S637-A RC group was not accompanied by notable changes in BAT morphology, which was comparable to that of control GFAP:GFP RC animals.

In chapter 4 we have shown that inhibition of mitochondrial fission in astrocytes of the NTS was sufficient to prevent BAT lipid droplets enlargement and a white-like phenotype of BAT in HFD-fed animals, independently of food intake. Thus, if we consider this evidence, we could infer that HFD is likely to be an important factor in BAT lipid droplet enlargement, and this could be prevented by inhibition of mitochondrial fission in the astrocytes of the NTS alone. However, the activation of mitochondrial fission in astrocytes of the NTS of regular chow fed rats alone is not sufficient to recapitulate the BAT morphological changes we observed in HFD.

In regards to BAT mass, it has previously been shown that the size of BAT depots is dependent upon expression of *PPARG* in BAT, and *PPARGC*$_{BAT}$ knock out mice have significantly smaller BAT pads and thermogenic genes expression, showing that PPARG is required to maintain thermogenic capacity of mature brown adipocytes (Lasar et al., 2018). Interestingly, our qPCR analysis revealed significantly lower levels of expression of PPARG in GFAP:S637-A RC animals when compared to GFAP:GFP RC controls. It would then be reasonable to speculate that the lower levels of BAT we observed in GFAP:S637-A animals could be due to lower expression of PPARG in this tissue, however more investigations would be needed to prove this.

Importantly, our qPCR analysis also revealed significant downregulation of other thermogenesis related markers, namely *ADRB3* and *UCP1* in GFAP:S637-A RC animals when compared to GFAP:GFP RC controls. These results show that the activation of mitochondrial fission in astrocytes of the NTS of RC-fed animals, together with lower noradrenergic innervation of BAT, is sufficient to blunt the expression of these thermogenesis-related genes in regular chow-fed animals. Similarly, Manaserh et al. (2020) showed that IRKO^{GFAP} mice exhibited lower *ADRB3* transcripts than IRloxp controls; moreover *UCP1* mRNA levels were also decreased in female IRKO^{GFAP} mice, whilst a trend towards decrease was observed in male IRKO^{GFAP} mice. The evidence presented by Manaserh et al. (2020) support our findings,

which strengthen the idea that astrocytes are important contributors in the control of BAT thermogenesis, and insulin sensitivity in astrocytes may play an important role in this process. Moreover, the role of mitochondrial dynamics in astrocytes in regulating insulin sensitivity in the NTS may represent a mechanism of interest in a potential pathway between NTS astrocytes and BAT thermogenesis.

We also observed a significant reduction in *CD36* mRNA transcripts in GFAP:S637-A RC animals compared to GFAP:GFP RC controls, which is the opposite of what we observed when we inhibited mitochondrial dynamics in the astrocytes of the NTS of HFD-fed rats (Chapter 4). This may suggest that mitochondrial dynamics in astrocytes of the NTS bidirectionally regulate the uptake of fatty acids into BAT via CD36 to drive thermogenesis; however, *CD36* mRNA downregulation does not affect the levels of CoQ in our model, suggesting that this is not the mechanism through which BAT thermogenesis is lower in our study. More investigations would be needed to elucidate the role of CD36 in BAT thermogenesis in our system.

There were higher levels of *TNFA* mRNA- a pro-inflammatory cytokine involved in acute inflammation and apoptosis- in the BAT of GFAP:S637-A RC rats when compared to GFAP:GFP controls. Importantly *TNFA* is elevated in the adipose tissues of obese humans (Kern et al., 1995), and it has been shown to mediate apoptosis in brown adipocytes and lead to defective BAT function in *ob/ob* mice together with mediating a decrease in the expression of β3 adrenergic receptors in *in vitro* and *in vivo* murine models (Nisoli et al., 2000). Whilst it is not clear how mitochondrial dynamics in astrocytes within the NTS could contribute to inflammatory signalling in BAT, this evidence showed that our model could induce pro-inflammatory markers in BAT that are typically associated with obesity in regular chow-fed animals. This could provide an interesting insight on potential mechanisms that connect BAT inflammation and lower thermogenic capacity to mitochondrial dynamics in astrocytes of the NTS.

In summary, our data has shown that the chronic activation of Drp1-mediated mitochondrial fission in astrocytes of the NTS is associated with higher body weight and food intake in regular chow-fed animals when compared to GFAP:GFP RC controls and induces insulin resistance in their NTS 12-hours after the infusion of insulin in this brain region. In addition,

we have shown that the activation of Drp1-mediated mitochondrial fission in all cells of the NTS significantly decreases BAT glucose uptake, and astrocytes alone are sufficient to sustain this effect. Finally, we revealed that noradrenergic innervation of BAT was lower in GFAP:S637-A RC animals, compared to GFAP:GFP RC controls, and this was accompanied by downregulation of mRNA transcripts associated with BAT thermogenesis, and upregulation of the pro-inflammatory gene *TNFA*. Here, together with the evidence we presented in chapters 3 and 4, we showed the relevance of bidirectional regulation of mitochondrial dynamics in astrocytes of the NTS in the control of BAT activation to regulate whole body energy expenditure. We also demonstrated, for the first time, that mitochondrial fission in astrocytes of the NTS may contribute to the development of obesity, providing a potential target for therapeutic interventions.

Chapter 6

Effect of the manipulation of mitochondrial dynamics in the NTS on the liver

6.1 Beyond the fat: effects of alterations of mitochondrial dynamics in the NTS on the liver and circulating insulin and triglycerides

6.1.1 The role of the liver in the regulation of systemic metabolism

The liver is central in the control of lipid homeostasis, and the three major sources for FA in this organ are dietary lipids, adipose tissue-derived FA and *de novo* synthesis of FA; additionally, the liver serves as a major storage for FA and TG that are kept specifically by hepatocytes (Seebacher et al., 2020). In the post-prandial period, dietary FA are resynthesised into TG by enterocytes and packaged into chylomicrons in the plasma (Iqbal and Hussain, 2009) and the majority are taken up by the WAT and muscle to support the activity of lipoprotein lipase, whilst the rest is taken up by the liver, where FA are released intracellularly via lysosomal processing (Cohen and Fisher, 2013). Upon fasting or restricted energy input, plasma insulin concentration decreases, and a lipolytic program is initiated in the WAT to release albumin-bound FA in the circulation to support liver uptake of TG (Donnelly et al., 2005). Plasma FA are the major source of VLDL in fasting and fed states (Donnelly et al., 2005), which are produced by the liver, and released in the circulation to supply body tissues with TG (Converse and Skinner, 1992). A high-carbohydrate diet triggers hepatic *de novo* synthesis of FA, a fundamental biosynthesis pathway in the liver, and substrates for this process are provided via glycolysis and carbohydrate metabolism (Strable and Ntambi, 2010; Menezes et al., 2013). Interestingly, it has been speculated that *de novo* lipogenesis can significantly contribute to hepatic steatosis together with enhanced hepatic FA uptake in pathological states (Donnelly et al., 2005).

Importantly, the liver plays a critical role in the storage, synthesis, metabolism and release of glucose and it is highly responsive to the body nutritional status; for example, upon feeding, the liver decreases glucose production from both glycogen stores and gluconeogenesis, whilst glycolysis and glycogen deposition are increased (Han et al., 2016). Conversely, during the fasting state, glycogen is broken down and gluconeogenesis promoted (Han et al., 2016). Such mechanisms clearly show the dynamic role of the liver in maintaining glucose homeostasis to support the whole-body energy needs. In states of chronic overnutrition, the liver can develop

insulin resistance, which results in decreased capacity of insulin to decrease glucose output from the liver (Hatting et al., 2018), leading to increased concentration of blood glucose. In fact, insulin is a potent suppressor of gluconeogenesis, and IR deletion in the liver of mice increases hepatic gluconeogenesis, leading to hyperglycaemia and glucose intolerance (Michael et al., 2000). Similarly, Biddinger et al. (2008) revealed that IR KO limited to the liver in mice is associated with severe hepatic insulin resistance and glucose intolerance. Chronic inflammation, which occurs in obesity, causes insulin resistance in the liver leading to increased hepatic glucose production in mice, ultimately resulting in hyperglycaemia and hyperinsulinemia (Okin and Medzhitov, 2016). Moreover, inflammation increases the ability of glucagon to stimulate hepatic glucose production (Chen et al., 2012), which further contributes to elevated plasma glucose levels in obesity.

Physiologically, the liver processes large quantities of FA, but only stores less than 5% in form of TG within cytoplasmic lipid droplets, because the combination of FA uptake from the circulation and *de novo* synthesis within the liver are equalised by FA oxidation and secretion in the plasma of TG- enriched VLDL/TG. Hepatic *de novo* lipogenesis is the biochemical process through which FA, most commonly derived from carbohydrate catabolism, are synthesised within the liver; glucose and fructose are the most common suppliers of carbon units for hepatic *de novo* lipogenesis (Sanders and Griffin, 2016). In the context of metabolic disorders, such as obesity, *de novo* lipogenesis is abnormally increased, and considered to contribute to the pathogenesis of NAFLD (Donnelly et al., 2005). Interestingly, a 2020 study by Smith et al. revealed that *de novo* lipogenesis is involved in the pathogenesis of hepatic steatosis in humans, and that increases in plasma glucose and insulin are major drivers of *de novo* lipogenesis in obese subjects and in NAFLD. Further, this research supports the idea that selective hepatic insulin resistance is involved in the pathogenesis of NAFLD in humans (Smith et al., 2020). Hepatic insulin resistance also determines post-prandial metabolism of lipoproteins in both diabetic and prediabetic patients according to the “CORDIOPREV” clinical trial (Leon-Acuna et al., 2016), increasing the risk of cardiovascular disease in these patients. Furthermore, a human study found that the association between elevated blood glucose and NAFLD increases 1.6-fold in people with fasting hyperglycaemia and 2.3-fold in T2DM patients compared to control with normal fasting blood glucose (Jimba et al., 2005). Altogether this

evidence supports the importance of hepatic insulin sensitivity in the pathogenesis of NAFLD during chronic overnutrition.

In pathological states, TG also accumulate in the liver leading to steatosis, one of the main hallmarks of NAFLD, which associate with obesity, T2DM and dyslipidaemia and is mainly occurring in presence of insulin resistance (Birkenfeld and Shulman, 2014). To summarise, in the presence of metabolic abnormalities including chronic over nutrition and systemic insulin resistance, accumulation of TG in the liver occurs through a combination of three main mechanisms, namely: (1) increased FA uptake from the circulation- both dietary and released from the WAT -as observed by Donnelly et al. (2005) in NAFLD patients; this increase in FA uptake could potentially be aggravated by overexpression of fatty acid transporter CD36 in the liver, as demonstrated in a mice model of NAFLD (Koonen et al., 2007). (2) Increased *de novo* synthesis of TG, driven by increased levels of insulin in response to systemic insulin resistance via the mammalian target of rapamycin complex 1 (mTORC1) and insulin-induced gene 2A (INSIG2A) as demonstrated with a combination of *in vivo* studies on rodents and *in vitro* modelling (Li et al., 2010; Yecies et al., 2011). (3) Alteration of fatty acid oxidation via the mitochondrial β oxidation; in particular, in NAFLD patients with insulin resistance this consisted of impaired ATP production in patients, whilst it involved an increase in the rate of fatty acid oxidation in patients with NAFLD only (Cortez-Pinto et al., 1999; Schmid et al., 2011). Importantly, insulin resistance is associated with fat accumulation in the liver and a potential increase in oxidative stress within the organ (Sanyal et al., 2001; Satapati et al., 2012).

6.1.2 Central control of hepatic functions

The liver, as other peripheral organs, constantly requires adequate nutrient supply to exert its functions, and the central nervous system has the unique ability to control the function of nearly every tissue and organ system via the sympathetic and parasympathetic branches of the autonomous nervous system. To do so, the brain receives cues from the peripheral organs that communicate their nutritional status and integrates this information to coordinate its response to alter nutrient availability to the periphery of the body via both hormonal signalling and direct innervation (Morton et al., 2006).

Glucose production in the liver, and glucose clearance via hormonal signalling are the major mechanisms underlying the control of plasma glucose levels (Moore et al., 2012; Han et al., 2016) together with the direct action of insulin (Röder et al., 2016), and the central nervous system critically controls hepatic functions (Uyama et al., 2004; O'Hare and Zsombok, 2016; Metz and Pavlov, 2018). For example, endogenous glucose production and glycogenolysis are driven by sympathetic activation of the liver, whilst glucose storage and decrease in glucose production are promoted by the parasympathetic branch of the autonomous nervous system (Püschel, 2004). In particular, the activation of preganglionic parasympathetic neurons in the DMX of the brainstem signal to the liver to decrease HGP and increase glycogen synthesis (Yi et al., 2010).

The hypothalamus and brainstem are particularly important in the regulation of systemic glucose levels via interaction with the liver, and specialised neuronal populations that sense hormones (insulin, leptin) and nutrients (glucose, fatty acids), have been identified in these regions (Obici et al., 2002; Lam et al., 2005; Pocai, Morgan, et al., 2005; Könner et al., 2007; Lin et al., 2010; Yue et al., 2015). For example, insulin receptor KO in AgRP neurons of the ARC of the hypothalamus failed to suppress HGP in mice during euglycemic clamp (Könner et al., 2007), whilst selective re-expression of IR in AgRP neurons restored insulin suppression of HGP in *IR -/-* mice (Lin et al., 2010). Conversely, the restoration of insulin action in POMC neurons in the same brain region exacerbated insulin resistance and increased HGP in *IR -/-* mice (Lin et al., 2010). Moreover, intracerebroventricular infusion of leptin targeting the 3rd ventricle of the brain promotes hepatic TG export and suppresses *de novo* lipogenesis in regular chow and HFD-fed rats (Hackl et al., 2019). Importantly, the effect of intracerebroventricular infusion of oleic acid in the third ventricle of rats inhibits HGP and food intake via central activation of K_{ATP} channels (Obici et al., 2002), whilst the selective blocking of long-chain fatty acids via intracerebroventricular infusion of glibenclamide (a potent K_{ATP} channel blocker) abolishes the inhibitory effect of oleic acid infusion in the 3rd ventricle on HGP (Obici et al., 2002; Lam et al., 2005). Similarly, inhibition of long-chain fatty acid esterification in the mediobasal hypothalamus increases hepatic glycogenolysis (Lam et al., 2005), whilst leptin infusion in the third ventricle inhibits glucose production in HFD-fed rats by decreasing glycogenolysis (Pocai, Obici, et al., 2005) and this was sufficient to normalize glucose production in these animals.

Other systems have been reported to be involved in the central regulation of liver glucose metabolism; in particular, intracerebroventricular infusion of synthetic cannabinoid WIN 55,212-2, or cannabimimetic arachidonoyl-2'-chloroethylamide (ACEA) selectively activating type 1 cannabinoid receptors (CB1) acutely impaired insulin action in the liver of wild type rats, whilst in a rat model of HFD-induced insulin resistance, CB1 antagonism restored insulin sensitivity in the liver (O'hare et al., 2011).

Yue et al. (2015) demonstrated that direct activation of NMDA receptors with glycine in the DVC, and oleic acid infusion in the MBH suppresses hepatic VLDL-TG secretion in rats; remarkably, hepatic vagal innervation is required for this process, suggesting the existence of a neurocircuitry between the MBH, DVC and the liver in the regulation of hypothalamic FA sensing. Moreover, upper intestinal infusion of lipids lowers HGP and plasma glucose via activation of brain-gut axis (Wang et al., 2008), and this is dependent on activation of PKA-mediated vagal afferents signalling (Rasmussen et al., 2012). This signal is transmitted to the brain via glutamatergic vagal terminals in the DVC, and subsequent activation of glutamatergic receptors in this brain region, which in turns signals to the liver via vagal efferent to control HGP (Wang et al., 2008; Cheung et al., 2009).

6.1.3 The role of astrocytes and mitochondrial dynamics in the control of hepatic functions

Whilst the role of neurons in the control of hepatic regulation of metabolism and glucose homeostasis has been extensively studied, as reviewed elsewhere (Ruud et al., 2017), very little research has explored the contribution of astrocytes in this process. For example, the metabolism of lactate to pyruvate in the mediobasal hypothalamus has been reported to regulate HGP (Lam, 2007), and Arrieta-Cruz et al. (2013) hypothesised that because astrocytes and neurons are metabolically coupled through lactate transfer via the astrocyte-neuron lactate shuttle, these glial cells may be involved in the hypothalamic regulation of hepatic glucose metabolism. Using a rat model, the authors found that hypothalamic and systemic infusion of proline, which in astrocytes is metabolised to pyruvate, acutely lowered blood glucose via decrease of HGP, a response that was secondary to inhibition of glycogenolysis,

gluconeogenesis and flux of glucose-6-phosphatase (Arrieta-Cruz et al., 2013). This suggests that astrocytes of the hypothalamus are involved in the regulation of HGP.

Glutamate is the major neurotransmitter utilised by vagal afferents terminating in the NTS, and this neurotransmitter is a complementary energy substrate for the brain; specifically, astrocytes take up glutamate to generate ATP via oxidative glutamate dehydrogenase (GDH) activity (Karaca et al., 2011), and this activity is abolished in absence of GDH (Karaca et al., 2015). Importantly, Karaca et al. (2015) showed that lack of glutamate oxidation in the brain induced profound changes in the regulation of the autonomic nervous system, resulting in increased sympathetic discharge to the liver to increase HGP. This indicates the importance of astrocyte mediated GDH activity in the NTS in the regulation of peripheral energy availability.

Moreover, activation of PPARγ in the CNS has been reported to influence energy intake and expenditure (Lu et al., 2011; Di Giacomo et al., 2017; Fernandez et al., 2017) and PPARγ is equally expressed in neurons and astrocytes from key brain areas in the regulation of energy homeostasis (Warden et al., 2016). Indeed, Fernandez et al. (2017) observed that conditional KO of PPARγ in astrocytes resulted in impaired glucose tolerance and hepatic steatosis in mice, and this was not worsened by HFD.

However, the role of astrocytes in the DVC in the regulation of hepatic lipid metabolism has never been addressed. Moreover, mitochondrial dynamics in the brain are involved in the regulation of hepatic functions. In the hypothalamus Mfn2 but not Mfn1 deletion in POMC neurons resulted in increased HGP, and the authors speculate that POMC neurons may propagate this signalling via sympathetic mediated α-MSH, a neuropeptide derived from POMC neurons (Schneeberger et al., 2015). However, the role of brain mitochondrial dynamics in the regulation of hepatic lipid metabolism has never been investigated, and no literature is currently available to define the role of astrocytes in the NTS in this process.

6.1.4 Study rationale

Altogether this evidence led to the hypothesis that astrocytes in the brainstem may also be involved in the regulation of hepatic functions and here we focused on hepatic lipid metabolism and how this may be regulated by mitochondrial dynamics within the astrocytes of the NTS. The liver of HFD-fed animals presents signs of steatosis, which is the first step towards the development of NAFLD. We hypothesise that inhibition of mitochondrial fission in the NTS of HFD fed rats prevents the development of steatosis in the liver and decreases TG content in HFD fed rats; equally, we hypothesised an increase in steatosis and TG content in the liver of RC-fed animals in which mitochondrial fission is activated within the astrocytes of the NTS. Additionally, we hypothesised that there would be changes in the expression of genes associated with liver inflammation and lipids metabolism, and in particular upregulation of genes associated with adverse hepatic outcomes in HFD fed animals and RC-fed animals that received the astrocyte-specific constitutively active form of Drp1 in their NTS and a decrease in the expression of these genes in HFD-fed animals that received the astrocyte-specific dominant negative form of Drp1 in their NTS.

Finally, we aimed to determine the levels of FA, TG, insulin, and glucose in the circulation to understand how the liver may adapt in response to nutritional sensing from the systemic circulatory system. If these data are confirmed, this would be the first evidence linking astrocytic mitochondrial dynamics in the NTS of the brainstem and hepatic metabolic health. Please note that the data presented in this chapter have been collected and analysed by myself (FA assay, TAG assay, H&E preparation, RNA extraction, cDNA preparation) and by Gao Qiyu, a MSc student in Infection, Immunity and Human disease at the University of Leeds (RNA extraction, cDNA preparation, qPCR, H&E analysis) under my direct supervision. The hepatic tissues used in this study are from the animal cohorts seen in Patel et al. (2021) and in Chapter 4 and 5 of this work.

6.2 Aims

Aim 1: To determine whether the inhibition of Drp1-dependent increase of mitochondrial fission in the NTS astrocytes of HFD-fed rats can prevent hepatic steatosis and hepatic TG accumulation and whether food intake is the major contributor to this process.

Aim 2: To determine whether the activation of mitochondrial fission in the NTS astrocytes can induce hepatic steatosis and hepatic TG accumulation in RC-fed rats and whether this affects genes involved in hepatic inflammation and lipids metabolism.

Aim 3: To determine the levels of insulin, glucose FA and TG in the circulation to understand the nutritional adaptation the liver may undergo in response to changes in concentrations of these factors in the plasma.

6.3 Short-term HFD induces triglycerides accumulation and steatosis in the liver of rats

Chronic overnutrition and obesity are associated with liver pathology, and in particular with hepatic lipid accumulation (steatosis), which eventually evolves into NAFLD, and can progress to a more severe form of liver disease known as NASH. We previously showed that 2-weeks of HFD are sufficient to blunt BAT dynamic glucose uptake in BAT (Chapter 3); moreover, we showed the appearance of unilocular, white-like adipocytes in BAT, as well as lower noradrenergic innervation, independent of food intake and changes in genes associated with inflammation and fatty acid oxidation (Chapters 4-5). Here we wanted to investigate whether our acute HFD model is sufficient to cause changes in the structure of the liver, namely, a build-up of TG in the liver. To this aim we employed histological and molecular analysis; we performed H&E staining (Section 2.2.14) to screen for steatosis. After staining sections were submitted for slide scanning to acquire images of the whole tissue section at 20x, and random ROI from the livers of n=4 animals from each of the GFAP:GFP RC and GFAP:GFP HFD groups were selected for analysis (n=9 technical repeats per animal).

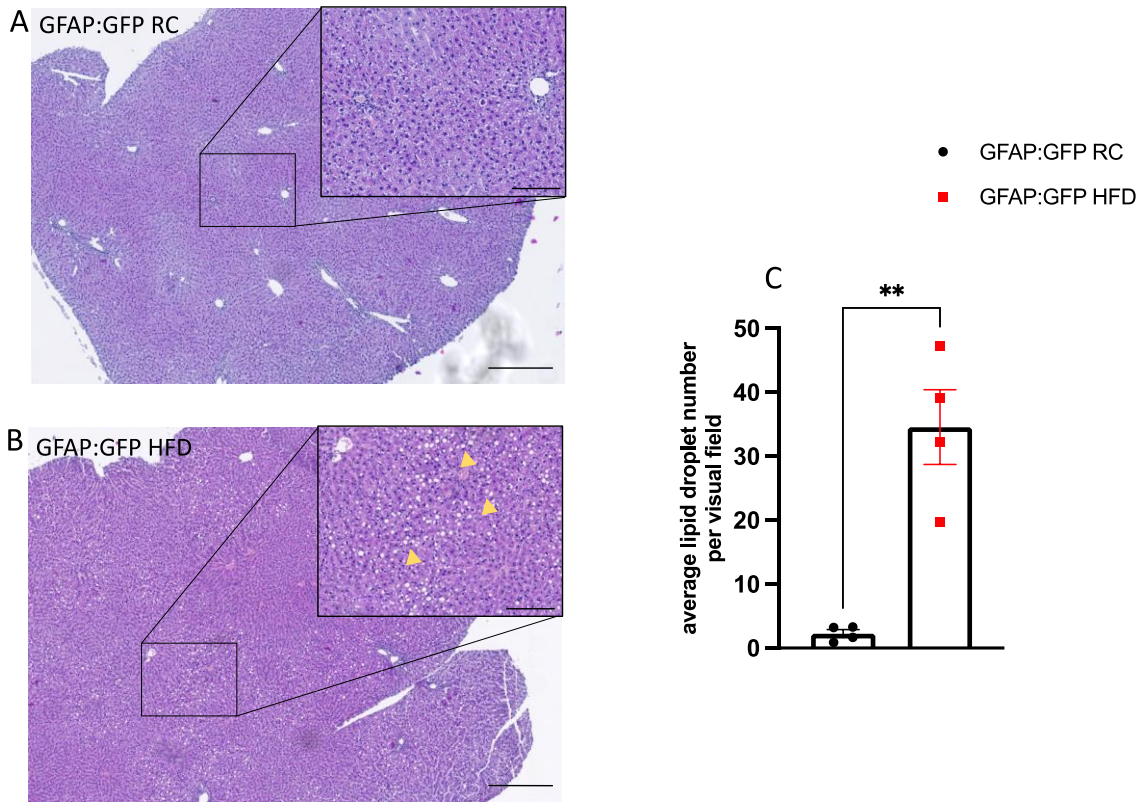

Figure 6.1: H&E staining of the liver shows lipids accumulation in the organ of rats fed with HFD for two weeks. *(A) Representative H&E on serial liver sections cut at 5 µm from a GFAP:GFP RC animal. (B) Representative H&E on serial liver sections cut at 5 µm from a GFAP:GFP HFD animal, yellow arrows indicate TG infiltration. (C) Lipid droplet quantification for GFAP:GFP RC (n=4, 9 technical repeats) and GFAP:GFP HFD (n=4, 9 technical repeats). Scale bar main figure= 100 µm, scale bar magnified figure= 50 µm. All data was tested for normality prior statistical tests using the Shapiro-Wilk normality test. Values are shown as mean ± SEM and single data point highlighted. $**p < 0.01$. Statistical test: Nested t-test.*

Remarkably, after 2-weeks of GFAP:GFP HFD (Fig 6.1B-C) animals exhibited significantly higher numbers of lipid droplets (34.6±5.85) within the liver per visual field when compared to GFAP:GFP RC animals (2.28±0.599) (Fig 6.1A-C) (**p<0.001). Moreover, the distribution of lipid droplets within the tissue appeared uniform and was not restricted to specific tissue landmarks (i.e., interlobular artery/vein, portal area, hepatic plate). Interestingly, GFAP:GFP HFD animals exhibited lipid (Figure 6.1B, yellow arrows) infiltration suggestive of a pattern of hepatic lipid accumulation during the early stages of HFD.

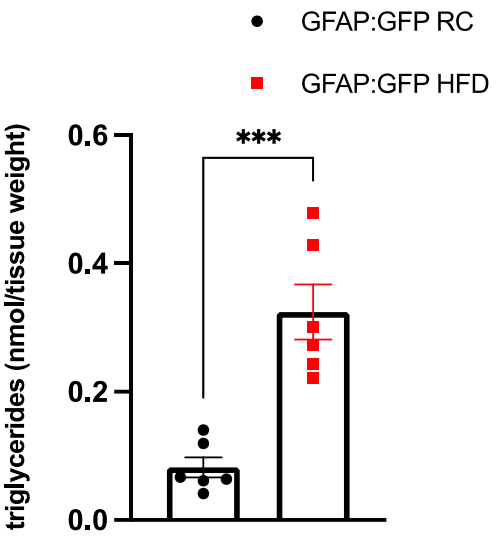

Figure 6.2: Hepatic triglyceride content is increased by HFD. *TG levels in nmol/tissue weight (g) measured in GFAP:GFP RC (n=6) and GFAP:GFP HFD (n=6) .All data was tested for normality prior statistical tests using the Shapiro-Wilk normality test. Values are shown as mean ± SEM and single data point highlighted. Statistical test:unpaired t-test.*

Next, to confirm and support the histological observations indicating steatosis occurring in the liver of rats fed HFD for 2 weeks we conducted a TG assay as described in Section 2.2.15. Briefly, liver was weighted and prepared for the assay and TG content in nmol was normalised to tissue weight. Remarkably we observed a 4-fold higher level of TG in the liver of GFAP:GFP HFD animals (0.324±0.0428 nmol/mg) when compared to GFAP:GFP RC animals (0.0821±0.0157 nmol/mg) (both n=6) (*** $p<0.001$) (Figure 6.2). This data confirmed that our model of short-term HFD is sufficient to induce a lipid accumulation in the liver and increase TG content within the tissue.

6.4 Inhibition of mitochondrial fission in NTS astrocytes of HFD-fed rats prevents HFD- induced triglyceride accumulation and steatosis independently of food intake [1]

Next, we aimed to establish whether the inhibition of mitochondrial fission in the astrocytes of the NTS is sufficient to prevent hepatic steatosis and TG accumulation in the liver. We also aimed to confirm whether it is the effect on food intake induced by the expression of the dominant negative form of Drp1 within astrocytes (Patel et al., 2021) that mediates this, or if our observations are a direct consequence of the manipulation of mitochondrial dynamics in astrocytes of the NTS. To this aim, a pair-feeding paradigm was employed.

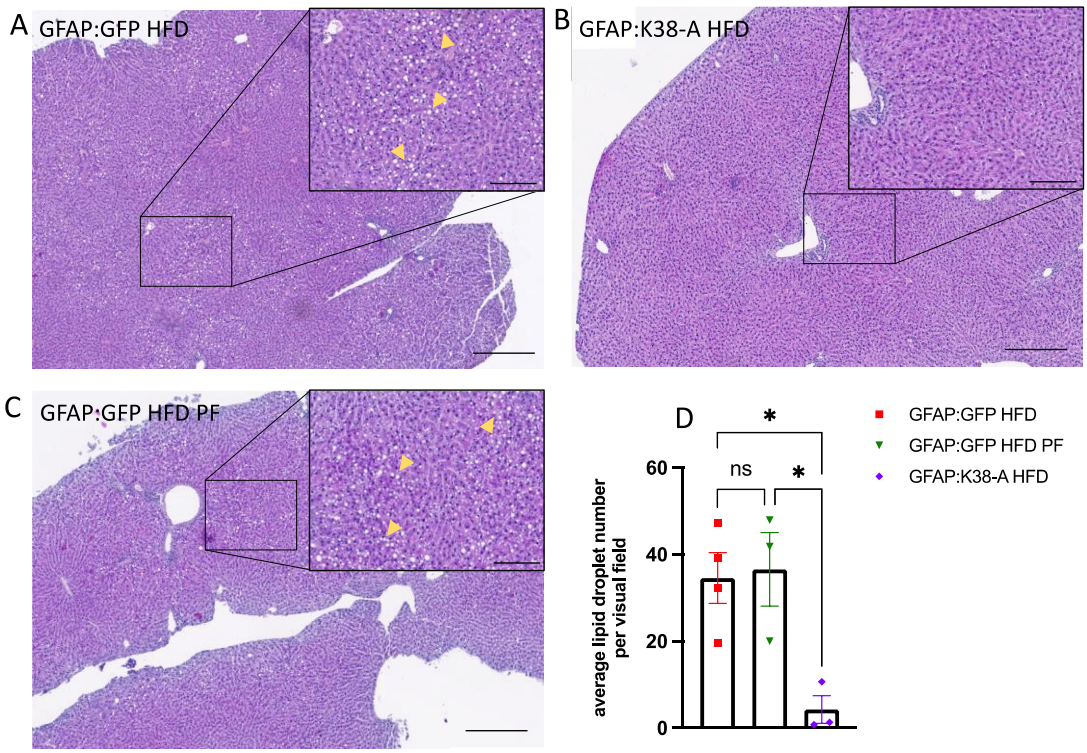

Figure 6.3: Inhibition of mitochondrial fission in astrocytes of the NTS ameliorates HFD-induced hepatic steatosis in a feeding independent manner. *(A) Representative H&E on serial liver sections cut at 5 µm from a GFAP:GFP HFD animal, blue arrows indicate hepatocytes enlargement and yellow arrows indicate TG infiltration. (B) Representative H&E on serial liver sections cut at 5 µm from a GFAP:K38-A HFD animal. (C) Representative H&E on serial liver sections cut at 5 µm from a GFAP:GFP HFD PF animal, yellow arrows indicate TG infiltration. (D) Lipid droplet quantification for GFAP:GFP HFD (n=4, 9 technical repeats), GFAP:GFP HFD PF (n=3, 9 technical repeats) and GFAP:K38-A HFD (n=3, 9 technical repeats). Scale bar main figure= 100 µm, scale bar magnified figure= 50 µm. All data was tested for normality prior statistical tests using the Shapiro-Wilk normality test. Values are shown as mean ± SEM and single data point highlighted. ⁎p < 0.05.Statistical test: Nested One Way ANOVA. Post-hoc:Tukey.*

First, H&E staining was performed (Section 2.2.14) to look for signs of steatosis in the pair-fed GFAP:GFP HFD group and in the K38-A groups and to determine the presence of steatosis. Random ROI from the livers of n=4 GFAP:GFP HFD and n=3 GFAP:K38-A HFD animals and GFAP:GFP HFD PF group were selected for analysis (n=9 technical repeats per animal). Surprisingly, whilst GFAP:GFP HFD control animals showed lipid infiltration, GFAP:K38-A

animals showed no signs of lipid infiltration; moreover GFAP:K38-A (4.27±3.22) had significantly lower lipid accumulation in the liver compared to GFAP:GFP HFD (34.6±5.57) anf GFAP:GFP HFD PF (36.6±8.47) groups (Figure 6.3.D) (*p<0.05). Moreover, GFAP:GFP HFD PF, similar to *ad libitum* GFAP:GFP HFD controls, showed signs of both lipid infiltration (Figure 6.3.A-C, yellow arrows). This data is suggestive of a direct involvement of mitochondrial dynamics, and in particular of mitochondrial fission in astrocytes of the NTS in the development of hepatic steatosis in HFD-fed rats, which is independent of food intake, as suggested by our pair-fed paradigm.

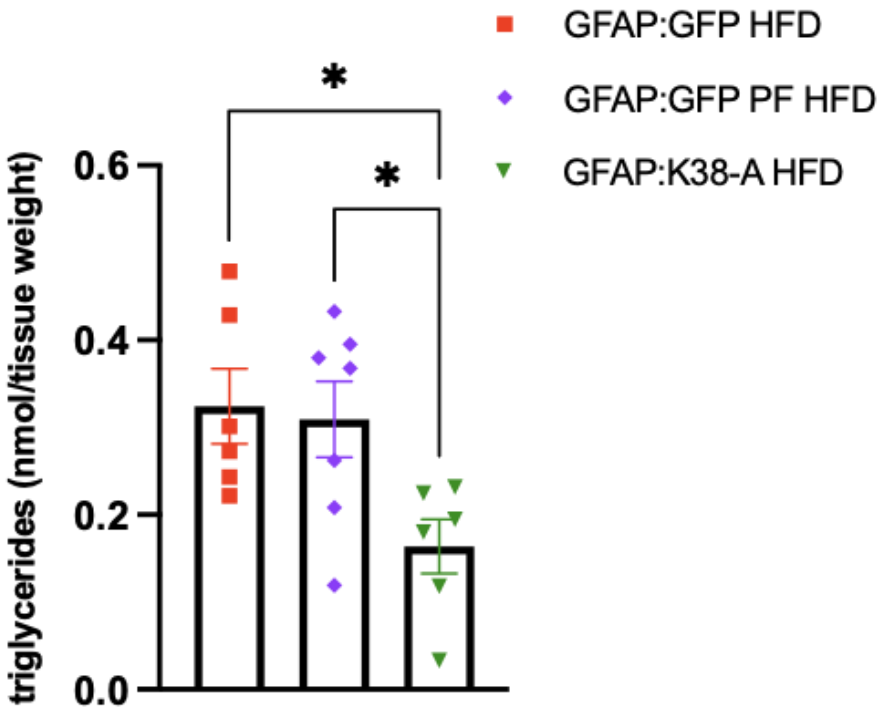

Figure 6.4: Inhibition of mitochondrial fission in astrocytes of the NTS reduce hepatic triglyceride accumulation independently of food intake. *TG levels in nmol/tissue weight (g) measured in GFAP:GFP HFD (n=6), GFAP:GFP HFD PF (n=7) and GFAP:K38-A HFD (n=6). All data were tested for normality prior statistical tests using the Shapiro-Wilk normality test. Values are shown as mean ± SEM and single data point highlighted. Statistical test: One-Way ANOVA. Post-hoc: Tukey.*

Next, to corroborate our histological findings we performed a molecular analysis to determine the concentrations of TG in the livers of these animals (Section 2.2.15); the livers were

weighed and prepared for the assay and measured TG content (nmol) was normalised to tissue weight. Notably, we observed significantly lower levels of TG in the liver of GFAP:K38-A HFD animals (0.164±0.0309 nmol/mg) when compared to both GFAP:GFP HFD animals (0.324±0.0428 nmol/mg) and GFAP:GFP HFD PF animals (0.309±0.0435 nmol/mg) (GFAP:GFP HFD and GFAP:K38-A HFD n=6, GFAP:GFP HFD PF n=7)(Figure 6.4) (* $p<0.05$ for both). Moreover, no significant differences in TG content were observed in GFAP:GFP HFD PF animals (0.309±0.0435 nmol/mg) when compared to GFAP:GFP HFD controls (0.324±0.0428 nmol/mg) ($p=0.961$) (Figure 6.4). This data confirmed that 2-weeks of HFD, independently of food intake, induce hepatic steatosis and increase TG content in the liver; moreover, the inhibition of mitochondrial fission in the astrocytes of the NTS prevent these effects, suggesting a role of astrocytic mitochondrial dynamics in the regulation of hepatic lipids content.

Importantly, this is the first evidence showing that mitochondrial dynamics, and in particular the inhibition of mitochondrial fission in astrocytes exert a protective role towards lipid accumulation in the liver in the context of HFD. The anorexigenic effect of the inhibition of mitochondrial fission in the astrocytes of the NTS (Patel et al., 2021) is not the driving factor in the hepatic resistance towards lipid accumulation that we observed in GFAP:K38-A animals, suggesting a direct role of astrocytic mitochondrial dynamics in this process. However, the underlying mechanisms to these observations remain unknown.

6.5 Activation of mitochondrial fission in astrocytes of the NTS induces hepatic triglyceride accumulation but not liver steatosis in regular chow fed animals

We previously showed that 2 weeks of HFD are sufficient to induce liver steatosis and increase TG content in the liver, regardless of food intake. Moreover, we showed that the inhibition of mitochondrial dynamics in the astrocytes of the NTS prevents these effects. Here we aim to establish whether the activation of mitochondrial fission in the astrocytes of the NTS can also affect the liver, and in particular hepatic lipid accumulation, in regular-chow fed rats, to a similar extent of that observed in control HFD-fed animals. To this aim H&E and TG assays were performed on the livers of GFAP:GFP RC (n=6) and GFAP:S637-A RC (n=4) animals as

previously described in Sections 6.3 and 6.4. ROI from n=4 livers for both GFAP:GFP RC group and GFAP:S637-A group were quantified (n=9 technical repeats per animal).

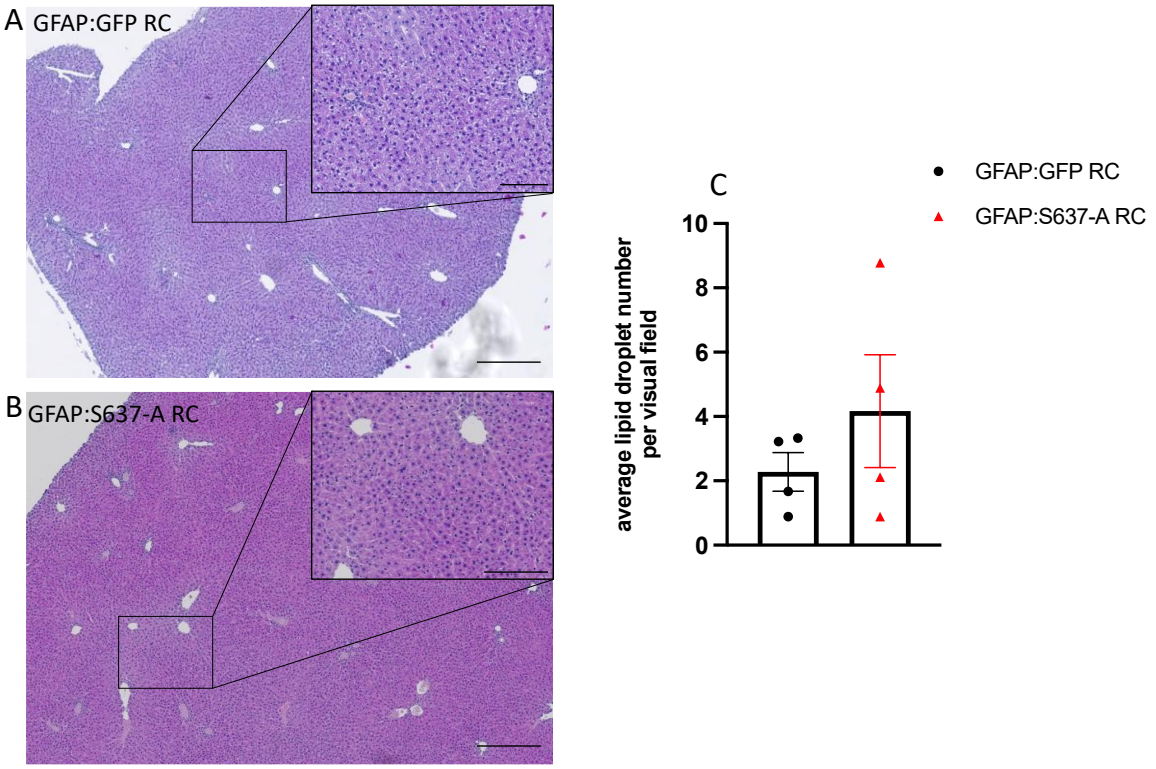

Figure 6.5: Activation of mitochondrial fission in astrocytes of the NTS does not induce hepatic steatosis. *(A) Representative H&E on serial liver sections cut at 5 µm from a GFAP:GFP RC animal. (B) Representative H&E on serial liver sections cut at 5 µm from a GFAP:S637-A RC animal. (C) Lipid droplets quantification for GFAP:GFP RC (n=4, 3 technical repeats), GFAP:S637-A RC (n=4, 3 technical repeats). Scale bar main figure= 100 µm, scale bar magnified figure= 50 µm. All data was tested for normality prior statistical tests using the Shapiro-Wilk normality test. Values are shown as mean ± SEM and single data point highlighted. ∗∗p < 0.01. Nested unpaired t-test.*

Here we found that in absence of HFD, the activation of mitochondrial fission in astrocytes of the NTS alone is not sufficient to induce hepatic steatosis in regular chow-fed animals; no significant differences were observed in the number of lipid droplets per visual field in GFAP:S637-A RC animals (4.17±1.75) (Figure 6.5B) when compared to GFAP:GFP RC controls (2.28±0.599) (Figure 6.5A) (p=0.349)(Figure 6.5C).

Next, we measured the TG content of the liver of GFAP:S637-A animals and GFAP:GFP animals to investigate whether the activation of mitochondrial fission in astrocytes of the NTS promotes TG accumulation prior to the development of steatosis.

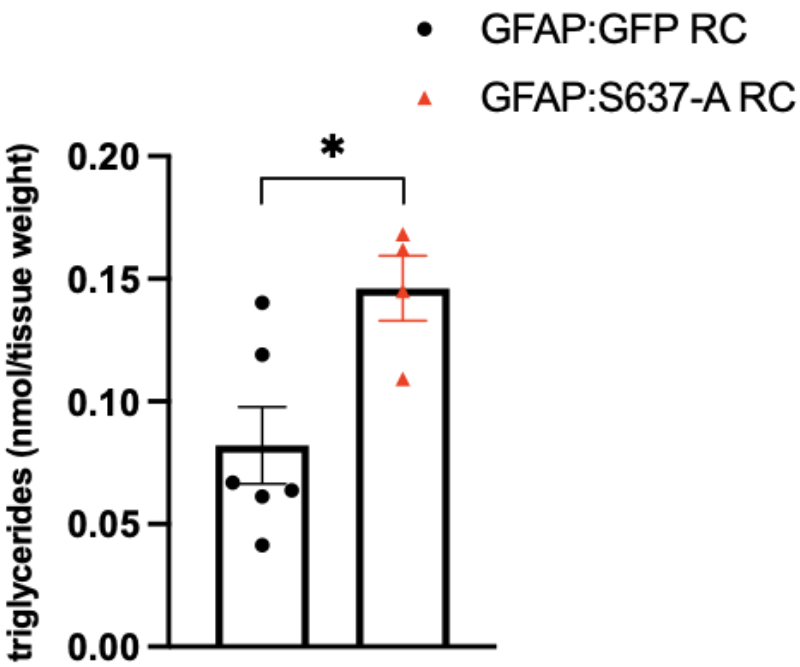

Figure 6.6: Activation of mitochondrial fission in astrocytes of the NTS induces hepatic triglyceride accumulation. *TG levels in nmol/tissue weight (g) measured in GFAP:GFP RC (n=6) and GFAP:S637-A RC (n=4). All data was tested for normality prior statistical tests using the Shapiro-Wilk normality test. Values are shown as mean ± SEM and single data point highlighted. Statistical test: unpaired t-test.*

Interestingly we found that GFAP:S637-A RC animals exhibited nearly double (0.146±0.0133 nmol/mg) the amount of hepatic TG of GFAP:GFP RC controls (0.0821±0.0157 nmol/mg) (*$p<0.05$) (Figure 6.6); however, the hepatic TG content, whilst increased is not comparable to that of control HFD-fed animals (0.324±0.0428 nmol/mg) (Figure 6.4). This could be explain why, despite the increase in hepatic TG content observed in GFAP:S637-A RC animals, we do

not observe an accumulation of TG within hepatocytes on a histological level; this suggests that higher concentrations of TG within the liver are needed for the development of steatosis, as seen in GFAP:GFP HFD animals.

6.6 Inhibition of mitochondrial dynamics in the astrocytes of the NTS of HFD-fed rats affects gene transcripts related to hepatic lipid metabolism in a feeding-dependent manner

Histological analysis revealed hallmarks of hepatic steatosis in rats acutely fed with HFD independently of food intake; we also showed that this was prevented by the inhibition of Drp1-dependent mitochondrial fission in astrocytes of the NTS. Here we determined whether these findings correlate with changes in mRNA transcript of genes associated with hepatic lipid metabolism, namely Diacylglycerol acyltransferase 1 (*Dgat1*), Diacylglycerol acyltransferase 2 (*Dgat2*), Acetyl- CoA Carboxylase α (*ACACA*) and Fatty acid synthase (*FAS*) and inflammation, i.e. Cluster of differentiation 68 (*CD68*) and C-reactive protein (*CRP*).

The ribosomal protein lateral stalk subunit P0 (*RPLP0*) was selected as housekeeping control following literature search highlighting its high stability in the hepatic tissue in presence of HFD (Fan et al., 2020). In accordance with this evidence, our results show a similar expression in *RPLP0* mRNA transcripts in GFAP:GFP RC (19.7±0.271) and GFAP:GFP HFD (20.3±0.411) ($p= 0.365$) (Figure 6.7) confirming that the expression of our housekeeping gene is similar in RC and HFD-fed animals.

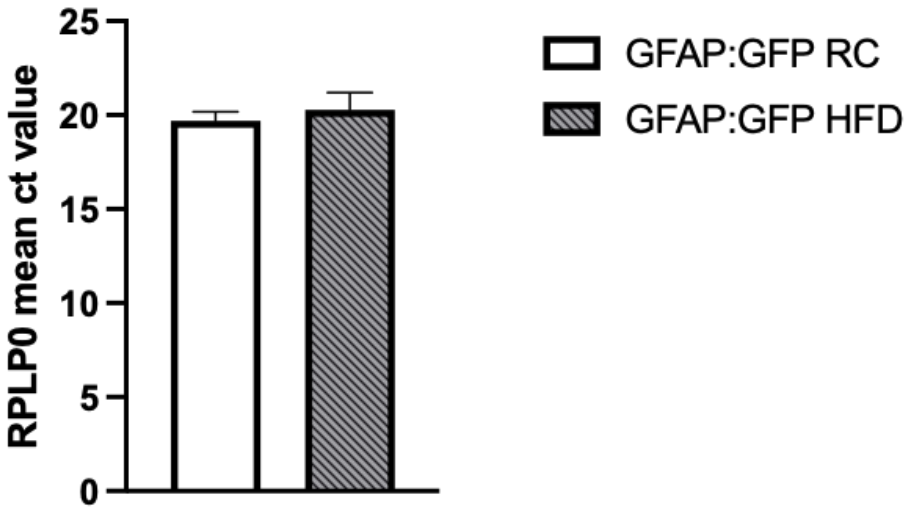

Figure 6.7: Expression of RPLP0 in regular-chow and HFD-fed animals to prove that the expression of the gene is stable regardless of the diet. *Values are shown as mean ± SEM. Statistical test: unpaired t-test.*

Primers for qPCR were tested and the products of the reactions were collected and electrophoresed on a 4% agarose gel (Section 2.2.13). The reactions produced a single product, whose size matched that predicted by in silico analysis, confirming the validity and specificity of the primers. Primers are presented starting from the left-hand side in the following order: *RPLP0* (165 bp), *Dgat1* (136 bp), *Dgat2* (135 bp), *ACACA* (145 bp), *FAS* (117 bp), *CD68* (80 bp) and *CRP* (77 bp). (Figure 6.8).

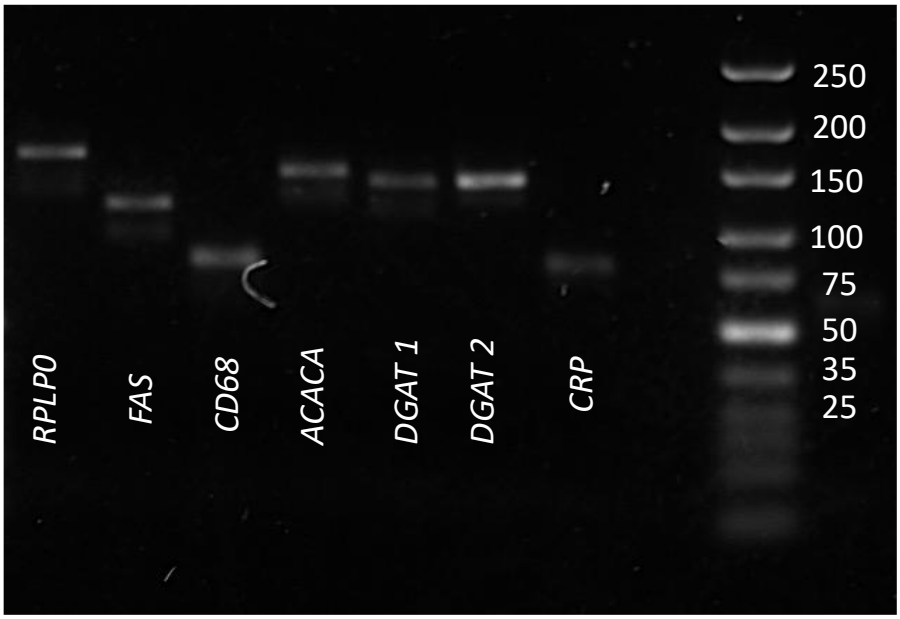

Figure 6.8: Representative agarose gel showing that the sizes of the primers employed in this study correspond to the in silico predicted size and that they produce a single clean product free of primer-dimer formations.

Next, we wanted to determine whether the inhibition of Drp1-dependent mitochondrial fission in astrocytes of the NTS can affect the expression of genes involved in hepatic lipid metabolism and inflammation. The relative mRNA expression in the liver *Dgat1, Dgat2, ACACA, FAS, CD68 and CRP* genes was investigated for this purpose and GFAP:GFP HFD group was used as control. Dgat1/2 catalyse the final step of TG synthesis, in particular FA esterification with diacylglycerol, resulting in TG formation (Li et al., 2015). The key role of ACACA is to provide malonyl-CoA substrate for the biosynthesis of fatty acids (Tong et al., 2006), and it encodes for the first committed enzyme in the hepatic *de novo* lipogenesis (Wan Kim et al., 2017). Similarly, FAS catalyses the *de novo* synthesis of fatty acids within the liver, with the aim of producing fat for energy storage during periods of nutrients excess (Jensen-Urstad and Semenkovich, 2012). Here we found that the inhibition of Drp1-dependent mitochondrial fission (GFAP:K38-A HFD) or reducing food intake using a pair-feeding paradigm (GFAP:GFP HFD PF) elicited significantly lower expression levels of *Dgat1 , ACACA, FAS* and *CD68* compared to control GFAP:GFP HFD. *Dgat1* (GFAP:K38-A HFD (0.328±0.0381), GFAP:GFP HFD PF (0.438±0.0391), GFAP:GFP HFD (1.05±0.162) ($p<0.0001$ and $p<0.0001$, respectively); *ACACA* (GFAP:K38-A HFD (0.699±0.0799), GFAP:GFP HFD PF (0.508±0.0658), GFAP:GFP HFD

(1.01±0.0856) ($p<0.05$ and $p<0.001$, respectively); *FAS* (GFAP:K38-A HFD (0.220±0.0448), GFAP:GFP HFD PF (0.0234±0.0442), GFAP:GFP HFD (1.04±0.134) ($p<0.0001$ and $p<0.0001$, respectively) (Figure 6.9). *Dgat2* was unchanged across the three groups (GFAP:K38-A HFD (1.05±0.0433), GFAP:GFP HFD PF (0.912±0.0465), GFAP:GFP HFD (1.035±0.127) (Figure 6.9) ($p=0.984$, $p=0.428$, respectively).

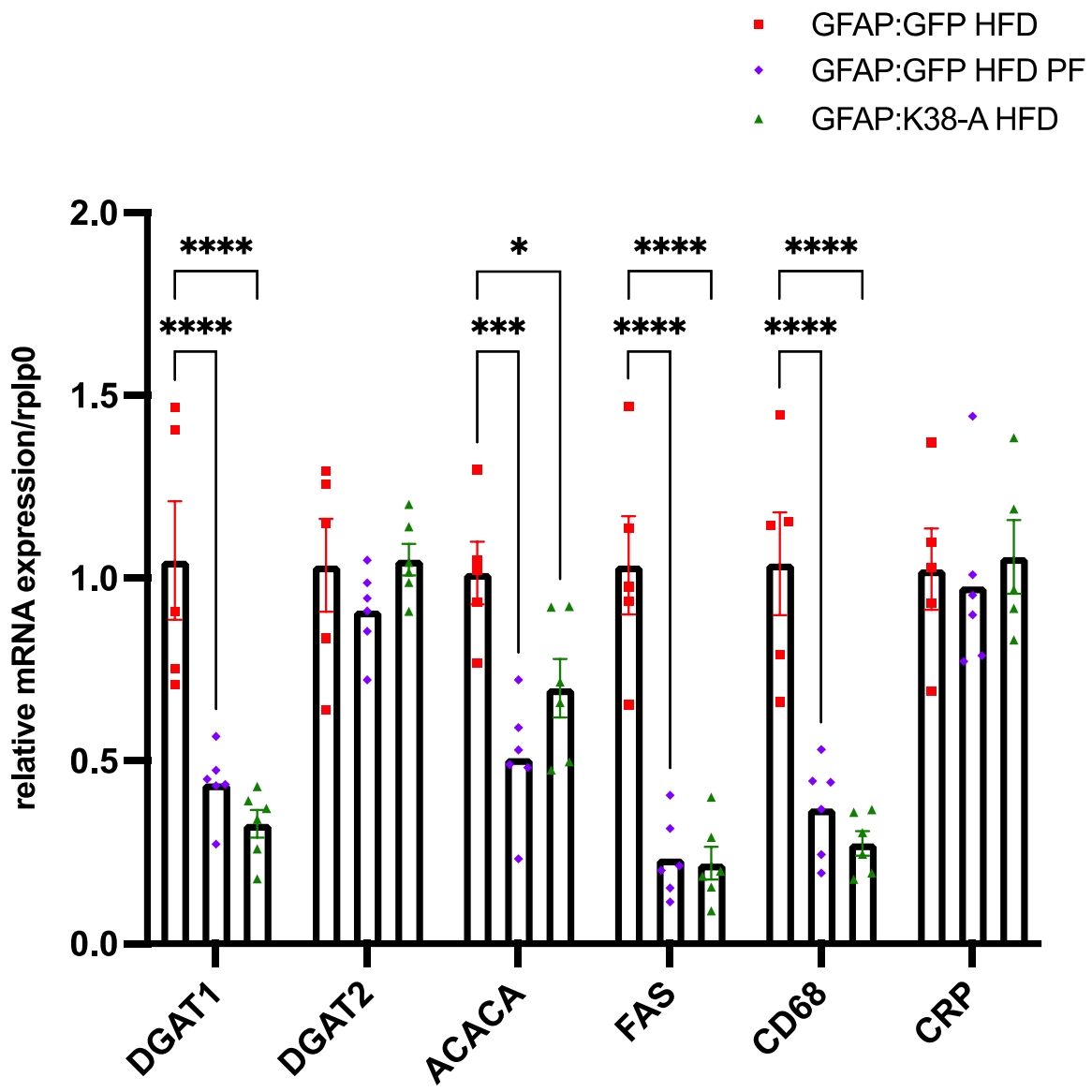

Figure 6.9: Quantitative polymerase chain reaction (qPCR) shows that genes associated with hepatic lipid metabolism and inflammation are lower upon inhibition of mitochondrial fission in astrocytes of the NTS of HFD-fed animals in a feeding-dependent manner. *Relative expression of genes of interest in GFAP:GFP HFD (n=5), GFAP:GFP HFD PF (n=6) and GFAP:K38-A HFD (n=6) animals fed ad libitum. Primers were run at separate times with internal controls to ensure gene expression consistency. All data was tested for normality prior statistical tests using the Shapiro-Wilk normality test. Values are shown as mean ± SEM and single data point highlighted. ****p<0.0001; ***p<0.001; *p<0.05. Statistical test: Two-Way ANOVA. Post-hoc: Tukey.*

We then looked at the expression of inflammatory genes *CD68* and *CRP* in GFAP:GFP RC and GFAP:GFP HFD. CD68 is a marker of Kupffer cells (KC), which are resident hepatic macrophages involved in the maintenance of liver functions (Nguyen-Lefebvre and Horuzsko, 2015). This is relevant since metabolic syndrome and insulin resistance-dependent accumulation of FA and lipids in hepatocytes could stimulate the innate immune response of KC leading to the development of NAFLD (Cha et al., 2018). CRP is a surrogate inflammatory marker of hepatic steatosis which in humans was found to be a robust predictor of NALFD (Yeniova et al., 2014). *CD68* levels were significantly lower in GFAP:K38-A HFD (0.274±0.0336) and GFAP:GFP HFD PF (0.371±0.0529), compared to GFAP:GFP HFD (1.04±0.141) ($p<0.0001$ and $p<0.0001$, respectively) (Figure 6.9) However, *CRP* was not affected (GFAP:K38-A HFD (1.06±0.101), GFAP:GFP HFD PF (0.978±0.100), GFAP:GFP HFD (1.025±0.111) ($p=0.973$, $p=0.945$, respectively) (Figure 6.9). These data suggest that the modulatory effect of the inhibition of Drp1-dependent mitochondrial fission in astrocytes of the NTS on hepatic lipid metabolism and inflammatory markers is dependent upon the modulation of feeding behaviour.

6.6 Activation of mitochondrial dynamics in the astrocytes of the NTS of RC-fed rats affects the expression of Diacylglycerol acyltransferases 2 (DGAT2) in the liver

Finally, we looked at the effect of the activation of Drp1-dependent mitochondrial fission in astrocytes of the NTS on the expression of these genes in regular-chow fed animals. The relative mRNA expression in the liver of *Dgat1, Dgat2, ACACA, FAS, CD68* and *CRP* genes was investigated and GFAP:GFP RC group was used as control.

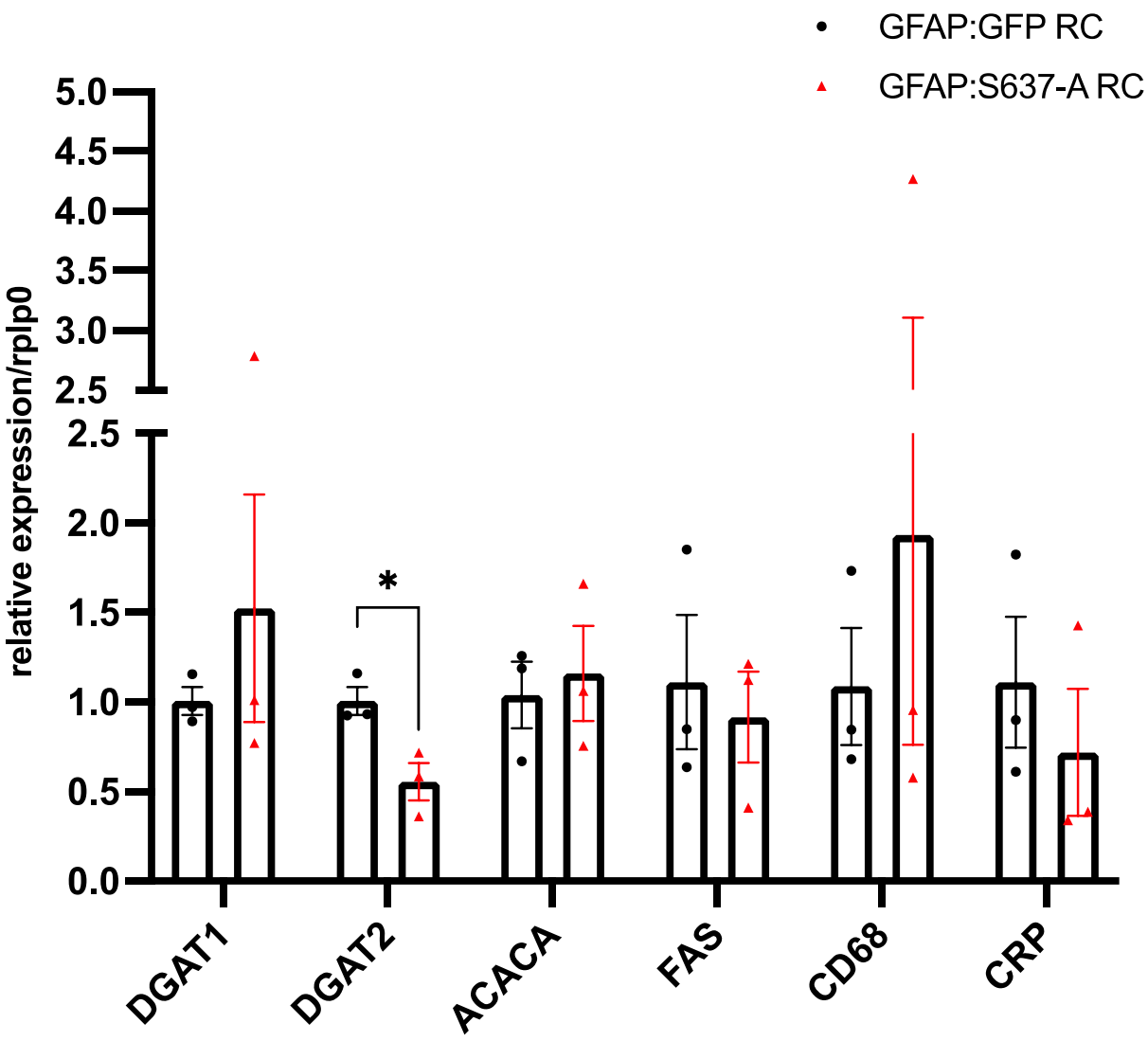

Figure 6.10: DGAT2 mRNA transcripts are lower in the liver upon activation of mitochondrial fission in astrocytes of the NTS of regular chow-fed rats. *Relative expression of genes of interest in GFAP:GFP RC (n=3), GFAP:S637-A RC (n= 3) animals fed ad libitum. Primers were run at separate times with internal controls to ensure gene expression consistency. All data was tested for normality prior statistical tests using the Shapiro-Wilk normality test. Statistical test: unpaired t-test. Values are shown as mean ± SEM and single data point highlighted.*

The relative expression of *Dgat2* was significantly lower in GFAP:S637-A animals (0.555±0.104) compared to GFAP:GFP RC controls (1.01±0.0775) ($p<0.05$). All the other markers were unaffected; *Dgat1* (GFAP:S637-A RC (1.523±0.635), GFAP:GFP RC (1.001±0.0780) ($p=0.464$); *ACACA* (GFAP:S637-A RC (1.07±0.120), GFAP:GFP RC (0.844±0.0581)) ($p=0.727$); *FAS* (GFAP:S637-A RC (0.916±0.254), GFAP:GFP RC (1.11±0.375))

(p=0.686); *CD68* (GFAP:S637-A (1.93±1.17), GFAP:GFP RC (1.09±0.327)) (p=0.525); *CRP* (GFAP:S637-A (0.719±0.355), GFAP:GFP RC (1.11±0.366)) (p=0.484) (Figure 6.10). Please note that only n=3 samples per group were available for this analysis and for this reason the interpretation of this data is limited. To overcome this, it would be beneficial to repeat this study in a larger cohort.

6.7 Inhibition of mitochondrial dynamics in the NTS of HFD-fed rats does not affect plasma triglycerides and FA but decreases plasma insulin and blood glucose levels

The next aim of our study was to measure the levels of TG in the plasma, but no significant differences were observed between the three groups; GFAP:K38-A (0.101±0.0113 nM), GFAP:GFP HFD PF (0.0698±0.0228 nM) GFAP:GFP HFD (0.124±0.0198 nM) (p=0.629, p=0.907, respectively) (Figure 6.11).

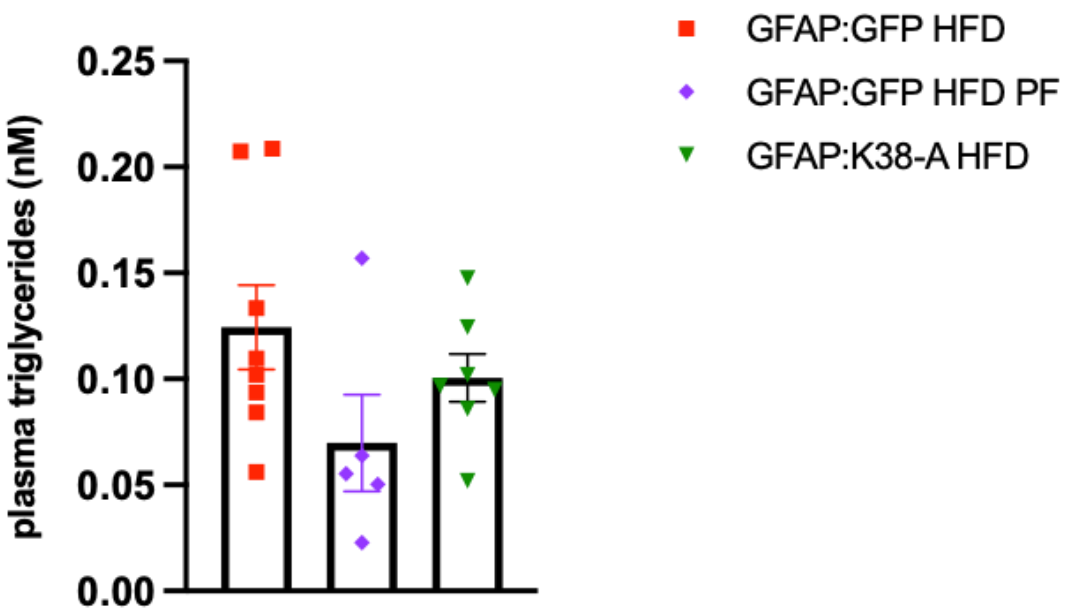

Figure 6.11: Inhibition of mitochondrial fission in astrocytes of the NTS does not affect circulating triglycerides. *TG levels in nM measured in GFAP:GFP HFD (n=8), GFAP:GFP HFD PF (n=5) and GFAP:K38-A HFD (n=7). All data was tested for normality prior statistical tests using the Shapiro-Wilk normality test. Values are shown as mean ± SEM and single data point highlighted. Statistical test: Two-Way ANOVA. Post-hoc: Tukey.*

We then assessed whether the increase in hepatic fat content we observed in our HFD model is associated with increased levels of plasma FA, as circulating FA are the main source of lipids in the liver in NAFLD (Donnelly et al., 2005). Please note that due to time constraints this experiment was not performed on the GFAP:GFP PF cohort.

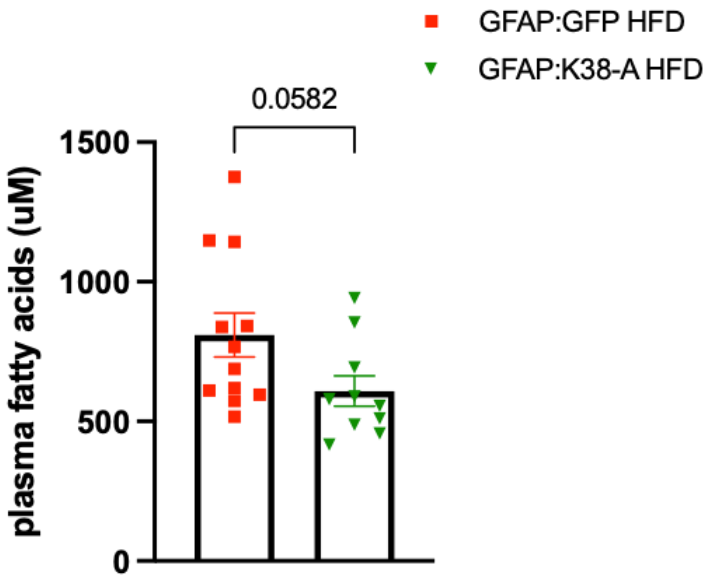

Figure 6.12: Plasma FA were lower in response to the inhibition of mitochondrial fission in astrocytes of the NTS. *Plasma FA levels in µM measured in GFAP:GFP HFD (n=12) and GFAP:K38-A HFD (n=10) .All data was tested for normality prior statistical tests using the Shapiro-Wilk normality test. Values are shown as mean ± SEM and single data point highlighted. Statistical test: t test.*

A trend towards decrease was observed in plasma FA of GFAP:K38-A HFD animals (608±54.4 μM) when compared to GFAP:GFP HFD animals (810± 79.2 μM) (p=0.0582) (Figure 6.12).

Next, given the role of the liver in insulin clearance (Najjar and Perdomo, 2019) and glucose production (Petersen et al., 2017), we measured circulating plasma insulin and blood glucose; 2 weeks of HFD were sufficient to induce hyperinsulinemia in rats (GFAP: GFP HFD 13.6±1.78 ng/mL). Interestingly, hyperinsulinemia was prevented in GFAP:K38-A animals (7.06±1.13 ng/mL) expressing the dominant negative form of Drp1 in their NTS when compared to GFAP:GFP controls (*p<0.05); however, when GFAP:K38-A group was compared to pair-fed control animals GFAP:GFP HFD PF, no discernible difference was identified (12.3 ±3.69 ng/mL) (p=0.182) (Figure 6.13).This result could mean that this is a feeding-dependent mechanism or

it could be due to the potential periods of intermittent fasting experienced by the pair-fed cohort as result of the experimental design.

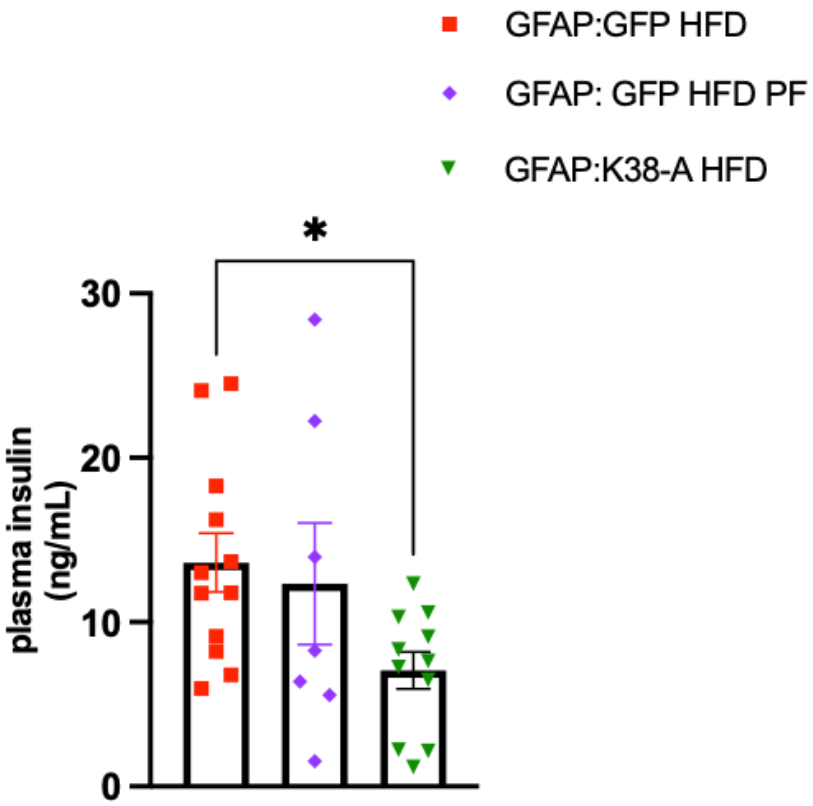

Figure 6.13: Inhibition of mitochondrial fission in astrocytes of the NTS prevents hyperinsulinemia. *Insulin levels in ng/ mL measured in GFAP:GFP HFD (n=11), GFAP:GFP HFD PF (n=7) and GFAP:K38-A HFD (n=11). All data was tested for normality prior statistical tests using the Shapiro-Wilk normality test. Values are shown as mean ± SEM and single data point highlighted. Statistical test: Two-Way ANOVA. Post-hoc: Tukey.*

Blood glucose levels were also measured in non-fasting animals; here we found that blood glucose levels were significantly lower in GFAP:K38-A HFD animals HFD (5.14± 0.0906mmol/L) compared to GFAP:GFP HFD controls (5.80± 0.322 mmol/L) (*p<0.05) . However, when GFAP:K38-A HFD group was compared to the pair-fed cohort GFAP:GFP HFD PF (5.23±0.176 mmol/L) no differences were observed (p=0.938) (Figure 6.14). This could have two explanations: (1) similarly to insulin, the effect of the inhibition of mitochondrial fission in astrocytes of the NTS is feeding dependent; (2) blood glucose levels are affected by the potential prolonged period of fasting experienced by the GFAP:GFP HFD PF.

Further, given that the GFAP:GFP HFD PF group has glucose levels similar to those of GFAP:GFP HFD animals (p=0.147), it is possible that the inhibition of mitochondrial fission in astrocytes of the NTS, rather than feeding behaviour alone, is required to affect blood glucose levels.

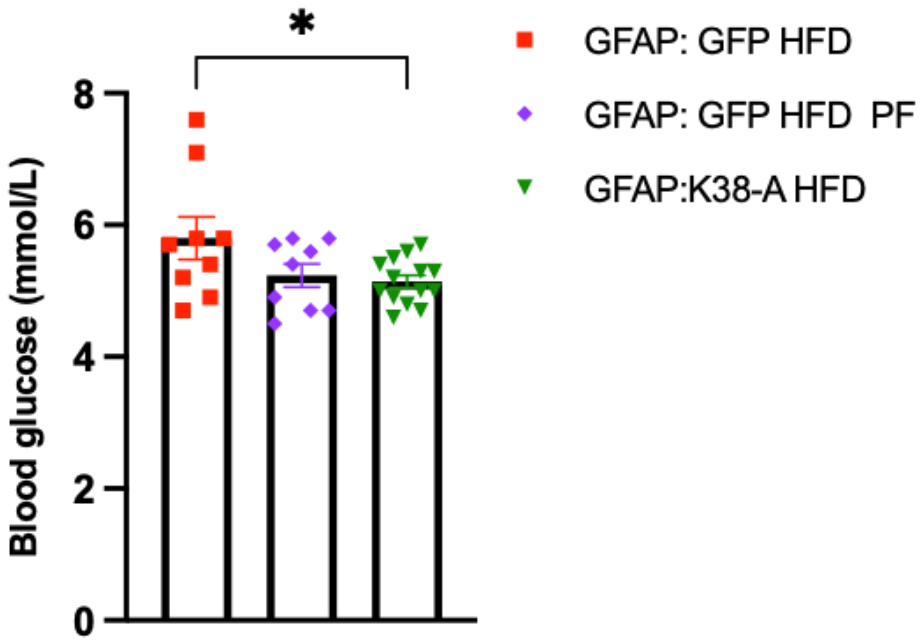

Figure 6.14: Inhibition of mitochondrial fission in astrocytes of the NTS results in lower circulating glucose levels in HFD compared to control animals. *Glucose levels in nmol/L measured in GFAP:GFP HFD (n=9), GFAP:GFP HFD PF (n=9) and GFAP:K38-A HFD (n=7). All data was tested for normality prior statistical tests using the Shapiro-Wilk normality test. Values are shown as mean±SEM and single data point highlighted. Statistical test: Two-Way ANOVA. Post-hoc: Tukey.*

6.8 Activation of mitochondrial dynamics in astrocytes in the NTS of RC-fed rats decreases plasma FA and triglycerides and increases plasma insulin levels without affecting blood glucose

Next, we wanted to establish whether the activation of mitochondrial fission in astrocytes in the NTS of RC-fed rats affects plasma FA; surprisingly, animals expressing the constitutively active form of Drp1 in astrocytes of the NTS had significantly lower levels of plasma FA (212±47.8 μM) than GFAP:GFP RC controls (659±114 μM) (**p<0.01) (Figure 6.15).

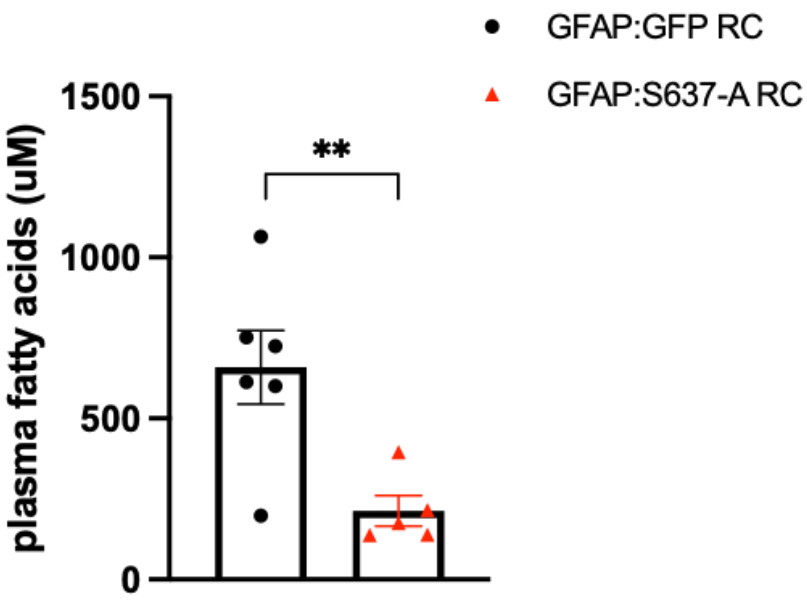

Figure 6.15: Plasma FA were lower in rats with activation of mitochondrial fission in astrocytes of the NTS compared to control animals. *Plasma FA levels in µM measured in GFAP:GFP RC (n=6) and GFAP:637-A RC (n=5) .All data was tested for normality prior statistical tests using the Shapiro-Wilk normality test. Values are shown as mean ± SEM and single data point highlighted. Statistical test: t test.*

Plasma TGs were also measured; a trend towards decrease could be observed in GFAP:S637-A RC (0.146 ±0.0133 nM) when compared to GFAP:GFP RC control (0.0821 ± 0.0157 nM) (p=0.0682) (Figure 6.16).

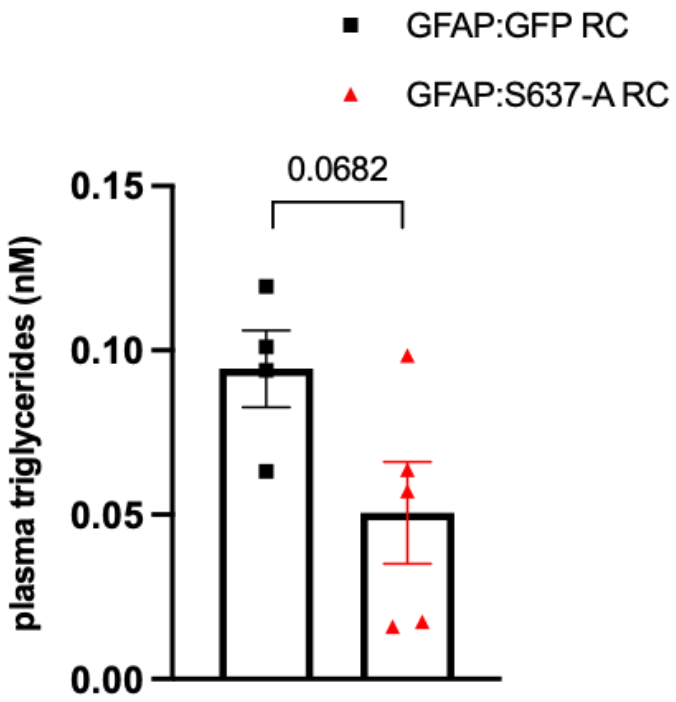

Figure 6.16: Plasma triglycerides were lower in animals with activation of mitochondrial fission in astrocytes of the NTS compared to control. *Plasma TG levels in nM measured in GFAP:GFP RC (n=4) and GFAP:637-A RC (n=5) .All data was tested for normality prior statistical tests using the Shapiro-Wilk normality test. Values are shown as mean ± SEM and single data point highlighted. Statistical test: t test.*

Plasma insulin and blood glucose were also measured. Interestingly, the activation of Drp1-dependent mitochondrial fission in astrocytes of the NTS of regular chow fed significantly increased circulating plasma insulin (12.7±1.61 ng/mL) compared to GFAP:GFP RC matching controls (6.98±1.56 ng/mL) (*$p<0.05$) (Figure 6.17), and to levels similar to those recorded in control HFD-fed animals, GFAP: GFP HFD (13.6±1.78 ng/mL) (Figure 6.11).

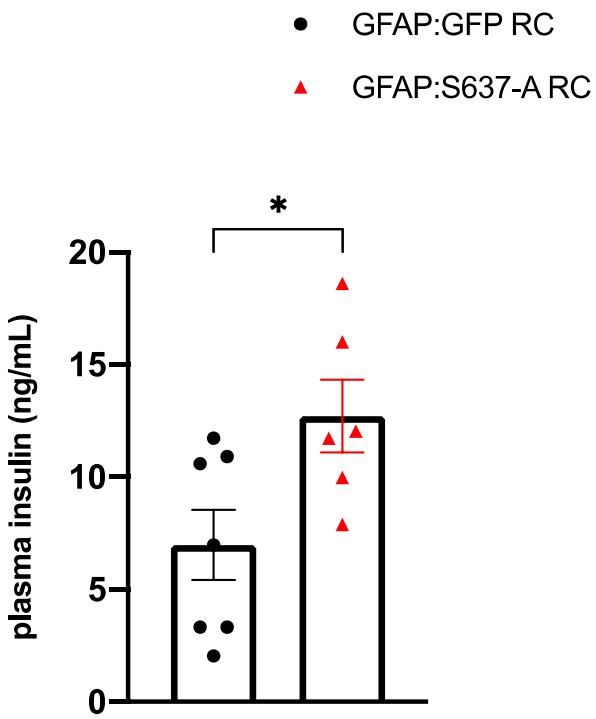

Figure 6.17: Activation of mitochondrial fission in astrocytes of the NTS induces hyperinsulinemia. *Insulin levels in ng/ mL measured in GFAP:GFP RC (n=7) and GFAP:S637-A (n=6). All data was tested for normality prior statistical tests using the Shapiro-Wilk normality test. Values are shown as mean ± SEM and single data point highlighted. Statistical test: unpaired t-test.*

Finally, blood glucose was measured, and no significant differences were found between the GFAP:S637-A RC group (5.42±0.291 mmol/mL) and GFAP:GFP RC control (5.09±0.114 mmol/mL) (p=0.286)(Figure 6.18). These data show that the activation of Drp1- dependent mitochondrial fission in astrocytes of the NTS regulates systemic insulin levels but not circulating glucose.

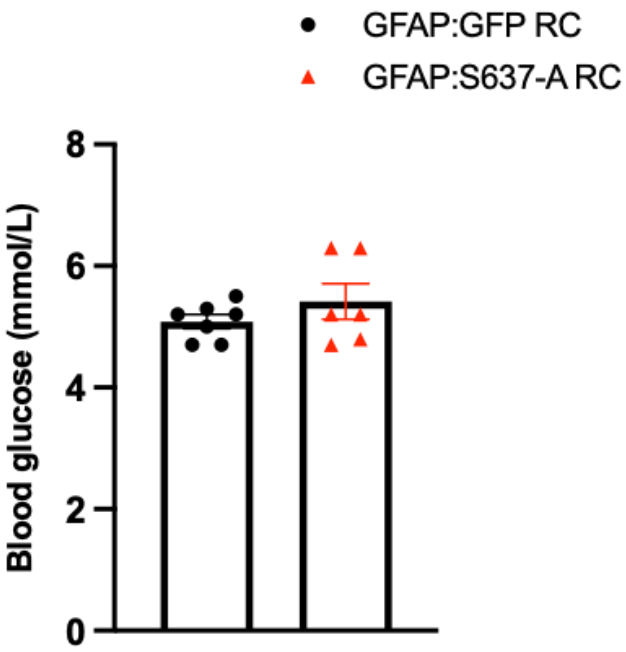

Figure 6.18: Activation of mitochondrial fission in astrocytes of the NTS does not affect circulating blood glucose. *Glucose levels in mmol/L measured in GFAP:GFP RC (n=6) and GFAP:S637-A (n=6). All data was tested for normality prior statistical tests using the Shapiro-Wilk normality test. Values are shown as mean ± SEM and single data point highlighted. Statistical test: unpaired t-test.*

6.9 Discussion

NAFLD is an increasingly prevalent hepatic disorder that affects more than 25% of the global population (Friedman et al., 2018), and it appears to be related to the growing prevalence of obesity and T2DM (Bellentani et al., 2010). NAFLD is characterised by excessive TG accumulation in the liver, and genetic vulnerability and high-fat intake are proposed mechanisms implicated in its development. In particular, increased consumption of fats, which is associated with metabolic and cardiovascular disease, insulin resistance and dyslipidaemia, could also underlie the genesis and progression of NAFLD (Basaranoglu and Neuschwander-Tetri, 2006). One of the theories proposed suggests that HFD-induced insulin resistance is the primary factor that contributes to steatosis as it triggers hepatic *de novo* lipogenesis and impairs FA transport; this is then followed by the activation of molecular signals involved in ER stress, mitochondrial dysfunction, apoptosis and alterations of autophagy, as well as in inflammatory responses (Lian et al., 2020). Overall, this theory

suggests that HFD increases hepatic fat deposition and induces IR in this organ, which increase the susceptibility to risk factors, which ultimately trigger NAFLD. Moreover, fat derived by diet is implicated in the disease progression in human and animals (Alkhouri et al., 2014; Mells et al., 2015); however a variety of events, including ER stress, gut microbiota imbalance, apoptosis, microRNAs dysregulation, genetic and epigenetic risks, inflammation and perturbation of autophagy appear to contribute in parallel (Lian et al., 2020), suggesting that NAFLD pathogenesis and progression comprises the involvement of a complex interplay of numerous factors.

6.9.1 HFD affects hepatic cytoarchitecture

The effects of long-term HFD on liver cytoarchitecture and lipid content are well characterised and widely reported in the literature (Chiazza et al., 2016; Soltis et al., 2017; Jensen et al., 2018; Tsuru et al., 2020). Here, we were able to show that the acute HFD protocol we employed in our study- which consisted of 2 weeks of 60% fat diet- was sufficient to induce hepatocytic enlargement and lipid infiltration, both of which are markers of hepatic steatosis. This is comparable to Rosenstengel et al (2011), which showed that 3-weeks of HFD were sufficient to induce lipid infiltration associated with hepatic steatosis in rats; this suggests that our model is an adequate representation of the morphological features of hepatic steatosis.

We also found that our acute HFD rat model GFAP:GFP HFD had increased TG content compared to matching GFAP:GFP RC control, suggesting that the cytoarchitectural alterations we observed are secondary to accumulation of TG accumulation within the liver. Importantly, when Drp1-dependent mitochondrial fission was inhibited in astrocytes of the NTS of HFD-fed rats, these animals were protected from hepatic TG accumulation, and the liver structure looked grossly preserved, indicating that our treatment successfully prevented HFD-dependent hepatic TG accumulation. This effect was independent from food intake, that, since PF animals showed a hepatocytic enlargement and lipidic infiltration to a level similar to that of GFAP:GFP HFD controls *ad libitum*. Hepatic steatosis is induced by multiple mechanisms in HFD and obesity; for example, increased uptake of plasma non-esterified fatty acids (NEFA)-as a response to insulin-insensitivity dependent WAT expansion can lead to increase hepatic lipids content; moreover, *de novo* lipogenesis could be stimulated by

hyperinsulinemia via activation of transcriptional upregulation factors such as ChREBP and SREBP1c (Kawano and Cohen, 2013). Alterations in lipid removal mechanisms, including mitochondrial FA oxidation and TG export as VLDL particles are also proposed to be involved in the genesis of hepatic steatosis (Kawano and Cohen, 2013). We showed that HFD-fed animals become hyperinsulinemic and this was prevented by inhibiting mitochondrial fission in astrocytes of the NTS. Furthermore, we showed that our treatment markedly decreased the mRNA transcripts of genes associated with hepatic steatosis, namely *Dgat1*, *ACACA* and *FAS*. Importantly, these genes are associated with TG synthesis (*Dgat1*), *de novo* lipogenesis and negative modulation of mitochondrial fat oxidation (*ACACA*) and *de novo* synthesis of FA (*FAS*); therefore, it appears that there is an association between the modulation of these genes and lower hepatic TG content in GFAP:K38-A animals. Whilst this suggests that the inhibition of mitochondrial fission in astrocytes of the NTS can modulate genes associated with hepatic lipid metabolism and alter lipid content within the liver, the molecular mechanisms involved in this pathway remain unknown. Moreover, we provided evidence showing lowered expression of *CD68* in the livers of GFAP:K38-A animals, suggestive of a decrease in hepatic inflammation. Importantly, our pair-fed study showed similar results, which implies that the modulation of genes associated with hepatic lipid metabolism and inflammation are dependent upon the regulatory effect of the inhibition of mitochondrial fission in astrocytes of the NTS on feeding behaviour (Patel et al., 2021); however, GFAP:GFP HFD PF controls showed an altered hepatic cytoarchitecture and levels of hepatic TG similar to those of the *ad libitum* GFAP:GFP HFD controls. Together this evidence suggests that mitochondrial dynamics in astrocytes of the NTS may regulate hepatic lipid metabolism via feeding-dependent and feeding-independent pathways.

6.9.2 Activation of mitochondrial fission in absence of HFD does not alter hepatic cytoarchitecture

We also measured the impact of the activation of mitochondrial fission in astrocytes of the NTS of RC-fed rats, observing that whilst the architecture of hepatocytes was not altered, GFAP:S637-A RC animals had increased TG content compared to GFAP:GFP RC controls. This could potentially indicate that whilst the activation of mitochondrial fission in astrocytes of the NTS increases hepatic TG content in HFD compared to the baseline of GFAP:GFP controls,

this is not sufficient to induce signs of hepatic steatosis. It would be interesting to observe, if more time was allowed for the study, whether chronic activation of mitochondrial fission in astrocytes of the NTS would induce discernible changes in the liver architecture. Interestingly, we also showed that animals expressing the constitutively active form of Drp1 in astrocytes of the NTS have lower levels of circulating FA compared to GFAP:GFP controls. This was an unexpected result but it would be intriguing to know if this would account for the increased TG content in the liver, given that FA accumulate in the liver via a combination of plasma uptake and *de novo* biosynthesis (Alves-Bezerra and Cohen, 2017). The use of isotope tracers would be required to be able to differentiate between FA uptake from the circulation and those synthesised locally within the liver (Umpleby, 2015). We also found that the activation of mitochondrial fission in astrocytes of the NTS induced hyperinsulinemia in RC-fed rat, showing that the effects of our treatment on insulin are not restricted to the DVC, in which we previously showed to cause insulin insensitivity, but it is a systemic effect occurring at similar levels to those observed in HFD-fed animals. Importantly, chronic hyperinsulinemia can stimulate *de novo* lipogenesis in the liver, and impaired insulin clearance can cause hepatic steatosis (Najjar and Perdomo, 2019). It would therefore be important to look at how hyperinsulinemia and impaired insulin clearance are involved in the genesis of hepatic steatosis.

6.9.3 Drp1 and ER stress: a potential mechanism involved in hepatic dysfunction during HFD

Drp1-dependent mitochondrial fission is associated with elevated ER stress in pancreatic β cells (Peng et al., 2011), whilst activation of Drp1 in the NTS of regular-chow fed rats induces ER-stress in this brain region (Filippi et al., 2017). Moreover, HFD inhibits DVC-insulin mediated decrease of HGP, and inhibition of Drp1 in the DVC negates HFD-induced ER stress in this brain region, which ultimately restored DVC control on HGP (Filippi et al., 2017). Given the effects of Drp1-dependent ER stress in the NTS on HGP, we speculated that Drp1-dependent mitochondrial fission and ER stress in this brain region may underlie the effects we observed on hepatic lipid metabolism. To answer this question, it would be worthwhile examining what would happen if we inhibited ER-stress mediators in the NTS. Remarkably, HFD and Drp1-overexpression (S637-A) in the NTS are associated with increased levels of iNOS

in this brain region (Patel et al., 2021). Importantly, iNOS is associated with insulin resistance (Carvalho-Filho et al., 2005) and activation of ER- stress related proteins in the liver (Ling Yang et al., 2015). Patel et al. (2021) used an shRNA (shiNOS) virus to knockdown iNOS, and the authors demonstrated that the delivery of shiNOS to the NTS protected HFD-animals from developing insulin resistance and decreased body weight and food intake. It would therefore be appealing to see if acting on the expression of this ER-stress mediator in the NTS could also affect hepatic functions, and in particular, lipid metabolism.

6.9.4 Conclusions

In conclusion, here we demonstrated that acute HFD is associated with increased TG content and hepatic steatosis that was prevented by the inhibition of mitochondrial fission in astrocytes of the NTS in a feeding-independent manner. The expression of genes associated with hepatic steatosis and inflammation was also lower upon inhibition of mitochondrial fission in astrocytes of the NTS, but this appeared to be dependent on lower food intake, as suggested by similar changes occurring in the pair-fed control group. The activation of mitochondrial fission in astrocytes of the NTS increased hepatic TG content without inducing steatosis. Interestingly, mitochondrial dynamics in astrocytes of the NTS were associated with systemic insulin levels, and in particular inhibition of mitochondrial fission in astrocytes of the NTS protected HFD animals from hyperinsulinemia whilst an increase in mitochondrial fission in astrocytes of the NTS induced hyperinsulinemia in regular chow-fed rats. However, whilst inhibition of mitochondrial fission in astrocytes of the NTS also lower blood glucose level in HFD-fed rats, the activation of mitochondrial fission in astrocytes in this brain region did not affect blood glucose.

Chapter 7: General discussion

7.1 Summary of findings

Our work demonstrated that the inhibition of HFD-induced, Drp1-dependent mitochondrial fission in astrocytes of the NTS is associated with higher glucose uptake to the BAT; moreover, it preserves noradrenergic innervation to the organ and BAT physiological cytoarchitecture in a feeding-independent manner. Conversely, we showed that activation of Drp1-dependent mitochondrial fission in astrocytes of the NTS is associated with lower BAT glucose uptake and noradrenergic innervation without affecting BAT morphology. Further, activating Drp1-dependent mitochondrial fission is astrocytes of the NTS also induced insulin insensitivity in this brain region. We also found that whilst HFD promotes higher hepatic TG content and induces steatosis, these effects were prevented by the inhibition of Drp1-dependent mitochondrial fission in astrocytes of the NTS, whilst liver TG were higher than controls upon activation of Drp1-dependent mitochondrial fission in astrocytes in this brain region in regular chow-fed animals (Figure 7.1).

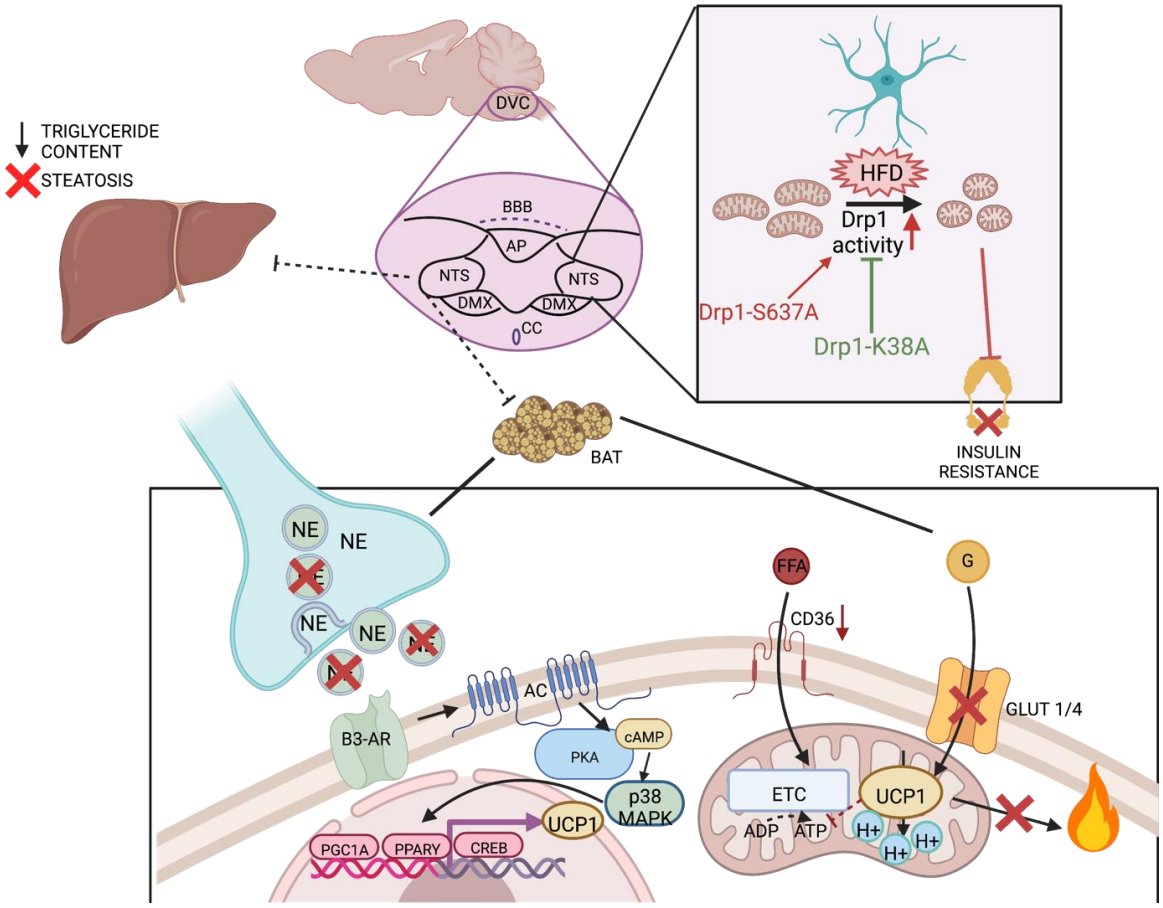

Figure 7.1: Summary of findings. *DVC=dorsovagal complex; BBB= blood brain barrier; NTS= nucleus tractus solitarius; AP=area postrema; DMX= dorsal motor nucleus of the vagus; CC= central canal; HFD=High fat diet; BAT= brown adipose tissue; NE= noradrenaline; B3-AR= Beta 3 adrenergic receptor; AC= adenylin cyclase; PKA= protein kinase A; cAMP=cycline adenosine monophosphate; p38 MAPK=; PGC1A= peroxisome proliferator activated receptor gamma coactivator 1 alpha; PPARY= peroxisome proliferator activated receptor gamma; CREB= cycline adenosine monophosphate response element binding protein; UCP1= uncoupling protein 1; ETC= electron transport chain; ADP= adenosine diphosphate; ATP= adenosine triphosphate; H+= hydrogen ion; GLUT1=glucose transport 1; GLUT4=glucose transporter 4; CD36= cluster of differentiation 36; FFA= free fatty acids; G= glucose.*

7.2 Discussion

7.2.1 Effects on the BAT

The NTS is a key brainstem centre for the integration of metabolic cues and other physiological information received from a range of peripheral organs, including vagal-relayed signals from the gut, liver, and adipose tissues. Remarkably, three days of HFD are sufficient to induce insulin resistance and promote Drp1-dependent mitochondrial fission in the NTS, which in turn elevated ER stress and iNOS levels in this brain region (Filippi et al., 2017; Patel et al., 2021). Moreover, Drp1-dependent mitochondrial fission induced weight gain, hyperphagia, insulin resistance and elevated abdominal fat expansion in HFD-fed rats and this effect was prevented by inhibiting Drp1 in all cells, and then specifically in astrocytes of the NTS of HFD-fed animals (Patel et al., 2021), suggesting a critical role of mitochondrial dynamics in the NTS to control metabolism.

Evidence has demonstrated that the NTS also participates in the regulation of energy expenditure via activation of BAT (Cao et al., 2010; Morrison et al., 2014; Madden et al., 2017; Conceição et al., 2017); moreover, the impact of mitochondrial dynamics in brain regions such as the hypothalamus and the NTS in altering the progression of metabolic disorders, such as obesity, is becoming apparent in rodents (Dietrich et al., 2013; Schneebergeret al., 2013; Toda et al., 2016; Filippi et al., 2017; Patel et al., 2021). However, it is not known what role mitochondrial dynamics in the NTS could play in the control of BAT activation. For this reason, the first aim of our study was to understand the role of mitochondrial dynamics in the NTS in the control of BAT thermogenesis, via dynamic ^{18}FDG PET scans, to study BAT glucose uptake, an indirect measurement of BAT thermogenic capacity. Our data demonstrated that 2-weeks of HFD are sufficient to blunt BAT glucose uptake. However, this effect was not detectable at thermoneutrality, and activation of BAT via IP injection of the β3 adrenergic agonist CL 316, 243 was required to appreciate differences in BAT activation between regular chow and HFD-fed animals. With this stimulation, we showed that inhibiting mitochondrial fission in all cells of the NTS and then specifically in astrocytes of HFD-fed animals was sufficient to induce higher BAT glucose uptake compared to HFD control animals. We speculate that BAT activation may be affected by the capacity of NTS astrocytes to maintain adequate glutamate

levels within the NTS. Whilst the mechanism behind this is yet to be elucidated, excess glutamate levels in the NTS could result in the activation of NTS neurons involved in the inhibition of BAT sympathetic premotor neurons, and astrocytes could participate in this process. Importantly, HFD leads to the increase of glutamatergic vagal discharge to the NTS to inhibit BAT activation (Madden and Morrison, 2016), and our GFAP:K38-A HFD model seems to indicate that in HFD, just stopping mitochondrial fission in the NTS reverses this suppression of BAT activation.

Importantly, inhibiting mitochondrial fission in the NTS of HFD-fed rats prevents insulin resistance in this brain region (Patel et al., 2021) and insulin sensing in astrocytes is critical for BAT thermogenesis; in fact, BAT of IRKO^{GFAP} mice exhibited lower levels of noradrenergic terminals and lower levels of expression of βAR3, and displayed significantly lower energy expenditure and basal body temperature than wildtype controls (Manaserh et al., 2020). As the inhibition of mitochondrial fission in the NTS is associated with insulin sensitivity in HFD-fed rats, here we speculate that the higher levels of BAT glucose uptake we observed when we inhibited Drp1-dependent mitochondrial fission in all cells, and then specifically in astrocytes of the NTS, may be due to preserved insulin sensitivity in astrocytes of the NTS. However, more experiments would be needed to confirm whether this could be the potential underlying mechanism linking mitochondrial dynamics in astrocytes of the NTS and BAT glucose uptake.

Another potential mechanism could revolve around the modulation of glutamatergic signalling, in which astrocytes play a vital role (Parpura and Verkhratsky, 2012). HFD is associated with increased glutamatergic vagal discharge to the NTS, which suppresses BAT activation (Madden and Morrison, 2016); glutamate, similarly to HFD, increases levels of iNOS in the DVC (Clyburn et al., 2018) and iNOS mainly colocalize with astrocytes within the NTS of rats (Patel et al., 2021). The inhibition of mitochondrial fission in these cells reduces iNOS expression and prevents hyperphagia and insulin resistance within the NTS, as well as reducing body weight gain and abdominal WAT mass compared to HFD control rats (Patel et al., 2021). It could therefore be of interest to investigate the role of mitochondrial dynamics in astrocytes of the NTS in relation to glutamate-dependent suppression of BAT activity.

Importantly, in this work we also showed that a bidirectional relationship between mitochondrial fission in the NTS and BAT glucose uptake exists; in fact, we found that the activation of Drp1-dependent mitochondrial fission in the NTS of regular chow-fed rats is associated with lower BAT glucose uptake in GFAP:S637-A RC compared to GFAP:GFP RC controls. Importantly, we confirmed that animals with the constitutively active form of Drp1 targeting astrocytes within their NTS went on to develop insulin resistance in this brain region, similarly to HFD control animals (Patel et al., 2021). This is a further indication that insulin sensitivity in NTS astrocytes may be important in regulating BAT activation.

HFD is associated with profound changes in BAT morphology, encompassing alterations in BAT cytoarchitecture so that it resembles that of white adipocytes. Importantly, it has been shown that one day of HFD is sufficient to induce such effect in rodents (Kuipers, Held, Panhuis, et al., 2019), which supports the notion that HFD acutely affects BAT morphology. Here we show that 2-weeks of HFD are sufficient to lower TH innervation of BAT, a marker of reduced noradrenergic discharge onto the organ and alter BAT morphology. Importantly, these effects were prevented by inhibiting Drp1-dependent mitochondrial fission in astrocytes of the NTS, independently of food intake. Similarly, activation of Drp1-dependent mitochondrial fission in astrocytes of the NTS reduces noradrenergic discharge to BAT but does not affect its morphology, suggesting that this is widely dependent on the presence of HFD in our model.

7.2.2 Effects on the liver

The liver is a fundamental organ in the regulation of whole-body energy metabolism; this organ is responsible for the execution of key physiological processes, including bile, proteins and cholesterol production, regulation of blood amino acids level and blood clotting, regulation of glucose metabolism, and bilirubin clearance, among others.

It is now well established that neuronal populations within the CNS project to the liver via multisynaptic pathways (Stanley et al., 2010), and these comprise NPY and POMC neurons in the brain stem and ARC, melanin-concentrating hormone (MCH) and orexin neurons in the lateral hypothalamus and corticotropic releasing hormone and oxytocin (Stanley et al., 2010).

POMC delivery in the NTS of rats using a recombinant adeno-associated viral vector showed that these animals have a 21-fold increased expression of α-MSH in their NTS, which is accompanied by a 26% decrease of hepatic TG content and a 35% and 34% decrease of serum TG and NEFA, respectively (Li et al., 2007). This suggests that the NTS plays a role in the regulation of hepatic lipid content. Further, recent work has shown that leptin receptors in the DVC modulate liver lipid metabolism; the authors showed that bilateral infusions of leptin in the DVC trigger vagal signalling to modulate hepatic lipid metabolism (Hackl et al., 2019). Importantly, the anti-steatosis effects of leptin generated in the DVC required hepatic vagal innervation (Hackl et al., 2019), suggesting the existence of brain-vagus-liver in control of hepatic lipid content. Further, MBH infusions of oleic acid lowered hepatic VLDL-TG in vivo to maintain lipid homeostasis (Yue et al., 2015); this mechanism was dependent upon protein kinase C delta type PKC-δ>K_{ATP} axis and NMDA-mediated neurotransmission in the DVC to convey efferent signalling to the liver to lower hepatic VLDL-TG (Yue et al., 2015).

The alteration of ER functionality, including ER stress has been implicated in cerebral metabolic disorders, including obesity (Özcan et al., 2004).The hypothalamus has been well characterised in the link between ER stress and overweight and obesity (Zhang et al., 2008; Çakir et al., 2013). A 2015 study by Schneeberger et al. revealed the involvement of mitochondrial protein Mfn2 in the regulation of cellular responses leading to ER-stress; in particular the authors found that Mfn2KO in hypothalamic POMC neurons of mice led to increased hepatic glucose production and hepatic gluconeogenesis which were dependent upon ER stress in this neuronal population (Schneeberger et al., 2015). Similarly, Drp1-dependent mitochondrial fission has been found to elevate ER stress in pancreatic β cells (Peng et al., 2011), and molecular activation of Drp1 in the DVC of healthy and lean rats was sufficient to induce ER stress in this brain region (Filippi et al., 2017). Furthermore, HFD prevented DVC-insulin from decreasing HGP, and inhibition of Drp1 negated HFD-induced mitochondrial fission and ER stress in the DVC, resulting in restored HGP (Filippi et al., 2017). Given this evidence, we put forward the hypothesis that Drp1-dependent mitochondrial fission and ER stress in the DVC may also affect hepatic lipid metabolism.

Our data showed that, in line with existing literature (Rosenstengel et al., 2011), acute HFD was sufficient to induce signs of hepatic steatosis in the liver of rats and promote higher hepatic TG content. Importantly, we demonstrated that upon inhibition of Drp1-dependent mitochondrial fission in astrocytes of the NTS, we could prevent accumulation of TG in the liver and associated alterations of the hepatic cytoarchitecture. When genes associated with hepatic lipid metabolism were analysed, we found a marked decreased in genes associated with hepatic steatosis and inflammatory response, but these seem to be feeding dependant as they were also observed in the pair-fed GFAP:GFP HFD PF cohort. Nevertheless, the pair-fed paradigm presents its limitations (Section 7.3), and it cannot be excluded that some of the observed effects are dependent upon the study design itself, namely the potential for prolonged periods of fasting.

Conversely, the activation of Drp1- dependent mitochondrial fission in astrocytes of the NTS induced higher hepatic TG content in regular chow-fed rats, without affecting the liver architecture, for which, it is possible that a high-fat intake from diet is required.

We also show that whilst GFAP:GFP HFD rats went on to develop hyperinsulinemia and had high blood glucose levels, these effects were prevented in GFAP:K38-A HFD rats, in a feeding dependent manner. GFAP:S637-A RC animals showed higher levels of serum insulin compared to GFAP:GFP RC controls, but no alterations were observed in blood glucose levels. Moreover, these animals showed a surprising reduction of circulating plasma FA of unclear cause. To address this, it could be useful to use radiolabelled FA tracers to assess if these animals have reduced circulating plasma FA secondary to an increase in FA uptake in relevant organs, such as the adipose tissues or the liver.

Together these data demonstrate that mitochondrial dynamics in the NTS play an important role in the pathogenesis of obesity, via central regulation of energy expenditure, hepatic lipid storage and circulating insulin and glucose.

7.3 How are we treating obesity and why we need new therapeutic targets?

Obesity incidence has tripled between 1975-2016 (WHO, 2017) and it is expected to rise. Obesity represents a major health challenge as it substantially increases the incidence of a range of comorbidities including T2DM, high blood pressure and vascular disease and increased risk of certain type of cancers, including colorectal and stomach, breast and liver cancers (National Institute of Health and Care Excellence, 2022). In the UK alone two thirds of adults are either overweight or obese (Public Health England, 2017) and this translates to substantial public expenditure, including £13.9 billions/year (9.8% NHS budget) for treatment of obesity and related comorbidities and £27 billions/year costs to the wider economy as a result of the incidence of overweight and obesity across the UK population (Public Health England, 2017).

Despite the clear trajectory of the obesity epidemic, its impact on both healthcare systems and wider economies worldwide, and the intense research effort that has been carried out in the past few decades, we still have not achieved long-term treatments options for obesity.
The first line of treatment for overweight and obesity consists of intensive lifestyle interventions, including restricted diet protocols, behavioural interventions, and increased amounts of exercise, or more often, a combination of these. Importantly, a 5% decrease in body weight, according to the "Look AHEAD" trial, is sufficient to reduce cardiovascular risk by reducing arterial blood pressure and blood lipid profile (The Look AHEAD Research Group, 2013). A 5% decrease in body weight is also the cut off value to determine whether pharmacological interventions are inducing a significant reduction in body weight; Pharmacological interventions are often a second line of treatment if lifestyle changes alone are not sufficient to reach target weight loss. In the UK, as of 2022 only three anti-obesity medication have been tested in clinical trials and approved for treatment of obesity: Orlistat, Liraglutide and Semaglutide (National Institute of Health and Care Excellence, 2022). The Orlistat mechanism of action involves reversible inhibition of lipases in the gastric tract and pancreas, limiting the digestion of dietary fats, namely the breaking down of TG into FA and monoglycerides that can be absorbed (Guerciolini, 1997). Whilst useful to decrease dietary fat absorption by approximately 30%, leading to decreased body weight, waist circumference and cholesterol levels, Orilstat is associated with a range of side effects, including GI

disturbances, increased risk of acute kidney injury and osteoporosis, and it known to interact with medications to manage diabetes, epilepsy and blood disorders (Bansal and Khalili, 2022). Liraglutide and Semaglutide are derivatives of GLP1, which binds to activate GLP1 receptors to increase glucose-dependent insulin secretion, suppress glucagon secretion and appetite and delay gastric emptying, leading to a significant decrease in body weight compared to placebo in people with obesity (O'Neil et al., 2018). Moreover, these medications induce only mild to moderate gastrointestinal side effects, which are generally well tolerated (National Institute of Health and Care Excellence, 2022). However, current guidance in the UK states that pharmacological treatment should be withdrawn if it fails to lead to at least 5% weight loss within the first three months of treatment (National Institute of Health and Care Excellence, 2022). Moreover, long-term use (beyond 12 months) for weight maintenance is dependent upon several factors including patients' drug tolerance and compliance (National Institute of Health and Care Excellence, 2022), which could lead in difficulties in maintaining the weight loss achieved with these medications over the long term.

If all appropriate non-surgical methods fail to induce and maintain adequate and clinically beneficial weight loss, the third and last line of action is bariatric surgery (gastric bypass and gastric sleeve). However, this requires fitness for anaesthesia and surgery, and extremely obese patients are at an increased risk of operative and post-operative complications (Soleimanpour et al., 2017). Moreover, surgical intervention require long-term commitment to follow ups and life-long life style changes to manage long-term risks and potential complications (National Institute of Health and Care Excellence, 2022).

Considering the restricted options available for the long-term treatment of obesity, and their variable success rate, it is critical to keep investigating basic mechanisms and potential therapeutic targets to shift the paradigm of obesity treatments. In this context, brown adipose tissue is of growing interest as a potential therapeutic target for obesity and HFD-related metabolic disorders. It is now well established that the autonomic control of BAT and its thermogenic processes is critical to maintain energy homeostasis; it then seems reasonable to speculate that targeting the autonomic control of thermogenesis could constitute a good therapeutic strategy for the treatment of obesity, especially after the recognition of the importance of BAT in human adults (Watanabe et al., 2006; Cypess et al.,

2009b; Saito et al., 2009a; Cypess et al., 2015b; Ahmed et al., 2021). In fact, studies have shown that upon cold-induced stimulation of BAT, lean and healthy subjects could burn an excess 25-400 kcal/day (Yoneshiro et al., 2011a; Muzik et al., 2013), and together with weight loss, BAT activation could have a positive impact on classic signs of metabolic syndrome, including insulin resistance, hyperglycaemia and increased concentration of circulating TG, due to the ability of BAT to take up lipids and glucose from the circulation to fuel thermogenesis (Bartelt et al., 2011a; Gunawardana and Piston, 2012; Chondronikola et al., 2014b). Existing studies have demonstrated that targeting central pathways to BAT activation, such as hypothalamic AMPK has beneficial effects on BAT thermogenesis, and the effect on body weight of drugs such as liraglutide that we discussed above, are mediated via hypothalamic AMPK signalling. However, our understanding of the central control of BAT thermogenesis is still limited and given the growing impact of obesity worldwide there is a great need than ever to explore alternative therapeutic targets for the treatment of obesity.
While the mechanisms involved in the regulation of NTS-mediated BAT activity and hepatic lipids metabolism remain unknown, our findings reveal a pertinent central-modulation approach of mitochondrial dynamics within the NTS that successfully modulate metabolism. Our data and previous literature (Filippi et al., 2017; Patel et al., 2021) suggest that insulin sensitivity within this region may be important for the control of metabolism, and it has also been implicated in BAT thermogenesis (Manaserh et al., 2020). Therefore, strategies oriented towards the restoration of insulin sensitivity within the DVC could be an efficient strategy to maintain BAT functionality. Moreover, stimulation of BAT using β3 adrenergic agonists, such as Mirabegron, which is characterised by lower side effects than typical β3 adrenergic agonists could be a useful treatment to improve obesity-derived metabolic damage.

It is important to remark that whilst the metabolic benefits of inducing BAT activation are an attractive target for the treatment of obesity there are concerns around its recruitment. For example, it is particularly tedious to achieve selective BAT activation in humans, and evidence shows that β3 adrenergic agonists may in fact require the activation of other β adrenergic receptors subtypes in BAT (Blondin et al., 2020; Riis-Vestergaard et al., 2020). Further, chronic adrenergic activation could cause tachycardia and hypertension and increase the risk of adverse cardiovascular events in a target population that is already at higher risk of these conditions (McNeill et al., 2021). Finally, it cannot be excluded that an increase in energy

expenditure could induce compensatory hyperphagia, as observed in mice studies (Ravussin et al., 2014).

7.4 Limitations

One of the major limitations of our study was the use of male rats only. Sex-differences in the development of metabolic disorders, including obesity in rodents are known (Hong et al., 2009; Mauvais-Jarvis, 2015; Casimiro et al., 2021). For example, a recent study has shown that diet-induced hyperphagia tends to be greater in males than females, but the latter tend to show an increased preference for HFD in a species-independent manner (Maric et al., 2022). Sex differences in visceral fat expansion upon HFD have also been noted in mice, with females showing a 5-fold increase in visceral fat compared to the 2-fold increase of males (Maric et al., 2022). If time had allowed, we would have repeated the experiment presented in this work on female rats to strengthen the validity of our results and ensure that these findings are not sex specific.

Another limitation that applies in this study is that experiments to confirm the viral constructs used to inhibit and activate mitochondrial fission in the experimental procedures were not performed. This is for two main reasons: (1) for the tissues obtained from animals shown in Patel et al. (2021) viral construct confirmation was done *in vitro* via quantification of Mitotracker immunofluorescence and (2) the viruses used in new cohort in this study were obtained from the same batch as the ones employed in Patel et al (2021). Further, the viral constructs were confirmed to manipulate mitochondrial morphology *in vivo* in Filippi et al. (2017) via electron microscopy. While it would have been against the 3Rs principle of reduction to perform again the electron microscopy data showed by Filippi et al (2017), reproducing the *in vitro* experiment using Mito tracker (Patel et al., 2021) would have strengthened the results presented in this work.

Some considerations should also be done about the pair-feeding paradigm employed in chapters 4 and 6. Pair-fed animals are food restricted and they are given a smaller amount of food than that which they would habitually consume. Due to unavailability of automatic feeding dispensers in the animal facility (yoke-feeders), the pair-fed rats were fed a single

meal, prior to the night-phase, the same amount that the control group (GFAP:K38-A) had consumed on the previous day. Whilst this was done according to the literature (Russell et al., 2008; De Meijer et al., 2010), we often found that by the following morning, most of the pair-fed rats had already consumed the amount of food given to them on the previous day. Therefore, they were food-restricted until the following food allotment was provided. This could have a significant impact on the study as it introduces variables related to intervals of prolonged fasting which could affect the secretion of metabolic hormones (Drazen et al., 2006; Korbonits et al., 2007; Ellacott et al., 2010; Kim et al., 2021) and gene expression in tissues (Trayhurn et al., 1995; Li et al., 2006; Bideyan et al., 2021). Given these considerations we accept that the experimental design could have an impact on our observed results, and the experiment would benefit from the use of automated food dispensers if available.

Another important limitation of this study is the uncertainty around the comparability of human and rodent BAT thermogenic function. For example, it is noted that BAT UCP1 homology is less than 80%, suggesting that functional differences between the two species may exist (Hughes et al., 2009). Further, whilst mouse BAT is restricted to well-defined anatomical locations and is homogenously made up of brown adipocytes, human BAT is more disperse and composed by white, brown and brite adipocytes (Jespersen et al., 2013), and their response to β adrenergic stimulation is also different (Liu et al., 2017). More studies would be needed to delineate difference and similarities between rodent and human BAT.

Differences in the thermoregulatory mechanisms of rodents and humans are also a limitation of this study. In fact, rodents present a higher metabolic rate than humans, a variable and unstable core temperature, a large surface area: body mass ratio and a high rate of thermal conductance which could affect the interpretability and translational value of our findings to humans (Gordon, 2017). As this study investigated BAT, a major organ involved in thermoregulation, it is important to take these differences into consideration. A recent study by Hankenson et al. (2018) suggested that higher housing temperatures than the standard 21-22°C may be required to fully reproduce the human condition in rodents. However, some characteristics of rodents, such as the elevated heat loss derived from high vascularisation of the tail (Hankenson et al., 2018) cannot be accounted for. We should therefore be cautious when thinking of the translational value of the findings of this study to human biology.

Some limitations also emerge from the experimental approach we used to investigate BAT recruitment. We used a histological approach to test noradrenergic innervation to the tissue, and we assumed the availability of TH in the tissue as an indirect measurement of the stimulation that BAT was receiving from the CNS. A better approach to this would have been the use of SNA recording, which allows capturing the electrophysiological activity of BAT upon stimulation with different agents and viral constructs. However, this experiment would have required a significant financial investment that was not possible to fulfil the scope of this work. Further, it would have required to extend the project and personal licences of the team involved in the animal work to cover the use of paralysing agents, which are required to study BAT SNA accurately. Lastly, as the final scope of this work investigated the significance of BAT in the treatment of human obesity it would have been important to replicate these experiments in a cohort of DIO rats, and if time would have allowed that would have been the next step of this study.

7.5 Future directions

The data presented has demonstrated that inhibition of Drp-1 dependent mitochondrial fission prevents HFD-induced blunting of noradrenergic BAT innervation, hypertrophy, and glucose uptake as well as hepatic TG accumulation. This work demonstrated a novel mechanism through which the NTS controls whole-body energy homeostasis, providing a foundation for future research in this brain area. Here we showed that the inhibition of mitochondrial dynamics in all cells and in astrocytes of the NTS associated with higher BAT glucose uptake in HFD-fed animals, compared to controls. However, we have not established whether this effect is dependent upon feeding; for this we would need to repeat the ^{18}FDG/CT scan in a cohort of pair-fed animals. As previously discussed, however, this paradigm would need improvements as alas, it is possible that intermittent fasting pattern could be a consequence of the study design, potentially introducing variables that can mask the real effect of the NTS treatment.

Previous studies within the Filippi group have shown the involvement of astrocytes in the control of several aspects of metabolism, including feeding behaviour and insulin homeostasis

(Patel et al., 2021), and here we demonstrated their involvement in BAT thermogenesis; however, the molecular mechanisms behind astrocytic modulation of BAT are unknown. To start answering this question it would be useful to set-up tracing studies; with ^{18}FDG/CT scan we could determine the average depth and width of BAT in adults rats, allowing a non-surgical approach to retrograde tracing studies from the BAT to the NTS, which is ideal to prevent accidental severing of sympathetic innervation to BAT, which could have substantial consequences to BAT ability to perform thermogenesis (Fischer et al., 2019). The tracer wheat germ agglutinin (WGA) is one of the most characterised wheat proteins, capable of binding to N-acetylglucosamine and sialic acid, a plasma-membrane bound sugar, and be readily transported in anterograde and retrograde directions with polysynaptic and some transsynaptic transport properties, allowing extensive networks mapping (Levy et al., 2015). However, as glial cells do not necessarily form synapses this approach could not be effective; in this case other solutions may be considered, such us adeno-associated virus (AAV) targeting using specific promoters, such as GFAP for astrocytes. To characterise neurons that are functionally connected to BAT in the NTS, an AAV-Cre-WGA could be injected within the BAT and an AAV-FLEx (loxP)-GFP within the NTS. This is because the FLEx (flip-excision) switch is a potent genetic tool that allows the manipulation of gene expression in vivo by using site-specific recombination (Sauer and Du, 1987). This tool exploits the orientation specificity of site-specific recombinases, namely Cre and FLP, which when binding to a DNA target induce a localised recombination event. Cre recombinase binds to Cre-loxP recombination sites (loxP), which will invert the flanked DNA sequence (floxed) between the sites, changing its orientation. In our case, cells infected with both AAV-Cre-WGA and AAV-loxP-GFP will express GFP as a result of Cre-dependent DNA recombination, labelling cells within the NTS that are functionally connected with the BAT; *in situ* hybridisation can then be used to characterise neuronal and glia populations within the NTS. This technique allows the visualisation of single RNA molecules in situ (Wang et al., 2012), allowing the identification and quantification of cells connected to BAT. Once these cells are identified, the next logical step would be to prove their functional connection with BAT, to this aim Cre can be expressed in populations of interest within the NTS and either chemogenetically activated using Cre-dependent DREADD (Zhu et al., 2016) or via optogenetics techniques- employing, for example- light-activated cation channel channelrhodopsin-2 (Madisen et al., 2012). Moreover, to understand the cellular mechanisms underlying BAT-modulation via manipulation of mitochondrial dynamics,

it would be interesting to look at several mechanisms and signalling molecules related to Drp1 activation in the NTS, including ER stress, insulin resistance and iNOS expression in astrocytes, which previous studies have found to be elicited by HFD, and associated with hyperphagia, higher body weight and adiposity, insulin resistance and alterations in HGP (Filippi et al., 2017; Patel et al., 2021).

Finally, if time allowed it would have been interesting to explore BAT activation in an obese rat model, to probe whether inhibition of Drp1-mediated mitochondrial fission in the NTS could also reverse the effects of HFD on the BAT and liver.

Overall, the future work we have proposed would be critical to establish the cellular populations in the NTS involved in BAT activation and thermogenesis. Further, this could provide a better understanding of the molecular mechanisms that associate mitochondrial dynamics in the NTS and BAT activation.

7.6 Final remarks

To conclude, this work has shown the role of Drp1-dependent mitochondrial fission in the regulation of BAT glucose uptake and in the development of NTS insulin resistance and systemic hyperinsulinemia and hyperglycaemia, with the latter being restricted to HFD-fed animals. In addition to this, we determined, for the first time, that astrocytes play a critical role in the development of these Drp1-dependent mechanisms. Finally, we demonstrated that short-term HFD is sufficient to induce hepatic steatosis and the inhibition of mitochondrial fission in astrocytes of the NTS is sufficient to prevent TG accumulation in the liver.

Chapter 8: References

8.1 References

Adamska-Patruno, E., Ostrowska, L., Goscik, J., Pietraszewska, B., Kretowski, A. and Gorska, M. 2018. The relationship between the leptin/ghrelin ratio and meals with various macronutrient contents in men with different nutritional status: A randomized crossover study. *Nutrition Journal*. **17**(1), pp.1–7.

Agius, L. 2009. Targeting Hepatic Glucokinase in Type 2 Diabetes: Weighing the Benefits and Risks. *Diabetes*. **58**(1), p.18.

Agulhon, C., Boyt, K.M., Xie, A.X., Friocourt, F., Roth, B.L. and Mccarthy, K.D. 2013. Modulation of the autonomic nervous system and behaviour by acute glial cell Gq protein-coupled receptor activation in vivo. *Journal of Physiology*. **591**(22), pp.5599–5609.

Ahmed, B.A., Ong, F.J., Barra, N.G., Blondin, D.P., Gunn, E., Oreskovich, S.M., Szamosi, J.C., Syed, S.A., Hutchings, E.K., Konyer, N.B., Singh, N.P., Yabut, J.M., Desjardins, E.M., Anhê, F.F., Foley, K.P., Holloway, A.C., Noseworthy, M.D., Haman, F., Carpentier, A.C., Surette, M.G., Schertzer, J.D., Punthakee, Z., Steinberg, G.R. and Morrison, K.M. 2021. Lower brown adipose tissue activity is associated with non-alcoholic fatty liver disease but not changes in the gut microbiota. *Cell Reports Medicine*. **2**(9), p.100397.

Aldiss, P., Symonds, M.E., Lewis, J.E., Boocock, D.J., Miles, A.K., Bloor, I., Ebling, F.J.P. and Budge, H. 2019. Interscapular and Perivascular Brown Adipose Tissue Respond Differently to a Short-Term High-Fat Diet. *Nutrients*. **11**(5).

Alfadda, A.A. and Sallam, R.M. 2012. Reactive oxygen species in health and disease. *Journal of Biomedicine and Biotechnology*. **2012**.

Alkhouri, N., Dixon, L.J. and Feldstein, A.E. 2014. Lipotoxicity in nonalcoholic fatty liver disease: not all lipids are created equal. *https://doi.org/10.1586/egh.09.32*. **3**(4), pp.445–451.

Allen, A.M. 2002. Inhibition of the Hypothalamic Paraventricular Nucleus in Spontaneously Hypertensive Rats Dramatically Reduces Sympathetic Vasomotor Tone. *Hypertension*. **39**(2 I), pp.275–280.

Allen, N.J. and Eroglu, C. 2017. Cell Biology of Astrocyte-Synapse Interactions. *Neuron*. **96**(3), pp.697–708.

Alvarez-Crespo, M., Csikasz, R.I., Martínez-Sánchez, N., Diéguez, C., Cannon, B., Nedergaard, J. and López, M. 2016. Essential role of UCP1 modulating the central effects of thyroid

hormones on energy balance. *Molecular Metabolism*. **5**(4), p.271.

Alves-Bezerra, M. and Cohen, D.E. 2017. Triglyceride metabolism in the liver. *Comprehensive Physiology*. **8**(1), p.1.

Amir, S. 1990. Intra-ventromedial hypothalamic injection of glutamate stimulates brown adipose tissue thermogenesis in the rat. *Brain Research*. **511**(2), pp.341–344.

Anderson, Courtney M, Kazantzis, M., Wang, J., Venkatraman, S., Goncalves, R.L.S., Quinlan, C.L., Ng, R., Jastroch, M., Benjamin, D.I., Nie, B., Herber, C., Van, A.-A.N., Park, M.J., Yun, D., Chan, K., Yu, A., Vuong, P., Febbraio, M., Nomura, D., Napoli, J., Brand, M.D. and Stahl, A. 2015. Dependence of Brown Adipose Tissue Function on CD36-Mediated Coenzyme Q Uptake. *Cell Rep*. **10**(4), pp.505–515.

De Andrade, I.S., Zemdegs, J.C.S., De Souza, A.P., Watanabe, R.L.H., Telles, M.M., Nascimento, C.M.O., Oyama, L.M. and Ribeiro, E.B. 2015. Diet-induced obesity impairs hypothalamic glucose sensing but not glucose hypothalamic extracellular levels, as measured by microdialysis. *Nutrition & Diabetes 2015 5:6*. **5**(6), pp.e162–e162.

Aponte, Y., Atasoy, D. and Sternson, S.M. 2011. AGRP neurons are sufficient to orchestrate feeding behavior rapidly and without training. *Nature Neuroscience*. **14**(3), pp.351–355.

Arch, J.R.S. 2002. β3-Adrenoceptor agonists: potential, pitfalls and progress. *European Journal of Pharmacology*. **440**(2–3), pp.99–107.

Arias-Salvatierra, D., Silbergeld, E.K., Acosta-Saavedra, L.C. and Calderon-Aranda, E.S. 2011. Role of nitric oxide produced by iNOS through NF-κB pathway in migration of cerebellar granule neurons induced by Lipopolysaccharide. *Cellular Signalling*. **23**(2), pp.425–435.

Au-Yong, I.T.H., Thorn, N., Ganatra, R., Perkins, A.C. and Symonds, M.E. 2009. Brown Adipose Tissue and Seasonal Variation in Humans. *Diabetes*. **58**(11), pp.2583–2587.

Bach, D., Pich, S., Soriano, F.X., Vega, N., Baumgartner, B., Oriola, J., Daugaard, J.R., Lloberas, J., Camps, M., Zierath, J.R., Rabasa-Lhoret, R., Wallberg-Henriksson, H., Laville, M., Palacín, M., Vidal, H., Rivera, F., Brand, M. and Zorzano, A. 2003. Mitofusin-2 Determines Mitochondrial Network Architecture and Mitochondrial Metabolism: A NOVEL REGULATORY MECHANISM ALTERED IN OBESITY *. *Journal of Biological Chemistry*. **278**(19), pp.17190–17197.

Bachman, E.S., Dhillon, H., Zhang, C.Y., Cinti, S., Bianco, A.C., Kobilka, B.K. and Lowell, B.B. 2002. βAR signaling required for diet-induced thermogenesis and obesity resistance. *Science*. **297**(5582), pp.843–845.

Bacon, S.J., Zagon, A. and Smith, A.D. 1990. Electron microscopic evidence of a monosynaptic pathway between cells in the caudal raphé nuclei and sympathetic preganglionic neurons in the rat spinal cord. *Experimental brain research*. **79**(3), pp.589–602.

Bae, J., Ricciardi, C.J., Esposito, D., Komarnytsky, S., Hu, P., Curry, B.J., Brown, P.L., Gao, Z., Biggerstaff, J.P., Chen, J. and Zhao, L. 2014. Activation of pattern recognition receptors in brown adipocytes induces inflammation and suppresses uncoupling protein 1 expression and mitochondrial respiration. *American Journal of Physiology - Cell Physiology*. **306**(10).

Ballestri, S., Zona, S., Targher, G., Romagnoli, D., Baldelli, E., Nascimbeni, F., Roverato, A., Guaraldi, G. and Lonardo, A. 2016. Nonalcoholic fatty liver disease is associated with an almost twofold increased risk of incident type 2 diabetes and metabolic syndrome. Evidence from a systematic review and meta-analysis. *Journal of gastroenterology and hepatology*. **31**(5), pp.936–944.

Bamshad, M., Song, C.K. and Bartness, T.J. 1999. CNS origins of the sympathetic nervous system outflow to brown adipose tissue. *The American journal of physiology*. **276**(6).

Bansal, A.B. and Khalili, Y. Al 2022. Orlistat. *xPharm: The Comprehensive Pharmacology Reference*., pp.1–3.

Barneda, D., Planas-Iglesias, J., Gaspar, M.L., Mohammadyani, D., Prasannan, S., Dormann, D., Han, G.S., Jesch, S.A., Carman, G.M., Kagan, V., Parker, M.G., Ktistakis, N.T., Klein-Seetharaman, J., Dixon, A.M., Henry, S.A. and Christian, M. 2015. The brown adipocyte protein CIDEA promotes lipid droplet fusion via a phosphatidic acid-binding amphipathic helix. *eLife*. **4**(NOVEMBER2015).

Barnes, M.B., Lawson, M.A. and Lee Beverly, J. 2011. Rate of fall in blood glucose and recurrent hypoglycemia affect glucose dynamics and noradrenergic activation in the ventromedial hypothalamus. *American journal of physiology. Regulatory, integrative and comparative physiology*. **301**(6).

Barraco, R., El-Ridi, M., Ergene, E., Parizon, M. and Bradley, D. 1992. An atlas of the rat subpostremal nucleus tractus solitarius. *Brain Research Bulletin*. **29**(6), pp.703–765.

Barroso, W.A., Victorino, V.J., Jeremias, I.C., Petroni, R.C., Ariga, S.K.K., Salles, T.A., Barbeiro, D.F., de Lima, T.M. and de Souza, H.P. 2018. High-fat diet inhibits PGC-1α suppressive effect on NFκB signaling in hepatocytes. *European journal of nutrition*. **57**(5), pp.1891–1900.

Bartelt, A., Bruns, O.T., Reimer, R., Hohenberg, H., Ittrich, H., Peldschus, K., Kaul, M.G., Tromsdorf, U.I., Weller, H., Waurisch, C., Eychmüller, A., Gordts, P.L.S.M., Rinninger, F., Bruegelmann, K., Freund, B., Nielsen, P., Merkel, M. and Heeren, J. 2011a. Brown adipose tissue activity controls triglyceride clearance. *Nature Medicine 2011 17:2*. **17**(2), pp.200–205.

Bartelt, A. and Heeren, J. 2013. Adipose tissue browning and metabolic health. *Nature Reviews Endocrinology 2013 10:1*. **10**(1), pp.24–36.

Bartness, T.J., Shrestha, Y.B., Vaughan, C.H., Schwartz, G.J. and Song, C.K. 2010. Sensory and sympathetic nervous system control of white adipose tissue lipolysis. *Molecular and Cellular Endocrinology*. **318**(1–2), pp.34–43.

Basaranoglu, M. and Neuschwander-Tetri, B.A. 2006. Nonalcoholic Fatty Liver Disease: Clinical Features and Pathogenesis. *Gastroenterology & Hepatology*. **2**(4), p.282.

Baskin, D.G., Breininger, J.F. and Schwartz, M.W. 1999. Leptin Receptor mRNA Identifies a Subpopulation of Neuropeptide Y Neurons Activated by Fasting in Rat Hypothalamus. *828 DIABETES*. **48**.

Becattini, B., Zani, F., Breasson, L., Sardi, C., D'Agostino, V.G., Choo, M.K., Provenzani, A., Park, J.M. and Solinas, G. 2016. JNK1 ablation in mice confers long-term metabolic protection from diet-induced obesity at the cost of moderate skin oxidative damage. *FASEB journal : official publication of the Federation of American Societies for Experimental Biology*. **30**(9), pp.3124–3132.

Bednar, I., Qian, M., Qureshi, G.A., Källström, L., Johnson, A.E., Carrer, H. and Södersten, P. 1994. Glutamate inhibits ingestive behaviour. *Journal of neuroendocrinology*. **6**(4), pp.403–408.

Beiroa, D., Imbernon, M., Gallego, R., Senra, A., Herranz, D., Villarroya, F., Serrano, M., Fernø, J., Salvador, J., Escalada, J., Dieguez, C., Lopez, M., Frühbeck, G. and Nogueiras, R. 2014. GLP-1 agonism stimulates brown adipose tissue thermogenesis and browning through hypothalamic AMPK. *Diabetes*. **63**(10), pp.3346–3358.

Bell, J.A., Reed, M.A., Consitt, L.A., Martin, O.J., Haynie, K.R., Hulver, M.W., Muoio, D.M. and Dohm, G.L. 2010. Lipid Partitioning, Incomplete Fatty Acid Oxidation, and Insulin Signal Transduction in Primary Human Muscle Cells: Effects of Severe Obesity, Fatty Acid Incubation, and Fatty Acid Translocase/CD36 Overexpression. *The Journal of Clinical Endocrinology & Metabolism*. **95**(7), pp.3400–3410.

Berglund, L., Berne, C., Svärdsudd, K., Garmo, H., Melhus, H. and Zethelius, B. 2012. Seasonal variations of insulin sensitivity from a euglycemic insulin clamp in elderly men. *Upsala Journal of Medical Sciences*. **117**(1), p.35.

Beutler, L.R., Corpuz, T. V., Ahn, J.S., Kosar, S., Song, W., Chen, Y. and Knight, Z.A. 2020. Obesity causes selective and long-lasting desensitization of AgRP neurons to dietary fat. *eLife*. **9**, pp.1–21.

Biddinger, S.B., Hernandez-Ono, A., Rask-Madsen, C., Haas, J.T., Alemán, J.O., Suzuki, R., Scapa, E.F., Agarwal, C., Carey, M.C., Stephanopoulos, G., Cohen, D.E., King, G.L., Ginsberg, H.N.N. and Kahn, C.R. 2008. Hepatic insulin resistance is sufficient to produce dyslipidemia and susceptibility to atherosclerosis. *Cell metabolism*. **7**(2), pp.125–134.

Bideyan, L., Nagari, R. and Tontonoz, P. 2021. Hepatic transcriptional responses to fasting and feeding. *Genes & Development*. **35**(9–10), pp.635–657.

Birkenfeld, A.L. and Shulman, G.I. 2014. Non Alcoholic Fatty Liver Disease, Hepatic Insulin Resistance and Type 2 Diabetes. *Hepatology (Baltimore, Md.)*. **59**(2), p.713.

Birsoy, K., Festuccia, W.T. and Laplante, M. 2013. A comparative perspective on lipid storage in animals. *Journal of Cell Science*. **126**(7), pp.1541–1552.

Blevins, J.E., Chelikani, P.K., Haver, A.C. and Reidelberger, R.D. 2008. PYY(3-36) induces Fos in the arcuate nucleus and in both catecholaminergic and non-catecholaminergic neurons in the nucleus tractus solitarius of rats. *Peptides*. **29**(1), pp.112–119.

Blondin DP, Nielsen S, Kuipers EN, Severinsen MC, Jensen VH, Miard S, Jespersen NZ, Kooijman S, Boon MR, Fortin M, Phoenix S, Frisch F, Guérin B, Turcotte ÉE, Haman F, Richard D, Picard F, Rensen PCN, Scheele C, Carpentier AC. Human Brown Adipocyte Thermogenesis Is Driven by β2-AR Stimulation. Cell Metab. 2020 Aug 4;32(2):287-300.e7.

Blouet, C. and Schwartz, G.J. 2012. Brainstem nutrient sensing in the nucleus of the solitary tract inhibits feeding. *Cell Metabolism*. **16**(5), pp.579–587.

Boden, G. 2008. Obesity and Free Fatty Acids. *Endocrinology and Metabolism Clinics of North America*. **37**(3), pp.635–646.

Bordi, M., Nazio, F. and Campello, S. 2017. The Close Interconnection between Mitochondrial Dynamics and Mitophagy in Cancer. *Frontiers in Oncology*. **7**, p.1.

Boucher, J., Kleinridders, A. and Ronald Kahn, C. 2014. Insulin Receptor Signaling in Normal and Insulin-Resistant States. *Cold Spring Harbor Perspectives in Biology*. **6**(1).

Bouillaud, F., Combes-George, M. and Ricquier, D. 1983. Mitochondria of adult human brown adipose tissue contain a 32 000-Mr uncoupling protein. *Bioscience Reports*. **3**(8), pp.775–780.

Bouillaud, F., Villarroya, F., Hentz, E., Raimbault, S., Cassard, A.M. and Ricquier, D. 1988. Detection of brown adipose tissue uncoupling protein mRNA in adult patients by a human genomic probe. *Clinical Science*. **75**(1), pp.21–27.

Bournat, J.C. and Brown, C.W. 2010. Mitochondrial dysfunction in obesity. *Current Opinion in Endocrinology, Diabetes and Obesity*. **17**(5), pp.446–452.

Boushel, R., Gnaiger, E., Schjerling, P., Skovbro, M., Kraunsøe, R. and Dela, F. 2007. Patients with type 2 diabetes have normal mitochondrial function in skeletal muscle. *Diabetologia*. **50**(4), pp.790–796.

Boutant, M., Kulkarni, S.S., Joffraud, M., Ratajczak, J., Valera-Alberni, M., Combe, R., Zorzano, A. and Cantó, C. 2017. Mfn2 is critical for brown adipose tissue thermogenic function. *The EMBO Journal*. **36**(11), pp.1543–1558.

Brandt, T., Cavellini, L., Kühlbrandt, W. and Cohen, M.M. 2016. A mitofusin-dependent docking ring complex triggers mitochondrial fusion in vitro. *eLife*. **5**(JUNE2016).

Brendle, C., Werner, M.K., Schmadl, M., la Fougère, C., Nikolaou, K., Stefan, N. and Pfannenberg, C. 2018. Correlation of Brown Adipose Tissue with Other Body Fat Compartments and Patient Characteristics: A Retrospective Analysis in a Large Patient Cohort Using PET/CT. *Academic radiology*. **25**(1), pp.102–110.

Brito, M.N., Brito, N.A., Baro, D.J., Song, C.K. and Bartness, T.J. 2007. Differential activation of the sympathetic innervation of adipose tissues by melanocortin receptor stimulation. *Endocrinology*. **148**(11), pp.5339–5347.

Broadwell, R.D. and Brightman, M.W. 1976. Entry of peroxidase into neurons of the central and peripheral nervous systems from extracerebral and cerebral blood. *Journal of Comparative Neurology*. **166**(3), pp.257–283.

Broeders, E.P.M., Nascimento, E.B.M., Havekes, B., Brans, B., Roumans, K.H.M., Tailleux, A., Schaart, G., Kouach, M., Charton, J., Deprez, B., Bouvy, N.D., Mottaghy, F., Staels, B., Van Marken Lichtenbelt, W.D. and Schrauwen, P. 2015. The bile acid chenodeoxycholic acid increases human brown adipose tissue activity. *Cell Metabolism*. **22**(3), pp.418–426.

Buckman, L.B., Thompson, M.M., Lippert, R.N., Blackwell, T.S., Yull, F.E. and Ellacott, K.L.J. 2015. Evidence for a novel functional role of astrocytes in the acute homeostatic

response to high-fat diet intake in mice. *Molecular Metabolism*. **4**(1), pp.58–63.

Çakir, I., Cyr, N.E., Perello, M., Litvinov, B.P., Romero, A., Stuart, R.C. and Nillni, E.A. 2013. Obesity Induces Hypothalamic Endoplasmic Reticulum Stress and Impairs Proopiomelanocortin (POMC) Post-translational Processing. *Journal of Biological Chemistry*. **288**(24), pp.17675–17688.

Cannon, B. and Nedergaard, J. 2004. Brown Adipose Tissue: Function and Physiological Significance. *Physiological Reviews*. **84**(1), pp.277–359.

Cano, G., Passerin, A.M., Schiltz, J.C., Card, J.P., Morrison, S.F. and Sved, A.F. 2003. Anatomical substrates for the central control of sympathetic outflow to interscapular adipose tissue during cold exposure. *The Journal of comparative neurology*. **460**(3), pp.303–326.

Cao, W.-H., Madden, C.J. and Morrison, S.F. 2010. Inhibition of brown adipose tissue thermogenesis by neurons in the ventrolateral medulla and in the nucleus tractus solitarius. *American Journal of Physiology-Regulatory, Integrative and Comparative Physiology*. **299**(1), pp.R277–R290.

Cao, W.H., Fan, W. and Morrison, S.F. 2004. Medullary pathways mediating specific sympathetic responses to activation of dorsomedial hypothalamus. *Neuroscience*. **126**(1), pp.229–240.

Cao, Y., Meng, S., Chen, Y., Feng, J., Gu, D., Yu, B., Nature, Y.L. 2017.MFN1 structures reveal nucleotide-triggered dimerization critical for mitochondrial fusion. *nature.com*.

Carlsen, H., Haugen, F., Zadelaar, S., Kleemann, R., Kooistra, T., Drevon, C.A. and Blomhoff, R. 2009. Diet-induced obesity increases NF-κB signaling in reporter mice. *Genes & Nutrition*. **4**(3), p.215.

Caron, A., Lee, S., Elmquist, J.K. and Gautron, L. 2018. Leptin and brain–adipose crosstalks. *Nature reviews. Neuroscience*. **19**(3), p.153.

Carvalheira, J.B.C., Ribeiro, E.B., Araújo, E.P., Guimarães, R.B., Telles, M.M., Torsoni, M., Gontijo, J.A.R., Velloso, L.A. and Saad, M.J.A. 2003. Selective impairment of insulin signalling in the hypothalamus of obese Zucker rats. *Diabetologia*. **46**(12), pp.1629–1640.

Carvalho-Filho, M.A., Ueno, M., Hirabara, S.M., Seabra, A.B., Carvalheira, J.B.C., De Oliveira, M.G., Velloso, L.A., Curi, R. and Saad, M.J.A. 2005. S-Nitrosation of the Insulin Receptor, Insulin Receptor Substrate 1, and Protein Kinase B/AktA Novel Mechanism of Insulin Resistance. *Diabetes*. **54**(4), pp.959–967.

Casimiro, I., Stull, N.D., Tersey, S.A. and Mirmira, R.G. 2021. Phenotypic sexual dimorphism in response to dietary fat manipulation in C57BL/6J mice. *Journal of Diabetes and its Complications*. **35**(2), p.107795.

Cassidy-Stone, A., Chipuk, J.E., Ingerman, E., Song, C., Yoo, C., Kuwana, T., Kurth, M.J., Shaw, J.T., Hinshaw, J.E., Green, D.R. and Nunnari, J. 2008. Chemical Inhibition of the Mitochondrial Division Dynamin Reveals Its Role in Bax/Bak-Dependent Mitochondrial Outer Membrane Permeabilization. *Developmental Cell*. **14**(2), pp.193–204.

Castell, F. and Cook, G.J.R. 2008. Quantitative techniques in 18FDG PET scanning in oncology. *British Journal of Cancer 2008 98:10*. **98**(10), pp.1597–1601.

Cawthorn, W.P., Scheller, E.L. and MacDougald, O.A. 2012. Adipose tissue stem cells meet preadipocyte commitment: going back to the future. *Journal of Lipid Research*. **53**(2), pp.227–246.

Cederberg, A., Gronning, L.M., Ahrén, B., Taskén, K., Carlsson, P. and Enerbäck, S. 2001. FOXC2 Is a Winged Helix Gene that Counteracts Obesity, Hypertriglyceridemia, and Diet-Induced Insulin Resistance. *Cell*. **106**(5), pp.563–573.

Cereghetti, G.M., Stangherlin, A., Martins De Brito, O., Chang, C.R., Blackstone, C., Bernardi, P. and Scorrano, L. 2008. Dephosphorylation by calcineurin regulates translocation of Drp1 to mitochondria. *Proceedings of the National Academy of Sciences of the United States of America*. **105**(41), pp.15803–15808.

Chalasani, N., Younossi, Z., Lavine, J.E., Charlton, M., Cusi, K., Rinella, M., Harrison, S.A., Brunt, E.M. and Sanyal, A.J. 2018. The diagnosis and management of nonalcoholic fatty liver disease: Practice guidance from the American Association for the Study of Liver Diseases. *Hepatology (Baltimore, Md.)*. **67**(1), pp.328–357.

Chami, N., Preuss, M., Walker, R.W., Moscati, A. and Loos, R.J.F. 2020. The role of polygenic susceptibility to obesity among carriers of pathogenic mutations in MC4R in the UK Biobank population. *PLOS Medicine*. **17**(7), p.e1003196.

Champigny, O., research, D.R. 1996. Evidence from in vitro differentiating cells that adrenoceptor agonists can increase uncoupling protein mRNA level in adipocytes of adult humans: an RT-PCR study. *Elsevier*.

Chan, O., Lawson, M., Zhu, W., Beverly, J.L. and Sherwin, R.S. 2007. ATP-sensitive K(+) channels regulate the release of GABA in the ventromedial hypothalamus during hypoglycemia. *Diabetes*. **56**(4), pp.1120–1126.

Chang, C.-R., Manlandro, C.M., Arnoult, D., Stadler, J., Posey, A.E., Hill, R.B. and Blackstone, C. 2010. A Lethal de Novo Mutation in the Middle Domain of the Dynamin-related GTPase Drp1 Impairs Higher Order Assembly and Mitochondrial Division. *The Journal of Biological Chemistry*. **285**(42), p.32494.

Chang, C.R. and Blackstone, C. 2007. Drp1 phosphorylation and mitochondrial regulation. *EMBO Reports*. **8**(12), pp.1088–1089.

Chang, C.R. and Blackstone, C. 2010. Dynamic regulation of mitochondrial fission through modification of the dynamin-related protein Drp1. *Annals of the New York Academy of Sciences*. **1201**(1), pp.34–39.

Chechi, K., Carpentier, A.C. and Richard, D. 2013b. Understanding the brown adipocyte as a contributor to energy homeostasis. *Trends in Endocrinology & Metabolism*. **24**(8), pp.408–420.

Chen, H., Detmer, S.A., Ewald, A.J., Griffin, E.E., Fraser, S.E. and Chan, D.C. 2003. Mitofusins Mfn1 and Mfn2 coordinately regulate mitochondrial fusion and are essential for embryonic development. *Journal of Cell Biology*. **160**(2), pp.189–200.

Chen, X.-M., Hosono, T., Yoda, T., Fukuda, Y. and Kanosue, K. 1998. Efferent projection from the preoptic area for the control of non-shivering thermogenesis in rats. *The Journal of Physiology*. **512**(3), pp.883–892.

Chen, Z., Sheng, L., Shen, H., Zhao, Y., Wang, S., Brink, R. and Rui, L. 2012. Hepatic TRAF2 Regulates Glucose Metabolism Through Enhancing Glucagon Responses. *Diabetes*. **61**(3), p.566.

Chiang, S.H., Bazuine, M., Lumeng, C.N., Geletka, L.M., Mowers, J., White, N.M., Ma, J.T., Zhou, J., Qi, N., Westcott, D., Delproposto, J.B., Blackwell, T.S., Yull, F.E. and Saltiel, A.R. 2009. The Protein Kinase IKKε Regulates Energy Balance in Obese Mice. *Cell*. **138**(5), pp.961–975.

Chiazza, F., Challa, T.D., Lucchini, F.C., Konrad, D. and Wueest, S. 2016. A short bout of HFD promotes long-lasting hepatic lipid accumulation. *Adipocyte*. **5**(1), p.88.

Chondronikola, M., Volpi, E., Børsheim, E., Porter, C., Annamalai, P., Enerbäck, S., Lidell, M.E., Saraf, M.K., Labbe, S.M., Hurren, N.M., Yfanti, C., Chao, T., Andersen, C.R., Cesani, F., Hawkins, H. and Sidossis, L.S. 2014b. Brown Adipose Tissue Improves Whole-Body Glucose Homeostasis and Insulin Sensitivity in Humans. *Diabetes*. **63**(12), pp.4089–4099.

Chrobok, L., Klich, J.D., Sanetra, A.M., Jeczmien-Lazur, J.S., Pradel, K., Palus-Chramiec, K.,

Kepczynski, M., Piggins, H.D. and Lewandowski, M.H. 2022. Rhythmic neuronal activities of the rat nucleus of the solitary tract are impaired by high-fat diet-implications for daily control of satiety. *The Journal of Physiology J Physiol*. **600**, pp.751–767.

Ciapaite, J., Van Den Broek, N.M., Te Brinke, H., Nicolay, K., Jeneson, J.A., Houten, S.M. and Prompers, J.J. 2011. Differential effects of short-and long-term high-fat diet feeding on hepatic fatty acid metabolism in rats.

Cinti, S. 2009. Transdifferentiation properties of adipocytes in the adipose organ. *American Journal of Physiology - Endocrinology and Metabolism*. **297**(5).

Clyburn, C. and Browning, K.N. 2019. Role of astroglia in diet-induced central neuroplasticity. *Journal of neurophysiology*. **121**(4), pp.1195–1206.

Clyburn, C., Travagli, R.A. and Browning, K.N. 2018. Acute high-fat diet upregulates glutamatergic signaling in the dorsal motor nucleus of the vagus. *American Journal of Physiology - Gastrointestinal and Liver Physiology*. **314**(5), pp.G623–G634.

Cohen, D.E. and Fisher, E.A. 2013. Lipoprotein Metabolism, Dyslipidemia and Nonalcoholic Fatty Liver Disease. *Seminars in liver disease*. **33**(4), p.380.

Collins, K.H., Paul, H.A., Hart, D.A., Reimer, R.A., Smith, I.C., Rios, J.L., Seerattan, R.A. and Herzog, W. 2016. A High-Fat High-Sucrose Diet Rapidly Alters Muscle Integrity, Inflammation and Gut Microbiota in Male Rats. *Nature Publishing Group*.

Collins, S., Kuhn, C.M., Petro, A.E., Swick, A.G., Chrunyk, B.A. and Surwit, R.S. 1996. Role of leptin in fat regulation. *Nature*. **380**(6576), p.677.

Collins, T.J., Berridge, M.J., Lipp, P. and Bootman, M.D. 2002. Mitochondria are morphologically and functionally heterogeneous within cells. *EMBO Journal*. **21**(7), pp.1616–1627.

Commins, S.P., Watson, P.M., Levin, N., Beiler, R.J. and Gettys, T.W. 2000. Central Leptin Regulates the UCP1 and obGenes in Brown and White Adipose Tissue via Different β-Adrenoceptor Subtypes *. *Journal of Biological Chemistry*. **275**(42), pp.33059–33067.

Commins, S.P., Watson, P.M., Padgett, M.A., Dudley, A., Argyropoulos, G. and Gettys, T.W. 1999. Induction of uncoupling protein expression in brown and white adipose tissue by leptin. *Endocrinology*. **140**(1), pp.292–300.

Conceição, E.P.S., Madden, C.J. and Morrison, S.F. 2017. Tonic inhibition of brown adipose tissue sympathetic nerve activity via muscarinic acetylcholine receptors in the rostral raphe pallidus. *The Journal of physiology*. **595**(24), pp.7495–7508.

Conceição, E.P.S., Reynolds, C.A., Morrison, S.F. and Madden, C.J. 2021. Activation of Transient Receptor Potential Vanilloid 1 Channels in the Nucleus of the Solitary Tract and Activation of Dynorphin Input to the Median Preoptic Nucleus Contribute to Impaired BAT Thermogenesis in Diet-Induced Obesity. *eNeuro*. **8**(2), pp.48–69.

Contreras, C., González-García, I., Seoane-Collazo, P., Martínez-Sánchez, N., Liñares-Pose, L., Rial-Pensado, E., Fernø, J., Tena-Sempere, M., Casals, N., Diéguez, C., Nogueiras, R. and López, M. 2017. Reduction of Hypothalamic Endoplasmic Reticulum Stress Activates Browning of White Fat and Ameliorates Obesity. *Diabetes*. **66**(1), pp.87–99.

Contreras, L., Drago, I., Zampese, E. and Pozzan, T. 2010. Mitochondria: the calcium connection. *Biochimica et biophysica acta*. **1797**(6–7), pp.607–618.

Converse, C.A. and Skinner, E.R. 1992. Lipoprotein analysis : a practical approach. , p.251.

Cortez-Pinto, H., Chatham, J., Chacko, V.P., Arnold, C., Rashid, A. and Diehl, A.M. 1999. Alterations in liver ATP homeostasis in human nonalcoholic steatohepatitis: a pilot study. *JAMA*. **282**(17), pp.1659–1664.

Cotero, V.E., Routh, Vanessa H and Routh, V H 2009. Insulin blunts the response of glucose-excited neurons in the ventrolateral-ventromedial hypothalamic nucleus to decreased glucose. *Am J Physiol Endocrinol Metab*. **296**, pp.1101–1109.

Cowley, M., Smart, J., Rubinstein, M., Nature, M.C. 2001.Leptin activates anorexigenic POMC neurons through a neural network in the arcuate nucleus. *nature.com*.

Cunningham, S., Leslie, P., Hopwood, D., Illingworth, P., Jung, R.T., Nicholls, D.G., Peden, N., Rafael, J. and Rial, E. 1985. The characterization and energetic potential of brown adipose tissue in man. *Clinical Science (London, England : 1979)*. **69**(3), pp.343–348.

Cypess, A.M., Doyle, A.N., Sass, C.A., Huang, T.L., Mowschenson, P.M., Rosen, H.N., Tseng, Y.H., Palmer, E.L. and Kolodny, G.M. 2013. Quantification of Human and Rodent Brown Adipose Tissue Function Using 99mTc-Methoxyisobutylisonitrile SPECT/CT and 18F-FDG PET/CT. *Journal of Nuclear Medicine*. **54**(11), pp.1896–1901.

Cypess, A.M., Lehman, S., Williams, G., Tal, I., Rodman, D., Goldfine, A.B., Kuo, F.C., Palmer, E.L., Tseng, Y.-H., Doria, A., Kolodny, G.M. and Kahn, C.R. 2009a. Identification and Importance of Brown Adipose Tissue in Adult Humans. *New England Journal of Medicine*. **360**(15), pp.1509–1517.

Cypess, A.M., Weiner, L.S., Roberts-Toler, C., Elía, E.F., Kessler, S.H., Kahn, P.A., English, J., Chatman, K., Trauger, S.A., Doria, A. and Kolodny, G.M. 2015a. Activation of human

brown adipose tissue by a β3-adrenergic receptor agonist. *Cell metabolism*. **21**(1), pp.33–38.

D'souza, A.M., Neumann, U.H., Glavas, M.M. and Kieffer, T.J. 2017. The glucoregulatory actions of leptin. *Molecular Metabolism*. **6**(9), p.1052.

Dallner, O.S., Chernogubova, E., Brolinson, K.A. and Bengtsson, T. 2006. β3-Adrenergic Receptors Stimulate Glucose Uptake in Brown Adipocytes by Two Mechanisms Independently of Glucose Transporter 4 Translocation. *Endocrinology*. **147**(12), pp.5730–5739.

Danese, A., Patergnani, BBA. 2017, Calcium regulates cell death in cancer: Roles of the mitochondria and mitochondria-associated membranes (MAMs). *Elsevier*.

Demas, G.E. and Bartness, T.J. 2001. Direct innervation of white fat and adrenal medullary catecholamines mediate photoperiodic changes in body fat. *American Journal of Physiology - Regulatory Integrative and Comparative Physiology*. **281**(5 50-5).

Denton, R.M. 2009. Regulation of mitochondrial dehydrogenases by calcium ions. *Biochimica et Biophysica Acta - Bioenergetics*. **1787**(11), pp.1309–1316.

Dienel, G.A. 2013. Astrocytic energetics during excitatory neurotransmission: What are contributions of glutamate oxidation and glycolysis? *Neurochemistry International*. **63**(4), pp.244–258.

Dietrich, M.O., Liu, Z.-W. and Horvath, T.L. 2013. Mitochondrial dynamics controlled by mitofusins regulate Agrp neuronal activity and diet-induced obesity. *Cell*. **155**(1), p.188.

Dijk, W., Heine, M., Vergnes, L., Boon, M.R., Schaart, G., Hesselink, M.K.C., Reue, K., van Marken Lichtenbelt, W.D., Olivecrona, G., Rensen, P.C.N., Heeren, J. and Kersten, S. 2015. ANGPTL4 mediates shuttling of lipid fuel to brown adipose tissue during sustained cold exposure. *eLife*. **4**(OCTOBER2015).

DiMicco, J.A. and Zaretsky, D. V. 2007. The dorsomedial hypothalamus: a new player in thermoregulation. *https://doi.org/10.1152/ajpregu.00498.2006*. **292**(1), pp.47–63.

Dimitriadis, G., Mitron, P., Lambadiari, V., Maratou, E. and Raptis, S.A. 2011. Insulin effects in muscle and adipose tissue. *Diabetes research and clinical practice*. **93 Suppl 1**(SUPPL. 1).

Dimitriadis, G., Parry-Billings, M., Bevan, S., Leighton, B., Krause, U., Piva, T., Tegos, K., Challiss, R.A.J., Wegener, G. and Newsholme, E.A. 1997. The effects of insulin on transport and metabolism of glucose in skeletal muscle from hyperthyroid and hypothyroid rats. *European Journal of Clinical Investigation*. **27**(6), pp.475–483.

Dockray, G.J. 2013. Enteroendocrine cell signalling via the vagus nerve. *Current Opinion in Pharmacology*. **13**(6), pp.954–958.

Dohm, G.L., Tapscott, E.B., Pories, W.J., Dabbs, D.J., Flickinger, E.G., Meelheim, D., Fushiki, T., Atkinson, S.M., Elton, C.W. and Caro, J.F. 1988. An in vitro human muscle preparation suitable for metabolic studies. Decreased insulin stimulation of glucose transport in muscle from morbidly obese and diabetic subjects. *The Journal of clinical investigation*. **82**(2), pp.486–494.

Donnelly, Kerry L, Smith, C.I., Schwarzenberg, S.J., Jessurun, J., Boldt, M.D. and Parks, E.J. 2005. Sources of fatty acids stored in liver and secreted via lipoproteins in patients with nonalcoholic fatty liver disease. *The Journal of Clinical Investigation*. **115**.

Del Dotto, V., Mishra, P., Vidoni, S., Fogazza, M., Maresca, A., Caporali, L., McCaffery, J.M., Cappelletti, M., Baruffini, E., Lenaers, G., Chan, D., Rugolo, M., Carelli, V. and Zanna, C. 2017. OPA1 Isoforms in the Hierarchical Organization of Mitochondrial Functions. *Cell Reports*. **19**(12), pp.2557–2571.

Douglass, J.D., Dorfman, M.D., Fasnacht, R., Shaffer, L.D. and Thaler, J.P. 2017. Astrocyte IKKβ/NF-κB signaling is required for diet-induced obesity and hypothalamic inflammation. *Molecular Metabolism*. **6**(4), pp.366–373.

Douris, N., Stevanovic, D.M., Fisher, F.M., Cisu, T.I., Chee, M.J., Nguyen, N.L., Zarebidaki, E., Adams, A.C., Kharitonenkov, A., Flier, J.S., Bartness, T.J. and Maratos-Flier, E. 2015. Central fibroblast growth factor 21 browns white fat via sympathetic action in male mice. *Endocrinology*. **156**(7), pp.2470–2481.

Drazen, D.L., Vahl, T.P., D'Alessio, D.A., Seeley, R.J. and Woods, S.C. 2006. Effects of a fixed meal pattern on ghrelin secretion: evidence for a learned response independent of nutrient status. *Endocrinology*. **147**(1), pp.23–30.

Duca, F.A., Swartz, T.D., Sakar, Y. and Covasa, M. 2012. Increased Oral Detection, but Decreased Intestinal Signaling for Fats in Mice Lacking Gut Microbiota. *PLOS ONE*. **7**(6), p.e39748.

Elias, C.F., Lee, C., Kelly, J., Aschkenasi, C., Ahima, R.S., Couceyro, P.R., Kuhar, M.J., Saper, C.B. and Elmquist, J.K. 1998. Leptin activates hypothalamic CART neurons projecting to the spinal cord. *Neuron*. **21**(6), pp.1375–1385.

Ellacott, K.L.J., Halatchev, I.G. and Cone, R.D. 2006. Characterization of leptin-responsive neurons in the caudal brainstem. *Endocrinology*. **147**(7), pp.3190–3195.

Ellacott, K.L.J., Morton, G.J., Woods, S.C., Tso, P. and Schwartz, M.W. 2010. Assessment of Feeding Behavior in Laboratory Mice. *Cell Metabolism*. **12**(1), pp.10–17.

Enriori, P.J., Evans, A.E., Sinnayah, P., Jobst, E.E., Tonelli-Lemos, L., Billes, S.K., Glavas, M.M., Grayson, B.E., Perello, M., Nillni, E.A., Grove, K.L. and Cowley, M.A. 2007. Diet-Induced Obesity Causes Severe but Reversible Leptin Resistance in Arcuate Melanocortin Neurons. *Cell Metabolism*. **5**(3), pp.181–194.

Enriori, P.J., Sinnayah, P., Simonds, S.E., Rudaz, C.G. and Cowley, M.A. 2011. Leptin action in the dorsomedial hypothalamus increases sympathetic tone to brown adipose tissue in spite of systemic leptin resistance. *The Journal of neuroscience : the official journal of the Society for Neuroscience*. **31**(34), pp.12189–12197.

von Essen, G., Lindsund, E., Cannon, B. and Nedergaard, J. 2017. Adaptive facultative diet-induced thermogenesis in wild-type but not in UCP1-ablated mice. *American Journal of Physiology - Endocrinology and Metabolism*. **313**(5), pp.E515–E527.

Eura, Y., Ishihara, N., Yokota, S. and Mihara, K. 2003. Two Mitofusin Proteins, Mammalian Homologues of FZO, with Distinct Functions Are Both Required for Mitochondrial Fusion. *Journal of Biochemistry*. **134**(3), pp.333–344.

Fan, W., Boston, B.A., Kesterson, R.A., Hruby, V.J. and Cone, R.D. 1997. Role of melanocortlnergic neurons in feeding and the agouti obesity syndrome. *Nature*. **385**(6612), pp.165–168.

Ferris, H.A. and Kahn, C.R. 2016. Unraveling the Paradox of Selective Insulin Resistance in the Liver: the Brain–Liver Connection. *Diabetes*. **65**(6), pp.1481–1483.

Filippi, B.M., Abraham, M.A., Silva, P.N., Rasti, M., LaPierre, M.P., Bauer, P. V., Rocheleau, J. V. and Lam, T.K.T. 2017a. Dynamin-Related Protein 1-Dependent Mitochondrial Fission Changes in the Dorsal Vagal Complex Regulate Insulin Action. *Cell Reports*. **18**(10), pp.2301–2309.

Filippi, B.M., Bassiri, A., Abraham, M.A., Duca, F.A., Yue, J.T.Y.Y. and Lam, T.K.T. 2014. Insulin Signals Through the Dorsal Vagal Complex to Regulate Energy Balance. *Diabetes*. **63**(3), pp.892–899.

Filippi, B.M., Yang, C.S., Tang, C. and Lam, T.K.T. 2012. Insulin activates Erk1/2 signaling in the dorsal Vagal complex to inhibit glucose production. *Cell Metabolism*. **16**(4), pp.500–510.

Fischer, A.W., Schlein, C., Cannon, B., Heeren, J. and Nedergaard, J. 2019. Intact innervation is essential for diet-induced recruitment of brown adipose tissue. *American Journal of*

Physiology - Endocrinology and Metabolism. **316**(3), pp.E487–E503.

Fischer, A.W., Shabalina, I.G., Mattsson, C.L., Abreu-Vieira, G., Cannon, B., Nedergaard, J. and Petrovic, N. 2017. UCP1 inhibition in cidea-overexpressing mice is physiologically counteracted by brown adipose tissue hyperrecruitment. *American Journal of Physiology - Endocrinology and Metabolism*. **312**(1), pp.E72–E87.

Fisher-Wellman, K.H. and Neufer, P.D. 2012. Linking mitochondrial bioenergetics to insulin resistance via redox biology. *Trends in Endocrinology & Metabolism*. **23**(3), pp.142–153.

Fisher, F.F., Kleiner, S., Douris, N., Fox, E.C., Mepani, R.J., Verdeguer, F., Wu, J., Kharitonenkov, A., Flier, J.S., Maratos-Flier, E. and Spiegelman, B.M. 2012. FGF21 regulates PGC-1α and browning of white adipose tissues in adaptive thermogenesis. *Genes & Development*. **26**(3), pp.271–281.

Florant, G.L., Richardson, R.D., Mahan, S., Singer, L. and Woods, S.C. 1991. Seasonal changes in CSF insulin levels in marmots: insulin may not be a satiety signal for fasting in winter. *https://doi.org/10.1152/ajpregu.1991.260.4.R712*. **260**(4 29/4).

Foster, D.O. and Frydman, M.L. 1979. Tissue distribution of cold-induced thermogenesis in conscious warm- or cold-acclimated rats reevaluated from changes in tissue blood flow: the dominant role of brown adipose tissue in the replacement of shivering by nonshivering thermogenesis. *Canadian journal of physiology and pharmacology*. **57**(3), pp.257–270.

Francy, C.A., Alvarez, F.J.D., Zhou, L., Ramachandran, R. and Mears, J.A. 2015. The Mechanoenzymatic Core of Dynamin-related Protein 1 Comprises the Minimal Machinery Required for Membrane Constriction. *The Journal of Biological Chemistry*. **290**(18), p.11692.

Friedman, J.E., Caro, J.F., Pories, W.J., Azevedo, J.L. and Dohm, G.L. 1994. Glucose metabolism in incubated human muscle: effect of obesity and non-insulin-dependent diabetes mellitus. *Metabolism: clinical and experimental*. **43**(8), pp.1047–1054.

Fromme, T. and Klingenspor, M. 2011. Uncoupling protein 1 expression and high-fat diets. *American Journal of Physiology - Regulatory Integrative and Comparative Physiology*. **300**(1), pp.1–8.

Garcia, C.A., Van Nostrand, D., Majd, M., Atkins, F., Acio, E., Sheikh, A. and Butler, C. 2004. Benzodiazepine-resistant 'brown fat' pattern in positron emission tomography: Two case reports of resolution with temperature control. *Molecular Imaging and Biology*. **6**(6),

pp.368–372.

Garofalo, M.A.R., Kettelhut, I.C., Roselino, J.E.S. and Migliorini, R.H. 1996. Effect of acute cold exposure on norpinephrine turnover rates in rat white adipose tissue. *Journal of the Autonomic Nervous System*. **60**(3), pp.206–208.

Garruti, G., Disord, D.R.-I.J.O.R.M. 1992. Analysis of uncoupling protein and its mRNA in adipose tissue deposits of adult humans. *Int J Obes Relat Metab Disord.* May;**16**(5):383-90.

Ge, Y., Shi, X., Boopathy, S., McDonald, J., Smith, A.W. and Chao, L.H. 2020. Two forms of opa1 cooperate to complete fusion of the mitochondrial inner-membrane. *eLife*. **9**.

Geerling, J.C., Shin, J.W., Chimenti, P.C. and Loewy, A.D. 2010. Paraventricular hypothalamic nucleus: Axonal projections to the brainstem. *Journal of Comparative Neurology*. **518**(9), pp.1460–1499.

Georgescu, T., Lyons, D., Doslikova, B., Garcia, A.P., Marston, O., Burke, L.K., Chianese, R., Lam, B.Y.H., Yeo, G.S.H., Rochford, J.J., Garfield, A.S. and Heisler, L.K. 2020. Neurochemical Characterization of Brainstem Pro-Opiomelanocortin Cells. *Endocrinology*. **161**(4), pp.1–13.

Gesta, S., Tseng, Y.H. and Kahn, C.R. 2007. Developmental origin of fat: tracking obesity to its source. *Cell*. **131**(2), pp.242–256.

Gill, J.A. and La Merrill, M.A. 2017. An emerging role for epigenetic regulation of Pgc-1α expression in environmentally stimulated brown adipose thermogenesis. *Environmental Epigenetics*. **3**(2).

Glick, Z., Teague, R.J. and Bray, G.A. 1981. Brown Adipose Tissue: Thermic Response Increased by a Single Low Protein, High Carbohydrate Meal. *Science*. **213**(4512), pp.1125–1127.

Glowacki, S., Synowiec, E. and Blasiak, J. 2013. The Role of Mitochondrial DNA Damage and Repair in the Resistance of BCR/ABL-Expressing Cells to Tyrosine Kinase Inhibitors. *International Journal of Molecular Sciences*. **14**(8), p.16348.

Golabi, P., Sayiner, M., Fazel, Y., Koenig, A., Henry, L. and Younossi, Z.M. 2016. Current complications and challenges in nonalcoholic steatohepatitis screening and diagnosis. *Expert review of gastroenterology & hepatology*. **10**(1), pp.63–71.

Gomes, L.C., Benedetto, G. Di and Scorrano, L. 2011. During autophagy mitochondria elongate, are spared from degradation and sustain cell viability. *Nature Cell Biology 2011 13:5*. **13**(5), pp.589–598.

Gordon, C. J. (2017) 'The mouse thermoregulatory system: Its impact on translating biomedical data to humans', *Physiology & Behavior*, 179, pp. 55–66. doi: 10.1016/J.PHYSBEH.2017.05.026.

Goto, K., Inui, A., Takimoto, Y., Yuzuriha, H., Asakawa, A., Kawamura, Y., Tsuji, H., Takahara, Y., Takeyama, C., Katsuura, G. and Kasuga, M. 2003. Acute intracerebroventricular administration of either carboxyl-terminal or amino-terminal fragments of agouti-related peptide produces a long-term decrease in energy expenditure in rats. *International journal of molecular medicine*. **12**(3), pp.379–383.

Gottero, C., Broglio, F., Prodam, F., Destefanis, S., Bellone, S., Benso, A., Gauna, C., Arvat, E., Van Der Lely, A.J. and Ghigo, E. 2004. Ghrelin: a link between eating disorders, obesity and reproduction. *Nutritional neuroscience*. **7**(5–6), pp.255–270.

Graham, F.L., Smiley, J., Russell, W.C. and Nairn, R. 1977. Characteristics of a human cell line transformed by DNA from human adenovirus type 5. *Journal of General Virology*. **36**(1), pp.59–72.

Greco, D., Kotronen, A., Westerbacka, J., Puig, O., Arkkila, P., Kiviluoto, T., Laitinen, S., Kolak, M., Fisher, R.M., Hamsten, A., Auvinen, P. and Yki-Järvinen, H. 2008. Gene expression in human NAFLD. *American journal of physiology. Gastrointestinal and liver physiology*. **294**(5).

Grenham, S., Clarke, G., Cryan, J.F. and Dinan, T.G. 2011. Brain-gut-microbe communication in health and disease. *Frontiers in Physiology*. **2 DEC**, p.94.

Grill, H.J. and Hayes, M.R. 2012. Hindbrain neurons as an essential hub in the neuroanatomically distributed control of energy balance. *Cell Metabolism*. **16**(3), pp.296–309.

Grill, H.J. and Hayes, M.R. 2009. The nucleus tractus solitarius: a portal for visceral afferent signal processing, energy status assessment and integration of their combined effects on food intake. *International journal of obesity (2005)*. **33 Suppl 1**(SUPPL. 1).

Group, T.L.A.R. 2013. Cardiovascular Effects of Intensive Lifestyle Intervention in Type 2 Diabetes. *https://doi.org/10.1056/NEJMoa1212914*. **369**(2), pp.145–154.

Guerciolini, R. 1997. Mode of action of orlistat. *International Journal of Obesity and Related Metabolic Disorders : Journal of the International Association for the Study of Obesity*. **21 Suppl 3**(SUPPL. 3), pp.S12-23.

Gunawardana, S.C. and Piston, D.W. 2012. Reversal of Type 1 Diabetes in Mice by Brown

Adipose Tissue Transplant. *Diabetes*. **61**(3), pp.674–682.

Gundersen, A.E., Kugler, B.A., McDonald, P.M., Veraksa, A., Houmard, J.A. and Zou, K. 2019. Altered mitochondrial network morphology and regulatory proteins in mitochondrial quality control in myotubes from severely obese humans with or without type 2 diabetes. *https://doi.org/10.1139/apnm-2019-0208*. **45**(3), pp.283–293.

Gunter, T.E., Buntinas, L., Sparagna, G.C. and Gunter, K.K. 1998. The Ca2+ transport mechanisms of mitochondria and Ca2+ uptake from physiological-type Ca2+ transients. *Biochimica et Biophysica Acta - Bioenergetics*. **1366**(1–2), pp.5–15.

Hackl, M.T., Fürnsinn, C., Schuh, C.M., Krssak, M., Carli, F., Guerra, S., Freudenthaler, A., Baumgartner-Parzer, S., Helbich, T.H., Luger, A., Zeyda, M., Gastaldelli, A., Buettner, C. and Scherer, T. 2019a. Brain leptin reduces liver lipids by increasing hepatic triglyceride secretion and lowering lipogenesis. *Nature Communications 2019 10:1*. **10**(1), pp.1–13.

Hahn, T.M., Breininger, J.F., Baskin, D.G. and Schwartz, M.W. 1998. Coexpression of Agrp and NPY in fasting-activated hypothalamic neurons. *Nature Neuroscience*. **1**(4), pp.271–272.

Haissaguerre, M., Ferrière, A., Simon, V., Saucisse, N., Dupuy, N., André, C., Clark, S., Guzman-Quevedo, O., Tabarin, A. and Cota, D. 2018. mTORC1-dependent increase in oxidative metabolism in POMC neurons regulates food intake and action of leptin. *Molecular Metabolism*. **12**, pp.98–106.

Han, H.S., Kang, G., Kim, J.S., Choi, B.H. and Koo, S.H. 2016a. Regulation of glucose metabolism from a liver-centric perspective. *Experimental & Molecular Medicine 2016 48:3*. **48**(3), pp.e218–e218.

Han, M.S., White, A., Perry, R.J., Camporez, J.P., Hidalgo, J., Shulman, G.I. and Davis, R.J. 2020. Regulation of adipose tissue inflammation by interleukin 6. *Proceedings of the National Academy of Sciences of the United States of America*. **117**(6), pp.2751–2760.

Hankenson FC, Marx JO, Gordon CJ, David JM. Effects of Rodent Thermoregulation on Animal Models in the Research Environment. Comp Med. 2018 Dec 1;68(6):425-438. Epub 2018 Nov 20.

Hansen, J.B. and Kristiansen, K. 2006. Regulatory circuits controlling white versus brown adipocyte differentiation. *Biochemical Journal*. **398**(2), pp.153–168.

Hany, T.F., Gharehpapagh, E., Kamel, E.M., Buck, A., Himms-Hagen, J. and Von Schulthess, G.K. 2002. Brown adipose tissue: a factor to consider in symmetrical tracer uptake in the neck and upper chest region. *European Journal of Nuclear Medicine and Molecular*

Imaging 2002 29:10. **29**(10), pp.1393–1398.

Hao, L., Scott, S., Abbasi, M., Zu, Y., Khan, M.S.H., Yang, Y., Wu, D., Zhao, L. and Wang, S. 2019. Beneficial Metabolic Effects of Mirabegron In Vitro and in High-Fat Diet-Induced Obese Mice. *The Journal of Pharmacology and Experimental Therapeutics*. **369**(3), p.419.

Haque, M.S., Minokoshi, Y., Hamai, M., Iwai, M., Horiuchi, M. and Shimazu, T. 1999. Role of the sympathetic nervous system and insulin in enhancing glucose uptake in peripheral tissues after intrahypothalamic injection of leptin in rats. *Diabetes*. **48**(9), pp.1706–1712.

Harms, M.J., Ishibashi, J., Wang, W., Lim, H.W., Goyama, S., Sato, T., Kurokawa, M., Won, K.J. and Seale, P. 2014. Prdm16 is required for the maintenance of brown adipocyte identity and function in adult mice. *Cell metabolism*. **19**(4), p.593.

Harney, D.J., Cielesh, M., Chu, R., Cooke, K.C., James, D.E., Stöckli, J. and Larance, M. 2021. Proteomics analysis of adipose depots after intermittent fasting reveals visceral fat preservation mechanisms. *Cell reports*. **34**(9).

Hatting, M., Tavares, C.D.J., Sharabi, K., Rines, A.K. and Puigserver, P. 2018. Insulin regulation of gluconeogenesis. *Annals of the New York Academy of Sciences*. **1411**(1), p.21.

Havel, R.J., Kane, J.P., Balasse, E.O., Segel, N. and Basso, L. V. 1970. Splanchnic metabolism of free fatty acids and production of triglycerides of very low density lipoproteins in normotriglyceridemic and hypertriglyceridemic humans. *The Journal of clinical investigation*. **49**(11), pp.2017–2035.

Hayes, M.R., Skibicka, K.P., Leichner, T.M., Guarnieri, D.J., DiLeone, R.J., Bence, K.K. and Grill, H.J. 2010. Endogenous Leptin Signaling in the Caudal Nucleus Tractus Solitarius and Area Postrema Is Required for Energy Balance Regulation. *Cell Metabolism*. **11**(1), pp.77–83.

He, A., Chen, X., Tan, M., Chen, Y., Lu, D., Zhang, X., Dean, J.M., Razani, B. and Lodhi, I.J. 2020. Acetyl-CoA Derived from Hepatic Peroxisomal β-Oxidation Inhibits Autophagy and Promotes Steatosis via mTORC1 Activation. *Molecular Cell*. **79**(1), pp.30-42.e4.

Heaton, J.M. 1972. The distribution of brown adipose tissue in the human. *Journal of Anatomy*. **112**(Pt 1), p.35.

Helle, S.C.J., Feng, Q., Aebersold, M.J., Hirt, L., Grüter, R.R., Vahid, A., Sirianni, A., Mostowy, S., Snedeker, J.G., Šarić, A., Idema, T., Zambelli, T. and Kornmann, B. 2017. Mechanical force induces mitochondrial fission. *eLife*. **6**.

Hemmings, B.A. and Restuccia, D.F. 2012. PI3K-PKB/Akt Pathway. *Cold Spring Harbor Perspectives in Biology*. **4**(9).

Hermes, S.M., Andresen, M.C. and Aicher, S.A. 2016. Localization of TRPV1 and P2X3 in unmyelinated and myelinated vagal afferents in the rat. *Journal of Chemical Neuroanatomy*. **72**, pp.1–7.

Herrera, D., Chao, M., Kirchner, M.K., Pham, C., Foppen, E., Denis, R.G., Castel, J., Morel, C., Montalban, E., Hassouna, R., Bui, L.-C., Renault, J., Mouffle, C., García-Cáceres, C., Tschöp, M.H., Li, D., Martin, C., Stern, J.E. and Luquet, S.H. 2022. Hypothalamic astrocytes control systemic glucose metabolism and energy balance via regulation of extra-synaptic glutamate signaling. *bioRxiv*., 2022.02.16.480737.

Hill, J.W. 2010. Gene Expression and the Control of Food Intake by Hypothalamic POMC/CART Neurons. *Open neuroendocrinology journal (Online)*. **3**, p.21.

Hillard, C.J., Beatka, M. and Sarvaideo, J. 2016. Endocannabinoid Signaling and the Hypothalamic-Pituitary-Adrenal Axis. *Comprehensive Physiology*. **7**(1), p.1.

Himms-Hagen, J. 1989. Brown adipose tissue thermogenesis and obesity. *Progress in lipid research*. **28**(2), pp.67–115.

Hiroshima, Y., Yamamoto, T., Watanabe, M., Baba, Y. and Shinohara, Y. 2018. Effects of cold exposure on metabolites in brown adipose tissue of rats. *Molecular Genetics and Metabolism Reports*. **15**, pp.36–42.

Hirosumi, J., Tuncman, G., Chang, L., Görgün, C.Z., Uysal, K.T., Maeda, K., Karin, M. and Hotamisligil, G.S. 2002. A central role for JNK in obesity and insulin resistance. *Nature 2002 420:6913*. **420**(6913), pp.333–336.

Hoffmann, L.S., Larson, C.J. and Pfeifer, A. 2016. cGMP and Brown Adipose Tissue. *Handbook of experimental pharmacology*. **233**, pp.283–299.

Hogan, S., Coscina, D. V. and Himms-Hagen, J. 1982. Brown adipose tissue of rats with obesity-inducing ventromedial hypothalamic lesions. *https://doi.org/10.1152/ajpendo.1982.243.4.E338*. **6**(4).

Holloway, G.P., Bonen, A. and Spriet, L.L. 2009. Regulation of skeletal muscle mitochondrial fatty acid metabolism in lean and obese individuals. *The American Journal of Clinical Nutrition*. **89**(1), pp.455S-462S.

Holmström, M.H., Iglesias-Gutierrez, E., Zierath, J.R. and Garcia-Roves, P.M. 2012. Tissue-specific control of mitochondrial respiration in obesity-related insulin resistance and diabetes. *American journal of physiology. Endocrinology and metabolism*. **302**(6), pp.731–739.

Holstege G, Kuypers HG. The anatomy of brain stem pathways to the spinal cord in cat. A labeled amino acid tracing study. Prog Brain Res. 1982;57:145-75. doi: 10.1016/S0079-6123(08)64128-X. PMID: 7156396.Gao, A.W. and Houtkooper, R.H. 2014. Mitochondrial fission: Firing up mitochondria in brown adipose tissue. *EMBO Journal*. **33**(5), pp.401–402.

Hondares, E., Iglesias, R., Giralt, A., Gonzalez, F.J., Giralt, M., Mampel, T. and Villarroya, F. 2011. Thermogenic activation induces FGF21 expression and release in brown adipose tissue. *Journal of Biological Chemistry*. **286**(15), pp.12983–12990.

Hong, J., Stubbins, R.E., Smith, R.R., Harvey, A.E. and Nu̇̃ez, N.P. 2009. Differential susceptibility to obesity between male, female and ovariectomized female mice. *Nutrition Journal*. **8**(1), p.11.

Hotamisligil, G.S., Shargill, N.S. and Spiegelman, B.M. 1993. Adipose expression of tumor necrosis factor-alpha: direct role in obesity-linked insulin resistance. *Science (New York, N.Y.)*. **259**(5091), pp.87–91.

Houmard, J.A., Pories, W.J. and Dohm, G.L. 2011. Is there a metabolic program in the skeletal muscle of obese individuals? *Journal of Obesity*. **2011**.

Houmard, J.A., Pories, W.J. and Dohm, G.L. 2012. Severe obesity: Evidence for a deranged metabolic program in skeletal muscle? *Exercise and Sport Sciences Reviews*. **40**(4), pp.204–210.

Hoyumpa, A.M., Greene, H.L., Dunn, G.D. and Schenker, S. 1975. Fatty liver: biochemical and clinical considerations. *The American journal of digestive diseases*. **20**(12), pp.1142–1170.

Hruby, A., Manson, J.A.E., Qi, L., Malik, V.S., Rimm, E.B., Sun, Q., Willett, W.C. and Hu, F.B. 2016. Determinants and Consequences of Obesity. *American Journal of Public Health*. **106**(9), p.1656.

Hrvatin, S., Sun, S., Wilcox, O.F. *et al.* Neurons that regulate mouse torpor. *Nature* **583**, 115–121 (2020).

Hugie, T., Halvorson, I. and Thornhill, J. 1992. Brown adipose tissue temperature responses following electrical stimulation of ventromedial hypothalamic and lateral preoptic areas or after norepinephrine infusion to long evans or sprague-dawley rats. *Brain Research*. **575**(1), pp.57–62.

Hughes DA, Jastroch M, Stoneking M, Klingenspor M. Molecular evolution of UCP1 and the evolutionary history of mammalian non-shivering thermogenesis. BMC Evol Biol. 2009 Jan 7;9:4. doi: 10.1186/1471-2148-9-4. PMID: 19128480; PMCID: PMC2627829.

Hussain, Z. and Khan, J.A. 2017. Food intake regulation by leptin: Mechanisms mediating gluconeogenesis and energy expenditure. *Asian Pacific Journal of Tropical Medicine*. **10**(10), pp.940–944.

Imai, J. and Katagiri, H. 2022. Regulation of systemic metabolism by the autonomic nervous system consisting of afferent and efferent innervation. *International immunology*. **34**(2), pp.67–79.

Iqbal, J. and Hussain, M.M. 2009. Intestinal lipid absorption. *American Journal of Physiology - Endocrinology and Metabolism*. **296**(6), p.E1183.

Item, F., Wueest, S., Lemos, V., Stein, S., Lucchini, F.C., Denzler, R., Fisser, M.C., Challa, T.D., Pirinen, E., Kim, Y., Hemmi, S., Gulbins, E., Gross, A., O'Reilly, L.A., Stoffel, M., Auwerx, J. and Konrad, D. 2017. Fas cell surface death receptor controls hepatic lipid metabolism by regulating mitochondrial function. *Nature Communications*. **8**(1), pp.1–10.

Ito, T., Tanuma, Y., Yamamoto, M. and Yokochi, C. 1975. The Occurrence of Brown Adipose Tissue in Perirenal Fat in Japanese. *Archivum histologicum japonicum*. **38**(1), pp.43–70.

Jäer, S., Handschin, C., St-Pierre, J. and Spiegelman, B.M. 2007. AMP-activated protein kinase (AMPK) action in skeletal muscle via direct phosphorylation of PGC-1alpha. *Proceedings of the National Academy of Sciences of the United States of America*. **104**(29), pp.12017–12022.

Javid, F.A., Bulmer, D.C., Broad, J., Aziz, Q., Dukes, G.E. and Sanger, G.J. 2013. Anti-emetic and emetic effects of erythromycin in Suncus murinus: Role of vagal nerve activation, gastric motility stimulation and motilin receptors. *European Journal of Pharmacology*. **699**(1–3), pp.48–54.

Jensen-Urstad, A.P.L. and Semenkovich, C.F. 2012. Fatty acid synthase and liver triglyceride metabolism: housekeeper or messenger? *Biochimica et Biophysica Acta*. **1821**(5), p.747.

Jensen, V.S., Hvid, H., Damgaard, J., Nygaard, H., Ingvorsen, C., Wulff, E.M., Lykkesfeldt, J. and Fledelius, C. 2018. Dietary fat stimulates development of NAFLD more potently than dietary fructose in Sprague-Dawley rats. *Diabetology and Metabolic Syndrome*. **10**(1), pp.1–13.

Jeong, J.H., Lee, D.K., Blouet, C., Ruiz, H.H., Buettner, C., Chua, S., Schwartz, G.J. and Jo, Y.H.

2015. Cholinergic neurons in the dorsomedial hypothalamus regulate mouse brown adipose tissue metabolism. *Molecular Metabolism*. **4**(6), pp.483–492.

Jespersen NZ, Larsen TJ, Peijs L, Daugaard S, Homøe P, Loft A, de Jong J, Mathur N, Cannon B, Nedergaard J, Pedersen BK, Møller K, Scheele C. A classical brown adipose tissue mRNA signature partly overlaps with brite in the supraclavicular region of adult humans. Cell Metab. 2013 May 7;17(5):798-805. doi: 10.1016/j.cmet.2013.04.011. PMID: 23663743.

Ježek, J., Cooper, K.F. and Strich, R. 2018. Reactive Oxygen Species and Mitochondrial Dynamics: The Yin and Yang of Mitochondrial Dysfunction and Cancer Progression. *Antioxidants (Basel, Switzerland)*. **7**(1).

Jheng, H.-F., Tsai, P.-J., Guo, S.-M., Kuo, L.-H., Chang, C.-S., Su, I.-J., Chang, C.-R. and Tsai, Y.-S. 2012. Mitochondrial Fission Contributes to Mitochondrial Dysfunction and Insulin Resistance in Skeletal Muscle. *Molecular and Cellular Biology*. **32**(2), pp.309–319.

Jimba, S., Nakagami, T., Takahashi, M., Wakamatsu, T., Hirota, Y., Iwamoto, Y. and Wasada, T. 2005. Prevalence of non-alcoholic fatty liver disease and its association with impaired glucose metabolism in Japanese adults. *Diabetic Medicine*. **22**(9), pp.1141–1145.

Jin, S., Yoon, N.A., Liu, Z.W., Song, J.E., Horvath, T.L., Kim, J.D. and Diano, S. 2021. Drp1 is required for AgRP neuronal activity and feeding. *eLife*. **10**.

Jocken, J.W.E., Moro, C., Goossens, G.H., Hansen, D., Mairal, A., Hesselink, M.K.C., Langin, D., Van Loon, L.J.C. and Blaak, E.E. 2010. Skeletal Muscle Lipase Content and Activity in Obesity and Type 2 Diabetes. *The Journal of Clinical Endocrinology & Metabolism*. **95**(12), pp.5449–5453.

Jung, K.M., Clapper, J.R., Fu, J., D'Agostino, G., Guijarro, A., Thongkham, D., Avanesian, A., Astarita, G., DiPatrizio, N. V., Frontini, A., Cinti, S., Diano, S. and Piomelli, D. 2012. 2-Arachidonoylglycerol signaling in forebrain regulates systemic energy metabolism. *Cell Metabolism*. **15**(3), pp.299–310.

Kajimura, S. and Saito, M. 2014. A New Era in Brown Adipose Tissue Biology: Molecular Control of Brown Fat Development and Energy Homeostasis. *http://dx.doi.org/10.1146/annurev-physiol-021113-170252*. **76**, pp.225–249.

Kakuma, T., Wang, Z.-W., Pan, W., Unger, R.H. and Zhou, Y.-T. 2000. Role of Leptin in Peroxisome Proliferator-Activated Receptor Gamma Coactivator-1 Expression*The nucleotide sequence(s) reported in this paper has been submitted to the GenBank nucleotide sequence databases, with the accession number(s) AB025784. We

acknowledge the grant support of the Department of Veterans Affairs Institutional Support, the National Institutes of Health (DK-02700–37), The National Institutes of Health/Juvenile Diabetes Foundation Diabetes Interdisciplinary Research Program, and. *Endocrinology*. **141**(12), pp.4576–4582.

Kalia, R., Wang, R.Y.R., Yusuf, A., Thomas, P. V., Agard, D.A., Shaw, J.M. and Frost, A. 2018. Structural basis of mitochondrial receptor binding and constriction by DRP1. *Nature*. **558**(7710), pp.401–405.

Kastanias, P., Mackenzie, K., Robinson, S. and Wang, W. 2017. Medical Complications Resulting from Severe Obesity. *Psychiatric Care in Severe Obesity*., pp.49–73.

Kawano, Y. and Cohen, D.E. 2013. Mechanisms of hepatic triglyceride accumulation in non-alcoholic fatty liver disease. *Journal of Gastroenterology*. **48**(4), p.434.

Kelly, T., Yang, W., Chen, C.S., Reynolds, K. and He, J. 2008. Global burden of obesity in 2005 and projections to 2030. *International journal of obesity (2005)*. **32**(9), pp.1431–1437.

Kern, L., Mittenbühler, M.J., Vesting, A.J., Ostermann, A.L., Wunderlich, C.M. and Wunderlich, F.T. 2019. Obesity-Induced TNFα and IL-6 Signaling: The Missing Link between Obesity and Inflammation—Driven Liver and Colorectal Cancers. *Cancers*. **11**(1).

Kershaw, E.E. and Flier, J.S. 2004. Adipose Tissue as an Endocrine Organ. *The Journal of Clinical Endocrinology & Metabolism*. **89**(6), pp.2548–2556.

Kim, B.H., Joo, Y., Kim, M.S., Choe, H.K., Tong, Q. and Kwon, O. 2021. Effects of Intermittent Fasting on the Circulating Levels and Circadian Rhythms of Hormones. *Endocrinology and Metabolism*. **36**(4), p.745.

Kim, D.Y., Heo, G., Kim, M., Kim, H., Jin, J.A., Kim, H.K., Jung, S., An, M., Ahn, B.H., Park, J.H., Park, H.E., Lee, M., Lee, J.W., Schwartz, G.J. and Kim, S.Y. 2020. A neural circuit mechanism for mechanosensory feedback control of ingestion. *Nature*. **580**(7803), pp.376–380.

Kim, E.M., O'Hare, E., Grace, M.K., Welch, C.C., Billington, C.J. and Levine, A.S. 2000. ARC POMC mRNA and PVN alpha-MSH are lower in obese relative to lean zucker rats. *Brain research*. **862**(1–2), pp.11–16.

Kim, J.D., Yoon, N.A., Jin, S. and Diano, S. 2019. Microglial UCP2 Mediates Inflammation and Obesity Induced by High-Fat Feeding. *Cell Metabolism*. **30**(5), pp.952-962.e5.

Kim, J.G., Suyama, S., Koch, M., Jin, S., Argente-Arizon, P., Argente, J., Liu, Z.W., Zimmer, M.R., Jeong, J.K., Szigeti-Buck, K., Gao, Y., Garcia-Caceres, C., Yi, C.X., Salmaso, N., Vaccarino,

F.M., Chowen, J., Diano, S., Dietrich, M.O., Tschöp, M.H. and Horvath, T.L. 2014. Leptin signaling in astrocytes regulates hypothalamic neuronal circuits and feeding. *Nature Neuroscience*. **17**(7), pp.908–910.

Kleiner, D.E., Brunt, E.M., Van Natta, M., Behling, C., Contos, M.J., Cummings, O.W., Ferrell, L.D., Liu, Y.C., Torbenson, M.S., Unalp-Arida, A., Yeh, M., McCullough, A.J. and Sanyal, A.J. 2005. Design and validation of a histological scoring system for nonalcoholic fatty liver disease. *Hepatology*. **41**(6), pp.1313–1321.

Kleiner, S., Mepani, R.J., Laznik, D., Ye, L., Jurczak, M.J., Jornayvaz, F.R., Estall, J.L., Bhowmick, D.C., Shulman, G.I. and Spiegelman, B.M. 2012. Development of insulin resistance in mice lacking PGC-1α in adipose tissues. *Proceedings of the National Academy of Sciences of the United States of America*. **109**(24), pp.9635–9640.

Klöckener, T., Hess, S., Belgardt, B.F., Paeger, L., Verhagen, L.A.W., Husch, A., Sohn, J.W., Hampel, B., Dhillon, H., Zigman, J.M., Lowell, B.B., Williams, K.W., Elmquist, J.K., Horvath, T.L., Kloppenburg, P. and Brüning, J.C. 2011. High-fat Feeding Promotes Obesity via Insulin Receptor/PI3k-Dependent Inhibition of SF-1 VMH Neurons. *Nature neuroscience*. **14**(7), p.911.

Klöting, N., Fasshauer, M., Dietrich, A., Kovacs, P., Schön, M.R., Kern, M., Stumvoll, M. and Blüher, M. 2010. Insulin-sensitive obesity. *American Journal of Physiology - Endocrinology and Metabolism*. **299**(3).

Knott, R.M., Trayhurn, P. and Hesketh, J.E. 1992. Changes in insulin-receptor mRNA levels in skeletal muscle and brown adipose tissue of weanling rats during fasting and refeeding. *British Journal of Nutrition*. **68**(3), pp.583–592.

Kobashi, C., Asamizu, S., Ishiki, M., Iwata, M., Usui, I., Yamazaki, K., Tobe, K., Kobayashi, M. and Urakaze, M. 2009. Inhibitory effect of IL-8 on insulin action in human adipocytes via MAP kinase pathway. *Journal of Inflammation (London, England)*. **6**, p.25.

Kogure, A., Yoshida, T., Sakane, N., Umekawa, T., Takakura, Y. and Kondo, M. 1998. Synergic effect of polymorphisms in uncoupling protein 1 and β3- adrenergic receptor genes on weight loss in obese Japanese [2]. *Diabetologia*. **41**(11), p.1399.

Könner, A.C., Janoschek, R., Plum, L., Jordan, S.D., Rother, E., Ma, X., Xu, C., Enriori, P., Hampel, B., Barsh, G.S., Kahn, C.R., Cowley, M.A., Ashcroft, F.M. and Brüning, J.C. 2007. Insulin Action in AgRP-Expressing Neurons Is Required for Suppression of Hepatic Glucose Production. *Cell Metabolism*. **5**(6), pp.438–449.

Kooijman, S., Boon, M.R., Parlevliet, E.T., Geerling, J.J., Van De Pol, V., Romijn, J.A., Havekes, L.M., Meurs, I. and Rensen, P.C.N. 2014. Inhibition of the central melanocortin system decreases brown adipose tissue activity. *Journal of Lipid Research*. **55**(10), p.2022.

Koonen, D.P.Y., Jacobs, R.L., Febbraio, M., Young, M.E., Soltys, C.L.M., Ong, H., Vance, D.E. and Dyck, J.R.B. 2007. Increased hepatic CD36 expression contributes to dyslipidemia associated with diet-induced obesity. *Diabetes*. **56**(12), pp.2863–2871.

Korbonits, M., Blaine, D., Elia, M. and Powell-Tuck, J. 2007. Metabolic and hormonal changes during the refeeding period of prolonged fasting. *European Journal of Endocrinology*. **157**(2), pp.157–166.

Korenblat, K.M., Fabbrini, E., Mohammed, B.S. and Klein, S. 2008. Liver, muscle, and adipose tissue insulin action is directly related to intrahepatic triglyceride content in obese subjects. *Gastroenterology*. **134**(5), pp.1369–1375.

Koves, T.R., Li, P., An, J., Akimoto, T., Slentz, D., Ilkayeva, O., Dohm, G.L., Yan, Z., Newgard, C.B. and Muoio, D.M. 2005. Peroxisome proliferator-activated receptor-γ co-activator 1α-mediated metabolic remodeling of skeletal myocytes mimics exercise training and reverses lipid-induced mitochondrial inefficiency. *Journal of Biological Chemistry*. **280**(39), pp.33588–33598.

Krashes, M.J., Shah, B.P., Koda, S. and Lowell, B.B. 2013. Rapid versus delayed stimulation of feeding by the endogenously released agRP neuron mediators GABA, NPY, and AgRP. *Cell Metabolism*. **18**(4), pp.588–595.

Kraus, F. and Ryan, M.T. 2017. The constriction and scission machineries involved in mitochondrial fission. *Journal of cell science*. **130**(18), pp.2953–2960.

Kuipers, E.N., Held, N.M., Panhuis, W. in het, Modder, M., Ruppert, P.M.M., Kersten, S., Kooijman, S., Guigas, B., Houtkooper, R.H., Rensen, P.C.N. and Boon, M.R. 2019. A single day of high-fat diet feeding induces lipid accumulation and insulin resistance in brown adipose tissue in mice. *American Journal of Physiology - Endocrinology and Metabolism*. **317**(5), pp.E820–E830.

De La Cour, C.D., Lindqvist, A., Egecioglu, E., Tung, Y.C.L., Surve, V., Ohlsson, C., Jansson, J.O., Erlanson-Albertsson, C., Dickson, S.L. and Håkanson, R. 2005. Ghrelin treatment reverses the reduction in weight gain and body fat in gastrectomised mice. *Gut*. **54**(7), pp.907–913.

Labban, R.S.M., Alfawaz, H., Almnaizel, A.T., Hassan, W.M., Bhat, R.S., Moubayed, N.M.S.,

Bjørklund, G. and El-Ansary, A. 2020. High-fat diet-induced obesity and impairment of brain neurotransmitter pool. *Translational Neuroscience*. **11**(1), p.147.

Labbé, Sebastien M., Caron, A., Lanfray, D., Monge-Rofarello, B., Bartness, T.J. and Richard, D. 2015. Hypothalamic control of brown adipose tissue thermogenesis. *Frontiers in Systems Neuroscience*. **9**(November), p.150.

Lafontan, M. and Langin, D. 2009. Lipolysis and lipid mobilization in human adipose tissue. *Progress in Lipid Research*. **48**(5), pp.275–297.

Lam, T.K.T., Pocai, A., Gutierrez-Juarez, R., Obici, S., Bryan, J., Aguilar-Bryan, L., Schwartz, G.J. and Rossetti, L. 2005. Hypothalamic sensing of circulating fatty acids is required for glucose homeostasis. *Nature Medicine*. **11**(3), pp.320–327.

Langley, M.R., Yoon, H., Kim, H.N., Choi, C. Il, Simon, W., Kleppe, L., Lanza, I.R., LeBrasseur, N.K., Matveyenko, A. and Scarisbrick, I.A. 2020. High fat diet consumption results in mitochondrial dysfunction, oxidative stress, and oligodendrocyte loss in the central nervous system. *Biochimica et biophysica acta. Molecular basis of disease*. **1866**(3), p.165630.

Lans, A.A.J.J. van der, Hoeks, J., Brans, B., Vijgen, G.H.E.J., Visser, M.G.W., Vosselman, M.J., Hansen, J., Jörgensen, J.A., Wu, J., Mottaghy, F.M., Schrauwen, P. and Lichtenbelt, W.D. van M. 2013. Cold acclimation recruits human brown fat and increases nonshivering thermogenesis. *The Journal of Clinical Investigation*. **123**(8), pp.3395–3403.

Lasar, D., Rosenwald, M., Kiehlmann, E., Balaz, M., Tall, B., Opitz, L., Lidell, M.E., Zamboni, N., Krznar, P., Sun, W., Varga, L., Stefanicka, P., Ukropec, J., Nuutila, P., Virtanen, K., Amri, E.Z., Enerbäck, S., Wahli, W. and Wolfrum, C. 2018. Peroxisome Proliferator Activated Receptor Gamma Controls Mature Brown Adipocyte Inducibility through Glycerol Kinase. *Cell Reports*. **22**(3), pp.760–773.

Lau, B.K., Murphy-Royal, C., Kaur, M., Qiao, M., Bains, J.S., Gordon, G.R. and Borgland, S.L. 2021. Obesity-induced astrocyte dysfunction impairs heterosynaptic plasticity in the orbitofrontal cortex. *Cell Reports*. **36**(7).

Law, J., Bloor, I., Budge, H. and Symonds, M.E. 2014. The influence of sex steroids on adipose tissue growth and function. *Hormone molecular biology and clinical investigation*. **19**(1), pp.13–24.

Le, W., Abbas, A.S., Sprecher, H., Vockley, J. and Schulz, H. 2000. Long-chain acyl-CoA dehydrogenase is a key enzyme in the mitochondrial β-oxidation of unsaturated fatty

acids. *Biochimica et Biophysica Acta - Molecular and Cell Biology of Lipids*. **1485**(2–3), pp.121–128.

Lean, M.E.J., James, W.P.T., Jennings, G. and Trayhurn, P. 1986a. Brown adipose tissue in patients with phaeochromocytoma. *International Journal of Obesity*. **10**(3), pp.219–227.

Lean, M.E.J., James, W.P.T., Jennings, G. and Trayhurn, P. 1986b. Brown adipose tissue uncoupling protein content in human infants, children and adults. *Clinical Science (London, England : 1979)*. **71**(3), pp.291–297.

Lebrun, P., Cognard, E., Bellon-Paul, R., Gontard, P., Filloux, C., Jehl-Pietri, C., Grimaldi, P., Samson, M., Pénicaud, L., Ruberte, J., Ferre, T., Pujol, A., Bosch, F. and Van Obberghen, E. 2009. Constitutive expression of suppressor of cytokine signalling-3 in skeletal muscle leads to reduced mobility and overweight in mice. *Diabetologia*. **52**(10), pp.2201–2212.

Lechan, R.M. and Toni, R. 2016. Functional Anatomy of the Hypothalamus and Pituitary. *Oxford Textbook of Endocrinology and Diabetes 3e*., pp.111–122.

Lee, J., Choi, J., Selen Alpergin, E.S., Zhao, L., Hartung, T., Scafidi, S., Riddle, R.C. and Wolfgang, M.J. 2017. Loss of Hepatic Mitochondrial Long-Chain Fatty Acid Oxidation Confers Resistance to Diet-Induced Obesity and Glucose Intolerance. *Cell Reports*. **20**(3), pp.655–667.

Lee, P., Swarbrick, M.M., Ting Zhao, J., Y Ho, K.K., Program, O., Vincent, S. and of Medicine, F.P. 2011. Inducible Brown Adipogenesis of Supraclavicular Fat in Adult Humans. *Endocrinology*. **152**(10), pp.3597–3602.

Leon-Acuna, A., Alcala-Diaz, J.F., Delgado-Lista, J., Torres-Peøa, J.D., Lopez-Moreno, J., Camargo, A., Garcia-Rios, A., Marin, C., Gomez-Delgado, F., Caballero, J., Van-Ommen, B., Malagon, M.M., Perez-Martinez, P. and Lopez-Miranda, J. 2016. Hepatic insulin resistance both in prediabetic and diabetic patients determines postprandial lipoprotein metabolism: From the CORDIOPREV study. *Cardiovascular Diabetology*. **15**(1), pp.1–10.

Levin, B.E., Routh, V.H., Kang, L., Sanders, N.M. and Dunn-Meynell, A.A. 2004. Neuronal GlucosensingWhat Do We Know After 50 Years? *Diabetes*. **53**(10), pp.2521–2528.

Levy, S.L., White, J.J. and Sillitoe, R. V. 2015. Wheat germ agglutinin (WGA) tracing: A classic approach for unraveling neural circuitry. *Neural Tracing Methods: Tracing Neurons and Their Connections*., pp.51–66.

Lewis, S.C., Uchiyama, L.F. and Nunnari, J. 2016. ER-mitochondria contacts couple mtDNA synthesis with Mitochondrial division in human cells. *Science*. **353**(6296).

Li, C., Li, L., Lian, J., Watts, R., Nelson, R., Goodwin, B. and Lehner, R. 2015. Roles of Acyl-CoA: Diacylglycerol acyltransferases 1 and 2 in triacylglycerol synthesis and secretion in primary hepatocytes. *Arteriosclerosis, Thrombosis, and Vascular Biology*. **35**(5), pp.1080–1091.

Li, G., Zhang, Y., Rodrigues, E., Zheng, D.H., Matheny, M., Cheng, K.Y. and Scarpace, P.J. 2007. Melanocortin activation of nucleus of the solitary tract avoids anorectic tachyphylaxis and induces prolonged weight loss. *American Journal of Physiology - Endocrinology and Metabolism*. **293**(1), pp.252–258.

Li, L.Y., Luo, X. and Wang, X. 2001. Endonuclease G is an apoptotic DNase when released from mitochondria. *Nature*. **412**(6842), pp.95–99.

Li, R.J.W., Batchuluun, B., Zhang, S.Y., Abraham, M.A., Wang, B., Lim, Y.M., Yue, J.T.Y. and Lam, T.K.T. 2021. Nutrient infusion in the dorsal vagal complex controls hepatic lipid and glucose metabolism in rats. *iScience*. **24**(4), p.102366.

Li, R.Y., Zhang, Q.H., Liu, Z., Qiao, J., Zhao, S.X., Shao, L., Xiao, H.S., Chen, J.L., Chen, M.D. and Song, H.D. 2006. Effect of short-term and long-term fasting on transcriptional regulation of metabolic genes in rat tissues. *Biochemical and Biophysical Research Communications*. **344**(2), pp.562–570.

Li, S., Brown, M.S. and Goldstein, J.L. 2010. Bifurcation of insulin signaling pathway in rat liver: mTORC1 required for stimulation of lipogenesis, but not inhibition of gluconeogenesis. *Proceedings of the National Academy of Sciences of the United States of America*. **107**(8), p.3441.

Li, Y., South, T., Han, M., Chen, J., Wang, R. and Huang, X.F. 2009. High-fat diet decreases tyrosine hydroxylase mRNA expression irrespective of obesity susceptibility in mice. *Brain Research*. **1268**, pp.181–189.

Lian, C.Y., Zhai, Z.Z., Li, Z.F. and Wang, L. 2020. High fat diet-triggered non-alcoholic fatty liver disease: A review of proposed mechanisms. *Chemico-Biological Interactions*. **330**, p.109199.

Liang, H., Yin, B., Zhang, H., Zhang, S., Zeng, Q., Wang, J., Jiang, X., Yuan, L., Wang, C.Y. and Li, Z. 2008. Blockade of Tumor Necrosis Factor (TNF) Receptor Type 1-Mediated TNF-α Signaling Protected Wistar Rats from Diet-Induced Obesity and Insulin Resistance. *Endocrinology*. **149**(6), pp.2943–2951.

Liang, W., Menke, A.L., Driessen, A., Koek, G.H., Lindeman, J.H., Stoop, R., Havekes, L.M.,

Kleemann., R. and Van Den Hoek, A.M. 2014. Establishment of a general NAFLD scoring system for rodent models and comparison to human liver pathology. *PLoS ONE*. **9**(12).

Lin, H. V., Plum, L., Ono, H., Gutiérrez-Juárez, R., Shanabrough, M., Borok, E., Horvath, T.L., Rossetti, L. and Accili, D. 2010. Divergent regulation of energy expenditure and hepatic glucose production by insulin receptor in agouti-related protein and POMC neurons. *Diabetes*. **59**(2), pp.337–346.

Lin, L., Lee, J.H., Bongmba, O.Y.N., Ma, X., Zhu, X., Sheikh-Hamad, D. and Sun, Y. 2014. The suppression of ghrelin signaling mitigates age-associated thermogenic impairment. *Aging*. **6**(12), pp.1019–1032.

Liu X, Cervantes C, Liu F. Common and distinct regulation of human and mouse brown and beige adipose tissues: a promising therapeutic target for obesity. Protein Cell. 2017 Jun;8(6):446-454.

Liu, J., Chen, Z., Zhang, Y., Zhang, M., Zhu, X., Fan, Y., Shi, S., Zen, K. and Liu, Z. 2013. Rhein Protects Pancreatic β-Cells From Dynamin-Related Protein-1–Mediated Mitochondrial Fission and Cell Apoptosis Under Hyperglycemia. *Diabetes*. **62**(11), pp.3927–3935.

Liu, T., Kong, D., Shah, B.P., Ye, C., Koda, S., Saunders, A., Ding, J.B., Yang, Z., Sabatini, B.L. and Lowell, B.B. 2012. Fasting activation of AgRP neurons requires NMDA receptors and involves spinogenesis and increased excitatory tone. *Neuron*. **73**(3), pp.511–522.

Lockie, S., Heppner, K.M., Chaudhary, N., Chabenne, J.R., Morgan, D.A., Veyrat-Durebex, C., Ananthakrishnan, G., Rohner-Jeanrenaud, F., Drucker, D.J., DiMarchi, R., Rahmouni, K., Oldfield, B.J., Tschöp, M.H. and Perez-Tilve, D. 2012. Direct control of brown adipose tissue thermogenesis by central nervous system glucagon-like peptide-1 receptor signaling. *Diabetes*. **61**(11), pp.2753–2762.

Loh, R.K.C., Formosa, M.F., La Gerche, A., Reutens, A.T., Kingwell, B.A. and Carey, A.L. 2019. Acute metabolic and cardiovascular effects of mirabegron in healthy individuals. *Diabetes, obesity & metabolism*. **21**(2), pp.276–284.

Lončar, D. 1991. Convertible adipose tissue in mice. *Cell and Tissue Research 1991 266:1*. **266**(1), pp.149–161.

López, M., Varela, L., Vázquez, M.J., Rodríguez-Cuenca, S., González, C.R., Velagapudi, V.R., Morgan, D.A., Schoenmakers, E., Agassandian, K., Lage, R., De Morentin, P.B.M., Tovar, S., Nogueiras, R., Carling, D., Lelliott, C., Gallego, R., OreŠič, M., Chatterjee, K., Saha, A.K., Rahmouni, K., Diéguez, C. and Vidal-Puig, A. 2010. Hypothalamic AMPK and fatty acid

metabolism mediate thyroid regulation of energy balance. *Nature Medicine 2010 16:9*. **16**(9), pp.1001–1008.

Ludwig, M.Q., Cheng, W., Gordian, D., Lee, J., Paulsen, S.J., Hansen, S.N., Egerod, K.L., Barkholt, P., Rhodes, C.J., Secher, A., Knudsen, L.B., Pyke, C., Myers, M.G. and Pers, T.H. 2021. A genetic map of the mouse dorsal vagal complex and its role in obesity. *Nature Metabolism*. **3**(4), pp.530–545.

Luedde, T. and Schwabe, R.F. 2011. NF-κB in the liver—linking injury, fibrosis and hepatocellular carcinoma. *Nature reviews. Gastroenterology & hepatology*. **8**(2), p.108.

Luquet, S., Perez, F.A., Hnasko, T.S. and Palmiter, R.D. 2005. NPY/AgRP neurons are essentials for feeding in adult mice but can be ablated in neonates. *Science*. **310**(5748), pp.683–685.

Ma, W., Yuan, L., Yu, H., Xi, Y. and Xiao, R. 2014. Mitochondrial dysfunction and oxidative damage in the brain of diet-induced obese rats but not in diet-resistant rats. *Life Sciences*. **110**(2), pp.53–60.

MacDonald, A.J. and Ellacott, K.L.J. 2020. Astrocytes in the nucleus of the solitary tract: Contributions to neural circuits controlling physiology. *Physiology and Behavior*. **223**, p.112982.

MacDonald, A.J., Holmes, F.E., Beall, C., Pickering, A.E. and Ellacott, K.L.J. 2020. Regulation of food intake by astrocytes in the brainstem dorsal vagal complex. *GLIA*. **68**(6), pp.1241–1254.

Madden, C.J. and Morrison, S.F. 2016. A high-fat diet impairs cooling-evoked brown adipose tissue activation via a vagal afferent mechanism. *American Journal of Physiology-Endocrinology and Metabolism*. **311**(2), pp.E287–E292.

Madden, C.J., Santos da Conceicao, E.P. and Morrison, S.F. 2017. Vagal afferent activation decreases brown adipose tissue (BAT) sympathetic nerve activity and BAT thermogenesis. *Temperature: Multidisciplinary Biomedical Journal*. **4**(1), p.89.

Madden, C.J., Tupone, D., Cano, G. and Morrison, S.F. 2013. α2 Adrenergic receptor-mediated inhibition of thermogenesis. *The Journal of neuroscience : the official journal of the Society for Neuroscience*. **33**(5), pp.2017–2028.

Madisen, L., Mao, T., Koch, H., Zhuo, J.M., Berenyi, A., Fujisawa, S., Hsu, Y.W.A., Garcia, A.J., Gu, X., Zanella, S., Kidney, J., Gu, H., Mao, Y., Hooks, B.M., Boyden, E.S., Buzsáki, G., Ramirez, J.M., Jones, A.R., Svoboda, K., Han, X., Turner, E.E. and Zeng, H. 2012. A toolbox

of Cre-dependent optogenetic transgenic mice for light-induced activation and silencing. *Nature Neuroscience 2012 15:5*. **15**(5), pp.793–802.

Madrigal, J.L.M., Moro, M.A., Lizasoain, I., Lorenzo, P., Castrillo, A., Boscá, L. and Leza, J.C. 2001. Inducible nitric oxide synthase expression in brain cortex after acute restraint stress is regulated by nuclear factor κB-mediated mechanisms. *Journal of Neurochemistry*. **76**(2), pp.532–538.

Mahmoud, S., Gharagozloo, M., Simard, C. and Gris, D. 2019. Astrocytes Maintain Glutamate Homeostasis in the CNS by Controlling the Balance between Glutamate Uptake and Release. *Cells*. **8**(2).

Malcolm W. Nason, J. and Mason, P. 2004. Modulation of Sympathetic and Somatomotor Function by the Ventromedial Medulla. *https://doi.org/10.1152/jn.00089.2004*. **92**(1), pp.510–522.

Manaserh, Iyad H, Maly, E., Jahromi, M., Chikkamenahalli, L., Park, J., Hill, J. and Hill, J.W. 2020. Insulin Sensing by Astrocytes Is Critical for Normal Thermogenesis and Body Temperature Regulation HHS Public Access. *J Endocrinol*. **247**(1), pp.39–52.

Maric, I., Krieger, J.P., van der Velden, P., Börchers, S., Asker, M., Vujicic, M., Wernstedt Asterholm, I. and Skibicka, K.P. 2022. Sex and Species Differences in the Development of Diet-Induced Obesity and Metabolic Disturbances in Rodents. *Frontiers in Nutrition*. **9**, p.141.

van Marken Lichtenbelt, W.D., Vanhommerig, J.W., Smulders, N.M., Drossaerts, J.M.A.F.L., Kemerink, G.J., Bouvy, N.D., Schrauwen, P. and Teule, G.J.J. 2009. Cold-Activated Brown Adipose Tissue in Healthy Men. *https://doi.org/10.1056/NEJMoa0808718*. **360**(15), pp.1500–1508.

Martin-Fernandez, M., Jamison, S., Robin, L.M., Zhao, Z., Martin, E.D., Aguilar, J., Benneyworth, M.A., Marsicano, G. and Araque, A. 2017. Synapse-specific astrocyte gating of amygdala-related behavior. *Nature Neuroscience*. **20**(11), pp.1540–1548.

Martinez-Carreres, L., Nasrallah, A. and Fajas, L. 2017. Cancer: Linking Powerhouses to Suicidal Bags. *Frontiers in Oncology*. **7**(SEP), p.1.

Martínez, V., Wang, L. and Taché, Y. 2001. Central TRH receptor 1 antisense blocks cold-induced gastric emptying but not brain c-Fos induction. *Peptides*. **22**(1), pp.81–90.

Mauvais-Jarvis, F. 2015. Sex differences in metabolic homeostasis, diabetes, and obesity. *Biology of Sex Differences*. **6**(1), pp.1–9.

McCorry, L.K. 2007. Physiology of the autonomic nervous system. *American journal of pharmaceutical education*. **71**(4).

McDougal, D.H., Hermann, G.E. and Rogers, R.C. 2011. Vagal Afferent Stimulation Activates Astrocytes in the Nucleus of the Solitary Tract Via AMPA Receptors: Evidence of an Atypical Neural-Glial Interaction in the Brainstem. *Journal of Neuroscience*.

McLaughlin, T., Lamendola, C., Coghlan, N., Liu, T.C., Lerner, K., Sherman, A. and Cushman, S.W. 2014. Subcutaneous Adipose Cell Size and Distribution: Relationship to Insulin Resistance and Body Fat. *Obesity (Silver Spring, Md.)*. **22**(3), p.673.

McNeill, B.T., Morton, N.M. and Stimson, R.H. 2020. Substrate Utilization by Brown Adipose Tissue: What's Hot and What's Not? *Frontiers in Endocrinology*. **11**.

Mears, J.A., Lackner, L.L., Fang, S., Ingerman, E., Nunnari, J. and Hinshaw, J.E. 2011. Conformational changes in Dnm1 support a contractile mechanism for mitochondrial fission. *Nature structural & molecular biology*. **18**(1), pp.20–27.

De Meijer, V.E., Le, H.D., Meisel, J.A., Sharif, M.R.A., Pan, A., Nosé, V. and Puder, M. 2010. Dietary fat intake promotes the development of hepatic steatosis independently from excess caloric consumption in a murine model. *Metabolism*. **59**(8), pp.1092–1105.

Mells, J.E., Fu, P.P., Kumar, P., Smith, T., Karpen, S.J. and Anania, F.A. 2015. Saturated fat and cholesterol are critical to inducing murine metabolic syndrome with robust nonalcoholic steatohepatitis. *The Journal of Nutritional Biochemistry*. **26**(3), pp.285–292.

Menezes, A.L., Pereira, M.P., Buzelle, S.L., dos Santos, M.P., de França, S.A., Baviera, A.M., Andrade, C.M.B., Garófalo, M.A.R., Kettelhut, I. do C., Chaves, V.E. and Kawashita, N.H. 2013. A low-protein, high-carbohydrate diet increases de novo fatty acid synthesis from glycerol and glycerokinase content in the liver of growing rats. *Nutrition Research*. **33**(6), pp.494–502.

Mengeste, A.M., Rustan, A.C. and Lund, J. 2021. Skeletal muscle energy metabolism in obesity. *Obesity*. **29**(10), pp.1582–1595.

Mercer, S.W. and Trayhurn, P. 1984. The development of insulin resistance in brown adipose tissue may impair the acute cold-induced activation of thermogenesis in genetically obese (ob/ob) mice. *Bioscience reports*. **4**(11), pp.933–940.

Metz, C.N. and Pavlov, V.A. 2018. Vagus nerve cholinergic circuitry to the liver and the gastrointestinal tract in the neuroimmune communicatome. *American Journal of Physiology - Gastrointestinal and Liver Physiology*. **315**(5), pp.G651–G658.

Michael, M.D., Kulkarni, R.N., Postic, C., Previs, S.F., Shulman, G.I., Magnuson, M.A. and Kahn, C.R. 2000. Loss of insulin signaling in hepatocytes leads to severe insulin resistance and progressive hepatic dysfunction. *Molecular Cell*. **6**(1), pp.87–97.

Minehira, K., Young, S.G., Villanueva, C.J., Yetukuri, L., Oresic, M., Hellerstein, M.K., Farese, R. V., Horton, J.D., Preitner, F., Thorens, B. and Tappy, L. 2008. Blocking VLDL secretion causes hepatic steatosis but does not affect peripheral lipidstores or insulin sensitivity in mice. *Journal of Lipid Research*. **49**(9), p.2038.

Minokoshi, Y., Haque, M.S. and Shimazu, T. 1999. Microinjection of leptin into the ventromedial hypothalamus increases glucose uptake in peripheral tissues in rats. *Diabetes*. **48**(2), pp.287–291.

Mittendorfer, B., Magkos, F., Fabbrini, E., Mohammed, B.S. and Klein, S. 2009. Relationship Between Body Fat Mass and Free Fatty Acid Kinetics in Men and Women. *Obesity*. **17**(10), pp.1872–1877.

Molina, A.J.A., Wikstrom, J.D., Stiles, L., Las, G., Mohamed, H., Elorza, A., Walzer, G., Twig, G., Katz, S., Corkey, B.E. and Shirihai, O.S. 2009. Mitochondrial Networking Protects β-Cells From Nutrient-Induced Apoptosis. *Diabetes*. **58**(10), pp.2303–2315.

Monge-Roffarello, B., Labbe, S.M., Roy, M.-C., Lemay, M.-L., Coneggo, E., Samson, P., Lanfray, D. and Richard, D. 2014. The PVH as a Site of CB1-Mediated Stimulation of Thermogenesis by MC4R Agonism in Male Rats. *Endocrinology*. **155**(9), pp.3448–3458.

Moonen, M.P.B., Nascimento, E.B.M. and van Marken Lichtenbelt, W.D. 2019. Human brown adipose tissue: Underestimated target in metabolic disease? *Biochimica et Biophysica Acta (BBA) - Molecular and Cell Biology of Lipids*. **1864**(1), pp.104–112.

Moore, M.C., Coate, K.C., Winnick, J.J., An, Z. and Cherrington, A.D. 2012. Regulation of Hepatic Glucose Uptake and Storage In Vivo. *Advances in Nutrition*. **3**(3), p.286.

Morak, M., Schmidinger, H., Riesenhuber, G., Rechberger, G.N., Kollroser, M., Haemmerle, G., Zechner, R., Kronenberg, F. and Hermetter, A. 2012. Adipose triglyceride lipase (ATGL) and hormone-sensitive lipase (HSL) deficiencies affect expression of lipolytic activities in mouse adipose tissues. *Molecular and Cellular Proteomics*. **11**(12), pp.1777–1789.

Morrison, S.F. 2001. Differential control of sympathetic outflow. *American journal of physiology. Regulatory, integrative and comparative physiology*. **281**(3).

Morrison, S.F. 2003. Raphe pallidus neurons mediate prostaglandin E2-evoked increases in brown adipose tissue thermogenesis. *Neuroscience*. **121**(1), pp.17–24.

Morrison, S.F. 1999. RVLM and raphe differentially regulate sympathetic outflows to splanchnic and brown adipose tissue. *https://doi.org/10.1152/ajpregu.1999.276.4.R962*. **276**(4 45-4).

Morrison, S.F. and Madden, C.J. 2014. Central nervous system regulation of brown adipose tissue. *Comprehensive Physiology*. **4**(4), pp.1677–1713.

Morrison, S.F., Madden, C.J. and Tupone, D. 2012. Central control of brown adipose tissue thermogenesis. *Frontiers in Endocrinology*. **3**(JAN), p.5.

Morrison, S.F., Madden, C.J. and Tupone, D. 2014. Central neural regulation of brown adipose tissue thermogenesis and energy expenditure. *Cell Metabolism*. **19**(5), pp.741–756.

Morrison, S.F. and Nakamura, K. 2011a. Central neural pathways for thermoregulation. *Frontiers in Bioscience-Landmark 2011, 16(1), 74-104*. **16**(1), pp.74–104.

Morrison, S.F., Sved, A.F. and Passerin, A.M. 1999. GABA-mediated inhibition of raphe pallidus neurons regulates sympathetic outflow to brown adipose tissue. *The American journal of physiology*. **276**(2).

Morton, G.J., Cummings, D.E., Baskin, D.G., Barsh, G.S. and Schwartz, M.W. 2006. Central nervous system control of food intake and body weight. *Nature*. **443**(7109), pp.289–295.

Mössenböck, K., Vegiopoulos, A., Rose, A.J., Sijmonsma, T.P., Herzig, S. and Schafmeier, T. 2014. Browning of White Adipose Tissue Uncouples Glucose Uptake from Insulin Signaling. *PLoS ONE*. **9**(10).

Motori, E., Puyal, J., Toni, N., Ghanem, A., Angeloni, C., Malaguti, M., Cantelli-Forti, G., Berninger, B., Conzelmann, K.K., Götz, M., Winklhofer, K.F., Hrelia, S. and Bergami, M. 2013. Inflammation-induced alteration of astrocyte mitochondrial dynamics requires autophagy for mitochondrial network maintenance. *Cell metabolism*. **18**(6), pp.844–859.

Münzberg, H., Flier, J.S. and Bjørbæk, C. 2004. Region-Specific Leptin Resistance within the Hypothalamus of Diet-Induced Obese Mice. *Endocrinology*. **145**(11), pp.4880–4889.

Muzik, O., Mangner, T.J., Leonard, W.R., Kumar, A., Janisse, J. and Granneman, J.G. 2013. O PET Measurement of Blood Flow and Oxygen Consumption in Cold-Activated Human Brown Fat. *J Nucl Med*. **54**, pp.523–531.

Myers, M.G., Cowley, M.A. and Münzberg, H. 2008. Mechanisms of leptin action and leptin resistance. *Annual review of physiology*. **70**, pp.537–556.

Nagdas, S. and Kashatus, D.F. 2017. The Interplay between Oncogenic Signaling Networks and Mitochondrial Dynamics. *Antioxidants (Basel, Switzerland)*. **6**(2).

Najjar, S.M. and Perdomo, G. 2019. Hepatic Insulin Clearance: Mechanism and Physiology. *Physiology (Bethesda, Md.)*. **34**(3), pp.198–215.

Nakamura, K., Matsumura, K., Kaneko, T., Kobayashi, S., Katoh, H. and Negishi, M. 2002. The rostral raphe pallidus nucleus mediates pyrogenic transmission from the preoptic area. *The Journal of neuroscience : the official journal of the Society for Neuroscience*. **22**(11), pp.4600–4610.

Nakamura, Y., Nakamura, K., Matsumura, K., Kobayashi, S., Kaneko, T. and Morrison, S.F. 2005. Direct pyrogenic input from prostaglandin EP3 receptor-expressing preoptic neurons to the dorsomedial hypothalamus. *European Journal of Neuroscience*. **22**(12), pp.3137–3146.

Nakamura, Y., Yanagawa, Y., Morrison, S.F. and Nakamura, K. 2017. Medullary Reticular Neurons Mediate Neuropeptide Y-Induced Metabolic Inhibition and Mastication. *Cell metabolism*. **25**(2), pp.322–334.

Nakandakari, S.C.B.R., Muñoz, V.R., Kuga, G.K., Gaspar, R.C., Sant'Ana, M.R., Pavan, I.C.B., da Silva, L.G.S., Morelli, A.P., Simabuco, F.M., da Silva, A.S.R., de Moura, L.P., Ropelle, E.R., Cintra, D.E. and Pauli, J.R. 2019. Short-term high-fat diet modulates several inflammatory, ER stress, and apoptosis markers in the hippocampus of young mice. *Brain, Behavior, and Immunity*. **79**, pp.284–293.

National Institute of Health and Care Excellence 2022. Recommendations | Obesity: identification, assessment and management | Guidance | NICE.

Nedergaard, J., Bengtsson, T. and Cannon, B. 2011. New powers of brown fat: fighting the metabolic syndrome. *Cell metabolism*. **13**(3), pp.238–240.

Nedergaard, J. and Cannon, B. 2010. The Changed Metabolic World with Human Brown Adipose Tissue: Therapeutic Visions. *Cell Metabolism*. **11**(4), pp.268–272.

Nedergaard, J., Petrovic, N., Lindgren, E.M., Jacobsson, A. and Cannon, B. 2005. PPARγ in the control of brown adipocyte differentiation. *Biochimica et Biophysica Acta (BBA) - Molecular Basis of Disease*. **1740**(2), pp.293–304.

Ngeles Fernández-Gil, M., Palacios-Bote, R., Leo-Barahona, M. and Mora-Encinas, J.P. 2010. Anatomy of the brainstem: a gaze into the stem of life. *Seminars in ultrasound, CT, and MR*. **31**(3), pp.196–219.

Nguyen, N.L.T., Barr, C.L., Ryu, V., Cao, Q., Xue, B. and Bartness, T.J. 2017. Separate and shared sympathetic outflow to white and brown fat coordinately regulates thermoregulation

and beige adipocyte recruitment. *American Journal of Physiology - Regulatory Integrative and Comparative Physiology*. **312**(1), pp.R132–R145.

Nicholls, D.G. and Locke, R.M. 1984. Thermogenic mechanisms in brown fat. *https://doi.org/10.1152/physrev.1984.64.1.1*. **64**(1), pp.1–64.

Nilsson, R., Schultz, I.J., Pierce, E.L., Soltis, K.A., Naranuntarat, A., Ward, D.M., Baughman, J.M., Paradkar, P.N., Kingsley, P.D., Culotta, V.C., Kaplan, J., Palis, J., Paw, B.H. and Mootha, V.K. 2009. Discovery of Genes Essential for Heme Biosynthesis through Large-Scale Gene Expression Analysis. *Cell Metabolism*. **10**(2), pp.119–130.

Nisoli, E., Briscini, L., Giordano, A., Tonello, C., Wiesbrock, S.M., Uysal, K.T., Cinti, S., Carruba, M.O. and Hotamisligil, G.S. 2000. Tumor necrosis factor α mediates apoptosis of brown adipocytes and defective brown adipocyte function in obesity. *Proceedings of the National Academy of Sciences of the United States of America*. **97**(14), pp.8033–8038.

O'hare, J.D., Zieli, E., Cheng, B., Scherer, T. and Buettner, C. 2011. Central Endocannabinoid Signaling Regulates Hepatic Glucose Production and Systemic Lipolysis.

O'Hare, J.D. and Zsombok, A. 2016. CNS Control of Metabolism: Brain-liver connections: role of the preautonomic PVN neurons. *American Journal of Physiology - Endocrinology and Metabolism*. **310**(3), p.E183.

O'Mara, A.E., Johnson, J.W., Linderman, J.D., Brychta, R.J., McGehee, S., Fletcher, L.A., Fink, Y.A., Kapuria, D., Cassimatis, T.M., Kelsey, N., Cero, C., Sater, Z.A., Piccinini, F., Baskin, A.S., Leitner, B.P., Cai, H., Millo, C.M., Dieckmann, W., Walter, M., Javitt, N.B., Rotman, Y., Walter, P.J., Ader, M., Bergman, R.N., Herscovitch, P., Chen, K.Y. and Cypess, A.M. 2020. Chronic mirabegron treatment increases human brown fat, HDL cholesterol, and insulin sensitivity. *The Journal of clinical investigation*. **130**(5), pp.2209–2219.

O'Neil, P.M., Birkenfeld, A.L., McGowan, B., Mosenzon, O., Pedersen, S.D., Wharton, S., Carson, C.G., Jepsen, C.H., Kabisch, M. and Wilding, J.P.H. 2018. Efficacy and safety of semaglutide compared with liraglutide and placebo for weight loss in patients with obesity: a randomised, double-blind, placebo and active controlled, dose-ranging, phase 2 trial. *The Lancet*. **392**(10148), pp.637–649.

Obici, S., Feng, Z., Morgan, K., Stein, D., Karkanias, G. and Rossetti, L. 2002. Central administration of oleic acid inhibits glucose production and food intake. *Diabetes*. **51**(2), pp.271–275.

Ohno, H., Shinoda, K., Ohyama, K., Sharp, L.Z. and Kajimura, S. 2013. EHMT1 controls brown

adipose cell fate and thermogenesis through the PRDM16 complex. *Nature*. **504**(7478), p.163.

Ohtomo, T., Ino, K., Miyashita, R., Chigira, M., Nakamura, M., Someya, K., Inaba, N., Fujita, M., Takagi, M. and Yamada, J. 2017. Chronic high-fat feeding impairs adaptive induction of mitochondrial fatty acid combustion-associated proteins in brown adipose tissue of mice. *Biochemistry and Biophysics Reports*. **10**, pp.32–38.

Okeke, K., Angers, S., Bouvier, M. and Michel, M.C. 2019. Agonist-induced desensitisation of β3-adrenoceptors: Where, when, and how? *British Journal of Pharmacology*. **176**(14), p.2539.

Okin, D. and Medzhitov, R. 2016. The Effect of Sustained Inflammation on Hepatic Mevalonate Pathway Results in Hyperglycemia. *Cell*. **165**(2), pp.343–356.

Okla, M., Wang, W., Kang, I., Pashaj, A., Carr, T. and Chung, S. 2015. Activation of Toll-like receptor 4 (TLR4) attenuates adaptive thermogenesis via endoplasmic reticulum stress. *The Journal of biological chemistry*. **290**(44), pp.26476–26490.

Oldfield, B.J., Giles, M.E., Watson, A., Anderson, C., Colvill, L.M. and McKinley, M.J. 2002. The neurochemical characterisation of hypothalamic pathways projecting polysynaptically to brown adipose tissue in the rat. *Neuroscience*. **110**(3), pp.515–526.

Olsen, J.M., Csikasz, R.I., Dehvari, N., Lu, L., Sandström, A., Öberg, A.I., Nedergaard, J., Stone-Elander, S. and Bengtsson, T. 2017. β 3 -Adrenergically induced glucose uptake in brown adipose tissue is independent of UCP1 presence or activity: Mediation through the mTOR pathway. *Molecular Metabolism*. **6**(6), pp.611–619.

Olsen, J.M., Sato, M., Dallner, O.S., Sandström, A.L., Pisani, D.F., Chambard, J.C., Amri, E.Z., Hutchinson, D.S. and Bengtsson, T. 2014. Glucose uptake in brown fat cells is dependent on mTOR complex 2-promoted GLUT1 translocation. *Journal of Cell Biology*. **207**(3), pp.365–374.

Ono, H., Pocai, A., Wang, Y., Sakoda, H., Asano, T., Backer, J.M., Schwartz, G.J. and Rossetti, L. 2008. Activation of hypothalamic S6 kinase mediates diet-induced hepatic insulin resistance in rats. *The Journal of Clinical Investigation*. **118**(8), pp.2959–2968.

Oppert, J.M., Vohl, M.C., Chagnonl, M., Dionne, F.T., Cassard-Doulcier, A.M., Ricquier, D., Perusse, L. and Bouchard, C. 1994. DNA polymorphism in the uncoupling protein (UCP) gene and human body fat. *International Journal of Obesity and Related Metabolic Disorders : Journal of the International Association for the Study of Obesity*. **18**(8),

pp.526–531.

Ota, T., Gayet, C. and Ginsberg, H.N. 2008. Inhibition of apolipoprotein B100 secretion by lipid-induced hepatic endoplasmic reticulum stress in rodents. *The Journal of clinical investigation*. **118**(1), pp.316–332.

Otera, H., Ishihara, N. and Mihara, K. 2013. New insights into the function and regulation of mitochondrial fission. *Biochimica et biophysica acta*. **1833**(5), pp.1256–1268.

Ouellet, V., Labbé, S.M., Blondin, D.P., Phoenix, S., Guérin, B., Haman, F., Turcotte, E.E., Richard, D. and Carpentier, A.C. 2012. Brown adipose tissue oxidative metabolism contributes to energy expenditure during acute cold exposure in humans. *Journal of Clinical Investigation*. **122**(2), pp.545–552.

Ouellet, V., Routhier-Labadie, A., Bellemare, W., Lakhal-Chaieb, L., Turcotte, E., Carpentier, A.C. and Richard, D. 2011. Outdoor Temperature, Age, Sex, Body Mass Index, and Diabetic Status Determine the Prevalence, Mass, and Glucose-Uptake Activity of 18F-FDG-Detected BAT in Humans. *The Journal of Clinical Endocrinology & Metabolism*. **96**(1), pp.192–199.

Ozcan, L., Ergin, A.S., Lu, A., Chung, J., Sarkar, S., Nie, D., Myers, M.G. and Ozcan, U. 2009. Endoplasmic Reticulum Stress Plays a Central Role in Development of Leptin Resistance. *Cell Metabolism*. **9**(1), pp.35–51.

Özcan, U., Cao, Q., Yilmaz, E., Lee, A.H., Iwakoshi, N.N., Özdelen, E., Tuncman, G., Görgün, C., Glimcher, L.H. and Hotamisligil, G.S. 2004. Endoplasmic reticulum stress links obesity, insulin action, and type 2 diabetes. *Science*. **306**(5695), pp.457–461.

Palmiter, R.D. 2018. The parabrachial nucleus: CGRP neurons function as a general alarm. *Trends in neurosciences*. **41**(5), p.280.

Pardina, E., Baena-Fustegueras, J.A., Llamas, R., Catalán, R., Galard, R., Lecube, A., Fort, J.M., Llobera, M., Allende, H., Vargas, V. and Peinado-Onsurbe, J. 2009. Lipoprotein lipase expression in livers of morbidly obese patients could be responsible for liver steatosis. *Obesity Surgery*. **19**(5), pp.608–616.

Park, J.W., Jung, K.H., Lee, J.H., Quach, C.H.T., Moon, S.H., Cho, Y.S. and Lee, K.H. 2015. 18F-FDG PET/CT monitoring of b3 agonist-stimulated brown adipocyte recruitment in white adipose tissue. *Journal of Nuclear Medicine*. **56**(1), pp.153–158.

Parpura, V. and Verkhratsky, A. 2012. Homeostatic function of astrocytes: Ca2+ and Na+ signalling. *Translational neuroscience*. **3**(4), p.334.

Patel, B., New, L.E., Griffiths, J.C., Deuchars, J. and Filippi, B.M. 2021. Inhibition of mitochondrial fission and iNOS in the dorsal vagal complex protects from overeating and weight gain. *Molecular Metabolism*. **43**, p.101123.

Pedersen, S.B., Bruun, J.M., Kristensen, K. and Richelsen, B. 2001. Regulation of UCP1, UCP2, and UCP3 mRNA Expression in Brown Adipose Tissue, White Adipose Tissue, and Skeletal Muscle in Rats by Estrogen. *Biochemical and Biophysical Research Communications*. **288**(1), pp.191–197.

Peng, L., Men, X., Zhang, W., Wang, H., Xu, S., Xu, M., Xu, Y., Yang, W. and Lou, J. 2011. Dynamin-related protein 1 is implicated in endoplasmic reticulum stress-induced pancreatic β-cell apoptosis. *International journal of molecular medicine*. **28**(2), pp.161–169.

Perea, G., Navarrete, M. and Araque, A. 2009. Tripartite synapses: astrocytes process and control synaptic information. *Trends in Neurosciences*. **32**(8), pp.421–431.

Perreault, M., Istrate, N., Wang, L., Nichols, A.J., Tozzo, E. and Stricker-Krongrad, A. 2004. Resistance to the orexigenic effect of ghrelin in dietary-induced obesity in mice: reversal upon weight loss. *International journal of obesity and related metabolic disorders : journal of the International Association for the Study of Obesity*. **28**(7), pp.879–885.

Petersen, K.F., Dufour, S., Savage, D.B., Bilz, S., Solomon, G., Yonemitsu, S., Cline, G.W., Befroy, D., Zemany, L., Kahn, B.B., Papademetris, X., Rothman, D.L. and Shulman, G.I. 2007. The role of skeletal muscle insulin resistance in the pathogenesis of the metabolic syndrome. *Proceedings of the National Academy of Sciences of the United States of America*. **104**(31), pp.12587–12594.

Petersen, M.C. and Shulman, G.I. 2018. Mechanisms of Insulin Action and Insulin Resistance. *Physiological reviews*. **98**(4), pp.2133–2223.

Pettinelli, P., del Pozo, T., Araya, J., Rodrigo, R., Araya, A.V., Smok, G., Csendes, A., Gutierrez, L., Rojas, J., Korn, O., Maluenda, F., Diaz, J.C., Rencoret, G., Braghetto, I., Castillo, J., Poniachik, J. and Videla, L.A. 2009. Enhancement in liver SREBP-1c/PPAR-α ratio and steatosis in obese patients: Correlations with insulin resistance and n-3 long-chain polyunsaturated fatty acid depletion. *Biochimica et Biophysica Acta (BBA) - Molecular Basis of Disease*. **1792**(11), pp.1080–1086.

Pickles, S., Vigié, P. and Youle, R.J. 2018. Mitophagy and Quality Control Mechanisms in Mitochondrial Maintenance. *Current Biology*. **28**(4), pp.R170–R185.

Pocai, A., Morgan, K., Buettner, C., Gutierrez-Juarez, R., Obici, S. and Rossetti, L. 2005. Central leptin acutely reverses diet-induced hepatic insulin resistance. *Diabetes*. **54**(11), pp.3182–3189.

Pocai, A., Obici, S., Schwartz, G.J. and Rossetti, L. 2005. A brain-liver circuit regulates glucose homeostasis. *Cell Metabolism*. **1**(1), pp.53–61.

Poole, S. and Stephenson, J.D. 1977. BODY TEMPERATURE REGULATION AND THERMONEUTRALITY IN RATS. *Quarterly Journal of Experimental Physiology and Cognate Medical Sciences*. **62**(2), pp.143–149.

Pouwels, S., Sakran, N., Graham, Y., Leal, A., Pintar, T., Yang, W., Kassir, R., Singhal, R., Mahawar, K. and Ramnarain, D. 2022. Non-alcoholic fatty liver disease (NAFLD): a review of pathophysiology, clinical management and effects of weight loss. *BMC Endocrine Disorders*. **22**(1), pp.1–9.

Preguiça, I., Alves, A., Nunes, S., Fernandes, R., Gomes, P., Viana, S.D. and Reis, F. 2020. Diet-induced rodent models of obesity-related metabolic disorders—A guide to a translational perspective. *Obesity Reviews*. **21**(12), p.e13081.

Preston, E., Triandafillou, J. and Haas, N. 1989. Colchicine lesions of ventromedial hypothalamus: Effects on regulatory thermogenesis in the rat. *Pharmacology Biochemistry and Behavior*. **32**(1), pp.301–307.

Public Health England, 2017. Health matters: obesity and the food environment - GOV.UK. [Accessed 5 November 2022]. Available from: https://www.gov.uk/government/publications/health-matters-obesity-and-the-food-environment/health-matters-obesity-and-the-food-environment--2.

Public Health England 2019. Health Survey for England 2019 [NS] - NHS Digital. [Accessed 7 October 2022c]. Available from: https://digital.nhs.uk/data-and-information/publications/statistical/health-survey-for-england/2019#.

Puigserver, P., Wu, Z., Park, C.W., Graves, R., Wright, M. and Spiegelman, B.M. 1998. A cold-inducible coactivator of nuclear receptors linked to adaptive thermogenesis. *Cell*. **92**(6), pp.829–839.

Püschel, G.P. 2004. Control of hepatocyte metabolism by sympathetic and parasympathetic hepatic nerves. *Anatomical Record - Part A Discoveries in Molecular, Cellular, and Evolutionary Biology*. **280**(1), pp.854–867.

Qi, Y., Yan, L., Yu, C., Guo, X., Zhou, X., Hu, X., Huang, X., Rao, Z., Lou, Z. and Hu, J. 2016.

Structures of human mitofusin 1 provide insight into mitochondrial tethering. *Journal of Cell Biology*. **215**(5), pp.621–629.

Quenneville, S., Labouèbe, G., Basco, D., Metref, S., Viollet, B., Foretz, M. and Thorens, B. 2020. Hypoglycemia-Sensing Neurons of the Ventromedial Hypothalamus Require AMPK-Induced Txn2 Expression but Are Dispensable for Physiological Counterregulation. *Diabetes*. **69**(11), p.2253.

Rahmouni, K., Morgan, D.A., Morgan, G.M., Liu, X., Sigmund, C.D., Mark, A.L. and Haynes, W.G. 2004. Hypothalamic PI3K and MAPK differentially mediate regional sympathetic activation to insulin. *The Journal of clinical investigation*. **114**(5), pp.652–658.

Rambold, A.S., Kostelecky, B., Elia, N. and Lippincott-Schwartz, J. 2011. Tubular network formation protects mitochondria from autophagosomal degradation during nutrient starvation. *Proceedings of the National Academy of Sciences of the United States of America*. **108**(25), pp.10190–10195.

Rambold, A.S., Kostelecky, B. and Lippincott-Schwartz, J. 2011. Together we are stronger: fusion protects mitochondria from autophagosomal degradation. *Autophagy*. **7**(12), pp.1568–1569.

Ramírez, S., Gómez-Valadés, A.G., Schneeberger, M., Varela, L., Haddad-Tóvolli, R., Altirriba, J., Noguera, E., Drougard, A., Flores-Martínez, Á., Imbernón, M., Chivite, I., Pozo, M., Vidal-Itriago, A., Garcia, A., Cervantes, S., Gasa, R., Nogueiras, R., Gama-Pérez, P., Garcia-Roves, P.M., Cano, D.A., Knauf, C., Servitja, J.M., Horvath, T.L., Gomis, R., Zorzano, A. and Claret, M. 2017. Mitochondrial Dynamics Mediated by Mitofusin 1 Is Required for POMC Neuron Glucose-Sensing and Insulin Release Control. *Cell Metabolism*. **25**(6), pp.1390-1399.e6.

Rana, A., Oliveira, M.P., Khamoui, A. V., Aparicio, R., Rera, M., Rossiter, H.B. and Walker, D.W. 2017. Promoting Drp1-mediated mitochondrial fission in midlife prolongs healthy lifespan of Drosophila melanogaster. *Nature Communications 2017 8:1*. **8**(1), pp.1–14.

Ravussin, Y., Xiao, C., Gavrilova, O. and Reitman, M.L. 2014. Effect of Intermittent Cold Exposure on Brown Fat Activation, Obesity, and Energy Homeostasis in Mice. *PLOS ONE*. **9**(1), p.e85876.

Rezai-Zadeh, K., Yu, S., Jiang, Y., Laque, A., Schwartzenburg, C., Morrison, C.D., Derbenev, A. V., Zsombok, A. and Münzberg, H. 2014. Leptin receptor neurons in the dorsomedial hypothalamus are key regulators of energy expenditure and body weight, but not food

intake. *Molecular metabolism*. **3**(7), pp.681–693.

Ribeiro, M., Rosenstock, T.R., Oliveira, A.M., Oliveira, C.R. and Rego, A.C. 2014. Insulin and IGF-1 improve mitochondrial function in a PI-3K/Akt-dependent manner and reduce mitochondrial generation of reactive oxygen species in Huntington's disease knock-in striatal cells. *Free Radical Biology and Medicine*. **74**, pp.129–144.

Richard, D. 2015. Cognitive and autonomic determinants of energy homeostasis in obesity. *Nature Reviews Endocrinology 2015 11:8*. **11**(8), pp.489–501.

Richard, D. and Picard, F. 2011. Brown fat biology and thermogenesis. *Frontiers in Bioscience*. **16**(4), pp.1233–1260.

Richardson, J., Cruz, M.T., Majumdar, U., Lewin, A., Kingsbury, K.A., Dezfuli, G., Vicini, S., Verbalis, J.G., Dretchen, K.L., Gillis, R.A. and Sahibzada, N. 2013. Melanocortin Signaling in the Brainstem Influences Vagal Outflow to the Stomach. *Journal of Neuroscience*. **33**(33), pp.13286–13299.

Ricquier, D., Bouillaud, F., Toumelin, P., … G.M.-J. of B. and 1986, Expression of uncoupling protein mRNA in thermogenic or weakly thermogenic brown adipose tissue. Evidence for a rapid beta-adrenoreceptor-mediated. *Elsevier*.

Ricquier, D. and Kader, J.C. 1976. Mitochondrial protein alteration in active brown fat: A sodium dodecyl sulfate-polyacrylamide gel electrophoretic study. *Biochemical and Biophysical Research Communications*. **73**(3), pp.577–583.

Ricquier, D., Mory, G. and Hemon, P. 1979. Changes induced by cold adaptation in the brown adipose tissue from several species of rodents, with special reference to the mitochondrial components. *Canadian Journal of Biochemistry*. **57**(11), pp.1262–1266.

Ricquier, D., Nechad, M., clinical, G.M.-T.J. 1982. Ultrastructural and biochemical characterization of human brown adipose tissue in pheochromocytoma. *europepmc.org*.

Riis-Vestergaard MJ, Richelsen B, Bruun JM, Li W, Hansen JB, Pedersen SB. Beta-1 and Not Beta-3 Adrenergic Receptors May Be the Primary Regulator of Human Brown Adipocyte Metabolism. J Clin Endocrinol Metab. 2020 Apr 1;105(4)

Röder, P. V., Wu, B., Liu, Y. and Han, W. 2016. Pancreatic regulation of glucose homeostasis. *Experimental & Molecular Medicine*. **48**(3), p.e219.

Rodriguez-Cuenca, S., Monjo, M., Frontera, M., Gianotti, M., Proenza, A.M. and Roca, P. 2007. Sex Steroid Receptor Expression Profile in Brown Adipose Tissue. Effects of Hormonal Status. *Cellular Physiology and Biochemistry*. **20**(6), pp.877–886.

Rodríguez-Cuenca, S., Pujol, E., Justo, R., Frontera, M., Oliver, J., Gianotti, M. and Roca, P. 2002. Sex-dependent thermogenesis, differences in mitochondrial morphology and function, and adrenergic response in brown adipose tissue. *The Journal of biological chemistry*. **277**(45), pp.42958–42963.

Rodríguez, A.M., Monjo, M., Roca, P. and Palou, A. 2002. Opposite actions of testosterone and progesterone on UCP1 mRNA expression in cultured brown adipocytes. *Cellular and Molecular Life Sciences CMLS 2002 59:10*. **59**(10), pp.1714–1723.

Rodríguez, A.M., Quevedo-Coli, S., Roca, P. and Palou, A. 2001. Sex-dependent dietary obesity, induction of UCPs, and leptin expression in rat adipose tissues. *Obesity research*. **9**(9), pp.579–588.

Rogers, R.C., Barnes, M.J. and Hermann, G.E. 2009. Leptin "gates" thermogenic action of thyrotropin releasing hormone in the hindbrain. *Brain research*. **1295**, p.135.

Ronveaux, C.C., Tomé, D. and Raybould, H.E. 2015. Glucagon-Like Peptide 1 Interacts with Ghrelin and Leptin to Regulate Glucose Metabolism and Food Intake through Vagal Afferent Neuron Signaling. *The Journal of Nutrition*. **145**(4), p.672.

Rose, J., Brian, C., Pappa, A., Panayiotidis, M.I. and Franco, R. 2020. Mitochondrial Metabolism in Astrocytes Regulates Brain Bioenergetics, Neurotransmission and Redox Balance. *Frontiers in Neuroscience*. **14**, p.1155.

Rosenstengel, S., Stoeppeler, S., Bahde, R., Spiegel, H.U. and Palmes, D. 2011a. Type of steatosis influences microcirculation and fibrogenesis in different rat strains. *Journal of investigative surgery : the official journal of the Academy of Surgical Research*. **24**(6), pp.273–282

Rosenwald, M., Perdikari, A., Rülicke, T. and Wolfrum, C. 2013. Bi-directional interconversion of brite and white adipocytes. *Nature cell biology*. **15**(6), pp.659–667.

Rossetti, L. and Giaccari, A. 1990. Relative contribution of glycogen synthesis and glycolysis to insulin-mediated glucose uptake. A dose-response euglycemic clamp study in normal and diabetic rats. *Journal of Clinical Investigation*. **85**(6), pp.1785–1792.

Rossi, M., Kim, M.S., Morgan, D.G.A., Small, C.J., Edwards, C.M.B., Sunter, D., Abusnana, S., Goldstone, A.P., Russell, S.H., Stanley, S.A., Smith, D.M., Yagaloff, K., Ghatei, M.A. and Bloom, S.R. 1998. A C-terminal fragment of Agouti-related protein increases feeding and antagonizes the effect of alpha-melanocyte stimulating hormone in vivo. *Endocrinology*. **139**(10), pp.4428–4431.

Rouru, J., Cusin, I., Zakrzewska, K.E., Jeanrenaud, B. and Rohner-Jeanrenaud, F. 1999. Effects of Intravenously Infused Leptin on Insulin Sensitivity and on the Expression of Uncoupling Proteins in Brown Adipose Tissue. *Endocrinology*. **140**(8), pp.3688–3692.

Rowe, I.C.M., Boden, P.R. and Ashford, M.L.J. 1996. Potassium channel dysfunction in hypothalamic glucose-receptive neurones of obese Zucker rats. *The Journal of Physiology*. **497**(2), pp.365–377.

Rui, L. 2014. Energy Metabolism in the Liver. *Comprehensive Physiology*. **4**(1), p.177.

Russell, J.C., Proctor, S.D., Kelly, S.E. and Brindley, D.N. 2008. Pair feeding-mediated changes in metabolism: stress response and pathophysiology in insulin-resistant, atherosclerosis-prone JCR:LA-cp rats. *American Journal of Physiology-Endocrinology and Metabolism*. **294**(6), pp.E1078–E1087.

Ruud, J., Steculorum, S.M. and Bruning, J.C. 2017. Neuronal control of peripheral insulin sensitivity and glucose metabolism. *Nature Communications*. **8**.

Sacks, H. and Symonds, M.E. 2013. Anatomical Locations of Human Brown Adipose Tissue: Functional Relevance and Implications in Obesity and Type 2 Diabetes. *Diabetes*. **62**(6), p.1783.

Sainsbury, A., Schwarzer, C., Couzens, M., Jenkins, A., Oakes, S.R., Ormandy, C.J. and Herzog, H. 2002. Y4 receptor knockout rescues fertility in ob/ob mice. *Genes and Development*. **16**(9), pp.1077–1088.

Saito, M., Okamatsu-Ogura, Y., Matsushita, M., Watanabe, K., Yoneshiro, T., Nio-Kobayashi, J., Iwanaga, T., Miyagawa, M., Kameya, T., Nakada, K., Kawai, Y. and Tsujisaki, M. 2009a. High incidence of metabolically active brown adipose tissue in healthy adult humans: Effects of cold exposure and adiposity. *Diabetes*. **58**(7), pp.1526–1531.

Sakaguchi, T. and Bray, G.A. 1989. Effect of norepinephrine, serotonin and tryptophan on the firing rate of sympathetic nerves. *Brain Research*. **492**(1–2), pp.271–280.

Sakamoto, T., Takahashi, N., Sawaragi, Y., Naknukool, S., Yu, R., Goto, T. and Kawada, T. 2013. Inflammation induced by RAW macrophages suppresses UCP1 mRNA induction via ERK activation in 10T1/2 adipocytes. *American Journal of Physiology - Cell Physiology*. **304**(8).

Sanders, F.W.B. and Griffin, J.L. 2016. De novo lipogenesis in the liver in health and disease: more than just a shunting yard for glucose. *Biological Reviews*. **91**(2), pp.452–468.

Santel, A., science, M.F.-J. 2001. *Control of mitochondrial morphology by a human mitofusin* [Online]. [Accessed 7 September 2022]. Available from:

https://journals.biologists.com/jcs/article-abstract/114/5/867/982.

Santoro, A., Campolo, M., Liu, C., Sesaki, H., Meli, R., Liu, Z.W., Kim, J.D. and Diano, S. 2017. DRP1 Suppresses Leptin and Glucose Sensing of POMC Neurons. *Cell Metabolism*. **25**(3), pp.647–660.

Sanyal, A.J., Campbell-Sargent, C., Mirshahi, F., Rizzo, W.B., Contos, M.J., Sterling, R.K., Luketic, V.A., Shiffman, M.L. and Clore, J.N. 2001. Nonalcoholic steatohepatitis: Association of insulin resistance and mitochondrial abnormalities. *Gastroenterology*. **120**(5), pp.1183–1192.

Sasaki, T., Beppu, K., Tanaka, K.F., Fukazawa, Y., Shigemoto, R. and Matsui, K. 2012. Application of an optogenetic byway for perturbing neuronal activity via glial photostimulation. *Proceedings of the National Academy of Sciences of the United States of America*. **109**(50), pp.20720–20725.

Sasser, T.A., Chapman, S.E., Li, S., Hudson, C., Orton, S.P., Diener, J.M., Gammon, S.T., Correcher, C. and Matthew Leevy, W. 2012. Segmentation and measurement of fat volumes in murine obesity models using X-ray computed tomography. *Journal of Visualized Experiments*. (62).

Satapati, S., Sunny, N.E., Kucejova, B., Fu, X., He, T.T., Méndez-Lucas, A., Shelton, J.M., Perales, J.C., Browning, J.D. and Burgess, S.C. 2012. Elevated TCA cycle function in the pathology of diet-induced hepatic insulin resistance and fatty liver. *Journal of Lipid Research*. **53**(6), pp.1080–1092.

Sattler, R., medicine, M.T. 2000. Molecular mechanisms of calcium-dependent excitotoxicity. *Springer*. **78**(1), pp.3–13.

Sauer, B. and Du, E.I. 1987. Functional expression of the cre-lox site-specific recombination system in the yeast Saccharomyces cerevisiae. *Molecular and Cellular Biology*. **7**(6), p.2087.

Savastano, D.M. and Covasa, M. 2005. Adaptation to a High-Fat Diet Leads to Hyperphagia and Diminished Sensitivity to Cholecystokinin in Rats. *The Journal of Nutrition*. **135**(8), pp.1953–1959.

Scarpace, P.J. and Matheny, M. 1998. Leptin induction of UCP1 gene expression is dependent on sympathetic innervation. *The American journal of physiology*. **275**(2).

Schade, K.N., Baranwal, A., Liang, C., Mirbolooki, M.R. and Mukherjee, J. 2015. Preliminary evaluation of β3-adrenoceptor agonist-induced 18F-FDG metabolic activity of brown

adipose tissue in obese Zucker rat. *Nuclear Medicine and Biology*. **42**(8), pp.691–694.

Schmid, A.I., Szendroedi, J., Chmelik, M., Krššák, M., Moser, E. and Roden, M. 2011. Liver ATP Synthesis Is Lower and Relates to Insulin Sensitivity in Patients With Type 2 Diabetes. *Diabetes Care*. **34**(2), pp.448–453.

Schmittgen, T.D. and Livak, K.J. 2008. Analyzing real-time PCR data by the comparative CT method. *Nature Protocols*. **3**(6), pp.1101–1108.

Schneeberger, M., Dietrich, Marcelo O., Sebastián, D., Imbernón, M., Castaño, C., Garcia, A., Esteban, Y., Gonzalez-Franquesa, A., Rodríguez, I.C., Bortolozzi, A., Garcia-Roves, P.M., Gomis, R., Nogueiras, R., Horvath, T.L., Zorzano, A. and Claret, M. 2013. Mitofusin 2 in POMC Neurons Connects ER Stress with Leptin Resistance and Energy Imbalance. *Cell*. **155**(1), pp.172–187.

Schneeberger, M., Gómez-Valadés, A.G., Altirriba, J., Sebastián, D., Ramírez, S., Garcia, A., Esteban, Y., Drougard, A., Ferrés-Coy, A., Bortolozzi, A., Garcia-Roves, P.M., Jones, J.G., Manadas, B., Zorzano, A., Gomis, R. and Claret, M. 2015. Reduced α-MSH Underlies Hypothalamic ER-Stress-Induced Hepatic Gluconeogenesis. *Cell Reports*. **12**(3), pp.361–370.

Schneeberger, M., Gomis, R. and Claret, M. 2014. Hypothalamic and brainstem neuronal circuits controlling homeostatic energy balance. *Journal of Endocrinology*. **220**(2), pp.T25–T46.

Schwartz, G.J. 2000. The role of gastrointestinal vagal afferents in the control of food intake: current prospects. *Nutrition (Burbank, Los Angeles County, Calif.)*. **16**(10), pp.866–873.

Scofield, M.D. and Kalivas, P.W. 2014. Astrocytic dysfunction and addiction: Consequences of impaired glutamate homeostasis. *Neuroscientist*. **20**(6), pp.610–622.

Scott, M.M., Williams, K.W., Rossi, J., Lee, C.E. and Elmquist, J.K. 2011. Leptin receptor expression in hindbrain Glp-1 neurons regulates food intake and energy balance in mice. *The Journal of Clinical Investigation*. **121**(6), pp.2413–2421.

Seale, P., Bjork, B., Yang, W., Kajimura, S., Chin, S., Kuang, S., Scimè, A., Devarakonda, S., Conroe, H.M., Erdjument-Bromage, H., Tempst, P., Rudnicki, M.A., Beier, D.R. and Spiegelman, B.M. 2008. PRDM16 Controls a Brown Fat/Skeletal Muscle Switch. *Nature*. **454**(7207), p.961.

Seale P, Conroe HM, Estall J, Kajimura S, Frontini A, Ishibashi J, Cohen P, Cinti S, Spiegelman BM. Prdm16 determines the thermogenic program of subcutaneous white adipose tissue

in mice. J Clin Invest. 2011 Jan;121(1):96-105. doi: 10.1172/JCI44271. Epub 2010 Dec 1. PMID: 21123942; PMCID: PMC3007155.

Sears, I.B., Macginnitie, M.A., Kovacs, L.G. and Graves, R.A. 1996. Differentiation-dependent expression of the brown adipocyte uncoupling protein gene: regulation by peroxisome proliferator-activated receptor gamma. *Molecular and Cellular Biology*. **16**(7), pp.3410–3419.

Seebacher, F., Zeigerer, A., Kory, N. and Krahmer, N. 2020. Hepatic lipid droplet homeostasis and fatty liver disease. *Seminars in Cell & Developmental Biology*. **108**, pp.72–81.

Seo, Y.S., Kim, J.H., Jo, N.Y., Choi, K.M., Baik, S.H., Park, J.J., Kim, J.S., Byun, K.S., Bak, Y.T., Lee, C.H., Kim, A.R. and Yeon, J.E. 2008. PPAR agonists treatment is effective in a nonalcoholic fatty liver disease animal model by modulating fatty-acid metabolic enzymes. *Journal of Gastroenterology and Hepatology*. **23**(1), pp.102–109.

du Sert, N.P., Ahluwalia, A., Alam, S., Avey, M.T., Baker, M., Browne, W.J., Clark, A., Cuthill, I.C., Dirnagl, U., Emerson, M., Garner, P., Holgate, S.T., Howells, D.W., Hurst, V., Karp, N.A., Lazic, S.E., Lidster, K., MacCallum, C.J., Macleod, M., Pearl, E.J., Petersen, O.H., Rawle, F., Reynolds, P., Rooney, K., Sena, E.S., Silberberg, S.D., Steckler, T. and Würbel, H. 2020. Reporting animal research: Explanation and elaboration for the ARRIVE guidelines 2.0. *PLOS Biology*. **18**(7), p.e3000411.

Shimizu, I., Aprahamian, T., Kikuchi, R., Shimizu, A., Papanicolaou, K.N., MacLauchlan, S., Maruyama, S. and Walsh, K. 2014. Vascular rarefaction mediates whitening of brown fat in obesity. *The Journal of clinical investigation*. **124**(5), pp.2099–2112.

Shimizu, I. and Walsh, K. 2015. The Whitening of Brown Fat and Its Implications for Weight Management in Obesity. *Current Obesity Reports 2015 4:2*. **4**(2), pp.224–229.

Shimizu, N., Oomura, Y., Plata-Salamán, C.R. and Morimoto, M. 1987. Hyperphagia and obesity in rats with bilateral ibotenic acid-induced lesions of the ventromedial hypothalamic nucleus. *Brain research*. **416**(1), pp.153–156.

Shin, H., Ma, Y., Chanturiya, T., Cao, Q., Wang, Y., Kadegowda, A.K.G., Jackson, R., Rumore, D., Xue, B., Shi, H., Gavrilova, O. and Yu, L. 2017. Lipolysis in Brown Adipocytes Is Not Essential for Cold-Induced Thermogenesis in Mice. *Cell metabolism*. **26**(5), pp.764-777.e5.

Simcox, J., Geoghegan, G., Maschek, J.A., Bensard, C.L., Pasquali, M., Miao, R., Lee, S., Jiang, L., Huck, I., Kershaw, E.E., Donato, A.J., Apte, U., Longo, N., Rutter, J., Schreiber, R.,

Zechner, R., Cox, J. and Villanueva, C.J. 2017. Global Analysis of Plasma Lipids Identifies Liver-Derived Acylcarnitines as a Fuel Source for Brown Fat Thermogenesis. *Cell metabolism*. **26**(3), pp.509-522.e6.

Sindhu, S., Thomas, R., Shihab, P., Sriraman, D., Behbehani, K. and Ahmad, R. 2015. Obesity Is a Positive Modulator of IL-6R and IL-6 Expression in the Subcutaneous Adipose Tissue: Significance for Metabolic Inflammation. *PLoS ONE*. **10**(7).

Singh, S., Allen, A.M., Wang, Z., Prokop, L.J., Murad, M.H. and Loomba, R. 2015. Fibrosis progression in nonalcoholic fatty liver vs nonalcoholic steatohepatitis: a systematic review and meta-analysis of paired-biopsy studies. *Clinical gastroenterology and hepatology : the official clinical practice journal of the American Gastroenterological Association*. **13**(4), pp.643-654.e9.

Sivitz, W.I., Walsh, S.A., Morgan, D.A., Thomas, M.J. and Haynes, W.G. 1997. Effects of Leptin on Insulin Sensitivity in Normal Rats. *Endocrinology*. **138**(8), pp.3395–3401.

Smirnova, E., Griparic, L., Shurland, D.-L. and Bliek, A.M. van der 2001. Dynamin-related Protein Drp1 Is Required for Mitochondrial Division in Mammalian Cells. *Molecular Biology of the Cell*. **12**(8), p.2245.

Smith, G.I., Shankaran, M., Yoshino, M., Schweitzer, G.G., Chondronikola, M., Beals, J.W., Okunade, A.L., Patterson, B.W., Nyangau, E., Field, T., Sirlin, C.B., Talukdar, S., Hellerstein, M.K. and Klein, S. 2020a. Insulin resistance drives hepatic de novo lipogenesis in nonalcoholic fatty liver disease. *The Journal of clinical investigation*. **130**(3), pp.1453–1460.

Smith, R.E. and Hock, R.J. 1963. Brown Fat: Thermogenic Effector of Arousal in Hibernators. *Science*. **140**(3563), pp.199–200.

Smith, R.E. and Horwitz, B.A. 1969. Brown fat and thermogenesis. *https://doi.org/10.1152/physrev.1969.49.2.330*. **49**(2), pp.330–425.

Soleimanpour, H., Safari, S., Sanaie, S., Nazari, M. and Alavian, S.M. 2017. Anesthetic Considerations in Patients Undergoing Bariatric Surgery: A Review Article. *Anesthesiology and Pain Medicine*. **7**(4), p.57568.

Solinas, G., Borén, J. and Dulloo, A.G. 2015. De novo lipogenesis in metabolic homeostasis: More friend than foe? *Molecular Metabolism*. **4**(5), pp.367–377.

Soltis, A.R., Kennedy, N.J., Xin, X., Zhou, F., Ficarro, S.B., Yap, Y.S., Matthews, B.J., Lauffenburger, D.A., White, F.M., Marto, J.A., Davis, R.J. and Fraenkel, E. 2017. Hepatic

Dysfunction Caused by Consumption of a High-Fat Diet. *Cell Reports*. **21**(11), pp.3317–3328.

Song, C.K., Vaughan, C.H., Keen-Rhinehart, E., Harris, R.B.S., Richard, D. and Bartness, T.J. 2008. Melanocortin-4 receptor mRNA expressed in sympathetic outflow neurons to brown adipose tissue: neuroanatomical and functional evidence. *https://doi.org/10.1152/ajpregu.00174.2008*. **295**(2), pp.417–428.

Song, Z., Chen, H., Fiket, M., Alexander, C. and Chan, D.C. 2007. OPA1 processing controls mitochondrial fusion and is regulated by mRNA splicing, membrane potential, and Yme1L. *Journal of Cell Biology*. **178**(5), pp.749–755.

Sonn, S.K., Seo, S., Yang, J., Oh, K.S., Chen, H., Chan, D.C., Rhee, K., Lee, K.S., Yang, Y. and Oh, G.T. 2021. ER-associated CTRP1 regulates mitochondrial fission via interaction with DRP1. *Experimental & Molecular Medicine 2021 53:11*. **53**(11), pp.1769–1780.

Stanley, S., Pinto, S., Segal, J., Pérez, C.A., Viale, A., DeFalco, J., Cai, X., Heisler, L.K. and Friedman, J.M. 2010. Identification of neuronal subpopulations that project from hypothalamus to both liver and adipose tissue polysynaptically. *Proceedings of the National Academy of Sciences of the United States of America*. **107**(15), pp.7024–7029.

Stark, R. and Roden, M. 2007. Mitochondrial function and endocrine diseases. *European Journal of Clinical Investigation*. **37**(4), pp.236–248.

Steculorum, S.M., Ruud, J., Karakasilioti, I., Backes, H., Engström Ruud, L., Timper, K., Hess, M.E., Tsaousidou, E., Mauer, J., Vogt, M.C., Paeger, L., Bremser, S., Klein, A.C., Morgan, D.A., Frommolt, P., Brinkkötter, P.T., Hammerschmidt, P., Benzing, T., Rahmouni, K., Wunderlich, F.T., Kloppenburg, P. and Brüning, J.C. 2016. AgRP Neurons Control Systemic Insulin Sensitivity via Myostatin Expression in Brown Adipose Tissue. *Cell*. **165**(1), pp.125–138.

Stefanidis, A., Wiedmann, N.M., Adler, E.S. and Oldfield, B.J. 2014. Hypothalamic control of adipose tissue. *Best Practice & Research Clinical Endocrinology & Metabolism*. **28**(5), pp.685–701.

Steinert, R.E., Feinle-Bisset, C., Asarian, L., Horowitz, M., Beglinger, C. and Geary, N. 2017. Ghrelin, CCK, GLP-1, and PYY(3–36): Secretory Controls and Physiological Roles in Eating and Glycemia in Health, Obesity, and After RYGB. *Physiological Reviews*. **97**(1), p.411.

Strable, M.S. and Ntambi, J.M. 2010. Genetic control of de novo lipogenesis: role in diet-induced obesity. *Critical reviews in biochemistry and molecular biology*. **45**(3), p.199.

Susin, S.A., Lorenzo, H.K., Zamzami, N., Marzo, I., Snow, B.E., Brothers, G.M., Mangion, J., Jacotot, E., Costantini, P., Loeffler, M., Larochette, N., Goodlett, D.R., Aebersold, R., Siderovski, D.P., Penninger, J.M. and Kroemer, G. 1999. Molecular characterization of mitochodrial apoptosis-inducing factor. *Nature*. **397**(6718), pp.441–446.

Swartz, T.D., Duca, F.A., De Wouters, T., Sakar, Y. and Covasa, M. 2012. Up-regulation of intestinal type 1 taste receptor 3 and sodium glucose luminal transporter-1 expression and increased sucrose intake in mice lacking gut microbiota. *British Journal of Nutrition*. **107**(5), pp.621–630.

Székely, M. 2000. The vagus nerve in thermoregulation and energy metabolism. *Autonomic Neuroscience*. **85**(1–3), pp.26–38.

Tabuchi, C. and Sul, H.S. 2021. Signaling Pathways Regulating Thermogenesis. *Frontiers in Endocrinology*. **12**, p.243.

Takahashi, T.M., Sunagawa, G.A., Soya, S. *et al.* A discrete neuronal circuit induces a hibernation-like state in rodents. *Nature* **583**, 109–114 (2020).

Tang, Q., Liu, Q., Li, J., Yan, J., Jing, X., Zhang, J., Xia, Y., Xu, Y., Li, Y. and He, J. 2022b. MANF in POMC Neurons Promotes Brown Adipose Tissue Thermogenesis and Protects Against Diet-Induced Obesity. *Diabetes*. **71**(11), pp.2344–2359.

Tanida, M., Yamamoto, N., Shibamoto, T. and Rahmouni, K. 2013. Involvement of Hypothalamic AMP-Activated Protein Kinase in Leptin-Induced Sympathetic Nerve Activation. *PLoS ONE*. **8**(2), p.56660.

Tanti, J.F., Ceppo, F., Jager, J. and Berthou, F. 2012. Implication of inflammatory signaling pathways in obesity-induced insulin resistance. *Frontiers in Endocrinology*. **3**(JAN).

Thangaraj, A., Sil, S., Tripathi, A., Chivero, E.T., Periyasamy, P. and Buch, S. 2020. Targeting endoplasmic reticulum stress and autophagy as therapeutic approaches for neurological diseases. *International Review of Cell and Molecular Biology*. **350**, pp.285–325.

Theander-Carrillo, C., Wiedmer, P., Cettour-Rose, P., Nogueiras, R., Perez-Tilve, D., Pfluger, P., Castaneda, T.R., Muzzin, P., Schürmann, A., Szanto, I., Tschöp, M.H. and Rohner-Jeanrenaud, F. 2006. Ghrelin action in the brain controls adipocyte metabolism. *Journal of Clinical Investigation*. **116**(7), pp.1983–1993.

Timper, K. and Brüning, J.C. 2017. Hypothalamic circuits regulating appetite and energy homeostasis: pathways to obesity. *Disease Models & Mechanisms*. **10**(6), p.679.

Titchenell, P.M., Lazar, M.A. and Birnbaum, M.J. 2017. Unraveling the Regulation of Hepatic

Metabolism by Insulin. *Trends in endocrinology and metabolism: TEM*. **28**(7), pp.497–505.

Toda, C., Kim, J.D., Impellizzeri, D., Cuzzocrea, S., Liu, Z.W. and Diano, S. 2016. UCP2 Regulates Mitochondrial Fission and Ventromedial Nucleus Control of Glucose Responsiveness. *Cell*. **164**(5), pp.872–883.

Tondera, D., Grandemange, S., Jourdain, A., Karbowski, M., Mattenberger, Y., Herzig, S., Da Cruz, S., Clerc, P., Raschke, I., Merkwirth, C., Ehses, S., Krause, F., Chan, D.C., Alexander, C., Bauer, C., Youle, R., Langer, T. and Martinou, J.C. 2009. SlP-2 is required for stress-induced mitochondrial hyperfusion. *EMBO Journal*. **28**(11), pp.1589–1600.

Trayhurn, P. 1979. Thermoregulation in the diabetic-obese (db/db) mouse. The role of non-shivering thermogenesis in energy balance. *Pflugers Archiv : European journal of physiology*. **380**(3), pp.227–232.

Trayhurn, P., Thomas, M.E.A., Duncan, J.S. and Vernon Rayner, D. 1995. Effects of fasting and refeeding on ob gene expression in white adipose tissue of lean and obese (ob/ob) mice. *FEBS Letters*. **368**(3), pp.488–490.

Trenker, M., Malli, R., Fertschai, I., Levak-Frank, S. and Graier, W.F. 2007. Uncoupling proteins 2 and 3 are fundamental for mitochondrial Ca2+ uniport. *Nature Cell Biology*. **9**(4), pp.445–452.

Tsou, K., Khachaturian, H., Akil, H. and Watson, S.J. 1986. Immunocytochemical localization of pro-opiomelanocortin-derived peptides in the adult rat spinal cord. *Brain research*. **378**(1), pp.28–35.

Tsukita, S., Yamada, T., Uno, K., Takahashi, K., Kaneko, K., Ishigaki, Y., Imai, J., Hasegawa, Y., Sawada, S., Ishihara, H., Oka, Y. and Katagiri, H. 2012. Hepatic glucokinase modulates obesity predisposition by regulating BAT thermogenesis via neural signals. *Cell metabolism*. **16**(6), pp.825–832.

Tsuru, H., Osaka, M., Hiraoka, Y. and Yoshida, M. 2020. HFD-induced hepatic lipid accumulation and inflammation are decreased in Factor D deficient mouse. *Scientific Reports 2020 10:1*. **10**(1), pp.1–10.

Tupone, D., Madden, C.J., Cano, G. and Morrison, S.F. 2011. An orexinergic projection from perifornical hypothalamus to raphe pallidus increases rat brown adipose tissue thermogenesis. *The Journal of neuroscience : the official journal of the Society for Neuroscience*. **31**(44), pp.15944–15955.

Ukropec, J., Anunciado, R.V.P., Ravussin, Y. and Kozak, L.P. 2006. Leptin Is Required for Uncoupling Protein-1-Independent Thermogenesis during Cold Stress. *Endocrinology*. **147**(5), pp.2468–2480.

Uldry, M., Yang, W., St-Pierre, J., Lin, J., Seale, P. and Spiegelman, B.M. 2006. Complementary action of the PGC-1 coactivators in mitochondrial biogenesis and brown fat differentiation. *Cell metabolism*. **3**(5), pp.333–341.

Umpleby, A.M. 2015. HORMONE MEASUREMENT GUIDELINES: Tracing lipid metabolism: the value of stable isotopes. *Journal of Endocrinology*. **226**(3), pp.G1–G10.

Uno, T. and Shibata, M. 2001. Role of inferior olive and thoracic IML neurons in nonshivering thermogenesis in rats. *American journal of physiology. Regulatory, integrative and comparative physiology*. **280**(2).

Uyama, N., Geerts, A. and Reynaert, H. 2004. Neural connections between the hypothalamus and the liver. *The Anatomical Record Part A: Discoveries in Molecular, Cellular, and Evolutionary Biology*. **280A**(1), pp.808–820.

Valentine, J.M., Ahmadian, M., Keinan, O., Abu-Odeh, M., Zhao, P., Zhou, X., Keller, M.P., Gao, H., Yu, R.T., Liddle, C., Downes, M., Zhang, J., Lusis, A.J., Attie, A.D., Evans, R.M., Rydén, M. and Saltiel, A.R. 2022. β3-Adrenergic receptor downregulation leads to adipocyte catecholamine resistance in obesity. *Journal of Clinical Investigation*. **132**(2).

Valve, R., Heikkinen, S., Rissanen, A., Laakso, M. and Uusitupa, M. 1998. Synergistic effect of polymorphisms in uncoupling protein 1 and β3-adrenergic receptor genes on basal metabolic rate in obese Finns. *Diabetologia 1998 41:3*. **41**(3), pp.357–361.

Valverde, A.M., Teruel, T., Navarro, P., Benito, M. and Lorenzo, M. 1998. Tumor Necrosis Factor-α Causes Insulin Receptor Substrate-2-Mediated Insulin Resistance and Inhibits Insulin-Induced Adipogenesis in Fetal Brown Adipocytes. *Endocrinology*. **139**(3), pp.1229–1238.

Vázquez-Vela, M.E.F., Torres, N. and Tovar, A.R. 2008. White Adipose Tissue as Endocrine Organ and Its Role in Obesity. *Archives of Medical Research*. **39**(8), pp.715–728.

Verty, A.N.A., Allen, A.M. and Oldfield, B.J. 2009. The Effects of Rimonabant on Brown Adipose Tissue in Rat: Implications for Energy Expenditure. *Obesity*. **17**(2), pp.254–261.

Villanueva, C.J., Monetti, M., Shih, M., Zhou, P., Watkins, S.M., Bhanot, S. and Farese, R. V. 2009. Specific role for acyl CoA:diacylglycerol acyltransferase 1 (Dgat1) in hepatic steatosis due to exogenous fatty acids. *Hepatology*. **50**(2), pp.434–442.

Vitali, A., Murano, I., Zingaretti, M.C., Frontini, A., Ricquier, D. and Cinti, S. 2012. The adipose organ of obesity-prone C57BL/6J mice is composed of mixed white and brown adipocytes. *Journal of Lipid Research*.

Voits, M., Förster, S., Rödel, S., Voigt, J.P., Plagemann, A. and Fink, H. 1996. Obesity induced by unspecific early postnatal overfeeding in male and female rats: hypophagic effect of CCK-8S. *Naunyn-Schmiedeberg's archives of pharmacology*. **354**(3), pp.374–378.

Waldén, T.B., Hansen, I.R., Timmons, J.A., Cannon, B. and Nedergaard, J. 2012. Recruited vs. nonrecruited molecular signatures of brown, 'brite,' and white adipose tissues. *American journal of physiology. Endocrinology and metabolism*. **302**(1).

Wang, F., Flanagan, J., Su, N., Wang, L.C., Bui, S., Nielson, A., Wu, X., Vo, H.T., Ma, X.J. and Luo, Y. 2012. RNAscope: A Novel in Situ RNA Analysis Platform for Formalin-Fixed, Paraffin-Embedded Tissues. *The Journal of Molecular Diagnostics*. **14**(1), pp.22–29.

Watanabe, M., Houten, S.M., Mataki, C., Christoffolete, M.A., Kim, B.W., Sato, H., Messaddeq, N., Harney, J.W., Ezaki, O., Kodama, T., Schoonjans, K., Bianco, A.C. and Auwerx, J. 2006. Bile acids induce energy expenditure by promoting intracellular thyroid hormone activation. *Nature 2005 439:7075*. **439**(7075), pp.484–489.

Weir, G., Ramage, L.E., Akyol, M., Rhodes, J.K., Kyle, C.J., Fletcher, A.M., Craven, T.H., Wakelin, S.J., Drake, A.J., Gregoriades, M.L., Ashton, C., Weir, N., van Beek, E.J.R., Karpe, F., Walker, B.R. and Stimson, R.H. 2018. Substantial Metabolic Activity of Human Brown Adipose Tissue during Warm Conditions and Cold-Induced Lipolysis of Local Triglycerides. *Cell Metabolism*. **27**(6), pp.1348-1355.e4.

WHO, Obesity. *2017*. [Online]. [Accessed 5 November 2022]. Available from: https://www.who.int/health-topics/obesity#tab=tab_1.

WHO, Global Health Observatory. [Accessed 5 October 2022a]. Available from: https://www.who.int/data/gho.

WHO World Obesity Atlas 2022 | World Obesity Federation. [Accessed 28 October 2022e]. Available from: https://www.worldobesity.org/resources/resource-library/world-obesity-atlas-2022.

Wikstrom, J.D., Mahdaviani, K., Liesa, M., Sereda, S.B., Si, Y., Las, G., Twig, G., Petrovic, N., Zingaretti, C., Graham, A., Cinti, S., Corkey, B.E., Cannon, B., Nedergaard, J. and Shirihai, O.S. 2014. Hormone-induced mitochondrial fission is utilized by brown adipocytes as an amplification pathway for energy expenditure. *The EMBO journal*. **33**(5), pp.418–436.

Willems, P.H.G.M., Rossignol, R., Dieteren, C.E.J., Murphy, M.P. and Koopman, W.J.H. 2015. Redox Homeostasis and Mitochondrial Dynamics. *Cell metabolism*. **22**(2), pp.207–218.

Williams, D.L., Bowers, R.R., Bartness, T.J., Kaplan, J.M. and Grill, H.J. 2003. Brainstem melanocortin 3/4 receptor stimulation increases uncoupling protein gene expression in brown fat. *Endocrinology*. **144**(11), pp.4692–4697.

Wortley, K.E., Anderson, K.D., Garcia, K., Murray, J.D., Malinova, L., Liu, R., Moncrieffe, M., Thabet, K., Cox, H.J., Yancopoulos, G.D., Wiegand, S.J. and Sleeman, M.W. 2004. Genetic deletion of ghrelin does decrease food intake but influences metabolic fuel preference. *Proceedings of the National Academy of Sciences of the United States of America*. **101**(21), pp.8227–8232.

Wu, C., Cheng, W., Sun, Y., Dang, Y., Gong, F., Zhu, H., Li, N., Li, F. and Zhu, Z. 2014. Activating brown adipose tissue for weight loss and lowering of blood glucose levels: A microPET study using obese and diabetic model mice. *PLoS ONE*. **9**(12).

Wu, J., Boström, P., Sparks, L.M., Ye, L., Choi, J.H., Giang, A.H., Khandekar, M., Virtanen, K.A., Nuutila, P., Schaart, G., Huang, K., Tu, H., Van Marken Lichtenbelt, W.D., Hoeks, J., Enerbäck, S., Schrauwen, P. and Spiegelman, B.M. 2012b. Beige Adipocytes Are a Distinct Type of Thermogenic Fat Cell in Mouse and Human. *Cell*. **150**(2), pp.366–376.

Wu, Z., Puigserver, P., Andersson, U., Zhang, C., Adelmant, G., Mootha, V., Troy, A., Cinti, S., Lowell, B., Scarpulla, R.C. and Spiegelman, B.M. 1999. Mechanisms Controlling Mitochondrial Biogenesis and Respiration through the Thermogenic Coactivator PGC-1. *Cell*. **98**(1), pp.115–124.

Xie, D., Li, J., Jiang, P., Xue, X., Wu, L. and First People's Hospital, J. 2022. Effect of adipose-derived exosome and exosomal miRNA on glycolipid metabolism. *Clinical and Translational Discovery*. **2**(3), p.e134.

Xu, B., Goulding, E.H., Zang, K., Cepoi, D., Cone, R.D., Jones, K.R., Tecott, L.H. and Reichardt, L.F. 2003. Brain-derived neurotrophic factor regulates energy balance downstream of melanocortin-4 receptor. *Nature Neuroscience 2003 6:7*. **6**(7), pp.736–742.

Xu, S., Jay, A., Brunaldi, K., Huang, N. and Hamilton, J.A. 2013. CD36 enhances fatty acid uptake by increasing the rate of intracellular esterification but not transport across the plasma membrane. *Biochemistry*. **52**(41), pp.7254–7261.

Xue, B., Rim, J.S., Hogan, J.C., Coulter, A.A., Koza, R.A. and Kozak, L.P. 2007. Genetic variability affects the development of brown adipocytes in white fat but not in interscapular brown

fat. *Journal of lipid research*. **48**(1), pp.41–51.

Yamashita, S., Hirano, K.I., Kuwasako, T., Janabi, M., Toyama, Y., Ishigami, M. and Sakai, N. 2007. Physiological and pathological roles of a multi-ligand receptor CD36 in atherogenesis; insights from CD36-deficient patients. *Molecular and Cellular Biochemistry*. **299**(1–2), pp.19–22.

Yan, L., Qi, Y., Huang, X., Yu, C., Lan, L., Guo, X., Rao, Z., Hu, J. and Lou, Z. 2018. Structural basis for GTP hydrolysis and conformational change of MFN1 in mediating membrane fusion. *Nature structural & molecular biology*. **25**(3), pp.233–243.

Yang, Ling, Calay, E.S., Fan, J., Arduini, A., Kunz, R.C., Gygi, S.P., Yalcin, A., Fu, S. and Hotamisligil, G.S. 2015. S-Nitrosylation links obesity-associated inflammation to endoplasmic reticulum dysfunction. *Science*. **349**(6247), pp.500–506.

Yang, Liang, Qi, Y. and Yang, Y. 2015. Astrocytes Control Food Intake by Inhibiting AGRP Neuron Activity via Adenosine A1 Receptors. *Cell Reports*. **11**(5), pp.798–807.

Yapa, N.M.B., Lisnyak, V., Reljic, B. and Ryan, M.T. 2021. Mitochondrial dynamics in health and disease. *FEBS Letters*. **595**(8), pp.1184–1204.

Ye, Q., Zou, B., Yeo, Y.H., Li, J., Huang, D.Q., Wu, Y., Yang, H., Liu, C., Kam, L.Y., Tan, X.X.E., Chien, N., Trinh, S., Henry, L., Stave, C.D., Hosaka, T., Cheung, R.C. and Nguyen, M.H. 2020. Global prevalence, incidence, and outcomes of non-obese or lean non-alcoholic fatty liver disease: a systematic review and meta-analysis. *The lancet. Gastroenterology & hepatology*. **5**(8), pp.739–752.

Yecies, J.L., Zhang, H.H., Menon, S., Liu, S., Yecies, D., Lipovsky, A.I., Gorgun, C., Kwiatkowski, D.J., Hotamisligil, G.S., Lee, C.H. and Manning, B.D. 2011. Akt stimulates hepatic SREBP1c and lipogenesis through parallel mTORC1-dependent and independent pathways. *Cell metabolism*. **14**(1), pp.21–32.

Yeo GS, Farooqi IS, Aminian S, Halsall DJ, Stanhope RG, O'Rahilly S. A frameshift mutation in MC4R associated with dominantly inherited human obesity. Nat Genet. 1998 Oct;20(2):111-2. doi: 10.1038/2404. PMID: 9771698.

Yi, C.X., la Fleur, S.E., Fliers, E. and Kalsbeek, A. 2010. The role of the autonomic nervous liver innervation in the control of energy metabolism. *Biochimica et Biophysica Acta (BBA) - Molecular Basis of Disease*. **1802**(4), pp.416–431.

Yildiz, B.O., Suchard, M.A., Wong, M.L., McCann, S.M. and Licinio, J. 2004. Alterations in the dynamics of circulating ghrelin, adiponectin, and leptin in human obesity. *Proceedings of*

the National Academy of Sciences of the United States of America. **101**(28), pp.10434–10439.

Yoneshiro, T., Aita, S., Matsushita, M., Kameya, T., Nakada, K., Kawai, Y. and Saito, M. 2011. Brown adipose tissue, whole-body energy expenditure, and thermogenesis in healthy adult men. *Obesity*. **19**(1), pp.13–16.

Yoneshiro, T., Aita, S., Matsushita, M., Kayahara, T., Kameya, T., Kawai, Y., Iwanaga, T. and Saito, M. 2013. Recruited brown adipose tissue as an antiobesity agent in humans. *Journal of Clinical Investigation*. **123**(8), pp.3404–3408.

Yoneshiro, T., Matsushita, M. and Saito, M. 2019. Translational aspects of brown fat activation by food-derived stimulants. *Handbook of Experimental Pharmacology*. **251**, pp.359–379.

Yoneshiro, T., Ogawa, T., Okamoto, N., Matsushita, M., Aita, S., Kameya, T., Kawai, Y., Iwanaga, T. and Saito, M. 2012. Impact of UCP1 and β3AR gene polymorphisms on age-related changes in brown adipose tissue and adiposity in humans. *International Journal of Obesity 2013 37:7*. **37**(7), pp.993–998.

Yoshida, K., Li, X., Cano, G., Lazarus, M. and Saper, C.B. 2009. Parallel Preoptic Pathways for Thermoregulation. *Journal of Neuroscience*. **29**(38), pp.11954–11964.

Yoshioka, K., Yoshida, T., Nishioka, H., Kondo, M. and Wakabayashi, Y. 1989. The role of insulin in norepinephrine turnover and thermogenesis in brown adipose tissue after acute cold-exposure. *Endocrinologia japonica*. **36**(4), pp.491–499.

Young, P., Arch, J.R.S. and Ashwell, M. 1984. Brown adipose tissue in the parametrial fat pad of the mouse. *FEBS Letters*. **167**(1), pp.10–14.

Younossi, Z.M. 2019. Non-alcoholic fatty liver disease - A global public health perspective. *Journal of hepatology*. **70**(3), pp.531–544.

Yu, D., Chen, G., Pan, M., Zhang, J., He, W., Liu, Y., Nian, X., Sheng, L., Xu, B. and Liang Sheng, C. 2017. High fat diet-induced oxidative stress blocks hepatocyte nuclear factor 4α and leads to hepatic steatosis in mice.

Yu, R., Lendahl, U., Nistér, M. and Zhao, J. 2020. Regulation of Mammalian Mitochondrial Dynamics: Opportunities and Challenges. *Frontiers in Endocrinology*. **11**, p.374.

Yue, J.T.Y., Abraham, M.A., Lapierre, M.P., Mighiu, P.I., Light, P.E., Filippi, B.M. and Lam, T.K.T. 2015. A fatty acid-dependent hypothalamic–DVC neurocircuitry that regulates hepatic secretion of triglyceride-rich lipoproteins. *Nature Communications* **6**(1), pp.1–11.

Zaretskaia, M. V., Zaretsky, D. V., Shekhar, A. and DiMicco, J.A. 2002. Chemical stimulation of

the dorsomedial hypothalamus evokes non-shivering thermogenesis in anesthetized rats. *Brain Research*. **928**(1–2), pp.113–125.

Zechner, R., Kienesberger, P.C., Haemmerle, G., Zimmermann, R. and Lass, A. 2009. Adipose triglyceride lipase and the lipolytic catabolism of cellular fat stores. *Journal of Lipid Research*. **50**(1), pp.3–21.

Zenisek, D. and Matthews, G. 2000. The Role of Mitochondria in Presynaptic Calcium Handling at a Ribbon Synapse. *Neuron*. **25**(1), pp.229–237.

Zhan, C., Zhou, J., Feng, Q., Zhang, J. en, Lin, S., Bao, J., Wu, P. and Luo, M. 2013. Acute and long-term suppression of feeding behavior by POMC neurons in the brainstem and hypothalamus, respectively. *The Journal of neuroscience : the official journal of the Society for Neuroscience*. **33**(8), pp.3624–3632.

Zhang, D., Liu, Z.X., Cheol, S.C., Tian, L., Kibbey, R., Dong, J., Cline, G.W., Wood, P.A. and Shulman, G.I. 2007. Mitochondrial dysfunction due to long-chain Acyl-CoA dehydrogenase deficiency causes hepatic steatosis and hepatic insulin resistance. *Proceedings of the National Academy of Sciences of the United States of America*. **104**(43), pp.17075–17080.

Zhang, R., Dhillon, H., Yin, H., Yoshimura, A., Lowell, B.B., Maratos-Flier, E. and Flier, J.S. 2008. Selective Inactivation of Socs3 in SF1 Neurons Improves Glucose Homeostasis without Affecting Body Weight. *Endocrinology*. **149**(11), pp.5654–5661.

Zhang, W.X., Fan, J., Ma, J., Rao, Y.S., Zhang, L. and Yan, Y.E. 2016. Selection of suitable reference genes for quantitative real-time PCR normalization in three types of rat adipose tissue. *International Journal of Molecular Sciences*. **17**(6).

Zhang, X., Zhang, G., Zhang, H., Karin, M., Bai, H. and Cai, D. 2008b. Hypothalamic IKKβ/NF-κB and ER Stress Link Overnutrition to Energy Imbalance and Obesity. *Cell*. **135**(1), p.61.

Zhang, Y., Kerman, I.A., Laque, A., Nguyen, P., Faouzi, M., Louis, G.W., Jones, J.C., Rhodes, C. and Münzberg, H. 2011. Leptin-receptor-expressing neurons in the dorsomedial hypothalamus and median preoptic area regulate sympathetic brown adipose tissue circuits. *The Journal of neuroscience : the official journal of the Society for Neuroscience*. **31**(5), pp.1873–1884.

Zhang, Z., Liu, L., Wu, S. and Xing, D. 2016. Drp1, Mff, Fis1, and MiD51 are coordinated to mediate mitochondrial fission during UV irradiation-induced apoptosis. *FASEB journal : official publication of the Federation of American Societies for Experimental Biology*.

30(1), pp.466–476.

Zhao, X., Gang, X., He, G., Li, Z., Lv, Y., Han, Q. and Wang, G. 2020. Obesity Increases the Severity and Mortality of Influenza and COVID-19: A Systematic Review and Meta-Analysis. *Frontiers in Endocrinology*. **11**, p.1007.

Zheng, J.Q., Seki, M., Hayakawa, T., Ito, H. and Zyo, K. 1995. Descending projections from the paraventricular hypothalamic nucleus to the spinal cord: anterograde tracing study in the rat. *Okajimas folia anatomica Japonica*. **72**(2–3), pp.119–135.

Zheng, Z., Zhang, C. and Zhang, K. 2010. Role of unfolded protein response in lipogenesis. *World Journal of Hepatology*. **2**(6), p.203.

Zhou, L., Xu, L., Ye, J., Li, D., Wang, W., Li, X., Wu, L., Wang, H., Guan, F. and Li, P. 2012. Cidea promotes hepatic steatosis by sensing dietary fatty acids. *Hepatology*. **56**(1), pp.95–107.

Zhu, H., Aryal, D.K., Olsen, R.H.J., Urban, D.J., Swearingen, A., Forbes, S., Roth, B.L. and Hochgeschwender, U. 2016. Cre-dependent DREADD (Designer Receptors Exclusively Activated by Designer Drugs) mice. *Genesis (New York, N.Y. : 2000)*. **54**(8), pp.439–446.

Zhu, P.P., Patterson, A., Stadler, J., Seeburg, D.P., Sheng, M. and Blackstone, C. 2004. Intra- and intermolecular domain interactions of the C-terminal GTPase effector domain of the multimeric dynamin-like GTPase Drp1. *The Journal of biological chemistry*. **279**(34), pp.35967–35974.

Zhu, X.H., Qiao, H., Du, F., Xiong, Q., Liu, X., Zhang, X., Ugurbil, K. and Chen, W. 2012. Quantitative imaging of energy expenditure in human brain. *NeuroImage*. **60**(4), pp.2107–2117.

Zhu, Z., Spicer, E.G., Gavini, C.K., Goudjo-Ako, A.J., Novak, C.M. and Shi, H. 2014. Enhanced sympathetic activity in mice with brown adipose tissue transplantation (transBATation). *Physiology and Behavior*. **125**, pp.21–29.

Zietlow, A., Nakajima, H., Taniguchi, H., Ludwig, K. and Takahashi, T. 2010. Association between plasma ghrelin and motilin levels during MMC cycle in conscious dogs. *Regulatory Peptides*. **164**(2–3), pp.78–82.

Zou, H., Li, Y., Liu, X. and Wang, X. 1999. An APAf-1 · cytochrome C multimeric complex is a functional apoptosome that activates procaspase-9. *Journal of Biological Chemistry*. **274**(17), pp.11549–11556.

Chapter 9: Appendix

9.1 Personal license for animal use in research

Home Office

PERSONAL LICENCE

Arianna Fozzato

A personal licence on its own does not authorise you to perform regulated procedures on protected animals. You apply regulated procedures of the category or categories specified below to animals of the species or groups specified below at places specified in authorised project licences subject to the restrictions and provisions contained in the Act and the conditions and restrictions below.

You are required to keep a record of all regulated procedures that you have carried out, and to make this record available to the Home Office upon request. If you cease to work at the establishment given as the primary availability on your licence, or it ceases to be the place where you wish your licence to be primarily available, you must notify the Home Office.

This licence shall be in force until it is revoked by the Home Office and shall be subject to periodic review.

Primary establishment

The University of Leeds

Leeds LS2 9JT

Animal types

- Mice (Mus musculus)
- Rats (Rattus norvegicus)

Procedures

Categories

- **A.** Minor / minimally invasive procedures not requiring sedation, analgesia or general anaesthesia.
- **B.** Minor / minimally invasive procedures involving sedation, analgesia or brief general anaesthesia. Plus surgical procedures conducted under brief non-recovery general anaesthesia
- **C.** Surgical procedures involving general anaesthesia. Plus - administration and maintenance of balanced or prolonged general anaesthesia.

Additional conditions

None

Standard conditions

1. In exercising his or her responsibilities, the licence holder shall act at all times in a manner that is consistent with the principles of replacement, reduction and refinement.
2. The licence holder is entrusted with primary responsibility for the welfare of the animals on which he or she has performed regulated procedures; the licence holder must ensure that animals are properly monitored and cared for.
3. The licence holder must not apply a regulated procedure to an animal if the procedure may cause the animal severe pain, suffering or distress that is likely to be long-lasting and cannot be ameliorated.
4. The licence holder must not apply a regulated procedure to an animal unless the holder has taken precautions to prevent or reduce to the minimum consistent with the purposes of the procedure any pain, suffering, distress or discomfort that may be caused to the animal.
5. Where the licence holder is applying a regulated procedure to an animal the holder must ensure that any unnecessary pain, suffering, distress or lasting harm that is being caused to the animal is stopped.
6. Where the licence holder is applying or has applied a regulated procedure which is causing the animal severe pain, suffering or distress the holder must take steps to ameliorate that pain, suffering or distress.
7. The licence holder shall ensure that where the holder applies a regulated procedure death as the end-point of the procedure is avoided as far as possible and is replaced by an early and humane endpoint.
8. In all circumstances where an animal which is being, or has been, subjected to a regulated procedure is in severe pain, suffering or distress which is likely to be long-lasting and cannot be ameliorated, the licence holder must ensure that the animal is immediately killed in accordance with section 15A.
9. The licence holder may apply a regulated procedure without the use of general or local anaesthesia only if the holder is satisfied that— (a) the procedure will not inflict serious injuries capable of causing severe pain; and (b) the use of general or local anaesthesia would be more traumatic to the animal than the procedure itself or would frustrate the purposes of the procedure.
10. When anaesthesia (whether general or local) is used, it shall be of sufficient depth to prevent the animal from being aware of pain arising during the procedure.
11. If the licence holder applies a regulated procedure to an animal with the use of general or local anaesthesia the holder must, unless it would frustrate the purpose of the procedure, use such

analgesics or other pain-relieving methods as may be necessary to reduce any pain that the animal may experience once the anaesthesia wears off.

12. The licence holder must use analgesia or another appropriate method to ensure that the pain, suffering and distress caused by regulated procedures are kept to a minimum.

13. It is the responsibility of the personal licence holder to notify the project licence holder as soon as possible when it appears either that the severity limit of any procedure listed in the project licence or that the constraints upon adverse effects described in the project licence have been or are likely to be exceeded.

14. The licence holder shall ensure that suitable arrangements exist for the care and welfare of animals during any period when the personal licence holder is not in attendance.

15. The licence holder shall ensure that, whenever necessary, veterinary advice and treatment are obtained for the animals in his or her care.

16. The licence holder shall ensure that all cages, pens or other enclosures are clearly labelled. The labelling must be such as to enable Inspectors, named veterinary surgeons and named animal care and welfare officers to identify the number of the project licence authorising the procedures, the project licence protocol in which the animals are being used, the date the protocol was started, and the responsible personal licence holder.

17. In order to ensure that regulated procedures are performed competently, the licence holder shall not apply regulated procedures unless given the appropriate level of supervision by the project licence holder or an experienced personal licence holder deputed by him/her for such time as may be needed to achieve competence.

18. The licence holder is authorised to delegate to assistants, who do not themselves possess the requisite personal licence authority but are under his or her control, the delegable tasks which form an integral part of the regulated procedures the licence holder is authorised to perform by this licence. The tasks must not require technical knowledge or skill, and delegation shall be in accordance with any relevant guidance published by the Secretary of State under section 21.

19. The licence holder must take all reasonable steps to ensure appropriate personal and project licence authorities exist before performing regulated procedures. The licence holder must be aware of the nature of the authorities given by this licence and the project licence, and of the conditions of issue attached to the licences.

20. The licence holder shall maintain a record of all animals on which procedures have been carried out, including details of supervision and declarations of competence by the project licence holder as appropriate. This record shall be retained for at least five years and shall, on request, be submitted to the Secretary of State or made available to an Inspector.

21. The licence holder must give any necessary assistance to inspectors carrying out visits by virtue of section 18(2A)(b) ; and to experts of the European Commission carrying out duties under Article 35 of the Animals Directive.

22. The licence remains the property of the Secretary of State, and shall be surrendered to him on request.

9.2 Appendix: source of qPCR primers

Table 1

PRIMER	SOURCE	AUTHOR	DOI
36B4	Primer3	-	-
RPLP0	Literature	Xiuqin et al., 2020	10.3389/fnut.2020.589771
ACACA	Literature	Romero et al., 2007	10.1186/1743-7075-4-26
ACADL	Primer3	-	-
ADRB3	Literature	Whittle et al., 2012	10.1016/j.cell.2012.02.066
CD36	Primer3	-	-
CD68	Primer3	-	-
CIDEA	Primer3	-	-
CRP	Primer3	-	-
DDIT3	Literature	Williams and Lipkin, 2006	10.1128/JVI.00836-06
DGAT 1	Literature	Li et al., 2016	10.1016/j.bbrc.2016.09.160
DGAT 2	Primer3	-	-
DNML1	Literature	Lou et al., 2013	10.1007/s00204-012-0942-z
FAS	Primer3	-	-
INSR	Primer3	-	-
PNPLA2	Literature	Turnbull et al., 2015	10.1371/journal.pone.0120136
HSL	Primer3	-	-
MFN2	Literature	Ling et al., 2011	10.2337/db10-0331
NFKβ	Literature	Habibi et al., 2016	10.15171/apb.2016.015
PPARG	Literature	Cystyhakov et al., 2015	10.1111/jnc.13101
PPARGC1A	Literature	Ni et al., 2019	10.1016/j.nutres.2019.01.005
SLC2A1	Literature	Zhang et al., 2012	10.1371/journal.pone.0042406
SLC2A4	Primer3	-	-
TNFα	Literature	Salas et al., 2007	10.1186/1471-2164-8-292
UCP1	Primer3	-	-